

Lecture Notes in Mechanical Engineering

S. Seetharamu

K. Bhanu Sankara Rao

Raghunath Wasudev Khare *Editors*

# Proceedings of Fatigue, Durability and Fracture Mechanics

 Springer

# **Lecture Notes in Mechanical Engineering**

Lecture Notes in Mechanical Engineering (LNME) publishes the latest developments in Mechanical Engineering—quickly, informally and with high quality. Original research reported in proceedings and post-proceedings represents the core of LNME. Also considered for publication are monographs, contributed volumes and lecture notes of exceptionally high quality and interest. Volumes published in LNME embrace all aspects, subfields and new challenges of mechanical engineering. Topics in the series include:

- Engineering Design
- Machinery and Machine Elements
- Mechanical Structures and Stress Analysis
- Automotive Engineering
- Engine Technology
- Aerospace Technology and Astronautics
- Nanotechnology and Microengineering
- Control, Robotics, Mechatronics
- MEMS
- Theoretical and Applied Mechanics
- Dynamical Systems, Control
- Fluid Mechanics
- Engineering Thermodynamics, Heat and Mass Transfer
- Manufacturing
- Precision Engineering, Instrumentation, Measurement
- Materials Engineering
- Tribology and Surface Technology

More information about this series at <http://www.springer.com/series/11236>

S. Seetharamu · K. Bhanu Sankara Rao  
Raghunath Wasudev Khare  
Editors

# Proceedings of Fatigue, Durability and Fracture Mechanics

 Springer

*Editors*

S. Seetharamu  
Central Power Research Institute  
Bengaluru, Karnataka  
India

K. Bhanu Sankara Rao  
Mahatma Gandhi Institute of Technology  
Hyderabad, Telangana  
India

and

Institute of Structural Integrity  
and Failure Studies (ISIFS)  
Bengaluru, Karnataka  
India

Raghunath Wasudev Khare  
Institute of Structural Integrity  
and Failure Studies (ISIFS)  
Bengaluru, Karnataka  
India

ISSN 2195-4356

ISSN 2195-4364 (electronic)

Lecture Notes in Mechanical Engineering

ISBN 978-981-10-6001-4

ISBN 978-981-10-6002-1 (eBook)

<https://doi.org/10.1007/978-981-10-6002-1>

Library of Congress Control Number: 2017948209

© Springer Nature Singapore Pte Ltd. 2018

This work is subject to copyright. All rights are reserved by the Publisher, whether the whole or part of the material is concerned, specifically the rights of translation, reprinting, reuse of illustrations, recitation, broadcasting, reproduction on microfilms or in any other physical way, and transmission or information storage and retrieval, electronic adaptation, computer software, or by similar or dissimilar methodology now known or hereafter developed.

The use of general descriptive names, registered names, trademarks, service marks, etc. in this publication does not imply, even in the absence of a specific statement, that such names are exempt from the relevant protective laws and regulations and therefore free for general use.

The publisher, the authors and the editors are safe to assume that the advice and information in this book are believed to be true and accurate at the date of publication. Neither the publisher nor the authors or the editors give a warranty, express or implied, with respect to the material contained herein or for any errors or omissions that may have been made. The publisher remains neutral with regard to jurisdictional claims in published maps and institutional affiliations.

Printed on acid-free paper

This Springer imprint is published by Springer Nature

The registered company is Springer Nature Singapore Pte Ltd.

The registered company address is: 152 Beach Road, #21-01/04 Gateway East, Singapore 189721, Singapore

# Preface

This volume contains 37 technical papers from the 2016 Conference, Fatigue Durability India. The theme of this 2nd International conference was fatigue, durability and fracture mechanics. As in the past conference, the format consisted of keynote talks, invited lectures, contributed papers, exhibition and contributed posters. A total of 220 delegates participated in the conference, and 72 papers were presented in Fatigue Durability India 2016.

The conference began with the domain experts Shri. R.J. Patel—BARC; Shri. B. Jaypal—Defence; Prof. Dattaguru—Former Professor, IISC; Shri. B.N. Suresh—Former Member of Space Commission; Prof. Pingsha Dong—Director, Welded Structures Lab, University of Michigan, USA, introducing various contemporary technical aspects in the areas of fatigue, durability and fracture mechanics in nuclear energy, defence, aerospace and welded structures. This was followed by keynote talks from Prof. Dattaguru, Prof. Pingsha Dong, Prof. Kamran Nikbin—Imperial College London and Dr. Omar Ibrahim—MD Process Optimisation, USA.

In the parallel sessions that followed on the first day as well as second and third days, 68 contributed paper presentations were made.

The second-day keynote presentations are made by Prof. Adolfo B. Matamoros—The University of Texas at San Antonio; Dr. G. Raghava—Chief Scientist at CSIR; Dr. Ramesh Chadwani Managing Director of Zentech International, UK; Dr. Asim Ghosal—Consulting Engineer/Technologist at GE Aviation, Bangalore. The third-day proceedings were further enriched by the following keynote speakers: Prof. Xiaosheng Gao—University of Akron; Dr. Yogesh K. Potdar—Manager at GE Global, India; Dr. U. Kamachi Mudali—Outstanding scientist and Associate Director at IGCAR, Kalpakam; Dr. R.C. Prasad—Former Professor at IIT Bombay; Dr. Rabindra Nath Ghosh—Chair Professor at IIT Kharagpur; Mr. M. Mohan Kumar—Senior Scientist, SSTD, CSIR-NAL and Mr. Vitthal Londhe—Technical Specialist at Siemens Industry Software, Pune.

All the presented papers led to detailed interactions in the areas of crack growth in nonlinear problems, advances in master S-N curve method for fatigue evaluation and welded structures, fracture mechanics-based structured integrated problems,

realistic fatigue life predictions, fatigue studies in water power reactors, viscoelastic parameters, behaviour of stainless steel at high temperatures, thermal stripping studies in dynamic sodium environment, potentiality of small punch test to generate J-R curve, materials characterisation and productive modelling, failure analysis studies, civil engineering applications, high-temperature crack growth behaviour, effectively induced residual stress, investigations and real size components, technology trends in aircraft engines, multi-axial fatigue tests, environmental effects, structural integrity assessment of UAV structures, fatigue strength of Al-Mg alloy processed by cryorolling, failure studies and coatings, creep-fatigue evaluation life assessment extension and certification, application in automotives, bridges, piping, operating machines, elasticity and ductile fracture, corrosion fatigue and hydrogen embrittlement, importance of structural test developments and significance and importance of durability for engineering components. The conference ended with the three awards of presentations to Mr. J. Veerababu of IGCAR, Chennai, Mr. Anjaneya Dixit of IIT Delhi and Mr. Siddappaji B. of ADE, DRDO.

The conference was sponsored by IOCL, KPCL, ISRO, BISS, Ansys, ICAT, Altair, CADMarC, NETZSCH Technologies, TII Techno Testing Services, TCR Engineering Services and IIPE.

This volume contains 37 papers featuring significant aspects of fatigue durability and fracture mechanics emphasising structural integrity of components as addressed through materials characterisation, productive modelling, environmental as well as service conditions component fabrications roots and damage diagnosis along with condition assessment and defect tolerance potential.

We thank all the sponsors, participants and exhibitors for their contributions to Fatigue Durability India 2016. We specially thank the authors and reviewers of the papers in this volume. Special thanks to all organising committee members and programme committee members of Fatigue Durability India 2016.

Bengaluru, India  
Hyderabad, India  
Bengaluru, India

Dr. S. Seetharamu  
Dr. K. Bhanu Sankara Rao  
Dr. Raghunath Wasudev Khare

# Contents

<b>Finite Element Analysis-Based Approach for Stress Concentration Factor Calculation</b> . . . . .	1
Yuvaraj Hodhigere, Jyoti S. Jha, Asim Tewari and Sushil Mishra	
<b>Evaluation of Viscoplastic Parameters of an Austenitic Stainless Steel at High Temperature</b> . . . . .	7
A.K. Asraff, Merin V. George, Krishnajith Jayamani and S. Sarath Chandran Nair	
<b>Potentiality of Small Punch Test Using Damage Model to Generate J-R Curve of 20MnMoNi55</b> . . . . .	29
Pradeep Kumar, B.K. Dutta, J. Chattopadhyay and R.S. Shrivastaw	
<b>Experimental Facility for Thermal Striping Studies in Dynamic Sodium Environment</b> . . . . .	41
S. Vijayaraghavan, P. Rajasundaram, T. Chandran, M. Shanmugavel, B. Babu and P. Selvaraj	
<b>Linear Elastic Fracture Mechanics (LEFM)-Based Single Lap Joint (SLJ) Mixed-Mode Analysis for Aerospace Structures</b> . . . . .	53
B.K. Mahesha, D. Thulasi Durai, D. Karuppannan and K. Dilip Kumar	
<b>Study of Fatigue Crack Growth Rate of AA6061 at Different Stress Ratios</b> . . . . .	67
Rajesh P. Verma and K.N. Pandey	
<b>Cooler Casing Fatigue Analysis: An ASME Approach</b> . . . . .	75
Prathapkumar Ramamoorthy, David K. Harper and Sam P. Joseph	
<b>Failure Analysis of HSS Punch Tool: A Case Study</b> . . . . .	93
Suraj Desai, B.V. Dilip Kumar Bhat, Guruvinder Singh, G.J. Naveen, P. Rangasamy, B. Jayadeva, P. Sampathkumaran, S. Seetharamu, G. Venkataramudu and H.B. Niranjana	



<b>Evaluation of Fatigue Strength of Alloy Steel Pipe Under Influence of Hydrostatic Pressure</b> . . . . .	103
Deepak Kumar Rout and Raghu V. Prakash	
<b>Estimation of Fatigue Life of Notched Specimens of P91 Steel by Analytical Approaches</b> . . . . .	117
J. Veerababu, Sunil Goyal, R. Sandhya and K. Laha	
<b>Effect of Induced Residual Stress and Its Contribution to the Failure of an IC Engine Valve Material</b> . . . . .	129
Gurunathan, Jitendra Sharma and Velshankar	
<b>Fatigue Analysis of Offshore Structures in Indian Western Offshore</b> . . .	143
Nitin Nehra, Praveen Bhat and N. Panneerselvam	
<b>Crack Effect on Rotors Using Mode-I Failure Model with Transfer Matrix Approach</b> . . . . .	153
Ved Prakash Singh and J. Srinivas	
<b>Multiaxial Fatigue Analysis—Approach Toward Real-World Life Prediction</b> . . . . .	167
Pradip Pujari	
<b>Effect of Loading Rate and Constraint on Dynamic Ductile Fracture Toughness of P91 Steel</b> . . . . .	185
S. Sathyanarayanan, Jashveer Singh, A. Moitra, G. Sasikala, S.K. Albert and A.K. Bhaduri	
<b>Fatigue Life Prediction of Commercial Dental Implant Using Analytical Approach and Verification by FEA</b> . . . . .	203
Pankaj Dhattrak, Uddhav Shirsat, Vijay Deshmukh and S. Sumanth	
<b>Layered Microstructure Generated by Multipass Friction Stir Processing in AZ91 Alloy and Its Effect on Fatigue Characteristics</b> . . .	213
Raja Allavikutty, Vivek Pancholi and Banu K. Mishra	
<b>Grain Refinement Mechanism and Its Effect on Strength and Fracture Toughness Properties of Al–Zn–Mg Alloy</b> . . . . .	223
P.K. Mandal	
<b>Evolution of Tertiary Carbides and Its Influence on Wear Behavior, Surface Roughness and Fatigue Limit of Die Steels</b> . . . . .	237
Tarang Shinde and N.B. Dhokey	
<b>Lakshya: Life Assessment, Extension and Certification</b> . . . . .	253
Manu Jain, S. Rajashekar, V. Ashok Rangan and V. Subramanian	
<b>Creep–Fatigue Damage Evaluation of 2.25Cr-1Mo Steel in Process Reactor Using ASME-NH Code Methodology</b> . . . . .	267
Sagar R. Dukare and Nilesh R. Raykar	

**Analysis and Design Optimization for Improved Fatigue Life of One-Way Clutch Drive Used in Starter Motor** . . . . . 283  
 Varatharaj Neelakandan, Bharath Kumar, Thulasirajan Ganesan and Praveen Chakrapani Rao

**Creep–Fatigue Assessment for Interaction Between IHX Seal Holder and Inner Vessel Stand Pipe in a Pool-Type Fast Reactor as Per RCC-MR** . . . . . 299  
 Sanjay Kumar Pandey, S. Jalaldeen, K. Velusamy and P. Puthiyavinayagam

**Probabilistic Fatigue Life Estimation of Plate with Multiple Stress Concentration Zones** . . . . . 307  
 T. Sivaranjani, K. Abhirama and M. Manjuprasad

**Creep–Fatigue Interaction Study on Gas Turbine Engine Alloy** . . . . . 323  
 Neeta Paulose, D. Chandru Fernando, Amborish Banerjee, J.K. Sahu and S.N. Narendra Babu

**Evaluation of Implicit Reliability Level Associated with Fatigue Design Criteria of Nuclear Class-1 Piping** . . . . . 335  
 J. Mishra and V. Balasubramaniyan

**The Tensile Fatigue Behaviour of Aligned MWNT/Epoxy Nanocomposites** . . . . . 351  
 Sasidhar Jangam, A. Hema Devi, S. Raja, K. Hemachandra Reddy and G. Vijay Kumar

**Thermo-Mechanical Creep and Recovery of CTBN–Epoxy Shape Memory Polymers Under Saline Environment** . . . . . 361  
 A. Revathi, M. Sendil Murugan and Sandhya Rao

**Fatigue Life Estimation of Components Mounted on PCB Due to Vibration** . . . . . 369  
 Debadatta Mishra, Manish Trikha, D. Kamesh, K. Venkatesh and M. Ravindra

**Modified Rainflow Counting Algorithm for Fatigue Life Calculation** . . . . . 381  
 Vaibhav Shinde, Jyoti Jha, Asim Tewari and Sushil Miashra

**Damage Prognosis of Plain Concrete Under Low-Cycle Fatigue Using Piezo-Based Concrete Vibration Sensors** . . . . . 389  
 Anjaneya Dixit, Abhinav Bindal and Suresh Bhalla

**Asymmetric Cyclic Behaviour of Fine- and Coarse-Grained Commercially Pure Copper and Aluminium** . . . . . 397  
 Jayanta Kumar Mahato, Partha Sarathi De, Amrita Kundu and Pravash Chandra Chakraborti

<b>High-Temperature Fatigue Crack Growth Behaviour of SS 316LN . . . .</b>	<b>413</b>
M. Nani Babu, G. Sasikala and Shaju K. Albert	
<b>Numerical Simulation of Fracture in Coatings Subjected to Sudden Temperature Change Using Element-Free Galerkin Method . . . . .</b>	<b>423</b>
Sahil Garg and Mohit Pant	
<b>Measurement of Residual Stress Distribution and Fatigue Life Assessment of Similar and Dissimilar Butt-Welded Joint . . . . .</b>	<b>433</b>
Varun Ravichandran, E.R. Revanth, D. Varun Kumar, M. Sandeep and A. Harish	
<b>Fatigue Life Prediction of Spot Welded Joints: A Review . . . . .</b>	<b>445</b>
Vipin Wagare	
<b>Crystal Orientation Effect on SIF in Single Crystals: A Study Based on Coupled Framework of XFEM and Crystal Plasticity Model . . . . .</b>	<b>457</b>
Rajwinder Singh and Dhiraj K. Mahajan	

## About the Editors

**Dr. S. Seetharamu** received his Ph.D. in Mechanical Engineering from the Indian Institute of Science (IISc) in 1982 after obtaining his M.E. in Mechanical Engineering from IISc in 1976 and B.E. in Mechanical Engineering from Bangalore University in 1974. Dr. S. Seetharamu worked in Central Power Research Institute (CPRI) since 1985 and retired as Director in June 2015. Energy Technology and Materials Engineering are his areas of interest, and special thrust is towards management of coordination with the professional working teams for collaborations, accreditations as well as custom-specific training programmes. He has worked in the Industry and has also served as a Faculty at Toyohashi University of Technology, Japan. Dr. S. Seetharamu is a leading Scientist in the Central Power Research Institute which is contributing towards the development of electrical industry in India. He is the recipient of several awards, holder of many patents and a member of multiple professional bodies.

**Dr. K. Bhanu Sankara Rao** FASM, FNAE, FIIM, FASc, formerly served as Head, Mechanical Metallurgy Division at the Indira Gandhi Centre for Atomic Research, Kalpakkam. Presently, he is a Ministry of Steel Chair Professor in the Mahatma Gandhi Institute of Technology, Hyderabad. He has received his B.E. (Metallurgy) from Visvesvaraya Regional College of Engineering, Nagpur, M.Tech. (Physical Metallurgy) from the Indian Institute of Technology Bombay (IIT Bombay) and Ph.D. (Metallurgical Engineering) from University of Madras. His current research interests are Mechanical Metallurgy, Physical Metallurgy, Welding Science and Technology and Powder Metallurgy. He has published 250 research papers. He has been serving as an Editor of International Materials Reviews, International Review Board Member of Metallurgical and Materials Transactions and Materials Engineering and Performance since 1995. He is a member of the Technical Books Committee of ASM International. He has been the recipient of the Best Metallurgist Award from the Ministry of Steel (1995), MRSI Medal (1997), NASA Appreciation (1994), Binani Gold Medal of IIM (1990), SAIL Gold Medal (Certificate of Merit) of IIM (2000), I.T. Mirchandani (1990), H.D. Govindaraj (1990), Nucor (1996) and D&H Schechron (1994) Awards of the

Indian Institute of Welding. He has served as National Research Council Fellow of USA at the NASA Lewis Research Centre, Cleveland, and as a Guest Scientist at Nuclear Research Centre, Juelich, Germany, and University of Siegen, Germany.

**Dr. Raghunath Wasudev Khare** has 35+ years of experience in Finite Element Method, Materials, Metallurgy, Fatigue and Failure Assessment. He holds his Master's and Doctorate from the Department of Mechanical Engineering, Indian Institute of Science, Bangalore. Dr. Raghunath Khare started his career with the Foundry and Forge Division of Hindustan Aeronautics Limited and later worked with various organisations as a Material & Failure Expert. He is the lead auditor for the failure investigation projects from Central Power Research Institute [CPRI] and Triveni Turbines, DHIO Research and Engineering Pvt Ltd., and so on. He has solved various industrial failure cases ranging from auto, aero and power plant companies. Dr. Raghunath Khare currently heads the Institute of Structural Integrity and Failure Studies [ISIFS], consortium of experts with decades of experience in solving the real-time industrial fatigue, fracture, failure problems associated with design, engineering, material, process related with insight of theoretical, analytical, experimental and computational simulation knowledge.

# Finite Element Analysis-Based Approach for Stress Concentration Factor Calculation

Yuvaraj Hodhigere, Jyoti S. Jha, Asim Tewari and Sushil Mishra

**Abstract** The geometric discontinuity often causes the ‘stress raiser’ or the stress concentration ( $K_t$ ). The fatigue life of a structure depends on the stress concentration, and hence it is very much required to calculate the ‘ $K_t$ ’ value correctly. The calculation of exact ‘ $K_t$ ’ value is cumbersome task. Here a VBA-based tool has been developed to calculate the ‘ $K_t$ ’ which is well validated with other approach.

**Keywords** Fatigue and damage tolerance (F&DT) life analysis · Stress concentration factor · Geometrical discontinuity

## 1 Introduction

The fatigue and damage tolerance (F&DT) life calculation is required to check the structural integrity of a component. There are various tools available for fatigue and damage tolerance analysis. While doing the fatigue and damage tolerance, the engineers often required ‘ $K_t$ ’ value, for the structure, which they directly get from handbook. To reduce the effort, VBA-based code has been developed which includes ‘ $K_t$ ’ value for all the different types of geometry. To other approach has also been suggested which is based on finite element analysis.

---

Y. Hodhigere (✉) · J.S. Jha · A. Tewari · S. Mishra  
Department of Mechanical Engineering, Indian Institute of Technology Bombay, Powai  
400076, Mumbai, India  
e-mail: yuvaraj.shivaraj25@iitb.ac.in

J.S. Jha  
e-mail: jyoti.jha@iitb.ac.in

A. Tewari  
e-mail: asim.tewari@iitb.ac.in

S. Mishra  
e-mail: sushil.mishra@iitb.ac.in

## 2 Stress Concentration Factor

An abrupt change in the geometrical cross sections gives rise to high stress gradient values at the localized areas such as holes, notches and fillet, etc. Hence the irregularity in the stress distribution causes the stress concentration as shown in Fig. 1.

Stress concentration factor defined the ratio of the maximum stress located at the discontinuity of a component to the nominal stress. Figure 2 shows the stress gradient for a plate with hole subjected to axial tension load.

$$K_t = \sigma_{\max} / \sigma_n$$

$\sigma_{\max}$  Maximum stress at the discontinuity.

$\sigma_n$  Nominal stress is calculated through the general stress equations.

**Analytical formula to calculate the nominal stress:**

$$\sigma_n = \text{load} / \text{Cross sectional area}$$

**Fig. 1** Stress concentration for a plate with V-notch subjected to axial tension load

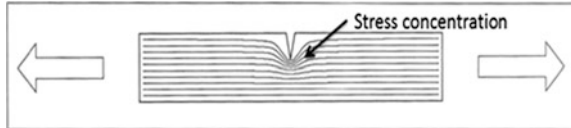
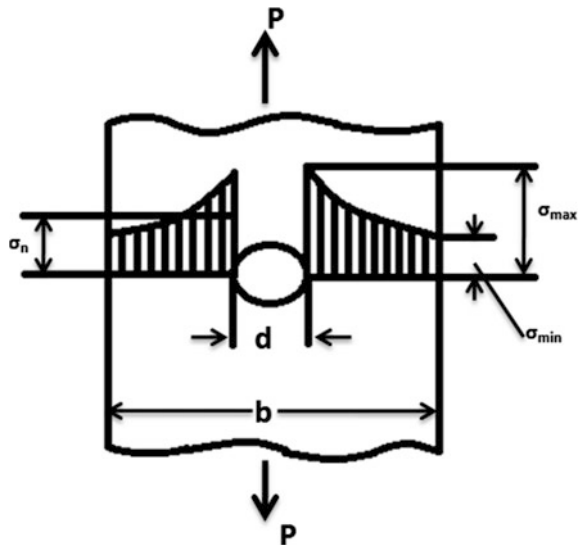


**Fig. 2** Stress gradient for a plate with hole subjected to axial tension load



**Numerical formula to calculate the nominal stress:****Axial case:**

$$\sigma_n = A_{k_t} / \text{Distance}$$

**In plane bending case:**

The area under the pure bending stress gradient is:

$$A_{k_t} = 1/2 \sigma_n * \text{Distance from neutral axis}$$

$$\sigma_n = 2 * A_{k_t} / \text{Distance from neutral axis}$$

### 3 Methodology

Methodology for stress concentration calculation.

#### 3.1 *Finite Element Analysis Based has been Used to Determine the Worst Principle Stress*

FEA software (ANSYS workbench) post-processor provides an integration calculation via path operation, from that extract worst principle stress along the distance at abrupt changes in geometric location. And hence these stress—distance profiles can be further used as input data to calculate the stress concentration factor.

#### 3.2 *VBA Code-Based Analytical Approach to Calculate the Stress Concentration Factor*

In Microsoft excel area under the curve method has been used to determine the stress concentration factor. It consists of two methods (1) integration method and (2) trapezoidal method. In this paper both the methods have been used to calculate the stress concentration factor.

##### 3.2.1 **Integration Method**

In this method calculate the area under the curve by doing definite integrals between two points. This method gives more accuracy compared to trapezoidal method.



$$y = \int f(x) dx \quad (1)$$

### 3.2.2 Trapezoidal Method

In this method discrete the points within a specified intervals and its considered as a trapezoid. Based on the trapezoidal formula calculate the area under the curve for particular segment [4]. For example area under the curve for segment  $x$  and  $y$  is given in Fig. 3.

$$AUC_{xy} = (S_y + S_{(y+1)})/2 * (D_x - D_{(x-1)}) \quad (2)$$

This method is less accurate compared to integration method because last segment is not considered for the summation to calculate the area under the curve.

### Flowchart for stress concentration factor

Based on the two inputs stress and distance graph get's plot, then its fit the curve using polynomial trend-line type and generate a sixth-order polynomial equation. This equation can further be used for the integration to calculate area under a curve. Depends on the load case nominal stress should be calculated. Maximum stress gets it from ANSYS post-processing result, and finally stress concentration factor can be determined (Fig. 4).

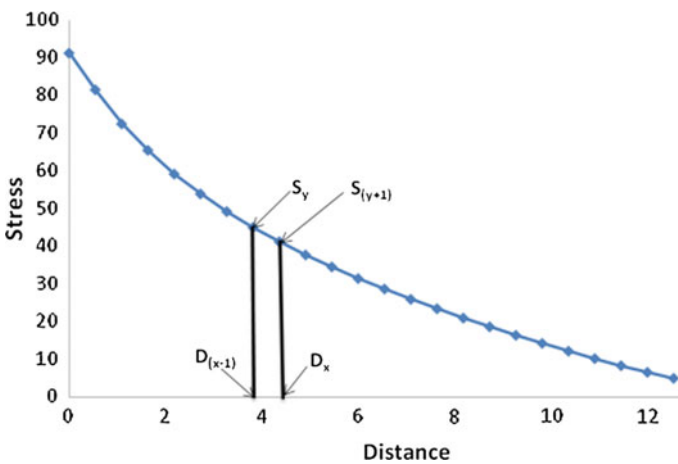


**Fig. 3** Area under the curve using for segment  $x$  and  $y$

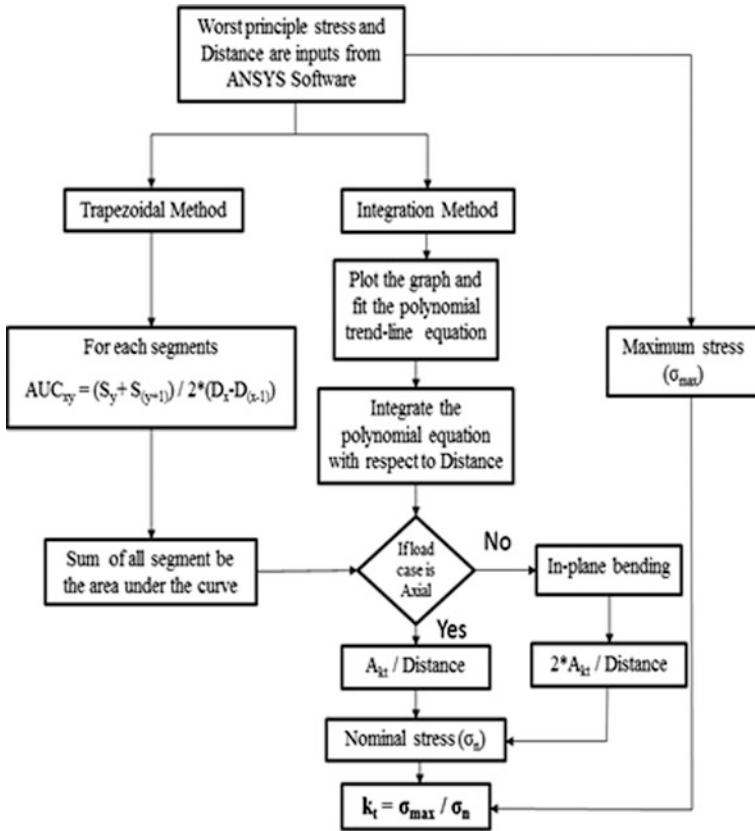


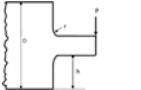


Fig. 4 Flowchart for stress concentration factor

### 4 Comparative Study

Comparative study has been done to validate the numerical results with the analytical results. Some standard geometries are selected from Roark’s handbook to ensure the accuracy of the stress concentration factor calculator (Table 1).

**Table 1** Result

No.	Type of geometry	Geometric data (mm)	Stress concentration factor	
			Analytical ( $k_t$ )	Numerical ( $k_t$ )
1		$r = 0.25$ $D = 1.50$	2.30	2.3
2		$r = 2.5$ $D = 40.0$ $h = 5.0$	3.04	3.1
3		$r = 12.70$ $D = 76.20$ $h = 25.40$	1.33	1.4

## 5 Conclusions

Finite element analysis-based stress concentration factor calculation gives very close to analytical approach. The excel-based tool using VBA for FE simulation/analytical is very simple to use.

## References

1. Muminovic AJ et al (2013) Analysis of stress concentration factor using different computer software solutions. University of Sarjevo, Faculty of Mechanical Engineering, Bosnia and Herzegovina
2. Kisija J et al (2009) Determination of stress concentration factor via numerical methods: bar of circular cross section with U-shaped groove subjected to tension and bending. Mechanical Engineering Faculty Zenica, Bosnia and Herzegovina
3. Kacmarcik J, Beslagic E, Spahic D (2008) New mathematical model of stress concentration factor in tension of rectangular bar with opposite edge U-notches. 12th international research/expert conference TMT
4. Yeh ST et al (2002) Using trapezoidal rule for the area under a curve calculation. pp 229–27
5. Santos A (2013) Determination of stress concentration factor on flat plate of structural steel, Universidad Pontificia Bolivariana Seccional Bucaramanga. Floridablanca, Colombia
6. Enab TA (2014) Stress concentration analysis in functionally graded plates with elliptic holes under biaxial loadings. Ain Shams Eng J 5(3):839–850
7. Sburlati R (2013) Stress concentration factor due to a functionally graded ring around a hole in an isotropic plate. Int J Solids Struct 50(22–23):36–3649
8. Duris R et al (2011) Determination of stress concentration factor using FEM
9. Young WC et al (2002) Roark's formula for stress and strain, 7th edn. McGraw Hill, New York
10. Pilkey WD, Pilkey DD (2008) Peterson's stress concentration factors, 3rd edn. Wiley, New York
11. Shigley JE, Mischke CR, Budynas RG (2004) Mechanical engineering design, 7th edn. McGraw-Hill, New York. ISBN 007-252036-1

# Evaluation of Viscoplastic Parameters of an Austenitic Stainless Steel at High Temperature

A.K. Asraff, Merin V. George, Krishnajith Jayamani and S. Sarath Chandran Nair

**Abstract** Metals at high temperatures are sensitive to strain rate effects and exhibit viscoplastic behavior. The Perzyna model is one of the most widely used ones to study rate-dependent plasticity. This paper presents the details of calibration of Perzyna model parameters of an austenitic stainless steel from tension tests and calibration of Chaboche and Voce model parameters from low-cycle fatigue test at 1000 K. Tests are conducted in an INSTRON 8862 electromechanical UTM. Perzyna model parameters are validated by comparing tension test results with finite element simulations using ANSYS (Version 16.0) software. Sensitivity of Perzyna model parameters on viscoplastic behavior is investigated for monotonic as well as cyclic loading situations. Perzyna model is combined with the Chaboche–Voce cyclic plasticity model for investigating cyclic loading. Finally, viscoplastic cyclic stress analysis of a double-walled rocket engine thrust chamber is carried out using a combination of Perzyna, Chaboche and Voce models and its cyclic life evaluated.

**Keywords** ANSYS · Chaboche model · Voce model · Perzyna model  
Stainless steel · UTM · Viscoplasticity

## 1 Introduction

Plasticity in metals can be classified into two: classical plasticity which is time independent and viscoplasticity which is time or rate dependent. For time-dependent plasticity, the stress–strain behavior is dependent on rate of loading and whether the loading is strain- or stress-controlled [1]. Viscoplasticity in metals

---

A.K. Asraff (✉) · K. Jayamani · S. Sarath Chandran Nair  
Structural Dynamics & Analysis Group, Liquid Propulsion Systems Centre, ISRO,  
Trivandrum, India  
e-mail: akasraff@yahoo.com

M.V. George  
Department of Civil Engineering, Mar Athanasius College of Engineering,  
Kothamangalam, Ernakulam, India

is observed when the operating temperature is above  $0.5 T_m$  where  $T_m$  is the melting point in kelvin. The strain rate effect is also significant under dynamic loading [2]. Most theories of viscoplasticity are formulated by adding the strain rate effects to classical theory of plasticity. The total strain rate may be additively decomposed into elastic and inelastic parts as given in Eq. 1:

$$\dot{\epsilon} = \dot{\epsilon}^e + \dot{\epsilon}^i \quad (1)$$

where  $\dot{\epsilon}^e$  represents the elastic effects and  $\dot{\epsilon}^i$  represents combined viscous and plastic effects. It is important to note that in this equation, viscous and plastic effects cannot be separated and are combined together.

The behavior of structures operating at elevated temperatures beyond the yield limit requires taking into account material viscosity and hardening properties. For modeling the rate-dependent plastic deformation of metals and alloys, two types of constitutive equations have been used. In one approach, no yield surface is assumed and plastic deformation starts from the onset of loading although its value might be negligible under certain levels of stress. This approach is usually referred to as the unified creep plasticity theory because there is no separation between time-dependent (creep) and time-independent deformations. In the second approach, a yield surface is assumed after which plastic deformation develops. Viscoplastic models fall in this category. This approach uses the notion of static yield surface and dynamic loading surface. The positive difference between the current dynamic stress and corresponding static stress is known as the overstress measure [3]. The fundamental empirical equation of Cowper and Symonds provides the simplest description of dynamic behavior of a viscoplastic material (see Eq. 2).

$$\frac{\sigma_d}{\sigma_s} = 1 + \left( \frac{\dot{\epsilon}}{D} \right)^m \quad (2)$$

where  $\sigma_d$  is the rate-dependent or dynamic yield stress,  $\sigma_s$  is the static yield stress (yield stress at zero strain rate),  $\dot{\epsilon}$  is the strain rate,  $D$  has the same unit as that of strain rate and is called the material viscosity parameter.  $m$  is called the material strain rate hardening parameter and  $0 < m < 1$ . The ratio of dynamic yield stress to static yield stress ( $\sigma_d/\sigma_s$ ) is known as ‘stress ratio’ [4]. In order to describe viscoplastic behavior, many constitutive laws have been developed, Anand [5], Perzyna [6] and Chaboche [7, 8] being some of them. Out of these, Perzyna model is one of the simplest ones. Yang and Luo [9] conducted a series of tensile experiments at a single temperature and different strain rates as well as under the same strain rate and different temperatures on carbon constructional quality steels, and the experimental results were analyzed theoretically. Furthermore, the rheological models of carbon steels were built combining the strong points of Perzyna and Johnson–Cook models. Results proved that the model can reflect the temperature effect and strain rate effect of these steels better. Safari et al. [2] developed a constitutive equation for austenitic stainless steel 310S at high temperature taking into account viscosity and strain rate effects. For this, the authors performed both

static and dynamic tension tests at various temperatures. To verify the model, the tension test results were compared with numerical results using ABAQUS program. Kłosowski and Mleczek [10] dealt with identification of parameters for Perzyna and Chaboche viscoplastic models for aluminum alloy at elevated temperature. Results of these were verified by numerical simulation of the laboratory tests. The material parameters were calculated on the basis of uniaxial tension test. The authors emphasized that a simple constitutive law like Perzyna model can very well represent viscoplastic material behavior. Yang et al. [11] conducted detailed viscoplastic structural analysis of a double-walled thrust chamber wall to study its damage process, phase by phase. Analysis revealed that under the same level of thermal structural loading, the duration of startup and shutdown phases plays an important role in the stress and strain evolution.

In this work, a series of tension tests are conducted on specimens made of austenitic stainless steel at 1000 K and different strain rates. From the test results, the viscoplastic parameters are determined by curve fitting based on the procedure developed by Kłosowski and Mleczek [10]. Sensitivity of different model parameters is investigated for monotonic and cyclic loadings from finite element simulations. Cyclic plasticity model parameters of the material are calibrated from LCF tests. The Chaboche–Voce model combination has been used for cyclic plastic modeling. Two-dimensional finite element modeling and cyclic stress analysis of a double-walled thrust chamber has been conducted using a combination of Perzyna, Chaboche and Voce models and its cyclic life evaluated.

## 2 Viscoplastic Models in ANSYS

The following viscoplastic models are available in ANSYS [5]: (1) Anand model, (2) Pierce model, (3) Perzyna model and (4) Chaboche model. This work uses the Perzyna viscoplastic model. It has to be combined with a suitable classical plasticity model to represent the elastoplastic part. The Perzyna model is obtained by rearranging the basic Cowper and Symonds equation as follows:

$$\dot{\epsilon} = D \left( \frac{\sigma_d}{\sigma_s} - 1 \right)^{1/m} \quad (3)$$

The parameters  $D$ ,  $m$  and  $\sigma_s$  are evaluated by curve fitting from tension tests at the desired temperature [10].

### 3 Tensile Testing of Austenitic Stainless Steel

Tensile tests are conducted in an INSTRON 8862 electromechanical UTM. Photograph of the machine is shown in Fig. 1. Salient features of the machine are listed below:

- Load frame rating: 100 kN
- Test temperature range: 30–1400 °C
- Induction heating system
- Water-cooled environment chamber inside which tests can be conducted
- Argon purging system
- Water-cooled pull rods.

Tests are done at 1000 K (727 °C) and strain rates of  $1 \times 10^{-4}/s$ ,  $5 \times 10^{-4}/s$ ,  $1 \times 10^{-3}/s$ ,  $5 \times 10^{-3}/s$ ,  $1 \times 10^{-2}/s$ . On average, three specimens per strain rate are tested. The specimen design and testing procedure conform to ASTM E8 standards [12]. Dimensions of the specimen are shown in Fig. 2. The austenitic stainless steel considered for the study is equivalent to SS-321 which has a material composition listed in Table 1.

Photographs of a specimen before and after testing are shown in Figs. 3 and 4, respectively.

**Fig. 1** Photograph of universal testing machine



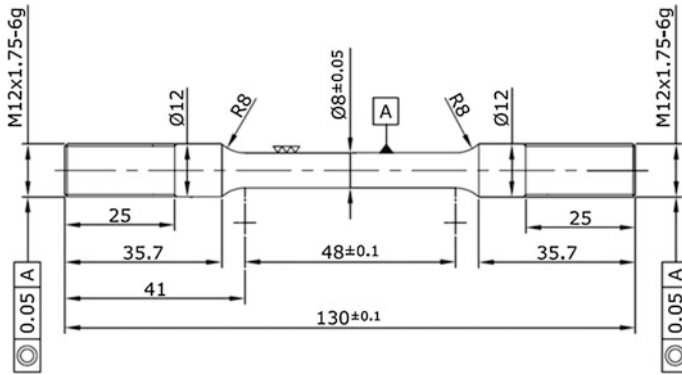


Fig. 2 Dimensions of the tension test specimen

Table 1 Material composition of SS-321

Alloying element	% by weight
Carbon	0.12 max
Chromium	17–19
Nickel	9–12
Titanium	0.7 max
Iron	Balance

Fig. 3 Specimen before testing



Fig. 4 Specimen after testing



The stress–strain curve, yield and ultimate strengths, percentage elongation and percentage reduction in area of each specimen are recorded from the tests. A total of 15 specimens are tested. Stress–strain curves at each strain rates tested are shown in Fig. 5. The average yield strength at each strain rate is listed in Table 2, and the variation of yield strength with strain rate is illustrated in Fig. 6. The static yield strength (yield strength corresponding to zero strain rate) is found to be  $199.2 \text{ N/mm}^2$  which is obtained by extrapolating the curve in Fig. 6 to zero strain rate.



**Fig. 5** Stress–strain graphs at different strain rates

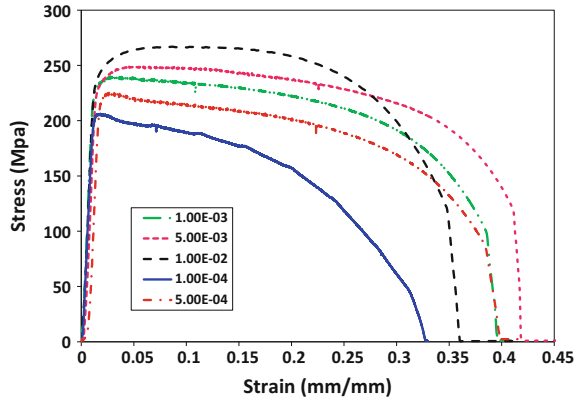
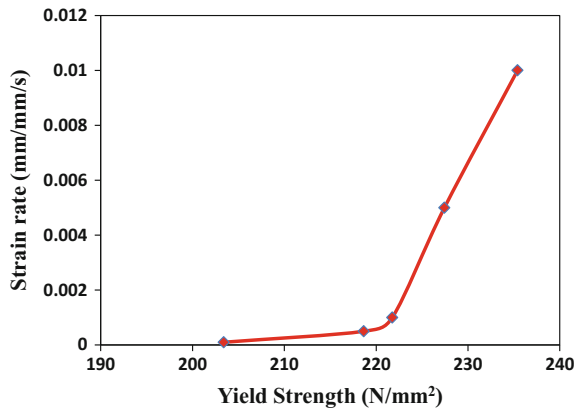


**Table 2** Average yield strength from tension tests

Strain rate (mm/mm/s)	Yield strength (N/mm <sup>2</sup> )
$1 \times 10^{-4}$	206.03
$5 \times 10^{-4}$	218.63
$1 \times 10^{-3}$	221.75
$5 \times 10^{-3}$	227.43
$1 \times 10^{-2}$	235.4

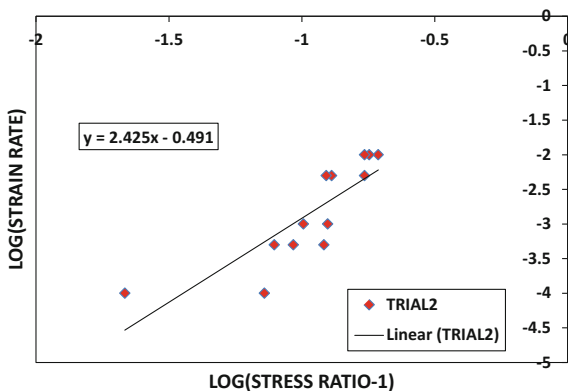
**Fig. 6** Variation of average yield strength with strain rates



### 4 Determination of Perzyna Parameters

The Perzyna model parameters are evaluated based on the methodology reported by Klosowski and Mleczek [10]. The logarithmic values of (stress ratio-1) and strain rate are determined and are plotted in linear scale as shown in Fig. 7 so that the equation for the linear curve is obtained.

**Fig. 7** Determination of Perzyna parameters



The equation for the linear curve is

$$y = 2.425x - 0.491 \quad (4)$$

By taking logarithm on both sides of Eq. 3 and rearranging, we get:

$$\log \dot{\epsilon} = \frac{1}{m} \log \left( \frac{\sigma_d}{\sigma_s} - 1 \right) + \log D \quad (5)$$

By comparing Eqs. 4 and 5, we get:

$$1/m = 2.425, m = 0.412, \log D = -0.491, D = 0.322$$

The Perzyna model for the stainless steel can thus be expressed as:

$$\dot{\epsilon} = 0.322 \left( \frac{\sigma_d}{\sigma_s} - 1 \right)^{1/0.412} \quad (6)$$

## 5 Numerical Examples

This section covers two examples to illustrate viscoplastic modeling and analysis. The specimen geometry, material model adopted and different load cases considered are discussed below.

### 5.1 Stress Analysis of a Tension Specimen Under Monotonic Loading

The purpose of this exercise is to validate the above-developed viscoplastic model. It is done by comparing actual tension tests with Perzyna based finite element simulations. Due to the symmetry of the tension test specimen (see Fig. 2) along axes  $X$  and  $Y$ , a quarter portion is idealized as illustrated in Fig. 8. Four noded axisymmetric solid elements PLANE182 are used for meshing. Perzyna model is combined with the rate-independent multi-linear isotropic hardening (MISO) plasticity model for analysis of monotonically loaded structures. The material properties used are shown in Table 3, and MISO model graph is shown in Fig. 9. True stress–true strain properties corresponding to a strain rate of  $1 \times 10^{-3}/s$  are used for MISO modeling.

All the nodes along the line AD are arrested in the radial direction, while the nodes along line CD are supported in the axial direction (refer Fig. 8). All the nodes along line AB are coupled together and pulled up in  $Y$  direction to simulate the displacement loading pattern as in a UTM. A small reduction in diameter is modeled at mid-length of the specimen in order to force the neck formation at this location. Displacement loading is applied on the top nodes in increments till the specimen failed. Failure is indicated by a non-convergence of equilibrium iterations signaling tensile rupture of the specimen. The following investigations are made:

**Fig. 8** FE model and boundary conditions

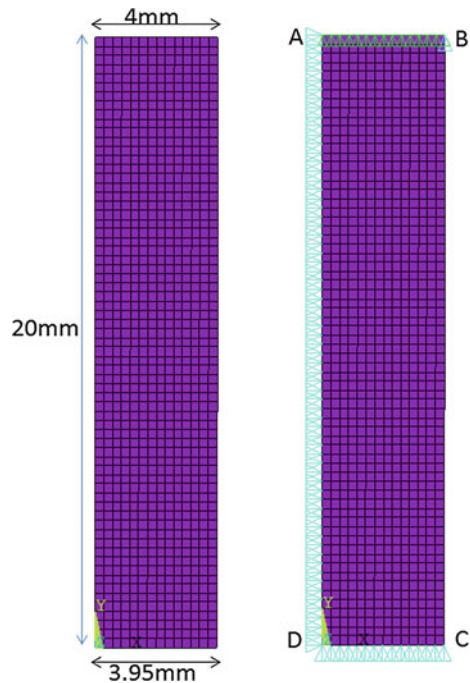
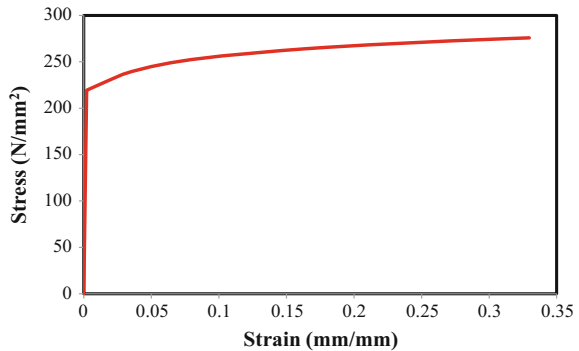


**Table 3** Viscoplastic properties used for SS-321

Property	Value	Unit
$E$	105582.2	MPa
$\nu$	0.3	–
$m$	0.412	–
$D$	0.322	mm/mm/s

**Fig. 9** MISO model graph for SS-321



- Sensitivity study of duration of application of load
- Sensitivity study of parameter  $m$
- Sensitivity study of parameter  $D$
- Comparison of stress–strain behavior with actual tension test results.

**Sensitivity study of duration of application of load**

Different durations are considered from 40 to 40000 s (strain rate ranging from 0.01 to 0.00001 mm/mm/s) for load application, and the stress–strain graphs plotted for each case. The plots are compared with the experimental stress–strain curve for the strain rate of  $1 \times 10^{-3}$  mm/mm/s, the actual duration of application of load being 400 s. An elastoplastic analysis is also done without considering the Perzyna model. This graph is also included in Fig. 10. From this figure, it is clear that duration of application of load has got a significant effect on the stress–strain response. It can be seen that as duration increases the yield strength decreases (i.e., as strain rate reduces, the yield strength decreases). The shape of simulation curve matches fairly with the test curve for a duration of 130 s.

**Sensitivity study of parameter  $m$**

In order to study the effect of parameter  $m$ , simulations are run with  $m$  ranging from 0.162 to 0.612. Duration considered for this study is 400 s. The value of  $m$  could not be decreased below 0.162 due to computational difficulties. Stress–strain graphs plotted for different values of  $m$  are illustrated in Fig. 11. From this figure, it is observed that as  $m$  approaches zero, the effect of viscoplasticity becomes predominant while as the value approaches one the viscoplastic effect is lower. For a value of 0.212, the test curve matches well with the simulation curve up to a strain of 0.3 mm/mm.

**Fig. 10** Sensitivity study of load application duration

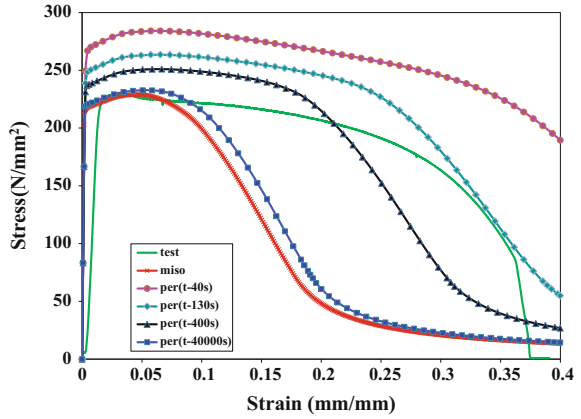
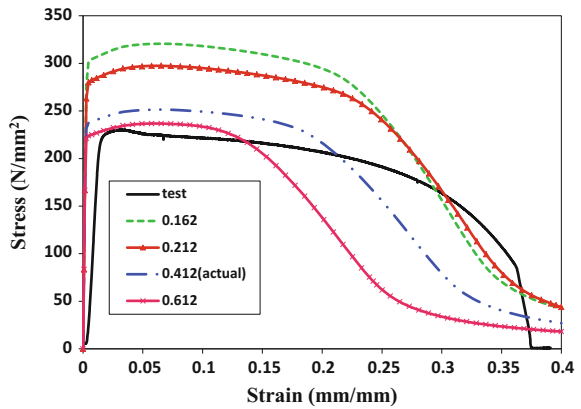


**Fig. 11** Study of parameter *m*



**Sensitivity study of parameter *D***

*D* is varied from 0.012 to 0.522/s. The obtained stress–strain curves are plotted along with the test curve as shown in Fig. 12. It is found that as *D* decreases the yield strength increases. It can be seen that the shape of the simulation curve matches fairly with the test curve for *D* = 0.082/s.

**Validation of Perzyna model**

Validation of the above-developed Perzyna model is done by comparing ANSYS simulations with test results. The stress–strain graph obtained with *m* = 0.412 and *D* = 0.322/s at a strain rate of  $1 \times 10^{-3}$  mm/mm/s for the actual test duration of 400 s is plotted in Fig. 13 together with the corresponding test graph. It is found that both the graphs do not match well. However, for a simulated test duration of 130 s, the test graph and Perzyna prediction match reasonably. This indicates that the fitted values of *m* = 0.412 and *D* = 0.322/s based on tension test data derived from 15 specimens do not represent the true viscoplastic behavior of the material. Therefore, a larger number of specimens should have been tested to get better

**Fig. 12** Study of parameter  $D$

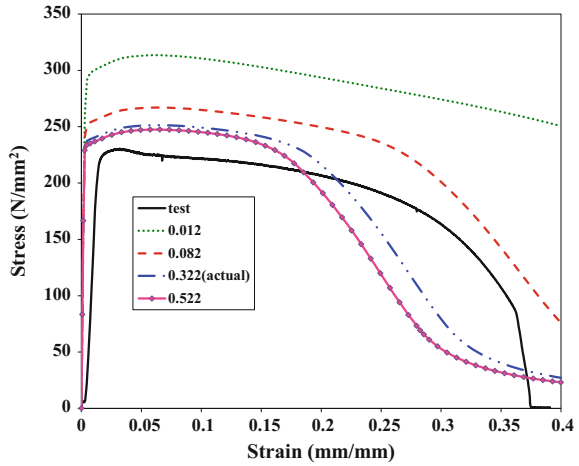
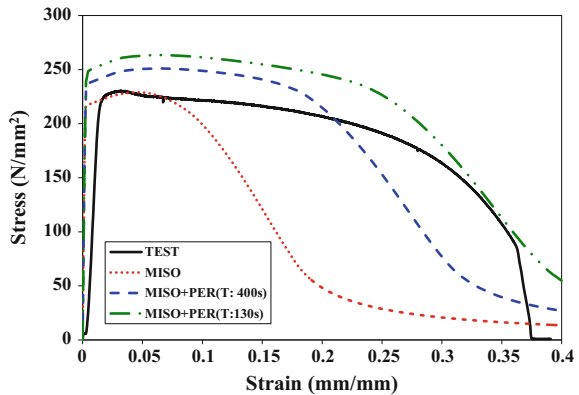


**Fig. 13** Validation of Perzyna model for tension specimen



estimates of the Perzyna parameters. However, the Perzyna model gives a better stress–strain response for the stainless steel tested compared to the MISO-based classical plasticity model which gives an odd pattern of the stress–strain graph after peak stress point.

## 5.2 Cyclic Stress Analysis of a Simple Block

The following material models are studied to check their suitability for analysis of cyclically loaded structures:

- Chaboche nonlinear kinematic hardening plasticity model [8]
- Chaboche + Perzyna model

- Chaboche + Voce model [13]
- Chaboche + Voce + Perzyna model.

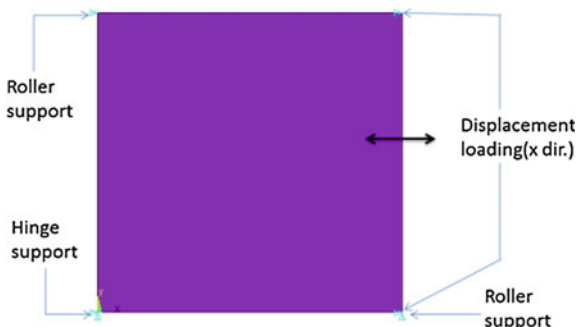
A single plane stress element is used for two-dimensional cyclic stress analysis with an element size of 1 mm as shown in Fig. 14. Displacement loading of  $\pm 0.05$  mm is applied on one edge of the element for two cycles as shown in Fig. 15. The cyclic stress–strain graph obtained using the above material model combinations is shown in Fig. 16. From this figure, it is observed that a combination of Chaboche, Voce and Perzyna models is well suited for modeling cyclic plasticity combined with viscoplasticity. The stress corresponding to a given strain with this model is found higher compared to other models.

### Sensitivity study of $m$ and $D$

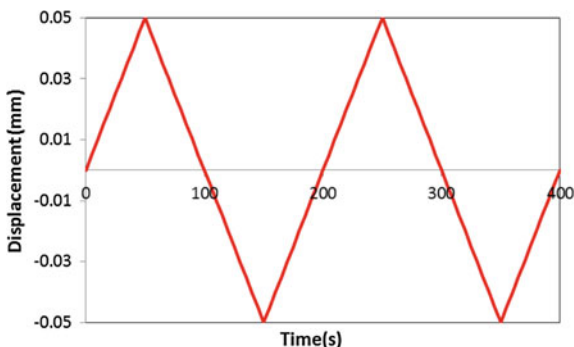
Sensitivity study of  $m$  and  $D$  parameters is conducted for cyclic loading of the simple block with a combination of Chaboche, Voce and Perzyna models. Different values for  $m$  and  $D$  are investigated, and the corresponding stress–strain graphs are plotted as shown in Fig. 17. It is found that as  $m$  decreases while keeping  $D$  constant, the yield strength increases. Similarly, as  $D$  decreases, keeping  $m$  constant, the yield strength increases.

Thus, the Perzyna model as implemented in ANSYS could be successfully used in association with a combination of Chaboche and Voce cyclic plasticity models to analyze cyclically loaded structures.

**Fig. 14** FE model of 2D block



**Fig. 15** Cyclic displacement loading pattern



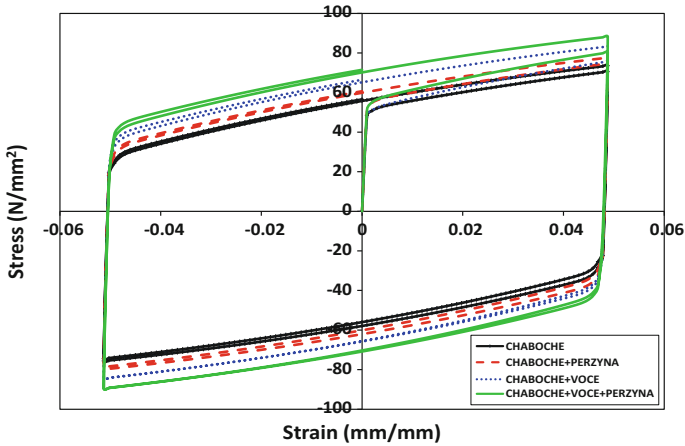


Fig. 16 Stress–strain graph for different material models

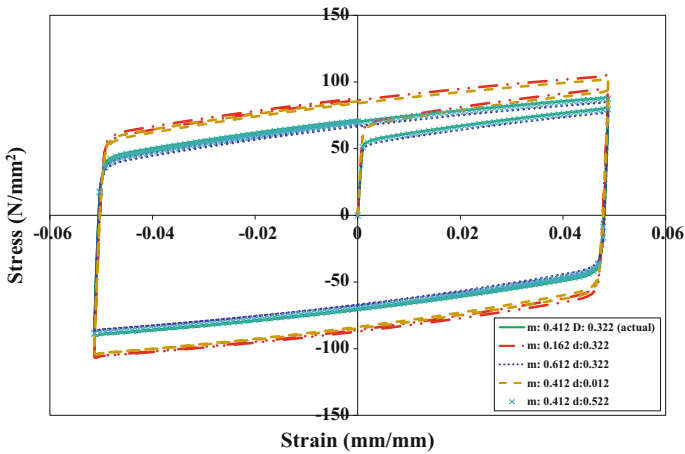


Fig. 17 Results of sensitivity study of  $m$  and  $D$  parameters

## 6 Calibration of Chaboche and Voce Model Parameters of SS-321

For simulating cyclic hardening of a material, it is required to combine the Chaboche nonlinear kinematic hardening model with the Voce nonlinear isotropic hardening model.

**Chaboche model:** To model smooth nonlinear stress–strain behavior, the Chaboche model, as given below, is commonly used:



$$\alpha_i = \frac{2}{3} C_i \varepsilon^p - \gamma_i \alpha dp \quad (7)$$

where  $\alpha$  = back stress,  $dp$  = accumulated plastic strain,  $c$ ,  $\gamma$  = material parameters. A third-order Chaboche model is found sufficient and hence used for the current idealization as given below:

$$\alpha = \sum_{i=0}^3 \alpha_i \quad (8)$$

A third-order Chaboche model has 7 parameters  $\sigma_0$ ,  $C_1$ ,  $\gamma_1$ ,  $C_2$ ,  $\gamma_2$ ,  $C_3$  and  $\gamma_3$ .

**Voce model:** This model is used for materials exhibiting a smooth exponential transition from the linear elastic region to a final constant linear strain hardening slope. It is given below:

$$\sigma_y = k + R_o \varepsilon^p + R_\infty (1 - e^{-b\varepsilon^p}) \quad (9)$$

where  $\sigma_y$  = yield strength,  $\varepsilon^p$  = plastic strain,  $k$  = elastic limit (initial yield point, which is the first tensile peak stress point in the cycling),  $R_o$  = slope of linear plastic region,  $R_\infty$  = stress intercept,  $b$  = exponential hardening term. The specialty of this model is that it can represent cyclic hardening or softening of a material when combined with the Chaboche model resulting in the translation and expansion of yield surface.

In the combined Chaboche–Voce model, the former one represents the characteristics of the stabilized stress–strain graph (hysteresis loop), while the latter simulates the cyclic hardening (or softening) of the material from the virgin state to the final state. These parameters are calibrated by performing a cyclic stress analysis of a simple block under displacement loading (uniaxial tension–compression loading), and the resulting cyclic stress–strain graph is compared with the LCF test results. The parameters are adjusted by trial and error till both the curves match well.

The FE model of the simple block made of SOLID185 element is shown in Fig. 18. Figure 19 represents the cyclic displacement load used for calibration studies. The steps involved in the calibration process of SS-321 at 1000 K and strain rate of  $1 \times 10^{-3}$  mm/mm/s are as under:

- Step 1: LCF cyclic stress–strain graph of SS-321 at 1000 K is plotted using MS Excel. Yield strength is noted. The stress–strain curve got stabilized after a few number of cycles.
- Step 2: From the LCF test results, it is possible to plot a graph with cycle number versus peak tensile stress in each cycle as shown in Fig. 20. This graph gives the cyclic hardening or softening characteristic of a material as well its cyclic stabilization. The cycle number at which the graph becomes stabilized can be found out from this curve. It is found that at the tenth cycle, the graph got stabilized.

**Fig. 18** FE model of a simple block

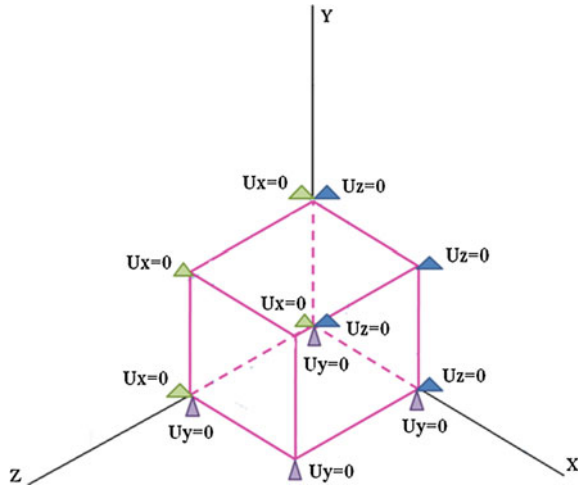


**Fig. 19** Cyclic displacement load

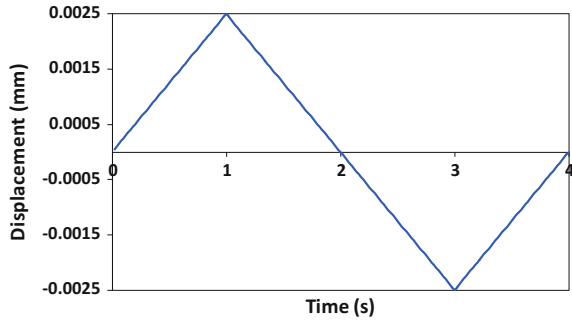
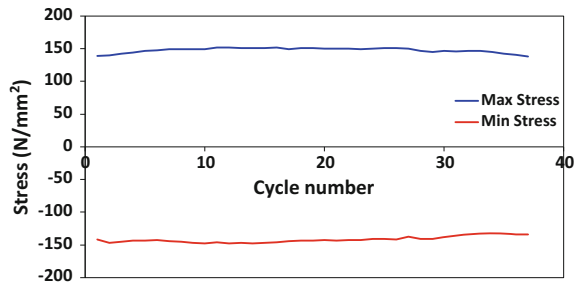


**Fig. 20** Cycle number versus peak tensile stress graph



- Step 3: The stabilized cyclic stress–strain graph is plotted in this step. A sample cyclic stress–strain graph and the procedure for evaluation of the Chaboche model constants are shown in Fig. 21.

The cyclic stress–strain graph typically consists of three regions: (I) a linear elastic region, (II) a curvilinear transition from elastic to elastoplastic region and (III) a gently curved strain hardening region. Initial values of the six Chaboche model parameters are taken as follows:  $C_1$  is taken as the slope at the beginning of region I,  $C_2$  as the slope at the middle of region II, and  $C_3$  as the slope of region III.  $\gamma_1$  is taken as the rate at which  $C_1$  reduces decays to  $C_2$ ,  $\gamma_2$  is the rate at which  $C_2$  decays to  $C_3$ , and  $\gamma_3$  is the rate at which  $C_3$  decays. With the above-evaluated initial values of the Chaboche model parameters, a cyclic stress analysis of the simple block under uniaxial tension–compression is conducted, under displacement- or strain-controlled loading for a strain range of  $\pm 0.5\%$  (displacement =  $0.005 \times 0.5 = 0.0025$  mm). From this analysis, the stabilized stress–strain graph can be obtained. The Chaboche model parameters are fine-tuned by comparing the computed cyclic stress–strain curve with the LCF test results as shown in Fig. 22. This is done by trial and error till both curves match reasonably. The final values of Chaboche model parameters are tabulated in Table 4.

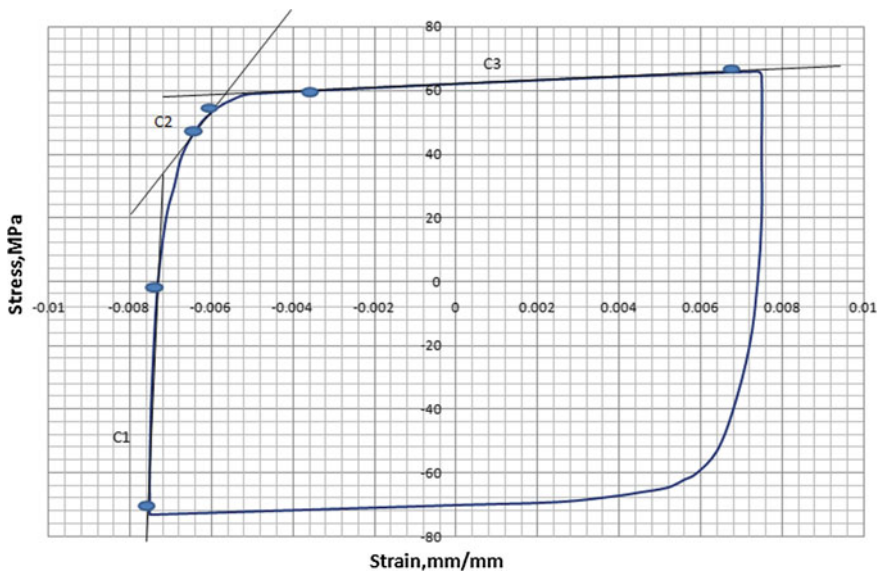


Fig. 21 Graphical method of evaluation of initial Chaboche parameters

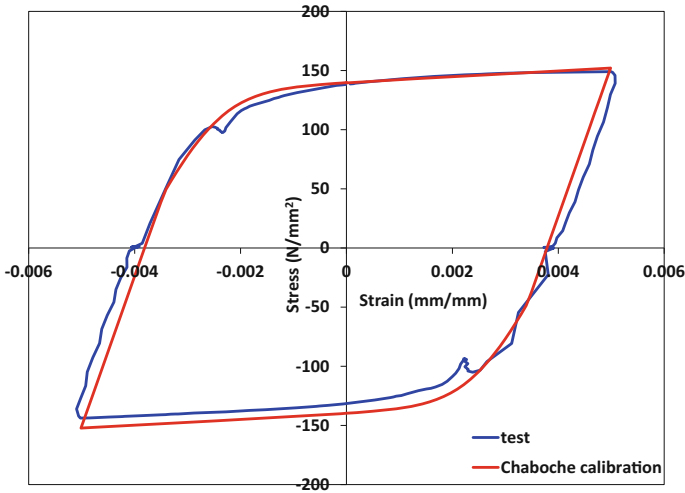


Fig. 22 Comparison of Chaboche graph with test graph

Table 4 Calibrated Chaboche and Voce parameters

Chaboche	Parameter	$C_1$	$\gamma_1$	$C_2$	$\gamma_2$	$C_3$	$\gamma_3$	$\sigma_o$
		Value	55000	2750	45000	1940	2500	5
Voce	Parameter	$K$	$R_o$	$R_\infty$	$b$	–	–	–
		Value	90	0	10	20	–	–

- Step 4: The original Voce model relates the variation of yield stress against plastic strain as seen in Eq. 9, but in the absence of this information, we can fit an approximate equation for peak tensile stress against cycle number as described in Step 2. Since the material stabilizes to a constant stress–strain graph, the slope of the curve in the plastic region,  $R_o$ , would be zero. Only one parameter  $b$  needs to be fitted from the above curve based on trial and error.
- Step 5: Now do a combined Chaboche exact model and Voce approximated model modeling of the material and perform cyclic stress–strain analysis till stabilization of stress–strain graph is achieved. The Voce model parameters  $b$  can be calibrated by trial and error by comparing the computed cyclic stress–strain graph with the LCF test results. Analysis is continued till a reasonable match is obtained between the two curves as shown in Fig. 23. Table 4 shows the calibrated Voce parameters.

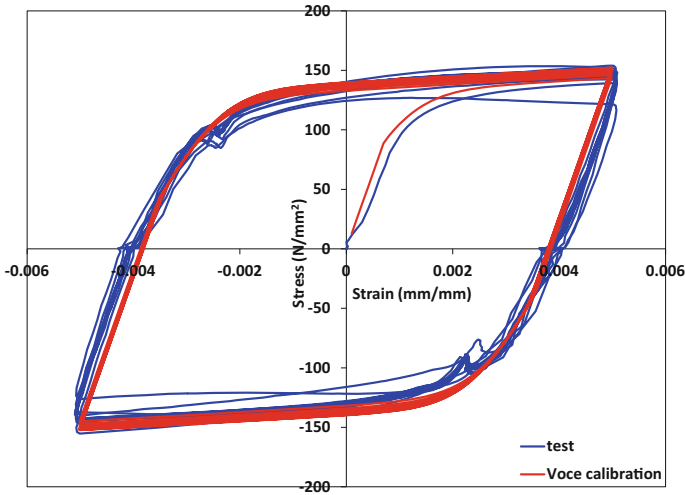


Fig. 23 Comparison of Chaboche and Voce simulations with test results

## 7 Cyclic Stress Analysis of Thrust Chamber

Thrust chamber is one of the important subsystems of a rocket engine. The thrust chamber generates propulsive thrust force for the flight of the rocket by ejection of combustion products at supersonic speeds. A double-walled construction is employed for these chambers where in the inner wall and ribs are made up of copper alloy up to area ratio 10 and stainless steel beyond area 10. The outer walls are made up of stainless steel throughout. The pressure and temperature load varies throughout the length of the chamber. So a section which experiences maximum temperature is taken for the cyclic stress analysis which is at area ratio 100. As the temperature is high, this location will experience viscoplastic effect.

FE model of a cyclic symmetric sector of the chamber cross section, with appropriate circumferential symmetric boundary condition, is used for analysis as shown in Fig. 24. Two-dimensional plane strain model of the thrust chamber cross section is modeled using PLANE182 elements. Two-dimensional analysis is carried out using Chaboche + Voce and Chaboche + Voce + Perzyna material model combinations, and the results are compared. Analysis is carried out considering temperature and pressure loads during seven stages of a single hot run of the engine: (a) pre-cooling, (b) ignition start, (c) hot test condition, (d) hold time for 7200 s (720 s with a factor of safety of 10), (e) initiation of shutdown, (f) post-cooling, (g) back to ambient. Duration of application of all loads except hold period is considered to be 1 s. Analysis is done for two hot tests. With these loads, the cyclic life of the thrust chamber is computed using both the model combinations. Figure 25 shows the hoop cyclic stress–strain curves at mid-channel gas side wall for two cycles of both the models combinations.

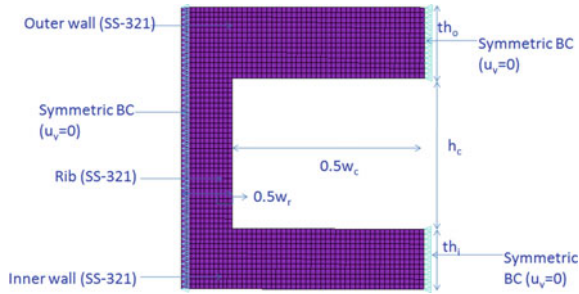


Fig. 24 Plane strain model of thrust chamber cross section

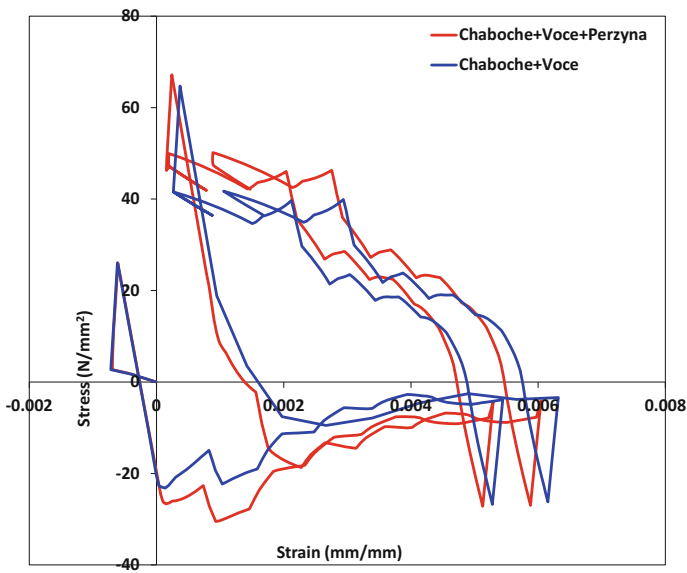


Fig. 25 Hoop cyclic stress–strain graph

From Fig. 25 it is observed that the hoop stress corresponding to Perzyna model is higher and strains lower compared to the model without Perzyna model. Also peak strain at the end of the third load step is lower by  $1.5E-04$ .

### 7.1 Life Cycle Prediction of Thrust Chamber

The failure mechanisms, viz. LCF and ratcheting, contribute by varying degrees to the failure of the chamber. These damages are summed up to get the total damage

(known as cumulative damage technique), the reciprocal of which gives the life of the chamber.

- Low-cycle fatigue damage: Damage due to LCF is simply the reciprocal of the number of cycles to fatigue failure as expressed below:

$$D_{LCF} = \frac{1}{N_f} \quad (10)$$

$$\text{where } N_f = \left( \frac{\varepsilon_f}{2\Delta\varepsilon} \right)^2 \quad (11)$$

$\varepsilon_f$  is the fracture strain expressed as

$$\varepsilon_f = \ln \left( \frac{1}{1 - RA} \right) \quad (12)$$

where RA is the reduction in area in fraction form and  $\Delta\varepsilon$  is the strain range expressed as  $\Delta\varepsilon = \varepsilon_{\max} - \varepsilon_{\min}$ .

For a temperature of 1000 K and strain rate of  $1 \times 10^{-3}$  mm/mm/s RA = 0.867,  $\varepsilon_f = 2.019$  and  $\Delta\varepsilon$  is obtained from Fig. 26. Considering a factor of safety of 4,  $D_{LCF} = 1.43 \times 10^{-4}$  (for Chaboche + Voce combination) and  $1.36 \times 10^{-4}$  (for Chaboche + Voce + Perzyna combination).

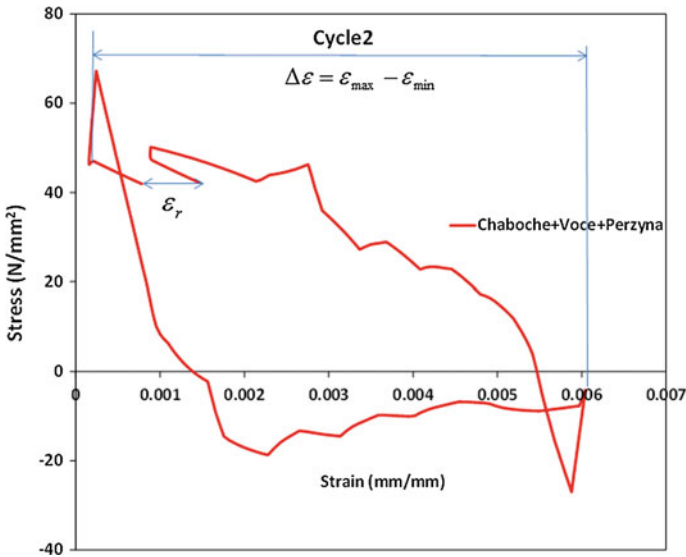


**Fig. 26** Determination of strain range

- Ratcheting damage: It is the ratio of accumulated plastic tensile strain in a cycle to the fracture strain of the material. It is expressed as:

$$D_{\text{ratcheting}} = \frac{\varepsilon_r}{\bar{\varepsilon}_f} \quad (13)$$

where  $\varepsilon_r$  is the ratcheting strain (as shown in Fig. 26) and  $\bar{\varepsilon}_f$  is the elongation (37.53% for  $1 \times 10^{-3}$  mm/mm/s).

Thus,  $D_{\text{ratcheting}} = 2.09 \times 10^{-3}$  (for Chaboche + Voce combination) and  $1.87 \times 10^{-3}$  (for Chaboche + Voce + Perzyna combination).

- Total damage is obtained as  $D_{\text{tot}} = 4 \times D_{\text{LCF}} + 2 \times D_{\text{ratcheting}}$  where 4 and 2 are the factor of safety considered for LCF and ratcheting, respectively. Number of cycles to failure is the reciprocal of total damage expressed as

$$N_f = \frac{1}{D_{\text{tot}}} \quad (14)$$

$N_f$  is obtained as 210 (for Chaboche + Voce combination) and 233 (for Chaboche + Voce + Perzyna combination).

**Study on duration of load application:** The material model considered for this study is a combination of Chaboche, Voce and Perzyna models. Duration of application of load steps is varied from 1 to 3 s. It is found that the corresponding life decreases from 233 to 225 cycles.

## 8 Conclusion

Perzyna viscoplastic model parameters are calibrated for an austenitic stainless steel using the methodology reported by Klosowski and Mleczek from tension tests conducted at 1000 K, at different strain rates. These parameters are validated by comparing actual tension tests with finite element simulations using ANSYS. Increase in dynamic yield strength of the material due to strain rate effects is clearly seen both in tests as well as in numerical simulations. A combination of Perzyna and MISO model is found to give good results for simulating monotonic loading. For cyclic loading, Perzyna model combined with Chaboche nonlinear kinematic hardening model and Voce nonlinear isotropic hardening model is found excellent. The sensitivity of parameters ' $m$ ' and ' $D$ ' in the Perzyna model is also investigated. It is found that when ' $m$ ' and ' $D$ ' reduce, the rate-dependent effects increase. Calibration of Chaboche and Voce parameters at 1000 K for a strain rate of  $1 \times 10^{-3}$  mm/mm/s and strain range of  $\pm 0.5\%$  has also been done.



Cyclic stress analysis of a double-walled rocket engine thrust chamber has been performed for a region which experiences high temperature. The material model used for the viscoplastic analysis is a combination of Perzyna, Chaboche and Voce models, whereas only the Chaboche–Voce model combination is used for classical elastoplastic based thermostructural analysis. Plane strain model of the required cross section is adopted for both the analyses. Number of cycle to low-cycle fatigue failure is found to be 210 for Chaboche + Voce combination and 233 for Chaboche + Voce + Perzyna combination. When the duration of application of load steps is varied from 1 to 3 s, the corresponding cycle life varies from 233 to 225 cycles. It is also observed that the hoop stress corresponding to Perzyna model is higher and strains lower compared to the model without Perzyna model. Because of this, the predicted cyclic life is higher for Perzyna model.

**Acknowledgements** The second author gratefully thanks Director, LPSC/ISRO, for granting permission to do her M. Tech thesis. Thanks are also due to Dr. R. Muthukumar, Deputy Director, MDA/LPSC, for permitting her to use the creep test facility and computational resources of SDAG for this work.

## References

1. Wu HC (2005) Continuum mechanics and plasticity, vol 3, 2nd edn. CRC Press Company, Washington D.C., pp 225–231
2. Safari AR, Forouzan MR, Shamanian M (2013) Thermo-viscoplastic constitutive equation of austenitic stainless steel 310s. *Comput Mater Sci* 68:402–407
3. Lubliner Jacob (2008) Plasticity theory. Dover Publications Inc., New York, pp 117–150
4. Nordberg H (2004) Note on the sensitivity of stainless steels to strain rate. Avesta Polarit Research Foundation, Research report no. 04.0-1
5. ANSYS Mechanical APDL (2015) Version 15. ANSYS Inc, USA
6. Perzyna P (1968) Fundamental problems in viscoplasticity. *Adv Appl Mech Acad Press* 9:313–377
7. Lin RC, Betten J, Brocks W (2006) Modeling of finite strain viscoplasticity based on the logarithmic corotational description. *Arch Appl Mech* 75:693–708
8. Chaboche JL (1989) Constitutive equations for cyclic plasticity and cyclic viscoplasticity. *Int J Plast* 5(3):247–302
9. Yang L, Luo Y (2008) Constitutive model depending upon temperature and strain rate of carbon constructional quality steels. *J Central South Univ Technol* 15:43–46
10. Kłosowski P, Mleczek A (2014) Parameters Identification of Perzyna and Chaboche viscoplastic models for aluminum alloy at temperature of 120 °C. *Eng Trans* 62(3):291–305
11. Yang J, Chen T, Jin P, Cai G (2014) Influence of the startup and shutdown phases on the viscoplastic structural analysis of the thrust chamber wall. *Aerosp Sci Technol* 34:84–91
12. Anonymous (2015) ASTM-E8/E8M-15a, Standard test methods for tension testing of metallic materials. American Society for Testing and Materials, Philadelphia, USA
13. Voce E (1955) A practical strain-hardening function. *Metallurgia*, pp 219–225
14. Asraff AK, Sheela S, Paul A, Mathew A, Savithri S. Cyclic stress analysis of a rocket engine thrust chamber using Chaboche, Voce and Creep constitutive models. *Trans Indian Inst Metals* 69(2):495–500

# Potentiality of Small Punch Test Using Damage Model to Generate J-R Curve of 20MnMoNi55

Pradeep Kumar, B.K. Dutta, J. Chattopadhyay and R.S. Shrivastaw

**Abstract** This study explored the determination of J-R curve and  $J_i$  (fracture toughness) of nuclear structural materials using small punch test of 3 mm disk. The punch load versus central deflection data are collected up to fracture which is signified by the rapid drop in load carrying capability of the specimens. The experimental data for 20MnMoNi55 material is then used to evaluate yield strength and ultimate tensile strength making use of available correlations in the previous studies. These material data are then used to calculate Ramberg–Osgood hardening exponent leading to the generation of complete true stress–strain data. The next task is to determine GTN parameters of the materials which can simulate average  $P/t_0^2$  versus biaxial strain up to fracture. These GTN parameters along with true stress–strain data are then used to generate J-R curves of the materials by finite element modeling of ASTM standard CT specimen. Calculated J-R curves are then compared with the experimental values of previous studies. The proposed methodology has the potential to determine J-R curve and  $J_i$  (fracture toughness) of irradiated material using small punch test.

**Keywords** Miniaturized SPT specimens · Finite element analysis  
Gurson model · J-R curve · Biaxial strain

---

P. Kumar (✉) · B.K. Dutta · J. Chattopadhyay  
Homi Bhabha National Institute, Anushaktinagar, Mumbai 400094, India  
e-mail: pradeep.dgfs@gmail.com

B.K. Dutta  
e-mail: bk Dutta@barc.gov.in

J. Chattopadhyay  
Reactor Safety Division, Bhabha Atomic Research Centre, Hall-7,  
Mumbai 400085, India  
e-mail: jchatt@barc.gov.in

R.S. Shrivastaw  
Post Irradiation Examination Division, Bhabha Atomic Research Centre,  
Mumbai 400085, India  
e-mail: rsshri@barc.gov.in

## 1 Introduction

In those conditions where determination of mechanical properties is necessary but due to limited availability material such as aged materials or in-service components, standard test cannot be conducted. There are now several nonstandard test techniques available which solves such difficulty. The miniaturized small punch test (MSPT) technique is one of them in use to determine change in mechanical properties of the materials, such as yield stress, ultimate stress, ductility and fracture toughness [1–12]. Mao et al. developed 3 mm diameter and 0.25 mm thickness disk bending technique to determine mechanical and fracture properties of several materials in which equivalent fracture strain has been chosen as a fracture parameter for the SP specimen [1, 2]. The acceptable ductile fracture toughness result was found with this fracture parameter. Furthermore, the fracture toughness of aged material has been determined by several researchers using same fracture parameter for the SP test [2–12]. Misawa et al. successfully used this test technique for the identification of change in cracking mode in low toughness steel from low temperature to high temperature and perform statistical analysis of equivalent biaxial strain and fracture toughness [3]. Using such tests, Finarelli et al. [4] estimated mechanical properties of austenitic steel and martensitic steels which were irradiated in a spallation environment with 530 meV protons. Guan et al. [5] implemented small punch test technique to assess fracture toughness of CrMo low alloy steels subjected to long-term reactor service conditions. Similarly, using small punch test specimens, Rodríguez et al. [6] tested a hot-rolled API X-70 steel plate and its heat affected zone at room temperature to estimate elasto-plastic fracture toughness. Furthermore, workers have used material damage GTN model to study the variation in nucleation porosity ( $f_N$ ), critical porosity ( $f_C$ ) and failure porosity ( $f_F$ ) [7, 8]. One of the major challenges at present is to obtain the fracture toughness and J-R curve of a material from this type of test. The main objective of this work is to extend existing methodology of single fracture parameter evaluation to complete J-R of material using SPT. Yield strength (YS) and ultimate tensile strength (UTS) are evaluated using proposed Garcia et al. equations [9]. These strength values from SP test are used to evaluate Ramberg–Osgood hardening exponent and complete true stress and plastic strain data points up to 100% plastic strain. However, GTN damage model is used to simulate the load-central deflection curve obtained from small punch test (SPT) for obtaining the constitutive materials parameters like initial void volume fraction, nucleation void volume fraction, void volume fraction at coalescence and fracture. Furthermore, these numerically calculated GTN material constant values and same true stress and plastic strain data points obtained from SP experiment test are used to generate J-R curve obtained from CT specimen. Finally, some numerical modifications have been carried out in J-R curve using phenomenological form of  $q_2$  parameter in GTN model. Dutta et al. have proposed a phenomenological equation with a statement that  $q_{2a} = 0.3$  and  $q_{2b} = 8$  will be same for SA333 Gr.6 and 22NiMoCr37 materials [10]. The advantage of this material independency of  $q_{2a}$  and  $q_{2b}$  parameters is utilized in this

paper for 20MnMoNi55, which improves J-R initiation as well as remaining part of J-R curve. The numerically modified J-R curve using phenomenological equation is compared with experimental plot. The experimental J-R plot for the validation purpose is taken from published research work [10].

## 2 Materials Used and Experimental Procedure

### 2.1 Materials

This study has been explored for 20MnMoNi55 nuclear structural materials. The chemical composition and mechanical properties at room temperature are shown in Tables 1 and 2, respectively [10].

### 2.2 Small Punch Test Experimental Setup

A Schematic diagram of small punch bend test setup is shown in Fig. 1a, b. The circular disk with  $\phi$  3 mm and initial thickness ( $t_0$ ) is loaded centrally in lower die by the plunger with a hemispherical ball of  $\phi$  1 mm. The fixture has an upper die, a lower die and a plunger. Both the dies are firmly tightened with each other using LN screws as shown in figure. The function of this fixture is to prevent cupping of specimen in upward during loading and, therefore, material is plastically deformed in the region below steel ball. The small punch test experiments have been performed at a crosshead speed of 0.2 mm/min at room temperature at PIED lab BARC, Mumbai.

### 2.3 Small Punch Test Experiment

The specimens were then tested using 5 kN test machine with a load cell of capacity 1000 N having a provision for mounting LVDT. The tests were conducted under

**Table 1** Chemical composition (wt%)

Material	C	Si	Mn	S	P	Ni	Cr	Mo	V	Al	Cu	Nb	W	N	Fe
20MnMoNi55 [10]	0.19	0.23	1.33	0.001	0.007	0.52	0.062	0.53	-	0.056	-	-	-	0.009	bal

**Table 2** Mechanical properties at room temperature

Material	Properties	$E$ (MPa)	$J_i$ (N/mm)	$\sigma_Y$ (MPa)	$\sigma_u$ (MPa)
20MnMoNi55 [10]		2.0E5	150	440	580

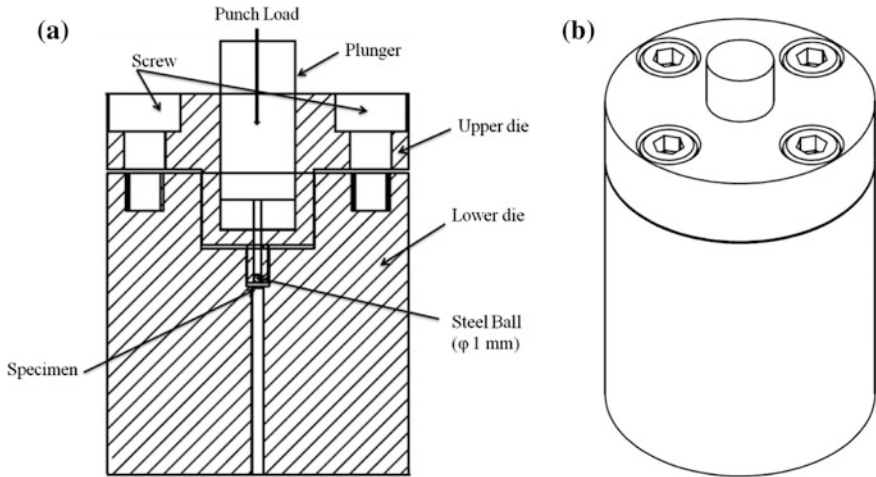


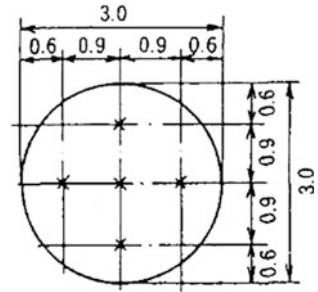
**Fig. 1** a Schematic diagram of small punch test (SPT) fixture, b schematic external view of the SPT fixture along with LN screws

**Table 3** Variation of thickness in SPT specimens of 20MnMoNi55 materials

No. of specimens	T1 (mm)	T2 (mm)	T3 (mm)	T4 (mm)	T5 (mm)	$T_{avg}$ (mm) = $(T1 + T2 + T3 + T4 + T5)/5$
A	0.239	0.235	0.239	0.241	0.235	0.238
B	0.228	0.229	0.223	0.228	0.222	0.226
C	0.220	0.216	0.224	0.217	0.224	0.220

displacement controlled loading with a constant punch velocity of 0.2 mm/min. The experimental load versus central deflection curves are shown in Fig. 3 for all specimens. The standard features in a load versus central deflection curve of SPT as reported in [1], viz., elastic bending, elastic-plastic bending, work hardening, geometrical softening and local necking, micro-cracks initiation, coalescence and complete damage of material are visible in this plot. It is planned to have initial thickness of 0.25 mm for all the specimens. However, after preparation, thickness is found to vary between the specimens as well as within a specimen as shown in Table 3. Thickness is measured at five locations within a specimen. Locations of such measurement are shown in Fig. 2. Average value of initial thickness for each specimen was taken for further analysis.

**Fig. 2** Locations of thickness measurements



### 2.4 Estimation and Comparison of Yield Strength and Ultimate Tensile Strength Using SPT Data

The yield strength (YS) and ultimate tensile strength (UTS) of the materials using SPT data were evaluated using Eqs. (1) and (2) proposed by Garcia et al. [9]. The evaluated yield and ultimate strength using experimental SPT data are shown in Table 4. It is shown in Fig. 3 that specimen’s initial thickness has major influence

**Table 4** Yield strength and ultimate tensile strength of nuclear materials determined by SPT data

Material name	$P_{Y\_Mao}/t_0^2$	$P_m/t_0^2$	Yield strength (MPa)		UTS (MPa)	
			YS values calculated using Eq. 1	% Variation of average values with standard test values	UTS values calculated using Eq. 2	% Variation of average values with standard test values
20MnMoNi55	891	5036	394	8.15	596	3.12

**Fig. 3** Load versus central deflection plot of 20MnMoNi55 steel

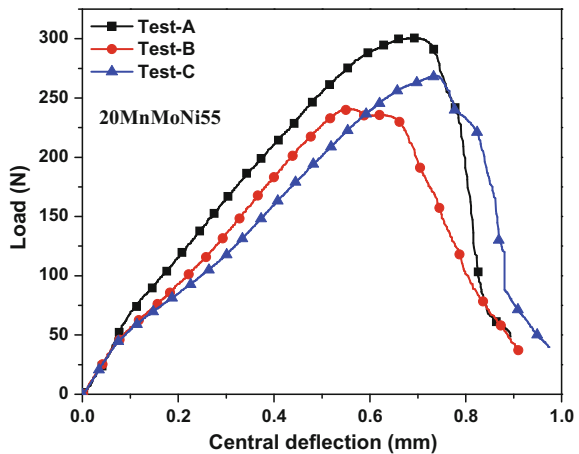
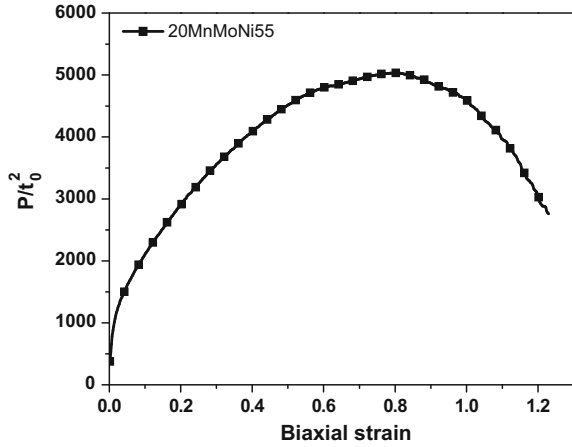


**Fig. 4** Average experimental plot of  $P/t_0^2$  versus biaxial strain



on the SPT curve; therefore, it is worthful to transform experimental SPT data to the average  $P/t_0^2$  versus equivalent biaxial strain up to fracture as shown in Fig. 4. Equivalent biaxial strain was evaluated using equation proposed by Kumar et al. [11]. However, the dependency of initial specimen thickness is practically eliminated when yield and ultimate load are divided by square of initial specimen thickness ( $t_0^2$ ) [1, 9]. Moreover, the average percentage variation of yield strength and ultimate tensile strength with standard test values for 20MnMoNi55 are shown in Table 4.

$$\text{YS (MPa)} = 0.442 \frac{P_{Y-Mao}}{t_0^2} \quad (1)$$

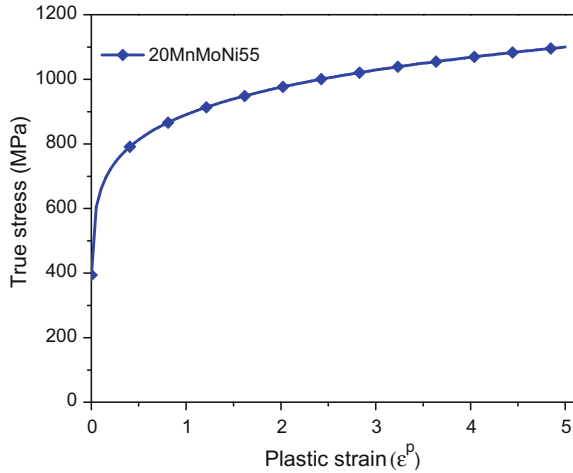
$$\text{UTS (MPa)} = 0.065 \frac{P_m}{t_0^2} + 268.81 \quad (2)$$

## 2.5 Calculation of Ramberg–Osgood Strain-Hardening Exponent and True Stress–Strain Data

The YS and UTS values determined above are further used to determine strain-hardening exponent and true stress–strain data of the material and assumed to follow Ramberg–Osgood hardening law shown in Eq. (3).

$$\frac{\varepsilon^p}{\varepsilon_0^e} = \alpha \left( \frac{\sigma}{\sigma_0} \right)^n \quad (3)$$

**Fig. 5** Generated stress–strain data for three materials using SPT data



Here,  $\epsilon_0^e$  is elastic strain at yield =  $\sigma_0/E$ ,  $\alpha$  is a dimensionless parameter such that  $\alpha(\frac{\sigma_0}{E}) = 0.002$ ,  $n$  is hardening constant,  $\epsilon^p$  and  $\sigma$  are true plastic strain and true stress, respectively. For each material, the values of  $\epsilon_0^e$  and  $\alpha$  are calculated using the average value of yield strength quoted in Tables 4. Using values of  $\epsilon_0^e$  and  $\alpha$  in Eq. (3), a set of true stress–plastic strain data are generated for various trial values of hardening parameter  $n$ . The true stress–plastic strain data are then converted to engineering stress–strain data to know the ultimate stress associated with various trial values of hardening parameter  $n$ . The hardening parameter  $n$  corresponding to which the ultimate stress matches with the value quoted in above Tables 4 is taken as the hardening parameter of that material. This procedure is used not only to know the hardening parameter but also to generate entire true stress–strain curve of the material (Fig. 5).

### 3 FEA Modeling and Determination of Gurson Parameters

#### 3.1 Finite Element Modeling

The axis-symmetric FE models of miniaturized small punch test (MSPT) of 3 mm diameter disk and 0.25 mm initial thickness were developed and simulated using the in-house finite element implicit code MADAM (MAterial DAamage Modeling) [12]. The code has the ability to solve both two- and three-dimensional structures. The quasi-static nonlinear FEA analysis of SP test was performed with quadratic fully integrated axisymmetric elements based on force-based contact model using augmented Lagrange contact algorithm method. Meshing was done using



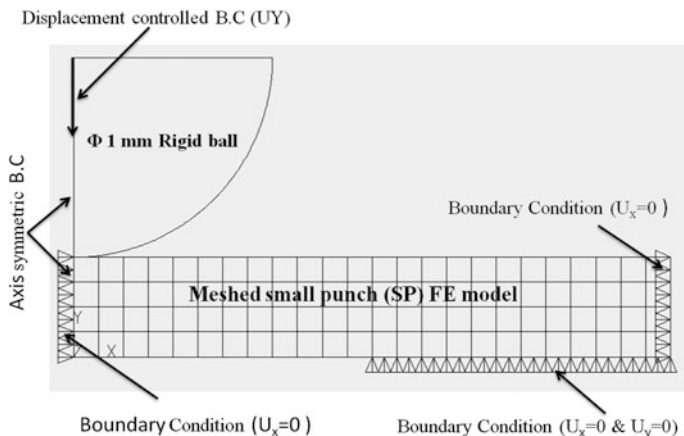


**Fig. 6** FE mesh and boundary conditions of small punch specimen

eight-noded quadratic fully integrated axisymmetric elements with an element size of 0.0625 mm along the radial direction and four equal layers in thickness direction, in accordance with the sensitivity analysis performed in previous studies [8, 11]. The hemispherical steel ball of diameter 1 mm was modeled as rigid body. SP specimen was centrally loaded by hemispherical ball under displacement controlled loading. The boundary conditions are shown in Fig. 6. The coefficient of friction between hemispherical ball and SPT specimen was set to 0.25, in accordance with the contact frictional analysis performed in a previous study [8].

### 3.2 Numerical Calibration of Gurson Material Parameters

For the calibration of Gurson material damage parameters, SPT experiments have been performed. Furthermore, the FE analysis of small punch test was carried out to generate load-central deflection data points with initial thickness of 0.25 mm. However, the experimental and numerical load-central deflection curves were transformed into  $P/t_0^2$  versus biaxial strain ( $\epsilon_q$ ) curves as shown in Fig. 7. Hence, transformed curves reveal that single FE model could be sufficient. On utilizing this concept, three Gurson material parameters viz. nucleation void volume fraction ( $f_N$ ), void volume fraction at coalescence ( $f_C$ ) and void volume fraction at failure ( $f_F$ ) have been evaluated after trial and error method. The other six Gurson material parameters have assumed to be constant according to the literature. Determination of all these parameters is done by comparing numerically calculated  $P/t_0^2$  versus biaxial strain ( $\epsilon_q$ ) curves curve with the average of experimentally measured values. The comparison method includes the rate of load drop/slop with the central

**Fig. 7** Average experimental and numerical plot of  $P/t_0^2$  versus biaxial strain and corresponding Gurson parameters for 20MnMoNi55

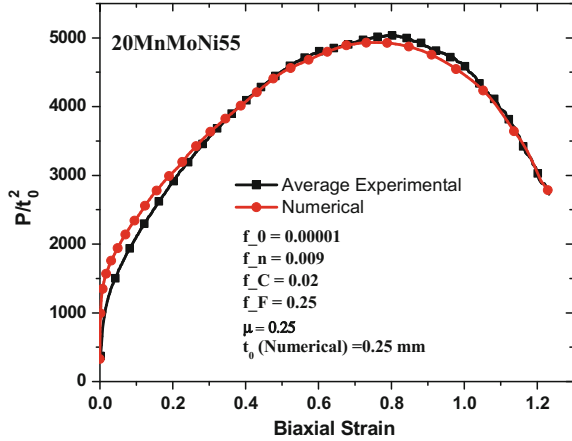


**Table 5** Numerically calibrated GTN and friction parameters

Material	GTN and friction parameters	Numerically calibrated values
20MnMoNi55	Initial porosity ( $f_0$ )	0.00001
	Nucleation porosity ( $f_N$ )	0.009
	Critical porosity ( $f_C$ )	0.02
	Failure porosity ( $f_F$ )	0.25
	Coefficient of friction ( $\mu$ )	0.25

displacement/biaxial strain must be same for both because this region of curve is the manifestation of fracture process in the specimen. Gurson parameters determined numerically are also listed in Table 5.

## 4 Estimation of J-R Curve Using SPT Data

### 4.1 Finite Element Modeling of CT Specimen

The Gurson parameters shown above are then used to generate J-R curve. For this purpose, an ASTM E1820 standard CT specimen was modeled by finite elements. The geometrical details and FE model with the zoomed view near to crack tip region are shown in Fig. 8. The 8-noded 2-D isoparametric plane strain finite elements are used for the modeling. Only half of the CT specimen is modeled with appropriate symmetric boundary conditions as shown in Fig. 8. Seven hundred and forty elements with 2343 nodes are employed to model the specimen. The minimum size of the element in FE model surrounding the crack tip is 0.2 mm  $\times$  0.2 mm. This element size leads to the average distance between two Gauss points as

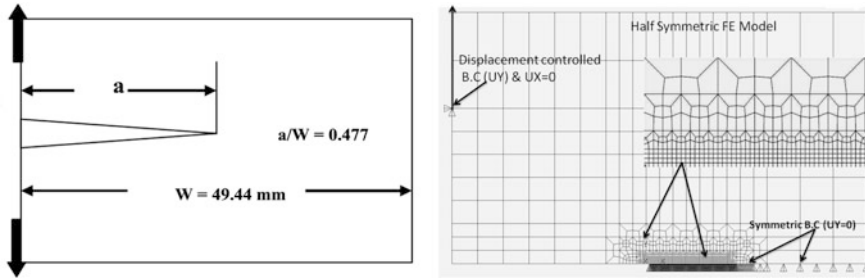


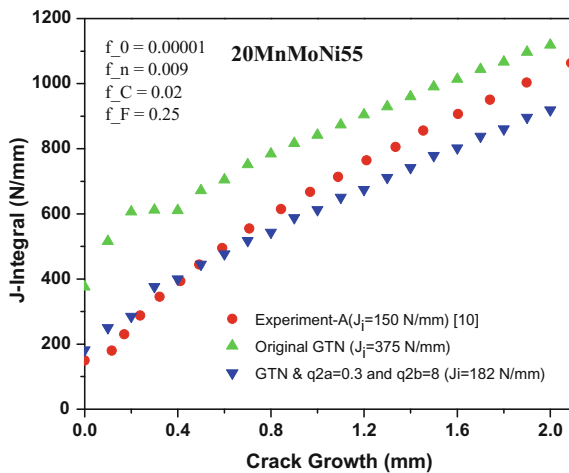
**Fig. 8** Detailed schematic diagram of CT specimen and FE model with the zoomed view of the crack tip region

0.1 mm along the crack line. This average distance is same as the characteristic length  $l_c$  in Gurson material model. The loading is assumed to be displacement controlled.

### 4.2 Numerical Estimation of J-R Curve

The true stress–plastic strain data points and Gurson parameters estimated from SPT data are used for J-R curve estimation from CT specimen. The J-integral at the crack tip as a function of load was calculated as per standards ASTM E-1820. The crack growth is determined by calculating the maximum distance between crack tip and Gauss points which are lying along the crack line and completely damaged. The numerically evaluated load versus load-line-displacement and crack increment data points are then used to get J-R curves, which are shown Fig. 9. The same figure also shows the experimental values of J-R curves taken from the literature [10]. It may

**Fig. 9** Predicted J-R curves using Gurson material model in comparison with experimental values for 20MnMoNi55 materials



be seen that the slope of the calculated J-R curves match well with the experimental values. However, calculated J-R curves are bodily shifted upwards with respect to experimental values leading to much higher values of J-initiation. Similar difficulty was reported in [13].

### 4.3 Numerical Modification of J-R Curves Estimation

To overcome the difficulty described above, computations are redone incorporating the suggestions of [13]. Dutta et al. [13] suggested a phenomenological form of  $q_2$  Gurson parameter to improve the prediction of J-initiation and also the entire J-R curve. The suggested form of  $q_2$  parameter is shown in Eq. (4).

$$q_2 = 1 + q_{2a} e^{-(r/l_c)/q_{2b}} \quad (4)$$

The values of two additional material constants which are used to describe  $q_2$  are  $q_{2a} = 0.3$  and  $q_{2b} = 8$  for two ferritic steels [13]. Same values of  $q_{2a}$  and  $q_{2b}$  are used in the present analysis. Figure 9 shows the modified J-R curves using such variation of  $q_2$  near the crack tip. A remarkable improvement in prediction of J-initiation and entire J-R curve may be seen in Fig. 9.

## 5 Conclusions

The following conclusions are summarized as below.

1. Yield strength and ultimate tensile strength of 20MnMoNi55 obtained in SP experiment are acceptable values as compared to standard.
2. Ramberg hardening exponent and stress-strain curve obtained by small punch test simulates acceptable plot of average  $P/t_0^2$  versus biaxial strain up to fracture.
3. The Gurson material parameters are verified with bilateral experimental test results, viz., SP test with average  $P/t_0^2$  versus biaxial strain up to fracture and CT test with J-R curve.
4. Numerically evaluated Gurson parameters with  $q_{2a} = 0.3$  and  $q_{2b} = 8$  produce acceptable J-R curve and J-initiation values for each materials.

## References

1. Mao X, Takahashi H (1987) Development of a further miniaturized specimen of 3 mm diameter for TEM disk ( $\varphi$  3 mm) small punch tests. J Nucl Mater 150:42–52
2. Mao X, Takahashi H, Kodaira T (1992) Supersmall punch test to estimate fracture toughness  $J_{ic}$  and its application to radiation embrittlement of 2.25 Cr–1Mo steel. Mater Sci Eng A150:231–236

3. Misawa T, Nagata S et al (1989) Fracture toughness evaluation of fusion reactor structural steels at low temperatures by small punch tests. *J Nucl Mater* 169:225–232
4. Finarelli D, Roedig M, Carsughi F (2004) Small punch test on austenitic steel and martensitic steels irradiated in a spallation environment with 530 MeV protons. *J Nucl Mater* 328:146–150
5. Guan Kaishu, Hua Li et al (2011) Assessment of toughness in long term service CrMo low alloy steel by fracture toughness and small punch test. *Nucl Eng Des* 241:1407–1413
6. Rodríguez C, Cardenas E et al (2013) fracture characterization of steels by means of the small punch test. *Exp Mech* 53:385–392
7. Alegre JM, Cuesta II, Bravo PM (2011) Implementation of the GTN damage model to simulate the small punch test on pre-cracked specimens. *Procedia Eng* 10:1007–1016
8. Kumar P, Dutta BK, Chattopadhyay J, Shriwastaw RS (2016) Numerical evaluation of J-R curve using small punch test data. *Theor Appl Fract Mech* (2016), [dx.doi.org/10.1016/j.tafmec.2016.08.003](https://doi.org/10.1016/j.tafmec.2016.08.003)
9. Garcia TE, Rodriguez C et al (2014) Estimation of the mechanical properties of metallic materials by means of the small punch test. *J Alloy Comp* 582:708–717
10. El-Fadaly MS, El-Sarrage TA, Eleiche AM, Dahl W (1995) Fracture toughness of 20MnMoNi55 steel at different temperatures as affected by room-temperature pre-deformation. *J Mater Process Technol* 54:159–165
11. Kumar P, Chattopadhyay J, Dutta BK (2016) On the correlation between minimum thickness and central deflection during small punch test. *J Nucl Mater* 475:37–45
12. In house finite element code MADAM (MAterial DAmage Modeling) developed by Reactor Safety Division (RSD), BARC technical report (1999), India
13. Dutta BK, Guin S, Sahu MK, Samal MK (2008) A phenomenological form of the q2 parameter in the Gurson model. *Int J Press Vessels Pip* 85:199–210

# Experimental Facility for Thermal Striping Studies in Dynamic Sodium Environment

S. Vijayaraghavan, P. Rajasundaram, T. Chandran,  
M. Shanmugavel, B. Babu and P. Selvaraj

**Abstract** In the Prototype Fast Breeder Reactor [PFBR], sodium coolant streams flowing out through the various fuel and blanket subassemblies mix in the sodium pools. This mixing interface is unstable, oscillating and the component structures nearby are subjected to the effects of oscillating temperature conditions causing stresses to be induced in the components. Thermal striping [TS] occurs due to the random thermal cycling of a structural component by a flow stream resulting from the mixing of nonisothermal jets near that component. The random thermal cyclic load leads to development of surface cracks and assist in crack growth which in turn may lead to failure of the structural component due to crack initiation by the high cycle fatigue mode. TS has been a critical mode of failure which has been studied in many FBR systems worldwide. An experimental facility has been constructed and commissioned at FRTG to study TS by conducting in-sodium experiments simulating the fuel-blanket interface to measure the temperature fluctuations on the surface due to mixing of nonisothermal jets in sodium. This paper brings out the spectrum of activities involved in establishing this test facility, focusing on its features, the challenges overcome, testing philosophy adopted for the effective utilisation of experimental facilities for conducting the TS experiments.

**Keywords** INSOT · Fatigue · Experiments · Thermal striping · Sodium Operation Loop

---

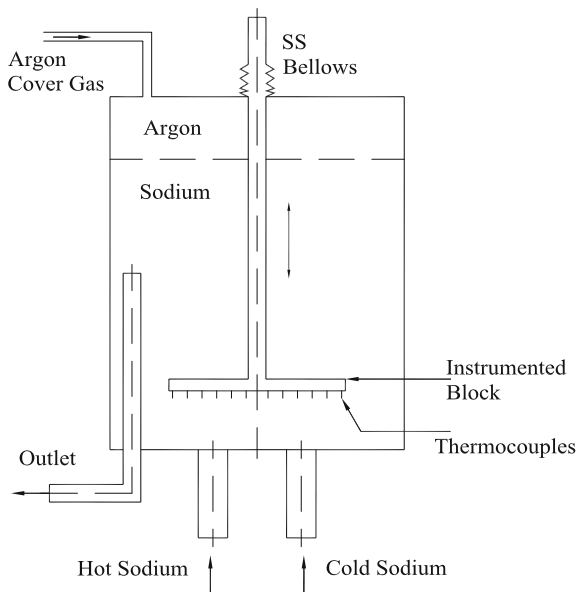
S. Vijayaraghavan (✉) · P. Rajasundaram · T. Chandran · M. Shanmugavel  
B. Babu · P. Selvaraj  
Fast Reactor Technology Group [FRTG], Indira Gandhi Centre for Atomic Research  
[IGCAR], Kalpakkam, India  
e-mail: svrag@igcar.gov.in

© Springer Nature Singapore Pte Ltd. 2018  
S. Seetharamu et al. (eds.), *Proceedings of Fatigue, Durability and Fracture Mechanics*, Lecture Notes  
in Mechanical Engineering, [https://doi.org/10.1007/978-981-10-6002-1\\_4](https://doi.org/10.1007/978-981-10-6002-1_4)

## 1 Introduction

Thermal striping [TS] is a thermal hydraulic phenomenon which occurs due to random thermal cycling created due to the mixing of different temperature streams of sodium flow on the surface of structural components. The structural components could fail if the temperature fluctuations are high in magnitude and oscillation. Hence, it is important to study the mixing behaviour in sodium, where thermal fluctuation is transferred to the component surface without much attenuation at the boundary layer due to high thermal conductivity of liquid sodium. With this objective, an experimental set-up has been incorporated in the existing fatigue loop of **IN-SODium Test** facility for materials testing [INSOT]. To study the temperature fluctuations of two nonisothermal jets, a simulation of cold and hot streams of sodium with definite temperature difference of  $150\text{ }^{\circ}\text{C}$ , impinging on an instrumented plate immersed in a dynamic sodium pool has been created in the TS test set-up (Fig. 1). The results of the In-sodium experiments conducted will be utilised to validate the computational analysis of the mixing phenomena.

**Fig. 1** TS at the interface of two parallel nonisothermal jets



## 2 Objective of the Experiments

The objectives of carrying out the TS studies in sodium are as follows;

- (a) To understand the thermal hydraulic phenomena in the mixing region of nonisothermal streams in sodium.
- (b) To arrive at an appropriate extrapolation rule, that can improve accuracy of prediction from studies conducted in water.
- (c) To assess the Boundary Layer Attenuation (BLA) of thermal fluctuations in case of sodium.
- (d) These studies will also be utilised for validation of numerical codes.
- (e) To study the fatigue damage assessment due to TS.

In sodium cooled FBR's, situations exist where sodium streams having a temperature difference of 100–150 °C mix in the vicinity of the structural parts. These situations occur in the mixing of fuel and blanket sodium flows below the control plug, fuel and control rod subassembly flows near control and safety rod drive, mechanism (CSRDM), intermediate heat exchanger (IHX) outlet primary sodium near main vessel and inner vessel, etc. The TS studies earlier were carried out in scaled down models using water as stimulant [1]. It is possible to extrapolate the fluid thermal fluctuations as measured in water into sodium condition using appropriate similarity laws. However, the thermal fluctuations as seen by the structures in sodium cannot be directly estimated from the studies carried out in water since the attenuation of thermal fluctuations in the boundary layer is less in case of sodium than water due to the higher thermal conductivity of sodium.

## 3 Experimental Facility

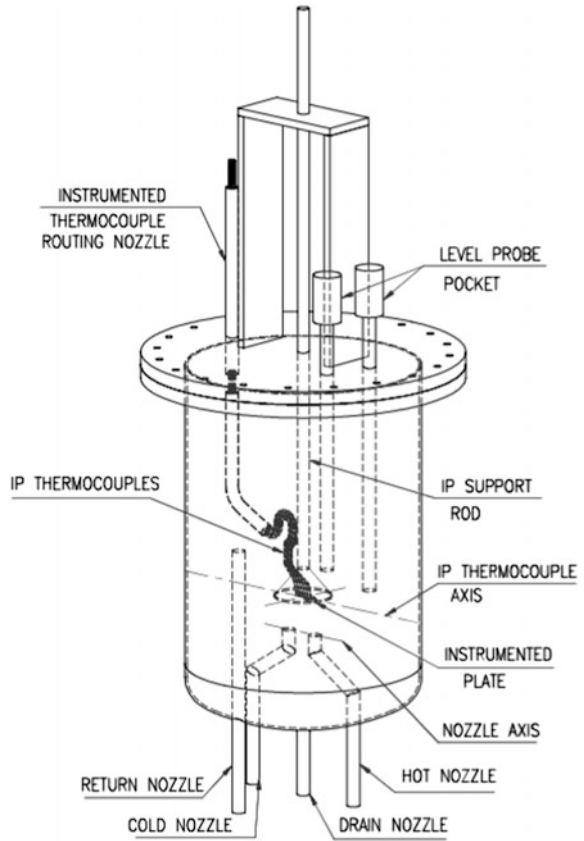
Fatigue loop of INSOT has been integrated with [8] the thermal striping test set-up [TSTS] consisting of sodium thermal striping test vessel [TSTV] with the testing mechanism, heater vessels and the connecting stainless steel pipelines. It was ensured that there was no ingress of atmosphere, metallic burrs, oils into the loop during modification works to avoid addition of any impurities such as oxygen, moisture, carbon to the system. The components required have been fabricated, inspected and qualified for sodium service.

## 4 Thermal Striping Test Vessel (TSTV) and Piping

The TSTV is shown in Fig. 2; its size is 600 mm inner diameter and 961 mm in height. The vessel has been fabricated from 316 L grade stainless steel [SS] materials and is covered by a gasket-sealed top flange. The TSTV consists of two



**Fig. 2** View of thermal striping test vessel



inlet circular jet nozzles connected to the loop piping for maintaining hot and cold sodium jets at different temperatures. An instrumented plate [IP] is mounted on a 30 mm diameter rod supported from the top flange by a screw-nut mechanism through a bellows sealing arrangement (Fig. 6). Position of the IP has been calculated to ensure that it is completely immersed in the dynamic pool of sodium maintained in the test vessel during its vertical travel to and from the nozzles. The sodium level is continuously monitored and indicated by continuous and discrete mutual inductance [MI] level probes mounted on the top flange nozzles. The hot and cold nozzles, the inlet hot and cold sodium piping, drain and return sodium pipelines are supported from the bottom dished end of the TSTV.

### 5 Operation Philosophy and Process Requirements

The operation philosophy is to fill the loop with sodium after conducting all checks, circulate in the loop and purify the sodium with TSTV isolated. Sodium is then admitted into the TSTV, purified and operated at an isothermal temperature of 300 °C. Purity of sodium is maintained within acceptable level by continuous online cold trapping, and the impurity level is periodically monitored using plugging indicator. Sodium in the storage tank is kept isolated. The loop temperature is steadily increased to the test condition required in the hot and cold nozzles of the test vessel by means of immersion heater vessels in incremental stages ensuring stabilisation of the system at each step. The TSTS has an arrangement of hot and relatively cold sodium jet passing to the TSTV through a heat exchanger and heater arrangement. The heat balance in the thermal stripping test section and the utility of the bye-pass line provided to maintain the cold and hot stream temperatures has been evaluated and found adequate [7]. During these test campaigns, operation parameters of sodium system like flow rate, purity, level, temperature were monitored and maintained as per the test requirements. Sodium to sodium heat exchanger, immersion heater vessels, sodium to air heat exchanger (NAX) and EM pump have been provided in the loop to maintain the hot and cold jet temperatures with the required velocities. Sodium-air heat exchanger has been used intermittently as a heat sink to maintain the temperature of cold leg region of the loop below 350 °C. Figure 3 gives the schematic layout of fatigue loop with the TS section.

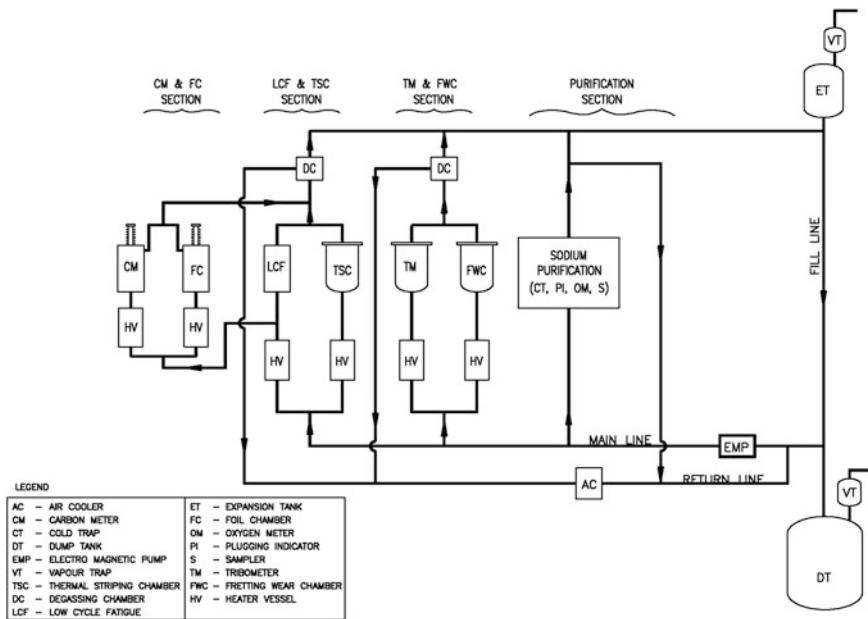


Fig. 3 Schematic diagram of fatigue loop with TS set-up

## 6 Experimental Methodology

The experimental phase of a TS campaign commences as soon as the test parameters of temperature and flow is established and the system has stabilised. The temperature distribution across the mixing zone of the two inlet circular jet nozzles inside the test vessel is measured by the Instrumented Plate thermocouples (IPTC) embedded on the IP. During each test condition, the test data from the embedded thermocouples on the IP, cold, hot sodium inlet nozzles and mixed outlet pipeline of the TSTV were acquired in real time by a high-speed, portable data acquisition system. Temperature profile was also measured in two mutually perpendicular planes, and the temperature data were recorded. The readings were taken at every 10 mm interval vertical positions of the IP by varying the distance between IP and the hot and cold nozzles levels using a screw-nut mechanism mounted on top flange of test vessel. The TS experiment has been conducted with hot sodium jet temperature range of 450–550 °C and cold sodium (relatively cold) jet temperature range of 300–450 °C, with total sodium flow rate varied from 0.1 m<sup>3</sup>/h to a maximum of 1 m<sup>3</sup>/h as per the experimental parameters.

## 7 Experimental Scheme for TS Studies at INSOT Loop

The nozzle outlet geometry for the full series of experiments is circular outlet. The following parametric studies have been planned and carried out during the experiments [11].

- (a) Validating our experiment with published data in the literature (Wakamatsu Model) [14].
- (b) Effect of Peclet number (Pe) variation with same velocity ratio between hot and cold jet.
- (c) Effect of Pe variation with same Reynolds (Re) ratio between hot and cold jet.
- (d) Effect of Pe variation with same Pe ratio between hot and cold jet.

Process parameter requirements such as flow, temperature ratios have been worked out for each experimental campaign [10].

### *7.1 Scheme for Fixing and Routing of the Thermocouples for the Instrumented Plate*

The TS phenomenon changes rapidly with time; hence, fast response thermocouples are used to measure the temperature and these data are acquired by means of a high-speed data acquisition system [DAS]. The surface temperature fluctuations along with the fluid temperature fluctuations are measured using 13 numbers of

0.65 mm diameter SS sheathed K-type thermocouples which have been embedded on an instrumented plate [IP]. The challenge faced was to safely route these delicate thermocouples from the IP to the exit pipe located on the top flange of the TSTV. Since the IP is a mobile assembly; the thermocouples have been carefully bunched together, ensuring that the routing arrangement is flexible enough with the right slack to allow for the vertical movement during experiments. This arrangement has performed well during the test campaigns.

## 7.2 *Data Acquisition of Experimental Data*

A dedicated DAS has been employed to monitor and store the experimental temperature data from the thirteen IPTC, three thermocouples of hot and cold sodium inlet nozzles and mixed sodium outlet nozzle during each TS experiment. The elevation of the IP has been varied from 5 to 155 mm from the nozzle exit in steps of 5 and 10 mm. Analysis of these temperature data focuses mainly on two parameters; mean temperature distribution and the peak-to-peak temperature fluctuation for the thermal characterisation of the mixing phenomena. Figure 4 shows the view of thermocouples fixed on the IP.

**Fig. 4** Thermocouples (IPTC) fixed on IP



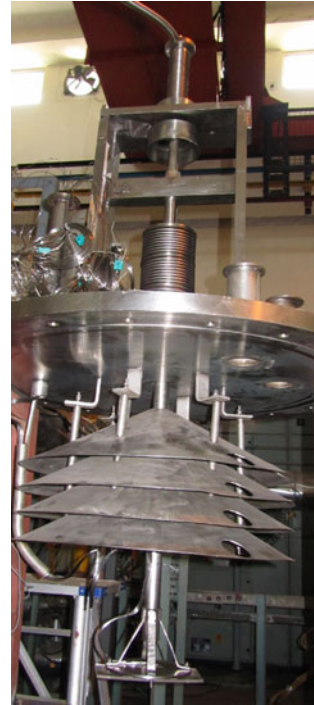
## 8 Commissioning of Thermal Striping Test Set-up (TSTS)

TSTS has been subjected to quality control checks including pressure hold test, the response of all the sensors in cold and hot argon atmosphere in the test vessel, IPTC and the vertical movement of the IP have been carried out to assess the performance and found satisfactory. The functionality and precommissioning checks of the MI level probes, flow, pressure, temperature indicators/controllers, wire- and plug-type leak detectors, SID systems and gas communication clearance for all fill paths were checked before filling of sodium in the loop. All the control and safety interlocks for the safe and systematic operation of fatigue loop were checked and confirmed [6]. Then, the entire loop was preheated to a temperature of 200 °C, monitored and controlled through the PLC-PC-based data acquisition and control system. The cold commissioning works for the TSTS have been carried out systematically including the cold and hot purging with argon gas to ensure that the oxygen and moisture levels in the TSTS were brought down to acceptable levels. The actuation mechanism arrangement erected on the top flange of the TSTV (Fig. 5) for enabling the vertical adjustment of the IP was operated and checked for proper actuation. After checking the performance of the preheating system, cover gas system, sodium system, electrical system, instrumentation system, etc. the loop was made ready for sodium filling. Figure 6 shows a view of the actuation mechanism provided for vertical movement of the IP in the TSTV.

**Fig. 5** Thermal striping test vessel (TSTV)



**Fig. 6** Mechanism for actuation of IP



### ***8.1 Operation of TSTS at 300 °C and Conduct of in-Sodium Trial Test***

The sodium was filled, circulated in the loop, purification of loop sodium was carried out [9] and the sodium was admitted into the TSTS. Sodium level rise was monitored by the MI type continuous and discrete level probes in the TSTV. The temperature of loop sodium was maintained at 300 °C, sodium flow rate was maintained in the cold and hot inlet nozzles of the TSTV. The loop with TSTS was operated at 300 °C steady state, isothermal condition. The operation parameters like flow rate, sodium purity, sodium level and temperature were monitored and maintained to meet the test requirements. The in-sodium trial test was carried out for duration of 120 min. Test data from the IPTC, cold, hot sodium inlet nozzles and mixed outlet pipeline of the TSTV were acquired by DAS. The performance of TSTS in sodium with respect to the establishing of the process conditions and acquiring test data was demonstrated.

## 8.2 Conducting TS Experiments up to 550 °C

The temperatures of cold and hot nozzles have been maintained at a  $\Delta T$  of 150 °C as per the process requirements for testing. Initially, experiments with a relatively cold sodium jet temperature of 300 °C and hot sodium jet temperature of 450 °C have been carried out. The sodium flow rates in the hot and cold nozzles have been varied, established and stabilised for each set of hot and cold nozzle temperatures and sodium flow rate requirements for carrying out the planned TS experiments. Subsequently, experiments with a relatively cold sodium jet temperature of 400 °C and hot sodium jet temperature of 550 °C were carried out. Performance of the immersion heater vessels for maintaining the temperature of hot and cold sodium streams within  $\pm 1$  °C, with its control system operating continuously at high temperatures up to 625 °C, was satisfactory. Many parametric studies have been carried out with various combinations of hot and cold jet sodium flow rate and their temperature difference. Seven successive test campaigns have been carried out from and all planned 156 numbers of TS experiments have been completed [3]. Basic studies in small-scale model to investigate influence of various nondimensional numbers and jet geometry on thermal mixing phenomena have been carried out successfully [2].

## 9 Safety Ethos Followed

Safety has been integrated in every part of the design, construction, erection, commissioning and operation of the sodium system [12, 13]. Design, fabrication and inspection of the components and piping have been carried out as per the standard codes of ASME. Flexibility analysis of piping has been carried out for operation up to 600 °C. Helium leak test of components has been carried out to ensure leak tightness below  $10^{-8}$  std atm.cc/s and qualified for sodium service. All butt weld joints exposed to sodium service have been subjected to LPI and 100% X-radiographed. Wire-type leak detectors have been provided on the surface of pipe lines and components. Leak collection trays are provided below each of the components and piping. Plug-type leak detectors have been provided in the bellows sealed valves. Nondestructive examination comprising of visual testing, liquid penetrant inspection [LPI] and Eddy current testing were conducted to check and qualify the integrity of the thin-walled cross sections of the heater element sleeve of the immersion heater vessels has been carried out between high temperature test campaigns on these areas. Sodium aerosol detector (SAD) is used for detecting global sodium leak from the loop. Adequate quantity of DCP fire extinguishers has been provided in the loop area. The operation, removal, sodium cleaning and installation procedure for each experiment have been followed as per check lists [4, 9]. Early detection, prevention and mitigation approaches to events are inbuilt in the systems for safe operation.

## 10 Future Direction

In-sodium experiments on different material specimens are also in the pipeline to investigate the metallurgical effects of TS. TS experiments with higher flow rates of sodium are being pursued at another test facility in FRTG in order to generate experimental data in sodium to give realistic and practical inputs to the designers and operation personnel.

## 11 Conclusion

The successful operation of the thermal striping test set-up in fatigue loop has been realised by adopting safe work procedures, surveillance, preventive maintenance and inspections of all systems in the facility [4, 5, 9] and ensured the availability of facility for conducting the TS experiments characterisation of thermal mixing due to mixing of two nonisothermal parallel sodium jets in the vicinity of an instrumented plate has been studied. The experimental data generated from these basic studies are very useful for component design and validation of numerical code. The authors wish to acknowledge the teamwork and contribution of the members from the INSOT facilities section and experimental thermal hydraulics section of FRTG, IGCAR in conducting these studies.

## References

1. Banerjee I et al (2009) Experimental simulation of thermal striping phenomena in control plug components of PFBR, NURETH-13, Japan, Sept–Oct 2009
2. Thermal striping studies in sodium at INSOT facility—phase—I, FRTG/ 99518/ EX/ 3015/REV-A, Apr 2014
3. Commissioning and conduct of thermal striping experiments in fatigue loop of INSOT Facility, FRTG/ ID&SD/ 99136/ EX/ 3074/ R-A, Oct 2013
4. Operation procedure for thermal striping test setup in fatigue loop of INSOT, FRTG/IDSD/IFS/99136/ON/3066/R-A, Feb 2013
5. Technical specifications for INSOT operation, FRTG/SFD/99136/TS/3002/Rev-H, Sept 2012
6. I&C modification on fatigue loop for Tribology, Thermal striping and fretting wear experiments, FRTG/STG/99136/DN/3042/R-A, July 2010
7. Heat balance calculation of heat exchanger, heater and NaX provided in thermal striping experiment loop of INSOT, FRTG/ ETHS/ 99518/DN/3009/R-A, June 2010
8. Proposal for introduction of thermal striping and fretting wear experimental set-up in fatigue loop of INSOT facility—safety report”, FRTG/STG/99136/SR/3039/R-A, May 2010
9. Check list for operation in creep and fatigue loops of INSOT facility, FRTG/STG/99136/ON/3041/Rev-A, Sept 2009
10. Process requirement and model size for two jet thermal striping studies in sodium, FRTG/ETHS/99518/EX/3006, Mar 2009
11. Experimental proposal for thermal striping studies in sodium, FRTG/ETHS/99518/EX/3004/R-B, May 2008



12. INSOT fatigue loop operation manual, IGC/MMD/INSOT/OM/Rev-D, Apr 2008
13. INSOT safety report IGC/MDD/INSOT/SR/ Rev-3, 1998
14. Wakamatsu M, Nei H, Hashiguchi K (1995) Attenuation of temperature fluctuations in thermal striping. J Nucl Sci Technol 32(8):752–762

# Linear Elastic Fracture Mechanics (LEFM)-Based Single Lap Joint (SLJ) Mixed-Mode Analysis for Aerospace Structures

**B.K. Mahesha, D. Thulasi Durai, D. Karuppannan  
and K. Dilip Kumar**

**Abstract** This paper investigates the study of crack propagation on single lap joint (SLJ) using cohesive zone modeling (CZM) for aerospace applications. To carry out the above task, linear elastic fracture mechanics (LEFM) approach using finite element methods was used to study the damage propagation in adhesively bonded joints. A traction–separation law was used to simulate the mode-II and mixed-mode-I+II interfacial fractures of adhesively bonded specimens loaded (quasi-static) in three-point bending and mixed-mode bending. An initial crack opening was introduced at the interfaces of the adherend/adhesive. The boundary conditions for SLJ have been set to carry out the interlaminar mode-II (shear mode) and mixed-mode fracture analysis by end notched flexure (ENF) and mixed-mode bending (MMB) methods. Optimized cohesive parameters from the literature survey were used for simulation of the tests, and same parameters have been validated to continue the research work focusing mainly on progressive delamination in SLJ. The total displacement of 10 mm was applied at free end, and as a result the reaction forces at fixed end steadily progressed up to 60% of applied displacement; further it has been observed the model starts failing by reduction in load versus displacement slope curve.

**Keywords** Crack · Linear elastic fracture mechanics · Cohesive zone modeling  
Mode-II fracture toughness · Mixed-mode analysis

---

B.K. Mahesha (✉) · K. Dilip Kumar  
NMAM Institute of Technology, Nitte, India  
e-mail: maheshabk9@gmail.com

D. Thulasi Durai  
CSMST, CSIR-NAL, Kodihalli, Bangalore, India

D. Karuppannan  
ACD, CSIR-NAL, Kodihalli, Bangalore, India

## Nomenclature

SLJ	Single lap joint
LEFM	Linear elastic fracture mechanics
SERR	Strain energy release rate
CZM	Cohesive zone model
ENF	End notched flexure
MMB	Mixed-mode bending
$G_C$	Critical strain energy release rate/fracture toughness
$G_T$	Total strain energy release rate
$G_{IC}$	Fracture toughness in pure mode-I direction
$G_{IIC}$ , $G_{IIIC}$	Fracture toughness in pure mode-II and mode-III direction
$\eta$	Exponent in B–K law
$K_{NN}$ , $K_{SS}$ and $K_{TT}$	Elastic parameters for traction–separation law in the normal direction and the two shear directions
$N_{max}$ , $S_{max}$ , $T_{max}$	Maximum stresses for traction–separation law in the normal direction and the two shear directions
$\Delta L_c$	Characteristic length of the cohesive element
$a_o$	Initial crack length
$\delta$	Delamination length
$t_{ply}$	Cured ply thickness

## 1 Introduction

Fracture mechanics methodology was developed and experimentally demonstrated for the prediction of the growth of bond-line flaws in an adhesively bonded structure that has been with success applied to several engineering problems in recent years. The damage tolerance design concept, originally adopted in the aircraft industry, was based mainly on the well-established concept of linear elastic fracture mechanics (LEFM), and it has gradually gained ground in other engineering fields. Many studies dealing with adhesive joints use the strain energy release rate (SERR),  $G$ , and respective critical value or fracture toughness,  $G_C$ , instead of stress intensity factors because these are not easily determinable when the crack grows at or near to an interface. Linear elastic fracture mechanics (LEFM) has proven to be an efficient tool for analysis of the criticality and propagation rate of an interlaminar defect for a given structural component and service conditions [1]. The scalar quantities which are in use to characterize the resistance of an interlaminar interface to crack propagation are: (a) fracture toughness under static loading for principal loading modes and (b) Paris law parameters and thresholds for cyclic loading [2]. Cohesive zone models (CZMs) can be considered to model the interfacial fracture behavior based on the concept of local stresses and fracture mechanics using continuum approach of either equally or differentially oriented

plies in stacked composites or the adhesive/adherend interface to simulate adhesive failure [3].

Interlaminar fracture toughness tests were conducted under pure mode-I, pure mode-II, and mixed-mode-I+II loading [4]. Test data were used for development of numerical simulations and their validation [4]. Mode-I, mode-II and mixed-mode-I+II fracture toughness tests are conducted as per ASTM D5528, ASTM D7805, and ASTM D6671 [5–7]. The test procedure and fracture toughness calculations are not presented in current work since it is well defined in the open literature. However, a brief detail of all tests and measured fracture toughness is presented, and this detail can be found in the literature [4, 8]. Cohesive zone models are based on interface elements where propagation occurs without any user intervention which has the ability to simulate crack initiation and crack propagation [9–11]. From Benzeggagh–Kenane (B–K) law [12] the measured fracture toughnesses  $G_{IC} = 325 \text{ J/m}^2$ ,  $G_{IIC} = 2492 \text{ J/m}^2$ . These data are used for development and validation of numerical simulation for ENF and MMB test. A bilinear traction–separation description of a cohesive zone model was employed to simulate progressive damage in the adhesively bonded joints [13]. The single lap joint has been modeled and analyzed using the geometrically nonlinear finite element method [14]. A damage law used was able to simulate damage evolution prior to crack growth using power law relationship to define damage rate [15]. Mode-II cohesive zone parameters were used directly from the previously determined mode-I parameters [4] to predict the fracture and deformation of mixed-mode geometries [8].

## 1.1 Scope of the Work

Adhesive bonded joints are ideal for joining parts in highly contoured, low-observable composite structures for aerospace structural applications; it is also critical in certifying the repaired bonded joints in assemblies [3]. In view of above-said scientific problems, there is a need to understand the behavior of adhesively bonded joints under complex bilateral loading conditions, which includes statics and dynamics. This research will address the durability damage and fracture development in adhesive composite joints.

The delamination process is frequently met in composite materials, and in most cases it results from mode-I, mode-II, or mixed-mode-I+II delamination. The present study concerns the simulation of delamination initiation and propagation in the mode-II and mixed-mode loadings.

Cohesive zone model (CZM) was developed in a continuum damage mechanics framework and made use of fracture mechanics concepts to improve its applicability [2]. The advantage of using CZM is their ability to simulate onset and growth of damage without the requirement of an initial flaw, unlike classical fracture mechanics approach. CZM fits seamlessly into available FE tools to model the fracture behavior of adhesively bonded joints and thus opening a scope and possibilities to carry out the research problem.

## 2 Approach

The aim of this investigation is to study types of damages and their propagations in SLJs to establish simplicity in design and to increase service efficiency. Presently large amount of databases has been archived on experimental methods to understand SLJ and always been the subject of considerable research. In-line to this finite element method will play a significant role in SLJ structural analysis and are capable of solving problems with various types of damages in adhesively bonded joints; combining with the concepts of linear elastic fracture mechanics based CZM provides a practical and convenient means of studying the damage propagation in adhesively bonded joints. The damage modes in SLJ and the damage propagation were studied and presented in this paper as a nonlinear finite element analysis.

The CZM is an advanced numerical analysis technique in the area of fracture mechanics to understand the separation of the surfaces involved in crack propagation across an extended crack tip or cohesive zone. The limitation of CZM is restricted by cohesive tractions. The CZM formulation brings out robustness, stability, and integrity of FE model by evaluating cohesive parameters (penalty factor and  $\delta_{\text{ratio}}$ ). CZM implicitly represents traction–separation laws to model interfaces or finite elements. The analyzed results will be used to demonstrate the use of cohesive zone approaches for the design of adhesively bonded SLJ and to validate approaches for determining the relevant properties to define mixed-mode (tension and shear) interaction in SLJ [16]. An eight-noded cohesive element for modeling delamination was used between shell elements on the basis of a 3D cohesive element previously developed by authors [4, 10] is proposed.

In addition to mode-II analysis, this paper also focuses on different ratios of  $G_{\text{II}}/G_{\text{T}}$  MMB modals to show good agreement with assumptions and boundary conditions in literature [10, 16]. The quadratic interaction between the tractions is proposed to predict delamination propagation for the mixed-mode fracture toughness. In post-processing ABAQUS/Standards, the validation part will reproduce load–displacement response of (i) ENF and (ii) MMB from literature [8]. Finally, SLJ will be modeled in 2D to show cohesive element for shells which can be used to represent the onset propagation of delamination in composite structures.

### 2.1 Fracture Mechanics Approach

#### 2.1.1 Cohesive Zone Modeling

A relatively effective method for prediction of delamination and growth within the framework of damage mechanics is cohesive zone model (CZM). CZM can be used to predict both the initiation of a new crack and growth of an existing crack [8]. CZM is widely used in finite element tools for interfacial failure or disbond/delamination modeling. The increased application of cohesive element

with ABAQUS has both standard (implicit) and explicit solution procedures enabling the user to model a defined plane of finite or zero thickness where the crack is expected to develop in the structure. The interface response in cohesive element modeling is defined by parameters such as fracture energy is obtained from fracture toughness test. The constitutive response of these elements depends on the specific model and certain assumptions about the deformation and 3D stress vectors.

**2.1.2 Bilinear Traction Separation Law**

The law states that cohesive elements should follow linear path governed by its elastic parameters such as  $K_{NN}$ ,  $K_{SS}$ , and  $K_{TT}$ . Once the traction reaches the nominal value of  $N_{max}$ ,  $S_{max}$ , and  $T_{max}$  the stiffness of the element reduces gradually. Traction–separation based modeling is opted for these simulation(s) [8]. Response of the traction–separation law is defined within the base framework of CZM [10]. The element follows a linear (or exponential) degradation post-initiation response.

The work done to completely degrade the cohesive element stiffness to approximate zero is called fracture energy  $G_C$ . Further degraded cohesive element acts only as a contact region to deny any physically impermissible crossover of the two base structures close to overlap zone. The element fails completely with final displacement  $\delta_{fail}$  (Fig. 1).

All the above cohesive element parameters are material dependent as shown in the equations

$$N_{max} = 2 \frac{G_{IC}}{\delta_{fail}} \tag{1}$$

$$S_{max} = T_{max} = 2 \frac{G_{IIC}}{\delta_{fail}} \tag{2}$$

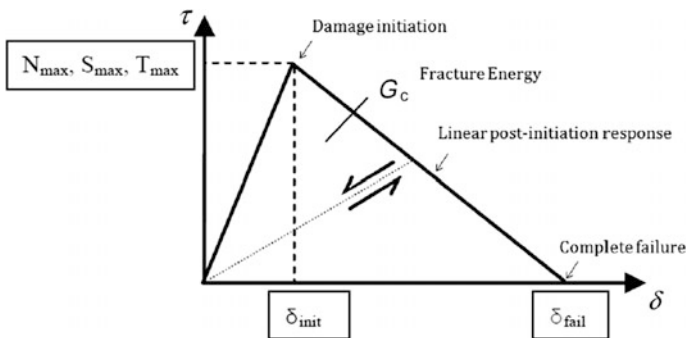


**Fig. 1** Traction–separation law for cohesive elements

$$K_{NN} = 2 \frac{G_{IC}}{\delta_{ratio} \times \delta_{fail}^2} \quad (3)$$

$$K_{SS} = K_{TT} = 2 \frac{G_{IIC}}{\delta_{ratio} \times \delta_{fail}^2} \quad (4)$$

where penalty factor =  $\delta_{fail}/\Delta L_c$  and  $\delta_{ratio} = \delta_{init}/\delta_{fail}$ .  $G_{IC}$  and  $G_{IIC}$  are the fracture energies measured from mode-I and mode-II fracture toughness tests experimentally, in this case from literature [4].  $G_{IIIC}$  is assumed to be equal to  $G_{IIC}$ .  $\Delta L_c$  is decided by the over meshing factor (OMF). OMF is the ratio of structural mesh to cohesive zone mesh. The cohesive zone mesh need to finer than the surrounding structural mesh based on modeling experience by the authors [8].

### 2.1.3 Benzeggagh and Kenane (B–K) Law

In the analyses presented herein, energy-based Benzeggagh and Kenane (B–K) law was used for damage evolution criterion as shown in Eq. (5). In general, each load case is a combination of mode-I/II thus bringing the mixed-mode B–K criterion to play vital role for damage evolution. Interface failure is expected for a given mixed-mode ratio  $G_{II}/G_T$ , when  $G_T$  exceeds the  $G_C$ .

$$G_{IC} + (G_{IIC} - G_{IC}) \left( \frac{G_{II}}{G_T} \right)^\eta = G_T \quad (5)$$

It is assumed that the onset of damage can be predicted by quadratic normal stress criterion. Damage is assumed to initiate when nominal stress ratios reaches a value of 1 given in Eq. (6).

$$\left( \frac{N}{N_{max}} \right)^2 + \left( \frac{S}{S_{max}} \right)^2 + \left( \frac{T}{T_{max}} \right)^2 = 1 \quad (6)$$

## 3 Simulation and Validation

It is important to use proper stiffness definition of cohesive elements in numerical simulation of delamination or disbond [8]. Cohesive element poses numerical convergence issues if softening constitutive model stiffness is not optimized. Furthermore, cohesive parameters like penalty factor and  $\delta_{ratio}$  affect computation time, accuracy of results and output file size. The stress and stiffness for cohesive elements in opening mode were calculated from the fracture toughness measured from test data using Eqs. (1–4).

### 3.1 Parametric Study of Cohesive Elements from Simulation of ENF and MMB Tests

Using the ABAQUS/CAE (Pre-processor), the finite element model of ENF specimen was modeled. The model is composed of two sub-laminates, each of 1.8 mm thick. The initial crack length  $a_0$  is 41 mm, and total laminate length ( $L$ ) is 120 mm and width ( $w$ ) is 25 mm. Each sub-laminate has a stacking sequence of  $[0_{10}]$ . The material properties and dimensions of ENF specimen used in modeling are mentioned in Table 1 and Fig. 2, respectively. The laminate consists of 20 plies (all  $0^\circ$  orientation), with the initial delamination at the midplane. Figure 2 shows the configuration of the specimen along with the boundary conditions applied [8].

Each sub-laminate was modeled with four-noded shell elements (S4R) and a layer of eight-noded cohesive element (COH3D8) was modeled at mid plane next to the pre-crack region to simulate progressive damage growth under mode-II loading. Tie constraints were used to tie the top and bottom faces of cohesive element layer to the shell elements. The thickness of cohesive elements was taken as 0.01 mm. In order to aid the convergence of simulation in the nonlinear region, viscosity parameter of  $1 \times 10^{-5}$  was used for cohesive elements [8]. OMF of five has been used as found in Diehl's work [10]. A mesh convergence study was conducted while assuming penalty factor and  $\delta_{\text{ratio}}$  of 0.08 and 0.5, respectively (Table 2).

Using above-said parameters and properties, MMB specimen has been modeled. The specimen was composed of two sub-laminates each of 1.67 mm thick. The initial crack length ( $a_0$ ) is 27.5 mm, and the total specimen length ( $L$ ) is 100 mm and width ( $w$ ) is 25 mm. Each sub-laminate has a stacking sequence of  $[0_{10}]$ .

In MMB test, the failure is assumed in the specimen once crack growth initiates and crack growth leads to unstable. The cohesive element layer was modeled only up to 10 mm from crack tip along the length of specimen. Different  $G_{II}/G_T$  ratios (literature [8]) were simulated by applying different displacement boundary conditions using kinematic coupling feature available in ABAQUS/standard.

The advantage of kinematic coupling is that different mode ratios can be simulated simply by changing the length  $C$  of loading lever. A schematic of the developed numerical model (specimen, interface elements and applied boundary conditions) is shown in Fig. 3. The green line in Fig. 3 represents loading lever which is connected to the specimen with hinged boundary conditions. Loading lever transferred only load without generating any moment at the connection.

**Table 1** Material properties of IMA/M21 prepreg

$E_{11}$	115 Gpa
$E_{22}$	10 Gpa
$G_{12}$	5.2 Gpa
$\nu_{12}$	0.302
$t_{\text{ply}}$	0.182 mm
$a$	41 mm



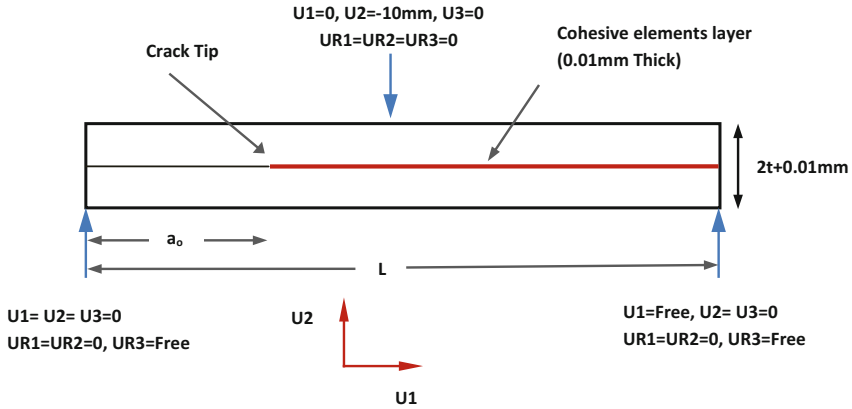


Fig. 2 Schematic of ENF specimen model

Table 2 Optimized cohesive element parameters

Cohesive element parameter	Refined value
Penalty factor	0.08
$\delta_{ratio}$	0.5

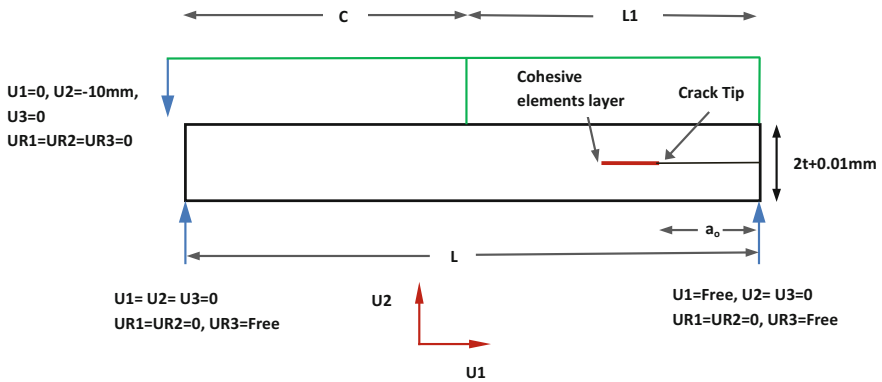
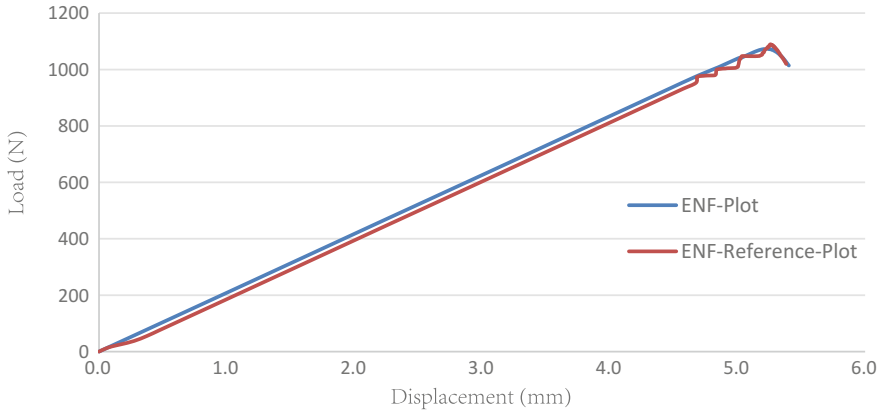


Fig. 3 Schematic view of MMB specimen model

### 4 Results and Discussion

The model of ENF specimen uses 9600 structural (S4R) elements of 1 mm × 1 mm size and 6900 cohesive elements (COH3D8) of size 0.2 mm × 0.2 mm. The numerical simulation of ENF test typically takes about 7 h of CPU time and generates an output file size of about 4 GB.



**Fig. 4** Comparison of reaction load versus applied displacement for simulation of ENF test with literature

The global response of the tested ENF specimens in terms of load (RF2) versus displacement (U2) curves is depicted from numerical simulation, and it was observed that accurate results were obtained by comparing it with the model from literature [4]. From Fig. 4, we can observe that a good repeatability of the results exhibits an initially linear response, followed by increasing nonlinearities, as the crack begins to propagate. The crack propagated in a stable manner during the displacement control fracture testing of models.

In similar way, the model of MMB specimen uses 5000 structural (S4R) elements and 62,500 cohesive elements (COH3D8). The plot of reaction load (RF2) versus applied displacement (U2) for different mode ratios was generated from numerical simulation for all load cases and compared with reference data from literature. Figure 5 shows the load–displacement data which show good agreement with reference data. The FE analysis were forcefully terminated once crack start to grow due to a fact that numerical simulation faces convergence issues for simulation of sudden drop in stiffens and requires high computation time.

The numerical simulation of MMB test typically takes about 50 h of CPU time and generates an output file size of about 11 GB.

By validating ENF and MMB numerical simulations, the model is comparable with literatures with optimized parameters and properties. Henceforth, same methodology has been taken to develop a single lap joint mixed-mode analysis in next section.

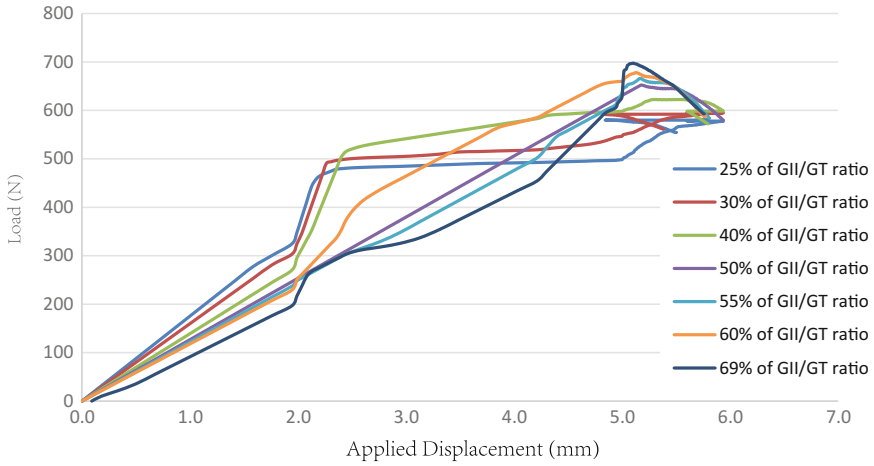


**Fig. 5** Comparison of reaction load versus applied displacement for simulation of MMB test with literature

### 5 Numerical Modeling of SLJ

The standard single lap joint was modeled by two laminates of size 175 × 125 mm (approximately) as shown in Fig. 6 and bonded together alongside the components. As the surface preparation plays important role on adhesive strength, the component and traveler panel shall undergo the same treatment and at the same time.

For the SLJ, the finite element model of the mixed-mode specimen was developed in preprocessor ABAQUS/CAE. The specimen is composed of two sub-laminates, each of 1.80 mm thick with four-noded plane stress shell elements

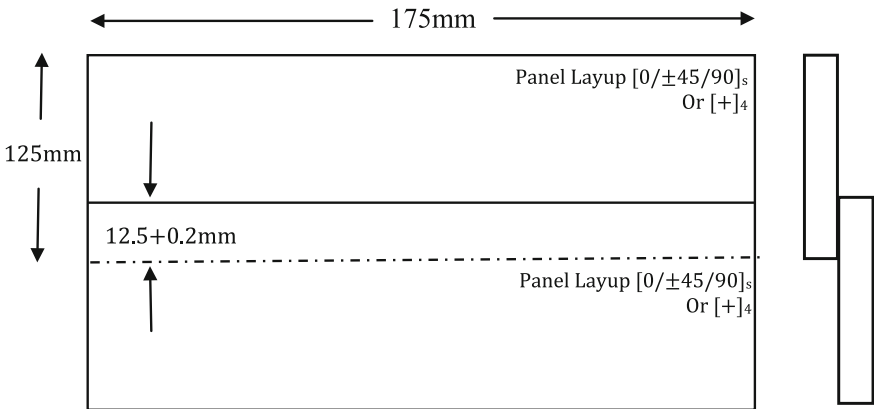


**Fig. 6** Dimensional panel for modeling bonded assembly

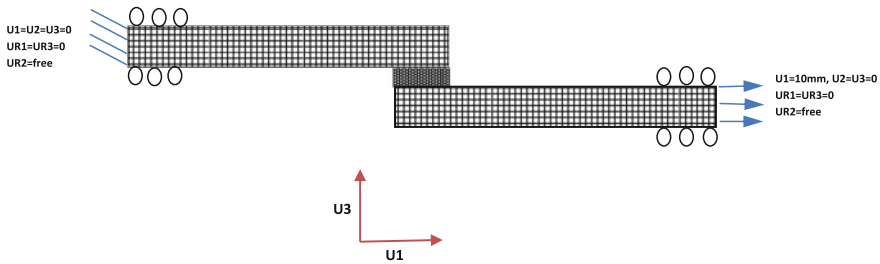


**Fig. 7** Boundary conditions for the single lap joint assembly

(S4R) were used for the substrates and to study the progressive damage in the adhesive, one layer of eight-noded cohesive elements (COH3D8) with the bilinear traction–separation descriptions as defined in earlier sections were utilized.

Cohesive element was modeled at mid plane and placed between two laminates with (12.5 + 0.2) distance from each lamina. Moreover, one end of the substrate was constrained by an encastre constraint ( $u_1 = u_2 = u_3 = 0$ ), while the transverse displacement and rotation about the out of plane axis of the other end were constrained ( $u_1 = 10\text{ mm}$ ,  $u_2 = u_3 = 0$ ) as shown in Fig. 7.

Top and bottom faces of cohesive element layer were tied to the shell elements using tie constraints. The thickness of cohesive element was taken as 0.01 mm. From the previous analysis, penalty factor and  $\delta_{ratio}$  are assumed to be 0.05 and 0.5 in order to avoid mesh convergence issues. The quadratic stress criterion was used to predict damage initiation in the cohesive elements. A higher mesh density was used near the cohesive elements to obtain more accurate results (Fig. 7). It is assumed that there is no friction between the cohesive and the laminates during the test, so that we use frictionless interaction property in this case.

The number of elements used in model is 70,525 (55,125 linear hexahedral elements of type COH3D8 and 15,400 linear quadrilateral elements of type S4R), and the number of nodes is 167,180. The reaction force for above model is plotted against applied displacement (Fig. 8). The main output parameters include QUADSCRT and SDEG. QUADSCRT indicates whether the maximum nominal stress damage initiation criterion has been satisfied at a material point. When QUADS reaches 1.0, it means that the damage initiates. SDEG is the overall value of the scalar damage variable. The parameter SDEG increases from 0.0 to 1.0, which stands for the damage evolution, and the evolution is finished when SDEG equals to 1.0, which means that the cohesive element is fully damaged and therefore a crack is formed.

The numerical simulation of mixed-mode model typically takes about 168 h of CPU time and generates an output file size of about 15 GB. Figure 8 shows the load versus displacement response for SLJ, and the plot shows failure near to 5 mm displacement for the applied displacement of 10 mm.

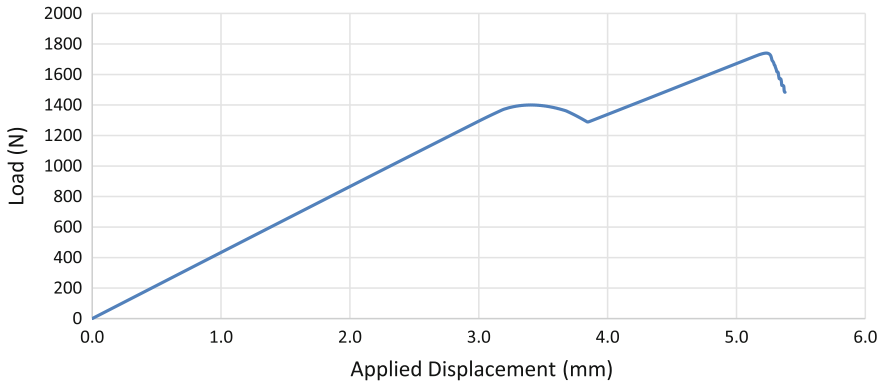


**Fig. 8** Load versus applied displacement curve for single lap joint mixed mode test

**Table 3** Output database

Model name	Total no. of elements	CPU time (h)	Output file size (GB)
ENF test (from literature)	55,375	10	8
ENF modeled	16,500	7	10
MMB tests (literature)	11,300	50	8
MMB tests	31,750	50	11
SLJ mixed-mode	70,525	168	15

## 6 Conclusion

A pure mode-II and mixed-mode cohesive zone model has been used to simulate the propagation of adhesively bonded specimen loaded by three-point bending and mixed-mode bending. The material properties required to define traction separation law, i.e., strength and stiffness were calculated using refined cohesive element parameters.

A quadratic normal stress criterion is used for onset of delamination and subsequently B–K law is used for damage evaluation in numerical simulations. Cohesive element parameters  $\delta_{ratio}$  and penalty factor are refined for optimum solution by ENF test and MMB test. The characteristic strength for the mode-II traction separation law was essentially identical to the cohesive strength of the interface. The reaction forces on a single lap joint (SLJ) subjected to 3ENF test using the parameters described in above sections are shown in Fig. 8. A method is presented for the prediction of crack growth in specimens under pure mode-II and mixed-mode tests using ABAQUS cohesive elements. Table 3 gives a brief detail about testing procedures for various models simulated for analysis. Numerical predictions for the reaction loads versus displacements are obtained using cohesive zone modeling. In order to capture the unstable onset of delamination growth in the

simulation, displacement and time period of the simulation had been resolved with convergence issues. The proposed mixed-mode criteria for SLJ can predict the strength of composite structures that exhibit progressive delamination.

## 7 Future Scope of Work

Numerical results will be validated with the experimental test data for better understanding of the crack propagation, and acoustic emission testing will be carried out to characterize the fracture initiation and damage propagation.

## References

1. Song K, Davila CG, Rose CA (2008) Guidelines and parameter selection for the simulation of progressive Delamination. NASA Langley Research Center, Hampton. Abaqus users conference
2. Džugan J, Viehrig HW (2006) Crack initiation determination for three-point-bend specimens. *J Test Eval* 35(3), Paper ID JTE12611
3. Girolamo D, Dávila CG, Leone FA, Lin SY (2013) Cohesive laws and progressive damage analysis of composite bonded joints, a combined numerical/experimental approach. National Institute of Aerospace, NASA Langley Research Center, Hampton, VA, 23681, USA
4. Viswamurthy SR, Masood SN, Siva M, Ramachandra HV (2013) Interlaminar fracture toughness characterization of unidirectional carbon fiber composite (IMA/M21 prepreg). NAL Project Document PD-ACD/2013/1013
5. ASTM D 5528: Standard test method for mode-I interlaminar fracture toughness of unidirectional fibre reinforced polymer matrix composites (2013)
6. ASTM D 7905: Standard test method for determination of the mode II interlaminar fracture toughness of unidirectional fiber-reinforced polymer matrix composites (2014)
7. ASTM D 6671: Standard test method for mixed mode I-mode II interlaminar fracture toughness of unidirectional fiber reinforced polymer matrix composites (2013)
8. Masood SN, Singh AK, Viswamurthy SR (2016) Simulation and validation of delamination growth in CFRP specimens under mixed mode loading using cohesive elements. INCCOM-14, Hyderabad January 22–23
9. Turon A, Dávila CG, Camanho PP, Costa J (2005) An engineering solution for using coarse meshes in the simulation of delamination with cohesive zone models. NASA/TM-2005-213547
10. Diehl T (2006) Using ABAQUS cohesive elements to model peeling of an epoxy-bonded aluminum strip: a benchmark study for inelastic peel arms. DuPont Engineering Technology, Abaqus users conference
11. ABAQUS version 6.11 documentation (2011). ABAQUS Inc., Rhode Island, USA
12. Benzeggagh ML, Kenane M (1996) Mixed-mode delamination fracture toughness using MMB apparatus for unidirectional glass/epoxy. *Compos Sci Technol* 56:439–449
13. Khoramishad H, Crocombe AD, Katnam KB, Ashcroft IA (2010) Predicting fatigue damage in adhesively bonded joints using a cohesive zone model. *Int J Fatigue* 32:1146–1158
14. Tsai MY, Morton J (1994) Morton: an evaluation of analytical and numerical solutions to the single-lap joint. *Int J Solids Struct*

15. Ashcroft IA, Shenoy V, Critchlow GW, Crocombe AD (2010) A comparison of the prediction of fatigue damage and crack growth in adhesively bonded joints using fracture mechanics and damage mechanics progressive damage methods. *J Adhes* 86:1203–1230
16. Li S, Thouless MD, Waas AM, Schroeder JA, Zavattieri PD (2006) Mixed-mode cohesive zone models for fracture of an adhesively bonded polymer-matrix composite. *Eng Fract Mech* 73
17. O'Brien TK, Johnston WM, Toland GJ (2010) Mode II interlaminar fracture toughness and fatigue characterization of a graphite epoxy composite material. National Aeronautics and Space Administration Langley Research Center Hampton, Virginia 23681–2199

# Study of Fatigue Crack Growth Rate of AA6061 at Different Stress Ratios

Rajesh P. Verma and K.N. Pandey

**Abstract** In the present work, fatigue crack growth behaviors of AA6061 are studied at different stress ratios,  $R = 0.1, 0.5$  and  $0.9$ . The fatigue crack growth rate and stress intensity factors at steady-state regime were determined by fatigue test on compact tension specimens. Fatigue tests were performed according to ASTM standards using Biss 25-kN, servo-hydraulic testing machine with graphic interface and auto-calibration. Lower fatigue crack growth rate as well as a higher fatigue crack growth threshold for stress ratio,  $R = 0.1$ , was observed and compared to  $R = 0.5$  and  $0.9$ . The dependency of crack growth on stress ratio is also modeled based on Walker approach, and Walker exponent was identified to model the dependency of fatigue crack growth rate of AA6061-T6 on stress ratios. The mathematical model developed shows 95% adj  $R$  square, which is acceptable.

**Keywords** Aluminum alloy · AA6061 T6 · Fatigue crack growth rate  
Stress intensity factor · Stress ratio · Modeling

## 1 Introduction

AA6061 aluminum alloys are widely used in structural application due to its high strength-to-weight ratio, high extrudability and high formability. These advantages of the alloy attract it to use in automobile, aerospace, architectural and naval structural applications [1]. Fatigue failure of structural components is one of the major challenges for the reliability of components as the structural components undergo repeatedly mechanical and vibrating stresses [2]. The fatigue load causes

---

R.P. Verma (✉)

Department of Mechanical Engineering, Graphic Era University (GEU), Dehradun, Uttarakhand, India

e-mail: rajesh\_dival@yahoo.in

K.N. Pandey

Department of Mechanical Engineering, Motilal Nehru National Institute of Technology (MNNIT), Allahabad, UP, India

© Springer Nature Singapore Pte Ltd. 2018

S. Seetharamu et al. (eds.), *Proceedings of Fatigue,*

*Durability and Fracture Mechanics*, Lecture Notes

in Mechanical Engineering, [https://doi.org/10.1007/978-981-10-6002-1\\_6](https://doi.org/10.1007/978-981-10-6002-1_6)



the growth of the preexisting micro-crack in material. The micro-crack subsequently grows to macro-crack and ultimately results into the failure of the components even before the first detection of the crack on surface. So, the study of crack growth phenomena is very important to understand the failure mechanism of any structure.

Usually fatigue crack growth can be divided into three regimes: slow crack growth regime, steady crack growth regime and unstable crack growth regime. It is very difficult to control the crack growth once the crack becomes unstable. So the stable crack growth regime is the main concern of researchers and designers to investigate the critical crack length and corresponding crack properties. Paris pointed out the stress intensity factor range ( $\Delta K$ ) as a main parameter that controls the rate of crack growth ( $da/dN$ ) and proposed the behavior of fatigue crack growth in relation to the change in stress intensity factor [3]. The stress intensity factor range below which the fatigue crack will not propagate is known as threshold stress intensity factor ( $\Delta K_{th}$ ), and the stress intensity factor at which material will fail (unstable crack growth occurs) is known as critical stress intensity factor ( $K_C$ ). It is needed to evaluate  $\Delta K_{th}$  and  $K_C$ , which are the important parameters to study the crack growth for estimating the residual lifetime of a component.

The real-life components are basically subjected to variable amplitude fatigue loading, and a complex mathematics is required to study it in the majority of cases [4]. By knowing the fatigue behavior of a material at different stress ratios, the fatigue study of real components can be performed effectively and accurately to some extent without bothering about the complex mathematics involved in study under variable amplitude loading [5]. In the present work, fatigue crack growth behaviors of AA6061-O aluminum alloy are studied at different stress ratios ( $R = 0.1, 0.5$  and  $0.9$ ). A mathematical relation between the crack growth rate and stress ratio for AA6061-T6 alloy is also presented.

## 2 Experimental Details

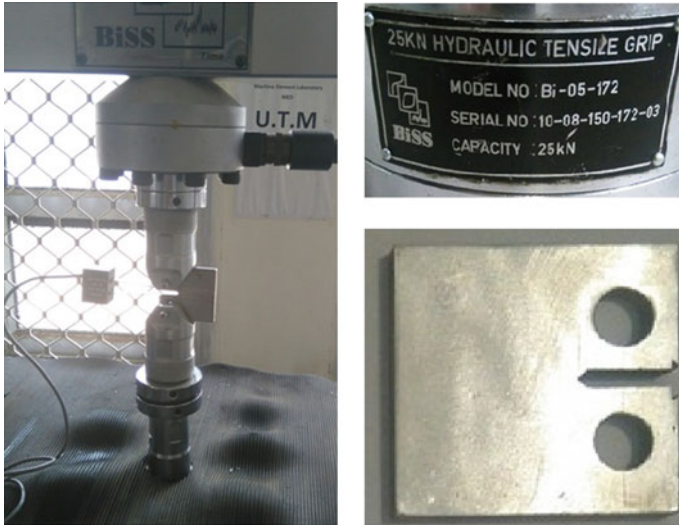
The fatigue crack growth rate test was performed to evaluate crack growth rate and threshold stress intensity factor using the standard compact tensile (CT) specimens. The CT specimens were cut from commercial plates of AA6061-T6 of 6-mm thickness using power hacksaw and then machined to the required dimensions. The chemical compositions of the alloy are presented in Table 1. The tensile properties of material have been evaluated as per ASTM B-557 M from the load extension plots and are presented in Table 2. ASTM E647-08 guidelines were followed for

**Table 1** Chemical composition of material AA6061-T6

Material	Si	Cu	Fe	Zn	Mg	Ni	Mn	Cr	Ti	Sn	Pb	Al
6061 T6	0.79	0.19	0.0	0.07	0.98	0.03	0.17	0.04	0.03	0.02	0.02	Balance

**Table 2** Tensile properties of material AA6061-T6

Material	AA6061-T6
Tensile strength (MPa)	285.4
% elongation	14.2
Modulus (GPa)	70
Room temperature (°C)	27

**Fig. 1** Photographs of fatigue testing machine and a sample of compact tensile specimen

preparing the test specimens and for performing the crack growth tests. A pre-crack of 8 mm was made on the CT specimens to make the testing results more accurate. Fatigue tests were performed on Biss 25-kN, servo-hydraulic testing machine with graphic interface and auto-calibration at 20 Hz frequency (Fig. 1).

### 3 Results and Discussion

#### 3.1 Fatigue Crack Growth Data

Crack growth was monitored through graphical interface at three stress ratios,  $R = 0.1, 0.5$  and  $0.9$ . The experimental data were used to obtain the relationship between the fatigue crack growth rate ( $da/dN$ ) and the stress intensity factor amplitude ( $\Delta K$ ) in the stable crack growth regime by curve fitting using Paris-Erdogan crack growth law [3]:

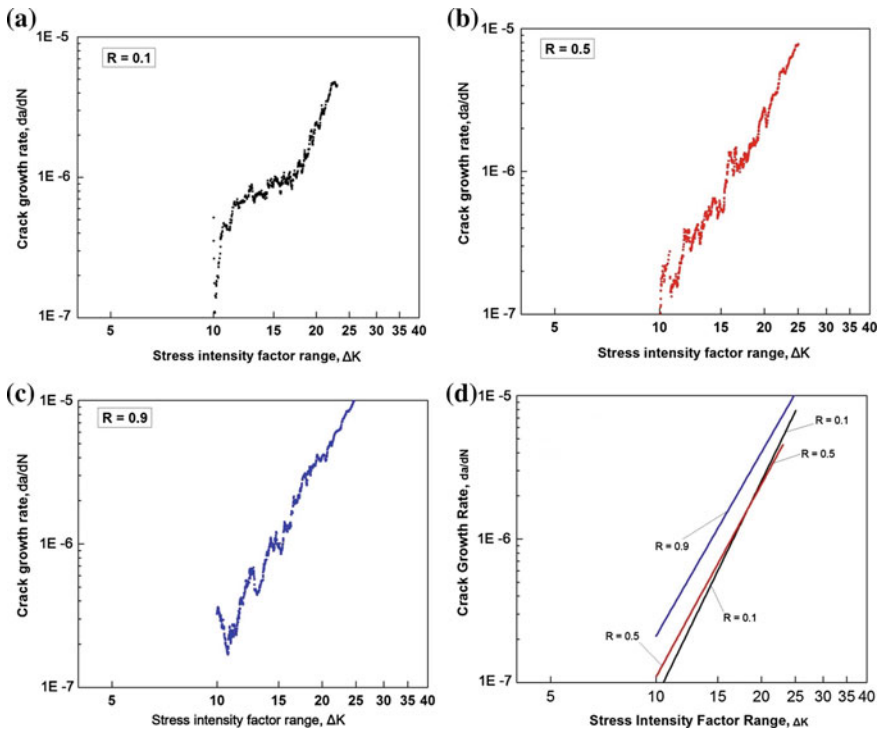
**Table 3** Paris constants obtained for material AA6061-T6

Paris constants	Stress ratio		
	$R = 0.1$	$R = 0.5$	$R = 0.9$
Exponent, $m$	4.25	4.47	5.01
Intercept, $C$	$1.76 \times 10^{-8}$	$1.38 \times 10^{-8}$	$2.70 \times 10^{-8}$

$$da/dN = C(\Delta K)^m \tag{1}$$

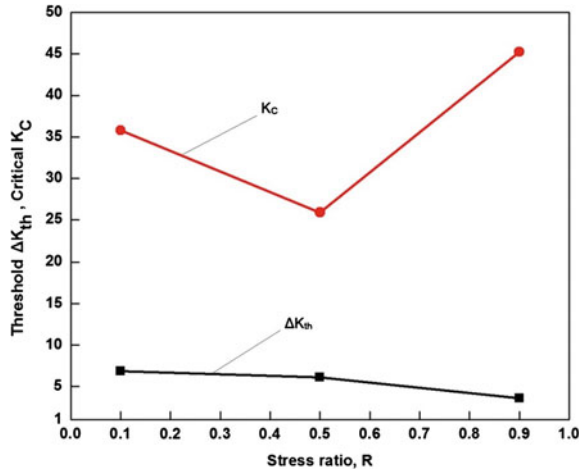
where  $C$  and  $m$  are material constants, which were determined by experimental data fitting (Table 3).

Figure 2 shows the comparison between the steady crack growth behaviors of alloys 6061-T6 near-threshold value at stress ratios,  $R = 0.1, 0.5$  and  $0.9$ . The linear regression of the  $\Delta K_{th}$  and  $K_C$  versus the stress ratios is also shown in Fig. 3. In Fig. 3, it is clear that the  $\Delta K_{th}$  decreases with the increase in stress ratio from 0.1 to 0.9.



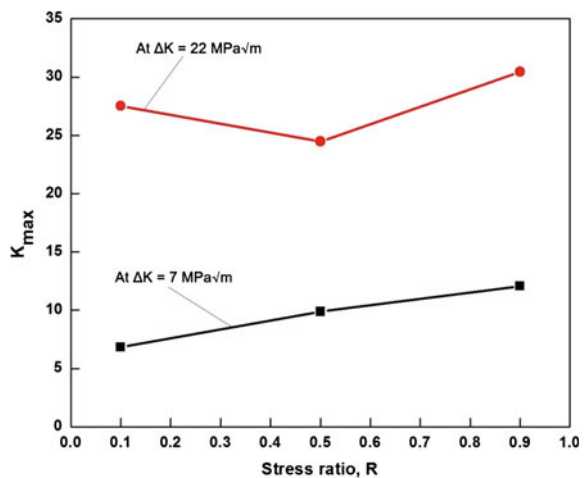
**Fig. 2** a Experimental curve at stress ratio = 0.1, b experimental curve at stress ratio = 0.5, c experimental curve at stress ratio = 0.9, d fitted curve (adj  $R^2 = 0.98$ ) of fatigue crack growth rate  $da/dN$  (mm/cycle) versus mode I stress intensity factor range  $\Delta K$  (MPa $\sqrt{m}$ )

**Fig. 3** Threshold  $\Delta K_{th}$  ( $\text{MPa}\sqrt{\text{m}}$ ) and critical stress intensity factor,  $K_C$  ( $\text{MPa}\sqrt{\text{m}}$ ) at different stress ratios,  $R$



Comparatively lower crack growth rate was observed for stress ratio  $R = 0.1$ . The stress ratio  $R = 0.9$  showed the greatest crack growth rate. Noroozi et al. [6] proposed two important parameters, stress intensity factor range ( $\Delta K$ ) and maximum stress intensity factor ( $K_{max}$ ), that control the growth of a crack under fatigue loading. A larger  $K_{max}$  is obtained with the increase in stress ratio at the same  $\Delta K$ , and it results in greater crack growth driving force and lower threshold,  $\Delta K_{th}$ . In Fig. 4, it is clear that the stress ratio,  $R = 0.9$ , exhibits larger  $K_{max}$  and hence exhibits faster crack growth. After  $\Delta K = 20 \text{ MPa}\sqrt{\text{m}}$ , the slower crack growth rate was observed at stress ratio  $R = 0.5$  than  $R = 0.1$ . The reason might be that the plastic zone at crack tip becomes large with increased  $\Delta K$  and that leads to great difficulty in crack growth [7]. Also, a larger  $K_{max}$  was observed at  $R = 0.1$  than  $R = 0.5$  at  $\Delta K = 22 \text{ MPa}\sqrt{\text{m}}$  as shown in Fig. 4.

**Fig. 4**  $K_{max}$  ( $\text{MPa}\sqrt{\text{m}}$ ) at different stress ratios,  $R$



### 3.2 *Mathematical Modeling of Crack Growth Based on Walker Approach*

The crack closure governs the crack growth driving force at crack tip in variable amplitude loading conditions, which may induced by plasticity, oxide at aluminum alloy surface or rough surface finish [5]. The repetitive compressive loads also induce crack closure effect at crack tip near-threshold regime. The larger positive stress ratio opens a crack longer during a stress cycle; subsequently, a larger part of the cycle contributes to crack propagation. The crack closure effect is accounted by many investigators in terms of the effective stress intensity factor range ( $\Delta K_{\text{eff}}$ ) [3].

An another approach was proposed by Walker to deal such situations by the effective stress range ( $\Delta\sigma_{\text{Walker}}$ ) [8] as.

$$\Delta\sigma_{\text{Walker}} = (1 - R)^\gamma \sigma_{\text{max}} \quad (2)$$

where  $\sigma_{\text{max}}$  is maximum stress level and  $\gamma$  is arbitrary exponent that depends on material.

Expressing  $\sigma_{\text{max}}$  in terms of stress range ( $\Delta\sigma$ ) and stress ratio ( $R$ ), Eq. (2) becomes

$$\Delta\sigma_{\text{Walker}} = \frac{\Delta\sigma}{(1 - R)^{1-\gamma}} \quad (3)$$

Further expressing Eq. (3) in terms of the stress intensity factor range ( $\Delta K$ ),

$$\Delta K_{\text{Walker}} = \frac{\Delta K}{(1 - R)^{1-\gamma}} \quad (4)$$

Rearranging Eq. (4),

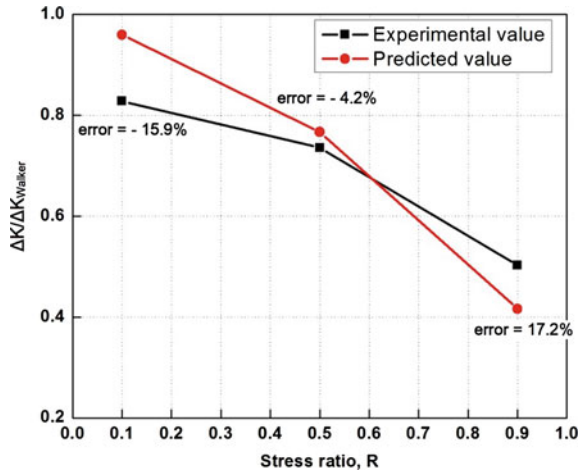
$$\Delta K = \Delta K_{\text{Walker}}(1 - R)^{1-\gamma} \quad (5)$$

Equation (5) is in power form as  $y = ax^b$ , where  $a = \Delta K_{\text{Walker}}$  and  $b = (1 - \gamma)$  are material-dependent constants.

The determination of  $\gamma$  in Eq. (5) requires that  $\Delta K$  is not the function of  $R$ , but it is not the case in crack propagation data. Many researchers have attempted to overcome this type of situation by fixing points in a region of  $da/dN$  or  $\Delta K$  [9]. The literature [10] showed that the determination of  $\gamma$  at different  $da/dN$  values has no much effect on the obtained Walker exponent,  $\gamma$ . Therefore,  $\gamma$  was determined at  $da/dN = 1 \times 10^{-7}$  mm/cycles (near  $\Delta K_{\text{th}}$  in steady-state regime) only.

The constants 'a' and 'b' were evaluated by curve-fitting method ( $\text{adj } R^2 = 95\%$ ) using the experimental data, and then,  $\gamma$  and  $\Delta K_{\text{Walker}}$  are calculated as 8.26 and 0.62, respectively. The proposed value of  $\gamma$  and  $\Delta K_{\text{Walker}}$  was confirmed (error <20%) by the experimental values as presented in Fig. 5. Generally,  $\gamma$  varies

**Fig. 5**  $\Delta K/\Delta K_{Walker}$  as a function of  $R$  for experimental and predicted values



between 0.3 and 0.8 at positive stress ratios, where lower limit indicates a strong and higher limit indicates a weak dependence on stress ratio [11]. The calculated Walker exponent  $\gamma = 0.62$  for AA6061-T6 alloy is toward higher side, and hence, the average dependency of crack growth on  $R$  was found.

#### 4 Conclusion

The fatigue crack growth behavior at different stress ratios was studied for AA6061-T6 alloy. The alloy shows a significantly higher resistance to crack propagation at lower stress ratio,  $R = 0.1$ , near-threshold point, but lower resistance to crack growth is observed toward critical point. At intermediate positive stress ratio,  $R = 0.5$ , higher crack growth resistance is observed near-threshold point than that at critical point compared to  $R = 0.1$ . The fastest crack growth rate was observed at stress ratio,  $R = 0.9$ . The proposed mathematical model based on Walker approach can be effectively used to model the crack growth of AA6061-T6 near-threshold region, as the calculated Walker exponent,  $\gamma = 0.62$ , is in permissible error range.

#### References

1. Moreira PMGP, de Jesus AMP, Ribeiro AS, de Castro PMST (2008) Fatigue crack growth in friction stir welds of 6082-T6 and 6061-T6 aluminium alloys: a comparison. Theoret Appl Fract Mech 50:81–91
2. Rodopoulos Chris A, Alexis T (2007) Kermanidis: understanding the effect of block overloading on the fatigue behaviour of 2024-T351 aluminium alloy using the fatigue damage map. Int J Fatigue 29:276–288

3. Jogia BF, Brahmanekar PK, Nanda VS, Prasad RC (2008) Some studies on fatigue crack growth rate of aluminum alloy 6061. *J Mater Process Technol* 201:380–384
4. Thomas WM (1986) The effect of single overloads upon fatigue cracks in 5083-H321 aluminium. *Eng Fract Mech* 23(6):1015–1029
5. Borrego LP, Ferreira JM, Costa JM (2001) Fatigue crack growth and crack closure in an AlMgSi alloy. *Fatigue Fract Eng Mater Struct* 24:255–266
6. Noroozi AH, Glinka G, Lambert S (2005) A two parameter driving force for fatigue crack growth analysis. *Int J Fatigue* 27:1277–1296
7. Bergner F, Zouhar G, Tempus G (2001) The material-dependent variability of fatigue crack growth rates of aluminium alloys in the Paris regime. *Int J Fatigue* 23:383–394
8. Mann T (2007) The influence of mean stress on fatigue crack propagation in aluminium alloys. *Int J Fatigue* 29:1393–1401
9. Kujawski D (2001) A new  $(\Delta K + K_{\max})^{0.5}$  driving force parameter for crack growth in aluminium alloys. *Int J Fatigue* 23:733–740
10. Kujawski D, Stoychev S (2003) Parametric study on the variability of opening load determination. *Int J Fatigue* 25:1181–1187
11. Schijve J (1981) Some formulas for the crack opening stress level. *Eng Fract Mech* 14(3):461–466

# Cooler Casing Fatigue Analysis: An ASME Approach

Prathapkumar Ramamoorthy, David K. Harper and Sam P. Joseph

**Abstract** Extended surface heat exchangers are widely adopted in centrifugal air compressors to transfer heat from compressed air to cooling water. These heat exchangers are enclosed in a casing which is made either by casting or fabrication. This paper reviews the cast casing fatigue qualification as per ASME Section VIII Division 2 guidelines. Casing is considered as a pressure vessel in industry which needs to be certified by ASME or PED or GB or CRN depending on the location of use. Machine operating parameters were used as inputs for fatigue screening criteria to determine whether the fatigue analysis is required as part of casing design. On failing the screening criteria, a detailed fatigue evaluation was performed. Coupled field analysis were ran in ANSYS and the maximum stress intensity values are used to compare against the material's fatigue criteria on the pressure boundary and non-pressure boundary regions separately, to qualify the casing.

**Keywords** Fatigue qualification · ASME fatigue screening · Coupled field pressure vessel analysis · Compressor load cycle and heat exchanger manufacturing

## 1 Introduction

The centrifugal compressor is a type of dynamic compressor where the kinetic energy imparted to the flow by a rotating impeller is subsequently converted to pressure energy with the help of a diffuser section and a scroll or volute casing.

---

P. Ramamoorthy (✉) · S.P. Joseph  
Compression Technologies & Services, Ingersoll-Rand Technologies & Services Private Limited, Bangalore, India  
e-mail: prathapkumar@irco.com

S.P. Joseph  
e-mail: Sam.Joseph@irco.com

D.K. Harper  
Compression Technologies and Services, Ingersoll Rand, Davidson, USA  
e-mail: David\_Harper@irco.com



The inflow and outflow directions are, characteristically, perpendicular to each other. The compressed fluid can be any gas of engineering importance, but air is the subject of this study.

The rise in temperature of air during compression limits the pressure level achieved by the single stage compression. Hence, multi-staging compression with inter-stage cooling helps in reducing temperature and volume of air, resulting in reduced power consumption. The after cooler (heat exchanger) reduces the compressed air temperature to that which can be tolerated by the end application—generally 5–10 °C above ambient. Heat exchangers are thus a vital component in any air compressor. Heat exchangers may be air-cooled or water-cooled. Air-cooled heat exchangers are limited to smaller compressors, while the water-cooled option is recommended for compressors with higher capacity. The latter is more effective because of its heat absorption capacity. For water-cooled heat exchangers used in the centrifugal air compression, the shell and tube construction, with extended heat transfer surfaces on the tubes, is the most preferred.

The construction consists of a cylindrical shell housing a group of tubes and extended surfaces, collectively called a cooling bundle or a tube bank. Wavy, extended surfaces (fins) are attached to the tubes to increase the heat transfer rate between the primary hot fluid (compressed air) and cold secondary fluid (water). Tube banks are usually arranged in an inline or staggered manner and typically the primary fluid moves over the tubes, while the secondary fluid at a different temperature passes through the tubes. Depending on the number of secondary fluid circulations within the control volume, heat exchangers are called single pass or multi-pass heat exchangers. Tube ends are securely attached to two perforated flat plates called tube sheets. Both the primary and secondary fluids come in contact with tube sheets. Tube sheets are either fixed to the shell or floating depending on its function and location. A fixed tube sheet is attached between the shell flange and the water bonnet flange surfaces by fasteners and holding the weight of the cooling bundle and maintaining tube bank alignment. A floating tube sheet is connected to the reversing plate through fasteners and does not carry cooling bundle weight. The water bonnet provides a connection for the inlet and outlet water connections, and the reversing plate on the other end returns the water to the bonnet. The number, length of tubes, and fin density are decided based on the required cold temperature difference (CTD), heat rejection, and cooling water temperature rise. During the heat transfer phase, water vapor present in compressed air condenses and is removed from the heat exchanger by condensate traps. If not properly designed, there will be condensate carry over issues in downstream equipment, after the compressed air exits the shell.

Heat exchanger fabrication requires welding, metal forming, drilling and cutting operations as well as precise adherence to dimensions and close tolerances, especially, for the tube bundles. Tubes are expanded into tube sheets at a uniform rate using advanced technologies to assure consistent expansion and leak-tight joints. In most modern constructions, computer-controlled machines make the tube to tube sheet joint in a uniform manner, with or without use of filler metal.

Alternatively, the shell may also be cast using ductile grades of cast iron. Owing to poor weldability of cast irons, flanging and bolting of sections are employed, e.g., for the end bonnets.

As the shell is to withstand the internal air pressure and the thermal–structural loading associated with centrifugal compression, the designer should consider this as a case of a pressure vessel with complex loading and the possibility of fatigue failure.

Most common failure mechanisms of a pressure vessel [1] under complex, cyclic loading are:

- Elastic deformation—Elastic instability or elastic buckling. Geometry and material of the vessel and its stiffness are to protect against buckling.
- Brittle fracture—Can occur at low temperatures (40–50 °F range) in vessels made of low carbon steel. This may be checked through suitable hydro-test procedures.
- Excessive plastic deformation—The primary and secondary stress limits are recommended by ASME Section VIII, Division 2, to prevent excessive plastic deformation and incremental collapse.
- Stress rupture—Progressive deformation and fracture as a result of fatigue or cyclic loading. Creep is a time-dependent phenomenon, whereas fatigue is a cycle-dependent phenomenon.
- High strain—Low cycle fatigue is strain-governed occurring mainly in lower-strength high-ductile materials.

It is against these failure modes that the designer must compare and interpret stress values. Design details and fabrication methods are as important as “allowable stress” in design of vessels for cyclic service. A logical design work flow would be to start with the choice of appropriate geometry, material and manufacturing process, followed by design using ASME Code, Section VIII, Divisions 1 and/or 2 guidelines and, if necessary, an FE Analysis of the shell design.

## 2 Material Selection

Considering the complex shapes achievable in the casting process and the ductility requirement for pressure vessel materials, ductile iron was the logical choice of material for this application.

In ductile irons, graphite inclusions are in the form of nodules rather than flakes as in gray iron. The iron matrix is mostly ferritic with some pearlite. Nodule formation is achieved by the addition of nodulizing elements, most commonly magnesium, to the melt. Under loading, graphite flakes provide likely stress concentration points within the metal matrix whereas rounded nodules inhibit the creation of cracks, thus improving ductility.

**Fig. 1** Stress–strain behavior in ductile iron compared with cast irons and mild steel [2]

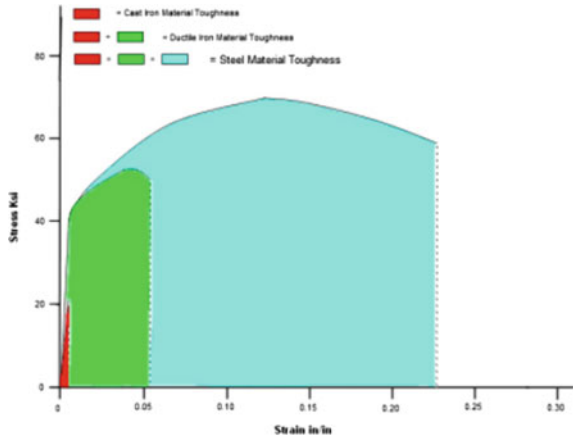


**Fig. 2** Relative deformation in a 180° bending test [2]



Ductile iron is also known as nodular cast iron or spheroidal graphite iron (SG iron). It also has much more impact and fatigue resistance than typical cast irons, due to its nodular graphite inclusions. A comparison of the stress–strain curves and relative bending test behavior of gray cast iron, ductile cast iron, and steel is shown in Figs. 1 and 2, respectively.

### 3 Design Methods

The ASME Boiler and Pressure Vessel Code (BPVC) is an American Society of Mechanical Engineers (ASME) standard that regulates the design and construction of boilers and pressure vessels. Every unfired pressure vessel in the USA is designed according to Division 1 and/or 2 of ASME Section VIII. In Division 1, by

using the predefined procedures, empirical relations, and charts, pressure vessels are designed. There are some additional specific guidelines and rules defined to handle discontinuities, thermal gradients and fluctuating loads. These procedures minimize the amount of analysis required to ensure the safety of the vessel. The allowable stresses in this code are based on a simplistic average membrane stress and assume large factors of safety in the stress concentrating regions and geometric discontinuities, leading to a conservative design. Division 1 does not cover every detail that the designer may want to use and does not explicitly consider the effects of combined stress or neither does it give detailed methods on how stresses are combined. This method is well identified as design by rule or design by formula approach.

When the vessel is subjected to complex loadings such as cyclic, thermal loads and where significant discontinuities exist, the more rigorous design by analysis approach is adopted. With these alternate rules, the designer is able to calculate stresses everywhere in the vessel and not just the average membrane stresses in regular sections such as cylinders and heads. The code invariably allows for the use of finite element tools, providing the opportunity to bring the calculated stresses closer to real stresses. Design by analysis approach helps to develop complex pressure vessel design with less material without compromising the safety. This design method removes the unnecessary conservatism of the design by rule approach.

In the design by analysis approach, a three-dimensional vessel geometry with loads is evaluated through detailed structural analysis. The basis of this analysis is the creation of a high-quality mesh followed by accurate load application and then the extraction and classification of stresses per the code. The structural analysis may be elastic or plastic in nature depending on the anticipated material behavior and loading conditions.

## 4 Fatigue Screening Criteria

Often, a vessel designed for static loading conditions may not survive the cyclic conditions due to damage accumulations in a localized region, and failures can occur at stress amplitudes considerably below the yield strength. Material behavior will not follow stress–strain relationship in the repeated loading situation. Detailed design plays a key role in eliminating regions of stress raisers and discontinuities. Fatigue cracks can grow slowly and without an easily detectable change in component dimension or performance. Upon reaching a critical size, catastrophic failure occurs.

ASME Code, Section VIII, Division 1 does not specifically provide design guidelines for pressure vessels under cyclic conditions. ASME Code, Section VIII, Division 2 has standard detailed criteria for determining when a vessel must be designed for fatigue. To determine the necessity of fatigue analysis, ASME section VIII Division 2 section 5.5.2 guidelines are provided. These screening guidelines are not applicable if the pressure vessel life requirements are more than  $10^6$  cycles, but instead the designer is advised to conduct detailed fatigue evaluation.

A screening assessment is the first step in performing a fatigue analysis. Three fatigue screening options given in ASME will assist the designers to decide the requirement of detailed fatigue analysis. If any one of the below mentioned screening criteria are satisfied, then a detailed fatigue analysis is not required as part of vessel design.

- **Method 1—Experience with comparable equipment operating under similar conditions**—New vessel fatigue evaluation is exempted if successful previous experience is attained with similar equipment design with similar operating conditions and similar loading histogram pattern is followed. In the case of a new vessel design, these data are not available, so another method must be selected.
- **Method 2—Based on materials of construction**—This method can only be used for the vessels with an ultimate tensile strength less than 552 MPa. SA-395 material's ultimate tensile strength is 414 MPa. So, this method can be used for screening. This method has seven steps.
  - Step 2a—Determine load history based on user specification—Some insight must be found in the machine's duty cycle, although this is often difficult to confidently know, but assumptions and generalizations can be made. Large industrial compressors will operate on a different duty cycle than smaller compressors. In applications with smaller compressors, there may be significantly more starts as it is more economical to turn off the compressor than to leave it running. It is also more likely the customer does not have as sophisticated set of controls. However, a smaller compressor would have a lower expected life due to its lower investment cost.
  - Step 2b—Full range load cycle,  $N_{\Delta FP}$  includes startup and shutdown. An application with a large industrial compressor like a centrifugal will probably start the machine only once per week or at most only once per day, at the start of the first shift due to its large start-up power. The customer probably has matched the compressor to his system and installed proper controls to protect his investment such that the compressor will stay within its normal operating limits so that it will not often reach surge conditions.
  - Step 2c—Operating pressure fluctuations,  $N_{\Delta PO}$ —The machine operating limits are also a factor in a fatigue analysis. The full range of pressures should be considered including the control band (the online and offline pressures). Cycles to be included depend on the method of pressure vessel construction. For integral vessels, the value is 20% and for non-integral vessels the value is 15%.
  - Step 2d—Overshoot pressure fluctuations—Pressure rises to surge, and the air systems overshoot pressure (the maximum observed pressure before the controller recognizes it and the compressor can respond to it). Air systems with large capacity help reduce fatigue stress of the compressor because they require a long time for the pressure to respond to changes in supply or demand, meaning the overshoot pressure is reduced and the time between fluctuations is extended.

- Step 2e—Effective changes in metal temperature,  $\Delta T_E$ —Temperature factor for fatigue screening criteria is given in Table 5.8 of Division 2. Temperature factor ranges from 0 to 20 depends on adjacent point temperature difference. An adjacent point value for shells and dished head is given by Eq. 1.

$$2.5\sqrt{Rt} \quad (1)$$

- Step 2f—For welded construction, determine thermal expansion coefficient value will be calculated using Eq. 2. For casted construction, this step will be skipped.

$$(\alpha_1 - \alpha_2)\Delta T \quad (2)$$

- Step 2g—Find out total number of cycles (pressure and temperature) and compare against the criteria given in Table 5.9 of Division 2. If the total number of cycles is more than the limiting value, then a fatigue analysis is required as a part of vessel design. In our case, the total number of cycles is more than 1000. So, fatigue analysis is required.
- **Method 3**—This method can be applied to all metals and requires design fatigue curves for evaluation. Annex 3-F of division 2 has fatigue material for materials and does not have SA-395 fatigue curve. So, fatigue curve available in Atlas of Fatigue Curves by Howard E. Boyer was used for fatigue evaluation.

- Step 3a—Determine load history based on user specification—similar as 2a.
- Step 3b—Determine screening criteria factors. These factors are available in Table 5.10 of Div. 2.
- Step 3c—Compare the full range pressure cycles,  $N_{\Delta FP}$  determined in Step 2b with Eq. 3. If the criteria were satisfied, proceed to step 3d.

$$N_{\Delta FP} \leq N(C_1 S) \quad (3)$$

- Step 3d—Compare the maximum range of operating pressure fluctuations determined in Step 2c and 2d and compare with Eq. 4. If the criteria were satisfied, proceed to Step 3e.

$$\Delta P_N \leq \frac{P}{S} \left( \frac{S_a(N_{\Delta P})}{S} \right) \quad (4)$$

- Step 3e—Compare the temperature difference,  $\Delta T_N$  between the adjacent points with Eq. 5. In our case, the criteria are not satisfied. So, the screening procedure stopped at this point, and a fatigue analysis was conducted.

$$\Delta T_N \leq \left( \frac{S_a(N_{\Delta TN})}{C_2 E_{ym}} \propto \right) \quad (5)$$

## 5 Finite Element Analysis

Since the pressure vessel is also a heat exchanger in our application, the thermal cycles and pressure cycles occur simultaneously. Primary and secondary stresses are induced. Primary stresses are because of pressure and secondary stresses are because of thermal loading. Non-essential geometries were de-featured to reduce element count. De-featured 3D model of the pressure vessel is presented in Fig. 3. Openings of the vessels are covered with thick plates to simulate the loads from compressed air and water pressure exerted by the bonnets. Hex dominant method with body sizing control was imposed to mesh the model with the average element quality of 0.75. Mesh was then supplied to ANSYS workbench for coupled analysis to determine the stress and deformation values.

The vessel body is constructed of nodular, ductile iron that conforms to ASME SA-395 Grade 60-40-18 which per spec implies an essentially ferrite structure with spheroidal graphite. This is equivalent to EU standard EN 1563:1997, EN-GJS-400-18-LT or Chinese standard GB-1348, QT400-18 (Table 1).

The vessel body undergoes various combinations of pressure and thermal conditions. Combined maximum operating pressure and steady state thermal is evaluated against fatigue code criteria. In all cases, vessel feet are restrained vertically and 1 foot is constrained and transverse to avoid rigid body motion.

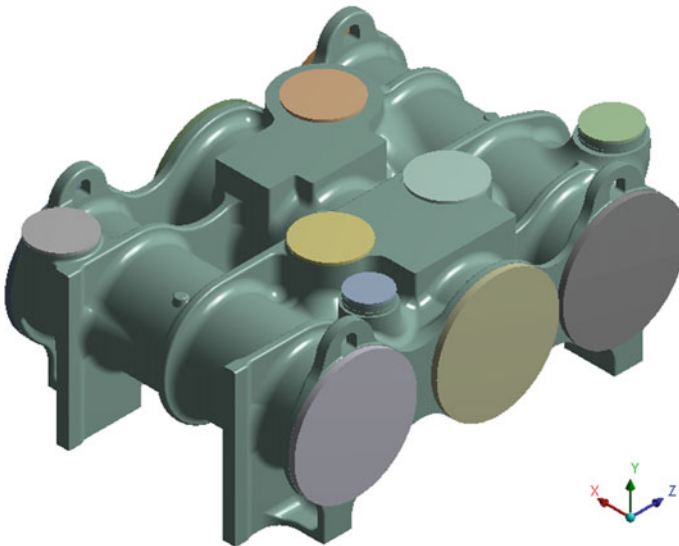


**Fig. 3** FEA model of vessel

**Table 1** SA-395 material properties

Property	Value
Density (kg/m <sup>3</sup> )	6920
Elastic modulus (Pa)	1.70E+11
Shear modulus (Pa)	6.52E+10
Poisson's ratio	0.29
Tensile strength (MPa)	414
Yield strength (MPa)	276
Elongation (%)	18
Thermal conductivity (W/m C)	52
Coefficient of linear thermal expansion (m/m/C)	1.01E-05

### 5.1 Steady-State Thermal

The vessel is a heat exchanger and as such has a thermal gradient between the hot and cold side of heat exchanger bundle, also between the body and water-filled bonnets (heads). The thermal gradient creates strains in the part that can fatigue it over time. In this condition, the most extreme steady state temperatures were assumed along with values for convection obtained through open literature on heat exchangers. This temperature gradient is modeled in ANSYS at the steady-state conditions using the nominal ambient temperature and maximum discharge temperature from the compressor stages. The external free air convection coefficient used for the vessel body is  $10 \text{ W/m}^2 \text{ K}$ , which is a typical average value for natural convection of a gas from published literature. The internal forced convection coefficient for a gas is  $50 \text{ W/m}^2 \text{ K}$ , again an average typical value seen in literature. The maximum compressor discharge temperature is applied on one half of the heat exchanger casing (Fig. 4) and the other half of the casing is applied with compressor suction side temperature (Fig. 5). These values are used as the bulk temperature inputs in the ANSYS steady-state thermal analysis. The ANSYS FEM model used is the same mesh as the structure with the 20 node solid 90. Temperature distribution is shown in Figs. 6, 7 and 8.

### 5.2 Maximum Pressure Standard Operation

The vessel chambers are experiencing different pressures ( $-0.85$ ,  $-0.25$  and  $1.1$ ) during its operation. Pressure magnitudes mentioned above are normalized values. This is the maximum pressure in each of the vessel chambers under the standard operation. Standard operation is defined as when the compressor discharge is in steady-state discharge (not surge), and maximum represents the highest discharge pressure under cold day conditions for the larger machine. This is not the design pressure of vessel body, but the loading condition that accumulates LCF fatigue



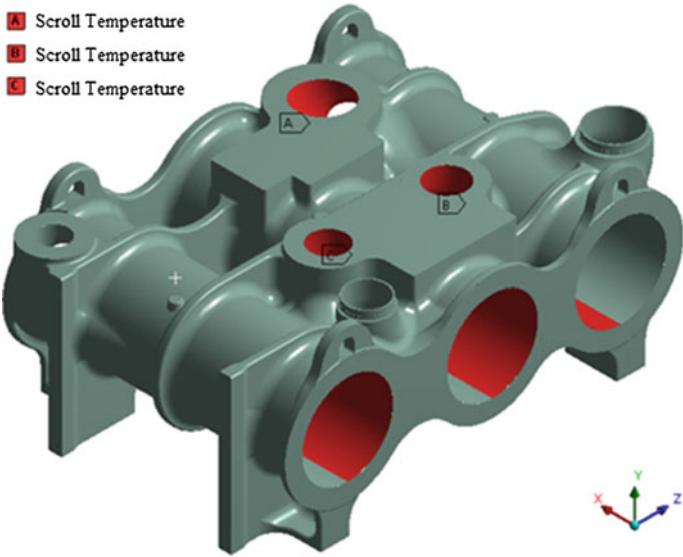


Fig. 4 Hot side or scroll temperature

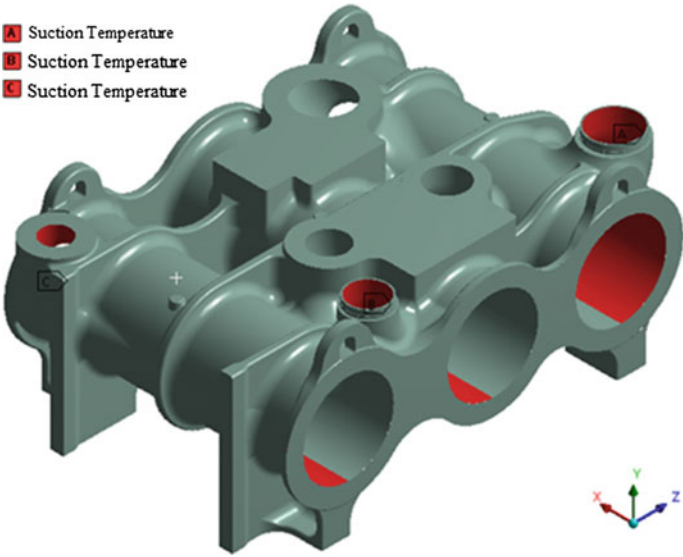
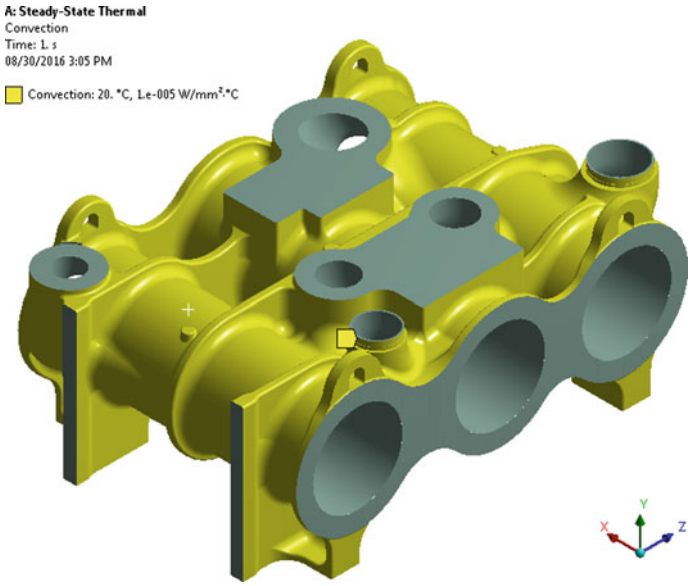
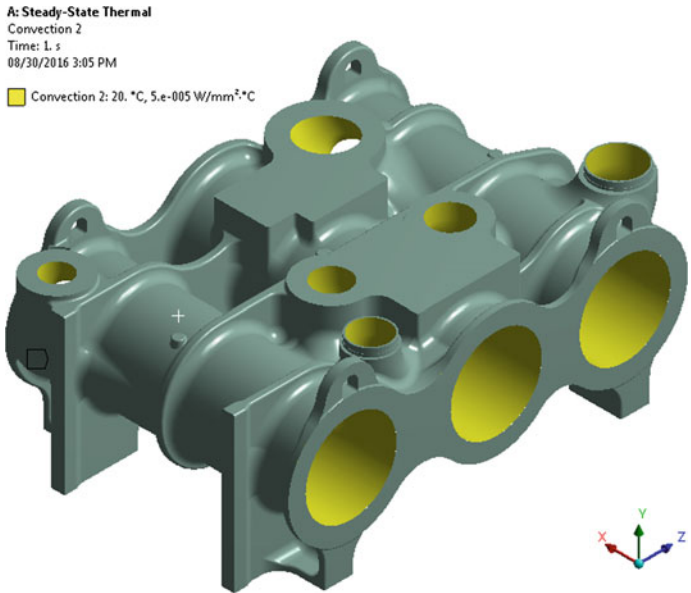


Fig. 5 Cold side or suction temperature



**Fig. 6** External free convection



**Fig. 7** Internal forced convection

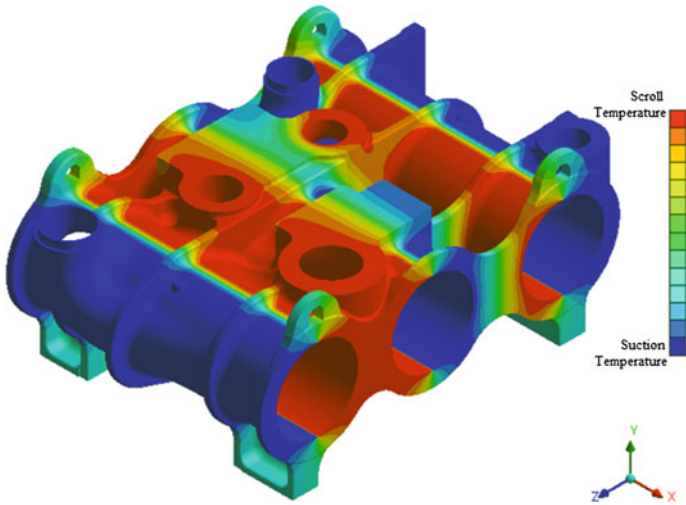


Fig. 8 Thermal analysis outcome with normalized values

cycles. The ANSYS FEM model used the same mesh as the thermal with the 10-node solid 187 (Fig. 9).

ANSYS multilinear, isotropic hardening method was used to predict the true stresses due to applied loading. In this plasticity method, linear stress–strain

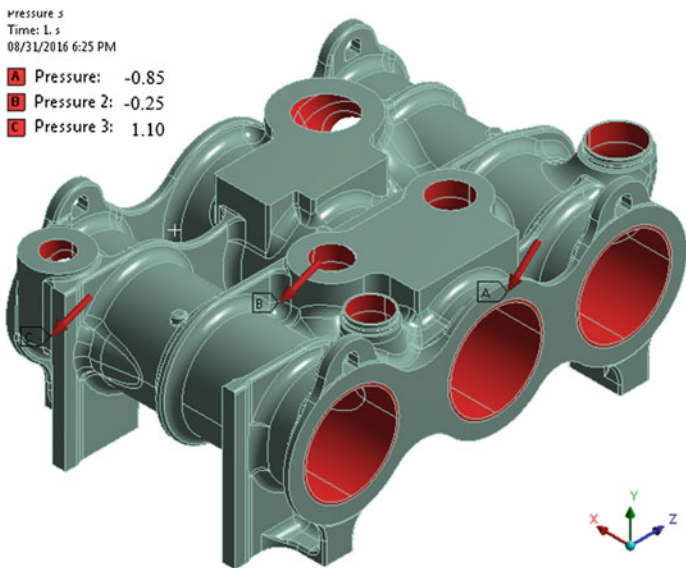


Fig. 9 Pressure vessel with normalized operating pressures values. End plates are concealed for clarity

behavior is followed till the yield point. Post the yield point, yield surface expands uniformly and follows plastic stress–strain curve data supplied to ANSYS. First point of the plastic stress–strain curve starts at yield point. ASME VIII division 2 offers a detailed and easy to follow approach to check the stress results against the stringent ASME requirements.

### 5.3 *Fatigue Assessment*

In fatigue assessment, highest stress from the coupled analysis is used on a material fatigue curve to determine the fatigue life. If the allowable number of cycles exceeds the actual number of cycles, then the vessel design is acceptable. On the other hand, the actual number of cycles exceeds the allowable number of cycles, and the vessel should be redesigned until an acceptable result is achieved.

Fatigue assessment is broken into two parts:

1. Vessel Pressure Boundary Fatigue Assessment
2. Vessel Non-Pressure Boundary Fatigue Assessment

It was separated in this way as the pressure boundary areas could rupture if a through crack from fatigue occurred. A fatigue crack away from the pressure boundary, while undesirable would not result in failure to contain pressure.

The fatigue strength of a material is normally defined by citing its fatigue limit, also called the endurance limit. The fatigue limit is the magnitude of the cyclic stress at which the fatigue life exceeds a specified number of cycles, usually  $10^6$ . Due to small defects such as graphite nodules and microshrinkage cavities existing in the structure, fatigue strength of ductile iron is lower than that of defect-free steel.

The maximum number of fatigue cycles expected during the life span of the vessel is calculated in screening methods. The fatigue curve obtained from the Atlas of Fatigue Curves by Howard E. Boyer for 60-40-18 ferritic cast ductile iron shown above runs out at 200,000 cycles, as it is primarily an HCF curve. The minimum fatigue strength at the lower minimum for 200,000 cycles will be used as a conservative value, at 275 MPa (Fig. 10).

#### 5.3.1 **Pressure Boundary Fatigue Assessment**

The combined maximum standard pressure and steady-state thermal condition were run in ANSYS, and the maximum local stress intensity was used to compare against the above fatigue criteria. In the case of the fatigue assessment of the pressure boundary vessel body, the maximum stress intensity is  $-0.13$  (normalized value) as shown in Fig. 13. This value is well below the 275 MPa requirement for  $>200,000$  cycles (Figs. 11 and 12).

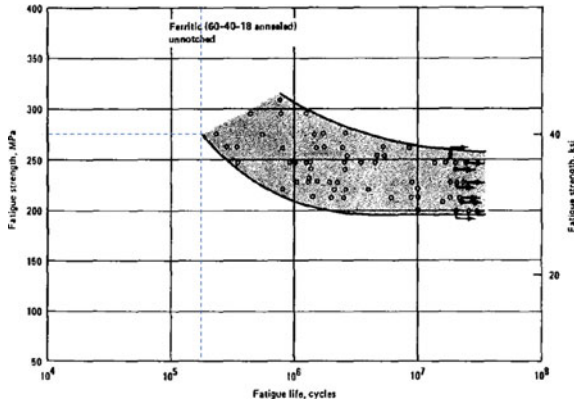


Fig. 10 Ductile cast iron fatigue curve [3]

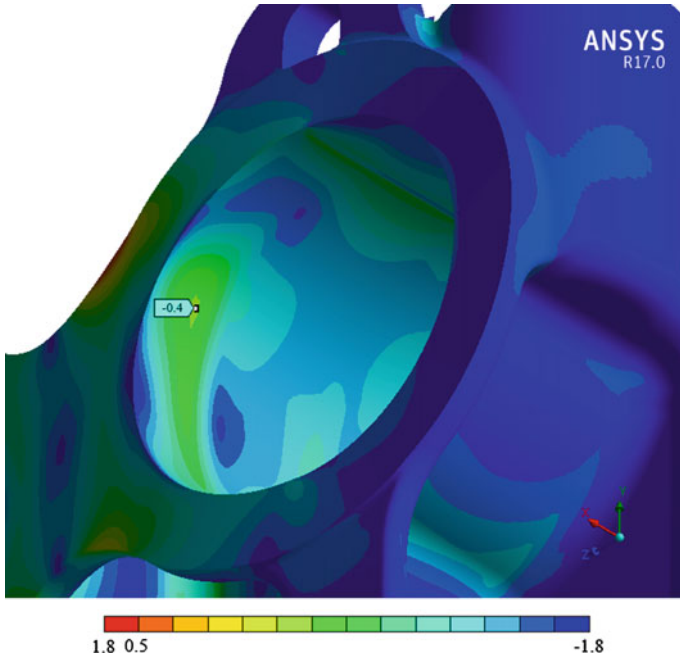
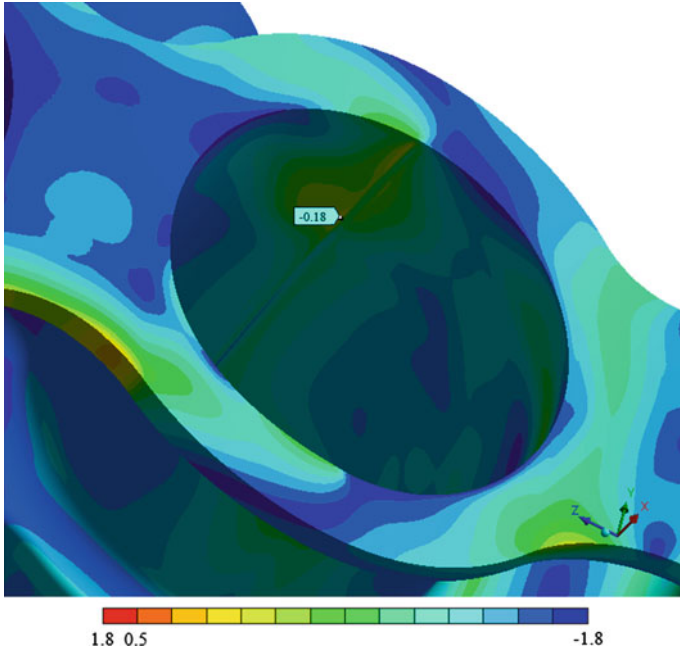
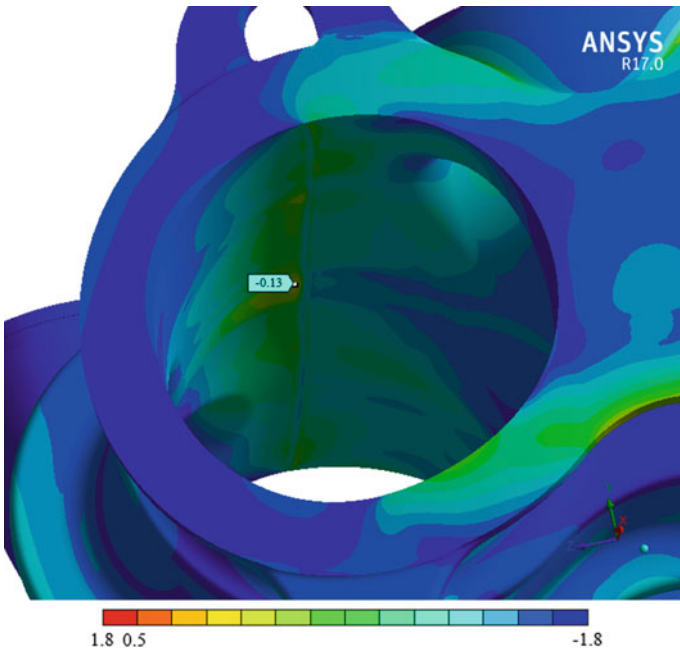


Fig. 11 Vessel 1 maximum stress (normalized value)—pressure boundary



**Fig. 12** Vessel 2 maximum stress (normalized value)—pressure boundary



**Fig. 13** Vessel 3 maximum stress (normalized value)—pressure boundary

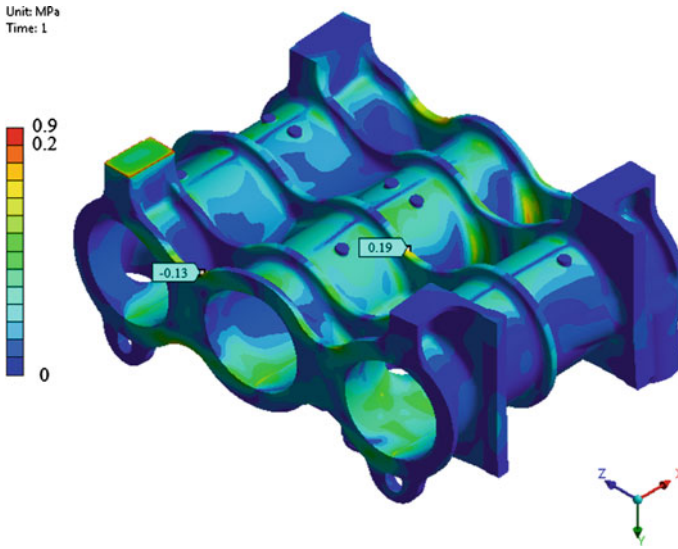


**Fig. 14** Non-pressure boundary stress (normalized value)

### 5.3.2 Non-pressure Boundary Fatigue Assessment

The combined maximum standard pressure and steady state stress intensity values for the entire vessel body occurs on the bottom strengthening ribs. The stress intensity is 0.19 (normalized value) shown in Fig. 14. This value is also below the 200,000 cycle limit, and thus the vessel body should experience no fatigue failures in its life.

## 6 Conclusion

Fatigue screening for the shell was performed as per ASME Division 2 guideline and subsequently; it was clear that detailed fatigue assessment is required. So, a nonlinear, coupled, thermal–structural analysis is performed using ANSYS. Pressure boundary and non-pressure boundary stress values are queried separately. Stress values obtained in the analysis is based on the vessel’s operating conditions and is found to be less than the material’s limiting fatigue value thus indicating an infinite life of the pressure vessel. Shell manufacture is proceeded as per the design and analysis above and is currently operational in centrifugal compressor installations in the field.

## References

1. Moss DR. Pressure vessel design manual
2. Keil B, Devletian J (2011) Comparison of the mechanical properties of steel and ductile iron pipe materials. Pipelines 2011: A Sound Conduit for Sharing Solutions © ASCE 2011, pp 1301–1312
3. Boyer HE. Atlas of fatigue curves. ASM international, p 261
4. ASME Section VIII Division 2, 5.5.2
5. Ansys Help Documentation



# Failure Analysis of HSS Punch Tool: A Case Study

Suraj Desai, B.V. Dilip Kumar Bhat, Guruvinder Singh, G.J. Naveen,  
P. Rangasamy, B. Jayadeva, P. Sampathkumaran, S. Seetharamu,  
G. Venkataramudu and H.B. Nirranjan

**Abstract** The work reports the failure investigations of HSS M35 grade steel that is used as a punch tool during cold forging process. The test samples were prepared from the heat-treated tool material and studied for composition, hardness, retained austenite, and microstructure. The punch tool operates at 800 MT during cold forging. It had produced 800 nos. of forged components before its failure. It is observed from the results that composition, hardness, and microstructure are conforming to the standard HSS M35 grade tool steel. The retained austenite (RA) percentage of the tool is within the acceptable limits. Fractographic studies were conducted on the failed sample using scanning electron microscope (SEM) to examine the fractured features. The cause of failure has been arrived at based on the fractographic analysis as well as macro-visual inspection of the fixture that is employed to clamp the punch tool. It is observed that, at the inner portion of the fixture, the presence of small pits and rubbing marks/ridges has caused stress concentration zone, leading to breakage/failure.

**Keywords** Punch tool · Cold forging · Fractography · Fatigue failure  
Failure investigation

---

S. Desai (✉) · B.V. Dilip Kumar Bhat · G. Singh · G.J. Naveen ·  
G. Venkataramudu · H.B. Nirranjan  
Department of Mechanical Engineering, Sambhram Institute of Technology,  
Bangalore 560097, India  
e-mail: desaisuraj13@gmail.com

P. Rangasamy · B. Jayadeva  
Essae Digitronics Pvt. Ltd., Bangalore 560099, India

P. Sampathkumaran · S. Seetharamu  
Central Power Research Institute, Bangalore 560080, India

## 1 Introduction

The manufacturing processes are classified into metal shaping, metal forming, metal cutting, metal treatment, and metal joining [1]. Each one of these deals with the different methodologies and is further divided into subgroups of the process catering to various applications. Forging is one of the key forming processes, which is further divided into hot forging, warm forging, and cold forging. Three types of process exist for the hot/cold forging process. They are hydraulic, mechanical, and screw types of systems [2]. There has been an increased use of the cold forging process in recent times because of its advantages such as: it is conducted at room temperatures, it is energy efficient, it produces near net-shaped products, it requires little to no finishing work, it provides improved dimensional control, and it has improved reproducibility. The scope of the work deals with the failure investigations of HSS material used as a punch tool in the cold forging process. The details regarding the material grade, heat treatment, procedure, history of the failure are covered in the following sections.

## 2 Materials and Methods

### 2.1 *Materials*

The breakage of HSS M35 grade steel used as punch tool has occurred, and the cause of failure has been investigated in this work. The punch is operated at 800 T load, and the forged equipment is produced at room temperature in one stroke. The tool has served for 800 nos. of such cold forged components and subsequently failed. The cause of failure has been investigated based on the metallurgical, mechanical and fractographic studies.

### 2.2 *Methods*

The various processes and investigation test methods adopted to find out the cause of failure of the punch tool are detailed below.

- Heat treatment schedule of the punch tool
- Cold forging methodology of producing a component using the punch tool
- Visual inspection
- Composition analysis
- Hardness test
- Microstructure analysis
- Retained austenite test
- Fractographic analysis

### 2.2.1 Heat Treatment Process

The heat treatment of the punch tool was carried out involving hardening at 1150 °C followed by three stages of stress relieving/tempering in the temperature range of 550–600 °C.

### 2.2.2 Cold Forging

The materials are made or reduced to standard shapes and process further to obtain component involving forming technique [2]. The primary metal forming process consists of rolling, forging, extrusion, drawing, etc. In forging, cold forging is one such method and it is defined as forming or forging of a bulk material at room temperature with no initial heating of the preform or intermediate stages [3]. Cold extrusion is a special type of forging process, wherein the cold metal flows plastically under compressive forces into a variety of shapes. These shapes are usually axisymmetric with relatively small non-symmetrical features, and, unlike impression-die forging, the process does not generate flash. The terms *cold forging* and *cold extrusion* are often used interchangeably and refer to well-known forming operations such as extrusion, upsetting or heading, coining, ironing, and swaging. These operations are usually performed in mechanical or hydraulic presses. The cold forged parts are generally used in various engineering applications such as aerospace, automotive industry for connecting rods, transmission shafts as they possess high strength and ductility (Fig. 1).

### 2.2.3 Visual Inspection

In the visual inspection, the tool that failed during cold forging has been inspected based on the macro-photographs.

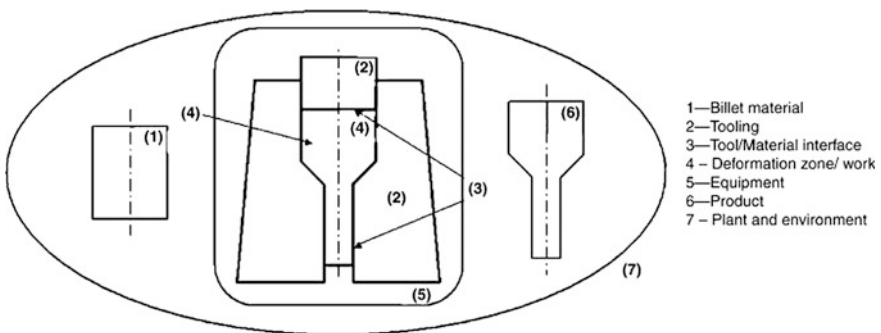


**Fig. 1** Cold forging as a system [3]

#### **2.2.4 Chemical Composition**

The composition of the tool material has been determined using optical emission spectrophotometer.

In this method, the sample is placed in its position and an arc is struck between the electrode and the sample. During the emission process, the sample is analyzed for the concentration involving optical/grating principles.

#### **2.2.5 Hardness**

The hardness measurement has been taken using Rockwell hardness tester (on 'C' scale). The load applied is 150 kg, and the type of indenter used is diamond cone (120°).

#### **2.2.6 Microstructure**

The sample is subjected to metallographical examination involving various stages of polishing—cloth polishing followed by etching (Nital) to reveal microstructure. The microstructure is observed using inverted metallurgical microscope (Neophot21).

#### **2.2.7 Retained Austenite**

The RA% has been measured using X-ray diffraction method (Rigaku stress analyzer) using Cr target at 30 kVA and 10 mA. The RA is determined by measuring the intensities of both alpha and gamma phases in the material.

#### **2.2.8 Fractography Analysis**

The failed sample is examined using scanning electron microscope (SEM) to study fractured features including origin of crack and propagation of crack.

### **3 Results and Discussion**

#### **3.1 Visual Inspection**

The macro-photographs of the failed sample M35 HSS grade steel are shown in Fig. 2a, b respectively, wherein Fig. 2a represents the top half of the tool which is clamped to the fixture and Fig. 2b is the bottom half of the failed tool.

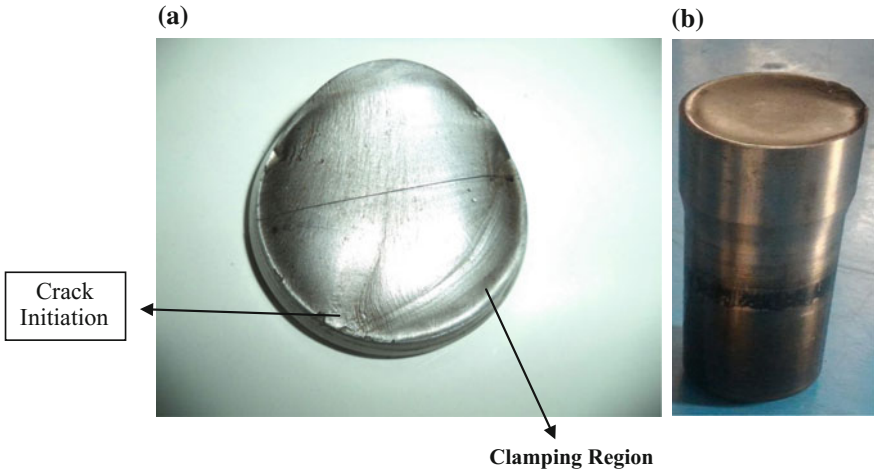


**Fig. 2**

The visual observation reveals moderately brittle type of failure revealing beach marks, cracks, matrix distortion, smooth and rough surfaces, etc. Further, the origin of crack and the region where the punch tool is clamped to the fixture of the cold forging machine are shown in the photograph (Fig. 2a).

### 3.2 Chemical Analysis

The result of the chemical composition of the tool steel sample is listed in Table 1. It is observed from Table 1 that the composition is conforming to the standard specification of M35 HSS grade steel.

### 3.3 Hardness Measurement

The hardness measurements of the failed HSS tool steel sample are given in Table 2. The hardness obtained is greater than 60 HRC, and it is found to be in accordance with the standard hardness value for M35 HSS grade steel.

**Table 1** Composition of the sample

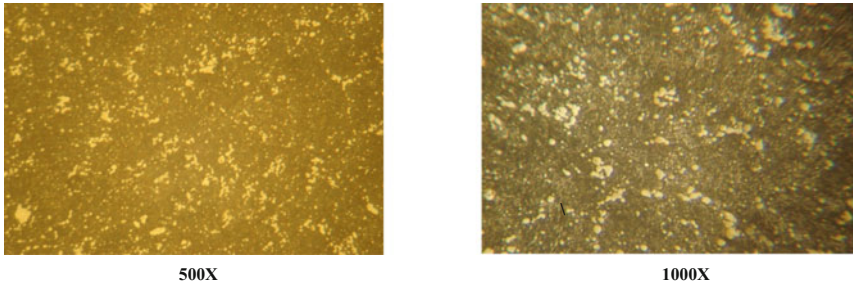
Elements	C	Si	Mn	Cr	Mo	Ni	Co	Cu	W
wt%	0.96	0.29	0.21	4.15	5.02	0.10	4.83	0.11	6.38

**Table 2** Hardness data

S. No.	Hardness (HRC)	Average hardness (HRC)
1	60, 62, 60, 64	62

### 3.4 Microstructure Analysis

The microstructure of the failed sample is carried out at two magnification levels: 500× and 1000×, and they are given below. The microstructure consists of spheroidal/angular carbides in a matrix of tempered martensite, which is conforming to the standard microstructure of M35 HSS grade steel. It is observed that the angular carbides are uniformly distributed in the matrix of tempered martensite.



### 3.5 Retained Austenite

The retained austenite (RA) % content of the tool sample is given in Table 3. The RA% is within 5%, which is the specified limit for this grade steel. Hence, it is well within the accepted level.

### 3.6 Fractographic Studies Using Scanning Electron Microscopy

The SEM pictures (Fig. 3a–d) show the fractographic features. Figure 3c shows the close-up view of the damaged surface. It is seen from Fig. 3a that the presence of beech marks in the form of striations is generally attributed to fatigue type of failure. It is reported in the literature [4] that concentric lines which are called as ripples or striations are observed as part of the fracture surface. These ripples are attributed to either the stress amplitude during cyclic loading or due to the sudden impact on the component, which affects the life of the component. It is also reported in the literature [4] that the distance by which the ripple is growing in one cycle is

**Table 3** Retained austenite data

S. No.	RA (%)	Av. RA (%)
1	1.0, 1.4, 1.3, 1.2	1.2

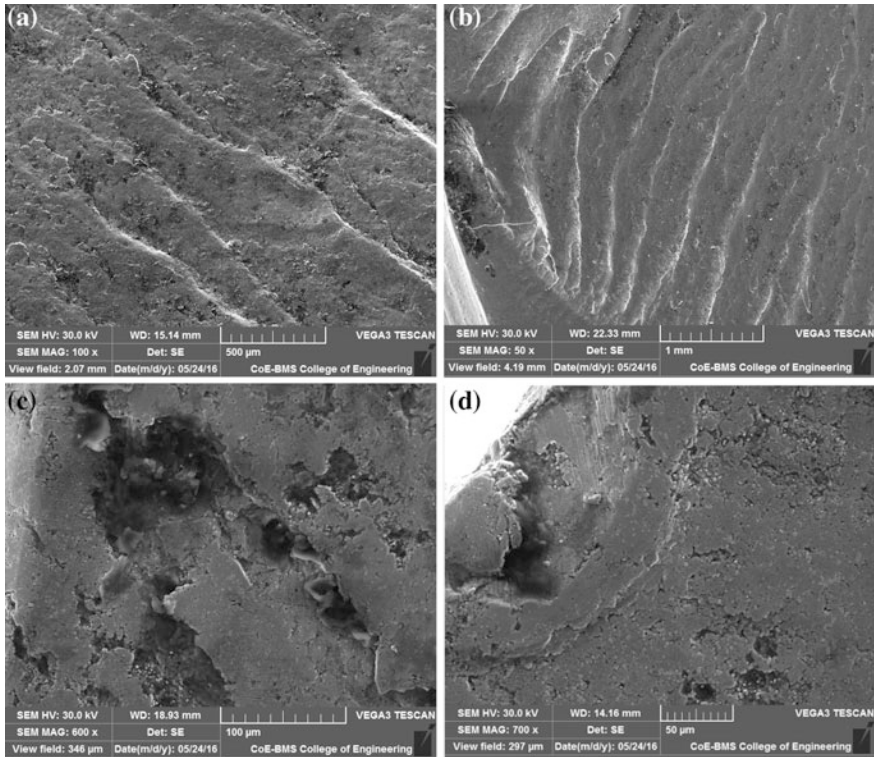


**Fig. 3**

equal to the width of the ripple. Also, it is the general observation of a fatigue failure that the rough granular part is attributed to fast crack growth after the critical condition is attained. The smooth portion of the fracture surface corresponds to slow crack growth.

In Fig. 3c, d, it is noticed that the damaged surface is indicating the presence of deep grooves due to severe plastic deformation, chip formation and network of cracks. These features are attributed to fast failure. It is reported [5] that the chip formation in the form of metallic pieces is one of the causing failures as they initiate cracks on the surface. The rubbing marks and pits of the fixture are observed in Fig. 4, and they are the root cause of initiating the cracks as they act as stress concentration regions.

The beech marks seen (Fig. 3a, b) on the failed punch tool are the indications to fatigue failure. As the punch tool has failed at the clamping end, it is held using a fixture on the top portion of the cold forging machine. The fatigue failure has occurred due to the sudden load application in one stroke. A slight misalignment of the tool, causing failure, has not been ruled out, as one could observe small pits/rubbing marks/ridges where the tool is fixed using fasteners. These pits acts as

**Fig. 4** Inner portion of the fixture to which the punch tool is clamped



stress raisers, and this has caused micro-cracks and aggravated further due to crack propagation, leading to fatigue failure. It is reported [4] that the failure of punch tool in most cases is attributed to misalignment causing fracture due to excessive load application. This would cause cracking due to irregular and excessive stresses, which would have acted on it. It is further reported that over-loading is to be avoided to prevent such failures. The procedure to reduce the failure of the tool deployed in cold forging has been reported [6]. This is based on the expertise, experience gained, and knowledge developed in the past. One of the methods suggested is the adoption of finite element simulation; a new design may be evolved to avoid the failure. The other method being measurement of residual stress and its analysis which will perhaps throw more light on the cause of the failure as one can get stress mapping at different regions of failure. No attempt has been made in this work to evaluate residual stress of the failed punch tool. The cold forged tools have complex geometry from high carbon to alloy steels as reported [6], having high forging pressure, and the ductility of the tool is low. In view of this, the tool life is not that long and the defects formed during forging limit the economic use of the cold forging process.

The fatigue limits are generally established experimentally (SN curve) on a smooth polished surface as the surface roughness, stress concentration, temperature, and nonmetallic inclusions are the factors which would reduce the fatigue strength [5]. Therefore, it is desirable to evaluate the fatigue strength experimentally.

Thus, in the present case, the fatigue fracture (beach marks) has occurred due to sudden load application, and moreover, the punch tool material being moderately brittle has cracked (chip formation and pits) and subsequently failed. Thus, this finding gets very good support from the literature report [4–6]. The remedial measure suggested is to adopt advanced coating methodology for the inner side of the fixture to minimize wear/pitting formation.



## 4 Conclusions

The following salient conclusions are drawn based on the above investigations.

- The chemical composition is meeting the standard specifications of M35 grade tool steel.
- The hardness value obtained is matching with that of the standard value of M35 grade tool steel.
- The microstructure reveals spheroidized carbides in a matrix of tempered martensite as it is in line with the M35 grade tool steel structure.
- The retained austenite % is much below the acceptable value of 5%.
- The fractographic analysis shows beech marks and moderately brittle type of fracture.
- The cause of failure is attributed to fatigue failure due to the ridges/rubbing marks seen at the inner portion of the fixture where the tool punch is clamped as they act as stress raisers.
- It is desirable to provide advanced coating to the inner portion of the fixture to reduce wear from the point of improving the surface integrity characteristics.

**Acknowledgements** The authors would like to thank the management of Sambhram Institute of Technology, Essae Digitronics Pvt. Ltd., and Central Power Research Institute for having accorded permissions to present the paper.

## References

1. Gupta HN, Gupta KC, Mittal A (2009) Book on manufacturing processes, 2nd edn. New Age International Publisher
2. Pandey PM. Metal forming process. <http://paniit.iitd.ac.in/pmpandey>
3. Ngaile G et al (ed) (2005) Cold and hot forging, fundamentals and applications. ASM International, Materials Park, OH, USA
4. Raghavan V (2010) Physical metallurgy; principles and practice. PHI Learning (P) Ltd., New Delhi, pp 153–158
5. Randedius M (2008) Influence of microstructure on fatigue and ductility properties of tool steel. Department of Materials Science, Royal Institute of Technology, Sweden
6. Failure Analysis and Prevention, ASM Handbook, vol 11. ASM International, Materials Park, OH, USA, 2002

# Evaluation of Fatigue Strength of Alloy Steel Pipe Under Influence of Hydrostatic Pressure

Deepak Kumar Rout and Raghu V. Prakash

**Abstract** The influence of hydrostatic pressure on the performance of the material is becoming increasingly important in several applications such as ocean engineering, nuclear engineering and petroleum engineering. It is required to meet the increasing demand to analyze the influence of hydrostatic pressure under fatigue load. The magnitude of hydrostatic pressure increases with increase in depth of the water from surface level. For example at a depth of 2 km from water surface, 200 bar hydrostatic pressure will act on the submerged body. In addition to that when components are used in subsea environment, corrosion will occur in the component. So it is necessary to determine what will be the effect on fatigue life of the components which are subjected to hydrostatic pressure with fatigue load in a corrosion environment. This analysis will be taken into consideration while designing machine element which is used for underwater application. High hydrostatic pressure alters the yield criterion of materials. Thus, it becomes essential to generate the fatigue strength data of structural steel in pressurized simulated sea water (3.5% NaCl solution) conditions. This paper presents the comparison of fatigue life data evaluated for alloy steel pipe under ambient conditions and under hyperbaric pressure conditions. To generate fatigue strength data under the influence of hydrostatic pressure, experiment has been done in MTS machine setup which consists of high-pressure chamber assembly and computer-controlled servo-hydraulic test system for applying cyclic load and differential hydrostatic pressure. Here both external and internal pressures are applied with the axial load to the specimen pipe. The S–N curve for alloy steel pipe (ASTM 106 grade B) is evaluated for two differential hydrostatic pressures at 10 bars internal with 30 bar external and 30 bar internal with 50 bar external pressure which are applied to the test specimen pipe.

---

D.K. Rout (✉)

Tata Consultancy Services, Bangalore, India  
e-mail: deepak.rout1985@gmail.com

R.V. Prakash

Mechanical Engineering Department, IIT Madras, Chennai, Tamil Nadu, India

© Springer Nature Singapore Pte Ltd. 2018

S. Seetharamu et al. (eds.), *Proceedings of Fatigue,*

*Durability and Fracture Mechanics*, Lecture Notes

in Mechanical Engineering, [https://doi.org/10.1007/978-981-10-6002-1\\_9](https://doi.org/10.1007/978-981-10-6002-1_9)

**Keywords** Alloy steel pipe · Hydrostatic pressure · Fatigue strength  
Hydrostatic fatigue · Fatigue life

## 1 Introduction

Nowadays, lots of mechanical components are used in ocean engineering, petroleum engineering and nuclear engineering. These mechanical components are subjected to both static and dynamic loads. When components are subjected to dynamic load (cycle/repeated variable), it is important to find the endurance strength (S–N curve) of the material. Endurance limit is known as the minimum stress value below which the component will be in service for infinite life cycle without any fail. But generally endurance limits are found at atmospheric pressure condition which may not be always the case. There are certain cases like ocean engineering, petroleum engineering and nuclear engineering where components are subjected to both hydrostatic stress and fatigue load.

The magnitude of hydrostatic pressure increases with increase in depth of the water from surface level. For example at a depth of 2 km from water surface, 200 bar hydrostatic pressure will act on the submerged body. In addition to that when components are used in subsea environment, corrosion will occur in the component. So it is necessary to determine what will be the effect on fatigue life of the components which are subjected to hydrostatic pressure with fatigue load in a corrosion environment. This analysis will be taken into consideration while designing machine element which is used for underwater application. For this analysis, some knowledge regarding fatigue and hydrostatic stress is required.

### 1.1 Fatigue

Fatigue is the progressive, localized, permanent structural change occurring in a material that is subjected to a condition that produces fluctuating stress and strain at some point or points and that may culminate in cracks and complete fracture after a sufficient number of fluctuations [1].

Fatigue is a surface phenomenon. Generally, fatigue starts with an initiation of a small crack; the crack may be so small and minute and cannot be seen without help of high-magnified electron microscope. The crack usually develops at a point of discontinuity in the material, such as scratches, a change in cross section, a keyway or a hole, pits, inclusion, or embrittled grain boundaries. Microcracks may be initially present due to welding, heat treatment or mechanical forming. Once a crack is initiated, the stress concentration effect becomes greater and the crack progresses more rapidly. As the stressed area decreases in size, the stress increases in magnitude until, finally, the remaining area is unable to sustain the load and the component fails suddenly.

The fatigue failure process can be divided into five stages [7]:

- (a) Cyclic plastic deformation prior to fatigue crack initiation
- (b) Initiation of one or more microcracks
- (c) Propagation or coalescence of microcracks to form one or more microcracks
- (d) Propagation of one or more macrocracks
- (e) Final failure

## 1.2 Hydrostatic Pressure

When a body submerged in water, it is subjected to hydrostatic pressure. Hydrostatic pressure depends on both density of the fluid and depth of the water column. Magnitude of hydrostatic pressure increases with increase in the depth.

Hydrostatic pressure

$$P = \rho gh \quad (1)$$

where

- $\rho$  density of the fluid in  $\text{kg/m}^3$
- $g$  acceleration due to gravity =  $9.81 \text{ m/s}^2$
- $h$  height or depth at which body is immersed (m)

## 2 Experimental Details

### 2.1 Methodology

To achieve the above-mentioned objective, following steps can be followed

- Design and manufacture of adapter to hold the fatigue test specimen in MTS 810 machine
- Prepare the fatigue test specimen (seamless alloy steel pipe in ASTM 106 grade B material)
- Conduct the tension test for specimen pipe in UTM machine
- Conduct the experiments in MTS 810 for various stress values under plain fatigue and differential hydrostatic pressure.
- Examination of fractured surface under SEM (scanning electron microscope)

## 2.2 Finite Element Analysis of Test Specimen Pipe

Before deciding on final dimension of the test specimen (seamless alloy steel pipe), finite element analysis has been done by using the software ANSYS® Work bench. Dimension details of the pipe used for finite element analysis are mentioned in Fig. 1. Tetrahedral solid element is used for finite element analysis.

## 2.3 Specimen Preparation

A seamless pipe made of ASTM 106 grade B steel is used for the experimental specimen whose chemical composition is given in the below table

Elements	Composition (%)
Carbon	0.3
Manganese	0.290–1.060
Phosphorous	0.035
Sulfur	0.035
Silicon	0.1
Chromium	0.4
Molybdenum	0.15
Nickel	0.4

The dimension of test specimen has been finalized for the manufacturing drawing of the specimen based on the finite element analysis. Twenty round fatigue specimens are prepared in CNC machine with high surface finish. The specimen has M26 x 1.5 threading on both sides to fix on fatigue loading arrangement assembly. The manufacturing drawing of the specimen is shown in Fig. 2.

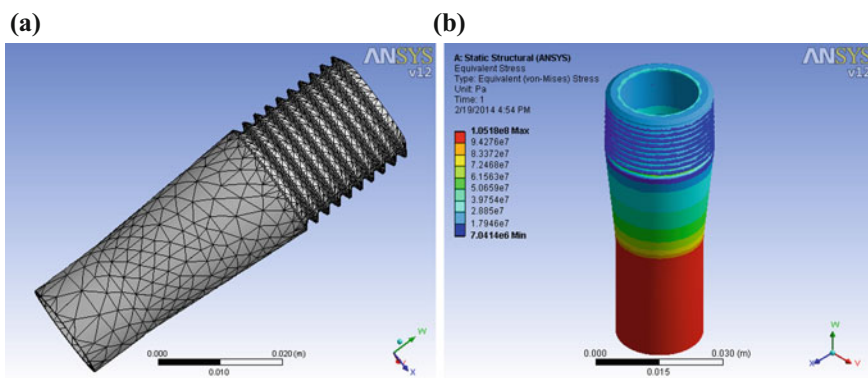


Fig. 1 a Mesh model of the test specimen, b finite element analysis model of the test specimen

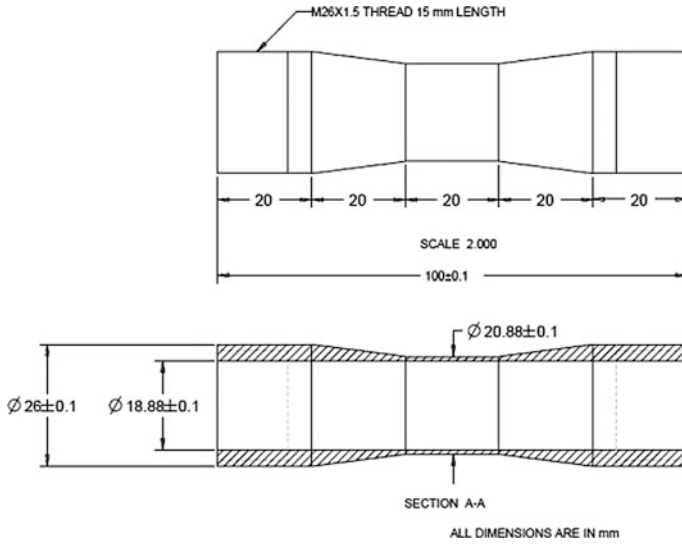


Fig. 2 Manufacturing drawing of fatigue specimen pipe

### 2.4 Schematic Diagram of Test Setup

It consists of a hand pump for pressurizing the 3.5% NaCl solution (simulated sea water) and non-return valve to allow the fluid in only one direction. The pressure gauge is used to monitor the pressure level in the high-pressure chamber. Air relief valve is provided in the chamber to relief the air accumulated in the pressure chamber. Drain valve is used to remove the water from the chamber after every experiment (Fig. 3).

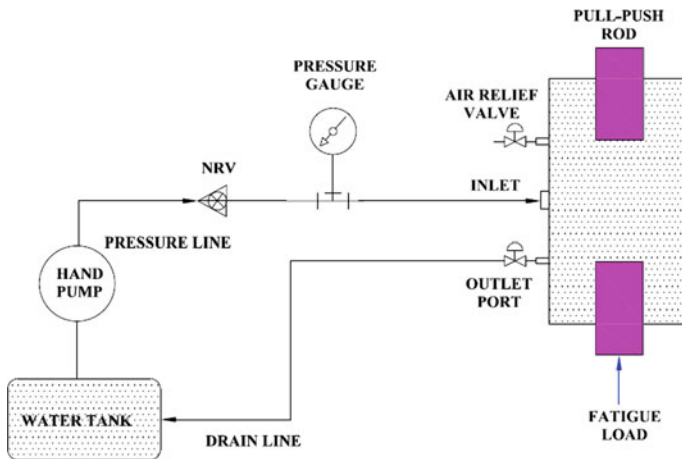


Fig. 3 Schematic diagram of test setup

## 2.5 Experimental Procedure

Axial fatigue test is carried out on the alloy steel pipe specimen by using MTS 810 fatigue testing machine. The effect of hydrostatic pressure on fatigue life of the test specimen is studied by applying the pressure on inside as well as outside diameter of the test specimen in specially designed chamber.

The procedure is followed during the experiment as follows: First mount the top and bottom pull push rod in MTS 810 machine, and then pressurize the test specimen assembly which contains adapter at both ends of specimen with non-return valve to the required fixed internal pressure using hand pump. After that, assemble the internally pressurized test specimen pipe in the pull push rod and then mount the pressure chamber with the end cap and tie rod and nuts above the stand. Then, pressurize the high-pressure chamber to the required pressure using water hand pump. The internal pressure created inside the pressure chamber acts as external pressure to the test pipe specimen. Prepare the test case in the computer system by assigning the stress value, frequency, data, log file name and interlock levels, and start the experiment. Monitor the experiments for peak/valley loads and displacements till the specimen fails. Note down the number of cycles for which specimen is broken. Repeat the experiments for different stress levels with same hydrostatic pressure and note down the corresponding number of cycles.

Plot the graph between stress amplitude and number of cycles (Fig. 4).

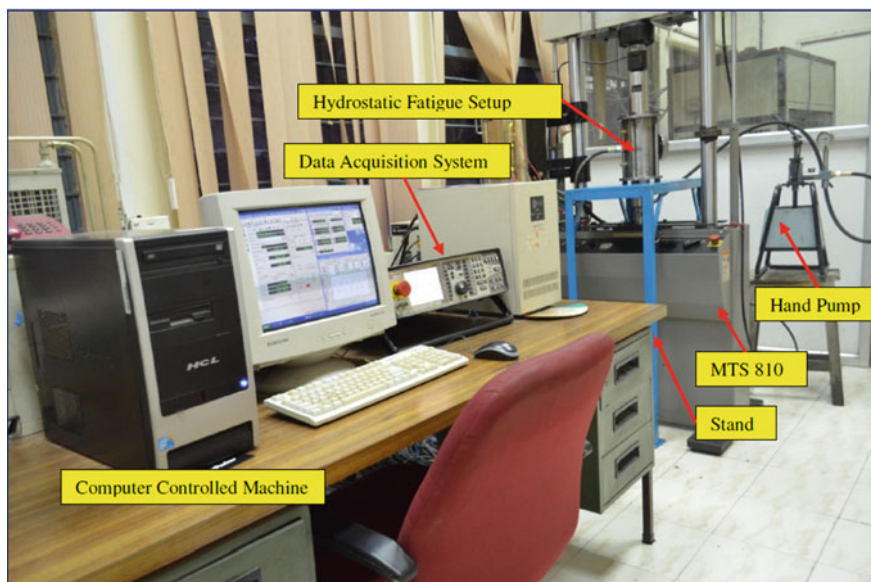


Fig. 4 Experimental setup

The fatigue tests are conducted under constant stress amplitude of 130, 168, 180, 192, 204 MPa at 3 Hz frequency and fully reversed condition. Tests are conducted at laboratory air environment and simulated sea water condition which is maintained at 10 bar and 30 bar internal hydrostatic pressure for the test specimen and 30 bar and 50 bar external hydrostatic pressure outside the test specimen, respectively. As the yield strength of the material is 240 MPa, the load calculation and the test matrix are prepared according to this yield strength.

### 3 Result and Discussion

Various experiments have been conducted on ASTM 106 grade B seamless pipe specimen to find the fatigue life of pipe material. This section explains about the tensile test which will give yield strength of the material; based on the yield strength, plain fatigue experiment has been done in the normal laboratory environment to find the fatigue life of the material. After that, hydrostatic pressure is applied both internally and externally in addition to the axial load to find the fatigue life. Analysis has been done on the influence of hydrostatic pressure on the fatigue life of the material. Finally, the fracture surface has been studied from the SEM image.

#### 3.1 Basquin Law

The method of fatigue life prediction from the magnitude of the fluctuating strain (rather than the stress) has begun with Basquin who introduced an empirical relation connecting the stress amplitude and life is shown in Eq. 2 [8]

$$\frac{\Delta\sigma}{2} = \sigma_a = \sigma'_f (2N_f)^b \quad (2)$$

where

- $\sigma_a$  stress amplitude (MPa)
- $\sigma'_f$  fatigue strength coefficient (MPa)
- $2N_f$  number of stress reversal to failure
- $b$  fatigue strength exponent



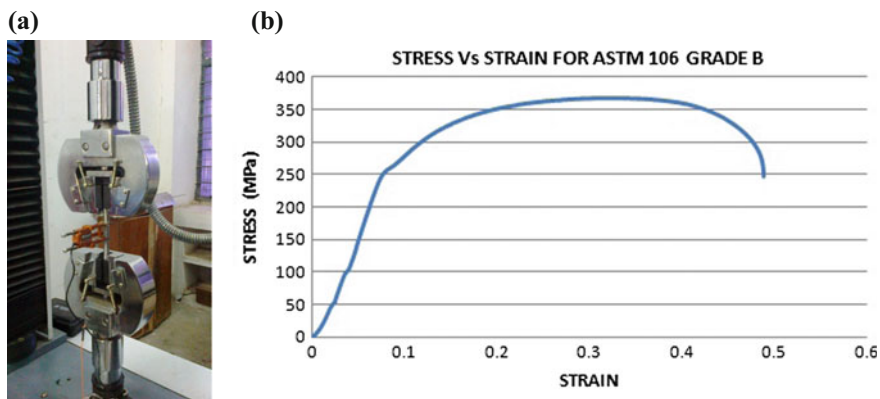


Fig. 5 a Tensile test setup, b stress strain curve from tensile test

### 3.2 Tensile Test

Tensile test has been conducted for the ASTM 106 grade B seamless pipe specimen in the UTM machine to find out the yield strength of the material. Experiment has been conducted for tensile test, and stress strain graph has been plotted for the material. 0.2% offset line has been drawn, and finally, the yield strength of the material has found to be 240 MPa. Figure 5 shows resultant stress–strain graph from experiment.

### 3.3 Plain Fatigue Test

Plain fatigue experiments have been conducted at different stress levels at a constant frequency of 3 Hz frequency in MTS 810 machine. Stress levels are varied as 204, 192, 182, 168, 130 MPa, and corresponding number of cycles to failure is noted. S–N curve was plotted in log scale for plain fatigue data and is shown in Fig. 6c. Power law was fitted to the data and related with Basquin law. The fatigue strength coefficient is 1086.3 MPa, and fatigue strength exponent is  $-0.165$ . It is very clear that the increased stress level decreases the number of cycles to failure. These data shown in Table 4.1 were taken as reference data to analyze the influence of hydrostatic pressure on the given material. The plain fatigue experiment setup has been shown in Fig. 4.2a and the pipe specimen before and after the plain fatigue test shown in Fig. 4.2b.

Specimen number	Stress amplitude (MPa)	No of cycles to failure	Frequency (Hz)
1	204	31,307	3
2	192	32,566	3

(continued)

(continued)

Specimen number	Stress amplitude (MPa)	No of cycles to failure	Frequency (Hz)
3	180	57,624	3
4	168	70,055	3
5	130	418,898	3
6	108	Run out for 17,26,578	3

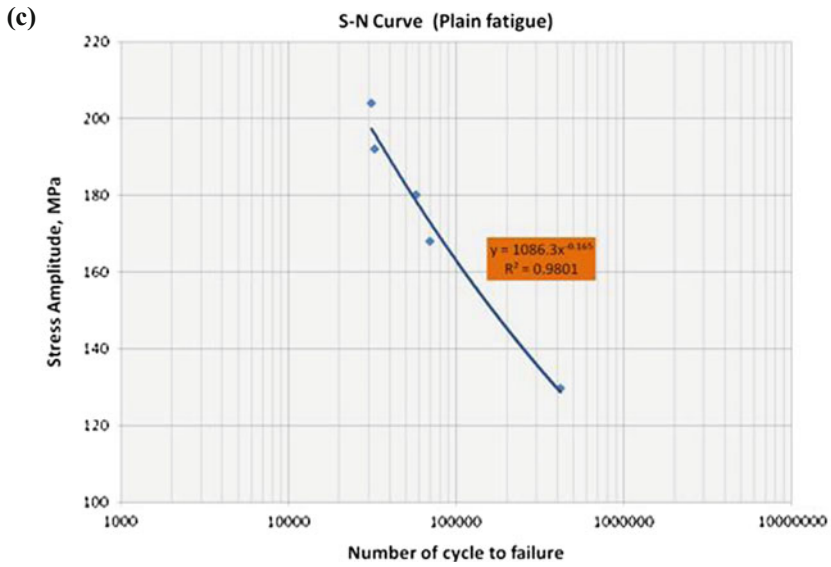
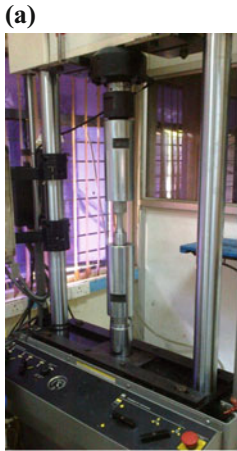


Fig. 6 a Plain fatigue test setup, b test specimen after and before plain fatigue test, c S–N curve for ASTM 106 grade B seamless pipe material under plain fatigue

### 3.4 *Hydrostatic Fatigue Test*

Hydrostatic fatigue test has been conducted by applying differential hydrostatic pressure both inside and outside of the test specimen which is kept inside the high-pressure chamber. Here constant hydrostatic pressure is maintained both inside and outside the specimen and different stress level applied at a constant frequency of 3 Hz. Five experiments have been done in these stress levels by applying 10 bar inside and 30 bar outside hydrostatic pressure in the test specimen pipe. Another five experiments have been done in the same stress level by applying 30 bar inside and 50 bar outside hydrostatic pressure. Figure 4.3 shows the test specimen under 30 bar internal pressure. Number of cycles to failure corresponding to each experiment has been noted down, and S–N graph has been plotted for these values (Fig. 7).

Specimen number	Stress amplitude (MPa)	Number of cycles to failure	Frequency (Hz)	Inside pressure of specimen (bar)	Outside pressure of specimen (bar)
1	130	77,100	3	10	30
2	168	43,578	3	10	30
3	180	23,280	3	10	30
4	192	15,034	3	10	30
5	204	8000	3	10	30
6	130	18,234	3	30	50
7	168	11,238	3	30	50
8	180	8257	3	30	50
9	192	6011	3	30	50
10	204	4377	3	30	50

### 3.5 *Comparison Between Plain and Hydrostatic Fatigue*

It is found from the graph that there is a decrease in life by an order of magnitude when a differential hydrostatic pressure has been applied compared to the plain fatigue. It has been also found the fatigue life decreases with increase in hydrostatic pressure.

Figure 8 shows S–N curves plotted for plain fatigue (laboratory air), hydrostatic fatigue by applying a differential pressure of (10 bar inside, 30 bar outside) and (30 bar inside, 50 bar outside) of the test specimen. Basquin power law is fitted, and its parameters are mentioned for each curve, as mentioned before the value of  $R^2$  which shows the deviation from the original data points. As the values are near to one, it seems as best fit curve for the given data.

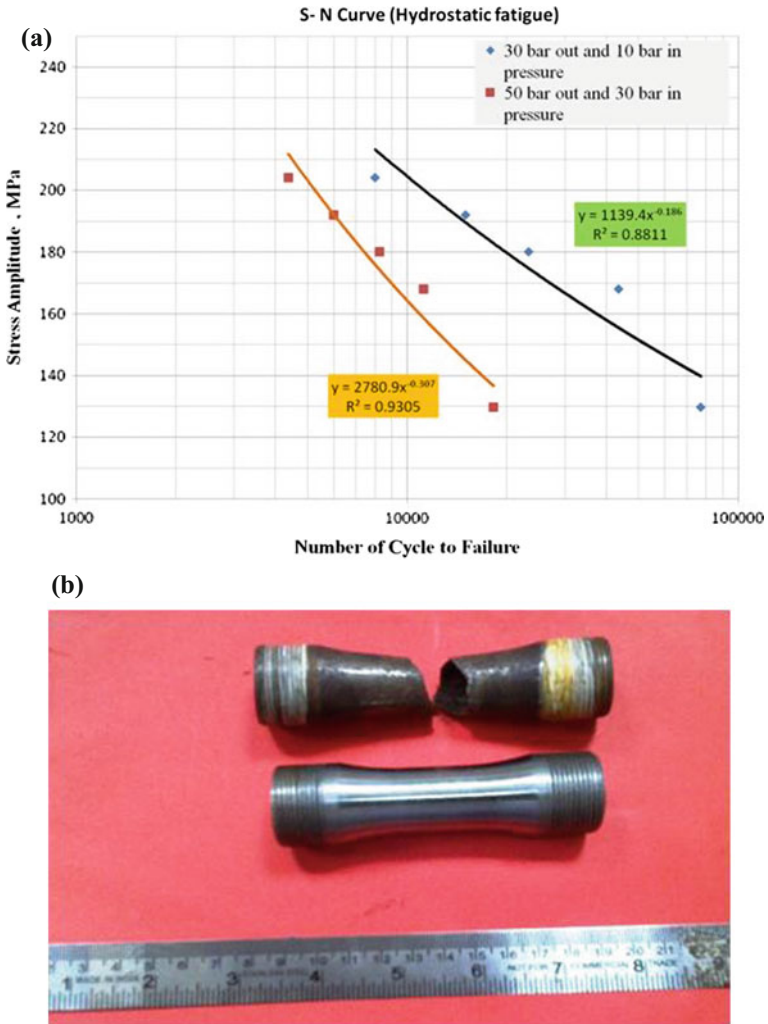


**Fig. 7** **a** S–N curve under hydrostatic fatigue, **b** test specimen after and before hydrostatic fatigue test

The fatigue strength exponent drops significantly from  $-0.165$  (plain fatigue) to  $-0.186$  (hydrostatic pressure fatigue). It is also found that the influence of hydrostatic pressure is dominant at high stress levels when compared to low stress levels.

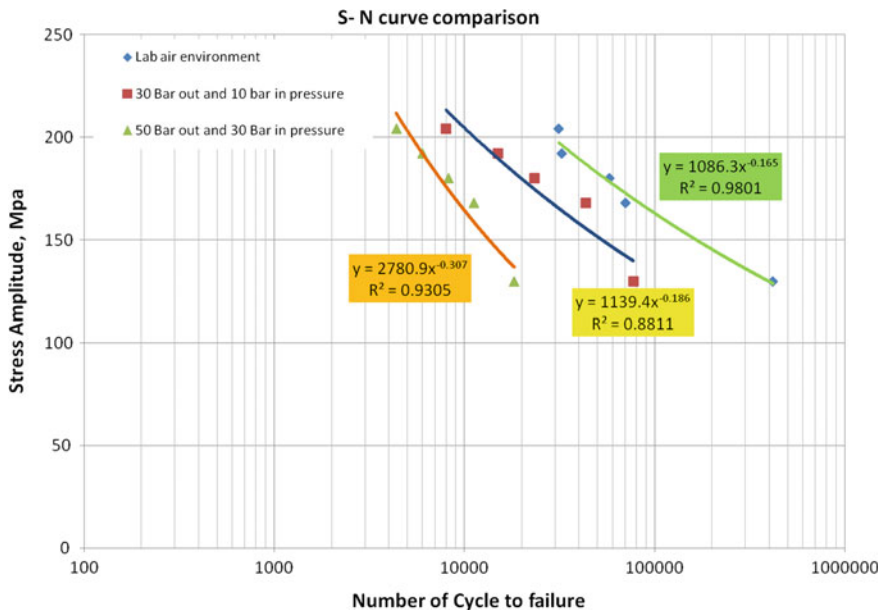


Fig. 8 S-N curve under hydrostatic fatigue

### 3.6 SEM Image of Plain Fatigue Test

Three distinct region of fatigue fracture is clearly seen in SEM image (Fig. 4.8). The three distinct regions are crack initiation, crack propagation and fast fracture in the material. The presence of dimples shows the ductile fracture in crack propagation and shear fracture in last region of failure. This experiment is conducted at a frequency of 3 Hz and stress amplitude of 180 MPa (Fig. 9).

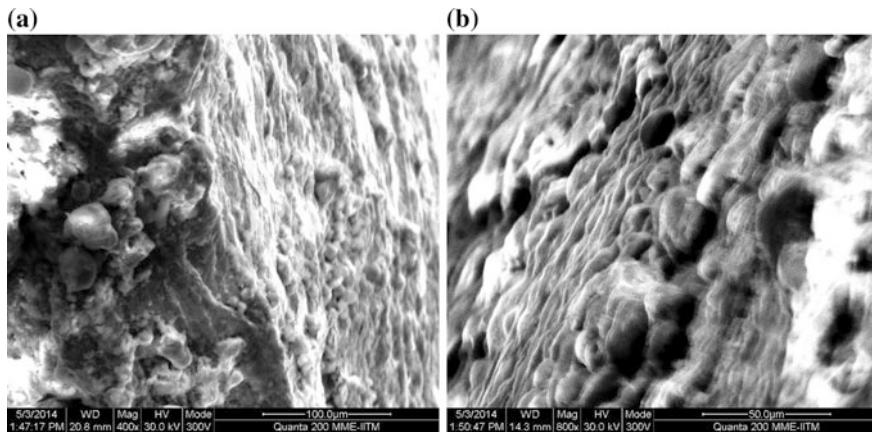


Fig. 9 a, b SEM image of fracture surface of specimen in plain fatigue test

### 3.7 SEM Image of Hydrostatic Fatigue Test

Hydrostatic fatigue SEM images are shown below. The fractured surfaces are covered with corrosive medium which are visible in the SEM images. Ultrasonic cleaning with acetone is carried out to clean the fracture surface before SEM. This experiment was conducted at a differential pressure of 10 bar inside and 30 bar outside hydrostatic pressure of the test specimen and stress amplitude of 180 MP (Fig. 10).

From the above SEM image of the fracture surface under hydrostatic pressure condition, it can be observed that there is a change in the mode of fracture in the surface. Due to hydrostatic pressure, the fracture surface contains both ductile and brittle mode of failure. The brittle fracture can be identified by multiple facets or cleavage on the surface, whereas the ductile fracture can be identified by the dimples.

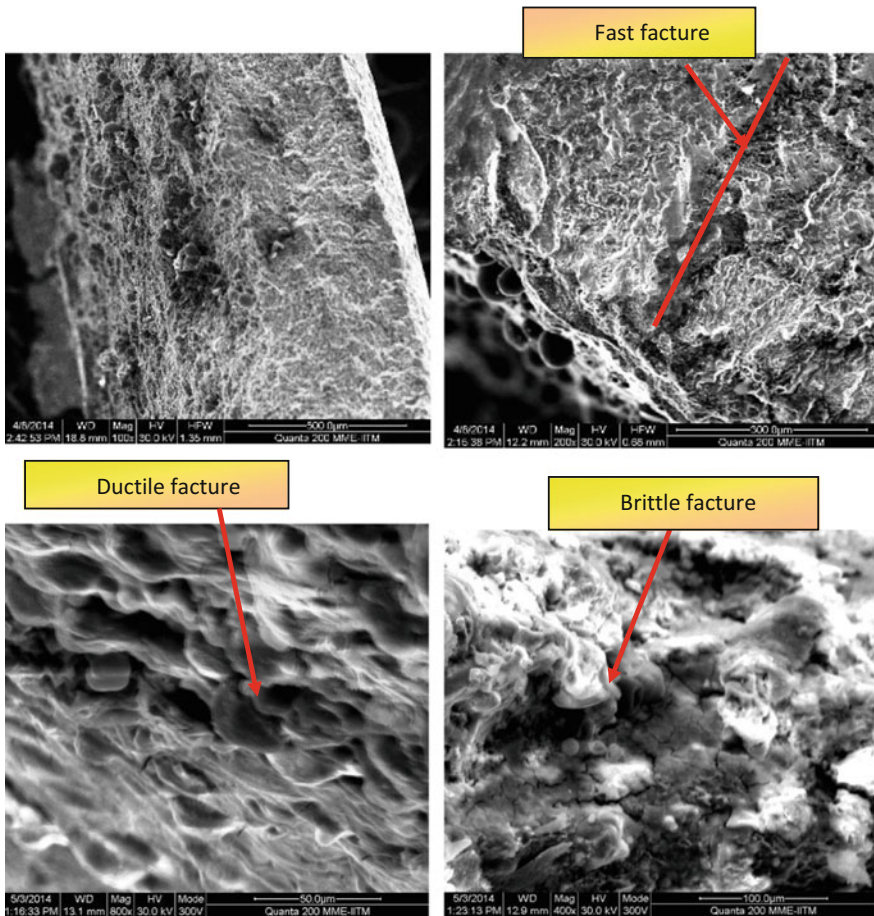


Fig. 10 a–d SEM image of fracture surface of specimen in hydrostatic fatigue test

After the SEM image analysis, it can be concluded that the mode of failure of the fracture surface is ductile in nature under plain fatigue, whereas the mode of failure under hydrostatic pressure condition is either a mixed failure which contains both brittle and ductile fracture

## 4 Conclusion

After the conduction of the experiment and analyzing the result, the following observations have been made; the corrosive environment is one of the responsible factors in addition to the axial load for the initiation of crack. Hydrostatic pressure has major influence on crack propagation stage, and with increase in hydrostatic pressure, the crack propagation rate becomes more faster. It is also found that the influence of hydrostatic pressure is dominant at high stress levels when compared to low stress levels. The fatigue strength exponent drops significantly from  $-0.165$  (plain fatigue) to  $-0.186$  (hydrostatic pressure fatigue). There is a decrease in life by an order of magnitude when the material is subjected to a differential hydrostatic pressure of 10 bar inside and 30 bar outside of the test specimen pipe. It is also quite interesting to note that the life further decreases when the differential hydrostatic pressure is increased. Fractographic analysis reveals a change in the mode of failure under hydrostatic pressure.

## References

1. ASM Hand book Vole: 19 (1996) Fatigue and fracture. ASM International Publication
2. Pang J, Wu PD, Huang Y, Chen XX, Lloyd DJ, Embury JD, Neale KW (2009) Effects of superimposed hydrostatic pressure on fracture in round bars under tension. *Int J Solids Struct* 46:3741–3749
3. Garson A (1977) Continuum theory of ductile rupture by void nucleation and growth. Part I. Yield criteria and flow rules for porous ductile media. *J Eng Mater Technol* 99:2–15
4. Wu PD, Chen XX, Lloyd DJ, Embury JD (2010) Effects of super imposed hydrostatic pressure on fracture in sheet metals under tension. *Int J Mech Sci* 52:236–244
5. Lefebvre DF (1989) The hydrostatic pressure effect on life prediction in biaxial low cycle fatigue. Mechanical Engineering Publication, London, pp 511–533
6. Thiruvengadam A (1972) Corrosion fatigue at high frequencies and high hydrostatic pressures. Stress corrosion cracking of metals—ASTM STP 518, pp 139–154
7. Anderson TL (2005) Fracture mechanics-fundamentals and applications, 3rd edn. Taylor & Francis
8. Suresh S (2003) Fatigue of materials, 2nd edn. Cambridge University Press

# Estimation of Fatigue Life of Notched Specimens of P91 Steel by Analytical Approaches

J. Veerababu, Sunil Goyal, R. Sandhya and K. Laha

**Abstract** To understand the effect of multiaxial state of stress at laboratory scale, specimens with different kinds of notches are widely used. In this investigation, the effect of notch root radii on low cycle fatigue life of P91 steel has been studied. Fatigue tests were carried out on notched specimens having notch radius of 1.25, 2.5 and 5.0 mm at net stress amplitudes of 250, 300 and 350 MPa at 823 K. To estimate the fatigue life in the presence of a notch based on local strain at the notch root, different analytical approximation methods such as linear rule, Neuber's rule and strain energy density approach have been employed. The fatigue life could be predicted within a factor of  $\pm 16$  on experimental fatigue life. The difference among the predicted fatigue lives by the different analytical methods decreased with increasing notch radii. The strain energy density method and linear rule predicted nearly equal fatigue lives in all the cases.

**Keywords** Analytical approximations · Low cycle fatigue · P91 steel  
Notched specimen · Life prediction

---

J. Veerababu (✉) · S. Goyal · R. Sandhya · K. Laha  
Mechanical Metallurgy Division, Indira Gandhi Centre for Atomic Research,  
Kalpakkam, India  
e-mail: veeraj@igcar.gov.in

S. Goyal  
e-mail: goyal@igcar.gov.in

R. Sandhya  
e-mail: san@igcar.gov.in

K. Laha  
e-mail: laha@igcar.gov.in



## 1 Introduction

Studying material fatigue behavior at laboratory scale is a key factor to assess the fatigue life of the component on site. If material undergoes strain-controlled cyclic loading conditions in service, standard strain-controlled low cycle fatigue (LCF) laboratory tests has to be performed on smooth specimens to understand its fatigue behavior. Coffin–Manson–Basquin relations are used to determine fatigue design parameters from obtained experimental data and further to estimate the fatigue life of component for unknown loading conditions. Nowadays, day-to-day technological developments demands to design more complicated structures which can withstand the complicated and diverse service conditions. Geometrical irregularities and microstructural inhomogeneities are inevitable in the design of such components. Combination of mode of service loadings with these discontinuities introduces multiaxial stress states. Specimens with different notch geometries are widely used to understand the effect of multiaxial state of stress at laboratory scale [1–3]. Notches behave like stress raisers in the specimens and hence constrain the deformation near to the notch root and this local deformation increases with decrease in notch root radius. Accurate estimation of the local plastic deformation is a key factor in the prediction of fatigue failure life of the notched components. Different analytical methods are in the practice to evaluate local stresses and strains at the notches [1]. The strain-life ( $\epsilon$ - $N$ ) approach is generally used to calculate the fatigue life of notched specimens. In this approach, knowledge of experimental fatigue data obtained from smooth specimens is used to estimate the fatigue life of notched specimens considering the estimated local stress and strain at notch root based on analytical approximations such as linear rule, Neuber's rule [4] and strain energy density (SED) method [5].

P91 (modified 9Cr–1Mo steel) steel is a candidate material for steam generator components in Prototype Fast Breeder Reactor (PFBR), Kalpakkam, India [6]. This steel has shown reliable high-temperature mechanical properties when compare to other chromium steels in steam generator side. Generally, this steel is used in optimized-tempered-martensitic structure condition. Hence, its microstructure consists of lath boundaries decorated with fine  $M_{23}C_6$  precipitates and fine V, Nb nitro-carbon precipitates at the lath boundaries as well as inside the lath structure. These fine precipitates provide very good creep resistance at elevated temperatures. LCF characterization on smooth specimens of this material has been studied earlier by various researchers [7–9]. Their reports mentioned that cyclic softening behavior of the material [7], reduction in fatigue life at low strain amplitudes and high temperatures due to oxidation [7], exhibition of inferior fatigue properties in hot forged alloy compared to hot rolled material [8], coarsening of  $M_{23}C_6$  precipitates and formation of laves phases which further causes reduction in LCF lives, as the result of prolonged aging [9].

In this investigation, LCF tests were conducted on smooth specimens of P91 steel and Coffin–Manson–Basquin's parameters were obtained. To study the notch effects on its fatigue life of this steel, experiments were conducted on notched

specimens. Different techniques, viz., linear rule, Neuber’s rule, SED method were applied to calculate local stress and strain at notch root. The accuracy of these models in the estimation of fatigue life of notched specimens has been assessed.

## 2 Experimental Details

The chemical composition of the steel is given in Table 1. The 110-mm length blanks in rolling direction were obtained from the as received 30 mm wall thickness rolled plate. These blanks were normalized at 1313 K/1 h + air cooling, followed by tempering at 1033 K/1 h + air cooling. LCF specimens of 25 mm gauge length with 10 mm diameter were fabricated from these heat-treated blanks and given 0.2 μm surface finishing. The fully reversed total strain-controlled low cycle fatigue tests were conducted on smooth specimens at the strain amplitudes ranging from ±0.3 to ±0.8% at 823 K under constant strain rate of  $3 \times 10^{-3} \text{ s}^{-1}$  using Instron electro-mechanical testing system. All the LCF tests were conducted according to the ASTM standard E606 [10].

Multiaxial state of stress had been introduced in the steel by incorporating circumferential grooves at the center of gauge length of smooth specimen as shown in Fig. 1. The minimum diameter of notched specimen was designed according to the code of practice [11]. Three different notches with root radius of 1.25, 2.5 and 5.0 mm were used to study the effect of notch root radii on the fatigue life of the steel. Fatigue tests on notch specimens were performed under stress-controlled mode (with frequency 0.2 Hz) at net stress amplitudes (at notch throat plane) of 250, 300 and 350 MPa corresponding to nominal stress amplitudes of 124.95, 149.95 and 174.95, respectively.

**Table 1** Chemical composition of modified 9Cr–1Mo steel

Element	C	Cr	Mo	Mn	V	Nb	Ni	S	P	Fe
Composition (wt%)	0.11	9.28	0.98	0.38	0.25	0.09	0.13	0.007	0.029	Bal.

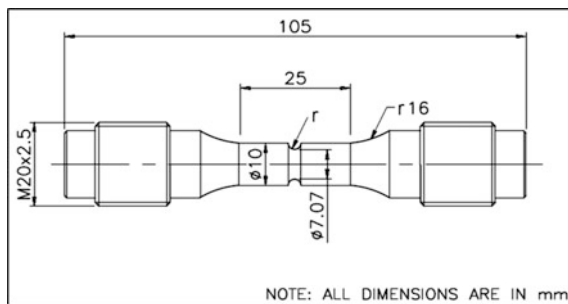


**Fig. 1** Typical notch specimen geometry with notch radius ( $r$ ) = 1.25 mm/2.5 mm/5.0 mm

### 3 Results and Discussion

#### 3.1 Fatigue Behavior of Smooth Specimens

Figure 2 depicts the effect of cyclic loading on tensile peak stress of the material at 823 K with different strain amplitudes. It can be observed that material is showing continuous cyclic softening till the initiation of macro crack and final failure at all the strain amplitudes except at strain amplitude of  $\pm 0.3\%$  at which small amount of initial hardening occurred. Cyclic softening is generally attributed to the annihilation of dislocations and degradation of lath structure [9]. Increase in strain amplitude increased the peak tensile stress and decreased the fatigue life of the material. Reduction in fatigue life with increase in strain amplitude indicates the increase in plastic deformation occurring in the material. Power law relation (Eq. 1) which correlates the tensile stress amplitude with plastic strain amplitude at half life of this material, and it is depicted in Fig. 3. Power law relation (cyclic stress–strain curve (CSSC)) may be expressed as:

$$\Delta\sigma/2 = K'(\Delta\varepsilon_p/2)^{n'} \quad (1)$$

where  $\Delta\sigma$ ,  $\Delta\varepsilon_p$ ,  $K'$  and  $n'$  are cyclic stress range, cyclic plastic strain range, cyclic strength coefficient and cyclic strain-hardening exponent, respectively. The values of  $K'$ ,  $n'$  were obtained by least square method as shown in Fig. 3 and listed in Table 2.

Decomposition of the total strain amplitude into the sum of elastic strain amplitude and plastic strain amplitude can be expressed as shown in Eq. (2). The relation between elastic strain amplitude and cycles to failure and the relation between plastic strain amplitude and cycles to failure can be represented by straight lines on log–log scale. These relations can be best represented analytically by

**Fig. 2** Cyclic stress response of modified 9Cr–1Mo steel at 823 K

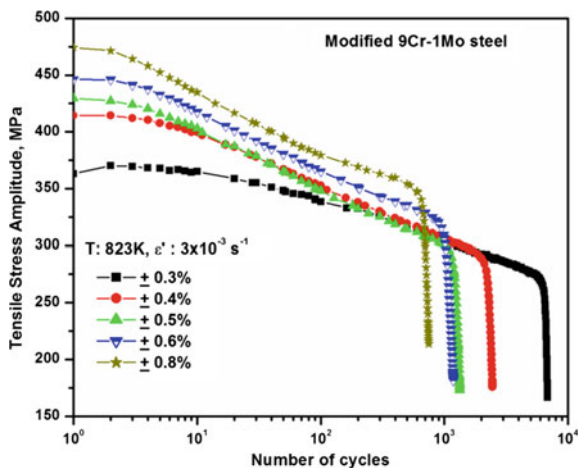
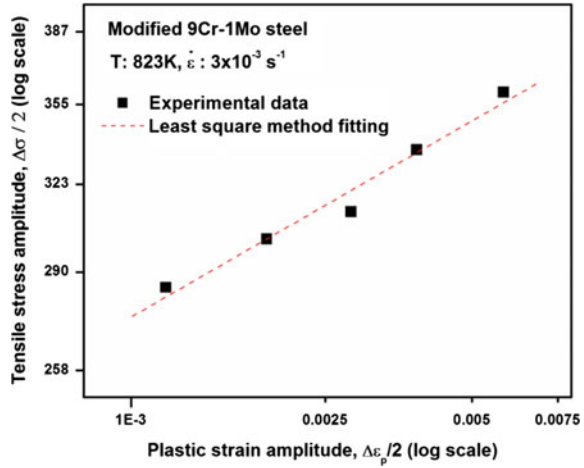


**Fig. 3** Cyclic stress–strain curve for modified 9Cr–1Mo steel at 823 K



Basquin’s equation (Eq. 3) and Coffin–Manson’s equation (Eq. 4), respectively. Hence, Eq. (2) can be further simplified and expressed as Eq. (5).

$$\frac{\Delta\varepsilon_t}{2} = \frac{\Delta\varepsilon_e}{2} + \frac{\Delta\varepsilon_p}{2} \tag{2}$$

$$\frac{\Delta\varepsilon_e}{2} = \frac{\sigma'_F}{E} (2N_f)^b \tag{3}$$

$$\frac{\Delta\varepsilon_p}{2} = \varepsilon'_f (2N_f)^c \tag{4}$$

$$\frac{\Delta\varepsilon_t}{2} = A(2N_f)^l \tag{5}$$

where  $\Delta\varepsilon_t$ ,  $\Delta\varepsilon_e$ ,  $\Delta\varepsilon_p$ ,  $N_f$ ,  $E$ ,  $\sigma'_f$ ,  $b$ ,  $\varepsilon'_f$  and  $c$  are total strain range, elastic strain range, plastic strain range, cycles to failure, Young’s modulus, fatigue strength coefficient, fatigue strength exponent, fatigue ductility coefficient and fatigue ductility exponent, respectively.  $A$ ,  $l$  are material constants in Eq. (5). Equations (1)–(5) have been applied to generated experimental data and are depicted in Fig. 4. The coefficients determined by least square curve fitting are listed in Table 2. Slope of the linear portion in first hysteresis loop and 0.2% offset in the linear part have been considered to calculate the young’s modulus and yield stress, respectively. These values have been calculated at the each strain amplitude and averaged over them. These values are listed in Table 2.

**Fig. 4** Coffin–Manson and Basquin relation plots for modified 9Cr–1Mo steel at 823 K

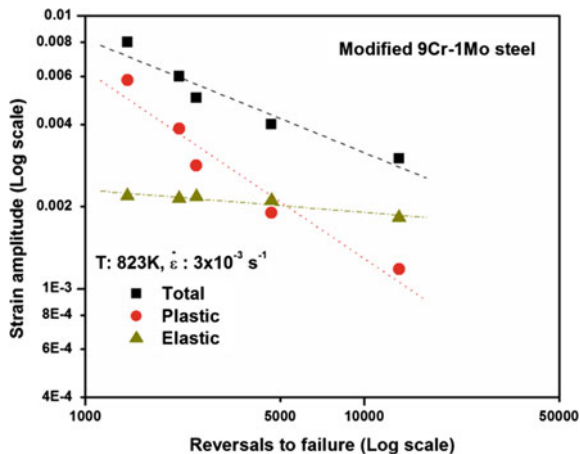


**Table 2** LCF material parameters for modified 9Cr–1Mo steel at 823 K

Cyclic stress–strain curve coefficients		Basquin relation coefficients		Coffin–Manson relation coefficients		Coefficients of Eq. (5) (total stain vs. life)	
$K'$ (MPa)	$n'$	$\sigma'_f$ (MPa)	$b'$	$\epsilon'_f$	$c'$	$A$	$l$
753.8	0.146	664.7	-0.0827	0.74	-0.69	0.1461	-0.4165
Young's modulus ( $E$ , GPa)		Yield stress ( $\sigma_y$ , MPa)					
163		258					

### 3.2 Fatigue Behavior of Notched Specimens

#### Experimental investigation

Fatigue tests have been conducted out in stress-controlled mode at net stress amplitudes of 250, 300 and 350 MPa on the notched specimens having notch root radius of 1.25, 2.5 and 5.0 mm. The effect of notch radius on fatigue life is shown in Fig. 5. Fatigue life was found to decrease with decrease in notch root radius and increase in applied stress. Figure 6 shows the fracture surface of fatigue tested smooth and notched specimens. It can be clearly seen that the cracks were initiated from the surface, for both the specimens. In the case of smooth specimen, cracks were nucleated in different locations across the specimen gage length due to availability of large surface area, whereas in the case of notched specimen, cracks nucleated in the notch throat plane due to presence of low cross-sectional area and concentration of stress at notch root.

#### Analytical approximations

Based on simplicity and easiness in applicability, the linear rule, Neuber's rule and SED method are widely in practice for local strain calculations. Within the elastic

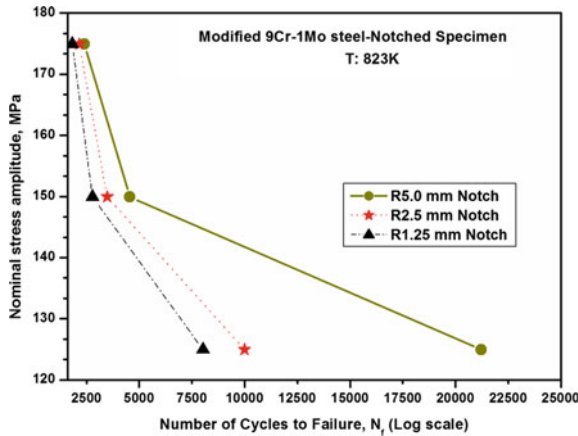


Fig. 5 Effect of notch radii and applied load on fatigue life

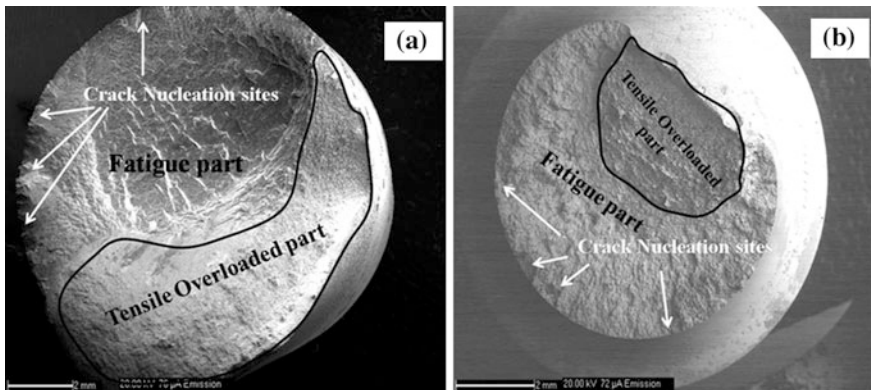


Fig. 6 Fractographs of modified 9Cr-1Mo steel **a** smooth specimen at strain amplitude  $\pm 0.6\%$  **b** notched specimen having notch root radius of 2.5 mm and applied net stress of 3000 MPa (applied nominal stress 149.95 MPa) at 823 K (check if you have any other images for (a) reflecting the same interpretation)

domain of material, theoretical stress concentration factor ( $K_t$ ) for cyclic loading (defined as the ratio of the maximum stress range ( $\Delta\sigma$ ) at notch root to the nominal stress range ( $\Delta S$ )) is used to measure the degree of elevated stresses and strains at notches. For simple geometries,  $K_t$  can be usually computed from theory of elasticity. Experimental methods like brittle-coating methods, grid method and photoelastic stress analysis, or numerical methods like the finite element analysis can be used for other complicated geometries. The linear rule assumes the equality of  $K_t$ , plastic stress concentration factor,  $K_\sigma$  (the ratio of local stress range,  $\Delta\sigma$  to the nominal stress range,  $\Delta S$ ) and plastic strain concentration factor,  $K_\epsilon$  (the ratio of

local strain range,  $\Delta\varepsilon$  to the nominal strain range,  $\Delta e$ ). Linear rule can be summarized as below equation:

$$\Delta\varepsilon = \Delta e K_t \quad (6)$$

in the cases of local stresses are above yield stress, Hooke's law no longer valid, hence  $K_t$  no longer relate the local stresses to nominal stresses. Neuber derived an equation while studying the grooved shafts which were under shear loadings. He proposed that geometrical mean of  $K_\varepsilon$  and  $K_\sigma$  equals to  $K_t$ .

$$K_\varepsilon K_\sigma = K_t^2 \quad (7)$$

By substituting  $K_\varepsilon$  and  $K_\sigma$  in above equation and considering elastic deformation at nominal location leads to:

$$\Delta\varepsilon \Delta\sigma = \frac{(K_t \Delta S)^2}{E} \quad (8)$$

By combining Eq. (8) with Ramberg–Osgood equation (Eq. (9), which relates the elasto-plastic behavior of the material under cyclic loading) leads to Eq. (10) which can be used for local strain calculations.

$$\Delta\varepsilon = \frac{\Delta\sigma}{E} + 2 \left( \frac{\Delta\sigma}{2K'} \right)^{1/n'} \quad (9)$$

$$\frac{(\Delta\sigma)^2}{E} + 2\Delta\sigma \left( \frac{\Delta\sigma}{2K'} \right)^{1/n'} = \frac{(K_t \Delta S)^2}{E} \quad (10)$$

Thus, notched specimen's local strain and stress can be evaluated by using smooth specimen's LCF data. The calculated  $K_t$  value based on the theory of elasticity depends only on geometry of the stress raisers. However, Topper et al. [12] proposed fatigue strength reduction factor or fatigue notch factor (the ratio of the fatigue strength of smooth specimen to the fatigue strength of notched specimen),  $K_f$ , instead of  $K_t$  in notch analysis by considering the plastic zone size ahead of the notch root. Below is the simplified equation proposed by Peterson [13] to evaluate  $K_f$  value:

$$K_f = 1 + \frac{K_t - 1}{1 + \frac{a}{r}} \quad (11)$$

$$a = 0.0254 \left( \frac{2070}{S_u} \right)^{1.8} \quad (12)$$

where  $r$  (in mm) is the notch root radius,  $a$  (in mm) is the material characteristic length,  $S_u$  is the ultimate tensile strength and its value for the present material is

340 MPa at 823 K. Glinka [5] proposed another approximation method similar to Neuber’s rule based on strain energy density, called SED method. This rule assumes that strain energy density (SED) at the notch tip is approximately same for linear-elastic behavior of notch and elastic-plastic behavior of notch, as long as plastic zone at notch tip is surrounded and controlled by elastic-stress field. The modified equation considering SED approach for fatigue loading condition can be defined as:

$$\frac{(\Delta\sigma)^2}{E} + \frac{4\Delta\sigma}{n' + 1} \left( \frac{\Delta\sigma}{2K'} \right)^{1/n'} = \frac{(K_t \Delta S)^2}{E} \tag{13}$$

$K_t$  values from hand book [14] were considered in present study to make the complete comparison among the earlier mentioned analytical approaches. Table 3 summarizes the values for  $K_t$  and  $K_f$  at different radii, and Tables 4, 5 and 6 summarize the estimated local strain by the different methods for the three net stresses with notch radius of 1.25, 2.5 and 5.0 mm, respectively.

By using Eq. (5), fatigue lives of notched specimens have been calculated for each estimated local strain given in Tables 4, 5 and 6. Figure 7 shows the comparison between predicted lives by the different methods and experimentally determined lives.

The linear rule, Neuber’s rule with  $K_t$  and  $K_f$ , SED method predicted the fatigue lives within the factor of  $\pm 16$  on experimental lives. All the methods overestimated the fatigue lives for all the testing conditions and notch geometries. Ascending order of over estimation of fatigue lives by different methods was Neuber’s rule with  $K_f$ , SED method, linear rule, Neuber’s rule with  $K_t$ . The difference among the

**Table 3**  $K_t$  and  $K_f$  values at different radii

Notch root radius (mm)	Theoretical stress concentration factor ( $K_t$ )	Fatigue notch factor ( $K_f$ )
1.25	2.0251	1.5678
2.5	1.6297	1.4058
5.0	1.3811	1.2527

**Table 4** Maximum local strains for three applied net stress amplitudes for the notch root radius of 1.25 mm

	Linear rule	Neuber’s rule		SED
		Using $K_t$	Using $K_f$	
$\Delta\epsilon_{max}$ at net stress 250 MPa	0.002861	0.003068	0.002484	0.002918
$\Delta\epsilon_{max}$ at net stress 300 MPa	0.003434	0.003919	0.003101	0.003574
$\Delta\epsilon_{max}$ at net stress 350 MPa	0.004006	0.004901	0.003812	0.004283



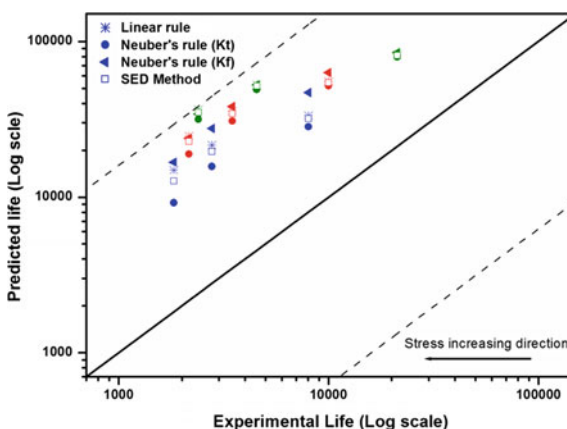
**Table 5** Maximum local strains for three applied net stress amplitudes for the notch root radius of 2.5 mm

	Linear rule	Neuber's rule		SED
		Using $K_t$	Using $K_f$	
$\Delta\epsilon_{max}$ at net stress 250 MPa	0.002319	0.002383	0.002197	0.002336
$\Delta\epsilon_{max}$ at net stress 300 MPa	0.002783	0.002961	0.002708	0.002831
$\Delta\epsilon_{max}$ at net stress 350 MPa	0.003247	0.003627	0.003288	0.003354

**Table 6** Maximum local strains for three applied net stress amplitudes for the notch root radius of 5.0 mm

	Linear rule	Neuber's rule		SED
		Using $K_t$	Using $K_f$	
$\Delta\epsilon_{max}$ at net stress 250 MPa	0.001972	0.001995	0.001941	0.001978
$\Delta\epsilon_{max}$ at net stress 300 MPa	0.002366	0.002439	0.002367	0.002385
$\Delta\epsilon_{max}$ at net stress 350 MPa	0.002761	0.002933	0.002839	0.002807

**Fig. 7** Comparison between predicted fatigue lives and experimental fatigue lives under three applied net stresses (stress increasing direction is right to left) for notch radius “ $r$ ” = 1.25 mm (blue marks), “ $r$ ” = 2.5 mm (red marks) and “ $r$ ” = 5.0 mm (olive marks) (blue symbols in figure should have Neuber's rule)



predicted fatigue lives by the different analytical methods decreased with increase in notch radii. This is because at higher notch root radius  $K_f$  value is approximately equals to  $K_t$  value. Analytical approximation methods which discussed in this study were providing better life predictions with decreasing radii or increasing  $K_t$  values. This may be due to larger strain gradients at the notch tip.

Analytical approximation methods which are used for local strain and stress calculations in notched specimens highly depend on plane strain and plane stress conditions. These two represent the two bounding conditions which occur at notch root. Earlier reports mentioned that linear rule, SED method were suitable in plain strain conditions and Neuber's rule was suitable for plain stress conditions [15, 16]. Better predictions of local strain and stress can be achieved by using modified versions of Neuber's rule and modified SED method [1]. Complexity involved in their usage makes them less convenient. All the above discussed different strain-based approaches predict the fatigue lives for crack to initiate and propagate to approximately 1 mm length [17]. Further crack propagation highly depends on crack tip stress field which has been taken into account in fracture mechanics studies. Hence, in general, total fatigue life to failure can be obtained by combining the life to crack initiation and the life to crack propagation [18].

## 4 Conclusions

The following conclusions can be made from the present study:

1. P91 steel showed cyclic softening till the final failure.
2. Analytical approximation methods (linear rule, SED method, Neuber's rule ( $K_t$ ), Neuber's rule ( $K_f$ )) overestimated the notched specimen fatigue failure life by a factor of  $\pm 16$  on experimental lives.
3. Analytical approximation methods were providing better life predictions with decreasing radii or increasing  $K_t$  values.
4. The strain energy density method and linear rule predicted nearly equal fatigue lives in all the cases.

**Acknowledgements** The authors are thankful to Dr. A.K. Bhaduri, Director, IGCAR, Kalpakkam, for his keen interest and support in this investigation. The authors also thank to Dr. C.R. Das, MTD, IGCAR for the help in SEM investigation.

## References

1. Zeng Z, Fatemi A (2001) Elasto-plastic stress and strain behavior at notch roots under monotonic and cyclic loadings. *J Strain Anal* 36(3):287–300
2. Goyal S, Veerababu J, Sandhya R, Laha K, Bhaduri AK (2016) Effect of notch on low cycle fatigue behaviour of 316 LN stainless steel. *Trans Indian Inst Met* 69(5):1015–1022
3. Agrawal R, Veerababu J, Goyal S, Sandhya R, Uddanwadiker R, Padole P (2016) Low cycle fatigue behaviour of 316 LN stainless steel in presence of notch. *Trans Indian Inst Met* 69(2):457–461
4. Neuber H (1961) Theory of stress concentration for shear-strained prismatical bodies with arbitrary nonlinear stress strain laws. *Trans ASME J Appl Mech* 28(4):544–550

5. Glinka G (1985) Energy density approach to calculation of inelastic stress-strain near notches and cracks. *Eng Fract Mech* 22(3):485–508
6. Raj B, Mannan SL, Vasudeva Rao PR, Mathew MD, Sadhana (2002) 27:527
7. Nagesha A, Valsan M, Kannan R, Bhanu Sankara Rao K, Mannan SL (2002) *Int J Fatigue* 24:1285
8. Ebi G, McEvily AJ (1984) *Fatigue Fract Eng Mater Struct* 17:299
9. Gieseke BG, Brinkman CR, Maziasz PJ (1993) Microstructure and mechanical properties of aging material. In: Liaw PK, Viswanathan R, Murty KL, Simonen EP, Frear D (eds) *The minerals metals and materials society*, p 197
10. “Standard test method for strain-controlled fatigue testing,” E606, ASTM International (2012)
11. Skelton RP, Wee ST, Webster GA (2001) Cyclic stress-strain behaviour of circumferentially notched cylindrical bars at high temperature. *Mater High Temp* 18(3):139–152
12. Topper TH, Wetzell RM, Morrow JD (1969) Neuber’s rule applied to fatigue of notched specimens. *J Mater* 4(1):200–209
13. Peterson RE (1974) *Stress concentration factors*. Wiley, New York
14. Pilkey WD (2005) *Formulas for stress, strain, and structural matrices*, 2nd edn. Wiley, Hoboken
15. Stephens RI, Fatemi A, Stephens RR, Fuchs HO (2000) *Metal fatigue in engineering*, 2nd edn. Wiley, New York
16. Sharpe WN Jr (1995) ASME 1993 Nadai Lecture—elastoplastic stress and strain concentrations. *Trans ASME J Eng Mater Technol* 117(1):1–7
17. Ellyin F (1997) *Fatigue damage, crack growth and life prediction*, 1st edn. Chapman & Hall, London
18. Dowling NE (2013) *Mechanical behavior of materials: engineering methods for deformation, fracture and fatigue*, 4th edn. Pierson Prentice Hall

# Effect of Induced Residual Stress and Its Contribution to the Failure of an IC Engine Valve Material

Gurunathan, Jitendra Sharma and Velshankar

**Abstract** The increasing engine demands such as high power, fuel efficiency and lesser emission have led to enormous modification in the intake and exhaust system of an engine. These improvements create additional loads on the valve train components as they have to cope with the increased speed as well as the efficiency and higher temperatures. Thus, engine valve materials must have high durability, high fatigue, wear resistance and temperature resistance. Intake valves generally made of martensitic steels will undergo high cyclic loads, and due to this higher stress in the material, chording of valve face occurs. Major cause for the failure of inlet valves is fatigue. A chorded inlet valve has been analyzed to see the root cause of the failure, and various factors contributed to the failure have been studied. Failure analysis has been done starting from the engine operating conditions to the production processes of the valve material to find out the failure initiation point. Metallurgical study of the chorded valve material through SEM reveals the microstructural details, composition and inclusions. Residual stress induced in the material during various points of production and operation has been observed to calculate the effect of inferring stress to failure. The amount of residual stress in induction-hardened valve material before and after stress relieving has been calculated to find out the contribution of stress relieving to remove the added tensile stress. Failure prevention modes are suggested based on the lowest possible residual stress value observed.

**Keywords** Inlet valves · Residual stress · Stress relieve · Microstructure  
Induction hardened · SEM · Inclusions

---

Gurunathan (✉) · J. Sharma · Velshankar  
Durovalves India Pvt Ltd, Waluj-Aurangabad, India  
e-mail: guru.r@varrogroup.com

J. Sharma  
e-mail: sharma.jitender@varrogroup.com

Velshankar  
e-mail: velshankar.m@varrogroup.com

## 1 Introduction

Engine valves become increasingly prone to severe temperature effects and fatigue cycles. Thus, to make them highly durable both structural and temperature effects need to be considered. Generally, inlet valves will be made of martensitic steel due to low-temperature operation and exhaust valves use bimetal or austenite material. Though titanium, hollow and sodium-filled valve works well with racing and high-rated engines, their adaptability with normal diesel engines is yet to be seen due to cost constraints. Exhaust valve has high hardened materials in seat area (stellite) to work in high temperatures. Since inlet valves work in lower temperatures, they mostly do not require stellite materials. However, to cope with increasing wear due to repeated working cycles certain hardening of martensitic materials has to be carried out to improve the durability and wear resistance. This can be done through induction hardening process. Induction hardening is a process through which hardness can be improved in localized areas such as seat, tip end and groove. This not only improves the hardness of the surface material but also has effect up to a certain depth depending upon the input parameters. Generally, the hardness of the inlet valve material will be improved from 30 HRC to about 55 HRC in localized areas through induction hardening process.

It has to be considered that hardness must be kept within the required limit since hardness is directly proportional to brittleness. Induction-hardened inlet valves fitted in engines work well even during high-cyclic-load operations. In some cases, it has been seen that the valve fails at an early stage of around 5000–6000 km after engine testing. The failed valve images have some uniformity as all failure occurred along the face to seat area. Chording of valve face material up to seat occurs due to fatigue in common. There can be four modes of possible failure for this (fatigue, temperature, erosion and wear). Since cracks are observed in the chord valve as shown in the figure, the failure might be due to fatigue (Fig. 1).



**Fig. 1** Chord of valve face

## 2 Failure Observations

### 2.1 Engine Observation

The fault check analysis has been carried out from the engine side after failure, and all the parameters are found to be well within the limits. Visual observation of cylinder block reveals scratch marks on the block due to broken valve piece. The image of the valve crack before taking out from the cylinder head is as shown in Fig. 2.

It can be observed that the cylinder block marks are not due to mechanical machining, thereby confirming that the failure of valve is due to high fatigue cycle which is responsible for the marks on block surface.

### 2.2 Valve Observation

The failed valve is taken for metallurgical analysis in a stepwise manner to find out the possibility of inclusions and the failure type. Visual observation of the failed valves clearly shows that the valve may have failed due to fatigue. After visual observation, the failed valves are cut to do tests using SEM. The sample from the cracked valve is kept inside SEM for the analysis. SEM structure at a magnification of around  $40\times$  to  $80\times$  reveals striation marks on its surface as shown in Fig. 3.

The crack seems to have started from outside of the circumferential direction toward the inside of the valve sample. It fatigue fracture due to presence of striation but its brittle fracture as the fracture/crack has progressed in one plane.

#### 2.2.1 Chemical Composition Analysis

The chemical composition of the failed sample needs to be checked to find out the fault in material after operation. Since due to temperature some oxidation layer

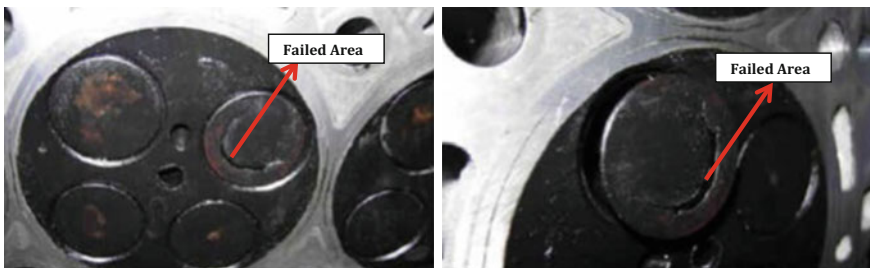


**Fig. 2** Failed valve in assembly state

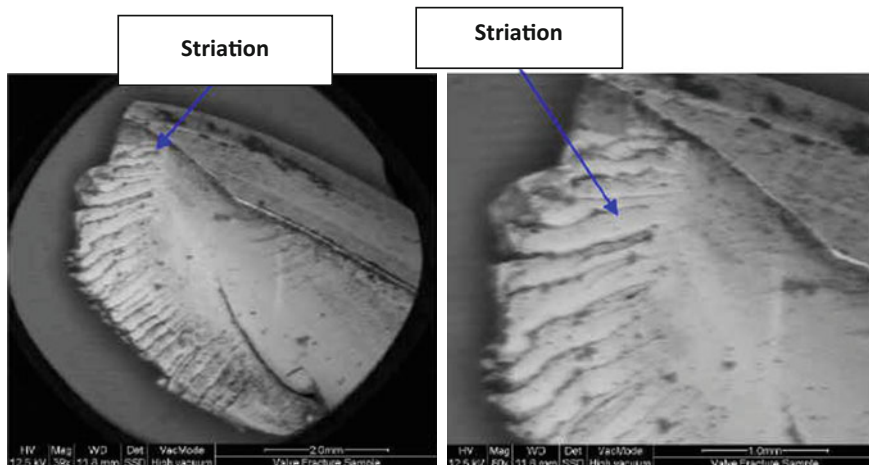


Fig. 3 SEM analysis of chord part

Table 1 Chemical composition of the failed valve

S. No	Test description	Specification values	Observed values
1	Carbon	0.40–0.50	0.42
2	Manganese	0.75 Max	0.41
3	Silicon	2.75–3.75	2.95
4	Chromium	7.50–9.50	8.35
5	Nickel	0.50 Max	0.17
6	Sulfur	0.003 Max	0.0006
7	Phosphorus	0.04 Max	0.001

forms on surface and it gets reacts with the surface material and thus the composition of the material which further reduces some properties of the material such as strength, wear resistance and hardness. The chemical composition can be checked either in the same SEM device or using the spectrometer device. The chemical composition revealed on SEM is as given in Table 1. This should conform with the specification of the martensitic valve material.

The chemical composition meets the specification values for martensitic grade materials used for inlet valves. Thus, the materials internal properties have remained the same.

### 2.2.2 Hardness Analysis

Hardness plays a vital role in determining wear and tear as well as the strength of the engine valve material. Thus, the valve sample is checked for hardness in the induction-hardened seat area to find the depth of the hardened layer (Table 2).

**Table 2** Hardness at various points

Distance from end (mm)	Hardness in HV
0.30	580
0.50	601
1.00	614
1.80	603
2.50	590
2.80	592

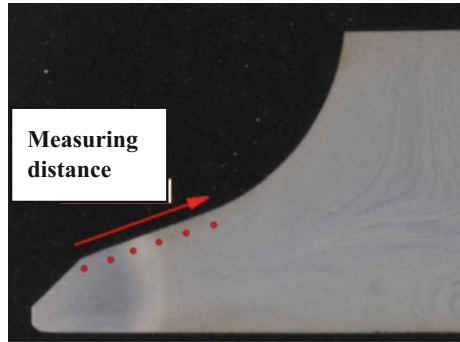
**Fig. 4** Hardness measuring points

Figure 4 explains the hardness-measuring locations. It is found that the hardness values are within the limits and specifications. Also, even hardness distribution has been observed along the case hardened zone. This confirms that the induction hardening process has no errors.

### 2.2.3 Inclusions Analysis

The microsample was prepared just near to the fracture surface to see the inclusion or any other defects in the failed valve sample. The microsample is analyzed in magnification of 100 $\times$ , 200 $\times$ , 300 $\times$  and 500 $\times$  using SEM, and the inclusions are observed. The detailed aspect of the observed inclusion images on various magnification factors is as shown in Fig. 5.

The sample is checked in unetched condition to see inclusions using EDAX analysis which will further confirm the added materials to the composition. EDAX analysis has been carried out for a magnification factor of around 1300 $\times$  in first step. The observed result shows microcrack layers on the surface which lead to initiation of the failure. The result of EDAX at 1300 $\times$  is shown in Fig. 6 and Table 3.



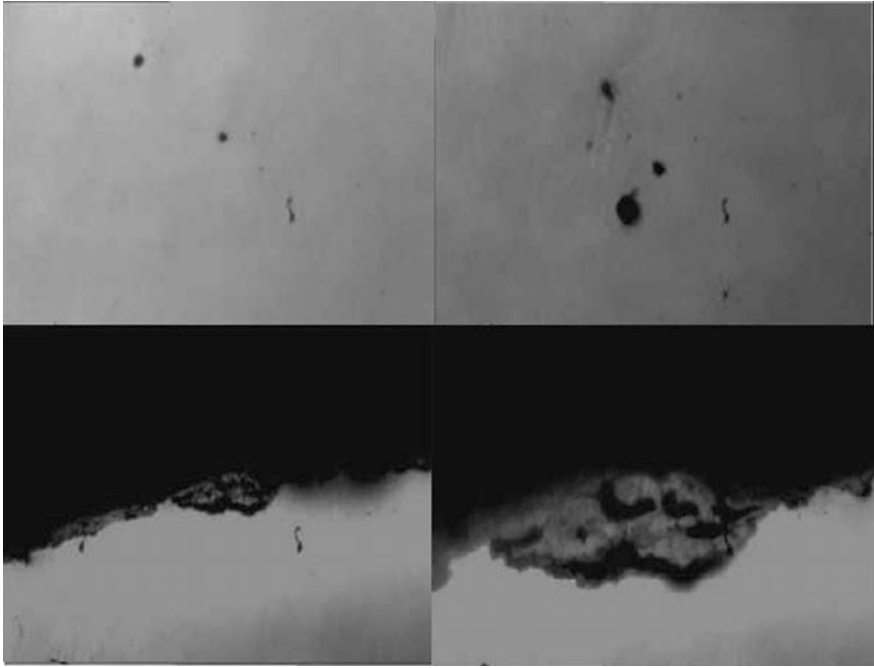


**Fig. 5** Observed inclusion at 100 $\times$ , 200 $\times$ , 300 $\times$  and 500 $\times$  in unetched condition

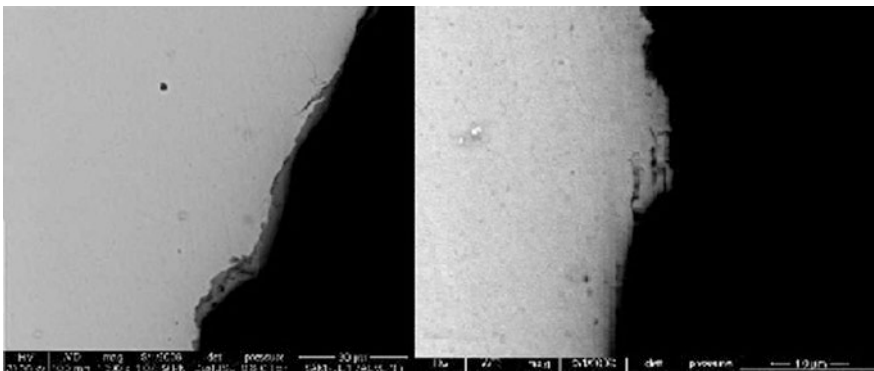


**Fig. 6** Visualization of microcracks

The result from EDAX shows inclusions of ferrous oxide along with aluminum, silicon, calcium and chromium. Thus, this concludes the inclusion analysis, but it has been seen that ferrous oxide inclusion has no part to play with the failure since it does not affect the overall property of the material. The hardness transverse is



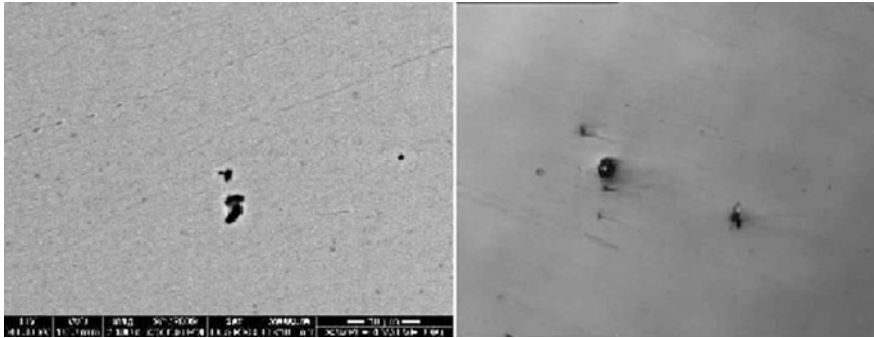


**Fig. 7** Inclusion image of etched surface

smooth which confirms the induction hardness process has no problems. However, microcracks are observed at magnification factors of around  $1300\times$  and  $2500\times$ . Microcracks and striation marks confirm the failure type as fatigue. The observed microcracks are shown in Fig. 6.

The same test is again conducted in etched condition of sample to confirm the inclusion and to obtain the microstructure (austenite or martensitic). Etching is done by using Nital solution. The etching results show martensitic matrix, thereby confirming the inlet valve material. The surface test at various magnification factors showed the same type of inclusions as that of those obtained using unetched test. The images shows below show the inclusions under etched condition at various magnification factors (Fig. 7).

No oxidation cracks are observed in this test, and thus, the failure is not due to high-temperature operation.

### **2.3 Process Observation**

After analyzing from both the engine side and the metallurgical side, the outcome was that the formation of microcracks leads to failure of the valve. Thus, the major processes such as forging and induction hardening are analyzed to find its effect on the engine valve material. As failure occurs along the face and seat region, the case may be due to induction hardening process. The machine parameters and the output hardness values are checked in the production lot and found to be ok. The effect of keeping the power constant and varying other parameters in induction hardness machine has been studied, and the output hardness and hardness transverse are found to be ok. The raw material inspection is also studied to confirm with the specification of the martensitic grade material. It is also found to be ok. Since all process parameters and the output are also found within the limit, the cause for failure is not associated with induction hardening or forging process.

### 3 Stress Calculations

#### 3.1 Stress Study

Valves having high hardness are prone to develop a stress, and these can develop a crack. These stressed valves can possibly generate microcracks and will fail in early stages of engine operation, thereby relieving the stress inside the material. Stress can be induced to the material through various possibilities such as sudden heating and cooling, high force production operations and high loads. The induced stress can be measured by using various techniques. The commonly used technique is X-ray diffraction. Since the valve failure resulted in a chord keeping all other parameters unchanged, it is required to measure the stress in the valve seat area. Another reason to check the stress in the seat area is that during induction hardening process the valve material is subjected to heating and quenching which may contribute to the added tensile stress.

#### 3.2 Residual Stress Measurement

An undamaged valve sample is taken from the production lot, and the face surface has been etched by using the Nital solution to find out the induction hardening heat-affected zone. The heat-affected zone will be visible after etching as shown in Fig. 8. The diameter of the valve face from the center is measured at 4 locations namely  $P1$ ,  $P2$ ,  $P3$  and  $P4$ . The distance between the points is set by taking some angles from  $P1$  to  $P4$ . Usually, the angles are separated by  $45^\circ$  each between each point.

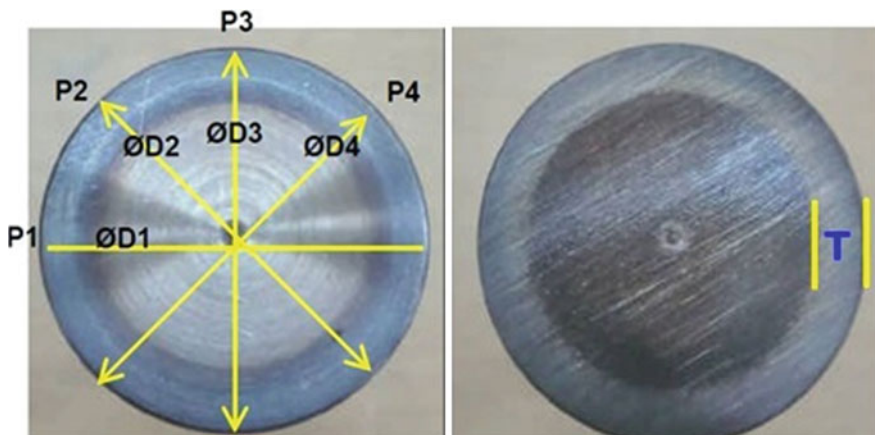
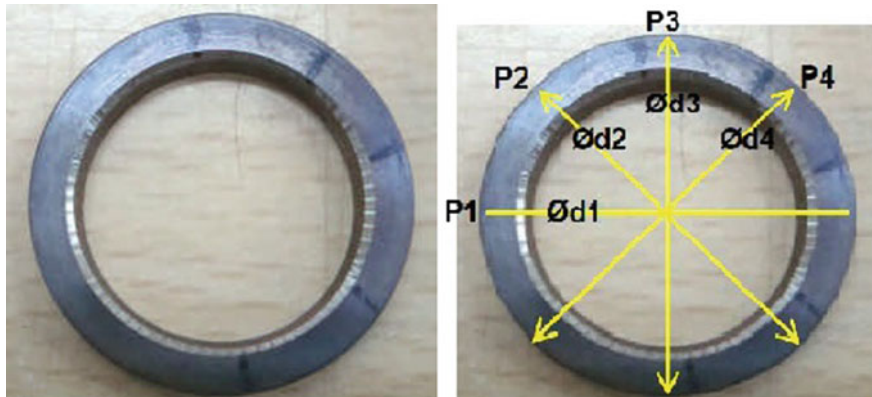


Fig. 8 Induction-hardened area and diameter



**Fig. 9** Hardened seat after cutting

Now, the valve will be cut using wire cutting technique so that the entire induction-hardened seat area is taken out. The new diameter from center to the four points is noted again. The wire-cut sample is as given in Fig. 9.

The old diameter  $D$  and new diameter  $d$  are compared to see any variations. According to standards, a maximum of 0.2% from the original diameter is accepted since the expansion (increased diameter) is due to the added stress stored in the valve material. It has been seen that the new diameter after cutting increased by about 20  $\mu\text{m}$  when compared with the original diameter. This confirms the residual stress available in the material after induction hardening process which leads to the failure of the valve. This stress stored will try to relieve, and it is the reason for the inlet valves to fail early. This diameter increase is directly proportional to internal residual stress.

## 4 Reduction of Inferring Stress

### 4.1 Stress Relieve Process

Since it has been seen that the stress induced in the valve material during induction hardening process is the reason behind the failure, sufficient measures are needed to be done to remove the induced inferring stress. The main reason behind the induced stress during the induction hardening process is the sudden heating followed by quenching process. Thus, it has been seen that providing some stress relive process after the induction hardening will reduce the amount of induced stress. Thus, some sample valves are taken after induction hardening process and stress relive process has been carried out at 150 °C and 1 h soak time for some samples. The same process has been repeated for other samples in which the temperature is kept at 170 °C and 1 h soak time. This is to compare the amount of stress which has been



relieved from the valve material. This is directly proportional to the change in diameter after cutting. So if the diameter change is very less then stress relieve process is very effective. Thus, the samples after stress relieve process have been cut using same technique and change is noted. The measured values are as shown in Table 4.

From the value, it can be understood that the stress relieved at  $170^{\circ}$  has reduced the increase in diameter to only about 1–3  $\mu\text{m}$  in all samples when compared with 18–20  $\mu\text{m}$  of normal induction-hardened valves without stress relieve. Thus, after induction hardening quenching stress relieve can be used for inlet valve material for prevention of valve face chord due to high induced residual stress.

## 5 Conclusions

Engine valve material failed after some initial running during engine testing operation. It has been seen that the face crack has occurred from face to seat area. Visual observations showed some cracks on the chord area and that the failure mode might be fatigue. Since valve failed at early stage, fatigue might not be the exact failure mode. Engine block and cylinder head parts are checked for issues, and cracks are observed in seat insert area due to the broken piece. Then, metal-lurgical studies are carried out to reveal the microstructure and other parameters. Microstructure reveals martensitic matrix and chemical composition observed through SEM matches with the material specification. The microcracks near the broken piece reveal the striation marks which confirm the failure is fatigue and type of fracture as brittle. Etched and unetched samples are tested for finding inclusions in material, and it is revealed that ferrous oxide along with aluminum, silicon and chromium are available. However, this does not contribute to failure of valve. Production parameters are checked to see any machine errors, and it is found ok. Stress study has been carried out to find the added tensile stress in the material during induction hardening process due to sudden heating and quenching. Wire cut sample reveal 20- $\mu\text{m}$  diameter increase. Thus, stress relieve process has been carried out at  $170^{\circ}\text{C}$  and 1 h soak time which reduced increase in diameter to 2  $\mu\text{m}$ . Furthermore, this will reduce the residual stress induced during the process, and hence, the failure of inlet valve due to inferring stress can be prevented.

## References

1. Lavhale YK, Salunke J (2014) Overview of failure trend of inlet & exhaust valves. *IJMET* 5(3):104–113
2. Londhe RT, Kshirsagar JM (2014) Experimental analysis of valve and valve seats wear in gases (CNG) fuelled engine. *IOSR J Mech Civil Eng (IOSR-JMCE)* 11(4) Ver. I:PP 56–62 (e-ISSN: 2278-1684, p-ISSN: 2320-334X)

3. Pandey A, Mandloi RK (2014) Effects of high temperature on the microstructure of automotive engine valves. *Int J Eng Res Appl* [www.ijera.com](http://www.ijera.com) 4(3) (Version 1):122–126 (ISSN: 2248-9622)
4. Raghuwanshi NK, Pandey A, Mandloi RK (2012) Failure analysis of internal combustion engine valves: a review. *Int J Innovative Res Sci, Eng Technol* 1(2):173–181
5. Kumar GU, Mamilla VR (2012) Failure analysis of internal combustion engine valves by using ANSYS. *Am Int J Res Sci, Technol, Eng Math* 6:1–25
6. Lewis R, Dwyer Joyce RS (2003) Combating automotive engine valve recession. *Tribol Lubr Technol* 59(10):48–51 (ISSN 0024-7154)
7. de Wilde EF (1967) Investigation of engine exhaust valve wear. *Wear* 10:231–244
8. Algieri A (2013) Fluid dynamic efficiency of a high performance multi-valve. *Therm Sci* 17(1):25–34
9. Wang YS, Schaefer SK, Bennett C, Barber GC (1995) Wear mechanisms of valve seat and insert in heavy duty diesel engine. *Soc Automot Eng*, Warrendale, PA, p 11 SAE paper 952476
10. Liang X, Strong G, Eickmeyer D, Myers K (1999) A study of valve seat insert wear mechanisms. *Soc Automot Eng*, Warrendale, PA, p 12 SAE Paper 1999-01-3673



# Fatigue Analysis of Offshore Structures in Indian Western Offshore

Nitin Nehra, Praveen Bhat and N. Panneerselvam

**Abstract** Oil and Natural Gas Corporation (ONGC), the national oil company of India, operates more than 270 steel tubular welded offshore structures which are piled to ocean bottom. All these structures have been designed to meet the strength and fatigue limit state requirements as per API RP 2A WSD. These offshore structures are subjected to continuous cyclic wave loads and hence fatigue susceptibility needs to be explored. In this paper, stochastic fatigue assessments of an existing offshore platform for life extension purpose have been discussed. The fatigue lives have been estimated as per parametric equations suggested by Efthymiou. A fatigue factor of safety value of 2.0 has been considered in this study, and  $S-N$  curves provided in API are used for cumulative damage (Palmgren Miner's Rule) assessment. All the joints which are found to have lower fatigue lives than design life have been included for type III inspection (as per API RP 2A-WSD) using state-of-the-art NDE techniques (NDT). These studies employed for drawing up the joint inspection campaigns.

**Keywords** Welded tubular joints ·  $S-N$  curves · NDT · Inspection campaign API RP2A · Stochastic fatigue

---

N. Nehra (✉) · P. Bhat · N. Panneerselvam  
Institute of Engineering & Ocean Technology-Oil & Natural Gas Corporation Limited,  
Navi Mumbai, India  
e-mail: nehra\_nitin@ongc.co.in

P. Bhat  
e-mail: bhat\_praveen@ongc.co.in

N. Panneerselvam  
e-mail: panneerselvam\_n@ongc.co.in

## 1 Introduction

Jacket-type fixed offshore platforms are the most commonly used fixed offshore structures installed in the western offshore of India, and these structures predominantly have two substructures one is jacket which is from bottom of the sea to few meters above the mean sea level and another one is deck which is placed on the jacket. The design life of these structures is 25 years, and many platforms have outlived their design lives but are still needed for 15–20 years. These offshore platforms are, in general, large and complex, three-dimensional framed structural systems, usually fabricated using steel tubular members interconnected through welded joints. These structures are predominantly subjected to oscillatory/cyclic environmental loads and due to this oscillating nature of load; fatigue characterizes a primary mode of failure of their components. Hence, fatigue life estimation is an integral part of design philosophy of offshore structures and to generate the inspection plans during the service life. The fatigue damage at any point in the structure depends on the complete stress history during the structures service life [1]. The calculation of this stress history and its effects on the material is a complex task. The irregular nature of the sea, size of structure, evaluation of stress concentration factors in welded joints and possible dynamic effects, etc., contribute to the complexity of the fatigue life assessment [1]. Fatigue in offshore structure is a typical high cycle fatigue phenomenon. Most damages are caused by the occurrence of many cycles of small stress ranges. The occurrence of few severe storms with return period more than one year is unimportant for fatigue damage consideration. The response of the structure in sea states of relatively low wave height and short mean wave period is of prime concern.

These offshore structures are designed as per established recommended practice/codes, e.g., NORSOK-N006/API RP2A WSD.

This paper presents the spectral fatigue analysis using SACS software for life estimation of existing jacket type of offshore structures based on  $S-N$  curve approach using Efthymiou's parametric equations for SCF and Palmgren Miner's Rule. This unmanned jacket platform is secured to seabed with four main piles and two skirt piles and installed in year 1976 in western Indian offshore. It has completed its design life and needs to check fit-for-purpose.

## 2 Fatigue in Offshore Tubular Structures

### 2.1 Fatigue Assessment

**Fatigue Damage** Total no of stress cycles required to failure is called fatigue damage and represented as follows:

$$\text{Fatigue Damage} = \frac{\text{No. of Stress cycles applied}}{\text{No. of Stress cycles resisted}} \tag{1}$$

Stress fluctuations normally occur predominantly as result of wave loads. These wave induced stresses are of variable magnitude and occur in random order [2]. The true time history of the local stresses is almost invariably simplified in that it is assumed to be adequately described in statistical terms by a reasonable number of stress blocks [2]. Each stress blocks consists of a number of cycles of constant stress range. Thus, the sequence of variation in the true stress history is lost. The cumulative effects of all stress blocks representing the stress history is estimated by Miner’s rule of liner accumulation of damage.

$$\text{Total Fatigue Damage} = \sum_{i=1}^s \frac{n_i}{N_i} \tag{2}$$

- s* Number of stress blocks considered
- n<sub>i</sub>* Actual number of stress cycles for stress block of range *i*
- N<sub>i</sub>* Number of stress cycles resisted of stress range *i*

Fatigue failure is to occur when the total fatigue damage reaches unity. In a fatigue analysis, this criteria can be considered as the definition of local fatigue failure. This does not necessarily imply a failure in reality, let alone a partial or complete collapse of the structure. Hence, fatigue life is defined as follows:

$$\text{Fatigue Life} = \frac{\text{Total Fatigue Damage}}{\text{Design Life}} \tag{3}$$

Before carrying out a cumulative damage calculation for any potential location at a tubular joint, it is necessary to determine the stress response over the range of sea conditions that structure can expect to experience during its life. Random sea conditions are usually described in the short term, i.e., over a period of a few hours, by one of the many directional wave spectrum formulae. These give the component of wave at each frequency and direction in terms of parameters such as significant wave height; mean zero crossing period and mean wave direction. The proportion of time for which each sea-state persist (over a period) (i-e probability) completes the description of sea.

**Stress Concentration Factor (SCF)** In offshore tubular joints, the welds are the most sensitive part due to the high local stress concentrations. Fatigue lives at these locations should be estimated by evaluating the hot spot stress range (HSSR) and using it as input into the appropriate *S-N* curve [3]. Thus, the SCF for a particular load type and at a particular location along the intersection of weld may be defined as:

$$SCF = \frac{\text{HSSR at the location}}{\text{Range of the nominal brace stress}} \quad (4)$$

The SCF should include all stress raising effects associated with the joint geometry and type of loading, except the local (microscopic) weld notch effect, which is included in the  $S-N$  curve [3]. Minimum eight locations (four on chord and four on brace) on welded joint section required to cover all relevant hot spot stress area. SCF approach is widely used for estimation of fatigue of tubular joints. Efthymiou SCF equations are considered to offer the best option for all joint types and load types (Figs. 1 and 2).

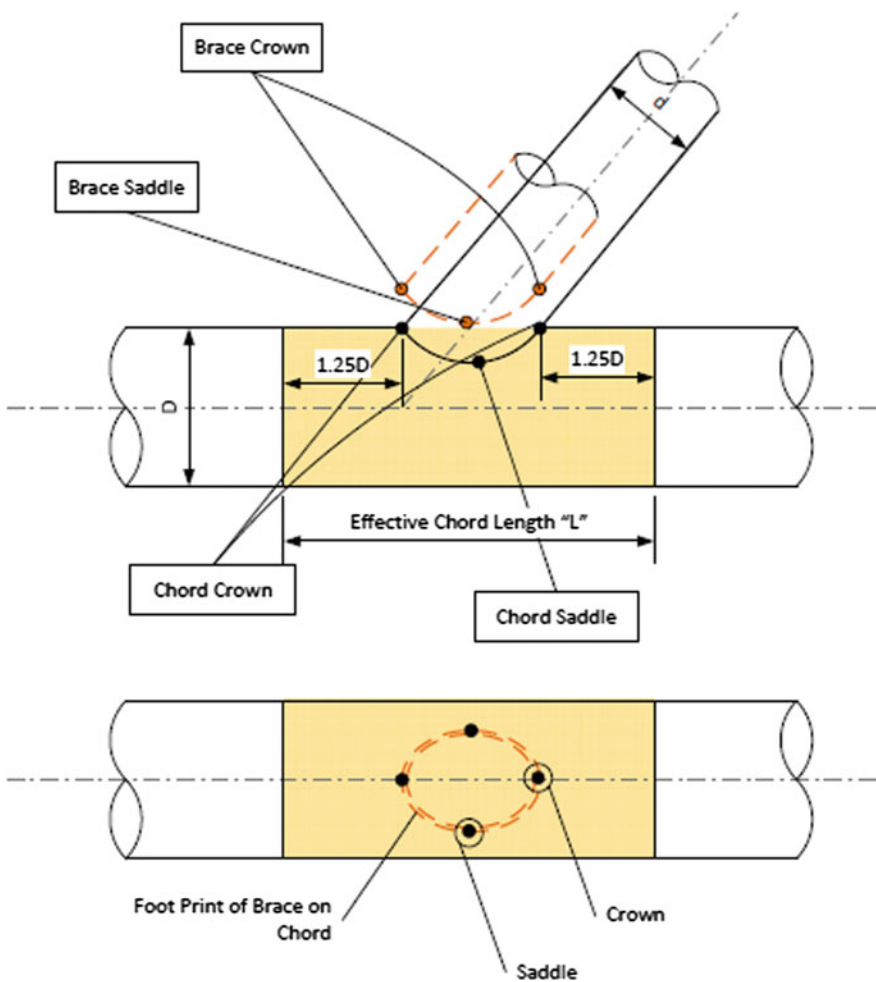


Fig. 1 Hot spot locations. Source <http://nptel.ac.in>

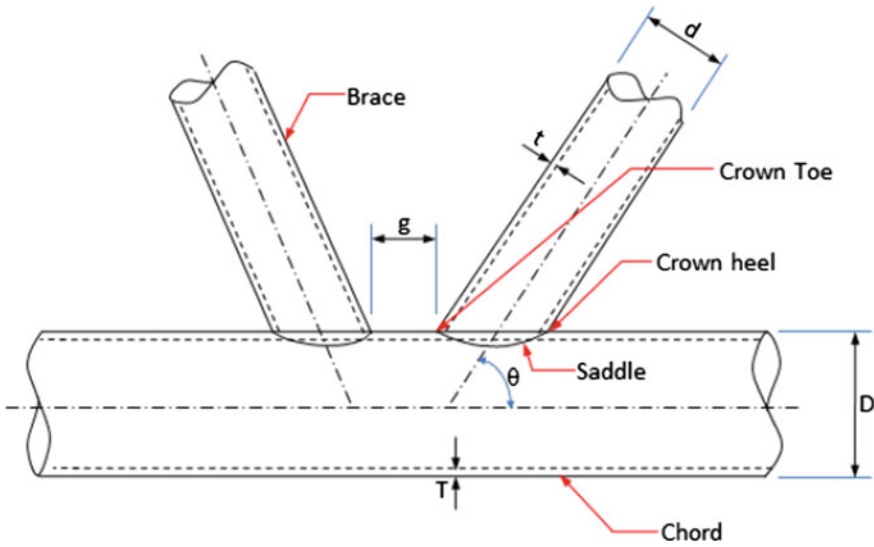


Fig. 2 Typical offshore tubular connection. Source API RP2A WSD 2007, p. 52

**S-N Curve.** Relation between stress ( $S$ ) and no of stress cycles ( $N$ ) and can be plotted on a logarithmic scale as a straight line and is referred as  $S-N$  curve. A typical  $S-N$  curve is given below for a welded tubular joint.

$$\text{Log}_{10}(N) = \text{Log}_{10}(K) - m \text{Log}_{10}(S) \tag{5}$$

where  $m$  is a slope of the curve and  $K$  is the geometric constant (Fig. 3)

**Sea State.** Oceanic sea state can be represented with energy spectrums. A spectrum is the relation between spectral density ( $S$ ) and wave frequency ( $\omega$ ). The different sea states are shown in Fig. 4.

In the current study, sea is considered fully developed and the Pierson-Moskowitz (P-M) spectrum described by Eq. (5) has been used.

$$S_{\eta}(\omega) = \frac{\alpha g^2}{(\omega)^5} e^{\{-\beta[\frac{\omega_0}{\omega}]^4\}} \tag{6}$$

where,

$\alpha$  Philip constant = 0.0081

$\beta$  0.74

$\omega_0$  Frequency corresponding to the peak value of the energy spectrum

The sea state is represented by selecting a sufficient number of frequencies for considering the jacket response transfer functions. The range of time periods selected varies between 1 and 15 s. 2% structural damping has been considered in the analysis (Fig. 5).

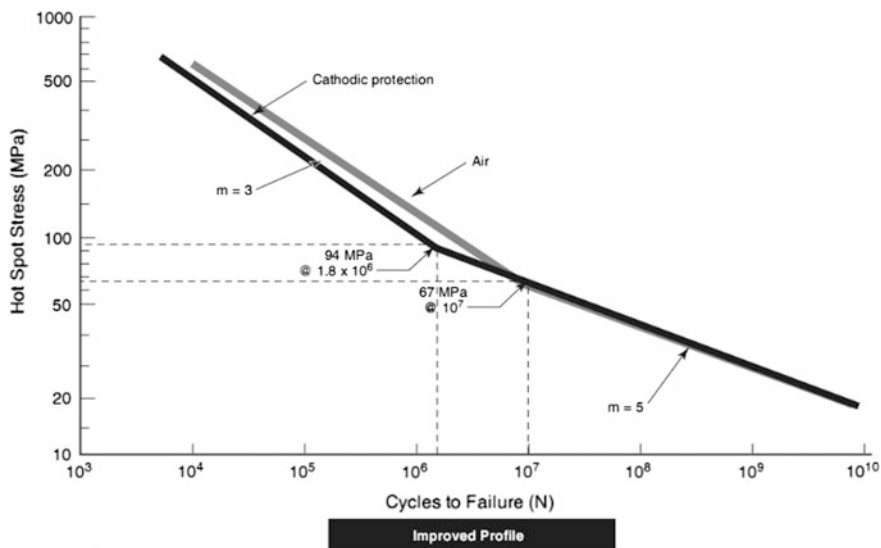


Fig. 3 S-N curve for offshore welded structures. Source API RP2A WSD 2007, p. 59

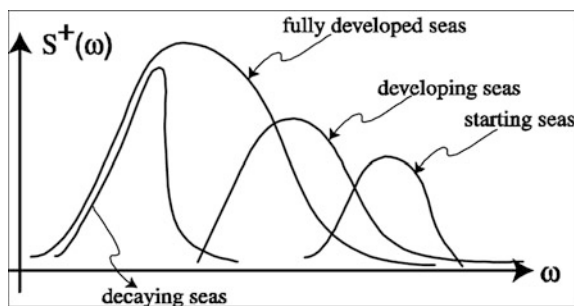


Fig. 4 Sea states. Source [web.mit.edu/13.42/www/handouts/reading-wavespectra.pdf](http://web.mit.edu/13.42/www/handouts/reading-wavespectra.pdf), p. 3

## 2.2 Analysis Methodology

Fatigue analysis involves using wave response to generate a transfer function for each wave direction which relates global load to excitation frequency, specifying a wave spectrum to which the structure will be subjected.

**Calculate Centre of Damage Wave Height** For fatigue analysis of offshore structure, a super element is created for soil properties due to the nonlinear behavior of soil. This super element is created for the center of damage (COD) wave that represents the spectrum of fatigue waves. This COD wave height ( $H_{cs}$ ) and time period ( $T_{cz}$ ) are calculated as follows:

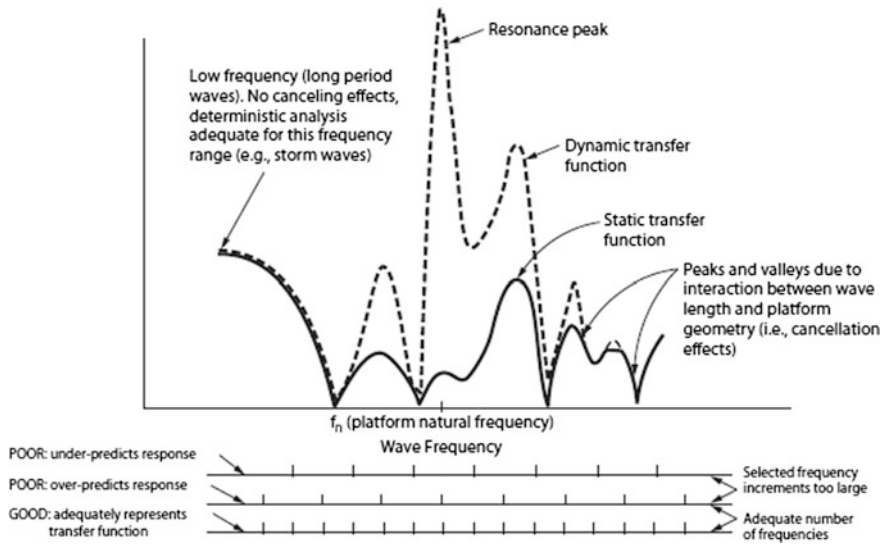


Fig. 5 Selection of frequencies for detailed analyses. Source API RP2A WSD 2007, p. 201

$$H_{cz} = \frac{\sum D_i H_{si}}{\sum D_i} \tag{7}$$

$$T_{cz} = \frac{\sum D_i T_{zi}}{\sum D_i} \tag{8}$$

where

- $D_i$  estimate damage of sea state  $i = (P_i H_{si}^m / T_{zi})$
- $P_i$  probability of occurrence of sea state  $i$
- $H_{si}$  significant wave height of sea state  $i$
- $T_{zi}$  zero crossing period of sea state  $i$
- $A$  1.8
- $m$  inverse slope of  $S-N$  curve

The fatigue analysis is represented in the following flow chart (Fig. 6).

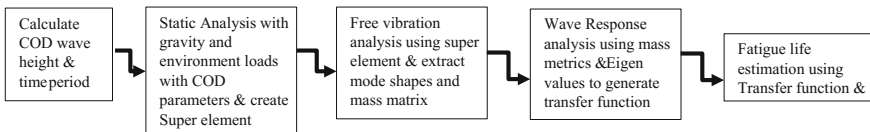
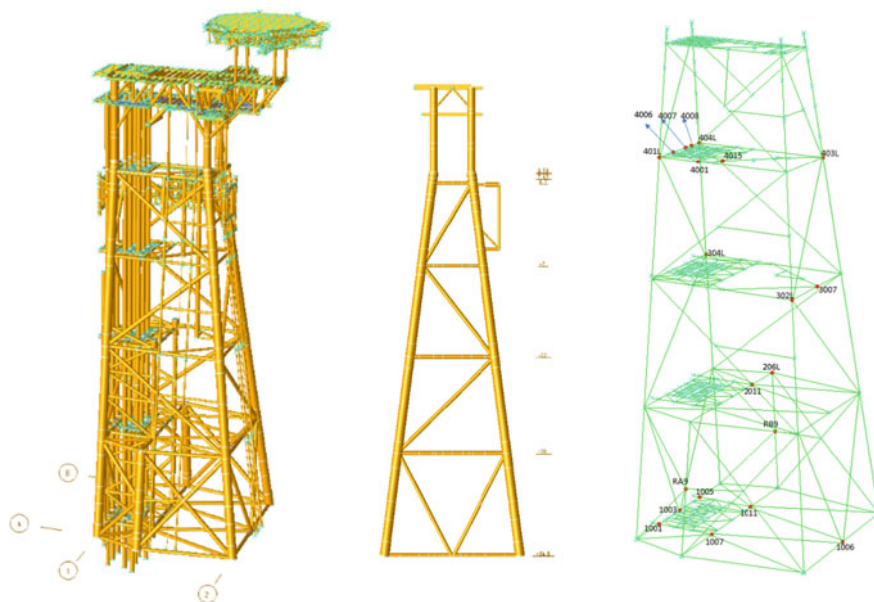


Fig. 6 Flow chart for spectral fatigue analysis



**Fig. 7** SACS model of the platform

### 3 Case Study

The offshore platform selected for the case study is located in western offshore of India in water depth of 54 m and installed in year 1976. The platform has four main legs and two skirt legs. The structural model is prepared using SACS software and shown in Fig. 7.

The center of damage wave height and time period for the sea state are 3.493 m and 6.196 s, respectively.

Marine growth and hydrodynamic coefficients have been considered as per API RP 2A WSD. In the free vibration analysis, first 30 modes have been extracted and fatigue life estimation of welded joints have been carried out.

#### 3.1 Results

This platform has lived 40 years and still required to be under operations till 2020. Factor of safety of 2.0 has been considered; hence, total fatigue life required is 88 years. The joints which are having fatigue life less than 88 years have been shown below:



Joint	Joint type	Fatigue damage	Service life (years)	Joint	Joint type	Fatigue damage	Service life (years)
1006	K	28.41381	3.167474	401L	TK	2.722906	33.05292
4007	T	19.67677	4.573921	302L	TK	2.192823	41.04298
4015	K	1.858529	48.42539	1005	T	2.086545	43.1335
4015	K	15.07281	5.971017	404L	TK	1.708574	52.6755
206L	T	5.722737	15.72674	4006	T	1.885135	47.74194
2011	T	4.728998	19.03152	1001	T	1.341135	67.10734
304L	TK	4.339304	20.74065	4008	T	1.309376	68.73502
RA9	K	3.644766	24.69294	1003	K	1.292088	69.6547
4001	TK	2.964391	30.36037	3007	K	1.09974	81.83755
403L	TK	2.683205	33.54198	1011	T	1.066322	84.40226
1007	T	1.032743	87.14655	RB9	K	1.048158	85.86492

These joints have been included for the type III inspection to be done during the scheduled underwater inspection for detection of damages, if any.

## 4 Conclusion

Offshore steel jacket structures are vulnerable to damage due to fatigue action of waves, and hence require to be adequately assessed from fatigue strength point of view. A stochastic analysis provides an efficient and reliable method for carrying out fatigue assessment of offshore structures as it simulates the prevalent distribution of wave energy over the entire frequency range and incorporates the representative structural dynamics in the analysis.

**Acknowledgements** We acknowledge the support and resources provided by ONGC required for carrying out this study. The study has been immensely beneficial in understanding the pertinent issues relevant to the structural behavior of jacket structures and is of vital importance in purview of ONGC’s operational requirements to carry out life extension studies of existing platforms. We extend our sincere thanks to Shri C. Tandi, ED-HoI, IEOT-ONGC for his generous support and encouragement. We are also immensely grateful for the continuous motivation received from Shri Dinesh Kumar, GGM–Head of Structures Section, IEOT-ONGC.

## References

1. Madhavan Pillai TM, Veena G (2006) Fatigue reliability analysis of fixed offshore structures: a first passage problem approach. *J Zhejiang Univ Sci A* 7:1839
2. Vughts JH, Kinra RK (1976) Probabilistic fatigue analysis of fixed offshore structures. In *Offshore technology conference*, Houston, Texas, 3–6 May
3. API RP 2A WSD: Recommended Practice for Planning, Designing and Constructing Fixed Offshore Platforms—Working stress Design (2007)
4. <http://www.nptel.ac.in>

# Crack Effect on Rotors Using Mode-I Failure Model with Transfer Matrix Approach

Ved Prakash Singh and J. Srinivas

**Abstract** This paper presents a crack identification in a rotor dynamic system based on changes in natural frequencies predicted from the transfer matrix approach using a crack point matrix defined in terms of stress intensity factors. A local flexibility of the system due to crack is employed and changes in natural frequencies of the system are illustrated. Effect of cracked and its location along the length is studied by using some interpolation formula. A generalized transfer matrix approach is applied after validating with the finite element model. Analytical results are compared with those obtained from numerical model through ANSYS. Fatigue analysis of cracked rotor shaft system containing the bearing at ends is performed using solid modeling tool. The results are compared and conclusions are drawn.

**Keywords** Identification · Transfer matrix · Breathing · Behavior  
Single-plane model

## 1 Introduction

Dynamic behavior of mechanical elements is important and should be monitor to access reliability of machinery. Most of the components used in high speeds often possess flaws due to cracks formed by cyclic loading, vibration and other types of loads. Due to loss of integrity, the dynamic properties such as natural frequencies of such systems are drastically affected and require a special attention. Compared with various nondestructive techniques such as ultrasonic testing, visual examination, vibration-based online monitoring for identification of crack location and severity has become more popular today. Vibration-based techniques follow two rules for

---

V.P. Singh (✉)  
NIT Rourkela, Rourkela, Odisha, India  
e-mail: ved.singhh@gmail.com

J. Srinivas  
Department of Mechanical Engineering, NIT Rourkela, Rourkela 769008, India  
e-mail: srin07@yahoo.co.in

detection of cracks. First one monitors synchronous vibration amplitude and phase. If such  $1 \times$  amplitude and phase exists, it implies the presence of crack. The second rule states that there also exists  $2 \times$  vibration in cracked rotor at half of the resonance speed. There are several papers published on this subject, and still various new methods are still under investigation. The constant rotation of the shaft with a crack has a periodic time varying stiffness characteristics. However, transfer cracks open and closed alternatively leading to breathing behavior. Here also the shaft stiffness variation is time periodic. Many investigations studied such parametric instability conditions in cracked rotor dynamics.

Meng and Gasch [1] studied stability of cracked Jeffcott rotor supported on journal bearing. Gasch [2] given an overview of cracked Laval rotor stability diagram. Nonlinear dynamic stability analysis of shaft disk system with crack was presented in some works [3–5]. Most of these works focused on simple systems having few degrees of freedom. Sinou [6] conducted the stability analysis by applying perturbation to nonlinear periodic solution and identified effect of crack on the instability region. When crack depth increases, the model must include additional flexibility term so as to generate an integral model. The stress intensity factors in the theory of fracture mechanics may be used for modeling open or breathing edge cracks. Local flexibility coefficients depend on the size of crack and crack length geometry. Often cracked section is replaced by single rotation spring representing local flexibility of crack. Investigators divided the edged crack problem into two categories. These are (1) direct problem where the effect of crack on the natural frequencies is studied and (2) inverse problem where the vibration data are used to predict location and size of the cracks. Cavelini et al. [7] calculated the additional flexibility introduced by the crack using linear fracture mechanics model. Tsai and Wang [8] investigated the position and size of crack on a stationary shaft by modeling crack as joint of local spring. Darpe [9] detected fatigue transverse crack in rotating shaft by using detection methodology exploiting both the typical nonlinear breathing phenomenon of the crack and the coupling of bending–torsional vibration due to presence of crack for its diagnosis. According to Gomez et al. [10], who detected crack in a rotating shaft by applying wavelet packet transverse energy combined with ANN (artificial neural network) with RBF (radial basis function) architecture. Attar [11] investigated mode and frequencies of stepped beam consisting of an arbitrary number of transverse cracks by using analytical approach and also calculated position and depth of crack opting transverse matrix method. Broda et al. [12] investigated longitudinal vibrations of beams with breathing cracks numerically and experimentally both. In all the above-mentioned works, it is assumed that the crack depth is relatively small in comparison with rotor diameter. Also most of the literature dealt with open crack modeling. In practice, the crack depth may elongate toward the centerline of the shaft and it requires additional flexibility consideration using fracture mechanics theory. In this line, present paper formulates an approach based on mode-1 failure to model the crack in terms of its depth function, and the frequency analysis of the rotor bearing system is carried out using transfer matrix approach. The breathing crack behavior is analyzed in detail with variations in natural frequencies and mode shapes. The remainder of the paper is organized in the following format. Section 2 deals with

mathematical modeling of the crack and rotor system. Section 3 presents results and discussion, and brief conclusions are given in Sect. 4.

## 2 Mathematical Modeling

This section deals with description of the breathing crack model along with a transfer matrix method employed in the present work. When the crack width is very small, it is known as gaping fatigue crack which is different from notch. Gaping cracks are difficult to manufacture. The shaft should be subjected to prolonged cyclic bending fatigue to initiate the crack. Compliance of a cracked shaft is a function of uncracked shaft compliance and additional compliance induced by the crack. Dimarogomas et al. [13] employed the fracture mechanics techniques for estimating crack compliance, where the strain energy release rate was used along with linear elastic fracture mechanics.

### 2.1 Additional Flexibility Due to Crack

A shaft element of length  $L$  having a transverse crack of depth  $h$  is located at the middle position as shown in Fig. 1.

By considering that there are six degrees of freedom at each station of the shaft element ( $i = 1-6$ ), the method is explained. If  $D = 2R$  is the diameter of the cross section,  $E$  is elastic modulus, and  $\nu$  is Poisson ratio of the material, then the additional strain energy  $U_c$  is given by the integration of the strain energy density function over the cracked area  $A_c$  as follows.

$$U_c = \frac{(1 - \nu^2)}{E} \int_{A_c} \left[ \left( \sum_{i=1}^6 K_{Ii} \right)^2 + \left( \sum_{i=1}^6 K_{IIi} \right)^2 + (1 + \nu) \left( \sum_{i=1}^6 K_{IIIi} \right)^2 \right] dA_c \quad (1)$$

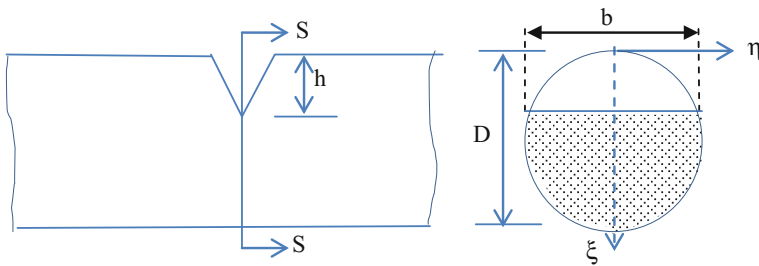


Fig. 1 Cracked shaft element

Here  $K_I$ ,  $K_{II}$ , and  $K_{III}$  are the stress intensity factors corresponding to opening, sliding, and shearing modes of the crack, 'i' denotes the applied load. Based on the stress distribution on the cross section of the crack, these stress intensity factors are determined. As mode-I (opening) is predominant on the crack flexibility, it is only considered in this work. This is expressed as

$$K_I = \sigma_i \sqrt{\pi a} f\left(\frac{h}{h_x}\right) \quad (2)$$

where  $\sigma_i$  is stress at the crack due to applied load  $P_i$ , and  $f$  is a shape function called crack configuration factor. The additional flexibility induced within the shaft due to crack is obtained as  $c_{ij} = \frac{\partial^2 U_c}{\partial P_i \partial P_j}$ . The elements of local flexibility matrix depends only on the degrees of freedom being considered for moments and forces applied on the crack cross section. The full compliance matrix is  $6 \times 6$ ; however, in present study, the flexural vibration of beam in one plane ( $X - Y$ ) is only considered so that the load  $P_5$  (moment) only comes in equations. That is the component of flexibility matrix  $C = c_{55}$  only exists in this case. The detailed derivation of this component for a circular section is given in Appendix.

## 2.2 Transfer Matrix Method

Transfer matrix method is useful techniques for solving the natural frequencies of the present rotor. Any section or station of the rotor is described by a state vector whose coordinates are physical quantities defining the vibration state of the section. In a 2-D bending, the state vector  $S$  is defined in terms of transverse displacement  $y$ , slope  $\theta$ , bending moment  $M$ , and shear force  $Q$ . The method consists in relating the ends of entire shaft line by means of several transfer matrices. Then the boundary conditions can be applied and natural frequencies or critical speeds are calculated. Several papers have been recently focused on the applications of transfer matrix method in rotor dynamics. Albuquerque and Barbosa [14] used transfer matrix method to predict the bending critical speeds of hydrogenerator shaft. Ghasemalizadeh et al. [15] analyzed a shaft system using transfer matrix method by considering gyroscopic effect. Albuquerque and Barbosa [16] predicted bending critical speed of a hydrogenerator shaft using transfer matrix method. More recently, Lee and Lee [17, 18] determined the solution to the free vibration characteristics of a tapered and twisted Bernoulli beam by finding the roots of differential equation. Figure 2 shows the rotor model in present work. Here, the station locations are also shown.

There are eight stations, and the rotating shaft is assumed to be bending in one plane. In applying the method, there are two sets of matrices (1) field matrix which relates the distributed effects such as shaft elements (2) point matrix which relates

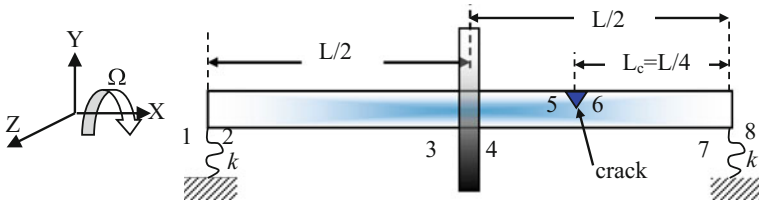


Fig. 2 Cracked rotor under study with station numbers

the lumped phenomena such as springs, crack, or disk. Following this, field and point matrices are used to compute overall transfer matrix [19].

Field matrix for the shaft elements:

$$[R_{23}(L/2)] = [R_{45}(L/4)] = [R_{67}(L/4)] [R] = \begin{bmatrix} S & \frac{T}{a} & -\frac{U}{a^2EI} & -\frac{V}{a^3EI} \\ aV & S & \frac{T}{aEI} & -\frac{U}{a^2EI} \\ -a^2EIU & -aEIV & S & \frac{T}{a} \\ -a^3EIT & -a^2EIU & aV & S \end{bmatrix} \quad (3)$$

with  $a = \sqrt{\omega} \sqrt{4 \frac{\rho A}{EI}}$ . Here,  $\rho$  and  $E$  are density and elastic modulus of shaft, while  $A$  and  $I$  are cross section and moment of inertia of the section. Also,  $\omega$  is natural frequency, while other terms are defined as:

$$S(al) = \frac{1}{2} [\cosh(al) + \cos(al)] \quad (4a)$$

$$T(al) = \frac{1}{2} [\sinh(al) + \sin(al)] \quad (4b)$$

$$U(al) = \frac{1}{2} [\cosh(al) - \cos(al)] \quad (4c)$$

$$V(al) = \frac{1}{2} [\sinh(al) - \sin(al)] \quad (4d)$$

Point matrix for bearing support with translation =  $[P_{12}] = [P_{78}]$

$$= \begin{bmatrix} 1 & 0 & 0 & 0 \\ 0 & 1 & 0 & 0 \\ 0 & 0 & 1 & 0 \\ k & 0 & 0 & 1 \end{bmatrix} \quad (5)$$

Point matrix for the disk with mass  $m$ , diametral moment of inertial  $I_d$ , and polar moment of inertia  $I_p$ :

$$[P_{34}] = P_2 = \begin{bmatrix} 1 & 0 & 0 & 0 \\ 0 & 1 & 0 & 0 \\ 0 & \omega(-I_p\Omega + I_d\omega) & 1 & 0 \\ -m\omega^2 & 0 & 0 & 1 \end{bmatrix} \quad (6)$$

Here,  $\Omega$  is speed of the shaft.

Point matrix for the cracked portion (discontinuity between the slopes revealed by bending moment and rotation)

$$[P_{56}] = P_3 = \begin{bmatrix} 1 & 0 & 0 & 0 \\ 0 & 1 & C & 0 \\ 0 & 0 & 1 & 0 \\ 0 & 0 & 0 & 1 \end{bmatrix} \quad (7)$$

The resultant overall transformation matrix is given by

$$[T] = [P_{78}][R_{67}][P_{56}][R_{45}][P_{34}][R_{23}][P_{12}] = \begin{bmatrix} T_{11} & T_{12} & T_{13} & T_{14} \\ T_{21} & T_{22} & T_{23} & T_{24} \\ T_{31} & T_{32} & T_{33} & T_{34} \\ T_{41} & T_{42} & T_{43} & T_{44} \end{bmatrix} \quad (8)$$

As both ends of the shaft after the support springs have free end conditions, the moment and shear become zero. Thus, the resultant characteristic equation is obtained as  $T_{31}T_{42} - T_{32}T_{41} = 0$ . The natural frequencies of the system are obtained by solving this equation for the frequency parameter  $a$ .

### 2.3 Breathing Crack

So far, only the studies of rotor with transverse open crack is studied. As shaft start to revolve the crack smoothly transits from fully open to fully closed mode. So, we use a cosine function to model this behavior.

Here Mayes' model is employed as:

$$\begin{aligned} K_{\text{maye}\xi} &= a_1 + b_1 \cos \theta \\ K_{\text{maye}\eta} &= a_2 + b_2 \cos \theta \end{aligned} \quad (9a)$$

or

$$K_{\text{maye}} = K_{\text{maye}\zeta} + iK_{\text{mayer}\eta} \tag{9b}$$

where  $K_{\text{maye}\zeta}$ ,  $K_{\text{mayer}\eta}$  are shaft stiffness with crack along  $\zeta$  and  $\eta$ , and  $\theta = \Omega t$  is angular displacement.

$$\begin{aligned} a_1 &= \frac{1}{2}(K_0 + K_\zeta), b_1 = \frac{1}{2}(K_0 - K_\zeta) \\ a_2 &= \frac{1}{2}(K_0 + K_\eta), b_2 = \frac{1}{2}(K_0 - K_\eta) \end{aligned} \tag{10}$$

Here if  $\theta = \pi$ ,  $K_{\text{maye}\zeta} = K_\zeta$ ,  $K_{\text{mayer}\eta} = K_\eta$  and if  $\theta = 0$ ,  $K_{\text{maye}\zeta} = K_0 = K_{\text{mayer}\eta}$ . First case is called, fully open crack and second case is called fully closed crack.

### 3 Results and Discussion

Initially, the problem is solved as direct analysis approach where the crack parameters are varied and the corresponding changes in natural frequencies are predicted. Dimensions of the rotor under consideration are given in Table 1.

A computer program is developed to obtain the natural frequencies of the system with variable crack dimensions at different speeds of operation and the support stiffness values. Without crack, the intact model of the rotor is tested for its natural frequencies using transfer matrix method. A comparison of the first three frequencies using finite element analysis using Timoshenko beam theory, ANSYS solution, is depicted in Table 2.

**Table 1** Geometric and material properties of system

Parameter	Value
Diameter of the shaft (mm)	15
Diameter of the disk (mm)	128
Thickness of the disk (mm)	10
Length of the shaft (mm)	328
Elastic modulus of shaft and disk (GPa)	200
Material density (kg/m <sup>3</sup> )	7850
Bearing stiffness k (N/m)	$1 \times 10^5$



**Table 2** First three natural frequencies (in Hz) of intact rotor

Method	Mode-1	Mode-2	Mode-3
Present transfer matrix	52.91	160.10	483.90
Timoshenko finite element	52.86	160.01	481.62
ANSYS	52.92	160.56	483.68

### 3.1 Effect of Crack Depth

Figure 3 shows variation of fundamental natural frequencies as function of local crack flexibility parameter.

As is obvious, it can be seen that as flexibility reduces from 0 to 0.01, the natural frequencies first increases and then decrease. In the next step, the relative crack depth ( $h/D$ ) is varied from 0.1 to 0.5, and the corresponding  $c_{55}$  values are computed, and the three natural frequencies are obtained in a similar manner as shown in Table 3. It is seen that there is a marked effect of crack depth on the natural frequency. In this paper, value of  $c_{55}$  is calculated by using the best fit formula [20] for solid circular shaft as a function of  $h/D$ . Table 3 shows the change in the value

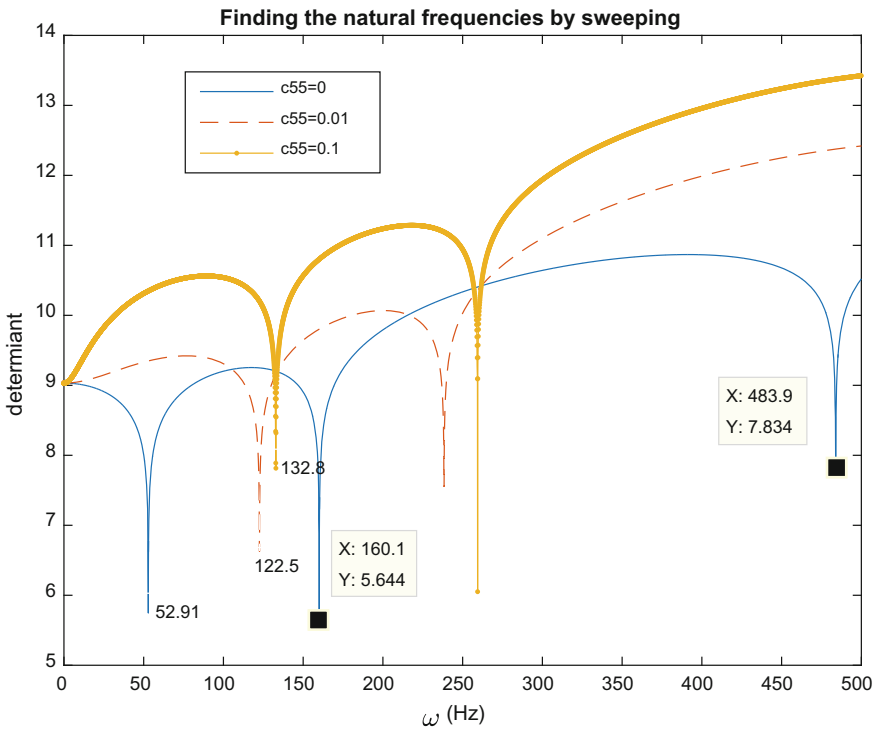


**Fig. 3** Natural frequencies as a function of local flexibility parameter

**Table 3** Variation of natural frequency with h/D

$h/D$	$c_{55}$ ( $10^{-6}$ )	Natural frequencies (Hz) (mode-1)	Natural frequencies (Hz) (mode-2)	Natural frequencies (Hz) (mode-3)
0.1	1.55	52.91	159.9	484.2
0.2	7.818	52.96	160	485
0.3	20.4	53.01	160	486.5
0.4	42.85	53.16	160.2	489.4
0.5	84.02	53.41	160.5	494.8

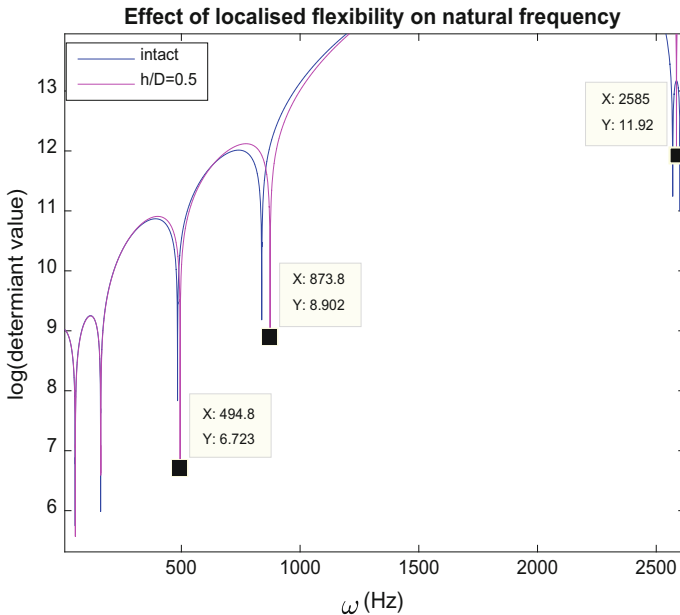


**Fig. 4** Variation of natural frequencies of cracked beam

of natural frequencies at different mode and by changing the value of  $c_{55}$  obtained from above reference and crack location is fixed at 82 mm from the right end of shaft.

It is clear that the natural frequencies with  $c_{55}$  have some change with respect to uncracked rotor from mode 3 onwards (Fig. 4).

### 3.2 Effect of Crack Location

Table 4 shows the effect of crack location on the natural frequencies of the system, and the variation are shown in table at the fix value of  $h/D$  ratio of the crack. From

**Table 4** Variation of natural frequencies (Hz) with the change of crack location

Non-dimensional crack location $L_c/L$	Mode-1	Mode-2	Mode-3
0.167	99.26	257.3	565.7
0.25 (initial location)	122.4	238.4	623.6
0.334	132.6	214.5	–

**Table 5** First five frequencies obtained from ANSYS

Mode	Intact	Fatigue crack (depth $h = 3$ mm, width $b = 6$ mm)
1	10.315	10.323
2	19.420	19.433
3	646.97	642.87
4	1453.1	1441.1
5	2423.1	2419.5

Table 4, it is clear that the natural frequencies vary as a function of crack location (Table 5).

### 3.3 Modeling of Crack in 2-D

ANSYS software is used to model the crack in the present shaft and analyze the system with two ends supported on spring elements. Figure 5 shows the 2-D model of the rotor with crack. Plane 183 elements are used to mesh the model.

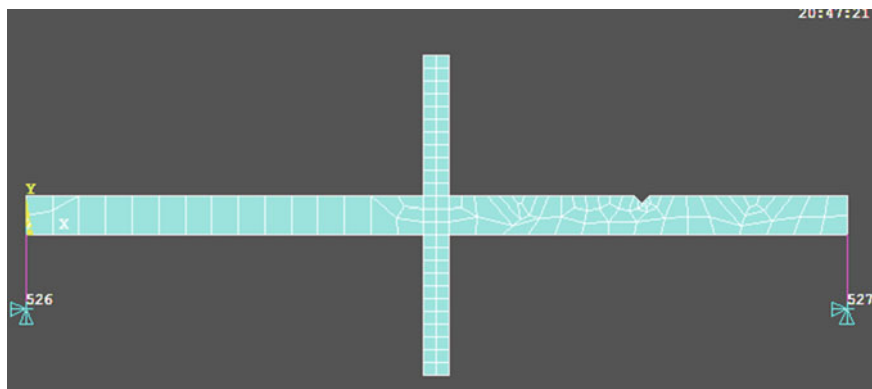


**Fig. 5** 2-D model for rotor and shaft

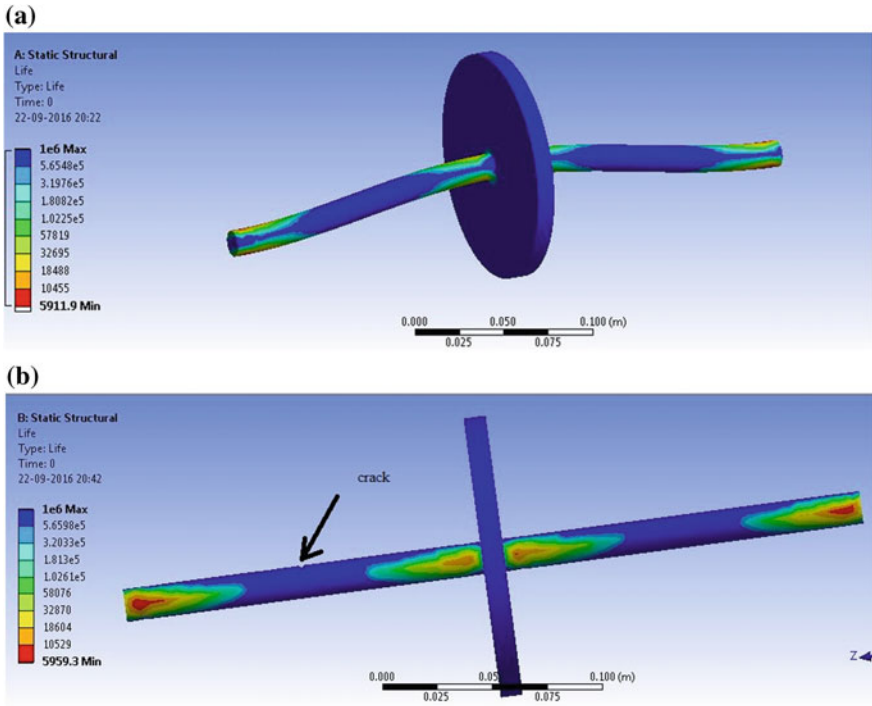


Fig. 6 a Fatigue life of system without crack. b Fatigue life of system with crack

### 3.4 Fatigue Analysis of System on Difference Condition

Using 3D solid modeling, fatigue analysis is done for with and without crack (depth 2 mm and width 3 mm) in ANSYS. Material used is stainless steel at rotation speed 500 rps. Result about life of system is shown in Figs. 6a, b. And it is clear that life of system decreases after introduction of crack.

## 4 Conclusions

In the context of this paper, various analyses are done for finding natural frequency of shaft and rotor system at different position and dimension of shaft. So it is clear that with variation of crack depth natural frequency increases. It can be also concluded from fatigue analysis that fatigue life of any shaft rotor system decreases with introduction of crack.

## Appendix: The Flexibility Coefficient Derivation

Stress Intensity Factor,

$$K_{I5} = \sigma_5 \times \sqrt{\pi \zeta F_{I5}}$$

Here,  $\sigma_5 = \frac{P_5 h}{2I}$  with  $P_5$  as bending moment and  $I$  is moment of inertia of cross section.

$\zeta$  and  $\eta$  are spatial variables to measure the crack length and width along crack plane

So,

$$\begin{aligned} c_{55} &= \frac{\partial^2}{\partial P_5^2} \left[ \int \frac{K_{I5}^2}{E} dA \right] \\ &= \frac{16D}{EI} \int_0^{a/D} \left\{ \int_{-P_1}^{P_1} (1 - 4\phi^2) (2\phi + \sqrt{1 - 4\phi^2} - 1) [H(\lambda)]^2 d\phi \right\} d\phi \end{aligned}$$

Here  $I = \frac{\pi D^4}{64}$  and  $P_1 = \sqrt{\phi - \phi^2}$  where,  $\phi = \frac{\zeta}{D}$ ,  $\phi = \frac{\eta}{D}$

$$H(\lambda) = \frac{\sqrt{\left(\frac{2}{\pi\lambda}\right) \tan\left(\frac{\pi\lambda}{2}\right) \left(0.923 + 0.199 \left(1 - \sin\left(\frac{\pi\lambda}{2}\right)^4\right)\right)}{\cos\left(\frac{\pi\lambda}{2}\right)}$$

where  $\lambda = \frac{2\phi + \sqrt{1 - 4\phi^2} - 1}{2\sqrt{1 - 4\phi^2}}$  for circular section.

## References

1. Meng G, Gasch R (2000) Stability and stability degree of a cracked flexible rotor supported on journal bearing. *J Vib Acoust, Trans-ASME* 122:116–125
2. Gasch R (2008) Dynamic behavior of Laval rotor with a transverse crack. *J. Mech Syst Signal Process* 22:790–804
3. Fu YM, Zheng YF, Hai ZK (2002) Analysis of nonlinear dynamic stability for a rotary shaft-disk with a transverse crack. *J. Sound Vib* 257:713–731
4. Dai LM, Chen CP (2007) Dynamic stability analysis of a cracked nonlinear rotor system subjected to periodic excitation in machinery. *J. Vib Control* 13:537–556
5. Chen CP, Dai LM, Fu YM (2007) Nonlinear response and dynamic stability of a cracked rotor. *J Commun Nonlinear Sci Numer Simul* 12:1023–1037
6. Sinou J (2007) Effects of crack on stability of a nonlinear rotor system. *J. Nonlinear Mech* 42:959–972
7. Cavalini AA Jr, Sanches L, Bachschmid N, Steffen V Jr (2016) Crack identification for rotating machines based on a nonlinear approach. *J. Mech Syst Signal Process* 79:72–85

8. Tsai TC, Wang YZ (1996) Vibration analysis and diagnosis of a cracked shaft. *J Sound Vib* 192:607–620
9. Darpe AK (2007) A novel way to detect transverse surface crack in a rotating shaft. *J Sound Vib* 305:151–171
10. Gomez MJ, Castejon C, Garcia JC (2016) Automatic condition monitoring system for crack detection in rotating machinery. *J Reliab Eng Syst Saf* 152:239–247
11. Attar M (2013) A transverse matrix method for free vibration analysis and crack identification of stepped beams with multiple edge cracks and different boundary condition. *J Int J Mech Sci* 57:19–23
12. Broda D, Pieczonka L, Staszewski WJ, Silberschmidt VV (2016) Generation of higher harmonics in horizontal vibration of beams with breathing cracks. *J J Sound Vib* 381:206–219
13. Dimarogonas AD, Paipetis SA, Chodros TG (2013) Analytical method is rotor dynamics, Springer, NY
14. Boiangie M, Ceausu V, Untaroiu CD (2016) A transfer matrix method for free vibration analysis of Euler-Bernoulli beam with variable cross section. *J Vib Control* 22:2591–2602
15. Ghasemalizabeh O, Mirzaee MR, Sadeghi H, Ahmadi MT (2008) Rotor bearing system analysis using transfer matrix method with thickness assumption of disk and bearing. *Int J Mech Ind Aerosp Eng* 2:206–213
16. Albuquerque RB, Barbosa DL (2012) Evaluation of bending critical speed of hydrogenerator shaft lines using the transfer matrix method. *J Mech Eng Sci Part-C*, 227:2010–2022
17. Lee JW, Lee JY (2016) Development of transfer matrix method to obtain exact solution for the dynamic characteristics of twisted uniform beam. *J Int J Mech Sci* 105:215–226
18. Lee Jung Woo, Lee Jung Youn (2016) Free vibration analysis using the transfer matrix method on a tapered beam. *J. Comput Struct* 164:75–82
19. Boiangio M, Ceausu V, Untaroiu CD (2016) A transfer matrix method for free vibration analysis of a euler bernoulli beams with variable cross sections. *J Vib Control* 22:2591–2602
20. Zheng DY, Kessissoglou NJ (2004) Free vibration analysis of cracked beam by finite element method. *J J Sound Vib* 273:457–475
21. Zheng DY, Fun SC (2003) Vibration and stability of cracked hollow sectional beams. *J Sound Vib* 267:933–954

# Multiaxial Fatigue Analysis—Approach Toward Real-World Life Prediction

Pradip Pujari

**Abstract** Conventional fatigue analysis procedures followed in daily practices are at least 10 or more years old. Typically, equivalent stress (on a plane) approach is used for fatigue analysis. However, variation of stresses/strains in a particular plane may not yield accurate results for fatigue life calculation. With new developments in analysis practices and better solver capabilities, it is imperative to evaluate these techniques for fatigue analysis followed today. One such need is to evaluate the fatigue life when loads are highly complex and nonproportional. Study is done here to perform multiaxial fatigue analysis of the structure. It is compared against the existing methods for applicability in terms of cost and solution time.  $n$ -code fatigue analysis module is used for the study based on multiaxiality. Multiaxial fatigue analysis requires use of yield criteria to fatigue under combined loading. With nonproportional loading, there is increased strain hardening which needs to be considered appropriately. Hence, based on nonproportionality and biaxiality, a decision matrix is prepared to decide the appropriate notch correction and equivalent stress or strain approach. Notch correction methods studied are Neuber, Hoffmann–Seeger, Glinka and Jiang Sehitoglu. Available  $n$ -code multiaxiality options are explored and comparative study among these approaches is summarized here. The  $n$ -code multiaxial fatigue analysis proposes two approaches to predict the fatigue life. Two-step analysis and multistep analysis give closer solution to fatigue life, but time required for solution increases drastically. Two-step analysis can be selected as a trade-off for life prediction with multiaxiality in terms of time taken for solution. Multiaxial fatigue analysis is performed on one of our vehicle structure to correlate the results with actual life of the components predicted from the rig test.

**Keywords** Equivalent stress • Multiaxial fatigue • Nonproportionality  
Biaxiality • Neuber correction • Hoffmann–Seeger • Critical plane approach

---

P. Pujari (✉)  
John Deere Technology Center, Pune, India  
e-mail: pujaripradip@johndeere.com

© Springer Nature Singapore Pte Ltd. 2018  
S. Seetharamu et al. (eds.), *Proceedings of Fatigue, Durability and Fracture Mechanics*, Lecture Notes in Mechanical Engineering, [https://doi.org/10.1007/978-981-10-6002-1\\_14](https://doi.org/10.1007/978-981-10-6002-1_14)

## 1 Introduction

Conventional fatigue analysis practices followed in daily practices today are at least 10 or more years old. Typically equivalent stress (on a plane) approach is used for fatigue analysis. However, variation of stresses/strains in a particular plane may not yield accurate results for fatigue life calculation. With development in analysis practices and better solver capabilities, it is imperative to evaluate these techniques for daily analysis practices.

One such need is to evaluate the fatigue life when loads are highly complex and nonproportional. Our products experience the loads in multidirection. So the variation of stress in a particular direction may not yield accurate results for fatigue calculation. Hence, performing multiaxial fatigue analysis appears to be the next step closer to correlate to fatigue failures.

### 1.1 *Multiaxial Fatigue Analysis*

Multiaxial fatigue analysis requires use of yield criteria to fatigue under combined loading. Based on loading history, the equivalent stress calculation is done for different conditions. Various methods for equivalent stress calculation such as maximum principal stress, Von Mises and maximum shear stress (Tresca) are studied for determination of equivalent stress under multiaxial loading situations [1, 2].

With nonproportional loading, there is increased strain hardening which needs to be considered appropriately. Hence, based on nonproportionality of the load and biaxiality ratio, a decision matrix is prepared to decide the appropriate notch correction and equivalent stress or strain approach. Notch correction methods studied are Neuber, Hoffmann–Seeger, Glinka and Jiang Sehitoglu, etc.

The multiaxial fatigue analysis methods based on stress (High cycle fatigue), strain (low cycle fatigue) and critical plane approach are studied and compared against each other with above considered parameters. Best method out of all these studied methods is proposed here for multiaxial fatigue analysis.

Multiaxial fatigue analysis is performed on SPFH (self-propelled forage harvester) machine to correlate the results with actual life of the components (Fig. 1).

### 1.2 *Necessity*

The day-to-day fatigue analysis considers equivalent stress approach. Actual variable loading suggests that failure does not coincide with the planes predicted by previous approach. Thus study of multiaxial fatigue cannot be made based on static



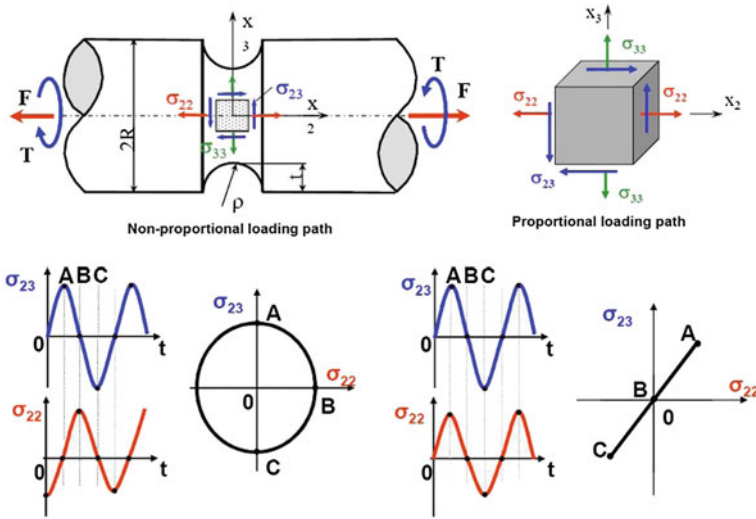


**Fig. 1** Proportional and nonproportional loading (reference: [https://www.efatigue.com/training/Multiaxial\\_Stresses.pdf](https://www.efatigue.com/training/Multiaxial_Stresses.pdf))

yield criteria. These approaches, though with all the corrections, cannot take into account the succession of stress states that define a multiaxial loading.

The general expression of multiaxial loading is given in following equation

$$X + I \sqrt{\tau} Y \ddot{u}$$

where  $X$  and  $Y$  are shear and normal stresses in certain planes considered to be critical, while  $I$  and  $\ddot{u}$  are values determined as functions of the material’s fatigue characteristics. This particular approach is termed as critical plane approach.

Critical plane approach recognizes that fatigue is essentially directional and considers the accumulation of damage on particular plane. There are various methods for calculating damage on a particular plane. Most commonly used method calculates damage for all possible planes (at say  $10^\circ$  intervals) and the worst or critical plane is selected.

Following are few examples of multiaxial loading situations.

- Crankshaft has torsion and bending—Biaxial stresses.
- Thin walled pressure vessel—Biaxial stresses.
- Stresses in notches—usually multiaxial.
- Stresses in bolt thread and main body of the bolt.

### 1.3 Terms Associated with Multiaxiality

(a) **Biaxiality Ratio ( $a_e$ ):**  $a_e = \zeta_2/\zeta_1$  (Fig. 2)

Stress state on free surface is biaxial—principal stresses  $\zeta_1$  and  $\zeta_2$  (where  $|\zeta_1| > |\zeta_2|$ ) lie in the  $x$ - $y$  plane Biaxiality analysis:

- $a_e = -1$  Pure Shear.
- $a_e = +1$  Equi-Biaxial.
- $a_e = 0$  Uniaxial.

(b) **Proportionality**

Orientation  $T$  of  $\zeta_1$  relative to local  $X$  axis (Fig. 3).

Proportional loading:  $T$  and  $a_e$  are fixed.

Nonproportional loading: either of  $T$  and  $a_e$  or both vary. Below are few situations where proportionality is explained (Fig. 4).

### 1.4 Fatigue Damage Modeling

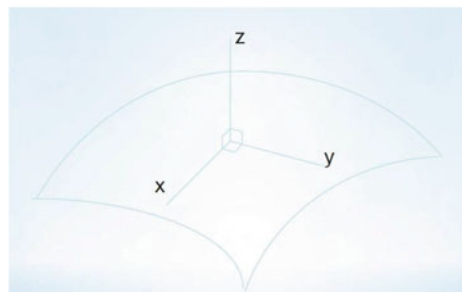
- Proportional loadings—Biaxiality ratio influences type of fatigue damage and choice of damage parameter.
- Nonproportional Loadings—Need method to capture varying stress orientation! (Table 1)

There are various methods available for modeling the damage based on stress or strain criteria. Out of the various methods, the few widely used approaches are listed in the table which are used widely by commercially available fatigue analysis softwares.

Table 2 shows the various damage modeling approaches used frequently.

Of the various methods listed in Table 2, following are the widely used models for fatigue analysis.

**Fig. 2** Free surface stresses  
(reference: <http://www.caefatigue.com/wp-content/uploads/CAEF-13-Multiaxial-Stress.pdf>)



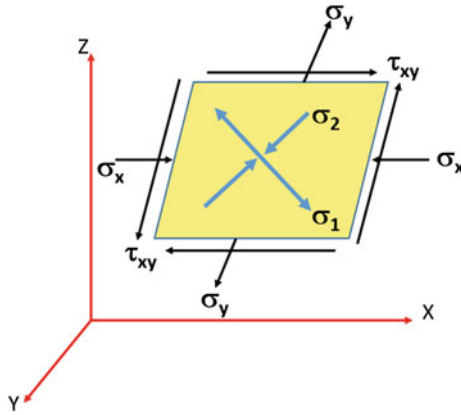


Fig. 3 Definition of proportionality

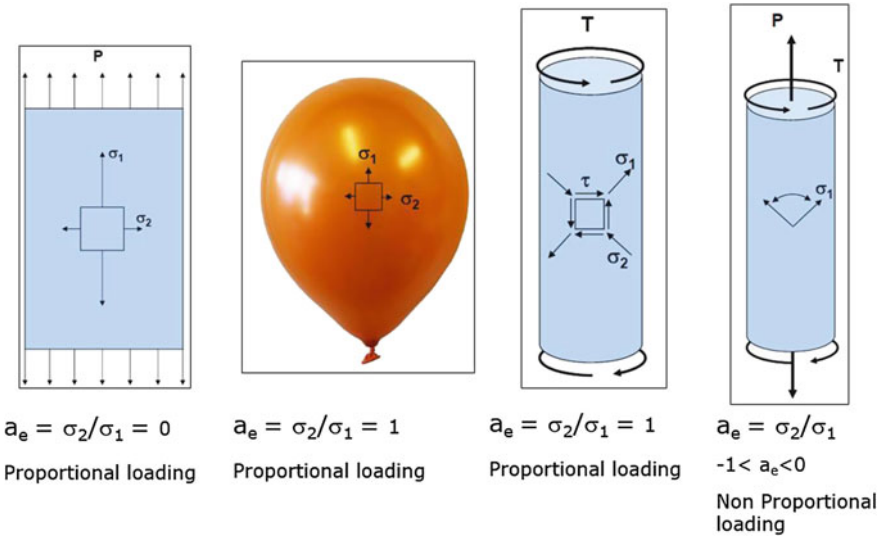


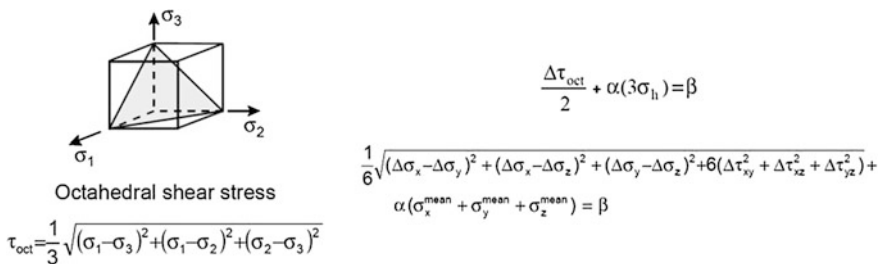
Fig. 4 Examples of loading (reference: [http://www.ncode.com/fileadmin/mediapool/nCode/downloads/events/Multiaxial\\_Fatigue\\_UGM\\_May\\_2012\\_Heyescompatibility\\_Mode\\_pdf](http://www.ncode.com/fileadmin/mediapool/nCode/downloads/events/Multiaxial_Fatigue_UGM_May_2012_Heyescompatibility_Mode_pdf))

Table 1 Basis for damage model definition

Type of loading	T	$a_e$
Uniaxial	Constant	0
Proportional multiaxial	Constant	$-1 < a_e < +1$
Nonproportional multiaxial	May vary	May vary

**Table 2** Fatigue damage modeling approaches

	Stress-based criteria		Strain based criteria	Energy based criteria
	Long life	Low life	Long/low life	
	Equivalent stress approach		Equivalent strain approach	Plastic work Total strain energy density per cycle
Critical plane models	Sines model		Brown and Miller	
	Findley		Fatemi Socie model	
	Dang Van model		Liu	
			Type B critical plane shear strain (TBCPS)	
			Wang Brown method	



**Fig. 5** Sines model

(a) Sines Model [1, 3]

- Sines method uses alternating octahedral shear stress for cyclic stresses and hydrostatic stress for mean stresses.
- Relatively easy and can be used for proportional loading with high cycle fatigue analysis (Fig. 5).

(b) Findley Model [1, 3]

- Fatigue crack plane considers the plane with maximum shear stress and maximum normal stress on this plane. *K* is the material constant.
- It requires search for critical plane. Hence computationally hard.
- It is suitable for long life calculations with proportional or nonproportional loading (Fig. 6).

(c) Dang Van Model [1, 3]

- Amplitude of the microscopic shear stresses and the magnitude of the hydrostatic stress.

**Fig. 6** Findley model

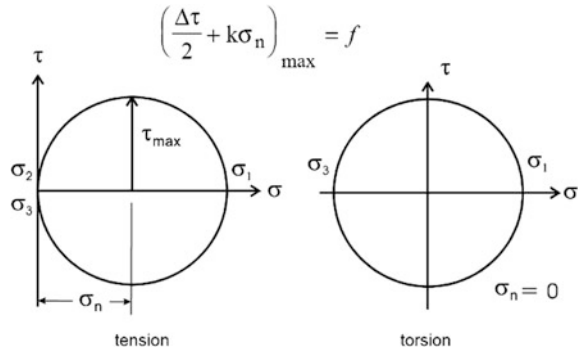


**Fig. 7** Dang Van model  
(reference: <https://www.efatigue.com/training/MultiaxialFatigue.pdf>)

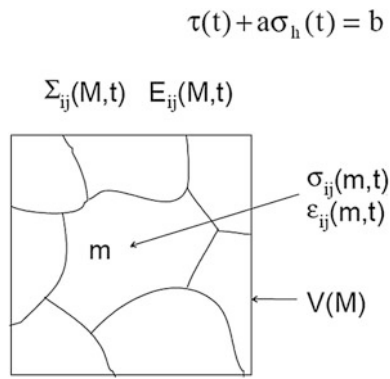


**Fig. 8** Brown and Miller model (reference: <https://fenix.tecnico.ulisboa.pt/downloadFile/395138338519/Extended%20abstract.pdf>)

$$\Delta \hat{\gamma} = \left( \Delta \gamma_{\max}^{\alpha} + S \Delta \epsilon_n^{\alpha} \right)^{\frac{1}{\alpha}}$$

$$\frac{\Delta \gamma_{\max}}{2} + S \Delta \epsilon_n = A \frac{\sigma_f' - 2 \sigma_{n,\text{mean}}}{E} (2N_f)^b + B \epsilon_f' (2N_f)^c$$

- Complicated way of estimating the microscopic residual stress.
  - High cycle fatigue with nonproportional loading (Fig. 7).
- (d) Brown and Miller Model [1, 3]
- Based on physical interpretation of mechanisms of fatigue crack growth.
  - Proposed that the shear strain and normal strain on the plane of maximum shear must be considered (Fig. 8).

(e) Fatemi and Socie Model [4]

- Based on physical interpretation of mechanisms of fatigue crack growth.
- Proposed that the shear strain and normal stress on the plane of maximum shear must be considered (Fig. 9).

(f) SWT Model [1, 3]

- Proposed the Maximum principal stress and principal strain as damage parameter (Fig. 10).

(g) Type B Critical Plane shear Strain (TBCPS) Model

- Out-of-plane shear strain on planes inclined at 45° to the free surface.
- Damage is calculated on the critical (maximum shear plane) whether type A or B (Figs. 11 and 12).

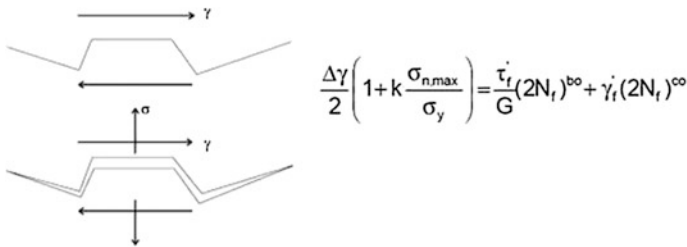


Fig. 9 Fatemi Soci model (reference: [http://www.abcm.org.br/symposium-series/SSSM\\_Vol2/Contents/SSSM\\_24.pdf](http://www.abcm.org.br/symposium-series/SSSM_Vol2/Contents/SSSM_24.pdf))

Fig. 10 SWT model (reference: <https://fenix.tecnico.ulisboa.pt/downloadFile/395138338519/Extended%20abstract.pdf>)

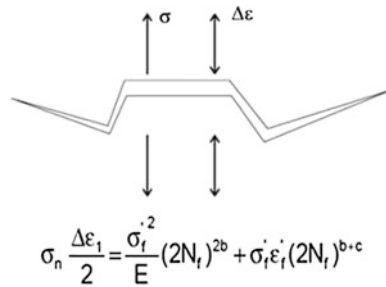
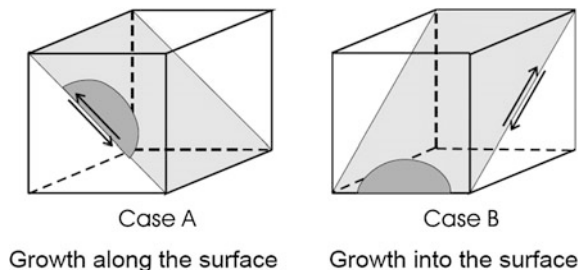


Fig. 11 Type of damage opening (reference: <https://www.efatigue.com/training/MultiaxialFatigue.pdf>)



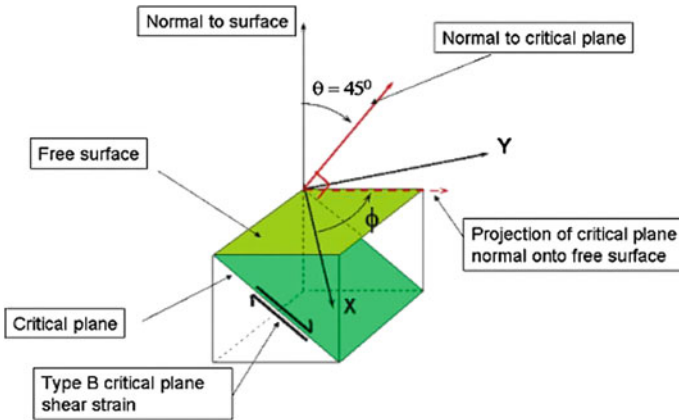


Fig. 12 TBCPS model (reference: [http://www.ncode.com/fileadmin/mediapool/nCode/downloads/events/UGM\\_15/2015\\_nCodeUGM\\_Multiaxial\\_Fatigue\\_Life\\_Prediction.pdf](http://www.ncode.com/fileadmin/mediapool/nCode/downloads/events/UGM_15/2015_nCodeUGM_Multiaxial_Fatigue_Life_Prediction.pdf))

(h) Wang Brown Model

- Calculates critical plane for each rainflow reversal.
- May be quite slow especially for long loading histories.
- Recommended for a variety of proportional and nonproportional loadings.
- For each reversal the damage is calculated on the critical (maximum shear plane) whether case A or B.

### 1.5 Mean Stress Correction

Mean stress corrections used in fatigue analysis mostly run around the methods proposed by Morrow and SWT. Based upon the various literature referred, following are the noted difference between two methods [5].

**Morrow Correction:**

- Suitable for high cycle fatigue.
- Mean stress effects are significant at low values of plastic strain, where the elastic strain dominates.
- The correction also reflects the trend that mean stresses have little effect at shorter lives, where plastic strains are large.

**SWT Correction:**

- Suitable for low as well as high cycle fatigue analysis.
- The physical interpretation of this approach assumes that no fatigue damage occurs when the maximum stress is compressive.

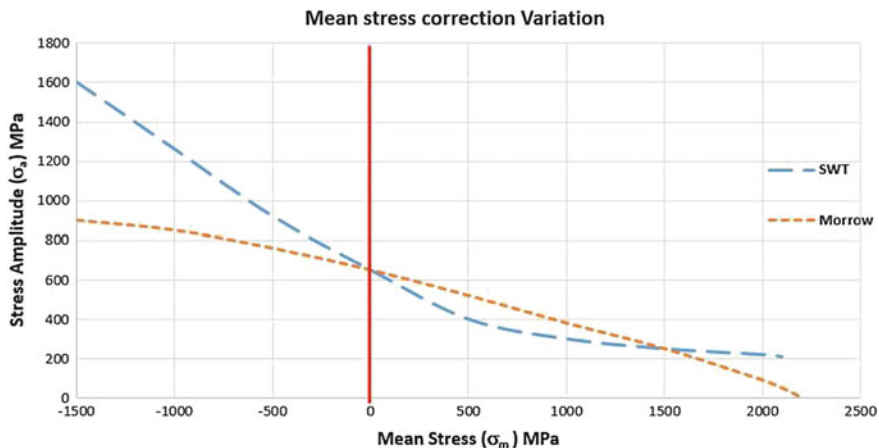


Fig. 13 Effect of mean stress correction

Figure 13 shows that Morrow correction shows conservative results for compressive mean stresses, whereas SWT model is more suitable for tensile mean stresses.

## 1.6 Multiaxial Plasticity

One of the complicated characteristics of nonproportional loading situations is the additional cyclic hardening due to the interaction of dislocations in different directions. Because of the change in direction of principal stresses and strains in the material, dislocations move in different directions, interact with each other and generate an additional hardening which is called nonproportional hardening. This additional hardening depends on loading conditions, temperature, and material hardness and microstructures. Therefore, one of the very first steps in analysis of fatigue life under nonproportional variable amplitude multiaxial loading is to evaluate the material response to the rotation of principal axes.

In general, a good multiaxial fatigue model should be physically based, sensitive to material deformation behavior, robust, and applicable to variable amplitude loading.

Final stress–strain state at the notch tip depends upon load path followed up incrementally as applied. Figure 14 explains how the stress strain response would vary for typical applied loading [6].

Therefore, the constitutive stress–strain relationships must be written in terms of increments because the current stress–strain increments depend on the previous stress/load path.



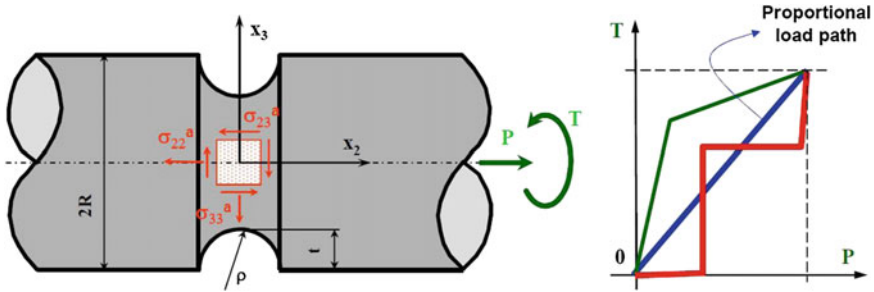
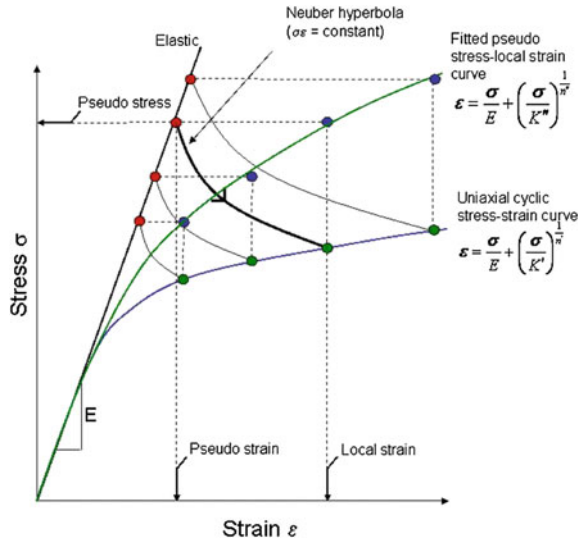


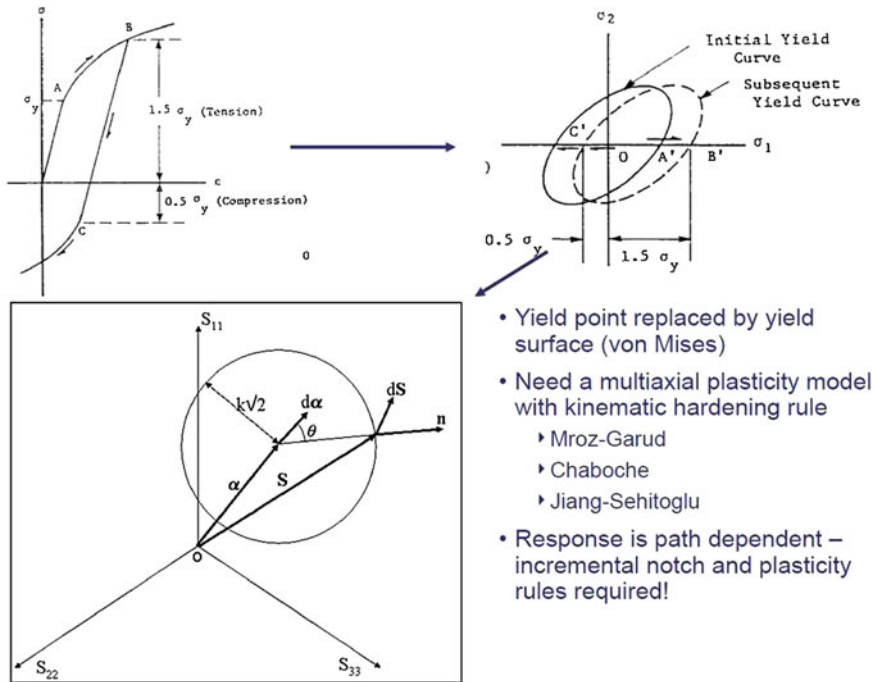
Fig. 14 Variation of load path

Fig. 15 Neuber correction  
 (reference: [http://www.ncode.com/fileadmin/mediapool/nCode/downloads/events/UGM\\_15/2015\\_nCodeUGM\\_Multiaxial\\_Fatigue\\_Life\\_Prediction.pdf](http://www.ncode.com/fileadmin/mediapool/nCode/downloads/events/UGM_15/2015_nCodeUGM_Multiaxial_Fatigue_Life_Prediction.pdf))



Based on these aspects, there are different models which suggest the plasticity correction.

- (a) **Neuber Correction**—Applicable to uniaxial or proportional loading [7, 8] (Fig. 15).
- (b) **Hoffmann–Seeger’s Correction**
  - The principal stress and strain axes are fixed in orientation.
  - The ratio of the in-plane principal strains is constant.
  - The uniaxial stress–strain curve can be extended for use with von Mises equivalent stress and strain under different states of stress.
  - Applicable to biaxial and proportional loading.



**Fig. 16** Jiang Seleh correction (reference: [http://www.ncode.com/fileadmin/mediapool/nCode/downloads/events/UGM\\_15/2015\\_nCodeUGM\\_Multiaxial\\_Fatigue\\_Life\\_Prediction.pdf](http://www.ncode.com/fileadmin/mediapool/nCode/downloads/events/UGM_15/2015_nCodeUGM_Multiaxial_Fatigue_Life_Prediction.pdf))

### (c) Seeger Heuler Correction

- Provides a variation on the Neuber or Hoffmann–Seeger methods that increases the amount of plasticity estimated when net section yielding is predicted, based on a shape factor.

### (d) Jiang Sehitoglu Notch Correction [9]

- Stress–strain relationship is very path dependent.
- Difficult to find closed cycles.
- An incremental formulation of the stress–strain relations and notch rules becomes necessary.
- Applicable to nonproportional loading (Fig. 16).

## 2 *n*-Code Multiaxial Fatigue Analysis Approach

Starting from *n*-code version 11 onward, it has the strong solver capability of performing multiaxial fatigue analysis. *n*-code has the option of performing multiaxial fatigue analysis in two different approaches.

1. Auto mode with standard assessment.
2. Multiaxial EN fatigue analysis glyph.

### Auto Mode With Standard Assessment

The Auto mode employs a two-pass approach. In the first pass, a calculation is made using the absolute maximum principal stress, and a standard multiaxial assessment is also carried out [8]. Based on the multiaxial assessment results, a second-pass calculation may be made using a different combined stress option (e.g., critical plane). Where a second-pass calculation is made, its results overwrite the first (Fig. 17).

This method provides a more robust measure of the biaxiality and nonproportionality of the local loading (stress state). The mean biaxiality and nonproportionality factors are reported in the analysis results, together with the dominant stress direction [8] (Fig. 18).

A second pass using a different stress combination method may be carried out IF the value of STRMAX (equivalent maximum stress) exceeds the percentage of the material strength (UTS) defined by zero damage stress percent and IF the non-proportionality and/or biaxiality values lie outside the ranges defined for the normal method by the relevant threshold values. The auto mode is summarized in Fig. 19.

### Multiaxial EN Fatigue Analysis Glyph

- Six-step analysis method.
- Critical plane calculations based on various combinations of biaxiality and nonproportionality.
- Computationally expensive. Hence, recommended only when highly nonproportional loading is involved (Fig. 20).

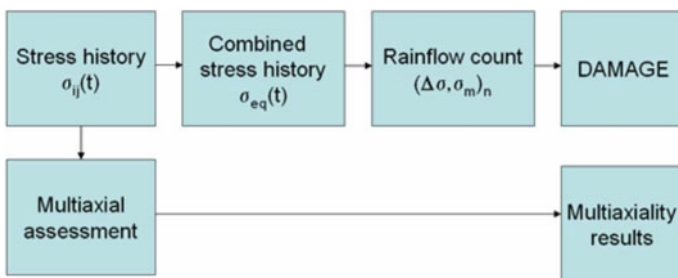


**Fig. 17** First-pass analysis with auto mode (reference: *n*-code design life theory guide. NC-DL-TH 8.00.13.0)

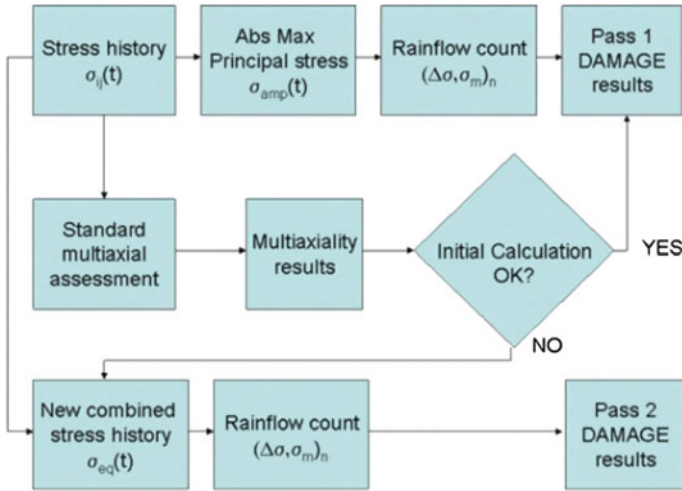
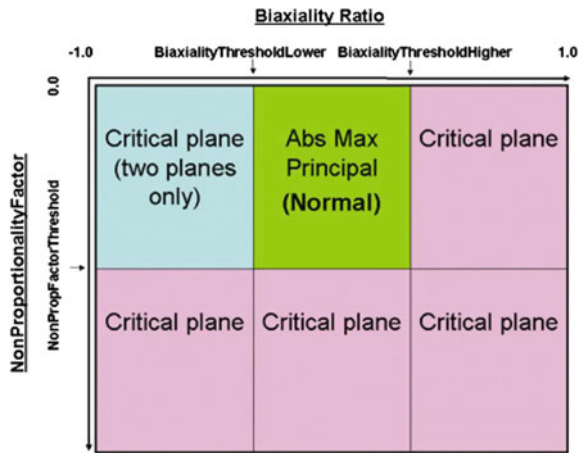


**Fig. 18** Second-pass with auto mode (reference: *n*-code design life theory guide. NC-DL-TH 8.00.13.0)

**Fig. 19** Decision matrix in auto model assessment (reference: *n*-code design life theory guide. NC-DL-TH 8.00.13.0)



A typical multiaxial EN analysis has the following basic steps, which are executed for each analysis entity (Node, Element, Node-on-Element) and shell surface, where appropriate:

- (i) The stress tensor history.
- (ii) The stress tensor is processed using a multiaxial plasticity model, combined with a notch correction, to generate an estimated local elastic-plastic strain and stress history.

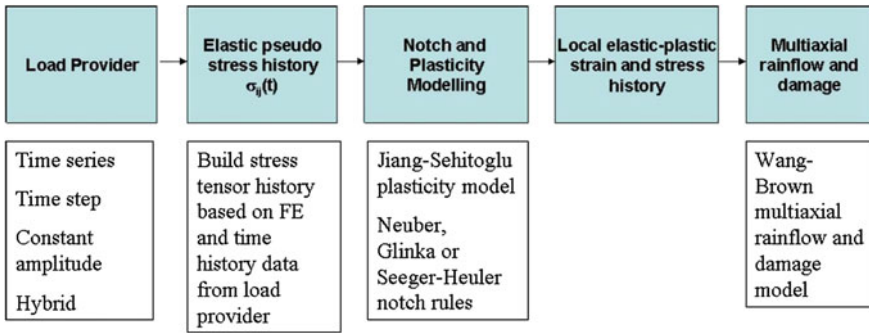


**Fig. 20** Multiaxial EN fatigue analysis (reference: *n*-code design life theory guide. NC-DL-TH 8.00.13.0)

**Fig. 21** Decision matrix in multiaxial EN fatigue glyph assessment (reference: *n*-code design life theory guide. NC-DL-TH 8.00.13.0)

		NonProportionalityFactor		
		$0 \leq \text{PROP} < 0.1$	$0.1 \leq \text{PROP} < 0.2$	$0.2 \leq \text{PROP}$
Mean Biaxiality Ratio	$-1 \leq a < 0.6$	Critical Plane Hoffmann-Seeger No MSC		Wang-Brown with mean Jiang-Sehitoglu/ Neuber
	$-0.6 \leq a < 0.25$	Abs Max Principal, Hoffmann-Seeger, Morrow	Critical Plane Hoffmann-Seeger Morrow	
	$0.25 \leq a < 0.6$	Signed Tresca Hoffmann-Seeger Morrow	TBCPS Hoffmann-Seeger Morrow	
	$0.6 \leq a \leq 1$	TBCPS Hoffmann-Seeger Morrow	TBCPS Hoffmann-Seeger Morrow	

- (iii) The elastic–plastic strain and stress history is fed through the different damage models listed below in decision matrix. The stress history undergoes multiaxial rainflow counting and damage procedures to get the final damage and life prediction (Fig. 21).

### 3 Multiaxial Fatigue Analysis and Discussion

Multiaxial fatigue analysis is carried out for one of our JD product, i.e., forage harvesting machine. A rig response test was carried out earlier in the laboratory. The measured strain histories with appropriate duty cycle are used for analysis (Fig. 22).

The multiaxial fatigue analysis is performed using three different approaches mentioned in earlier section. The results show good correlation with the life numbers predicted through multiaxial fatigue analysis.

The fatigue analysis is performed by considering the duty cycle of the machine. The various configuration set-up are run for respective % of the time. The test measurements are taken in terms of strain histories at different location. Inertia relief analysis is performed with unit loads at different wheel locations. Fatigue analysis is performed by using unit response at different location which is scaled with response from the measured strain histories.

Multiaxial fatigue EN analysis shows good co-relation with actual life predicted through test. However, the run time with two-step and multiple steps method increases significantly, so one need to be very deterministic in selecting the elements for these calculations. More the number of damaged elements filtered for further calculations more the time is taken for analysis. Hence, it is necessary to decide these numbers so that only the critical region elements get filtered for further calculation and run times minimal.

There are still few regions where the life numbers do not correlate with test. There is still some variation by a factor of 3–5 which is a common for any fatigue analysis method. This analysis, however, also dwells upon the aspect that critical region are highlighted which otherwise could have been missed with normal fatigue analysis.

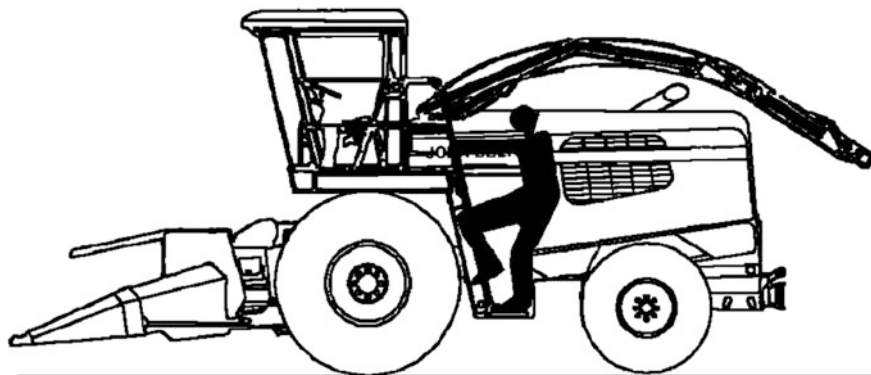


**Fig. 22** Typical agricultural machine (reference: GreenStar 2 System™—Forage Harvester, OPERATOR'S MANUAL, John Deere Works Zweibrücken, 2007)

## 4 Conclusion

- The multiaxial fatigue analysis reflects in reduction in life numbers based on biaxiality and nonproportionality. This would highlight the location which would have been missed with normal fatigue analysis.
- Various aspects considered in fatigue analysis such as notch corrections for plasticity, mean stress corrections do affect the fatigue life of the structure under highly nonproportional loading.
- It is the analysis engineer's call to decide which method is suitable for the specific problem on fatigue analysis.
- Many of the fatigue analysis problems should result in better solution with two-step analysis which would give the benefit on computational cost as well.
- Computation time with multiaxiality increases as it does calculations on every 10° rotation of the plane.
- Decision on selection of the fatigue analysis method to be done by judgment and vital experience on type of loading in the problem under life evaluation. Multiaxial fatigue analysis can further be evaluated with study of certain parameters which reduce the solution time.

## References

1. Meggiolaro MA, de Castro JT, de Oliveira Miranda AC (2009) Evaluation of multiaxial stress-strain models and fatigue life prediction methods under proportional loading. *Mechanics of Solids in Brazil, Brazilian Society of Mechanical Sciences and Engineering*
2. Somnath C (2012) Investigation of proportional and non-proportional loading. *American Society for Engineering Education*
3. dos Reis Cabrita AJ (2009) Analysis of the non proportionality between stress in multiaxial loadings in austenitic stainless steel (AISI 303). *Instituto Superior Técnico—Technical University of Lisbon, Portugal*
4. Fatemi A, Socie DF (1988) A critical plane approach to multiaxial fatigue damage including out-of- phase loading. *Fatigue Fract Eng Mater Struct* 11(3):149–165
5. Ince A, Glinka G (2011) A modification of Morrow and Smith–Watson–Topper mean stress correction models. *Fatigue Fract Eng Mater Struct* 34:854–867
6. Hancell PJ, Harvey SJ (1979) The use of kinematic hardening models in multiaxial cyclic plasticity. *Fatigue Fract Eng Mater Struct* 1:271–279 (Pergamon Press. Printed in Great Britain. *Fatigue of Engineering Materials Ltd.*)
7. n-code document on “Multiaxial\_Fatigue\_n-code\_Heyes\_Compatibility\_Mode (2015)”
8. nCode Design Life Theory Guide, version 11.0 (2015) HBM-nCode
9. Neuber H (1961) Theory of stress concentration for shear strained prismatic bodies with arbitrary nonlinear stress—strain law. *J Appl Mech* 28:544–55126
10. Socie DF. *Multiaxial Fatigue*. Department of Mechanical and Industrial Engineering University of Illinois at Urbana-Champaign

# Effect of Loading Rate and Constraint on Dynamic Ductile Fracture Toughness of P91 Steel

S. Sathyanarayanan, Jashveer Singh, A. Moitra, G. Sasikala, S.K. Albert and A.K. Bhaduri

**Abstract** The dynamic ductile fracture toughness ( $J_{0.2d}$  and  $J_a$ - $R$  curve) of P91 steel is an important parameter for design against failure of fast reactor sub-assembly wrappers under accidental loading conditions. Instrumented impact testing of pre-cracked Charpy specimens is well suited for this purpose due to their small size and resultant material economy for service-exposed materials. While the effect of impact loading rates on plastic deformation properties is well known, their effect on dynamic ductile fracture toughness is relatively less studied. Also, change in in-plane constraint is known to affect ductile fracture toughness under quasi-static loading conditions. Hence, a study was undertaken to evaluate the effect of loading rate and in-plane constraint on the dynamic  $J$ - $R$  curves. The main challenge in this is determination of current crack length ( $a$ ), which is required to evaluate  $J$ -integral. Though a few methodologies have been proposed in the literature for this purpose, there is no standard method as yet. The lowest impact loading rate has been chosen so as to ensure ‘low-blow’ conditions where the specimen is not fully broken. This enabled the usage of ‘normalization’ method of ASTM E 1820 standard to determine ‘ $a$ ’ for this loading rate. Further for the higher loading rate full-blow tests, the data from low-blow test specimens have been used as reference in the ‘Compliance Ratio’ key curve method to determine ‘ $a$ .’ The dynamic  $J$ - $R$  curves have been obtained from the ASTM E 1820 formulation of  $J$ -integral using as input the determined ‘ $a$ ’ and load–displacement data. Dynamic  $J$ - $R$  curves are found to be independent of loading rate in the range between 2.15 to 5 m/s and 1.5 to 5 m/s for short cracks ( $a/W \approx 0.3$ ) and long cracks ( $a/W \approx 0.5$ ), respectively. Short cracks ( $a/W \approx 0.3$ ) display higher  $J$ - $R$  curves than those for long cracks ( $a/W \approx 0.5$ ) beyond a crack extension of 0.3 mm. The validity of the dynamic  $J$ - $R$  curves obtained has also been explained.

---

S. Sathyanarayanan (✉) · A. Moitra · G. Sasikala · S.K. Albert · A.K. Bhaduri  
Metallurgy and Materials Group, Indira Gandhi Centre for Atomic Research,  
Kalpakkam 603102, Tamil Nadu, India

J. Singh  
Department of Mechanical Engineering, National Institute of Technology,  
Srinagar 190006, India



**Keywords** Dynamic  $J$ - $R$  curves · P91 steel · Smoothing  
Normalization method · ‘Compliance ratio’ key curve method

## 1 Introduction

The dynamic ductile fracture toughness ( $J_{0.2d}$  and  $J_d$ - $R$  curves) is an important parameter for structural integrity analysis of fast reactor in core wrappers to guard against ductile tearing under accidental loading conditions. While the 9Cr–1Mo steels are the chosen material [1–4] for this purpose, the use of instrumented pre-cracked Charpy tests (PCVN) for evaluation of  $J_{0.2d}$  and  $J_d$ - $R$  curves is gaining importance mainly because of smaller specimen size requirement and faster testing, facilitating economic experimentations on service-exposed materials. There are various successful efforts in the literature [5–8] toward determination of dynamic ductile fracture toughness. However, there is scope for further improvement in the methodologies appropriate for analytical approaches toward single specimen method determination of  $J$ .

Evaluation of  $J_{0.2d}$  and  $J_d$ - $R$  curves requires load ( $P$ ), displacement ( $d$ ) and current crack length ( $a$ ) triplets for the duration of the test. Un-smoothened  $P$ - $d$  plots are obtained from low-blow impact tests. The two main challenges toward determination of dynamic ductile fracture toughness are smoothing of  $P$ - $d$  plots and determination of  $a$ . The un-smoothened  $P$ - $d$  plots (due to inertial oscillations in an impact test) have been smoothed adopting a new way using linear regression fit [9] in the initial linear portion and by the moving average method [10, 11] in the elastic–plastic and crack growth regimes. The other major technological challenge has been the determination of the current crack length  $a$ , as the usual DCPD/ACPD and unloading compliance methods applied in quasi-static loading situations cannot be applied in dynamic circumstances. Though unequivocal standard methodologies to determine the parameter  $a$  are yet to evolve owing to the inherent experimental uncertainties involved in dynamic fracture experimentations, a few experiment-based techniques with mutual merits and demerits are available in the literature. These are, namely (a) ‘load ratio’ (LR) method [12], (b) power law ‘key curve’ (PLKC) method [7, 13], (c) three-parameter LMN method [14], (d) normalization method given in [9, 15] and (e) Compliance Ratio method [8]. It is of technological importance to compare and contrast the above-mentioned methodologies with respect to the experimental observations toward adopting a conservative approach to integrity analysis based on  $J_{0.2d}$  and  $J_d$ - $R$  curve approach. The ‘LR’ and ‘PLKC’ methods require only the initial crack length ( $a_0$ ) in addition to  $P$ - $d$  plots obtained from the impact tests. Hence, they can be applied to both impact test conditions where the specimen is fully broken (full-blow) and where the specimen is not fully broken (low-blow). The LMN and normalization methods require the final unbroken crack length. Hence, these methods can either be applied to low-blow tests or to full-blow tests with stoppers, ensuring that the specimen is not fully broken during impact. Though LMN and the normalization methods are

closely comparable, the latter uses a more rigorous functional form for plastic displacement. ‘Compliance Ratio’ method uses reference key curves generated from quasi-static or low-blow tests of identical specimens (where  $a$  can be determined) to determine  $a$  in the actual full-blow impact test. While the ‘LR’ and ‘PLKC’ methods have been proven for materials like HY 80 steel and SS316L(N) [7, 12, 13], respectively, they have not been successful for P91 steels. The ‘LR’ method requires that elastic displacement should be constant after peak load, whereas there is a significant decrease in this quantity for pre-cracked Charpy impact tests of P91 steel. The ‘PLKC’ method uses the  $P-d$  pairs after yield and before peak load only along with initial ligament length as input. The success of this method depends on whether the obtained constants in the power law fit give a linear shape to the ‘key curve’ after peak load. This does not happen for pre-cracked Charpy tests of P91 steels. It should be mentioned that ‘PLKC’ method was found to be successful for ‘low-blow’ impact tests of SS316L(N). It is well known that austenitic stainless steels exhibit higher amount of plastic deformation which can explain the difference in success of this method between SS316L(N) steel and the ferritic steels in this study. In this study, the normalization method has been used to determine ‘ $a$ ’ for low-blow impact tests. The low-blow impact tests (for which ‘ $a$ ’ is known) have been used as reference key curves in the ‘Compliance Ratio’ method to determine ‘ $a$ ’, for full-blow impact tests. The determined ‘ $a$ ’ along with  $P-d$  pairs from the impact test has been input in the ASTM E 1820-09e1 [9]  $J$  formulation to evaluate  $J_{0.2d}$  and  $J_a-R$  curves for P91 steel. The in-plane constraint effect has been studied by testing pre-cracked Charpy specimens with short and long crack lengths.

## 2 Material

For this study, 24-mm-thick plate of the Mod. 9Cr–1Mo steel in normalized and tempered (N&T) condition is the starting material. The steel was normalized at 1050 °C, and the holding time was 1 min/mm. It was tempered at 770 °C, and the holding time was 3 min/mm. Its chemical composition, in weight percent, is given as follows in weight percentage: C-0.105, Mn-0.411, P-0.016, S-0.0005, Si-0.207, Cu-0.062, Ni-0.202, Cr-8.937, Mo-0.861, Al-0.012, Nb-0.079, Zr-0.006, V-0.203, Ti-0.003, B-0.0004, N-0.0532, Fe-balance.

Charpy V-notch specimens were fabricated for P91 steel from rectangular blanks of 65 \* 15 \* 15 mm<sup>3</sup>. The drawing of the Charpy V-notch specimen is given in Fig. 1.

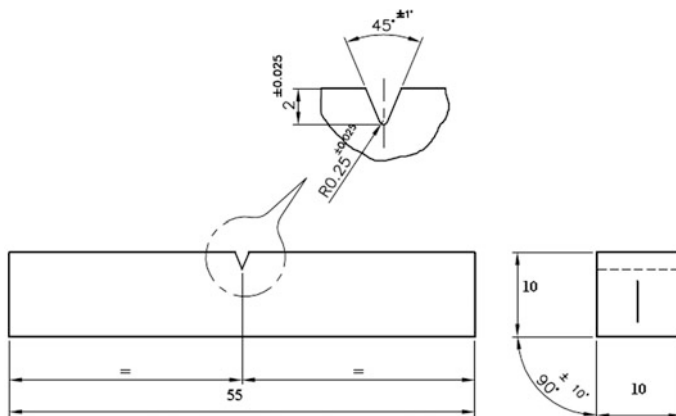


Fig. 1 Charpy V-notch specimen drawing with all dimensions in mm

### 3 Pre-cracking of Charpy V-Notch Specimens

Charpy impact test specimens were fatigue pre-cracked in a 3-point compression bend mode with an R-ratio of 0.10 in a 20-kN resonant fatigue testing machine. The initial resonant frequency for pre-cracking was 104 Hz, and it gradually decreased with crack growth. The initial peak to peak load was set at 5 kN and was reduced in steps of 0.5 kN, for every drop in the system frequency of 0.5 Hz, down to 3.0 kN. The stress intensity factor range ( $\Delta K$ ) during pre-cracking was within the range of 21.14–28.75 MPa $\sqrt{m}$ . The length of the fatigue crack was  $\sim 3$  and  $\sim 1$  mm from the end of the V-notch, to provide an  $a_0/W$  ratio  $\sim 0.5$  and  $\sim 0.3$ , where  $a_0$  is the initial crack length and  $W$  is width of the specimen.

### 4 Experimental

Impact testing for  $a/W \approx 0.5$  specimens of P91 steel was carried out at loading rates of 1.5, 3 and 5 m/s. Impact testing for  $a/W \approx 0.3$  specimens was carried out at loading rates of 2.15, 3 and 5 m/s.

The test temperature for all the tests was maintained at 100 °C to ensure ductile loading condition.

## 5 Smoothing of $P$ - $d$ Plots

Un-smoothened load–time plots are obtained as output from the impact tests which are converted to load–displacement  $P$ - $d$  plots. The inertial oscillations in an impact test are due to the interference of elastic stress waves with the actually experienced load by the specimen. These inertial oscillations make it difficult or not possible to obtain meaningful current crack length and  $J_{d}$ - $R$  curves. Hence, smoothing of the  $P$ - $d$  plots is a necessity. In this study, a new way of smoothing combining two available methodologies has been developed. The two methodologies that have been used are (a) linear regression fit given in ASTM-E1820-09e1 [9] and (b) moving average method given in [10, 11].

The linear regression fit [ASTM E 1820-09e1] smoothens the  $P$ - $d$  plot in the initial linear portion. This method does not cover the smoothing of the plot after the yield load.

The moving average method smoothens the entire  $P$ - $d$  plot. This method computes the value of the  $n$ th load ( $P$ ) point by taking the average of  $(m - 1)/2$  points before and after along with the  $n$ th point. It is given as

$$P_n = (1/m) * \sum_{n-[(m-1)/2]}^{n+[(m-1)/2]} P_i \quad (1)$$

where  $i$  is the index

$m$  total number of points taken for averaging.

This averaging is done on sliding basis covering the entire  $P$ - $d$  plot. The  $P$ - $d$  plot is averaged many number of times till the final smoothed plot is obtained.

The linear regression method [ASTM E 1820-09e1] gives a good fit to the un-smoothened initial linear portion. The moving average method gives a good fit to the data in the elastic–plastic and crack growth regimes starting at some distance after yield load. However, this method gives a steeper slope than the measured un-smoothened initial linear portion of the  $P$ - $d$  plot. Hence, smoothing of the  $P$ - $d$  plot will require usage of the linear regression fit to the initial linear elastic portion and the moving average method beyond the yield load. Since the moving average method starts giving a good fit to the un-smoothened data only some distance after the yield load, it was extended to intersect the initial linear regression line, thus completing coverage of the entire  $P$ - $d$  plot. The extension of moving average method to intersect the linear elastic portion was done by correlating  $P/b_o^2$  and  $d/W$  employing a four-parameter correlation formula (same as ASTM E 1820 normalization method) in the case of  $a/W \approx 0.5$  specimens and a polynomial fit of order 2 for  $a/W \approx 0.3$  specimens. In the above,  $P$  is the load by the moving average method and  $d$  is the total displacement.

## 6 Current Crack Length Estimation Methodologies

The second major challenge to evaluate dynamic  $J$  is determination of current crack length ‘ $a$ .’ The two methodologies to determine ‘ $a$ ’ for low-blow and full-blow tests, respectively, are summarized in this section.

### 6.1 Normalization Method

The ‘key curve’ is the basis of this method with a correlation between normalized load and plastic displacement in the form and with the procedure [9, 15] given herein:

Normalized load ( $P_{Ni}$ ) is given as

$$P_{Ni} = P_i / \left( W^* B^* (1 - a_{bi}/W)^{\eta_{pl}} \right) \quad (2)$$

where subscript  $i$  refers to the  $i$ th data point,  $P$ —load,  $W$ —width,  $B$ —thickness,  $a_{bi}$ —blunting corrected crack length and  $\eta_{pl} = 2$  (for TPB specimen) is the plastic eta factor.

$a_{bi}$  is given as

$$a_{bi} = a_o + (J_i / (2 * \sigma_f)) \quad (3)$$

where  $a_o$ —initial crack length,  $\sigma_f$ —flow stress =  $((\sigma_{ys} + \sigma_{uts})/2)$  and  $J_i$  is calculated as per ASTM E 1820-09e1 using  $a_o$ .  $\sigma_{ys}$  and  $\sigma_{uts}$  are the yield strength and ultimate tensile strength, respectively.

In the instrumented impact test using pre-cracked Charpy specimen, the dynamic yield stress,  $\sigma_{yd}$ , and dynamic flow stress,  $\sigma_{fd}$ , are obtained using the equations given below (Server et al. 1978):

$$\sigma_{yd} = (2.85 * P_{gy} * W) / (B * b_o^2) \quad (4a)$$

$$\sigma_{fd} = (2.85 * (P_{gy} + P_{pl}) * W) / (2 * B * b_o^2) \quad (4b)$$

where  $P_{gy}$ —yield load,  $P_{pl}$ —peak load,  $b_o$ —initial ligament length.

Normalized plastic displacement ( $d_{Npli}$ ) is obtained from

$$d_{Npli} = d_{pli} / W \quad (5)$$

where  $d_{pli}$  is the plastic displacement and obtained as

$$d_{pli} = d_i - (C_{el} * P_i) \quad (6)$$

with  $d_i$ —total displacement and  $C_{el}$  is the initial elastic compliance determined from the initial linear portion of  $P$ - $d$  plot.

$P_{Ni}$  and  $d_{Npli}$  are calculated for the points from yield load up to the point just preceding the peak load. They are also calculated for the final  $P$ - $d$  pair using the final crack length without blunting correction. They are then fitted with the given normalization function using least squares regression:

$$P_{Ni} = \left\{ C_1 + (C_2 * d_{Npli}) + \left( C_3 * (d_{Npli})^2 \right) \right\} / (C_4 + d_{Npli}) \quad (7)$$

where  $C_1$ ,  $C_2$ ,  $C_3$  and  $C_4$  are fitting constants.

Using the fitted equation, the current crack length is obtained iteratively starting from the point where  $d_{Npli} \geq 0.002$  and moving in a consecutive way for all the subsequent points.

## 6.2 Compliance Ratio ‘CR’ Key Curve Method

The CR method is an improved derivative of the load ratio method [12, 16]. The CR method does not need either the strain hardening exponent of the material or normalization functions or the measured final crack length.

Characteristic feature of the CR method is that the instantaneous specimen compliance of a ‘target specimen’ is calculated based on the experimentally measured load–displacement curve of a ‘source specimen.’ It is assumed that the key curves of source and target specimens are identical. The principle of the CR method is briefly described below.

At first, a source specimen is tested quasi-statically using the partial unloading compliance technique or by low-blow impact test. A load–displacement curve of the source specimen without crack growth (CR load,  $P$ ) can be determined according to Fig. 2. This curve is then normalized by the maximum load,  $P_{\max,source}$ , and elastic displacement at maximum load,  $d_{el,P\max,source}$ , in order to form the key curve.

The next step is to measure the load–displacement curve of the target specimen in a test without periodic unloadings which makes the method suited for dynamic loading conditions too. Generally, load signals from dynamic tests may show oscillations. Therefore, the data of the tests are smoothed to make them suitable for further analysis. Regardless of this, it is of great importance to optimize specimen instrumentation and loading parameters in dynamic tests before the signals are processed. The initial target specimen compliance,  $C_{0,target}$ , the maximum load,  $P_{\max,source}$ , and the corresponding displacement at maximum load,  $d_{el,P\max,source}$ ,

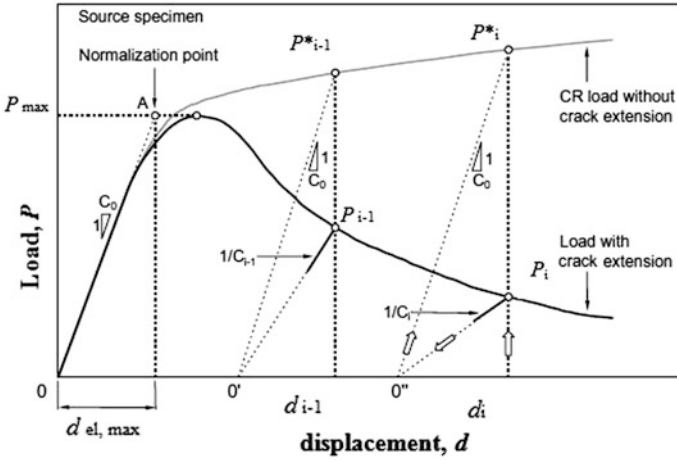
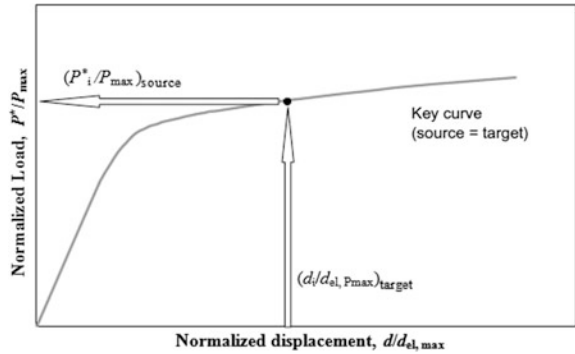


Fig. 2 Basis of compliance ratio method

Fig. 3 Determination of the normalized CR load ( $P_i^*/P_{max,source}$ )



then can be determined. The target specimen displacement values,  $d_{i,target}$ , are normalized by  $d_{el,Pmax,source}$  to  $(d_{el,Pmax})_{target}$ . According to Fig. 3, the key curve is entered with the normalized displacement,  $(d_{el,Pmax,source})_{target}$ , to obtain the normalized CR load,  $(P_i^*/P_{max})_{source}$ , from which the CR load of the target specimen,  $P_{i,target}^*$ , is calculated using:

$$P_{i,target}^* = P_{max,target} \left( \frac{P_i^*}{P_{max}} \right)_{source} \tag{8}$$

Subsequently, the compliance of the target specimen,  $C_{i,target}$ , is calculated by:

$$C_{i,target} = \left( \frac{P_i^*}{P_i} \right)_{target} C_0 \tag{9}$$

From the obtained  $C_{i,target}$ , the current crack length equation can be obtained for the Charpy specimen geometry under dynamic loading conditions using the following equation:

$$\frac{a}{W} = 1.17545 - 9.20345u + 50.40352u^2 - 179.15993u^3 \quad (10)$$

where

$$u = \frac{1}{E * C_{i,target} * B}$$

Essentially, the CR key curve was found to be independent of notch type, temperature and initial crack length [17]. Those parameters found to influence the shape of the key curves were specimen geometry and material. Therefore, the target specimens need to be of the same material and geometry as the source specimen. Since the ratio of maximum forces of source and target specimens is included in the CR procedure, the strain rate and temperature dependence of the mechanical properties of the materials are taken into account. The load–displacement record is the only information needed from the target specimen.

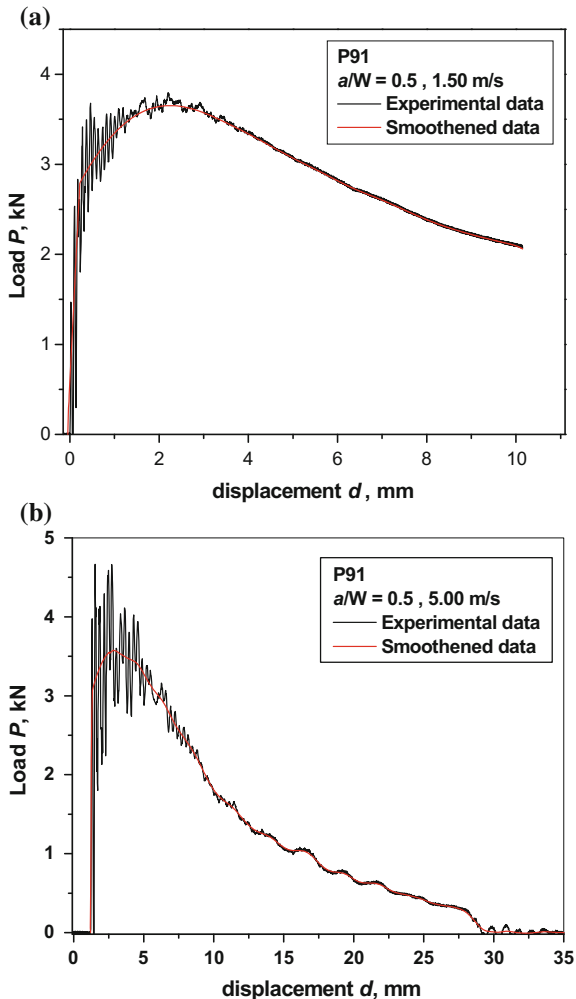
## 7 Results and Discussion

The testing and analysis of all the P91 steel specimens were carried out as given in the previous sections. The raw  $P$ - $d$  plots before peak load consist of high-amplitude superimposed oscillations which are due to interference of elastic stress waves generated in a dynamic loading test. It is known [18] that beyond a time span of  $\sim 3\tau$ , where  $\tau$  is the time period of oscillations, the amplitude of oscillations becomes negligible, and therefore any load measurement can be considered to be free from inertial effects. Kobayashi [19] has suggested the criterion of initial pendulum energy,  $E_o \geq 3E_T$ , where  $E_T$  is the total energy absorbed by the specimen, to avoid loss of contact effects during elastic–plastic fracture. Another point to note is that the  $P$ - $d$  plots are symptomatic of ductile fracture.

The evaluation of ductile fracture toughness ( $J$ - $R$  curve  $J_{0.2d}$ ) requires  $P$ - $d$ - $a$  triplets at each point of the plot. Hence, successful smoothing of the  $P$ - $d$  plot is an essential pre-requisite to enable determination of ‘ $a$ ,’ and therefore, the  $J$ -integral. The smoothing of the raw  $P$ - $d$  plots was done by a combination of linear regression fit given in ASTM E 1820-09e1 [9] and the moving average method [10, 11]. The comparison of the smoothed and un-smoothed  $P$ - $d$  plots is given in Fig. 4a, b for  $a/W \approx 0.5$  having loading rates of 1.5 and 5 m/s. Both the plots show good agreement between smoothed and un-smoothed data, confirming the correctness of the method employed. Similar results were obtained for all the tests.



**Fig. 4** **a** Raw un-smoothened and smoothed  $P$ - $d$  plot for 1.50 m/s for  $a/W \approx 0.5$  specimen, **b** raw un-smoothened and smoothed  $P$ - $d$  plot for 5.00 m/s for  $a/W \approx 0.5$  specimen



The comparison of smoothed  $P$ - $d$  plots for all the loading rates for  $a/W \approx 0.5$  specimens and that for  $a/W \approx 0.3$  samples is given in Figs. 5 and 6, respectively. It will be prudent to study the effect of loading rate on the plots. For  $a/W \approx 0.5$  specimens (Fig. 5), testing done at loading rates of 1.5 and 5 m/s is more or less superimposed, showing the lack of effect of the change in loading rate in the above range. The  $P$ - $d$  plot for the specimen having loading rate of 3 m/s is significantly higher than both the other specimens. This can be attributed to the difference in initial crack lengths between the specimens. While for specimens tested at 1.5 and 5 m/s, the ' $a_0$ ' is comparable at 5.82 and 5.95 mm, respectively, the ' $a_0$ ' for the specimen tested at 3 m/s is significantly lesser at 5.58 mm. For  $a/W \approx 0.3$  specimens (Fig. 6), testing done at loading rates of 3 and 5 m/s is more or less

**Fig. 5** Comparison of smoothed  $P$ - $d$  plot for  $a/W \approx 0.5$  specimen

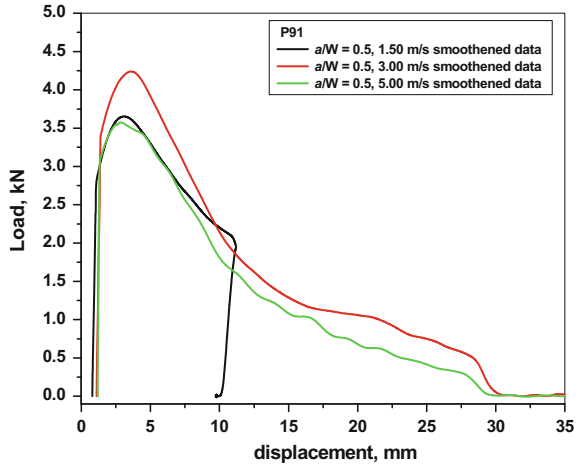
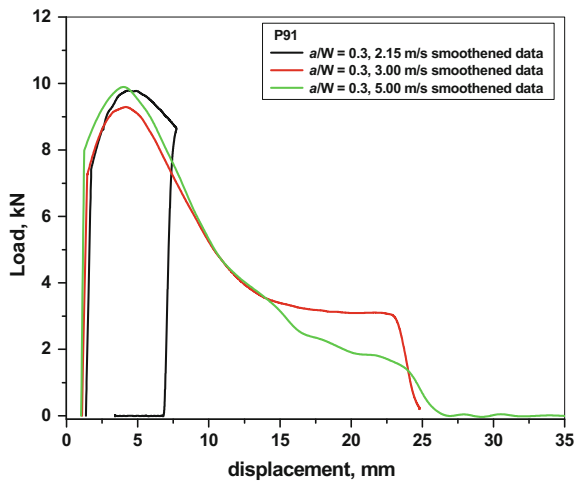


**Fig. 6** Comparison of smoothed  $P$ - $d$  plot for  $a/W \approx 0.3$  specimen



superimposed, showing the lack of effect of the change in loading rate in the above range. The  $P$ - $d$  plot for the specimen having loading rate of 2.15 m/s shows a higher curve after peak load with increasing deviation from the other two curves. The difference in  $P$ - $d$  plots after peak load in the lowest loading rate test is due to larger plastic zone size in short crack specimens. This point will be explained later during the discussion on  $J$ - $R$  curves.

The dynamic yield stress ( $\sigma_{yd}$ ) and dynamic flow stress ( $\sigma_{fd}$ ) calculated for all the specimens are given in Table 1. As expected, both increase with the increase in loading rate. Also, as can be seen from the tables for the specimens tested at 3 and 5 m/s, both quantities are comparable and independent of  $a/W$  ratio. These points confirm the validity of the  $P$ - $d$  plots obtained from tests at different loading rates.

**Table 1** The dynamic yield and dynamic flow stress for  $a/W \approx 0.5$  and  $a/W \approx 0.3$  specimens

A/W ratio	Impact velocity (m/s)	Dynamic yield stress $\sigma_{yd}$ (MPa)	Dynamic flow stress $\sigma_{fd}$ (MPa)
$a/W \approx 0.5$	1.5	455.5	526.5
	3	495.5	557.8
	5	531.6	577.3
$a/W \approx 0.3$	2.15	476.3	552.3
	3	486.9	554.0
	5	501.2	561.2

**Table 2** Final calculated and measured crack length for low-blow tests for  $a/W \approx 0.5$  and  $a/W \approx 0.3$  specimens

$a/W$ Ratio	Impact velocity (m/s)	Calculated final crack length (normalization method) (mm)	Measured final crack length (mm)	Measured initial crack length (mm)
$a/W = 0.5$	1.5	7.5240	7.5263	5.8263
$a/W = 0.3$	2.15	4.6991	4.7091	3.3365

After the smoothening of the  $P$ - $d$  plot, the next major challenge to evaluate dynamic  $J$ -integral is the determination of ‘ $a$ .’ In this work on P91 steel, ‘ $a$ ’ for the low-blow tests where the specimen is not fully broken has been determined by the ‘normalization’ key curve method. The low-blow test specimens have been used as ‘source’ specimens to determine ‘ $a$ ’ for the full-blow tests by the ‘Compliance Ratio’ key curve method. It is to be noted that specimen fractures fully in a full-blow impact test. The ‘CR’ key curve method has been used successfully [8] to determine ‘ $a$ ’ for low-blow impact tests of ductile cast iron TPB specimens using identical quasi-statically tested ‘source’ specimens.

The ‘normalization’ key curve method correlates  $P$ - $d$ - $a$  triplets, and hence, determination of  $J$ - $R$  curve depends on the success of the four-parameter formula used. Very good curve fits are obtained for the low-blow tests of both short and long cracks. The correlation coefficient ( $R^2$ ) is 0.99975 and 0.99961 for NT 34 ( $a/W \approx 0.5$ ) and NT 45 ( $a/W \approx 0.3$ ) data, respectively. The final calculated and measured crack length also shows very good agreement as can be seen from Table 2. The intermediate crack lengths between peak load and final unloading point are obtained iteratively using the fitted functional form. Now, it would be appropriate to analyze the rationale of the correctness of the ‘normalization’ method to describe the data. In this method, the load between yield point and peak load is normalized using an assumed blunting corrected crack length. However, the final load is normalized by the actually measured unbroken crack length. Hence, correctness of the functional fit to the data reflects the validity of this method and justifies the assumed blunting corrected crack length. The blunting correction is given as  $J/(m * \sigma_{fd})$  where  $m$  can have any value of 2 or above. The fact that usage of  $m = 2$  in our case has yielded good functional fit indicates that the size of crack

blunting is relatively very high compared to specimen dimensions for the pre-cracked Charpy specimens of P91 steel in this study.

Further, the Compliance Ratio (CR) key curve method has been used to determine current crack length ' $a$ ' for full-blow tests at 3 and 5 m/s for both  $a/W \approx 0.5$  and  $a/W \approx 0.3$  specimens. The 'CR' key curve obtained from the source specimens, NT 34 ( $a/W \approx 0.5$ , 1.5 m/s) and NT 45 ( $a/W \approx 0.3$ , 2.15 m/s), was used to determine ' $a$ ' for the full-blow test specimens. By taking the 'source' specimen from low-blow impact tests instead of quasi-statically tested sample, the usage of an extra servo-hydraulic machine has been avoided.

Having obtained  $P-d-a$  triplets, dynamic ductile fracture toughness ( $J-R$ ) curves were obtained for all the tested specimens using the ASTM E 1820-09e1 [9] formulation for  $J$ . For long crack ( $a/W \approx 0.5$ ) specimens, the  $J-R$  curves are given in Fig. 7 for all the three loading rates. It can be seen that  $J-R$  curves are independent of loading rate within the range 1.5–5 m/s. Similarly, for short crack ( $a/W \approx 0.3$ ) specimens, the  $J-R$  curves are independent of loading rate for specimens tested at 3 and 5 m/s as can be seen from Fig. 8. As is clearly evident from long crack (Fig. 7) specimen data,  $J-R$  curves consist of two linear lines with the change occurring at the peak load. This is symptomatic of ductile fracture behavior of long cracks of standard ( $a/W \approx 0.45-0.7$ ) length utilized in ASTM E 1820 standard.

The effect of in-plane constraint ( $a/W \approx 0.3$  and 0.5) is given by means of comparison of short crack and long crack  $J-R$  curves tested at 3 and 5 m/s in Figs. 9 and 10, respectively. As can be seen from the figures, the  $J-R$  curves are coincident up to 0.30 mm for 3 m/s data and up to 0.28 mm for 5 m/s data. After this initial coincidence,  $J-R$  curves for the respective  $a/W \approx 0.3$  specimens are higher than those of  $a/W \approx 0.5$  samples. The selection of  $a/W$  between 0.45 and 0.7 in ASTM E 1820 standard is to ensure the most conservative  $J-R$  curve which is also evident from our study. It is well known that short cracks have less constraint than long cracks of standard length.

**Fig. 7** Comparison of ASTM  $J-\Delta a$  curve for  $a/W \approx 0.5$  specimen

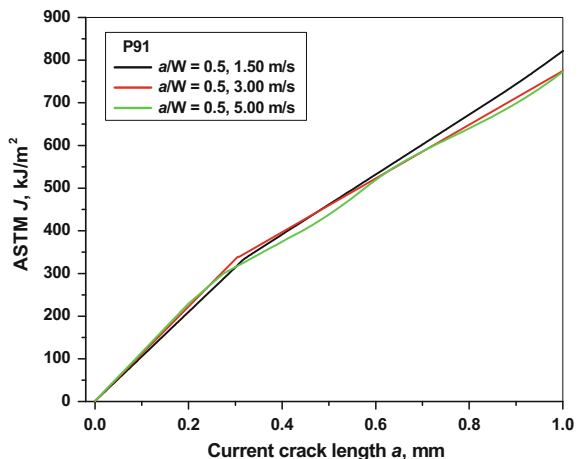


**Fig. 8** Comparison ASTM  $J$ - $\Delta a$  curve for  $a/W \approx 0.3$  specimen

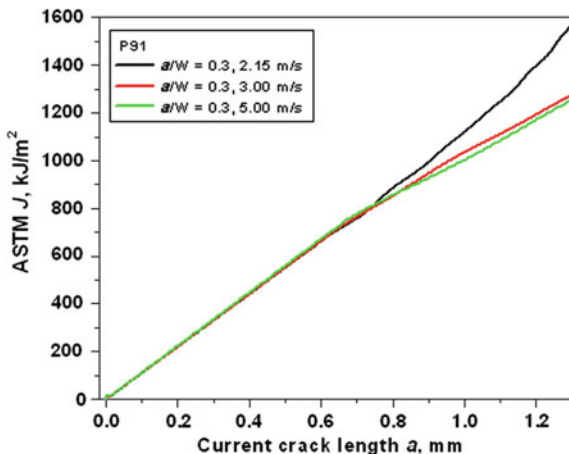
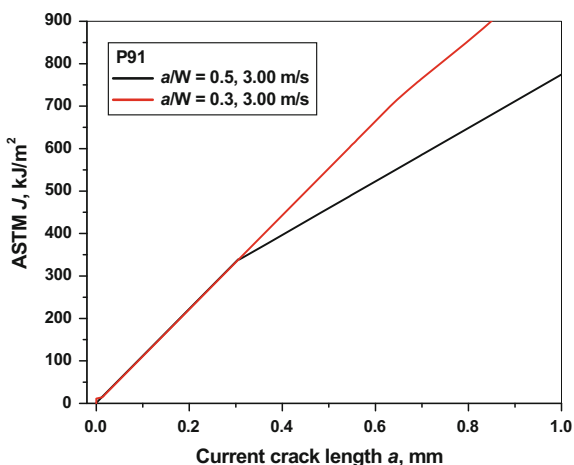


**Fig. 9** Comparison of ASTM  $J$ - $\Delta a$  curve for 3.00 m/s



$J_{0.2d}$  ( $J$  at  $\Delta a$  of 0.2 mm) for all the specimens is given in Table 3 and is almost of the same value varying between 210 and 229.8 kJ/m<sup>2</sup>. As was evident from the figures, it is independent of loading rate and constraint.

The ASTM E 1820 standard method is valid only under quasi-static loading conditions. While the same formula for  $J$  has been applied for the dynamic loading conditions, the acceptability of the dynamic  $J$ - $R$  curves has to be assessed. The main differences in the dynamic loading situation are smoothening of oscillations and the use of normalization method low-blow impact test data to determine ‘ $a$ ’ for full-blow tests by ‘Compliance Ratio’ key curve method. The correctness of the smoothening for  $P$ - $d$  data, normalization and Compliance Ratio key curve methods can be assessed by comparison of  $J$ - $R$  curves obtained at different loading rates. For all loading rate tests of long crack and short crack tests at 3 and 5 m/s, the dynamic

**Fig. 10** Comparison of ASTM  $J-\Delta a$  curve for 5.00 m/s

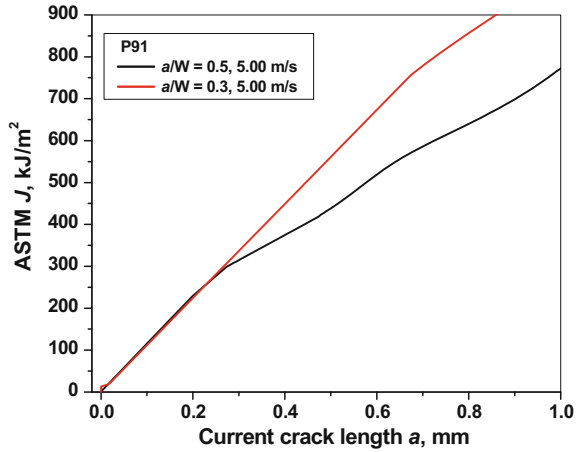


**Table 3**  $J_{0.2d}$  for  $a/W \approx 0.5$  and  $a/W \approx 0.3$  specimens

$a/W$ ratio	Impact velocity (m/s)	Fracture toughness $J_{0.2d}$ (kJ/m <sup>2</sup> )
$a/W \approx 0.5$	1.5	210.0
	3	224.5
	5	228.8
$a/W \approx 0.3$	2.15	222.0
	3	222.9
	5	229.8

$J-R$  curves are independent of loading rate which is in accordance with similar results of  $P-d$  plots for specimens having comparable initial crack length. This justifies the validity of the dynamic  $J-R$  curves obtained in this study. The only deviation is the higher  $J-R$  curve for  $a/W \approx 0.3$  specimen tested at lowest loading rate of 2.15 m/s. This  $J-R$  curve coincides with those of the higher loading rate specimens up to the blunting length of  $\Delta a = 0.74$  mm after which it shows increasing deviation from the other two curves. This is also in accordance with the behavior of the corresponding  $P-d$  plots. The blunting length (0.74 mm) corresponds to the peak load point in the corresponding  $P-d$  plots. The short crack specimens have longer blunting length when compared to those ( $\Delta a = 0.30$  mm) of long crack specimens. This reflects larger plastic zone size/deformation in short crack specimens which has resulted in the difference in fracture behavior with changing loading rate.

## 8 Conclusions

1. Dynamic  $J$ - $R$  curves have been obtained for P91 steel for both low-blow tests and full-blow tests. Smoothing of the inertial oscillations is done by the combination of linear regression curve fit and moving average method. Current crack length for low-blow test is obtained by 'normalization' method. For full-blow test, current crack length is obtained by 'Compliance Ratio' key curve method using low-blow tests as source data. The validity of the obtained dynamic  $J$ - $R$  curves has been explained.
2. Dynamic  $J$ - $R$  curves are independent of loading rate in the range between 1.5 and 5 m/s for long cracks ( $a/W \approx 0.5$ ) and 3 and 5 m/s for short cracks ( $a/W \approx 0.3$ ). The deviation in  $J$ - $R$  curve for short crack specimen at lowest loading rate of 2.15 m/s with the higher two loading rates is explained.
3. The effect of constraint was studied by a comparison of short crack and long crack results. At loading rates of 3 and 5 m/s, dynamic  $J$ - $R$  curves from the different  $a/W$  ratio specimens were coincident up to a crack extension of 0.30 mm and 0.28 mm for short cracks and long cracks, respectively. After the initial coincidence, short cracks display higher dynamic  $J$ - $R$  curves.
4. For all the loading rates and the different  $a/W$  ratios,  $J_{0.2d}$  values are comparable varying between 210 and 229.8 kJ/m<sup>2</sup>.

## References

1. Choudhary BK, Bhanu Sankara Rao K, Mannan SL (1994) Effects of strain rate and temperature on tensile deformation and fracture behavior of thick section 9Cr-1Mo steel forging. *Int J Press Vessels Pip* 58:151–160
2. Sathyanarayanan S, Moitra A, Sasikala G, Samuel KG, Ray SK, Singh V (2008) *Mater Sci Eng A* 488:519–528
3. Sathyanarayanan S, Moitra A, Sasikala G, Dasgupta A, Saroja S, Bhaduri AK, Raj B, Singh V (2011) *J Test Eval* 39(3):448–455
4. Sathyanarayanan S, Basu J, Moitra A, Sasikala G, Singh V (2013) *Metall Mater Trans A* 44(5):2141–2155
5. Kobayashi T, Yamamoto I, Niinomi M (1987) *Eng Fract Mech* 26(1):83
6. Kobayashi T, Niinomi M (1989) *Nucl Eng Des* 111:27–33
7. Sreenivasan PR, Mannan SL (1999) Dynamic  $J$ - $R$  curves and tension impact properties of AISI 308 stainless steel weld. *Int J Fract* 101:229–249
8. Baer Wolfram, Bösel Dieter, Eberle Arno, Klingbeil Dietmar (2010) *Eng Fract Mech* 77:374–384
9. ASTM E 1820–09e1, Standard test method for measurement of fracture toughness
10. Kobayashi T (1984) *Eng Fract Mech* 19:49–65
11. Tronskar JP, Mannan MA, Lai MO (2002) *Eng Fract Mech* 69:321–338
12. Hu JM, Albrecht P, Joyce JA. Fracture mechanics: 22nd symposium. ASTM STP 1131, pp 880–903
13. Sathyanarayanan S, Sasikala G, Ray SK (2004) *Int J Press Vessels Pip* 81:419–425

14. Zhen Z., Lee K., Herrera R. and Landes J.D., Elastic-Plastic Fracture Test Methods: The User's Experience. ASTM STP 1114, pp 42–56
15. Zhu XK, Joyce JA (2007) Eng Fract Mech 74:2263–2281
16. Chen X, Albrecht P, Wright W, Joyce JA (1995) In: Ruschau JJ, Donald JK (eds) Improved load ratio method for predicting crack length, special applications and advanced techniques for crack size determination. ASTM STP 1251. American Society for Testing and Materials, pp 83–103
17. Candra H, Wright WJ, Albrecht P (2002) Experimentally determined key curves for fracture specimens. Int J Fract 117:247–267
18. Ireland DR (1997) Proceedings of international conference on dynamic fracture toughness. The Welding Institute, Cambridge, UK, p 45
19. Kobayashi T, Yamamoto I, Niinomi M (1987) Eng Fract Mech 26(1):83



# Fatigue Life Prediction of Commercial Dental Implant Using Analytical Approach and Verification by FEA

Pankaj Dhatrak, Uddhav Shirsat, Vijay Deshmukh and S. Sumanth

**Abstract** Dental implants are nowadays commonly used as replacement for natural teeth when natural teeth get damaged due to injury, infection or old age. Despite high success rates of implantation, complications and failures of implants still occur. The aim of this study is to predict fatigue life of commercially available implant system using FEA and verification by analytical method. Implant is basically a mechanical screw made of titanium alloy Ti-6Al-4V with threads on its periphery. A three-dimensional finite element model (FE model) of implant prosthesis (implant, abutment, fitting screw and crown) is modeled using linear isotropic material properties for implant, abutment, cortical bone and cancellous bone using commercial software code. Occlusal load (vertical and lateral) on teeth is applied as static load on the crown to find the stresses around implant–bone interface. Analytical approach is used to predict fatigue life of implant. Good correlation is observed in analytical method and FEA results. The study is useful for better understanding of stress concentration location of implant systems. Guidelines for selecting the best implant can be suggested.

**Keywords** Fatigue life • Dental implant • FEA • Implant–bone interface

---

P. Dhatrak (✉)

MAEERS'S Maharashtra Institute of Technology, Pune, India  
e-mail: pankaj.dhatrak@mitpune.edu.in

U. Shirsat

Navsahyadri Institute of Technology, Pune, India  
e-mail: shirsatum@yahoo.com

V. Deshmukh

International Clinical Dental Research Organization, Pune, India

S. Sumanth

M.A. Rangoonwala College of Dental Science & Research Centre, Pune, India

© Springer Nature Singapore Pte Ltd. 2018

S. Seetharamu et al. (eds.), *Proceedings of Fatigue,*

*Durability and Fracture Mechanics*, Lecture Notes

in Mechanical Engineering, [https://doi.org/10.1007/978-981-10-6002-1\\_16](https://doi.org/10.1007/978-981-10-6002-1_16)

## 1 Introduction

Dental implants are subjected to repeated loading due to mastication forces, so it is necessary to study the fatigue life of dental implant. This fatigue life depends upon the size and material of implant and the physical properties of bone. For long-term success of a dental implant, the reliability and the stability of the implant–bone interface and implant–abutment connection play a great role. A study on the properties of the biomaterials available for the dental implants is done, and the effect of changes in the implant geometry with respect to different manufacturer has been studied. Finally, an implant based on the biomechanical parameters is proposed owing to the maximum life in fatigue failure.

Current study aims to analyze the conditions present at threaded implant–bone interface for better understanding of stress distribution pattern for selected dental implants and to predict the fatigue behavior of commercially available three different dental implants with analytical approach and verification by finite element-based commercial software code.

## 2 Implant System

### 2.1 *Implant Selection*

Commercially available implants from three implant companies were purchased directly from the supplier: Osstem Implant (diameter 3.5 mm, length 10 mm; Osstem Implant India Pvt. Ltd., Mumbai), connected with straight abutment, Biohorizon Implant (diameter 3.5 mm, length 10.5 mm; Katara Dental Pvt. Ltd., Pune), connected to a screw retained, internal hexagonal standard straight abutment, and Adin Implant (diameter 3.5 mm, length 10 mm; MIL Medical Dental System Pvt. Ltd., Nagpur). The sizes and the thread profile (V-thread) of the implant system were selected same for the purpose of comparative study as shown in Fig. 1.

### 2.2 *Implant–Bone Interface*

Once the implant is placed into the bone, a fast interaction takes place at the interface between bone and implant. Bone remodeling at the interface is responsible for stability of an implant. The success rate of implant prosthesis depends on the biological and biomechanical factors. The development of direct interaction between implant and surrounding bone is mostly biological. However, the biomechanical factors also play a vital role at the bone–implant interface [1, 2]. Selection of proper implant thread profile is the initial requirement at the time of implantation for perfect osseointegration. Once the implant is osseointegrated with

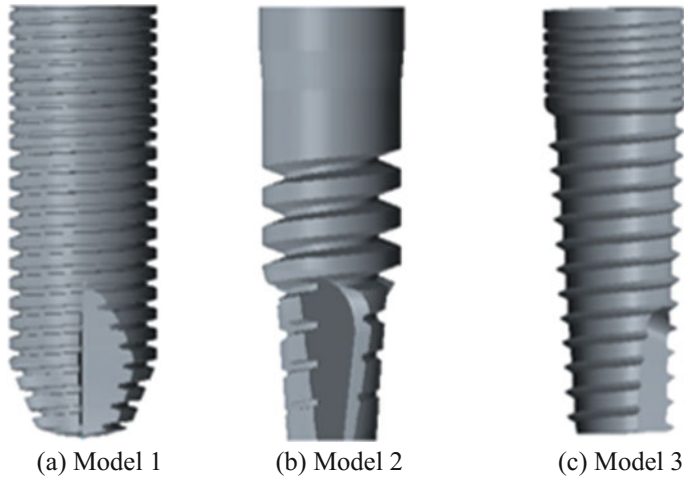


**Fig. 1** Implant systems: **a** Osstem implant (Model 1), **b** Biohorizon implant (Model 2) and **c** Adin implant (Model 3)

the bone, the primary stability is achieved. Due to high stress intensities and uneven stress distribution at the interface, the patient suffers unbearable pain. Therefore, the stress distribution along implant–bone interface should be uniform [3].

### 2.3 Interface Conditions

The interface between implant and bone was modeled as a continuous bond. This implies an ideal osseointegration, without any relative motion at the interface [4]. In other words, the implants were rigidly anchored in the bone, showing a fixed and same type of bond at all material interfaces.

## 3 Materials and Methods

### 3.1 Geometrical Modeling

The dimensions of the prosthetic element are measured using the non-contact-type optical profile meter. Profile meter is a measuring instrument used to measure a surface's profile dimensions of the implant prosthesis. The major implant dimensions such as diameter and overall length were available from manufacturer, whereas the detailed dimensions such as thread profile, depth and height of thread, and the thread pitch were measured using Optical Profile Projector (Accurate PP300TE) with 10X magnification lens, as shown in Fig. 2a. 3D CAD models of the implants were constructed using Creo Parametric software, as shown in Fig. 1.

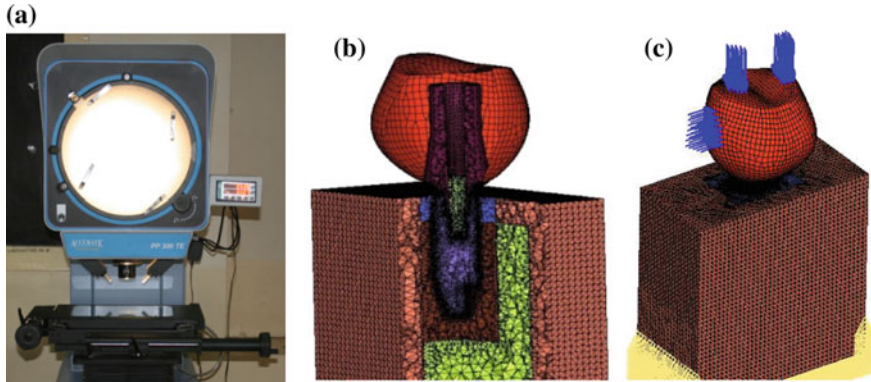


**Fig. 2** a Optical profile projector, b cut section of 3D FE model, c load and boundary conditions

### 3.2 FE Modeling

3D FE model of the implant prosthesis was meshed with element convergence criteria. The cut section of finite element model is shown in Fig. 2b. A tetrahedron element is used for implant prosthesis which has quadratic displacement behavior and is well suited for meshing irregular CAD geometry, whereas crown is modeled using shell element. Static stress analysis was performed using Hypermesh as a preprocessor and Nastran as a solver.

### 3.3 Material Properties

Titanium and titanium alloys have been widely used materials for dental implants due to their good biocompatibility, excellent corrosion resistance as well as suitable mechanical properties [5]. The material properties used for dental implant prosthesis in this study are shown in Table 1.

**Table 1** Mechanical properties of materials

Implant prosthesis	Material	Young’s modulus (MPa)	Poisson’s ratio
Implant, abutment and fitting screw	Ti–6Al–4V	113,000	0.33
Hard bone	Cortical bone	13,700	0.26
Soft bone	Cancellous bone	1370	0.31
Crown	Porcelain	70,000	0.19

### 3.4 Load and Boundary Conditions

During mastication load and boundary conditions involves a repeated pattern of cyclic impacts that causes loading to the implant components and distributes the force to the bone interface. The mean range of cyclic load is found to be 90–200 N depending on the age and gender [6]. In current study the load is selected as 116 N occlusal and 40 N lateral distributed over the artificial crown and the model was completely constrained at the sides and bottom of cortical bone as shown in Fig. 2c.

### 3.5 Assumptions

*Material properties:* For 3D analysis, homogenous isotropic elastic properties are assumed for implant prosthesis, cortical and cancellous bone, and crown.

*Bone modeling:* Cut section of mandible is taken as bone model. This assumption is with the consideration that the focus of analysis is on the stress distribution near implant–bone interface.

*Implant–bone interface:* The implant–bone is a biological system and undergoes continuous change as per the response of human body over a period of time. The implant–bone interface was assumed to be fully osseointegrated.

*Occlusal loads:* Cyclic loads are common in mastication cycle. For simplification only static vertical and lateral loading has been assumed from the point of view of major component of forces acting on the implant. The results are viewed and noted at the neck region of the implant–cancellous bone interface, i.e., at the proximal zone.

## 4 Experimental Procedure

### 4.1 Photoelastic Test Setup

Experimental stress analysis using the method of photoelasticity is a popular technique for measuring 2D stresses. The setup consists of a loading frame, light source with the facility of monochromatic as well as white light, polarizer and analyzer plates, quarter-wave plates and a load cell, as shown in Fig. 3a. Fringe pattern under loading was observed in white as well as monochromatic light. A 10X magnifying glass is available for facilitating the measurement of fringe orders. The fringe orders were evaluated around the implant–bone interface using Tardy's compensation technique [7], as shown in Fig. 3d.

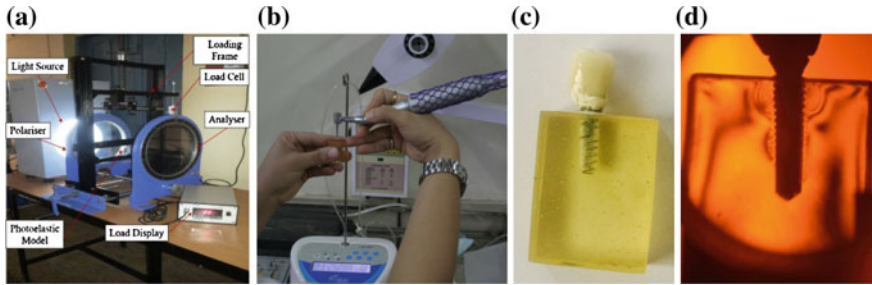


**Fig. 3** **a** Experimental photoelastic setup, **b** drilling and screwing of implant in the photoelastic model, **c** photoelastic block model with crown fitment, **d** measured photoelastic fringe pattern for implant model

## 4.2 Photoelastic Material Model

Epoxy resins are most commonly used material model for photoelastic experiment. Araldite CY-230 and Hardener HY-951 are used in a proportion of 10:1 to prepare photoelastic model blocks of dimensions 30 mm × 20 mm × 10 mm. A circular disk model was also fabricated in the same batch for calibration of photoelastic material. Fabrication was done at Engineering Equipment Enterprises, Pune. Photoelastic block model is shown in Fig. 3c.

## 4.3 Implant Fitment

Figure 3b shows the speed control and driving unit along with implant fitment set. This set mainly consists of drills and taps of various sizes. A torque wrench is also provided for tightening of implant.

## 5 Results and Discussion

Comparing FEA and photoelastic stress analysis results, the stress values are in close agreement. Stress intensity results in the cancellous bone–interface near the implant neck region (proximal region) are shown in Fig. 4. Experimental stress intensity result and FE model results were calculated and are summarized in Table 2.

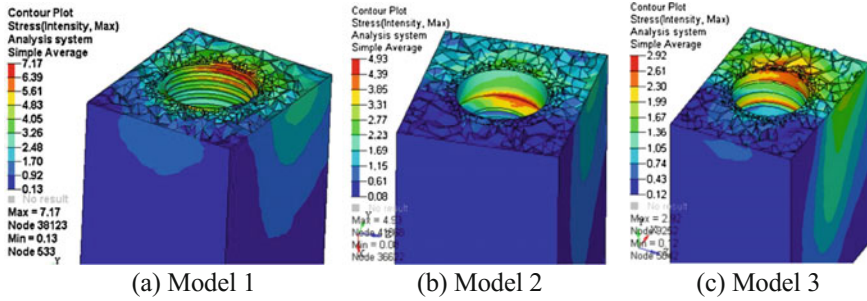


Fig. 4 Maximum stress intensity observed at proximal right region of implant model

Table 2 Experimental and FEA stress intensity result

Implant model	Region at implant–bone interface	Stress intensity (MPa)	
		Experimental	FEA
Model 1	Proximal (right)	7.02	7.17
Model 2	Proximal (right)	4.75	4.93
Model 3	Proximal (right)	2.86	2.92

## 6 Fatigue Life Predictions

For long-term success the dental implant design should satisfy the maximum fatigue life. In this study, static stress analysis of the dental implant results is taken as input to fatigue solver. FEMFAT software code is used to predict the fatigue life of implant. Post-processing of implant is done in HyperView. Fatigue life of dental implant was calculated analytically based on Goodman theory and FE model, as shown in Table 3.

From static stress analysis the maximum von Mises stresses obtained for all three models are shown in Fig. 5 and the minimum number of cycles obtained is shown in Fig. 6.

Table 3 Experimental and FEA stress intensity result

Implant model	Fatigue life (number of cycles)	
	Analytically	FEA
Model 1	1.50e8	2.46e8
Model 2	2.88e14	3.67e15
Model 3	1.16e8	1.26e7

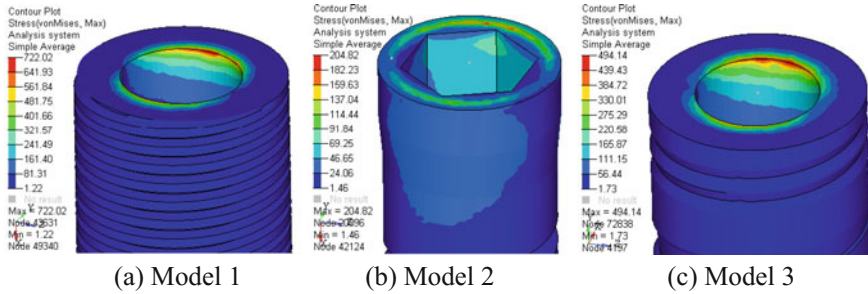


Fig. 5 Maximum von Mises stresses at the implant–abutment neck connection of implant models

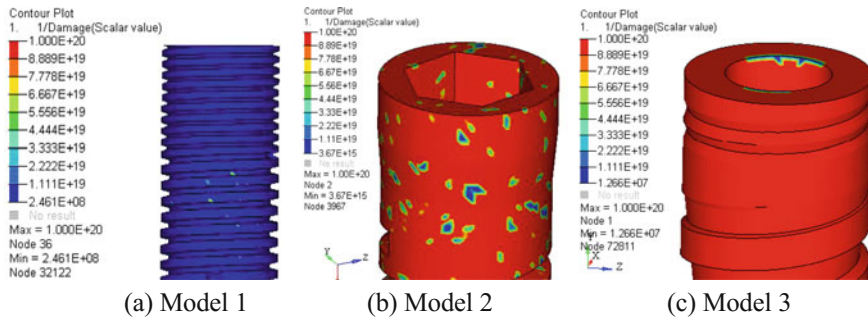


Fig. 6 Fatigue life predicted by FEA for the models

## 7 Conclusion

The success in implant dentistry depends on the biomechanical parameters which play an important role in predicting the fatigue life of the dental implant. Based on the results obtained conclusions can be drawn regarding the choice of implant on the basis of stress distribution at implant–bone interface. The implants from different manufacturers were compared for maximum stress intensity at the interface. Stresses were evaluated at proximal left and right regions. Within the limitations of the study, the following conclusions can be drawn.

1. It is found that the high stress intensity is observed in the areas of bone which are closer to the implant neck surface at proximal region and decrease in magnitude toward the outer region in Model 1.
2. Stress distribution is uniform in the dental implants along the implant–bone interface for all three models.
3. Stress intensity around the implant–bone interface is less in implant Model 3 and hence should be preferred for clinical use.



4. The fatigue life predictions of finite element-based model correlated fairly well to the analytical results obtained.
5. In the present study, a significant implant profile effect could be seen for the different implants on fatigue performance with Model 1 and 3 implants showing a classic comparable finite fatigue life behavior, while the Model 2 implant exhibits an infinite fatigue life behavior.

## References

1. Brunski JB, Moccia AF Jr, Pollack SR (1979) The influence of functional use of endosseous dental implant on tissue implant interface II. *J Res Dent* 58:1970–1980
2. Soballe K, Hanseen ES, B-Rasmussen H (2006) Tissue ingrowth into titanium and hydroxyapatite-coated implants during stable and unstable mechanical condition. *J Orthop Res* 10: 285–299 (Oct. 1994. Web Services. In: Nagel WE, Walter WV, Lehner W (eds) Euro-Par 2006, LNCS, vol 4128. Springer, Heidelberg, pp 1148–1158)
3. Abuhussein H, Pagni G, Rebaudi A, Wang HL (2010) The effect of thread pattern upon implant osseointegration. *Clin Oral Implant Res* 21:129–136
4. Kienapfel H, Sprey C, Wilke A, Griss P (1999) Implant fixation by bone in-growth. *J Arthroplast* 14(3):355–368
5. Hernandez-Rodriguez MAL, Contreras-Hernandez GR, Juarez-Hernandez A, Beltran-Ramirez B, Garcia-Sanchez E (2015) Failure analysis in a dental implant. *Eng Fail Anal* 57:236–242
6. Pérez MA (2012) Life prediction of different commercial dental implants as influence by uncertainties in their fatigue material properties and loading conditions. *Comput Methods Programs Biomed* 1277–1286
7. Fakhouri SF (2012) Photoelastic analysis of the vertebral fixation system using different screws. *Eng Technol Appl Sc Res* 2(2):190–195
8. Chang HS, Chen Y, Hsieh Y, Lun Hsu M (2013) Stress distribution of two commercial dental implant systems: a three-dimensional finite element analysis. *J Dent Sci* 1–11
9. Kayabas O, Yuzbasoglu E, Erzincanl F (2006) Static, dynamic and fatigue behaviors of dental implant using finite element method. *Adv Eng Softw* 37:649–658
10. Jamshidinia M, Wang L, Tong W, Ajlouni R, Kovacevic R (2015) Fatigue properties of a dental implant produced by electron beam melting (EBM). *J Mater Process Technol* 226:255–263
11. Ali B, Chikh EBO, Meddah HM, Merdji A, Bouiadjra BB (2013) Effects of overloading in mastication on the mechanical behavior of dental implants. *Mater Design* 47:210–217
12. Yona K (2012) Effect of dental implant diameter on Fatigue Performance part-I and part-II. *Clin Implant Dent Relat Res*
13. Shemtov-Yona K (2014) Identification of failure mechanisms in retrieved fractured dental implants. *Eng Fail Anal* 38:58–65
14. Bae J-S, Jeong H-Y (2012) Effects of material properties and hole designs of the jig on the fatigue life of dental implants. *J Mech Sci Technol* 26(3):759–766
15. ASM International (2009) Failure analysis of titanium-based dental implant. *J Fail Anal Prev* 10:138–142
16. Kim MG (2011) Fatigue properties on the failure mode of a dental implant in a simulated body environment. *Met Mater Int* 17(5):705–711
17. Park S, Won SY, Bae TS, Song KY, Park CW, Eom TG, Jeong CM (2008) Fatigue characteristics of five types of implant-abutment joint designs. *Met Mater Int* 14(2):133–138
18. Misch CE. Contemporary implant dentistry, 3rd edn. Elsevier, A division of Reed Elsevier India Private Limited

19. Duyck J, Naert I (1998) Failure of oral implants: aetiology, symptoms and influencing factors. *Clin Oral Invest* 2:102–114
20. Kobayashi E, Mochizuki H, Doi H, Yoneyama T, Hanawa T (2006) Fatigue life prediction of biomedical titanium alloys under tensile/torsional stress. *Mater Trans* 47(7):1826–1831
21. Misch CE, Bidez MW (1999) A scientific rationale for dental implant design. *Contemp Implant Dent*

# Layered Microstructure Generated by Multipass Friction Stir Processing in AZ91 Alloy and Its Effect on Fatigue Characteristics

Raja Allavikutty, Vivek Pancholi and Banu K. Mishra

**Abstract** Layered microstructure with three different configurations was developed by multipass friction stir processing (FSP) on as-cast (AC) AZ91 magnesium alloy using three different tools with probe lengths 7, 5 and 4 mm. They were half thickness processed (HFSP), surface modified (SFSP) and full thickness processed (FFSP). FSP was performed at tool rotation rate of 720 rpm and transverse speed of 150 mm/min. The large  $\beta$ -Mg<sub>17</sub>Al<sub>12</sub> particles with an average size of 20  $\mu$ m and  $\alpha$ -Mg matrix grains of 100  $\mu$ m were reduced to approximately 1 and 2  $\mu$ m, respectively, after multipass FSP. Texture of FSPed samples measured by X-ray diffraction technique had shown basal texture. Constant amplitude axial fatigue test was performed on all the microstructural configurations, with process direction parallel to loading axis. Life of the fatigue tested samples was found to increase with the increasing fraction of FSPed region in AZ91 alloy.

**Keywords** Fatigue · Microstructure variation · Multipass FSP  
AZ91 alloy · Texture

## 1 Introduction

Magnesium (Mg) alloys, due to their light weight, high specific strength and damping capacity, are used in high-performance applications and energy saving of machines and structures [1]. There are two categories of Mg alloys, namely cast and

---

R. Allavikutty · V. Pancholi (✉)

Department of Metallurgical and Materials Engineering, Indian Institute of Technology  
Roorkee, Roorkee, India  
e-mail: vivek.pancholi@gmail.com

R. Allavikutty  
e-mail: araja1407@gmail.com

B.K. Mishra  
Department of Mechanical and Industrial Engineering, Indian Institute of Technology  
Roorkee, Roorkee, India  
e-mail: bhanufme@iitr.ac.in

© Springer Nature Singapore Pte Ltd. 2018

S. Seetharamu et al. (eds.), *Proceedings of Fatigue, Durability and Fracture Mechanics*, Lecture Notes

in Mechanical Engineering, [https://doi.org/10.1007/978-981-10-6002-1\\_17](https://doi.org/10.1007/978-981-10-6002-1_17)

wrought Mg alloys. The mechanical properties of wrought alloys are better than cast alloys, so they are used in load-bearing applications. However, flexibility of casting into desired shape and cost saving are advantages of cast alloys. Therefore, cast Mg alloys are widely used in many structural applications like aerospace and automobile industries and electronics and sports equipments. As-cast AZ91 alloys have coarse-grained microstructure with thick secondary phase particles and casting defects. These secondary phase particles and casting defects act as a crack initiation site and reduce fatigue life of the alloy [2, 3]. Modifying the cast microstructure by grain refinement and elimination of casting defects can bring a significant improvement in the fatigue properties of AZ91 alloys [4–6].

Friction stir processing (FSP) is a novel solid-state processing technique developed from friction stir welding (FSW) [7]. It has advantage of processing Mg at room temperature which is highly difficult to achieve by any conventional processing methods like rolling, forging and extrusion or even by other severe plastic deformation (SPD) methods like equal channel angular processing (ECAP), accumulative roll boding (ARB) and high-pressure torsion (HPT); it is because of HCP crystal structure and availability of only two independent slip systems at room temperature for plastic deformation. Also, FSP can be used to change the microstructure locally [8] as well as bulk processing by multipass method. Hence, in this work the cast microstructure of AZ91 alloy is modified by using multipass FSP. To optimize the grain refinement process, three different tools with varying tool probe length have been used: one to modify the cast structure to half thickness (HFSP), second to modify the cast structure on both the surfaces (SFSP) and the final one to modify the cast structure completely throughout the thickness (FFSP). Load-controlled constant amplitude axial fatigue test was conducted and analysed the effect of this layered microstructure on the fatigue life of AZ91 alloy.

## 2 Experimental Method

The as-received cast AZ91 alloy billets were machined into plates of 10 mm thick, 100 mm width and 110 mm length and subjected to multipass FSP at a tool rotational speed of 720 rpm and a traverse speed of 150 mm/min with a tool tilt angle of 3°. To reduce the heat generated during the process copper backing plate was used. Three tools with different pin lengths, 7, 5 and 4 mm having shoulder diameter of 28 mm and threaded conical pin of diameter 8 mm at shoulder and 4 mm at tip, were used. To process the 70 width of the plate 30 passes of FSP were performed with 50% overlap towards the retreating side. After multipass FSP the 10-mm plates were machined to 6 mm. The FFSP samples were obtained from FSP of ‘7-mm pin length tool’ after machining the FSPed surface to 1 mm and bottom surface to 3 mm from the 10-mm plate. The HFSP samples were obtained from FSP of ‘5-mm pin length tool’ after machining 2 mm from both the surfaces. The SFSP samples were FSPed using ‘4-mm pin length tool’ first on one surface; then, 2 mm

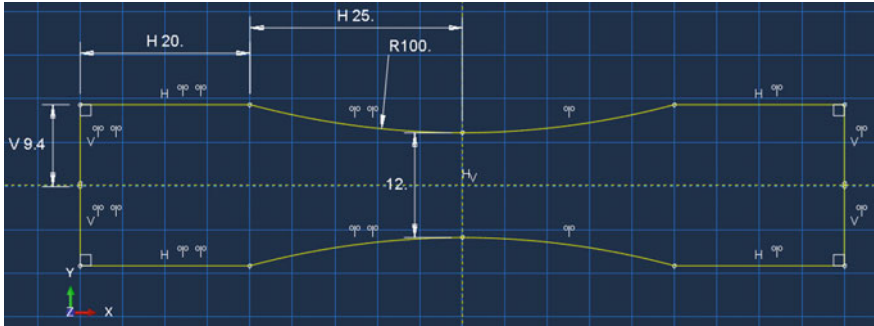


**Fig. 1** Dimensional details fatigue sample prepared according to ASTM E 466 standards

was machined from that surface and FSPed on another surface with the same forward direction and 2 mm was machined.

High-cycle fatigue (HCF) test specimens with continuous radius between ends with 6 mm thickness and 12 mm width were used. Other dimensions related to specimen design are shown in Fig. 1. The specimen was designed according to ASTM E466 standard. HCF experiments conducted at stress ratio,  $R = 0$  and a frequency of 20 Hz in a constant load-controlled axial fatigue testing method at different stress amplitudes ( $\sigma_a$ ). All these tests were performed on Instron 8800 servohydraulic testing system at ambient temperature using WaveMatrix software.

Microstructural characterization was carried out by optical microscope (Leica DMI 5000). Field emission scanning electron microscope (FESEM—FEI Quant 200F) was used for microstructural characterization, energy-dispersive spectroscopy (EDS) as well as fracture surface characterization. Rigaku SmartLab X-ray diffractometer was used for phase identification in AZ91 alloy before and after FSP, in which Cu  $K\alpha 2$  peak stripping and background subtraction were carried out using X'pert HighScore Plus software.

### 3 Results and Discussion

#### 3.1 Microstructure

The microstructure of as-cast (AC) material, HFSP, SFSP and FFSP is shown in Fig. 2. The AC material is characterized by large dendrites of 100  $\mu\text{m}$  and thick plate-like interdendrites of 20  $\mu\text{m}$  in Fig. 2a. In HFSP (Fig. 2b), half of the region has as-cast microstructure and remaining half of the region has a microstructure of FSPed region where there are no dendrites and interdendrites. Similarly in Fig. 2c, the as-cast region is sandwiched by FSPed region from both the surfaces in case of SFSP. Material that is FSPed over the full thickness (FFSP) has a completely homogeneous fine-grained microstructure as shown in Fig. 2d. Thus, after FSP the

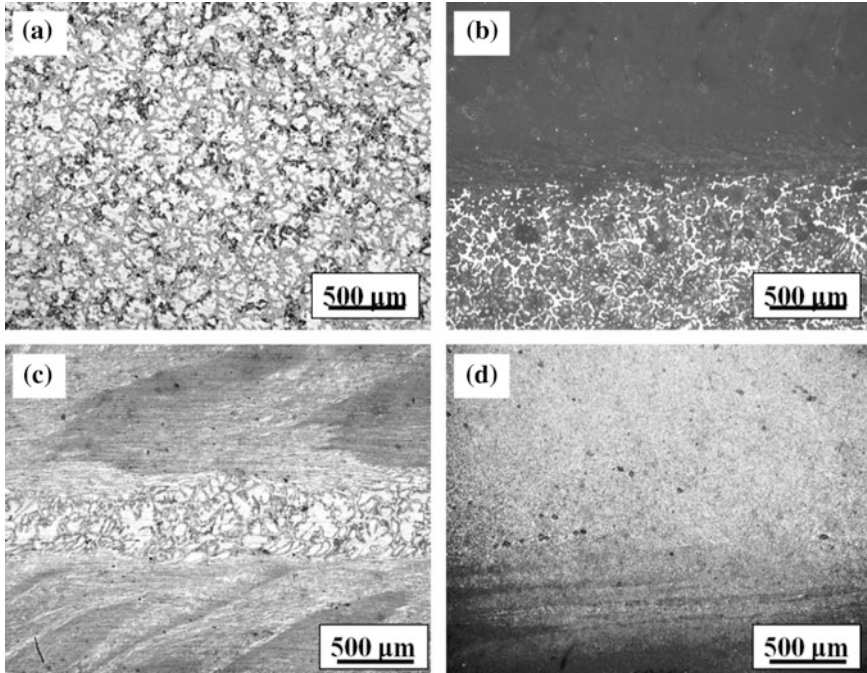


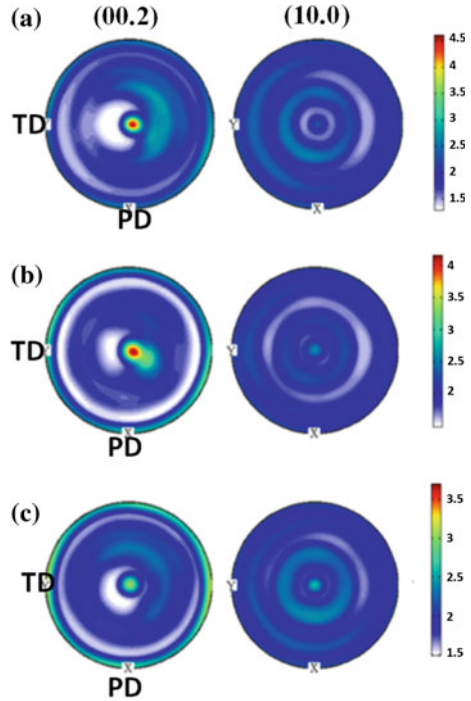
**Fig. 2** Microstructure of **a** AC, **b** HFSP, **c** SFSP and **d** FFSP samples

coarse Mg matrix and thick plate-like precipitates were broken up into fine and evenly distributed microstructure of 2- $\mu\text{m}$  sized  $\alpha$ -Mg matrix and 1- $\mu\text{m}$  sized  $\beta$ -precipitate. Multipass FSP of AZ91 alloy on copper backing plate, which acts as heat sink aided in controlling the grain growth after the process which results in very fine and homogeneous microstructure due to dynamic recrystallization [9].

### 3.2 Texture

Figure 3 shows (00.2) and (10.0) pole figures/texture plots for the processed materials. The pole figure measurements were taken from 2 mm below the normal surface of processed material. The intensity of the basal pole decreases from 4.5 in FFSP (Fig. 3a) to 4 in case of HFSP (Fig. 3b) and further decreases to approximately 3 in SFSP (Fig. 3c), and the basal poles in all the cases spread towards the processing direction. It can be correlated with length of the tool probe or thickness to which the material is processed. As thickness of material processed increases, the force exerted on the material under the shoulder also increases which accounts for the maximum intensity in FFSP material. This fact together with the tilted basal pole towards process direction ensures texture formed during FSP is ascribed to the

**Fig. 3** Macrotexture of **a** FFSP, **b** SFSP and **c** HFSP



material flow influenced by the tool shoulder [10]. The critical resolved shear stress (CRSS) for non-basal slip systems is predicted to be approximately 5 times higher than basal slip systems [11]. Therefore, in process direction basal slip dominates the deformation, whereas in the transverse direction, non-basal slip dominates the deformation. Hence, as a design criterion, fatigue tests were performed with process direction parallel to the loading axis in all the different microstructurally varied materials, including as-cast material.

### 3.3 Fatigue

The number of cycles to failure at different stress amplitudes for all the four variants, namely AC, HFSP, SFSP and FFSP, is presented in Table 1. AZ91 alloy has a characteristic of breaking early at stresses much higher than its fatigue limit. The AC samples fail in tension at 60 MPa, whereas it endured for 175,173 cycles at 40 MPa. HFSP has slightly higher fatigue life at the same stress amplitude when compared to AC material. The surface modified (SFSP) and full thickness FSPed material (FFSP) crossed  $10^6$  cycles without failure at 50 and 60 MPa, respectively. On comparing all the microstructurally different fatigue samples at 60 MPa, AC material fails to survive the load, HFSP has survived for very few cycles and failed

**Table 1** Number of cycles to failure at constant stress amplitude for all the four microstructurally different materials

	Stress amplitude in MPa						
	40	45	50	60	70	80	90
AC	175,173	36,650	19,960	Failed in tension			
HFSP	656,594	400,072	37,709	8756	Failed in tension		
SFSP			Run out at $10^6$ cycles	564,323	256,253	109,841	22,017
FFSP				Run out at $10^6$ cycles	325,784	127,265	38,826

before reaching the high-cycle regime of  $10^4$  cycles, SFSP has survived for  $5.6 \times 10^5$  cycles, and FFSP has run out at  $10^6$  cycles. It ensures that fatigue life of AZ91 alloy increases as processed region in the microstructure increases. Surface modification however significantly improves the fatigue life; complete modification of the microstructures by FSP ensures surface modification as well as elimination of internal casting defects and core, as-cast, structure and endured more number of cycles when compared to AC, HFSP and SFSP materials.

The fractograph of fatigue tested samples at specific stress amplitudes is shown in Fig. 4. The as-cast microstructures have facets in fatigue crack regions, and striations are observed in the fatigue crack region of FSPed materials. These facets and striations are almost  $45^\circ$  to the loading direction in all cases. These are due to the intrusion and extrusion of basal slips occurred during fatigue cycling. However, there is a difference in the origin of these cyclically reversible slips depending on the microstructure and applied stress amplitude. The fractographs of AC materials at 40 MPa and 45 MPa in Fig. 4a, b, respectively, show the difference in the size of the fatigue crack regions. At lesser stress amplitude of 40 MPa, fatigue region is larger than at 45 MPa. In case of HFSP, the fatigue crack region is observed in as-cast region at 40 MPa (Fig. 4c), whereas at 45 MPa fatigue region is observed from the corners and surface of FSPed region (Fig. 4d). Another important and interesting observation is that there is an observable difference in the distance between the facets in AC material and distance between the striations in FSPed region. In AC material, the size of striations is smaller at stress amplitude 40 MPa (Fig. 4e) when compared to the facet size at 45 MPa (Fig. 4f). In case of HFSP, the distinction of fatigue crack region at 40 and 45 MPa is quite clear from the magnified fractographs in Fig. 4g, h, respectively. The fractograph of SFSP at stress amplitudes 70 and 80 MPa is presented in Fig. 4i, j, respectively. It shows that fatigue crack origin is from interface of processed region and as-cast region at 70 MPa, whereas it is from as-cast region at 80 MPa. The fractographs of FFSP at stress amplitude 70 MPa (Fig. 4k) and 80 MPa (Fig. 4l) show too finer fatigue crack initiation regions with few inhomogeneities observed along the fracture surface. The magnified view of fatigue crack regions of SFSP at stress amplitude



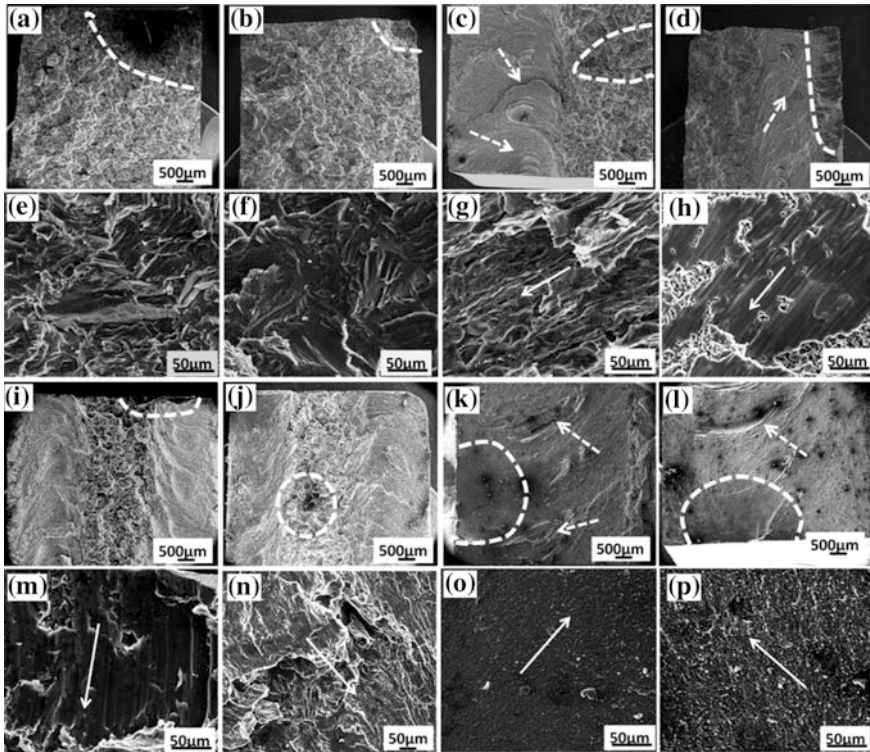


**Fig. 4** Fractograph of fatigue tested samples at specific stress amplitudes **a** AC at 40 MPa, **b** AC at 45 MPa, **c** HFSP at 40 MPa and **d** HFSP at 45 MPa with **e**, **f**, **g** and **h** is respective magnified fatigue crack growth regions marked in boxes, similarly **i** SFSP at 70 MPa, **j** SFSP at 80 MPa, **k** FFSP at 70 MPa and **l** FFSP at 80 MPa, while **m**, **n**, **o** and **p** are respective magnified fatigue growth regions. *Dotted arrows* indicate inhomogeneities, and *solid arrows* indicate crack growth direction

70 and 80 MPa is shown in Fig. 4m, n; corresponding fractographs of FFSP are shown in Fig. 4o, p, respectively. All the fractographs clearly indicate that as-cast microstructure and inhomogeneities present in the microstructure reduce the fatigue cycle. Hence, FFSP exhibited higher fatigue life among other materials, namely AC, HFSP and SFSP.

To understand the crack propagation, the optical micrograph on the transverse section of fractured surfaces was analysed from samples at specific stress amplitudes. In AC material, at the stress amplitude of 40 MPa, the reversible cyclic slip originated inside the matrix and the fracture profile is less irregular (Fig. 5a) than how it appears at 45 MPa in Fig. 5b. At the stress amplitude of 45 MPa, the fracture follows precipitate matrix interface, whereas when amplitude decreases, extrusion and intrusion of slip occur not only at the interface but all over the matrix. As-cast region of HFSP samples at the stress amplitudes 40 MPa (Fig. 5c) and 45 MPa (Fig. 5d) also has similar kind of fracture profile. The SFSP samples are

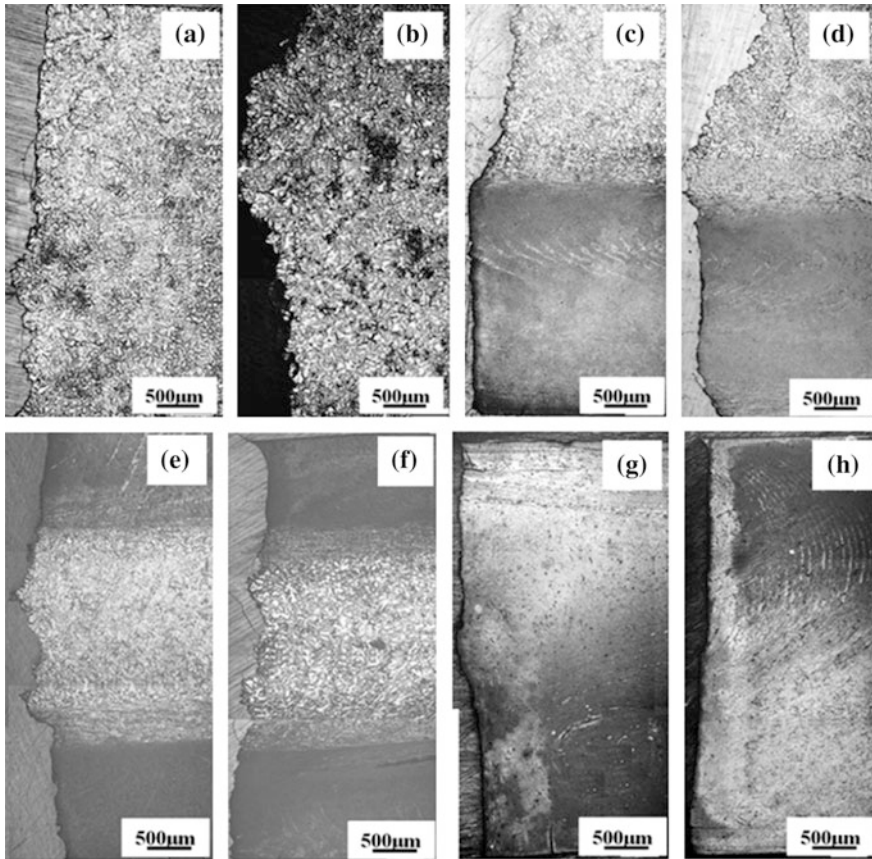


**Fig. 5** Subsurfaces of fatigue failed samples at specific stress amplitudes **a** AC at 40 MPa, **b** AC at 45 MPa, **c** HFSP at 40 MPa, **d** HFSP at 45 MPa, **e** SFSP at 80 MPa, **f** SFSP at 90 MPa, **g** FFSP at 80 MPa and **h** FFSP at 90 MPa

tested at such stress amplitudes which take their maximum stress values during fatigue test much higher than tensile strength of as-cast material. This causes as-cast region in SFSP to have irregular fracture profile as shown in Fig. 5e, f at both the stress amplitudes of 70 and 80 MPa. The fracture profile of FSPed samples is almost linear in either stress amplitudes as shown in Fig. 5g, h, and in the processed region of HFSP and SFSP too it has a similar kind of fracture profile.

Thus, reversible cyclic slip is reason for fatigue crack initiation in all the microstructures with a clear difference in fatigue crack surfaces of as-cast and processed region. It was reported that any decrease in grain size or decrease in working stress decreases the elastic strain per cycle. The reduction in size of the striations at 70 MPa (Fig. 6a) and 80 MPa (Fig. 6b) indicates this fact. In this study, also fatigue life increases with the increase in fraction of fine grain

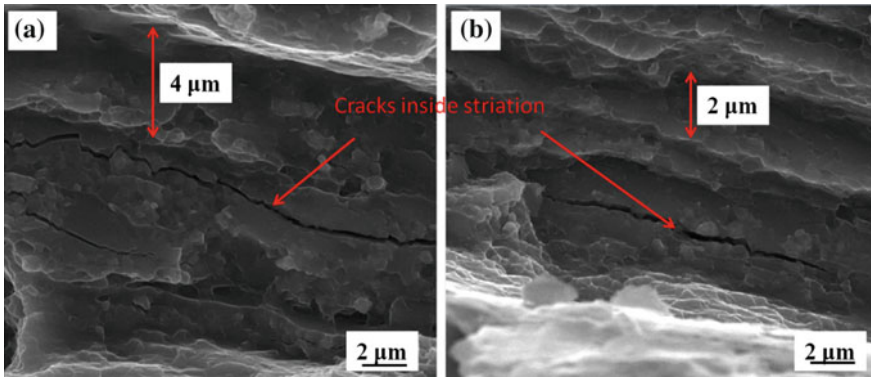


**Fig. 6** Fatigue cracked region with striations and cracks in FFSP material at stress amplitudes **a** 80 MPa and **b** 70 MPa

microstructure. Hence, fully FSPed material FFSP exhibited highest fatigue life, with SFSP, HFSP and AC materials have fatigue life in the descending order at specific stress amplitude

## 4 Conclusions

In order to find the optimum grain refinement of AZ91 alloy by multipass FSP to enhance the fatigue life of the material at high-cycle regime, microstructure of the material was modified using FSP tool with different probe heights. The microstructure was modified to half of the thickness (HFSP), modified on the surfaces (SFSP) and full thickness modified (FFSP). FFSP exhibited highest fatigue life due to the modification of surface microstructure as well as modified core, as-cast, structure. Hence, complete grain refinement by multipass FSP is necessary to achieve improvement in the fatigue life of AZ91 alloy.

## References

1. Fleming S (2012) An overview of magnesium based alloys for aerospace and automotive applications. Rensselaer Polytechnic Institute, Hartford
2. Ni DR, Wang D, Feng AH, Yao G, Ma ZY (2009) Enhancing the high-cycle fatigue strength of Mg–9Al–1Zn casting by friction stir processing. *Scr Mater* 61:568–571
3. Cavaliere P, De Marco PP (2007) Fatigue behaviour of friction stir processed AZ91 magnesium alloy produced by high pressure die casting. *Mater Charact* 58:226–232
4. Liu WC, Dong J, Zhang P, Korsunsky AM, Song X, Ding WJ (2011) Improvement of fatigue properties by shot peening for Mg–10Gd–3Y alloys under different conditions. *Mater Sci Eng A* 528:5935–5944

5. Tajiri A, Uematsu Y, Kakiuchi T, Tozaki Y, Suzuki Y, Afrinaldi A (2015) Effect of friction stir processing conditions on fatigue behavior and texture development in A356-T6 cast aluminum alloy. *Int J Fatigue* 80:192–202
6. Sharma S (2004) Effect of friction stir processing on fatigue behavior of A356 alloy. *Scr Mater* 51:237–241
7. Mishra RS, Ma ZY (2005) Friction stir welding and processing. *Mater Sci Eng R Rep* 50:1–78
8. Ma ZY, Pilchak AL, Juhas MC, Williams JC (2008) Microstructural refinement and property enhancement of cast light alloys via friction stir processing. *Scr Mater* 58:361–366
9. Asadi P, Besharati Givi MK, Akbari M (2016) Simulation of dynamic recrystallization process during friction stir welding of AZ91 magnesium alloy. *Int J Adv Manuf Technol* 83:301–311
10. Jain V, Yuan W, Mishra RS, Gupta AK (2012) Directional anisotropy in the mechanical behavior of friction stir processed and aged AZ91 alloy. pp 64–67
11. Agnew SR, Tom CN (2003) Study of slip mechanisms in a magnesium alloy by neutron diffraction and modeling. *Scr Mater* 48:1003–1008

# Grain Refinement Mechanism and Its Effect on Strength and Fracture Toughness Properties of Al–Zn–Mg Alloy

P.K. Mandal

**Abstract** Grain refinement has a significant effect on the mechanical properties. Grain refinement in cast Al–Zn–Mg alloy tends to reduce porosity, size and number of the pores. This improves the mechanical properties, specially fracture toughness. Inoculation effect is most important factor during feeding of liquid metal. For these reasons, most cast aluminium alloys are grain refined. Fluidity is another factor that increases formation of a coherent equiaxed dendritic network at the flow front. The degree of grain refinement is dependent on the level of scandium (Sc) concentration and the Zn/Mg ratio. Grain refiner namely Al–Sc master alloy is added in small amounts ( $>0.2$  wt% Sc) to molten aluminium alloys to control the grain structure in castings.  $Al_3Sc$  particles act as nucleating sites for the formation of primary  $\alpha$ -Al dendrites and promote a uniform and fine equiaxed structure. In addition, friction stir processing (FSP) is the most innovative solid-state surface modification technology that eliminates cast heterogeneity and refines grains under the depth of the processed zone of aluminium alloys. The basic principle is based on friction stir welding (FSW). Thus, three main causes for fine grains are severe plastic deformation, heat input and dynamic recrystallization. Therefore, FSP should result in heterogeneous nucleation and growth of  $Al_3Sc$  precipitates for diffusional mechanisms, which explains the rapid growth of precipitates in the processed zone. It has been experimentally proven that after as-cast (AC) + FSP condition aluminium alloy enhance mechanical properties such as 0.2% proof strength is 89.81 MPa, ultimate tensile strength is 187.1 MPa, elongation is 3.42%, and fracture toughness ( $K_{IC}$ ) is 25.10 MPa $\sqrt{m}$ . In the present study, further evaluation has been done with optical microscopy, EPMA, FESEM, SEM, and TEM of Al–Zn–Mg–Sc alloy.

**Keywords** Inoculation effects • FSP • Fracture toughness •  $Al_3Sc$  precipitates  
TEM analysis

---

P.K. Mandal (✉)

Department of Metallurgy, Amal Jyothi College of Engineering,  
Kanjirappally 686518, Kerala, India  
e-mail: pkmmet@yahoo.in

© Springer Nature Singapore Pte Ltd. 2018

S. Seetharamu et al. (eds.), *Proceedings of Fatigue, Durability and Fracture Mechanics*, Lecture Notes

in Mechanical Engineering, [https://doi.org/10.1007/978-981-10-6002-1\\_18](https://doi.org/10.1007/978-981-10-6002-1_18)

## 1 Introduction

The high strength Al–Zn–Mg-based aluminium alloy of 7075 series is widely used in many engineering fields such as cylinder heads, engine blocks, aerospace housings, gear pumps, aircraft fittings, general automotive castings and marine structures due to their high strength-to-density ratio, strong age-hardening ability, competitive weight savings, attractive mechanical properties and improvement of thermal properties [1–3]. The major strengthening precipitates in the aluminium alloy depends on the Zn:Mg ratio is over 2,  $MgZn_2$  phase formed. It is further observed that small addition of scandium (Sc) in aluminium alloy improves mechanical properties by refining microstructure and accelerating the age-hardening characteristics [4, 5]. The solution-treated 7075 Al alloy exhibits very disperse particles of  $Al_3Sc$  type and restraint of recrystallization, which is coherently bond with in matrix during  $T_6$ -ageing treatment. In addition, grain refinement due to addition of scandium has been considered from the precipitation of primary  $Al_3Sc$  particles in the melt, which act as potent nucleation sites for aluminium grains [6]. So, a nucleating particle should be larger than a critical size, which depends on the undercooling of the melt. Therefore, once the alloy cooled below the liquidus temperature, it has been suggested that  $Al_3Sc$  primary particles nucleate heterogeneously on oxides particles in the melt. The latent heat evolved as the particles grow while floating in the melt will be dissipated into the liquid phase which will be undercooled with respect to the liquidus. Thus,  $Al_3Sc$  particle effectively increases refinement in structure because shows analogy in respect of crystallography with Al is isomorphous inclusion. The nanosize of disperse  $Al_3Sc$  particles (3–10 nm) after ageing (nearly 300 °C), which causes a very strong hardening [7]. Further, it has been noted that 7075 Al alloy with Sc, mechanical properties can be further improved by a surface modification technique called friction stir processing. FSP does not cause any change in the density. Therefore, strength-to-density ratio of this alloy after FSP increases further. During FSP, a rotating tool is inserted into a cast plate and high plastic deformation is produced. The effect of FSP parameters such as tool rotational speed, traverse speed, axial compressive load, tool design, investigated change in microstructure, tensile properties and fracture toughness is discussed in this paper.

The AC + FSP 7075 Al alloy with Sc addition shows increasing mode of mechanical properties due to elimination casting defects and refinement of microstructure in the matrix. The minor Sc content (0.2 wt%) and moderate Zn content (6.7 wt%) alloy exhibited gradual increase in mechanical properties due to fine precipitates ( $MgZn_2$ ) and fine  $Al_3Sc$  particles through dynamic recrystallization mechanism during FSPed [8, 9]. The present study reveals grain refinement mechanism in aluminium alloy through Sc inoculation effect as well as adaptation of an advanced surface modification technique like double passes FSP generated ultra-fine grains and thereby improved their mechanical properties.

## 2 Experimental Procedure

### 2.1 Aluminium Alloy Preparation

The electrical resistance muffle furnace was used to melt the aluminium alloy. The melt was cast in the air using a mild steel mould of dimension  $160 \times 90 \times 24 \text{ mm}^3$ . The charge consists of commercially pure aluminium cut into small pieces which was fed to a graphite crucible. Scandium was added in the melt in form of master alloy (Al-2 wt% Sc). In order to prevent burning of Zn and Mg during melting of Al, both elements were added just before pouring. During melting following steps were followed: Step-1, pure Al was heated up to the  $780 \text{ }^\circ\text{C}$  for 2.5 h in graphite crucible (capacity 3.0 kg), and then Al-2% Sc master alloy was added and kept for half an hour. Step-2, hot crucible was brought outside the furnace, and then pure Mg and pure Zn were added in liquid metal gradually with carefully. Step-3, slag removed from the top of the melt, and molten metal was poured into metallic mould quickly. The fading effect of scandium on grain refinement was controlled by keeping the pouring temperature within  $780 \text{ }^\circ\text{C}$  in the metallic mould. Due to faster cooling, the grain refinement controlled the fading. It has to mention that avoiding excessive turbulence through lip to lip pouring of liquid metal, the pouring rate control was done. The cast sample was examined by chemical analysis using inductively coupled plasma atomic emission spectroscopy (ICP-AES) and atomic absorption spectroscopy (AAS) analysis. The nominal composition of prepared 7075 Al alloy was: Al-6.7 Zn-2.8 Mg-0.2Sc alloy.

### 2.2 Friction Stir Processing (FSP)

Surface modification of cast metal and alloy can be performed by advanced technique like double passes FSP. An indigenously designed and developed milling machine was used for FSP. A specially designed and developed fixture was used to hold the plate firmly in position during FSP. The processing plate (dimension  $150 \times 90 \times 8 \text{ mm}^3$ ) can be fixed on the working table with the proper fixer. The working position had three mutually perpendicular movements, horizontal (traverse speed), vertical (tool plunge) and across movement (overlap passes). A tool was made of martensitic stainless steel. During preparation of tool, it was normalized at the  $930 \text{ }^\circ\text{C}$  for 1.5 h then quenched in oil bath. Further, it was tempered at the  $750 \text{ }^\circ\text{C}$  for 1.5 h to obtain a Vicker's hardness of 211 HV. The schematic diagram of FSP set-up shown in Fig. 1. During processing, the traveling direction ( $x$ -direction) was parallel to the processed direction of the Al-plate. The transverse side ( $y$ -direction) of the plate was clamped using pressing plate to constrain the displacement of the plate during processing. The tilt angle of the tool was  $2.5^\circ$  with respect to Z-axis of the FSP machine. Figure 4 shows a typical micrograph containing various microstructural zones after FSP at 720 rpm (revolutions per minute)

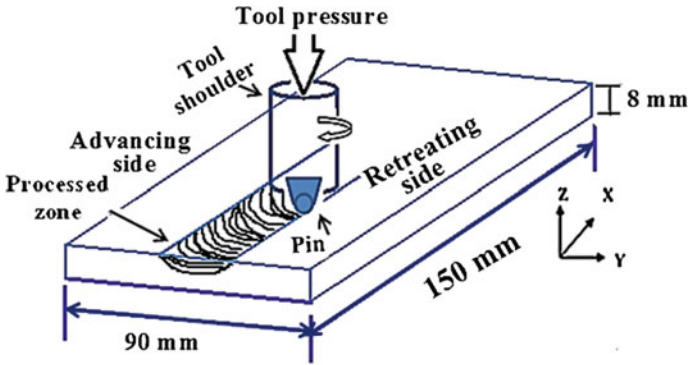


**Fig. 1** Schematic diagram of FSP set-up

and traverse speed (80 mm/min). The nugget zone or stir zone created in middle place, with adjacent right side and left side is called advancing side and retreating side, respectively. Next to the nugget zone is TMAZ (thermo-mechanically affected zone) where considerable plastic deformation takes place. Nearer to TMAZ region is called HAZ (heat affected zone) region.

### 2.3 Optical Microscopy (OM)

During metallographic studies, alloy has been thoroughly examined by optical microscopic (OM) technique, scanning electron microscopy (SEM) analysis, field-emission scanning electron microscopy (FESEM) analysis and transmission electron microscopy (TEM) analysis. The sample was cut it into small pieces and ground, and then polished with emery paper by sequentially by 1/0, 2/0, 3/0, and 4/0, respectively. Then cloth polishing was carried out with mechanically rotating wheel with  $\text{Al}_2\text{O}_3$  particles until fine scratches are removed. The final stage of polishing was done with diamond paste (0.5–1.0  $\mu\text{m}$ ) wet by sprayed liquid oil put on fine cloth by mechanically rotating the wheel until fine scratches were removed to obtain a mirror finish. Then the sample was cleaned with water and dried using a hot air dryer and etched with modified Keller's reagent (2.5 ml  $\text{HNO}_3$ (70%) + 1.5 ml  $\text{HCl}$  (38%) + 1 ml  $\text{HF}$ (40%) + 175 ml water). The microscope used for the study was a LEICA DMI 5000 M (Leica Microsystems, Buffalo Grove, IL) microscope.

### 2.4 Electron Probe Microanalysis (EPMA)

The as-cast sample was analyzed by electron probe microanalysis (EPMA) (Model no.: CAMECA SX100) with EDS to examined segregation on grain boundary and existence of scandium content as shown in Table 1.



**Table 1** Electron probe microanalysis (EPMA) in wt% of as-cast 7075 Al alloy

Set points	Al	Zn	Mg	Sc	Fe	Si	Total
1	92.13	3.97	1.49	0.03	0.03	0.02	97.66
2	89.37	5.58	1.53	0.15	0.02	0.04	96.68
3	88.12	5.64	3.03	0.10	0.05	0.05	96.89
4	90.63	3.43	1.72	0.15	0.03	0.02	95.95
5	89.13	4.16	2.66	0.03	0.05	0.01	89.13
Avg.	89.88	4.56	2.10	0.10	0.04	0.03	95.26

## 2.5 Transmission Electron Microscopy (TEM)

The TEM samples were prepared manually by polishing a thin specimen to obtain disc-shaped scratch-free surface.  $10 \times 10 \text{ mm}^2$  disc specimens were thinned down to 0.1 mm. Finally, 3-mm-diameter disc-shaped samples were cut from main polished  $10 \times 10 \text{ mm}^2$  sample which was considered for TEM analysis. Then, samples were polished using twin-jet electro-polishing (solution content 75%  $\text{CH}_3\text{OH}$  and 25%  $\text{HNO}_3$ ) at 12 V and  $-35^\circ\text{C}$ . The TEM imaging was carried out using Techai G<sup>2</sup> 20 S-TWIN at 200 kV as shown in Fig. 3.

## 2.6 Tensile Testing

The tensile test was performed on 7075 Al alloy at AC + FSP condition. The flat shape tensile specimens of full length 58 mm, gauge length 26 mm, width 4 mm and thickness 2 mm were tested with cross-head speed of 1 mm/min at room temperature. The test was conducted by Instron universal testing machine (UTM), and results are shown in Table 2. The tensile sample was collected from SZ during double passes FSP, and FSP piece for tensile sample preparation is shown in Fig. 7.

## 2.7 Fracture Toughness ( $K_{IC}$ ) Testing

The fracture toughness ( $K_{IC}$ ) value was evaluated by Instron testing machine which has thoroughly maintained a compact-tension (CT) specimen in pure mode-I fracture. It is based on the principle of linear-elastic fracture mechanics (LEFM) and contains three main steps: generation of crack in the test specimens, measurement of the load at failure stress, and crack depth. The dimension of CT specimen is  $62.5 \times 60 \times 6.25 \text{ mm}^3$ . The as-cast specimen after double passes FSP was notched by CNC Wire Cut Machine (Model no.: Sprintcut 734) made in Japan. The parameter selections for  $K_{IC}$  test are contained in Table 2. Determination of fracture

**Table 2** Mechanical properties have been evaluated of FSP 7075 Al alloy (AC + FSP condition)

Al-6.7 Zn-2.8 Mg-0.2Sc alloy	FSP parameters	Heat ratio (tool rotation rate/traverse speed)	Tensile properties after double passes FSP			$K_{IC}$ test parameters	Double passes FSP proceed through notch region of CT sample	vol% of porosity (as-cast condition)
			$\sigma_{0.2}$ (MPa)	$\sigma_u$ (MPa)	$\delta$ (%)			
	720(rpm), 80 (traverse speed)	9.0 (low heat input)	89.81	187.1	3.42	$R = 0.1$ ; applied load at 800 N; $f = 2$ Hz; 1000 no. of cycles at pre-cracked stage	Fracture toughness (plain-strain condition) values, $K_{IC}$ (MPa $\sqrt{m}$ ) tested by Instron Universal testing machine (Model no-8802)	6.60

N.B: Yield strength denoted at 0.2% proof strength offset from stress-strain curve; tool rotation rate  $\rightarrow$  rpm and traverse speed  $\rightarrow$  mm/min; the fracture toughness tests were conducted by four valid samples for this alloy

toughness ( $K_{IC}$ ) involves specimen preparation, testing procedure and calculation of  $K_{IC}$  values. As per ASTM E-399 standard (as shown in Fig. 6), the crack length is 0.25 mm. The crack was generated by applying fatigue load at a controlled condition of small load and amplitude to obtain a sharp fatigue pre-crack to ensure high stress distribution ahead of the crack tip. Therefore, predetermined crack was generated where crack length is 0.25 mm by Instron testing machine. The fracture toughness ( $K_{IC}$ ) results have been tabulated in Table 2.

## 2.8 Scanning Electron Microscopy (SEM)

The scanning electron microscopy (SEM) analysis has been done on CT fracture surface (Model no.: ZEISS EVO MA and LA series with EDAX analysis). The CT specimen was properly cleaned and dried for study of surface topography, pattern and different fracture mode. The EDAX analysis implies of impurity elements with Sc content in fracture surface as shown in Fig. 5.

## 3 Results and Discussion

It is well known that a fine and equiaxed grain microstructure has ample benefits in cast aluminium alloys, enhancing the mechanical properties, reducing shrinkage porosity, elimination of hot tearing, distribution of second phase particles and improved the toughness properties. In addition, the aged structure and the kinetics of ageing depend on the Zn + Mg content and Zn:Mg ratio and the temperature of solution and ageing temperatures. The Sc addition has been shown to greatly improve mechanical properties of 7075 Al alloy [10]. It is experimentally observed that a minor addition of Sc (0.2 wt%) in aluminium alloys induces the formation of fine equiaxed structures (30–35  $\mu\text{m}$ ), acting like a stronger inoculant when compared to the conventional Al–B, Al–Ti, Al–Ti–B and Al–Ti–C master alloys, which produces coarse grain structures and has affinity to induce fading phenomena. A latest study indicates that aluminium alloys can be grain refined by the use of an Al-2wt% Sc master alloy. Therefore, heterogeneous nucleation on the substrate would depend on compatibility between the crystal structure and lattice parameter of the phases involved. These factors indicate that  $\text{Al}_3\text{Sc}$  can be an efficient nucleant [6]. FSP is a fairly new solid-state technique of changing properties of a cast metal surface layer through severe localized plastic deformation. It is well known that FSW and FSP are based on same working principles which led the material a softened state ( $0.8 T_f$ ) without any liquid phase. The thermal sources governing the process mechanics are the frictional force and the plastic deformation, both decaying into heat [11]. According to the characteristics of the cast microstructure, the main contributions to hardening of the surface modified layers fabricated by double passes FSP are the fine grain size of the aluminium matrix, and the Orowan

strengthening due to the fine  $\text{Al}_3\text{Sc}$  particles dispersion. The improvement of hardness can be attained by controlling the grain size and heat input through the tool rotation speed and traverse speed. The enhancement of strength found to in FSP aluminium alloy is mostly due to recrystallized grains, residual stress due to axial compressive force, work hardening and  $\text{Al}_3\text{Sc}$  particles contribution [12, 13].

Moreover, the fracture toughness ( $K_{IC}$ ) depends primarily on crack propagation, which has a tendency towards strain localization in grain boundaries. Fine grain was considered to be effective in stopping premature fracture by reducing the dislocation pile-up length in the grain boundaries and exhibited better fracture toughness [14, 15]. Figure 2a presents optical micrograph of as-cast aluminium alloy which has exhibited fine grains due to minor Sc (0.2 wt%) inoculation effects. The cast inhomogeneity, grain boundary segregation and porosities are major drawbacks in cast microstructure, although minor Sc refines grain as 30–35  $\mu\text{m}$ . Main precipitates in 7075 Al alloy may be GP zones,  $\eta'$ , and  $\eta$  phases with  $\text{Al}_3\text{Sc}$  particles. A major achievement in as-cast alloy has reduced precipitation free zone (PFZ), which may reduce grain boundary failure, resulting in minimizing the intergranular fracture and improving the fracture resistance. The electron probe microanalysis (EPMA) indicates grain boundary segregation and minor Sc identification in cast aluminium alloy as shown in Fig. 2b and Table 1. Grain boundary segregation is clearly indicated with black line networks throughout in matrix. Figure 3a shows TEM micrograph with selective area diffraction (SAD) of as-cast alloy, which exhibits irregular shape of precipitates with random orientation due to minor Sc ( $\sim 0.2$  wt%) addition. Also, cast inhomogeneity is the main factor for coarse precipitates in matrix. The SAD image exhibited some of larger bright spots of coarse precipitates in matrix. Figure 3b shows TEM micrograph with SAD of  $T_6$  Al 7075 alloy, which exhibited fine dense and uniform precipitates throughout in matrix. The  $T_6$  ageing treatment implies critical dispersion of second phases and  $\text{Al}_3\text{Sc}$  particles with optimum size and density as a function time and temperature (140  $^\circ\text{C}$  for 6 h) phenomena in aluminium matrix. Main precipitates are GP zones (round shapes and uniform),  $\eta'$  (most dense, fine precipitates and uniform), some of

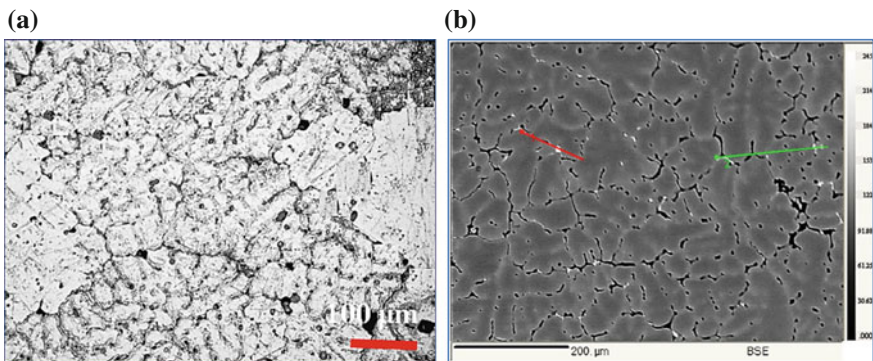


**Fig. 2** a Optical micrograph of as-cast 7075 Al alloy; b EPMA micrograph of as-cast 7075 Al alloy

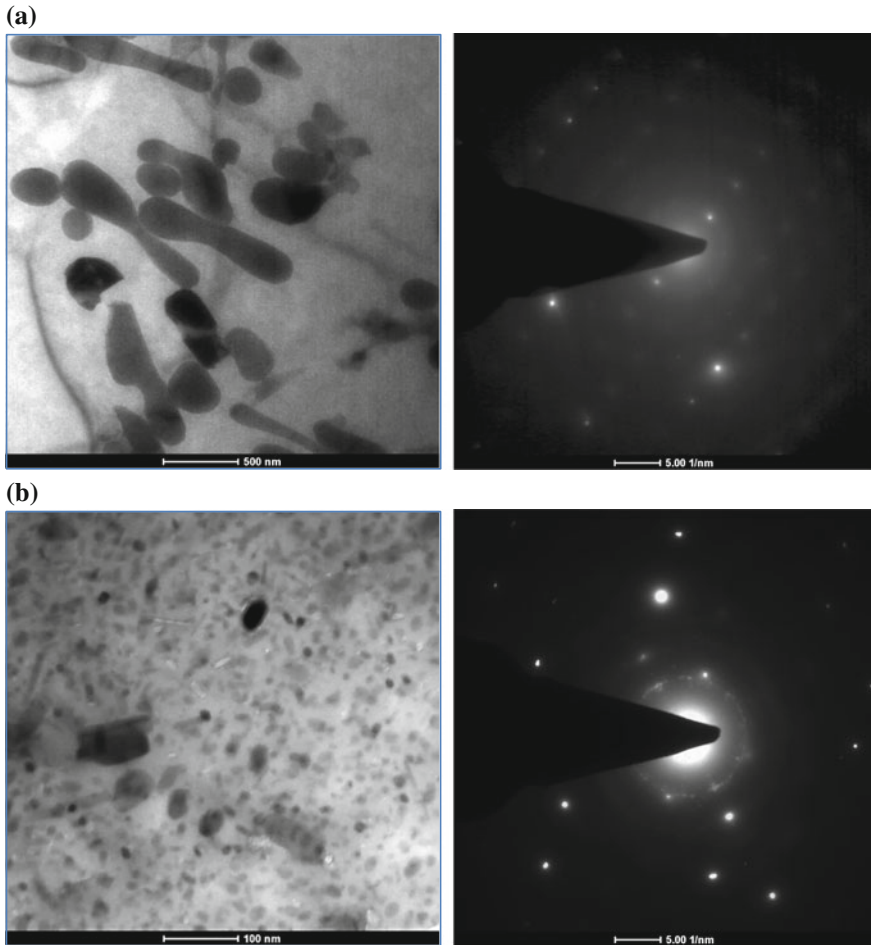


**Fig. 3** a TEM micrograph with SAD image of as-cast 7075 Al alloy; b TEM micrograph with SAD image of T<sub>6</sub> (aged at 140 °C/6 h) 7075 Al alloy

mostly large precipitates of complex phases and some of needle shapes ( $\eta$ ), and Al<sub>3</sub>Sc particles (mostly white spots and less population) in matrix. It has clearly indicated in SAD analysis that the large precipitates of bright spots are complex phases (cast inhomogeneity). Figure 4 shows optical micrograph of FSP 7075 Al alloy which has exhibited two distinct microstructural zones such as stir zone (SZ) and thermo-mechanically affected zone (TMAZ). The grain size achieved after FSP in SZ of 2–5  $\mu\text{m}$  and TMAZ of 5–10  $\mu\text{m}$ . The several black spots indicated Zn vaporization problem arise due to high heat generation ( $\sim 550$  °C) in SZ but more black spots exhibited in TMAZ may cause of torsional effects accelerate Zn vaporization, although lower heat ( $\sim 450$  °C) generated in this region. This advises that FSP refines grains but may not yield homogeneous grain size distribution

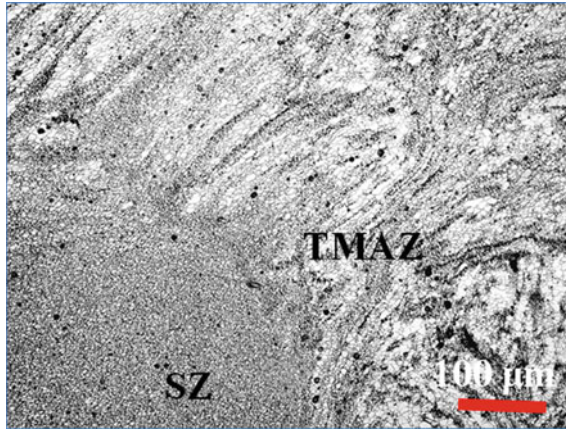


**Fig. 4** Optical micrograph exhibited several black spots due to Zn vaporization of FSP 7075 Al alloy (AC + FSP condition)

throughout processed region. According to literature survey, it is hypothesized that these heterogeneities are caused by non-uniform thermal cycles and strain rate distribution during FSP. These microstructures in the SZ are known to exhibit fine grain due to dynamic recrystallization [16, 17]. Figure 5 shows SEM CT-fractograph of FSP 7075 Al alloy after AC + FSP condition, showing the mixed fracture characteristics intergranular and transgranular types of planar features are more pronounced, covering the majority of the fracture surfaces. The fractograph of the present alloy revealed cleavage facets in the presence of sharp fine dimples. The fractograph also contains many large cracks (indicate by arrows) which may a source of crack initiation point or may source of Zn vaporization spots as revealed by optical microscopy after AC + FSP (Fig. 4).

The fracture toughness ( $K_{IC}$ ) and tensile properties of AC + FSP samples were tested as per ASTM standards as shown in Figs. 6 and 7, respectively. In Fig. 6 shows CT sample as per ASTM E-399 standard with double passes FSP proceed

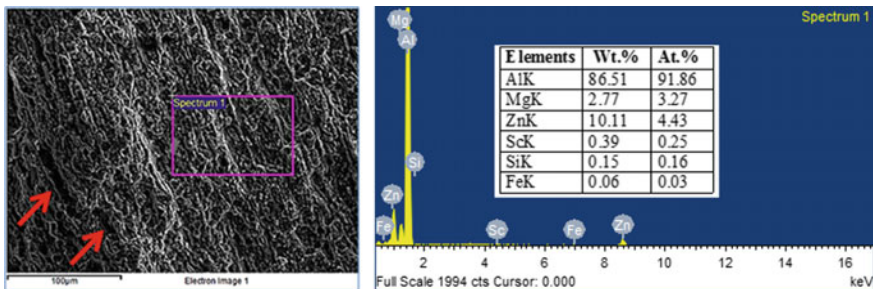


**Fig. 5** SEM compact-tension (CT) fractograph with EDX analysis of FSP 7075 Al alloy (AC + FSP condition)

through notch region (only 3.5 mm is processed zone) of aluminium alloy [18, 19]. The average of four samples of fracture toughness ( $K_{IC}$ ) value for this aluminium alloy is 25.10 MPa $\sqrt{m}$ . There is an important parameter such as low heat input ratio (9) affect the vital role of low Zn vaporization during FSP. It has to be mentioned that grain refinement, eliminate porosities, dispersion of second phases and  $Al_3Sc$  particles are main causes of enhanced fracture toughness, although only 3.5-mm portion has processed zone by FSP. Fine grain size has considered to be effective in preventing premature fracture by reducing the dislocation pile-up length in the grain boundaries and improved on fracture toughness after FSP. In addition, crystallographic disorientation across the grain boundary implies in crack plane tilt and twist, which reduces the effective driving force for crack growth phenomena. On the other hand, a smaller grain size and  $Al_3Sc$  dispersoids introduce more grain boundaries and can strongly pin dislocation and subgrain boundaries [20, 21]. Figure 7 shows tensile sample as per ASTM E-8/E8 M-11 sub-size standard with double passes FSP proceed to maintain half processed zone (1.25 mm) plus half unprocessed zone (1.25 mm) of aluminium alloy. The as-cast alloy has prone to high porosity content (6.60 vol%) although exhibited moderate 0.2% proof strength of 89.81 MPa, ultimate tensile strength of 187.1 MPa, and elongation of 3.42% after FSP. Thus,  $Al_3Sc$  ( $L1_2$ ) spherical particles can be finely dispersed to improve strength of aluminium alloy [22, 23].

## 4 Conclusions

In the present study, scandium inoculated cast aluminium alloy surface layer was successfully fabricated by double passes FSP. The microstructure, tensile and fracture toughness properties were evaluated observing the matrix grains and dispersion of the second phases. The following results have been drawn below:

- (1) The grain refinement of aluminium alloy is achieved by the addition of inoculant particles (e.g.  $Al_3Sc$ ) in the form of Al–Sc master alloy during melt practise.
- (2) Sc addition to Al–Zn–Mg–Sc alloy can produce fine coherent,  $Al_3Sc$  dispersoids that can efficiently pin the dislocations and subgrain boundaries and enhance the resistance to recrystallization of aluminium alloy.
- (3) TEM examination revealed after  $T_6$  ageing treatment implies critical dispersion of second phases and  $Al_3Sc$  particles with optimum size and density as a function time and temperature (140 °C for 6 h) phenomena in cast aluminium matrix.
- (4) Friction stir processing for 8-mm-thick as-cast plate of natural aged, high strength 7075 Al alloy was succeeded without any defects using double passes FSP.

- (5) Minor Sc addition (0.2 wt%) to Al–Zn–Mg–Sc alloy can achieve the 0.2% proof strength of 89.81 MPa, ultimate tensile strength of 187.1 MPa, elongation of 3.42%, and fracture toughness of 25.10 MPa√m after AC + FSP condition.
- (6) FSP at usually low rotational speed of 720 rpm and traverse speed 80 mm/min has shown better fracture toughness ( $K_{IC}$ ) of 25.1 MPa√m for Al–Zn–Mg–Sc alloy after AC + FSP condition. This is due to synergy effects of fine grains, elimination of porosity, breakup of cast inhomogeneity and fragmentation of  $Al_3Sc$  along with finely dispersion of  $MgZn_2$  and lower Zn vaporization problem (black spots revealed in optical metallography) due to low heat input ratio (9).

**Acknowledgements** The author is very much thankful to the research scholars in Metallurgical and Materials Engineering Department, Indian Institute of Technology Roorkee (IITR), Roorkee, India, for helping and providing Instron Testing Machine for conducting fracture toughness testing.

## Appendix

Design of CT and Tensile test samples:

See Figs. 6 and 7.

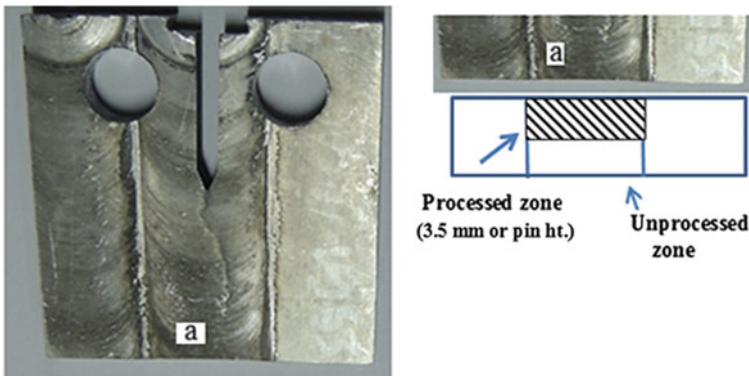
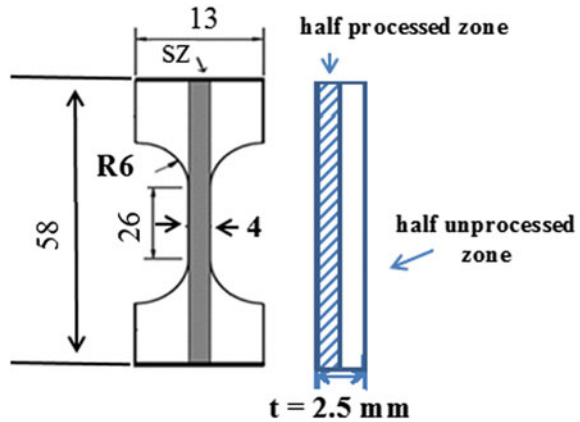


**Fig. 6** A compact-tension (CT) tested sample ( $62.5 \times 60 \times 6.25 \text{ mm}^3$ ) (ASTM E-399 standard) has exhibited double passes FSP at notch region. A cross section of “a” region indicated depth of processed zone (hatched region) (720 rpm and 80



**Fig. 7** A tensile test sample (ASTM: E-8/E8 M-11 sub-size) collected from SZ. Beside test sample a cross sectional view, which have indicated depth of processed zone (hatched region) (720 rpm and 80 traverse speed)



## References

1. Wu L-M, Seyfing M, Rettenmayr M, Wang W-H (2010) Characterization of precipitate evolution in an artificially aged Al-Zn-Mg-Sc-Zr alloy. *Mater Sci Eng A* 527:1068–1073
2. Mandal PK (2016) Study on GP-zones formation in the Sc inoculated ternary Al-Zn-Mg Alloys. *J Mater Metall Eng* 6(2):53–69
3. Löffler H, Kovacs I, Lendvai J (1983) Review decomposition processes in Al-Zn-Mg alloys. *J Mater Sci* 18:2215–2240
4. Fuller CB, Krause AR, Dunand DC, Seidman DN (2002) Microstructure and mechanical properties of a 5754 aluminium alloy modified by Sc and Zr additions. *Mater Sci Eng A* 338:8–16
5. Huang J-W, Yin Z-M, Fang J-F, Nie B, Wang T (2007) Aging characteristics of 7A52 Al-Zn-Mg alloy. *Mater Sci Forum* 546–549:867–870
6. Mandal PK (2015) Processing and characterization of  $Al_3Sc$  precipitates in cast aluminium alloy by Foundry Route. *J Adv Res Manuf Mater Sci Metall Eng* 2(3&4):1–6
7. Milman Y (2006) Structure and mechanical behavior of Al-Sc alloys. *Mater Sci* 519–521:567–572
8. Gholami S, Emadoddin E, Tajally M, Borhani E (2015) Friction stir processing of 7075 Al alloy and subsequent aging treatment. *Trans Nonferrous Met Soc China* 25:2847–2855
9. Wang K, Liu FC, Ma ZY, Zhang FC (2011) Realization of exceptionally high elongation at high strain rate in a friction stir processed Al-Zn-Mg-Cu alloy with the presence of liquid phase. *Scripta Mater* 64:572–575
10. Costa S, Puga H, Barbosa J, Pinto AMP (2012) The effect of Sc additions on the microstructure and age hardening behaviour of as cast Al-Sc alloys. *Mater Des* 42:347–352
11. Patel JB, Patil HS (2014) Simulation of peak temperature & flow stress during FSW of aluminium alloy AA6061 for various tool pin profiles. *Int J Mater Sci Eng* 2(1):67–71
12. Deng Y, Yin Z, Zhao K, Duan J, He Z (2012) Effects of Sc and Zr microalloying additions on the microstructure and mechanical properties of new Al-Zn-Mg alloys. *J Alloy Compd* 530:71–80
13. Kumar N, Mishra RS (2013) Ultrafine-grained Al-Mg-Sc alloy via friction-stir processing. *Metall Mater Trans A* 44A:934–945
14. Han NM, Zhang XM, Liu SD, He DG, Zhang R (2011) Effect of solution treatment on the strength and fracture toughness of aluminium alloy 7050. *J Alloy Compd* 509:4138–4145

15. Vratnica M, Cvijovic Z, Rakin M (2004) Fracture toughness modeling in high-strength Al-based alloys. *Mater Sci Forum* 453–454:181–186
16. Feng X, Liu H, Babu SS (2011) Effect of grain size refinement and precipitation reactions on strengthening in friction stir processed Al-Cu alloys. *Scripta Mater* 65:1057–1060
17. Su J-Q, Nelson TW, Sterling CJ (2006) Grain refinement of aluminium alloys by friction stir processing. *Phil Mag* 86(1):1–24
18. Mohan Kumar S, Pramod R, Shashi Kumar ME, Govindaraju HK (2014) Evaluation of fracture toughness and mechanical properties of aluminium alloy 7075, T6 with Nickel Coating. *Procedia Eng* 97:178–185
19. Reddy AC, Rajan SS (2005) Influence of ageing, inclusions and voids on ductile fracture mechanism in commercial Al-alloys. *Bull Mater Sci* 28(1):75–79
20. Ludtka GM, Laughlin DE (1982) The influence of microstructure and strength on the fracture mode and toughness of 7XXX series aluminium alloys. *Metall Trans A* 13A:411–425
21. Yan A, Chen L, Liu HS, Xiao FF, Li XQ (2015) Study on strength and fracture toughness of Al–Zn–Mg–Cu–Ti(–Sn) alloys. *J Min Metall Sect B: Metall* 51(1):73–79
22. Rhodes CG, Mahoney MW, Bingel WH, Calabrese M (2003) Fine-grain evolution in friction-stir processed 7050 aluminium. *Scripta Mater* 48:1451–1455
23. Zhenbo H, Zhimin Y, Sen L, Ying D, Baochuan S (2010) Preparation, microstructure and properties of Al–Zn–Mg–Sc alloy tubes. *J Rare Earths* 28(4):641–646

# Evolution of Tertiary Carbides and Its Influence on Wear Behavior, Surface Roughness and Fatigue Limit of Die Steels

Tarang Shinde and N.B. Dhokey

**Abstract** The fatigue is a primary mode of failure in many hot work die steels such as AISI H13 on account of severe thermal fatigue conditions as in hot forging. The present work involves hardening of AISI H13 die steel specimens at 1020 °C, oil quenching followed by double tempering at 500 °C and then cryogenic treatment at minus 185 °C at different cryosoaking periods from 8 to 32 h followed by soft tempering at 100 °C. The influence of tertiary carbide evolution on wear behavior, surface roughness and fatigue limit was studied. It has been established that there are reduction in wear rate, improvement in hardness, surface roughness and increasing the fatigue life on account of fine tertiary carbide precipitation.

**Keywords** AISI H13 · Wear · Surface roughness · Fatigue limit  
Cryogenic treatment

## 1 Introduction

The AISI H13 hot work die steel is frequently subjected to severe conditions of load and heat, widely used for mechanical working operations such as hot forging and extrusion, thereby limiting the life of the parts. It is necessary to increase the life of dies and prevent premature failure; various measures have been suggested in the literature, but very little has been mentioned about the cryogenic treatment of hot work die steels. Cryogenic treatment is used for cutting tool materials as described in many research projects. Koneshlou et al. [1] investigated the effect of cryogenic treatment on wear behavior of AISI H13 die steel, explaining the conversion of retained austenite into martensite as well as precipitation of fine carbides, thereby improving the mechanical properties and wear behavior of the materials. Perez et al.

---

T. Shinde (✉) · N.B. Dhokey  
College of Engineering, Pune, India  
e-mail: tarangshinde@gmail.com

N.B. Dhokey  
e-mail: nbdhokey@yahoo.co.in

[2] had elaborated upon the effect of cryogenic treatments on the mechanical properties of H13 steel wherein the increase in carbide density and toughness had been reported for the specimens with cryogenic treatment which was attributed to fine carbide network as well as the conversion of retained austenite into martensite. Meng et al. [3] explained the role of  $\eta$ -carbides precipitation in the improvement of performance of tool steel by cryogenic treatment. The cryogenic treatment enhances the preferential precipitation of fine  $\eta$ -carbides. These fine carbides increase the strength and toughness of martensite matrix, thereby improving the wear resistance. Dhokey et al. [4] had carried out an investigation on cryogenically treated AISI T42 steel with respect to its wear behavior in which case the optimum cryosoaking period was established at 8 h based on increased carbide density and hardness accompanied by a significant reduction in wear rate with proposed wear mechanisms as divided into mild delamination wear and severe wear regime. AISI H13 steel is subjected to fatigue loading conditions too, which needs to be taken into consideration. Fukaura et al. [5] have explained the fatigue crack formation on the basis of carbide morphology in cold work die steel. The authors have proposed that the fatigue crack initiation is dependent on the magnitude of applied alternating stress. The fracture initiates from the surface when the stress values are higher. At lower stress values, the crack initiates near the surface from the interior and spreads toward the surface. Ebara et al. [6] focused on the fatigue crack initiation and propagation of hot forging as well as cold forging die steels in low-cycle, high-cycle and giga-cycle fatigue regions. It has been discussed that smoother surface, i.e., the surface with minimum value of surface roughness, delivers higher fatigue strength, especially in low-cycle fatigue region. Vacuum heat treating has shown improvement in fatigue strength, and it is attributed to smaller size of carbides. The size of carbides has been reported to be smaller for vacuum-treated steels as compared to salt bath treatment. Fatigue crack starts at the surface, but due to the presence of these smaller carbides, the crack initiation was delayed and it was started at the subsurface rather than at the surface.

As per the analysis carried out, the cryosoaking period for H13 steel has not been optimized and there is no correlation established between the wear resistance with respect to surface roughness and carbide density as well as the effect of cryogenic treatment on fatigue limit. In this paper, an attempt has been made to study the influence of cryogenic treatment on wear resistance and fatigue life of die steels.

## 2 Experimental Methods

### 2.1 Material Heat Treatment

AISI H13 hot work die steel material was procured to make specimens with diameter 8 mm and height 10 mm. The spectroscopic analysis indicated the chemical composition of material as Fe-0.40C-0.30Mn-0.90Si-5.50Cr-1.40Mo-1.00V

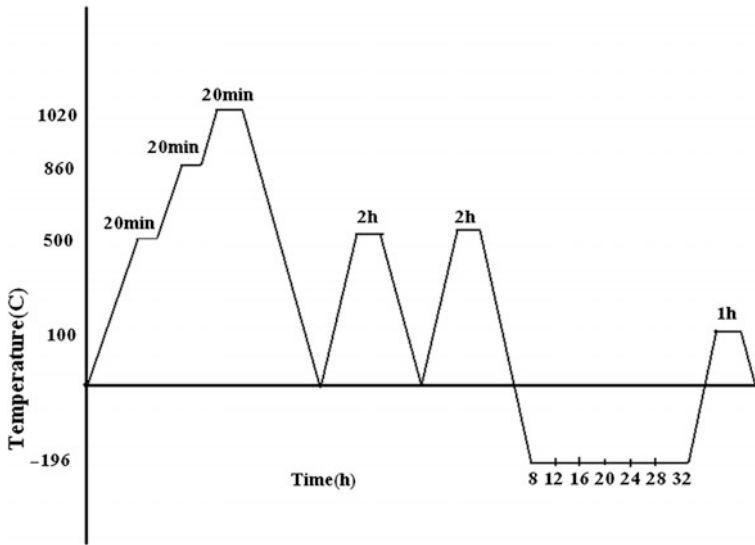


**Fig. 1** Cryogenic treatment cycle for AISI H13

(by weight %). AISI H13 specimens were hardened (*H*) at 1020 °C and oil quenched followed by double tempering (*T*) at 500 °C for 2 h. This treatment has been named as conventional heat treatment (HT).

The cryogenic treatment was performed on AISI H13 specimens as shown in Fig. 1, in computer-controlled setup, at a cooling rate of 3 °C/min by supplying calculated amount of liquid nitrogen through a solenoid valve. Different cryosoaking periods were used starting from 8 to 32 h, in the range of 4 h. After completion of each cryosoaking period, the specimens were taken out from cryobath and were transferred to thermocol box until they attain room temperature followed by soft tempering at 100 °C for 1 h to relieve the internal stresses generated in cryogenic treatment. The specimens were designated as HTC8, HTC12, HTC16, HTC20, HTC24, HTC28 and HTC32 with the number indicating cryosoaking period in hours.

## 2.2 Characterization

Microstructural analysis, of AISI H13 specimens, was carried out by optical micrography and scanning electron microscope (make: Zeiss). The H13 die steel specimens were polished on emery papers (1/0, 2/0, 3/0 and 4/0). Final polishing was carried out on a velvet cloth polishing machine with the application of fine suspensions of diamond paste, intermittently. A freshly prepared etchant 3% nital (30 s) was used for revealing microstructure of AISI H13 steel. The carbide

counting was performed on the optical microstructures (1000 X) as per ASTM E562-89 with expressing the number of carbide particles per unit area.

The hardness measurement, on C scale, was carried out using Rockwell hardness tester. The flat surface was prepared by polish paper of 1/0. A minor load of 10 kg was applied to seat the indenter properly which was followed by application of major load of 150 kg for 15 s, and resistance offered by the material to indentation was automatically recorded on the dial gauge. Hardness was measured as an average of five readings reported from the machine.

The conventionally treated (HT) and cryotreated (HTC8 to HTC32) specimens were machined on computerized numerical controlled milling machine with a spindle speed of 2500 revolutions per min and feed rate of 120 mm per min with depth of cut of 5 mm. Surface roughness of conventionally treated and cryogenically treated specimens was measured in contact-type surface roughness tester (make: Mitutoyo; model: SJ-410) as per DIN EN ISO 4287:1998 with travel path length of the probe as 10 mm. An average of three readings was reported as a measure of surface roughness.

### **2.3 Wear Testing**

Pin-on-disk method was used for testing the dry sliding wear of AISI H13 material in wear test. During testing, pin of AISI H13 steel specimen was kept stationary, while the disk was rotated. The apparatus consisted of a SAE 52100 steel disk (0.98% C and 1.40% Cr by wt and 63HRC) of diameter 215 mm, used as counter face. The test specimen was clamped in a holder and was held against the rotating steel disk as shown in Fig. 2. Specimens of AISI H13 steel (8 mm in diameter and 10 mm height) were subjected to wear test with a load of 4 kg for a sliding distance of 6000 m at a speed of 3 m/s with track radius of 60 mm [7] in dry condition at 300 K with approximate relative humidity of 60%. Wear was determined from the mass loss from the specimen material by electronic weighing balance. The mass loss was converted to volume loss with density of 7.8 g/cc and dividing the sliding distance. Three readings were captured for each cryosoaking period to record the average wear rate.

## **3 Results and Discussion**

### **3.1 Mechanism of Carbide Evolution**

The cryogenic treatment influences the microstructural features of the AISI H13 steel. Figures 2 and 3 show the optical microstructure and SEM micrograph of conventionally treated (HT) specimen, respectively, indicating the presence of

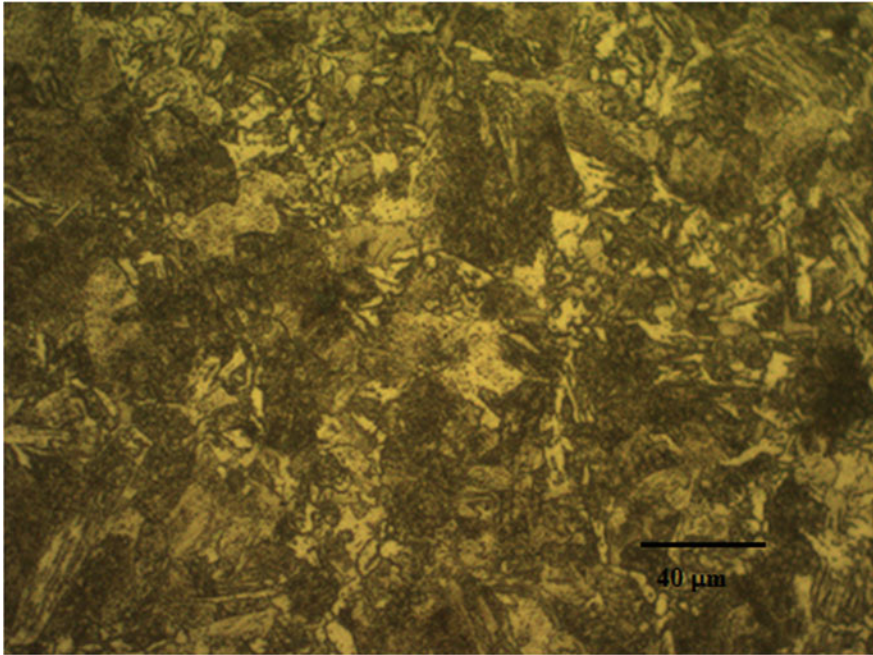


**Fig. 2** Optical microstructure of HT specimen indicating the retained austenite in the matrix of tempered martensite (500 X)

retained austenite. The microstructure also indicates the precipitation of primary and secondary carbides in the matrix of tempered martensite.

Figure 4 indicates SEM micrograph of HTC16 specimen which shows moderate distribution of fine tertiary carbides in the matrix of tempered martensite. The cryogenic treatment leads to conversion of retained austenite into martensite [3, 7] as well as it promotes the precipitation of nanoscale fine tertiary carbides [3]. During initial cryosoaking period, the carbide density is increasing (Fig. 6) due to increased carbide nucleation and availability of alloying elements for nucleation [4]. The carbide density reaches maximum at 16 h where maximum hardness has also been noted (Fig. 6).

Figure 5 indicates SEM micrograph of HTC32 specimen, indicating the carbide network at the grain boundary areas leading to weakening of grain boundary region. With the increase in cryosoaking period beyond 16 h especially, the kinetics of nucleation of carbides becomes sluggish which may be attributed to poor availability of alloying elements for nucleation of carbides and smaller carbide particles coalesce to form coarser carbides by Ostwald ripening mechanism, thereby reducing the surface energy. Thus, the growth becomes a dominant mechanism for the specimens subjected to cryogenic treatment beyond 16-h cryosoaking period. Due to carbide coarsening at higher cryosoaking period, there is a drop in carbide density (Fig. 6) as well as the drop in hardness (Fig. 7).

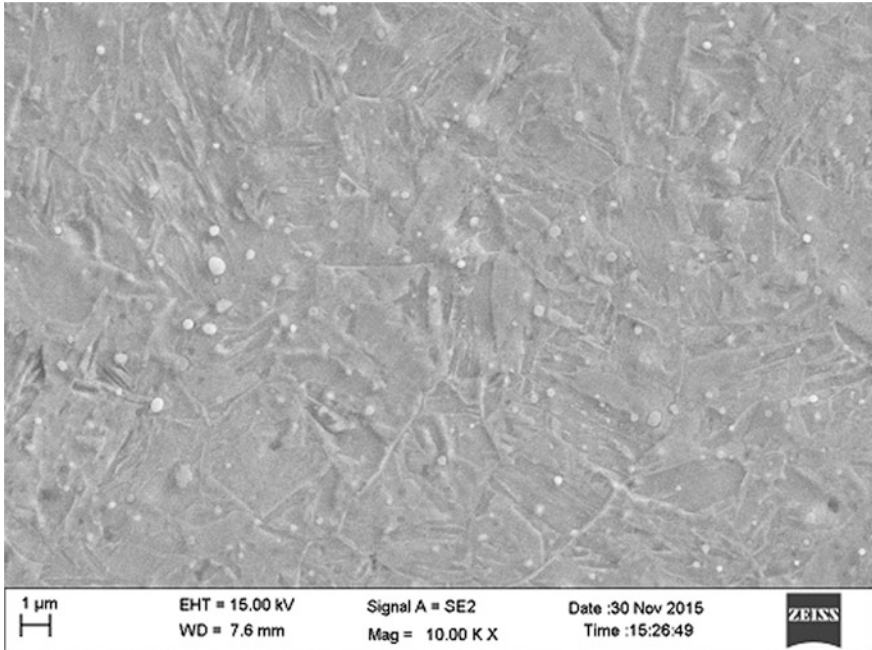


**Fig. 3** SEM micrograph of HT specimen indicating precipitation of primary and secondary carbides in the matrix of tempered martensite

### ***3.2 Carbide Density and Hardness***

Figures 6 and 7 indicate, with the increase in cryosoaking period, there is an increase in carbide density and hardness for cryogenically treated specimens till 16 h, as compared to conventionally treated specimens which is attributed to higher carbide nucleation rates in this regime till 16 h. Beyond 16 h, there is drop in carbide density as well as hardness on account of carbide coarsening by Ostwald ripening which is a growth-dominated regime as depicted in Fig. 6.

### ***3.3 Microstructural Impact on Surface Roughness***

Surface roughness affects the wear characteristics of materials since the material surface is subjected to impact load and high-temperature applications in case of hot work die steels. To cope up with such conditions, it is very important to have very high quality of surface finish as whenever the material is subjected to such severe loading and high temperature conditions, the surface roughness increases which leads to crack nucleation from the surface. Figure 8 indicates the variation of



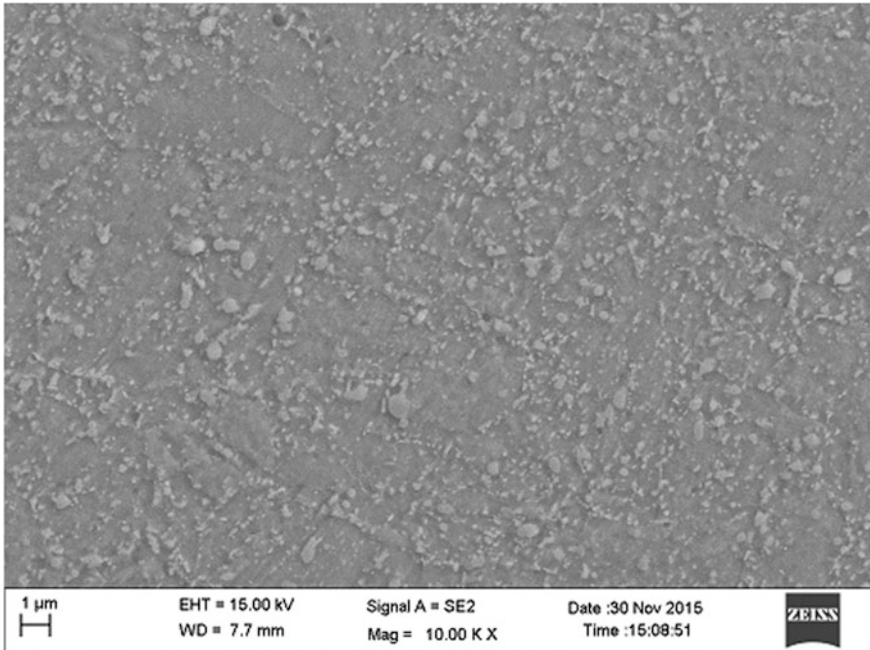


**Fig. 4** SEM micrograph of HTC16 specimen indicating moderate distribution of carbides in tempered martensitic structure

surface roughness ( $R_a$ ) with cryosoaking period wherein conventionally treated specimen (HT) indicates higher surface roughness, whereas surface roughness decreases to a minimum for 16-hr cryogenically treated specimens (HTC16). Higher value of surface roughness as in case of conventionally treated specimen (HT) indicates a much rough surface which resembles the notch-like pattern, acting as a potential site for nucleation of crack [8], leading to an increased wear rate (Fig. 9) as compared to smoother surface, in case of HTC16 specimen.

### **3.4 Wear Behavior**

The wear behavior was studied for AISI H13 specimens with different cryosoaking periods. The wear rate was seen to be reduced significantly in case of cryogenically treated specimens. The maximum reduction in wear rate was observed for specimens of 16-h cryosoaking period (HTC16). Figure 9 shows the variation of wear rate for conventionally treated specimens and specimens with different cryosoaking periods.

The decrease in roughness value is also seen along with the decrease in wear rate (Fig. 9). The minimum value of roughness is at 16-h cryosoaking period at which

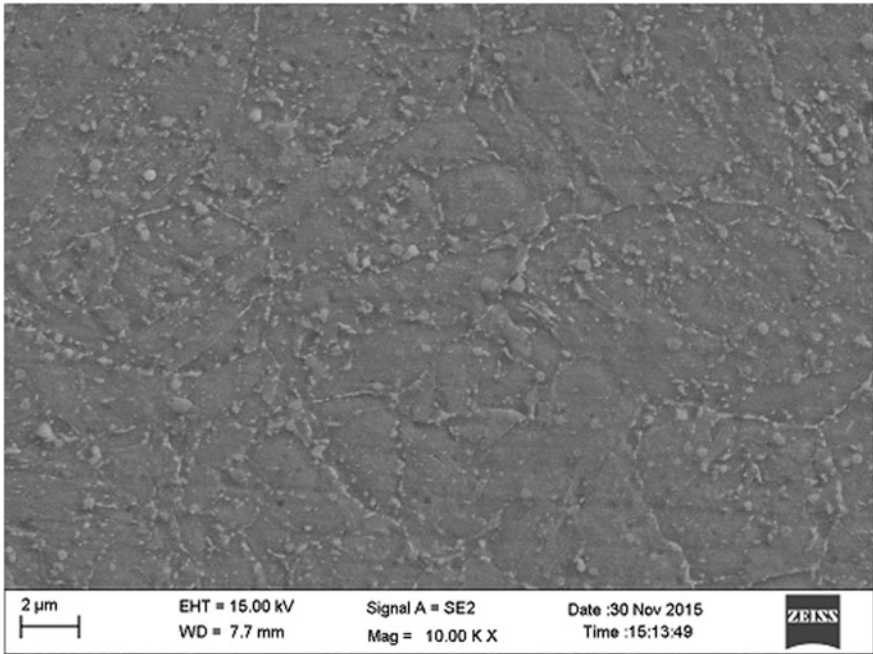


Fig. 5 Microstructure of HTC32 specimen indicating the carbide network along the grain boundaries

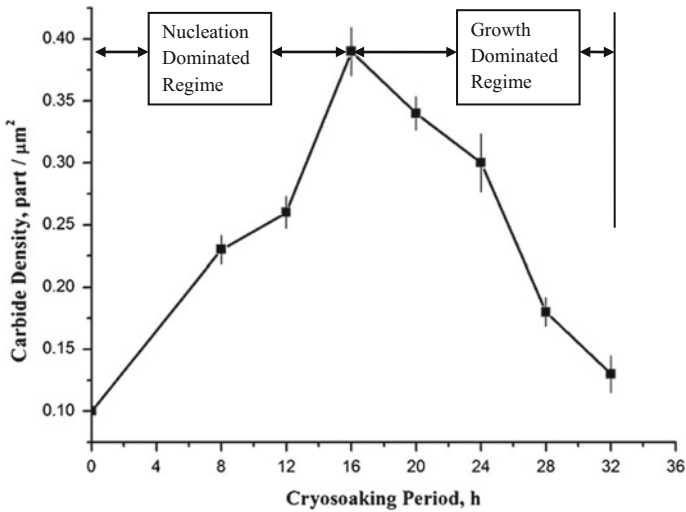


Fig. 6 Variation of carbide density with cryosoaking period

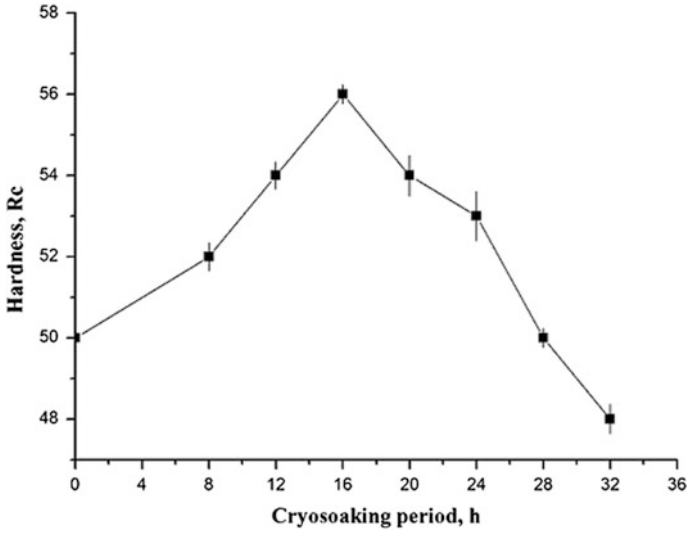


Fig. 7 Variation of hardness with cryosoaking period

Fig. 8 Variation of surface roughness (Ra) with cryosoaking period

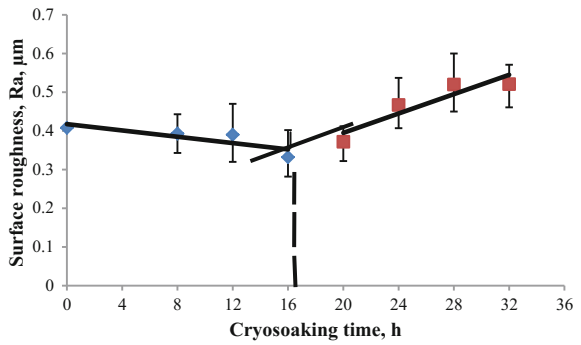
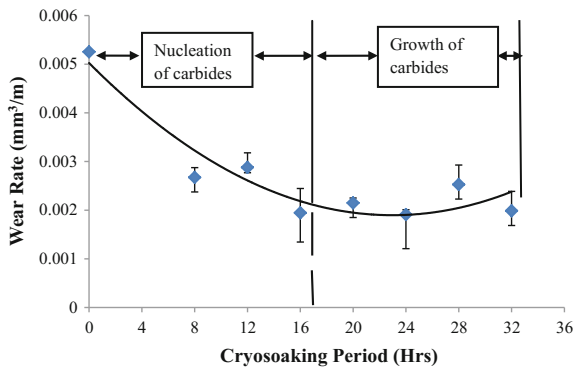


Fig. 9 Variation of wear rate with cryosoaking period



the wear rate also attains the minimum (Fig. 9). During initial cryosoaking period, there is a rejection of alloying elements by the matrix on account of thermal stresses which arise due to thermal shock as well as phase change from retained austenite to martensite [9, 10]. These elements form their respective carbides and precipitate in the tempered martensitic structure, thereby increasing the carbide density (Fig. 6) and increased hardness (Fig. 7) till 16-h cryosoaking period.

Beyond 16 h of cryogenic soaking, the wear rate is seen to be increasing with consequent decrease in hardness and increase in roughness values too. At higher cryosoaking period, the precipitation of carbides is dominated by coarsening due to reduction in surface energy of fine carbides as well as less availability of alloying elements from the matrix, leading to insignificant nucleation rate of carbides [10].

On the basis of the analysis of results obtained from hardness, surface roughness, carbide density and wear rate with respect to cryosoaking period, it is established that 16-h cryosoaking period could be optimized for AISI H13 die steel. Hence, fatigue behavior has been discussed for AISI H 13 specimens for 16-h cryosoaking period and a mechanism has been proposed to elaborate upon the improvement in fatigue life of the cryogenically treated specimens.

## 4 Fatigue Specimen

AISI H13 hot work die steel material was procured to make specimens with specimen dimensions as per DIN 50113 specifications (Fig. 10). The spectroscopic analysis indicated the chemical composition of material as Fe–0.40C–0.30Mn–0.90Si–5.50Cr–1.40Mo–1.00V (by weight %).

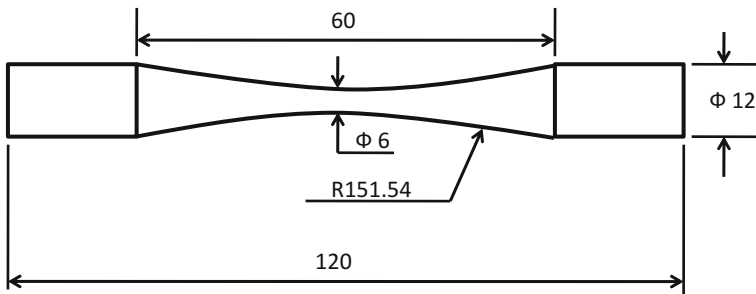


**Fig. 10** Specimen for fatigue test

### 4.1 Fatigue Test

The HT and HTC16 specimens were tested for fatigue loading on four-point rotating bending fatigue testing machine (Fig. 11) (make: Magnum, motor: 3000 rpm, maximum load: 50 kg) at 3000 rpm with a variation of load starting from 10 kg. As per standards, the load is selected at 75% of tensile strength of the material under test. The test was conducted at room temperature with load ratio of  $-1 (R = -1)$ . For each stress level, three specimens were tested and the number of cycles to failure was noted. The test was stopped if no failure occurred after  $10^6$  cycles. If three specimens complete  $10^6$  cycles on the same stress level, that stress level was considered as the fatigue or endurance limit for the material.

The fractured specimen surfaces were observed under scanning electron microscope (make: ZEISS) having a voltage range of 0 to 20 eV.

### 4.2 Effect of Roughness on Crack Nucleation

The hardness values of conventionally treated (HT) and cryogenically treated (HTC16) specimens were 50 and 56 HRC, respectively. The increase in hardness can be attributed to conversion of retained austenite to martensite [11] as well as precipitation of fine tertiary carbides.

The fatigue failure can be characterized into three steps: (1) crack initiation, involving formation of smaller crack at a point of high stress concentration.

(2) Crack propagation wherein crack advances incrementally with every stress cycle and (3) final failure which occurs when the crack has reached critical size. The cracks associated with fatigue failures are nucleating mainly at the surface of the material. Hence, the material surface is required to be harder to delay the crack nucleation. The surface roughness value for HT specimen is reported to be  $0.408 \mu\text{m}$ , whereas for HTC16 specimen, it is  $0.332 \mu\text{m}$ . Higher values of surface roughness lead to reduced fatigue limit as the rough surface contains the surface irregularities which will act as notches. The notched area will have higher stress concentration; hence, these notches become the favorable sites of crack nucleation.

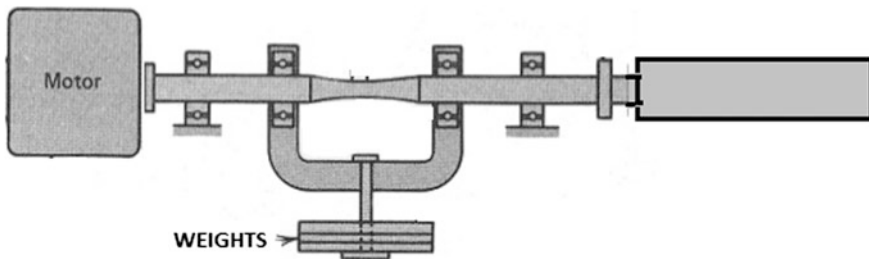
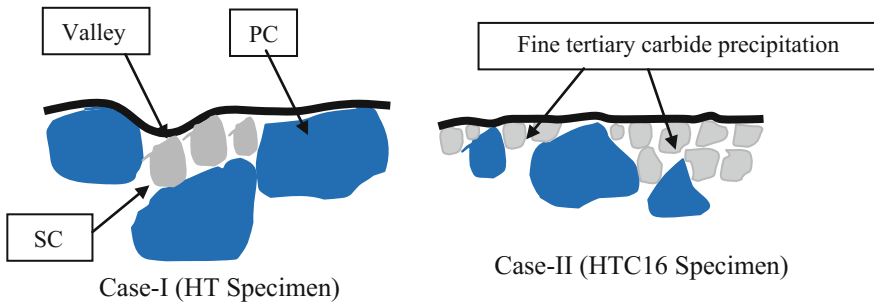


Fig. 11 Four-point rotating bending fatigue test machine



**Fig. 12** Case-I indicates crack nucleated at the valley present on the surface of the HT specimen due to higher surface roughness. Case-II indicates valleys present on the surface are preoccupied by fine tertiary carbide precipitation, thereby reducing the chances of crack nucleation (*PC* primary carbides, *SC* secondary carbides)

Any notch or geometrical discontinuity especially on the surface can act as stress raiser, thereby becoming a potential site for fatigue crack initiation. Hence, to improve fatigue limit, it is very necessary to have lower roughness values. The decrease in roughness value reported in the test may be attributed to the precipitation of fine carbides which will be occupying the valleys present on the surface, thereby reducing the surface roughness values as compared to conventional treatment [12] as the microstructural analysis of cryotreated specimens (HTC16) has indicated moderate and fine distribution of tertiary carbides, throughout the matrix of tempered martensite.

As far as the effect of surface roughness on the fatigue limit is concerned, it can be explained with the help of a model (Fig. 12). Figure 12 Case-I indicates the distribution of primary and secondary carbides and the gaps or valleys which are left behind acting as notched areas where cracks can originate and propagate further for HT specimen, whereas in case of cryogenically treated specimens (HTC16) (Fig. 12-Case-II), the valleys are occupied by fine tertiary carbides precipitated during cryogenic treatment, thereby reducing the tendency of notch formation as well as delaying the nucleation of cracks subsequently increasing the fatigue limit of the materials.

### 4.3 Fatigue Mechanism

Figure 13 indicates *S-N* curve for conventionally treated (HT) and 16-hr cryogenically treated (HTC16) AISI H13 specimens which clearly reveals that there is an improvement in fatigue limit for cryogenically treated specimens (HTC16). HTC16 specimen indicates moderate distribution of fine carbides in the matrix of tempered martensite as well as the retained austenite is converted to martensite [10] which leads to increase in hardness of the steel as compared to conventionally treated (HT) specimens. Most of the fatigue cracks initiate at the surface of the

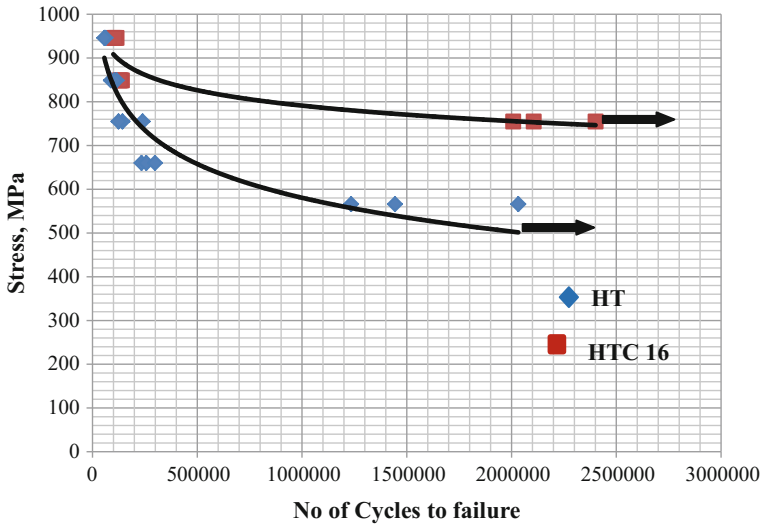


**Fig. 13** S-N curve for HT and HTC16 specimens

materials, and since this material AISI H13 experiences tremendous amount of thermal and mechanical stresses, there is greater possibility that the cracks initiate at the surface of this material. The increase in hardness is always beneficial to prolong the initiation of the crack, especially at the surface. One of the fundamental reasons for fatigue failure is slip. Any treatment that increases the hardness of the material will increase the stress level required for producing the slip which leads to increasing the fatigue limit of the material. Since 16-h cryogenically treated specimens (HTC16) indicate increased hardness as compared to conventionally treated (HT) specimens, this could be attributed to delayed crack initiation at the surface of HTC16 specimens leading to an increased fatigue limit of these cryogenically treated materials.

As far as the conventionally treated (HT) specimens are concerned, these specimens contain mainly primary and secondary carbides. The interface between the matrix and the primary or secondary carbide particles can act as a potential site for crack initiation. This could be a reason for much earlier initiation and propagation of cracks in case of these specimens, leading to failure at  $10^5$  number of cycles than HTC16 specimen.

Carbide morphology does have an impact on the mechanical properties of the steels [5, 11]. Conventionally treated (HT) specimens contain primary and secondary carbides, whereas HTC16 specimen contains fine tertiary carbides because cryogenic treatment is accountable for evolution of tertiary carbides. These cryogenically treated (HTC16) specimens indicate moderate distribution of carbides and higher carbide density as compared to HT specimen. The refined carbides lead to an increased fatigue limit of the materials as there would be less dislocation pile up at the finer carbides and the same are difficult to fracture [12, 13]. Figure 14 indicates

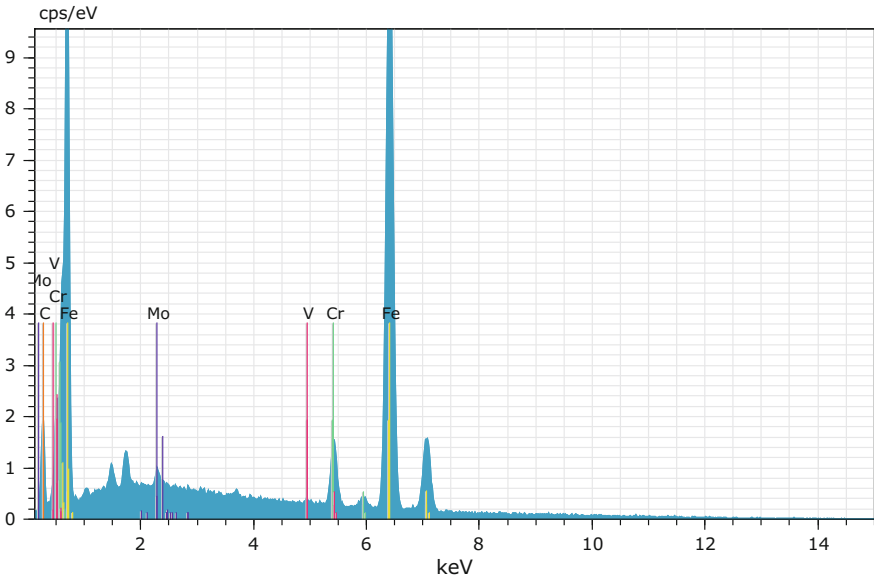
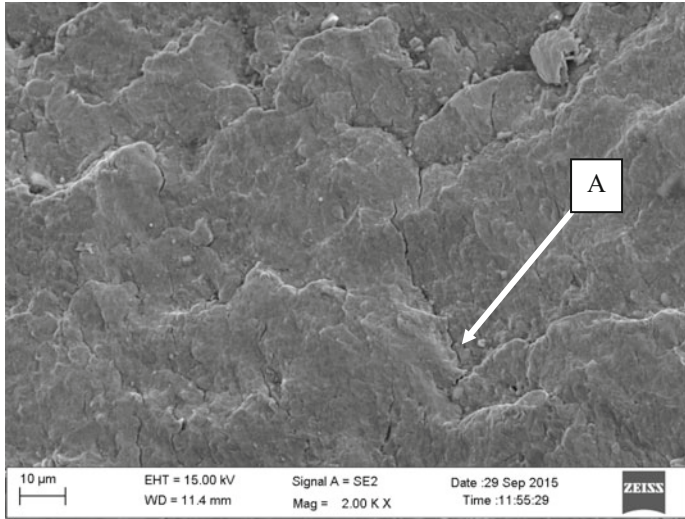


**Fig. 14** SEM fractograph of HTC16 specimen and EDS analysis of carbide particle 'A' which is present in the path of crack propagation and acting as a crack arrester

fractographs and EDS analysis for HTC16 specimen. It indicates the presence of carbide particles in the path of crack, thereby acting as an obstacle for crack propagation subsequently delaying the process of crack propagation and increasing the fatigue limit for cryogenically treated specimens as compared to conventionally treated (HT) specimens.



## 5 Conclusion

On the basis of results obtained for cryogenic treatment of AISI H13 die steel, following conclusions can be drawn.

1. Cryogenic treatment reduces the wear rate of AISI H13 specimens by 51% on account of fine tertiary carbide precipitation. Nucleation and growth phenomenon of carbides act as decisive factors for specimens with less than 16-h and greater than 16-h cryosoaking period, respectively.
2. Fatigue limit of 16-h cryogenically treated specimen has been increased by 25% on account of evolution of fine tertiary carbides, thereby imparting fatigue resistance to crack propagation than that of conventionally hardened and tempered specimens. Increased hardness values in case of cryogenically treated specimens also increase the fatigue crack initiation life, thereby improving the fatigue limit of the material.
3. Fatigue is a surface phenomenon, and decrease in surface roughness has been observed in case of 16-h cryogenically treated steels which may be attributed to precipitation of fine tertiary carbides.

**Acknowledgements** This work is supported under TEQIP project in the Department of Metallurgy and Materials Science, College of Engineering, Pune.

## References

1. Koneshlou M, Asl KM, Komamizadeh F (2011) Effect of cryogenic treatment on microstructure, mechanical and wear behaviour of AISI H13 hot work tool steel. *Cryogenics* 51:55–61
2. Perez M, Belzunce FJ (2015) The effect of cryogenic treatments on the mechanical properties of AISI H13 steel. *Mater Sci Eng A* 624:32–40
3. Meng F (1994) Role of eta-carbide precipitation in the wear resistance improvements of Fe–12–Cr–mo–V–1.4C tool steel by cryogenic treatment. *ISIJ Int* 34(20):205–210
4. Dhokey NB, Hake AR (2013) Instability in wear mechanism and its relevance to microstructural features in cryotreated T42. *Tribology*. W S Maney & Sons Ltd
5. Ebara R (2010) Fatigue crack initiation and propagation behavior of forging die steels. *Int J Fatigue* 32:830–840
6. Fukaura K, Yokoyama Y, Yokoi D, Tsujii N, Ono K (2004) Fatigue of cold-work tool steels: effect of heat treatment and carbide morphology on fatigue crack formation, limit and fracture surface observations. *Metall Mater Trans A* 35A:1289–1300
7. Wei M (2011) Effect of tempering conditions on wear resistance in various wear mechanisms of H13 steel. *Tribol Int* 44:898–905
8. Thamizhmanii S, Hasan S (2013) Surface roughness and tool wear on cryogenic treated CBN insert on titanium and inconel 718 alloy steel. *World Acad Sci Eng Technol* 77:1570–1575
9. Dhokey NB, Hake A, Kadu S, Bhoskar I, Dey GK (2013) Influence of cryoprocessing on mechanism of carbide development in cobalt-bearing high speed steel. *Metall Mater Trans A (ASM Int)*

10. Dhokey NB, Dandwate JV (2012) Study of wear stabilization in cryoprocessed cobalt-based high speed steel. *Trans IIM* 65(4):405–412
11. Mellouli D, Haddara N, Köster A, Ayedi HF (2014) Hardness effect on thermal fatigue damage of hot working tool steels. *Eng Fail Anal* 45:85–95
12. Okuno T (1987) Effect of microstructure on the toughness of hot work tool steels, AISI H13, H10, and H19. *Trans ISIJ* 51–59
13. Baldissera P, Delprete C (2008) Deep cryogenic treatment: a bibliographic review. *Open Mech Eng J* 2:1–11
14. Suh NP (1977) An overview of the delamination theory of wear. *Wear* 44:1–16

# Lakshya: Life Assessment, Extension and Certification

Manu Jain, S. Rajashekar, V. Ashok Rangan and V. Subramanian

**Abstract** Lakshya is a reusable pilot less target aircraft designed and developed by Aeronautical Development Establishment, which is used by all the three services of Indian armed forces. There is a large variation between storage facilities and use pattern of services which has necessitated the life extension of Lakshya beyond the original prescribed life. This has helped services to get maximum utilization of fleet with minimal cost. While extending the life of Lakshya, two factors have been kept in mind: (1) economic viability of the life extension (cost compared to the new aircraft) and (2) safety of operations in the extended life. This study presents the procedure followed in the life extension of Lakshya and lessons learnt during various field experiments. Suggestions for corrective/preventive actions leading to improvement in quality and reliability of the Lakshya are also documented.

**Keywords** UAV · Fuselage · Corrosion · Corrosion fatigue  
Nondestructive inspection (NDI) · Service life testing · Service life assessment

## 1 Introduction

'Lakshya' has undergone more than one hundred developmental flights and hundreds of user flights after induction into the services. It is launched from a zero-length launcher using a booster rocket motor and recovered either over sea or land using parachute.

Performance envelope of UAV reduces with age. In general, its systems and airframe structure performance can be significantly reduced by severe environmental conditions in which the aircraft operates during the service life.

---

M. Jain (✉) · S. Rajashekar · V. Ashok Rangan · V. Subramanian  
ADE, DRDO, New Tippasandra, Bangalore 560075, India  
e-mail: manujain@ade.drdo.in

© Springer Nature Singapore Pte Ltd. 2018  
S. Seetharamu et al. (eds.), *Proceedings of Fatigue, Durability and Fracture Mechanics*, Lecture Notes in Mechanical Engineering, [https://doi.org/10.1007/978-981-10-6002-1\\_20](https://doi.org/10.1007/978-981-10-6002-1_20)

The service life extension programs, for extending the aircraft service life, consist of a process of defining and executing the recommended additional procedures as aircraft monitoring and maintenance with required possible additional constraints and limits for the further aircraft service during the period of extended life, with issuing the appropriate certificate for airworthiness [1].

The primary focus of this study is the experimental NDT methods and preventive maintenance procedures which are used for finding, preventing the effects of corrosion and aging. These experiments and procedures have helped in extending the service life of Lakshya beyond the originally prescribed limit, i.e., calendar life and operational life without compromising on the reliability of operations.

## 2 Structural Design and Operational Life Assessment

### 2.1 Structural Design

Lakshya is similar to the manned aircraft in respect of its aerodynamic behavior and fabrication techniques including standards and specifications used in manufacture. There are certain differences arising out of operational, environmental parameters, and these unique requirements affect the structural design of Lakshya. Lakshya is subjected to high 'g' loads due to booster-assisted launch and parachute-based recovery. The structural loads considered for the design of Lakshya are broadly classified into the following main categories:

- Booster launch loads—11 g during booster motor operation—in  $x$  axis—once in each launch
- Flight maneuvering loads—up to 3 g—lateral plane—twice in each launch
- Loads during parachute recovery phase—16 g—in  $x$  axis—once in each launch
- Lift load of the wings—in  $z$  direction—during flight
- Fuel tank differential pressure loads—2 bar—four times in each launch
- Retrieval and ground handling loads—twice in each launch.

As Lakshya is mainly utilized from the sea shore ranges and recovered in the sea, use of corrosion resistant materials is mandated. Lakshya is required to float over the sea surface for a considerable time to facilitate the retrieval operation; this has a unique design requirement of water tight compartments for flotation and hermetically sealed avionic bay to minimize the sea water ingress. All these factors have been incorporated in the design of Lakshya, and its life was estimated to be 10 sea dunking or 10 calendar year of storage.

## 2.2 *Effects of Operations and Environment on Life of Lakshya*

**Fatigue:** The fatigue behavior leads to the reduction in structural stiffness of the airframe resulting in under-performance and compromise the safety of aircraft. In addition to vibration due to air loads, the airframe is subjected to significant fatigue due to cyclic and impact loads during the launch, cruise and recovery phases. The following joints/brackets are found critical to flight safety [2]:

- Engine mounting bracket—front
- Wing mounting brackets—front and rear
- Tail plane mounting brackets
- Transportation joint
- Parachute mounting bracket—Spider casting
- FEB—MFL joint
- Pylon mounting bracket
- Wing surface, spars and interior.

**Corrosion:** It is the deterioration of a material or its properties due to the reaction of that material with its chemical/saline environment. Corrosion has always been considered as a major factor in aging aircraft maintenance. The combined effect of corrosion and corrosion fatigue plays a significant role in damaging the aircraft structure.

In case of sea dunking, sea water ingresses into various modules of the aircraft such as fuselage, wing, tail plane, and this deteriorates the electrical points, avionics bay, control surfaces, actuation system and corrodes the exposed structural elements.

Effects of sea water ingress and saline environment [3].

- Corrosion inside the fuel tank
- Damage to the fuel tank ducts
- Damage the aluminum alloy end strip reinforced in the wing (GFRP)
- Stress corrosion at wing mounting brackets
- Damage the control surface (at self-plugging rivets and at end ribs)
- Control surface skin cracked due to stress corrosion
- De riveting aileron skin with stainless-steel end rib
- Galvanic corrosion on silver-coated copper wires.

Steel and aluminum alloys get corroded because of the environmental conditions like temperature, humidity, UV radiation, sea water, pollutants. This leads to corrosion and is aggravated by loads/aging which severely affects the integrity and safety of UAV structure.

### **2.3 Effect on Life of Lakshya**

All these operational and environmental factors lead to life being limited. Original life of Lakshya is defined as 10 years of storage or 10 sea dunking whichever is earlier. Fatigue combined with corrosion severely affects the structural integrity of the airframe and gradually degrades the life and performance of the aircraft over time. In general, the corrosion damage is a function of the calendar age of the aircraft or structure and the fatigue crack growth will depend upon the applied load spectrum. The effect of operational and environmental conditions on the aging of aircraft cannot be reversed, but this can be substantially reduced by taking proper preventive and corrective measures.

## **3 Service Life Extension Criteria**

Lakshya spends less than 0.1% of its total life flying. The usage patterns of services are quite different. In some cases, full flying life is consumed within 2 years and it is not advisable to discard the airframe as it still have a lot of residual calendar life. In other cases, full calendar life is completed without even reaching half of operational life and it is economically prudent to life extend the aircraft so that it can be utilized to its full potential.

Lakshya's life extension is done after the original prescribed life of 10 sea dunking/10 years of storage. This life extension is termed as major life extension. In this, Lakshya is brought to the base and stripped open. A thorough inspection is carried out and damages/corrosion is documented. A comprehensive plan for repair/replacement of parts is followed. Lakshya is subjected to all the base integration checks (mechanical and electrical), and if successful it is cleared for further 5 launches/2 years whichever is earlier.

After completion of extended life, i.e., 15 launches/12 years of storage, only minor life extension is carried out at the site. In this, inspection and damage repair/replacement of parts are done on the user premises and a subset of checks are used for clearing the Lakshya for further 2 launches/6 months whichever is earlier. Beyond this, life extension is not recommended as many electrical LRUs and engine also complete their life cycle which results in a high cost of retrofitting the UAV.

## **4 Economy of Life Extension**

As shown in Fig. 1, the cost of life extension is a fraction of the new UAV cost. If UAV goes through the full life extension cycle, i.e., one major and 3 minor, it results in reduced operational costs as shown in Fig. 2. Total savings are about 60% of a brand new UAV cost. Life extension procedure for UAV is simple and efficient which results in time saving compared to fabrication of a new UAV and better operationalization of fleet.

**Fig. 1** Original and life extension cost in %

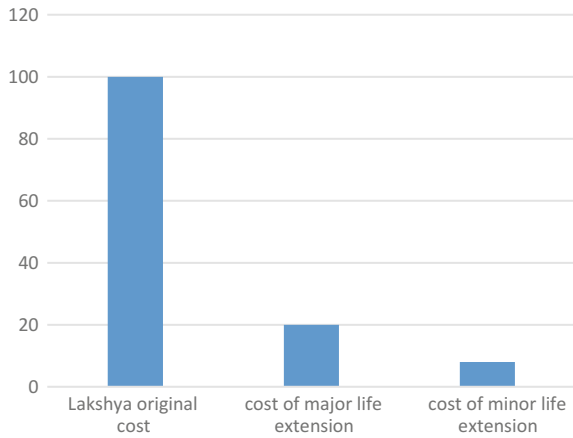
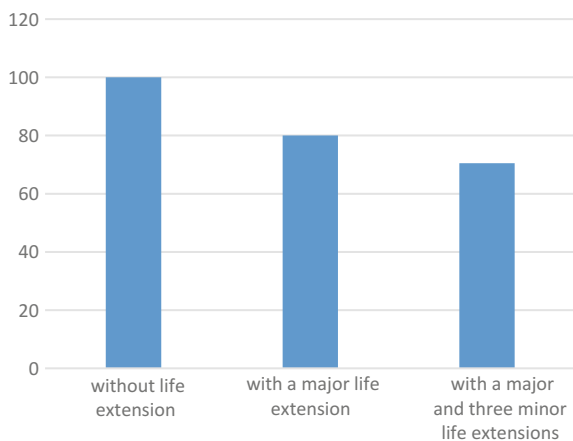


**Fig. 2** % cost per launch



## 5 Service Life Extension Procedure

A detailed methodology followed for Lakshya service life extension is given in the form of a flow chart as shown in Fig. 3 [2].

Before life extension, the followings are taken into account.

- History of use and life consumed
- Repairs during service life and concessions provided
- Availability of parts (obsolescence)
- Cost of the new equipment (economy of life extension)
- Service log book with detailed maintenance carried out.

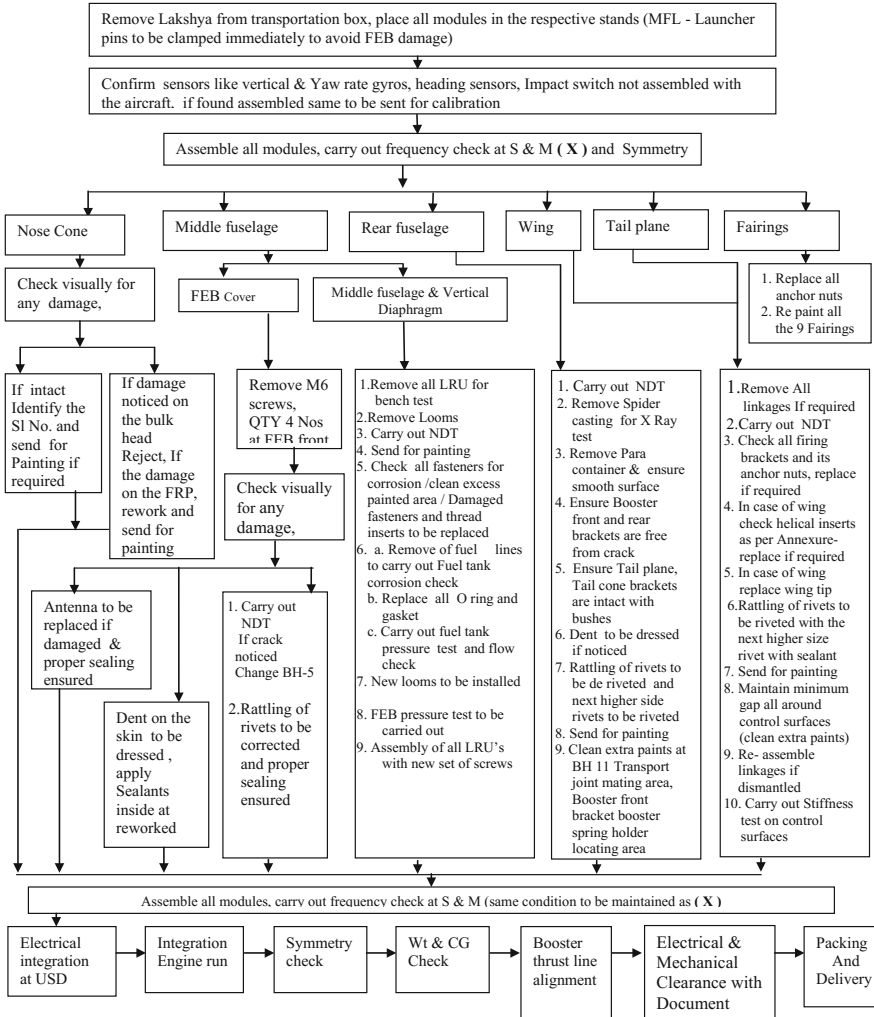


Fig. 3 Life extension procedure flow chart for Lakshya [2]

### 5.1 Stiffness and Integrity/Health Monitoring of Airframe [4]

The first step in the life extension of aircraft is the stiffness and integrity/health monitoring of the airframe. This is carried out by frequency measurement by mechanical impulse response test. The airframe alone is placed on the trolley by resting the trolley pins on the bungee cord to isolate trolley frequencies.

The stiffness and integrity—Health monitoring checks of the airframe are carried out by frequency measurement by vibration impulse response test. The airframe



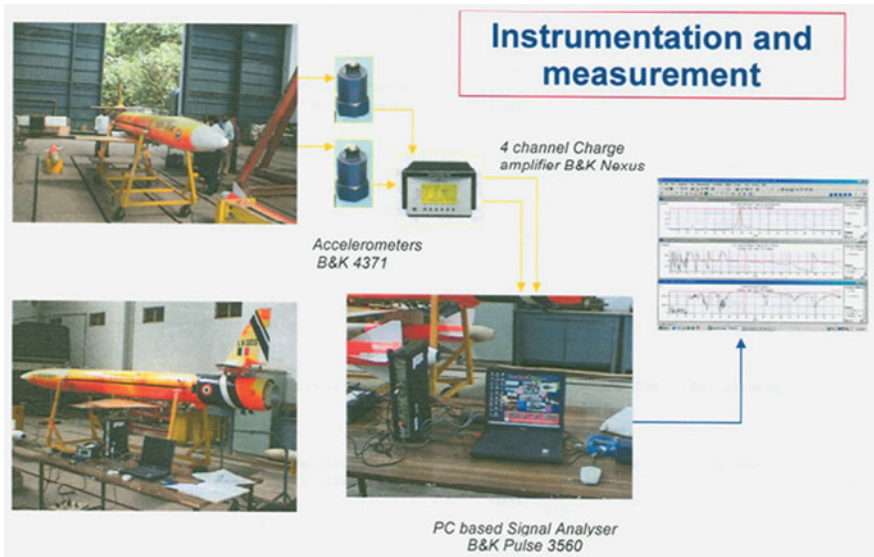


**Fig. 4** Instrumentation and frequency measurement setup

alone is placed on the trolley by resting the trolley pins on the bungee cord to isolate trolley frequencies.

A PC-based signal analyzer type B&K LANXI 3050-B-040 is employed for signal acquisition and analysis. Accelerometer type B&K ICP 4513 sensitivity 9.8 mv/g is used. Two numbers of sensors are used for the measurements. B&K signal analyzer type 3050-B-040 settings used are 800 lines, 100 Hz, CCLD,  $\Delta f$  0.125 Hz,  $\Delta t$  3.906  $\mu$ s,  $t = 8$  s 8 avg and  $T = 64$  s. Measurement and analysis type used is time domain and frequency domain—cross-spectrum magnitude, phase and coherence functions.

Figure 4 shows the frequency measurement setup used during life extension of Lakshya airframe.

Table 1 shows the defined frequencies for Lakshya airframe, and Table 2 shows the measured frequencies during life extension. The comparison study of the test results shows less than 1.5% deviations on wing and tail plane and 2.73% deviation on the fuselage. The allowable limit is 5.0%.

**Table 1** Typical Lakshya airframe defined frequencies

Structure	Magnitude (Hz)
Wing	28–31
Fuselage	40–47
Horizontal tail	46–55
Vertical tail	45–53

### 5.2 NDT of Critical Components

Second step in life extension is to examine the critical components/joints crucial for the operation and flight safety as identified in Sect. 2.1. After visual examination, these components are subjected to inspection and NDT to ascertain their integrity. Methods used are:

**Visual examination:** This is conducted on all critical airframe parts with the help of a magnifier. Glass magnifier and optical microscope are used for the assessment of the corrosion depth.

**Endoscope visual examination:** This is carried out for the non-accessible parts like inner wing areas and fuel tanks. Figure 5 shows the pitting damage inside the fuel tank due to corrosion.

**Liquid dye penetration examination** which is one of the most popular nondestructive examination (NDE) methods in the industry used to examine the surface-level cracks and damages of the critical areas. Some of the parts tested with dye penetration test are shown in Figs. 6 and 7. This method is more economical, versatile and easy to inspect the parts with complex shapes and requires minimal training when compared to other NDT methods.

**Radiography** is another nondestructive test which is carried out to examine the internal cracks of the bulk heads, spider castings and critical parts to rule out any internal cracks or damages as shown in Fig. 8.

**Table 2** Comparison of measured airframe frequencies of Lakshya (test case)

S. No.	Airframe flight No.	Structure frequencies, Hz			
		Wing (Hz)	Fuselage (Hz)	Tail plane	
				HT (Hz)	VT (Hz)
1	After 10 flights	29.50	41.75	49.25	47.75
2	After 15 flights	29.38	41.50	48.75	46.38
3	After 17 flights	29.13	41.38	48.50	46.38
4	After 19 flights	29.75	40.25	49.88	46.88

The coherence value for all these measurements are >0.95

**Fig. 5** Internal view of fuel tank showing pitting using endoscope/borescope



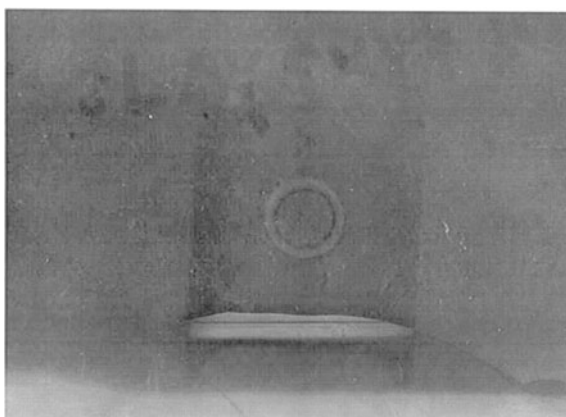
**Fig. 6** Liquid penetration test of tail plane mounting brackets



**Fig. 7** Liquid penetration test of wing mounting bracket



**Fig. 8** Radiography of fuel tank bulk head showing leak



### 5.3 *Corrective/Preventive Actions and Operational Readiness*

In the third step, a component found damaged during NDT is accessed and repaired, rectified or replaced based on the severity of fault, criticality of the part. Then preventive coating, painting and reassembly of airframe are completed. After this the airframe is again subjected to all the mandatory checks, i.e., leak test, control surface stiffness test and frequency checks. If all these test results are satisfactory, then airframe is cleared for further launches. The life-extended airframe is then electrically integrated and used.

## 6 Corrosion Due to Sea Water Ingress and Storage

A major part of Lakshya life is reduced due to corrosive environment in which it is operated. If the sea water ingresses during recovery and is not removed promptly, it slowly corrodes the components as shown in Fig. 9. The most prone area for sea water ingress is wing and tail interior (due to ducts and tooling holes) and fuel tank. These are hard to access and removing water from them is very difficult. This has resulted in local bulging and change of aerodynamic profile of wing as shown in Fig. 10.

### 6.1 *Detection, Prevention and Repair*

A detailed procedure has been formulated for refurbishment of Lakshya after every recovery. Adherence to this procedure has resulted in the low water ingress and less corrosion. A complete check of all fuel/smoke oil tanks is done every two years for detection of pitting. Any localized damage is repaired and treated with protective coatings and paints. Figures 11, 12, 13 and 14 show the damaged and repaired parts.

**Fig. 9** Corrosion of electrical wires

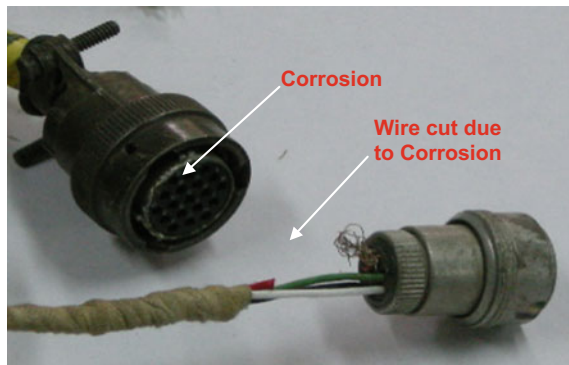


**Fig. 10** Change in the wing profile due to local bulging



**Fig. 11** Corrosion at wing and control surfaces



**6.2 Some Design Lessons Learnt from Sea Dunking of Lakshya are as Follows [3]**

- Fuel tank corrosion occurred due to ingress of sea water in the threaded hole, proper wall thickness to be maintained in the machined bulk head
- Sealants to be used to avoid ingress of sea water at wing and control surfaces during fabrication



**Fig. 12** Wing after repair and painting

**Fig. 13** Local indentation at fuel tank



**Fig. 14** Fuel tank after repair



- All self-plugging rivets to be impregnated into the bonding resin before riveting
- Before painting all, skin joints are to be filled with resin
- Tool marking/dents/deep scratches to be avoided, in turn, will prevent the initiation of stress corrosion
- Use nonmetallic, nonabsorbent insulators between the dissimilar metals to prevent galvanic corrosion
- Always avoid connecting small anodes to large cathodes
- Painting a galvanic couple can also be helpful in reducing the corrosion rate
- Use of protection compound and fuel mixture to avoid fuel tank corrosion. Fuel tank is kept in inhabited condition during long storage periods.

All these lessons have been incorporated in the series production of Lakshya. These have helped in prevention of corrosion to a large extent.

## 7 Certification

OEM's certification is mandatory for airworthiness of the aircraft which has completed the specified number of sea dunking before clearing the aircraft for integration and testing. The servicing team follows the life extension procedures in the presence of the resident inspector. After the successful completion of the repair/replacement procedure, certification is issued by the OEM. Flight data and maintenance records are audited periodically to ensure the reliability of operations. A re-certification program with a short training module is implemented to keep the knowledge and procedures followed by crew of Lakshya squadrons up to date.

## 8 Conclusion

The process of aircraft aging, structural and performance deterioration cannot be stopped, but it could be rather minimized using several practical approaches which include

- Use of analysis to identify the critical components and joint which are subjected to fatigue loads
- Quality control and preventive measures during production
- Following the maintenance schedules strictly and improving the crew awareness
- Implementing the lessons learnt by design changes.

The life extension and certification of Lakshya airframe are carried out by the established procedures under the strict supervision and inspection by quality control team. The life-extended aircrafts have successfully completed more than the designed flight sorties. This could be achieved by periodic and systematic maintenance of the aircraft. The life extension of aircrafts has proved that a considerable

amount of cost and time can be saved to the user. Many Lakshyas have achieved the life of 20 launches and more. Life extension program has also achieved the better launch, mission and recovery reliability for Lakshya fleet in turn enhancing the operational capability of squadrons.

**Acknowledgements** The authors thank Director ADE for his continuous encouragement for quality improvement and permitting to present this paper. The authors also acknowledge Shri V. Dakshina Murthy of Quality Assurance Division, ADE and support staff from assembly for valuable guidance and encouragement in writing this paper.

## References

1. Maksimović Stevan, Vasić Zoran, Došić Radoljub (2015) Service life extension program for aircraft structures. *Scientific Technical Review* 65(3):46–54
2. Singh SK, Jain M, Dakshina Murthy V, Ashok Rangan V (2009) Lakshya life extension procedure. Technical procedure document
3. Dakshina Murthy V, Swar SC, Kumarswamy ML (2008) Lesson learnt from Sea dunking of unmanned aerial vehicles. ReQUEST
4. Jain M, Rajashekhar S, Subramanian V, Ashok Rangan V (2009–2016) Lakshya life extension reports. Field trial reports



# Creep–Fatigue Damage Evaluation of 2.25Cr-1Mo Steel in Process Reactor Using ASME-NH Code Methodology

Sagar R. Dukare and Nilesh R. Raykar

**Abstract** Critical equipment of nuclear power plants and petrochemical industries is sometimes subjected to both creep and fatigue loading simultaneously. Under combined creep–fatigue loading, the creep deformation affects the fatigue behavior of the material depending on the relative duration of stress relaxation due to creep within service life. In the present paper, evaluation of creep and fatigue damage is carried out for a process reactor using elastic analysis method of ASME-NH code. The reactor material is 2.25Cr-1Mo steel. The stress evaluations are carried out at outlet nozzle where stresses are observed to be maximum. Effect of three parameters, that is, the maximum hold temperature, the duration of hold time at highest temperature and the rate of temperature change on combined creep–fatigue damage, is studied. This work provides guidelines for performing creep–fatigue analysis for similar pressure components.

**Keywords** ASME-NH • Creep–fatigue interaction • Creep ratcheting  
2.25Cr-1Mo steel

## Nomenclature

$D$	Total creep–fatigue damage
$K$	Local geometric concentration factor
$K_e$	Stress ratio factor at yield
$K_r$	Factor for reduction in extreme fiber bending stress due to effect of creep
$K_v$	Multiaxial plasticity and Poisson ratio adjustment factor
$P_b$	Primary bending equivalent stress
$P_L$	Local primary membrane equivalent stress
$P_m$	Primary membrane equivalent stress
$(Q_R)_{\max}$	Maximum secondary stress range

---

S.R. Dukare (✉) · N.R. Raykar  
Mechanical Engineering Department, Sardar Patel College of Engineering, Mumbai, India  
e-mail: sagardukare27@gmail.com

N.R. Raykar  
e-mail: Nilesh\_raykar@spce.ac.in

$S^*, \bar{S}$	Stress indicators
$S_{\text{alt}}$	Alternating stress intensity
$S_j$	Initial stress
$S_m$	Allowable stress
$S_{\text{rH}}$	Hot relaxation strength
$S_t$	Temperature and time-dependent stress intensity limit
$S_y$	Yield strength of material
$X$	Primary stress parameter
$Y$	Secondary stress parameter
$Z$	Dimensionless effective creep stress parameter
$\Delta \mathcal{E}_{\text{max}}$	Maximum equivalent strain range
$\Delta \mathcal{E}_{\text{mod}}$	Modified maximum equivalent strain range
$\Delta \mathcal{E}_c$	Creep strain increment
$\mathcal{E}_t$	Total strain range
$\sigma_c$	Effective creep stress
$\Delta t$	Duration of time interval

## 1 Introduction

A significant number of equipments experience fluctuating loads combined with high temperatures in the creep range as in case of steam generating systems of the power plant and reactors in petrochemical industries. For evaluation of damage and life prediction of such equipment, the effects of creep, fatigue and their interaction should be considered [1]. In such scenario, components are subjected to cyclic strains that are produced thermally and/or mechanically and the fatigue damage occurs under thermal strains which lead to crack initiation and subsequent crack growth [2]. The creep phenomenon has an important influence on the fatigue damage process.

Under cyclic loading, the creep deformations affect the fatigue response of the material depending on the relative duration through which creep deformations relax the cyclic stress. In systems like nuclear pressure vessels, high-pressure boilers, steam pipelines, nuclear reactor fuel cladding, heat exchangers, such effects are important at the design stage. The temperature loads are mostly accompanied by pressure loads which vary because of different operating conditions of underlying process [3].

Below certain temperatures, for a given material, the problem of creep is not of much concern and the stress and fatigue limits may be independently checked to assure the structural design integrity [4]. But at higher temperatures, the time-dependent creep and stress rupture effects become more significant and can no longer be neglected. The resulting extension of an involved component may

eventually produce a troublesome loss of dimensional tolerance and may ultimately lead to catastrophic rupture.

At elevated temperatures, the parameters related to thermal loading patterns such as hold time, hold temperature and the rate of temperature change are important in calculating inelastic strain and creep–fatigue damages. The effect of above-mentioned parameters should be included in the design of a system with creep service for safe and long-life operation.

The fatigue design of vessels operating below the creep regime itself is complex. One can fully appreciate difficulties inherent in the design of such vessels additionally subjected to elevated temperature service. At elevated temperatures, the yield strength of the material reduces significantly increasing plastic strain concentration effects which further complicates the damage evaluation. Creep rupture is a potential failure mode at elevated temperatures. The ratio of the time at a critical stress level to the time to rupture at the same temperature and stress level is commonly used as a measure of creep rupture damage.

The complex nature of cyclic creep–fatigue evolution has been studied through different perspectives by many researchers [2, 5, 6]. Some methods for evaluating the life of a component at elevated temperature service are developed since then such as RCC-MR code [7], hysteresis energy [8], ASME-NH code [9], strain range partition [10] and continuum damage mechanics [11, 12]. Aoto et al. [13] have explained creep–fatigue evaluation of normalized and tempered modified 9Cr-1Mo steel using conventional ductility exhaustion concept. Fournier et al. [6] conducted cyclic tests with tensile holding periods in air at 823 K on a modified 9Cr-1Mo martensitic steel, and effect of hold time at maximum load was studied. The dramatic lifetime reduction due to holding periods is highlighted and quantified by them. Koo and Yoo [4] have carried out an elevated temperature design of KALIMER reactor of 316 SS for creep and stress rupture effects with creep damage evaluation at different temperatures. It has been observed that very few researchers have carried out a combined creep–fatigue analysis and simultaneously studied effects of hold time and hold temperature for 2.25Cr-1Mo low-alloy steel.

The ASME Boiler and Pressure Vessel (B&PV) code Section III, Division 1, subsection NH [9] provides in detail the rules for elevated temperature design with creep–fatigue interaction. It includes both elastic and inelastic analysis methods for the evaluation. The use of inelastic analysis would seem natural method for pressure vessels at elevated temperature service. However, use of elastic analysis has been observed to be more practical and reliable in design applications [5].

The work presented here builds on the creep and fatigue damage evaluation of a pilot plant process reactor of 2.25Cr-1Mo steel carried out by Gurumurthy et al. [5]. In the present paper, the creep–fatigue damage investigation additionally includes effects of hold time, hold temperature and the rate of temperature change.

## 2 Creep–Fatigue Evaluation of a Process Reactor Outlet Nozzle

### 2.1 Main Design Features

In Fig. 1, the outline of pilot plant process reactor under investigation is shown. The material of construction is 2.25Cr-1Mo low-alloy steel. The discontinuity regions of a reactor are of specific interest. The prominent regions are inlet nozzle to top head junction, outlet nozzle to bottom head junction, quench nozzle to shell junction, catalyst nozzle to shell junction and skirt shell head junction. Based on the preliminary evaluation of geometry and loading conditions, the nozzle junctions at inlet and outlet were identified as possible candidates for further study. Initially, both the inlet and outlet nozzle junctions were analyzed separately to establish critical region for detailed investigation. Creep–fatigue damage is evaluated using elastic analysis method of ASME-NH for given operating conditions and load cycles.

**Fig. 1** Outline of pilot plant process reactor [5]

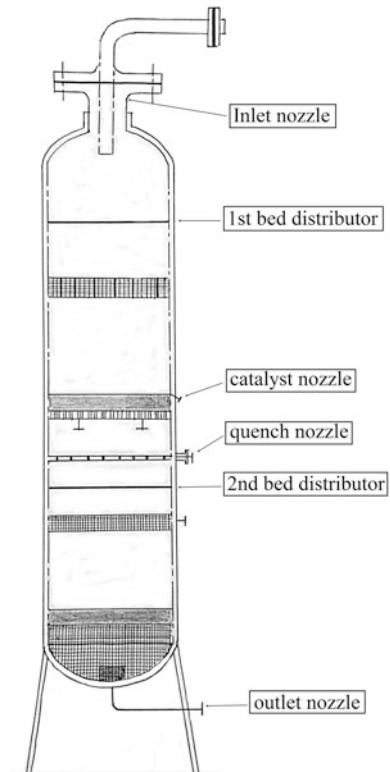


**Table 1** Design data of process reactor

	Items	Inside Dia. (mm)	Outside Dia. (mm)	Thickness (mm)	Material	Remark
1	Reactor shell (top)	1000	–	30	2.25Cr-1Mo	Main containment vessel
	Reactor shell (bottom)			36		
2	Ellipsoidal head (top portion)	–	–	30	2.25Cr-1Mo	–
3	Ellipsoidal head (bottom portion)	–	–	36	2.25Cr-1Mo	–
4	Inlet nozzle	480	710	14	2.25Cr-1Mo	Self-reinforced
5	Outlet nozzle	299	419	10	2.25Cr-1Mo	Self-reinforced

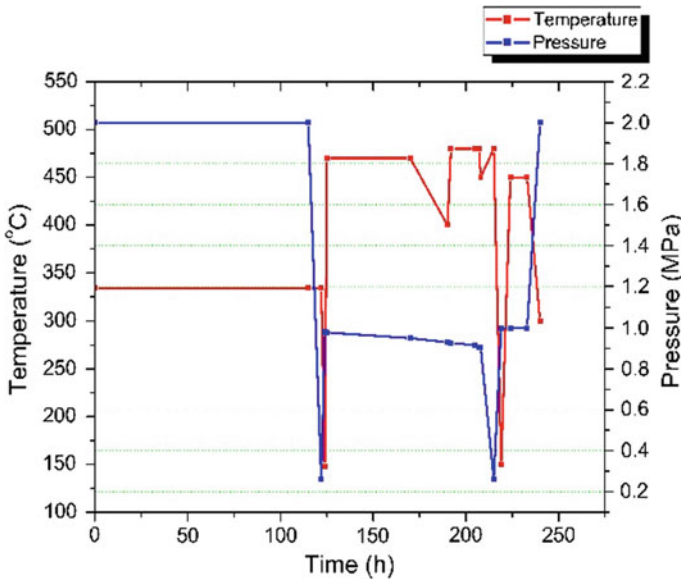


**Fig. 2** Operating pressure and temperature load cycle [5]

The reactor is designed as per ASME Section VIII, Division 1 [14] which has rules for construction of pressure vessels. The thickness calculations of reactor shell, head and nozzle were carried out using the same code.

The design data for the reactor are given in Table 1. The design temperature is 550 °C, and design pressure is 2.6 MPa. The typical operating pressure and temperature cycle is shown in Fig. 2. The total pressure–temperature load cycle time is 240 hours out of which the duration where the temperature is above creep range is 115 h. The design life of reactor is 20 years which corresponds to 730 load cycles.

## 2.2 Finite Element Analysis

A coupled transient thermal and structural analysis was carried out using analysis software ANSYS 14.5 [15] with axisymmetric 2D elements. All temperature-dependent properties of material 2.25Cr-1Mo were taken from ASME Section II, Part D [16]. The finite element analysis (FEA) models of inlet and outlet nozzle are shown in Fig. 3. The figure also shows stress evaluation point and stress classification line (SCL) along which linearized stresses were calculated for adopting ASME method.

An identical mesh was used for both transient thermal and transient structural analyses for direct mapping of nodal temperatures. First, a transient thermal analysis was carried out where a heat transfer coefficient of  $2000 \text{ W/m}^2 \text{ }^\circ\text{C}$  was applied on the inner surfaces of process reactor. A heat transfer coefficient of  $50 \text{ W/m}^2 \text{ }^\circ\text{C}$  was applied on the outside surface which accounts for the effect of both external thermal insulation and ambient air. The analysis was carried out for complete cycle duration, that is, for 240 h with 15 intermediate load steps. The results of transient thermal analysis of inlet and outlet nozzle are shown in Fig. 4.

Once the heat transfer analysis was over, the temperature distribution was mapped on a structural model for stress analysis. In the structural model, the reactor shell end nodes were fixed in all directions except in radial direction. Internal pressure and nozzle axial load (longitudinal stresses at nozzle neck) were applied on appropriate surfaces. The time steps in both thermal and structural analysis were kept same. The von Mises stress distribution for inlet and outlet nozzle is shown in Fig. 5. The stresses in outlet nozzle to bottom head junction were observed to be higher than those in inlet nozzle junction. Further creep–fatigue damage evaluation was performed only on outlet nozzle.

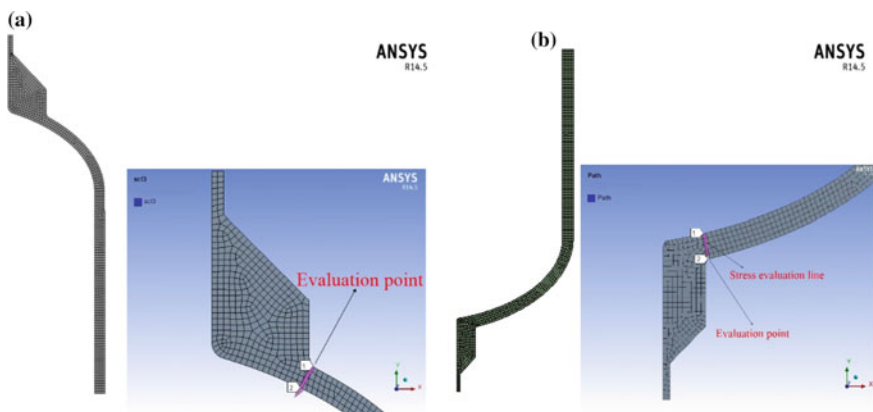


Fig. 3 Finite element model for **a** inlet nozzle and **b** outlet nozzle

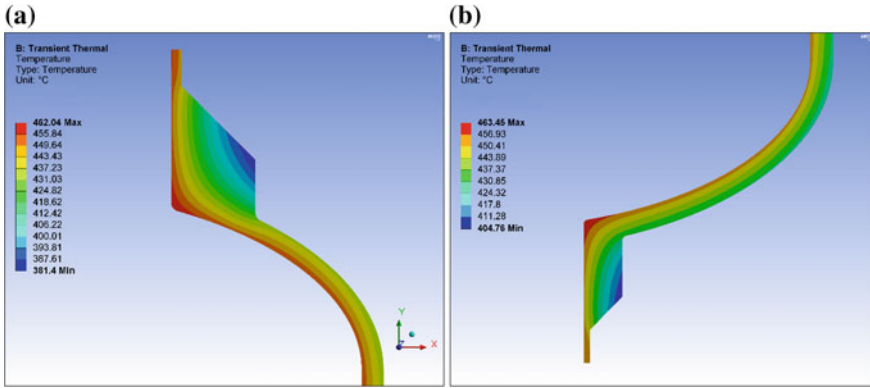


Fig. 4 Temperature distribution **a** inlet nozzle and **b** outlet nozzle at 124 h

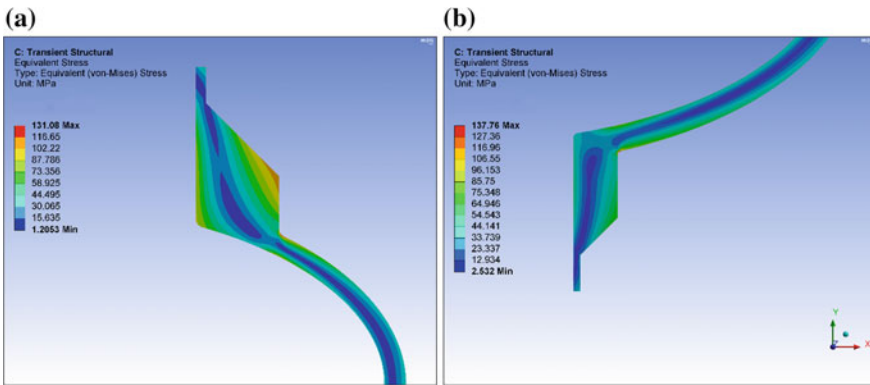


Fig. 5 von Mises stress distribution **a** inlet nozzle and **b** outlet nozzle at 124 h

### 2.3 ASME-NH Elastic Analysis of 2.25Cr-1Mo Process Reactor Outlet Nozzle

The flowchart in Appendix outlines the procedure followed in the evaluation of creep and fatigue damage as per ASME-NH. The stress distribution obtained during analysis of outlet nozzle was linearized to obtain membrane and bending stresses as per ASME section VIII, Division 2 [17]. These were used to calculate the equivalent stresses based on the von Mises criterion. The linearized stresses were classified in accordance with NH-3217. ASME Section III-NH requires the check of elastic ratcheting rules of T-1320 or T-1330. To satisfy the strain limits by elastic analysis method, the rules of NH-T-1320 (Test No. A-2) were followed. Table 2 shows the strain limit check carried out for the outlet nozzle.

Secondary stresses with elastic follow-up (i.e., pressure-induced membrane and bending stresses and thermally induced membrane stresses) were classified as

**Table 2** Strain limit check for outlet nozzle

Parameter	Values
$(P_L + P_b/K_t)_{\max}$	47.09
$(Q_R)_{\max}$	48.08
$S_y$ (MPa)	182
$X = (P_L + P_b/K_t)_{\max}/(S_y)$	0.258
$Y = (Q_R)_{\max}/(S_y)$	0.264
$X + Y (<1)$	0.522 < 1 (criteria satisfied)

**Table 3** Parameters for total strain range calculation

Maximum metal temperature ( $^{\circ}\text{C}$ )	480
Cycle duration (h)	240
Time duration above the creep range (h)	115
Number of cycles ( $n$ )	730
Alternating stress, $S_{\text{alt}}$ (MPa)	35.65
Initial stress, $S_i$ (MPa)	183
Maximum elastic strain range, $\Delta\mathcal{E}_{\max}$ (%)	0.0245
Equivalent stress concentration factor, K	1.632
Modified strain range, $\Delta\mathcal{E}_{\text{mod}}$ (%)	0.0425
Stress ratio factor at yield, $K_e$	1.0
Creep strain increment, $\Delta\mathcal{E}_c$ (%)	0.0382
Total strain range, $\mathcal{E}_t$ (%)	0.1048

primary stresses for applying the corresponding rules. Total strain range was calculated using NH-T-1432. The parameters required for total strain range calculation are shown in Table 3.

### 3 Results and Discussion

#### 3.1 Fatigue Damage

Fatigue damage is evaluated as the ratio of the applied number of cycles ( $n$ ) to the number of allowable design cycles ( $N_d$ ) at a design fatigue strain range. To obtain the number of allowable cycles ( $N_d$ ), total strain range,  $\mathcal{E}_t$ , was calculated as per NH-T-1432. Table 1420-1D of ASME-NH-III gives the total number of allowable design cycles at a given strain range and for a given temperature. From Table NH-T-1420-1D, the value of  $N_d$  for calculated total strain range  $\mathcal{E}_t$  (Table 3) is  $10^6$  cycles. As the evaluation point (Fig. 3) is in the vicinity of the weld ( $\pm 3$  times the thickness to either side of the weld centerline), reduced values of the allowable number of design cycles  $N_d$  and the allowable time duration  $T_d$  were used for the creep-fatigue evaluation (NH-T-1400) as per NH-T-1715. According to this, the value of the allowable number of design cycles ( $N_d$ ) is one-half the value permitted for parent material, that is,  $5 \times 10^5$  cycles. The calculated fatigue damage is 0.00146.



### 3.2 Creep Damage and Combined Creep–Fatigue Damage

The basis for calculating creep damage is to generate stress relaxation time history. The stress relaxation was evaluated at a constant hold temperature of 480 °C with the initial stress level  $S_j$  equal to 183 MPa. As  $\epsilon_r$  was less than  $3 \bar{S}_m/E$ , a single relaxation cycle was generated (NH-T-1433) for entire design life, that is, 730 cycles (83,950 h). The damage evaluation was done at the evaluation point (Fig. 3) near outside corner of a nozzle to head junction. The stress relaxation time history (Fig. 6) was obtained using isochronous stress–strain curve NH-T-1800-D-5.

The weld strength reduction factors as per NH-T-1715 are considered for calculating allowable time duration  $T_d$ . In this case, the weld strength reduction factor is 1.0. For acceptance, the creep and fatigue damage shall satisfy the following linear damage rule (NH-T-1400):

$$\sum \left( \frac{n}{N_d} \right)_j + \sum \left( \frac{\Delta T}{T_d} \right)_k < D \tag{1}$$

Figure 7 shows built-up of cumulative creep damage over entire design life. The cumulative creep damage at the end of design life of 730 cycles is calculated as 0.4127. Table 4 presents the creep and fatigue damage factors at 480 °C and hold time of 115 h.

It is observed that the creep damage is larger than fatigue damage, i.e., the failure is creep dominated. The combined effect of fatigue and creep was evaluated as per Eq. (1). The total damage is calculated as 0.4142 which is less than 1.0 and hence is acceptable. The fatigue and creep damage combination point is located over the creep–fatigue interaction envelop of 2.25Cr-1Mo (NH-T-1420-2) and is observed to be within the envelope and hence satisfying the design criterion.

**Fig. 6** Stress relaxation time history

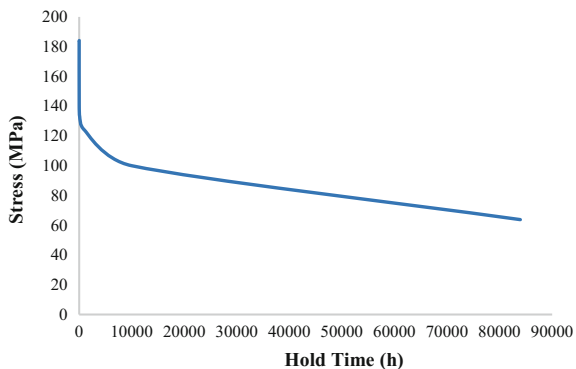


**Fig. 7** Cumulative creep damage

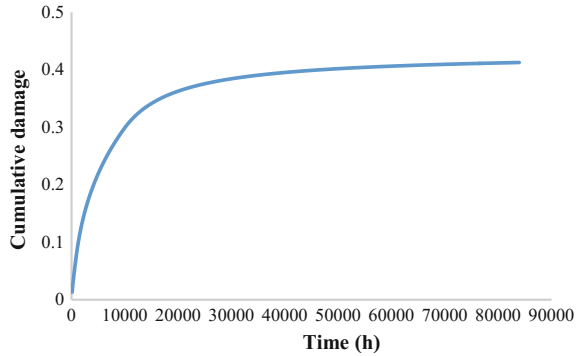


**Table 4** Creep–fatigue damage factors at 480 °C and hold time of 115 h

Parameter	Outlet nozzle
Fatigue damage	0.00146
Creep damage	0.4127
Total damage factor	0.4142

### 3.3 Effect of Hold Time, Hold Temperature and Rate of Temperature Change on Creep–Fatigue Damage

Three specific investigations have been performed in this study to investigate the effects of: hold time, hold temperature and rate of temperature change. The base analysis described till here is carried out at 480 °C. Fifteen cases (Table 5) were analyzed for a combination of three hold temperatures 400, 480 and 540 °C and five hold times 10, 25, 55, 85 and 115 h. In each case, the pressure cycle and other parameters were unchanged. The effect of hold time on combined creep–fatigue

**Table 5** Analysis cases and results of combined creep–fatigue damage

Case number	Temperature (°C)	Hold time (h)	Fatigue damage	Creep damage	Combined damage (<1)
1	400	115	0.00146	0.00246	0.0039
2		85		0.00193	0.0033
3		55		0.00139	0.0028
4		25		0.0008	0.0022
5		10		0.00041	0.0018
6	480	115	0.00146	0.4127	0.4142
7		85		0.409	0.4104
8		55		0.399	0.4004
9		25		0.363	0.3644
10		10		0.268	0.2695

(continued)

**Table 5** (continued)

Case number	Temperature (°C)	Hold time (h)	Fatigue damage	Creep damage	Combined damage (<1)
11	540	115	0.00146	0.738	0.7394
12		85		0.707	0.7084
13		55		0.660	0.6614
14		25		0.580	0.5814
15		10		0.486	0.4874

**Fig. 8** Combined damage at 400 °C (cases 1–5)

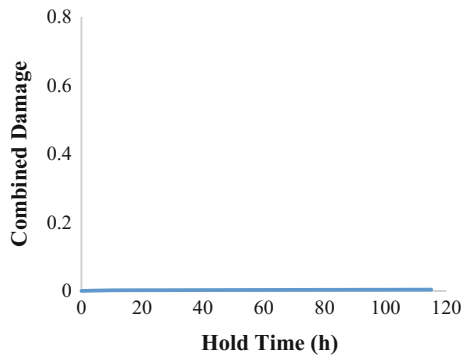
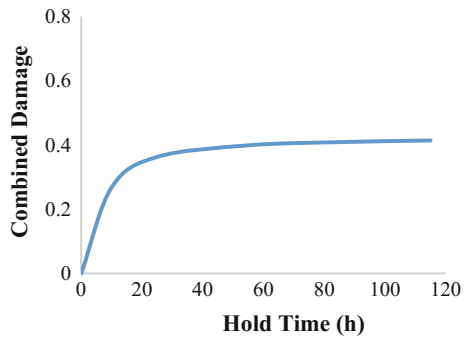


**Fig. 9** Combined damage at 480 °C (cases 6–10)



damage at 400, 480 and 540 °C is shown in Table 5 and in Figs. 8, 9 and 10, respectively. Figure 11 presents the effect of a change in hold temperature on combined creep–fatigue damage at a fixed hold time of 115 h.

The effect of rate of temperature change on creep–fatigue damage was investigated by changing the time duration of temperature ramp within operating temperature cycle (Fig. 2) at 124 h from original 2 to 1 and 0.5 h. Table 6 shows the values of total strain range and combined creep–fatigue damage obtained for

**Fig. 10** Combined damage at 540 °C (cases 11–15)

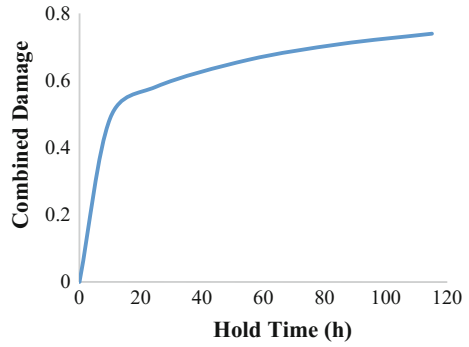


**Fig. 11** Effect of hold temperature at hold time of 115 h (cases 1, 6 and 11)

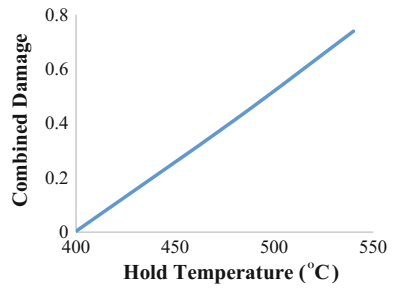


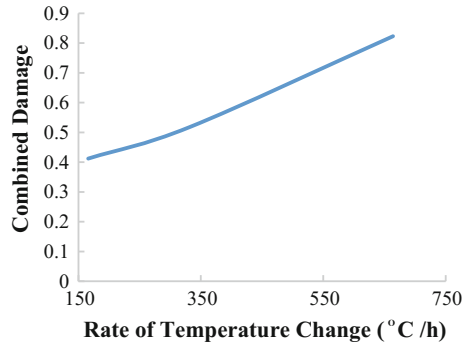
**Table 6** Effect of rate of temperature change

Duration of temperature ramp (h)	Rate of temperature change (°C/h)	Total strain range ( $\epsilon_T$ ) %	Combined damage
2	166	0.1048	0.4142
1	332	0.1051	0.518
0.5	664	0.1286	0.823

different rates of temperature change. The variation of creep–fatigue damage with respect to rate of temperature change is shown in Fig. 12.

As the rate of temperature change increases, the thermal gradient and hence the thermal stresses increase across the critical section of nozzle junction. Accordingly, the creep–fatigue damage increases almost linearly with rate of temperature change (Fig. 12).

**Fig. 12** Rate of temperature change versus combined damage



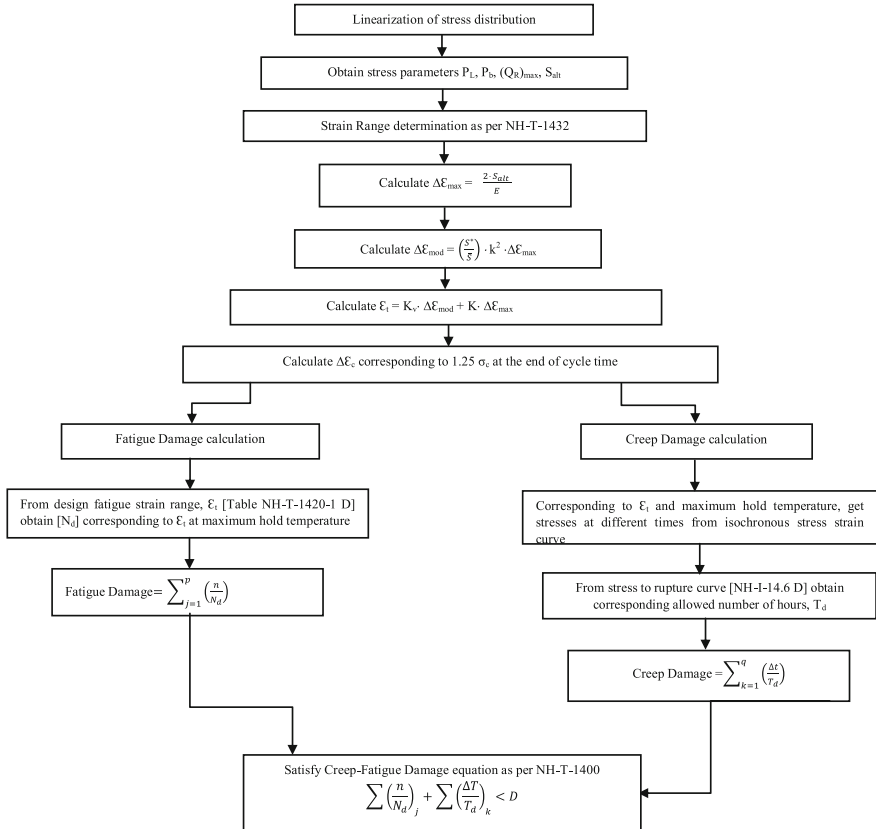
## 4 Conclusions

A combined creep–fatigue analysis has been successfully carried out for a pressure vessel component undergoing both pressure and thermal cyclic loading in the creep range using elastic analysis method of ASME-NH code. The creep damage exceeds that due to the fatigue, and the design is creep dominated.

For a given hold time, the creep damage increases linearly with increase in hold temperature. At lower temperature (400 °C in this case), the damage is negligible since the given material 2.25Cr-1Mo starts exhibiting significant creep behavior after 371 °C.

For a given hold temperature, the creep damage increases rapidly at lower hold times (<20 h in this study) and the damage slows down for higher hold times (beyond 20 h in this study). Increasing the rate of temperature change within thermal load cycle also has a significant detrimental effect on creep–fatigue damage. The methodology of analysis developed in this study can be adopted for assessment of damage of creep, fatigue and creep–fatigue interaction of similar pressure components.

## Appendix: Flowchart for Creep and Fatigue Damage Evaluation



## References

1. Plumbridge WJ, Dean M, Sand Miller DA (1982) The importance of failure mode in fatigue-creep interactions. In: Fatigue of engineering materials and structures, vol 5, pp 101–114
2. Hormozi R, Biglari F, Nikbin K (2015) Experimental and numerical creep-fatigue study of type 316 stainless steel failure under high-temperature LCF loading condition with different hold time. Eng Fract Mech 141:19–43
3. Jawad MH, Jetter RI (2009) “Creep-fatigue analysis” in design and analysis of ASME Boiler and pressure vessel components in the creep range. ASME Press, New York, pp 151–176

4. Koo GH, Yoo B (2000) Elevated temperature design of KALIMER internals accounting for creep and rupture effects. *J Korean Nucl Soc*, vol 32, pp 66–594
5. Gurumurthy K, Balaji S et al (2014) Creep-fatigue design studies for process reactor components subjected to elevated temperature service as per ASME-NH. *Procedia Eng* 86:327–334
6. Fournier B, Sauzay M et al (2008) Creep-fatigue oxidation interactions in 9Cr-1Mo martensitic steel. Part III: lifetime prediction. *Int J Fatigue* 30:1797–1812
7. AFCEN (2002) Design and construction rules for mechanical components of FBR Nuclear Islands. RCC-MR, 2002 edn. AFCEN
8. Oldham J, Abou-Hanna J (2011) Numerical investigation of creep-fatigue life prediction utilizing hysteresis energy as a damage parameter. *Int J Pressure Vessels Piping* 88:149–157
9. ASME Boiler and Pressure Vessel Code (2015) Section III, Subsection NH
10. Manson SS, Halford GR (2009) *Fatigue and durability of metals at high temperatures*. ASM International, Materials Park, Ohio
11. Guodong ZB, Yanfen Z et al (2011) Creep-fatigue interaction damage model and its application in modified 9Cr-1Mo steel. *Nucl Eng Des* 241:4856–4861
12. Fan ZC, Chen XD et al (2009) A CDM-based study of fatigue-creep interaction behavior. *Int J Pressure Vessels Piping* 86:628–632
13. Aoto K, Komine R et al (1994) Creep-fatigue evaluation of normalized and tempered modified 9Cr-1Mo. *Nucl Eng Des* 153:97–110
14. ASME Boiler and Pressure Vessel Code (2015) Section VIII, Division 1
15. ANSYS Workbench (2015) Release 14.5, ANSYS Inc.
16. ASME Boiler and Pressure Vessel Code (2015) Section II, Part D
17. ASME Boiler and Pressure Vessel Code (2015) Section VIII, Division 2
18. Koo GH, Lee JH (2006) High-temperature structural integrity evaluation method and application studies by ASME-NH for the next generation reactor design. *J Mech Sci Technol* 20:2061–2078

# Analysis and Design Optimization for Improved Fatigue Life of One-Way Clutch Drive Used in Starter Motor

Varatharaj Neelakandan, Bharath Kumar, Thulasirajan Ganesan and Praveen Chakrapani Rao

**Abstract** Durability of a starter motor system coupled with an engine is mostly determined by the durability of its components design strength. The starter drive one-way clutch is a component which transmits the torque from an electrical motor to a ring gear mounted on a cranking shaft in an engine thus cranks the engine. The one-way clutch also prevents the whole starter from damage caused by extremely high load and/or extremely high speed applied to the starter pinion from the engine. The variability in the design and material parameters has vital effect on the durability life. In order to achieve better performances together with improved safety, the new design methodology for one-way clutch drive is to be strictly followed to build good-quality starter motor. The new approach incorporates all the variability and uncertainties in the design phases with the help of computer simulation methods to guarantee design reliability. Present work deals with the analysis and design optimization for improved fatigue life of a one-way clutch drive and the methods to calculate the fatigue life of the one-way clutch drive barrel. Design parameters have been optimized on the basis of the component life requirement. The design involves the calculation of stress limit for the material stress values, and it is related to the fatigue life calculation, thereby improving the life of the one-way clutch with optimal factor of safety. The optimal factor of safety has been achieved by means of the various design features like increased wall thickness, increased fillets. Starter motor experienced high-impact loading loadings with respect to the working environments. These variable loadings affect the component life

---

V. Neelakandan (✉) · B. Kumar · T. Ganesan · P.C. Rao  
Comstar Automotive Technologies Pvt. Ltd, Chengalpatu, Tamil Nadu, India  
e-mail: nvaratha@comstarauto.com

B. Kumar  
e-mail: gbharath@comstarauto.com

T. Ganesan  
e-mail: gthulasi@comstarauto.com

P.C. Rao  
e-mail: cpraveen@comstarauto.com



abnormally, which may cause the damage of starter motor components within the defined life cycle. To enhance the product performance, fatigue life of the starter motor's one-way clutch has been predicted and design has been optimized for improved durability.

**Keywords** FEA · Fatigue life · One-way clutch · Optimization  
Starter motor · Engine

## 1 Introduction

Nowadays, vehicle design demands higher load capacity with optimum life to withstand the vehicle application in the various environments. Accordingly in the vehicle subsystems, components are designed to the maximum load capacity which can withstand the total life requirements. The starter motor is placed on to the engine connected to engine block by means of housing bracket and bolts as shown in Fig. 1.

The starter motor consist of Solenoid, motor, one-way clutches, shift lever, and Pinion gear system. One-way clutch is integrated with drive assembly to drive the ring gear when required. The one-way clutch is mounted on the motor shaft which gives torque input to when the solenoid is at the engaged situation. The typical starter motor schematic diagram as shown Fig. 2.

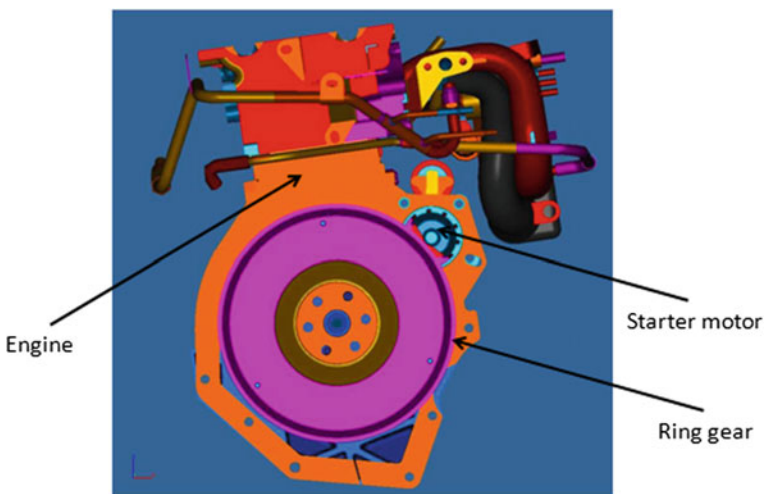


**Fig. 1** Starter mounting

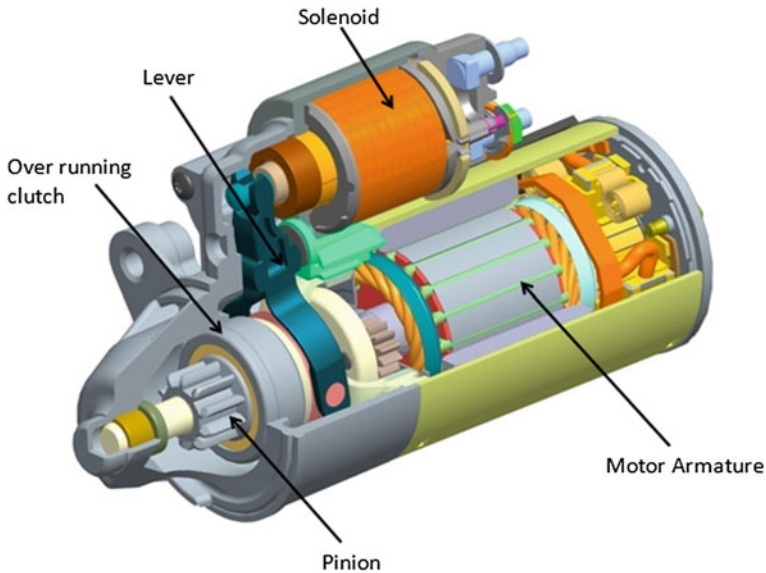


**Fig. 2** Starter motor

## 2 Design Methodologies

The one-way clutch assembly consists of parts named as barrel, pins, springs, and journal shaft. The one-way clutch is a special design which involves the package constraints, material selections, and strength to take care the load spectrum and the design for assembly. Barrel is one of the critical designs in starter motor to understand the operating behavior for better performance to satisfy the design needs that hold the pins while taking torque to the operation. The pinion is loaded and pinion meshes with the ring gear to transfer rotary motion, while cover retains the rollers and spring (Fig. 3).

The loads acting on the drive assembly is classified as shown Figs. 4 and 5 and it depends upon the engine ring gear load and vehicle drive cycle load. The procedure for designing the one-way clutch is started from the ring gear torque coming from the engine and that is converted to the pinion torque by gear ratio calculation procedure as shown Fig. 6. Then the total motor layout is prepared to finalize the drive assembly design to freeze the one-way clutch 3D modeling. The stress calculation is being done for the factor of safety calculation using empirical formulae. Starter drive clutch is a one-way roller clutch and a key component in a starter motor that is used to crank internal combustion engines. The starter drive clutch transmits torque from an electrical motor to a ring gear mounted on a cranking shaft in an engine, thus cranks the engine. The clutch also prevents the whole starter from damage caused by extremely high load and/or extremely high speed applied starter pinion from the engine.

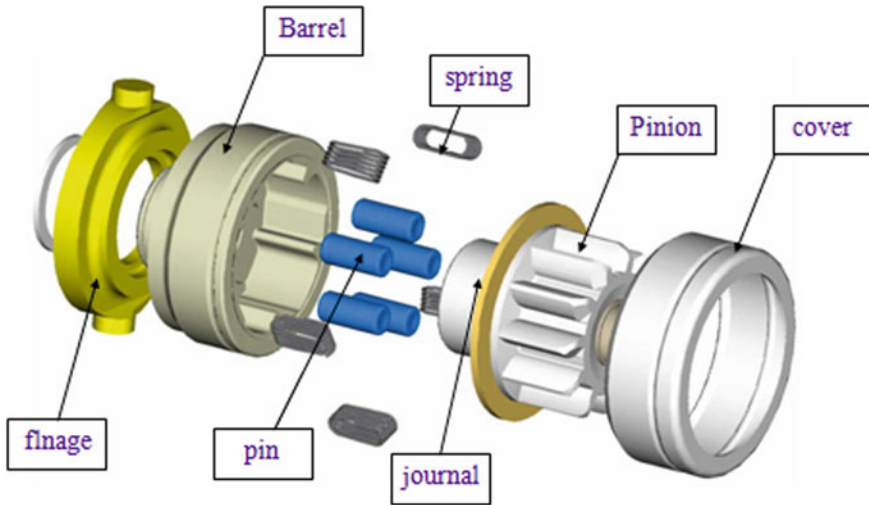


Fig. 3 One-way clutch exploded view

Fig. 4 Load classifications

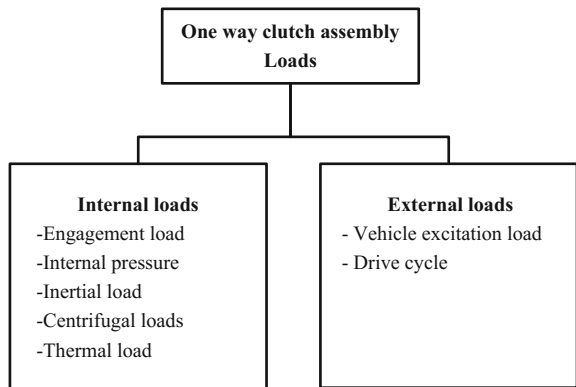


Figure 1 shows the cross section of the drive clutch. The clutch consists of one barrel, five springs, five rollers, and journal. The barrel has an internal spline to connect to external spline of an output shaft of a starter motor, and race is part of the starter pinion. Thus, power is transmitted from motor to pinion through the clutch during cranking engine.

When starter is not energized, rollers set at their initial position and slightly contact the race and barrel due to the spring force. When the starter motor is energized, an electrical motor drives the barrel, and the race is driven by the barrel through the friction between the barrel/rollers/journal. When the pinion engages to the ring gear, RPM of the barrel is greater than RPM of the race thus the rollers are forced to move to their working positions shown in Fig. 5 where the space between the barrel and journal is smaller.

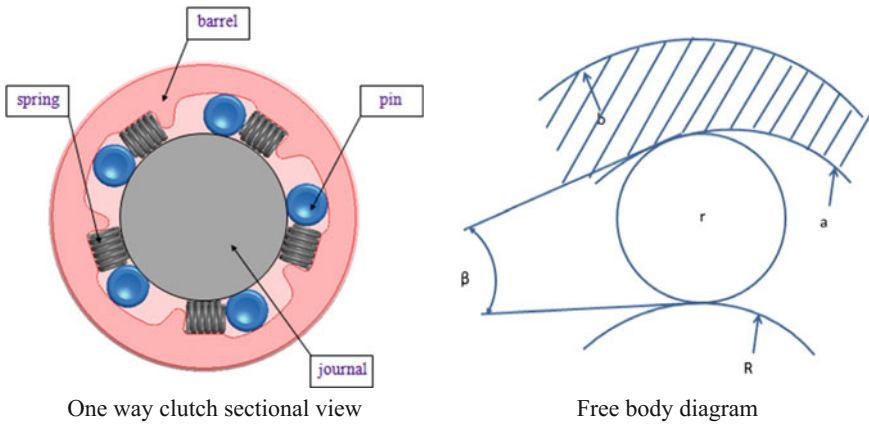


Fig. 5 One-way clutch sections and free body diagram

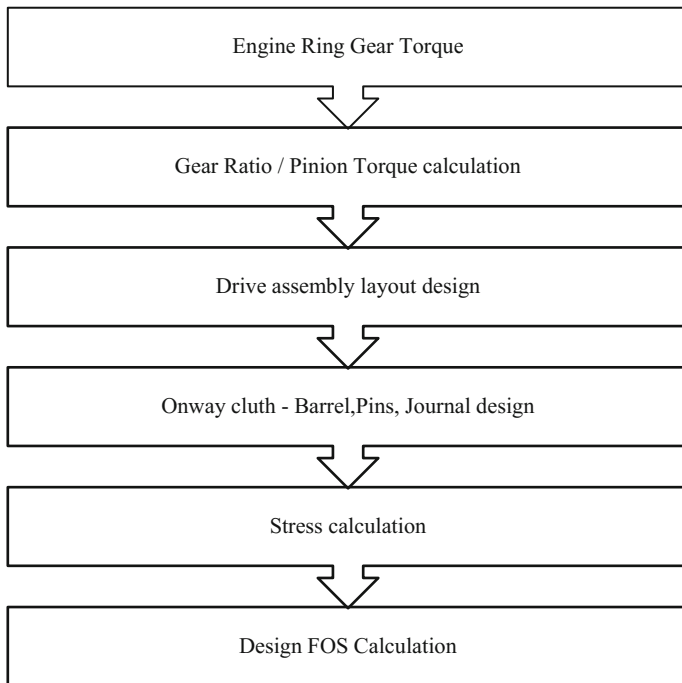


Fig. 6 Barrel stress calculation procedure

The pin contact stress between race surface and rollers is developed due to reduced space. The high contact stress is required; hence, the clutch can get high torque capacity and transmit sufficient torque. High torque capacity increases

circumferential stress in the barrel diameter. Drive assy slip and barrel crack are two major failure modes for starter drive assy failure. Insufficient torque capacity results in the drive slip, while excessive high circumferential stress on the clutch barrel ring causes barrel crack [1, 2]. To eliminate drive slip failure, the clutch has to be designed with high torque capacity. High torque capacity, however, is a cause of high circumferential stress on the barrel that may result in the cracked barrel failure. So, the barrel design required increased fatigue life.

Adding to the barrel design, the friction of the barrel machining quality and surface finish is playing big role on the fatigue life of the barrel and its components. Barrel is more depended on the pin and journal outer diameter surface finish.

Component assembly in the barrel also cause for the barrel design failure in relation to the fatigue life which will be seriously looked into the assembly. Here the concentration is on the fatigue life of the barrel improvement.

Figure 5 shows the free diagram of the barrel–roller–journal. The torque capacity of the clutch and the stresses on the race and barrel can be derived from Fig. 5. Since the torque is derived from the contact stress of the race by assuming the material property, the torque capacity ( $T$ ) of the clutch and the circumferential stress ( $\sigma_h$ ) on the barrel are key objectives and can be expressed as (1) and (2).

The equation which is used for circumferential stress is according to shell theory [2]. The maximum torque which can be applied on one-way clutch is given by [1]

$$T = Nnl \left( \frac{rR^2}{r+R} \right) \sin \beta \quad (1)$$

The circumferential stress developed in one-way clutch barrel, considering shell theory [2]

$$\sigma_h = Mnl \left[ \frac{rnR}{\pi(r+R)a} \right] \left[ \frac{b^2 + a^2}{b^2 - a^2} \right] \cos \beta \quad (2)$$

where

- $\sigma_h$  circumferential stress
- $r$  pin radius
- $R$  journal outer radius
- $a$  barrel inner radius
- $b$  barrel outer radius
- $n$  No. of pins
- $\beta$  Strut angle
- $T$  pinion torque
- $N$  torque constant = 8300
- $M$  stress constant = 49,800

From the above Eqs. 1 and 2, the barrel design is directly related to the pin radius, barrel inner, and outer radius, No. of pins, strut angle, and journal radius and that is formed as design function parameter as (3)

$$\text{One way clutch Barrel design parameters} = f(r, R, a, b, n, \beta) \quad (3)$$

### 3 One-Way Clutch Analysis Procedure

Effective analysis and optimization involves various approaches which deals with vehicle loads, internal loads as discussed. Important criteria [3] for the effective optimization are detailed and appropriate approach using FEA. The following approach in Fig. 7 is followed to analyze and optimize the one-way clutch barrel.

The one-way clutch drive assembly is taken into the analysis in the form of 3D model which consist of barrel, pins, journal, and pinion as shown Fig. 8. There are five numbers of roller pins distributing the loads into the barrel. The main focus area in a one-way clutch is barrel, and its material considered for design concept and analysis is Steel SAE J404 G8615H and its material properties as shown in Table 1.

The roller pins are having the frictional interaction with both journal and barrel, while torque applied on to the pinion as shown Fig. 8. The journal takes the load and transfer to the barrel through the pins and each parts contact the each other. This make the stiffness between the parts to the give output results in the analysis. Since the function is fully frictional contact, the high-level analysis methods used in the finite element analysis tools. The contact and target has been well established [4–6], each pairs of parts like journal to pins and pins to barrel as shown in Fig. 9.

The meshing has been established carefully to handle the contact solution for all the parts and specifically to the barrel. Fine meshing with increased mesh control is used for the barrel, pins, and journal as shown in Fig. 8. The barrel is fixed at the spline area where the one-way clutch is locked on the shaft. The coefficient of friction between the journal and pins and pins and barrel is 0.15 with respect to the material, surface quality, and lubricity condition [2, 7]. The software used for the analysis is high-level FEA capable software which can address all the complication in terms of analysis methods and pout put requirements.

The analysis results focused on the barrel as there is more potential failure mode causing major issue in the product development cycle. The observation is more important and is focused on von Mises stress and circumferential stresses along with radial displacement. Also to understand the contact pressure between the barrel and pins, pins and journal are also predicted. This paper discuss only on the stress-related parameter which are based on the stress analysis.

The initial design concept is made to finalize the design with help of finite element method, and then after seeing the stress results, the decision was made to go for more concepts to increase fatigue life of the barrel. There are more parameters which are contributing to improve barrel life which relates to the fatigue life of the one-way clutch design.

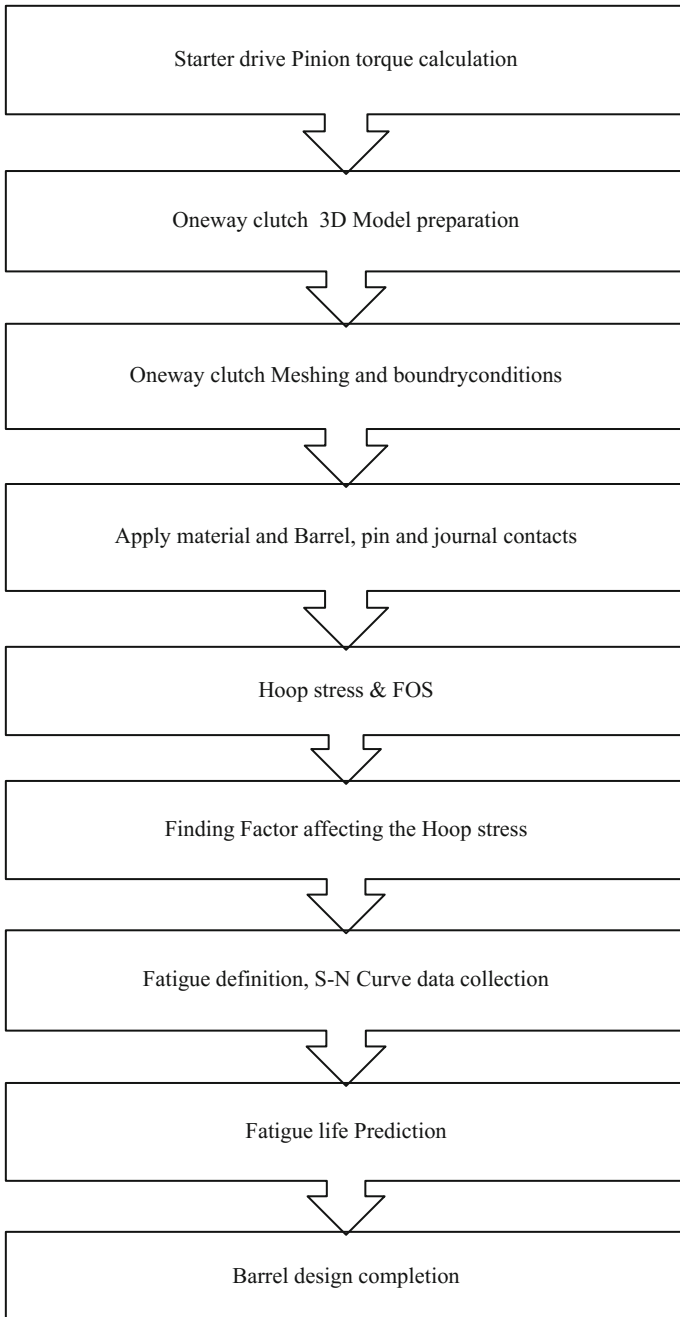


**Fig. 7** Barrel optimization approach

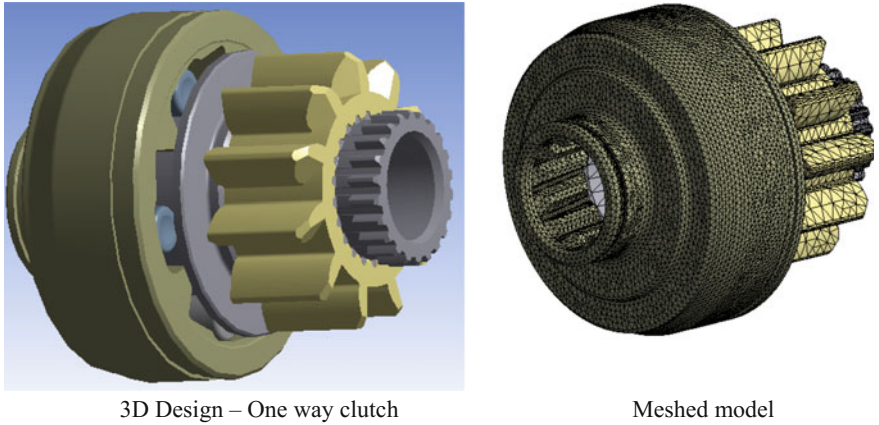


**Fig. 8** One-way clutch 3D Model and meshed model

**Table 1** Barrel material properties as per SAE J404 steel hardened

Material	SAE J404 G8615H
Density	7.84E-6 kg/mm <sup>3</sup>
Poisson's ratio	0.3
Modulus of elasticity	200 GPa
Yield stress	460 MPa
Core tensile stress	560 MPa
Hardness	RA 76.5–80.5
Case tensile strength	1744–2233 MPa

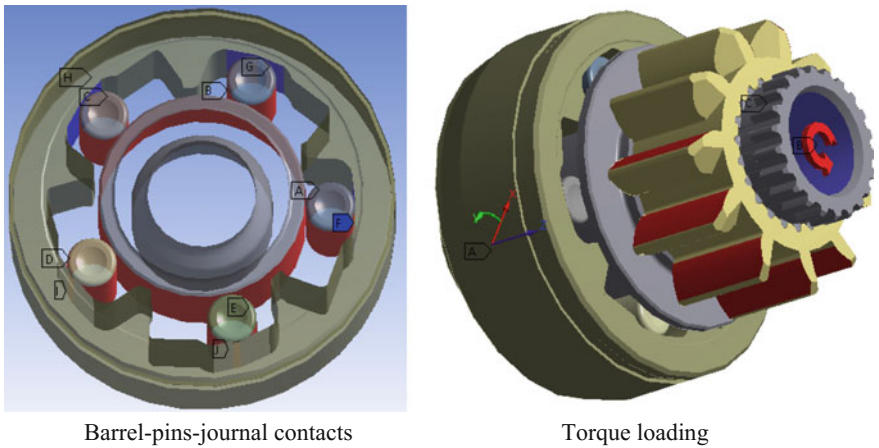


**Fig. 9** Contacts and loading



### 4 Initial Design Analysis and Results

Static contact analysis conducted for the one-way clutch, and the results have been reviewed for the initial design. The total one-way clutch assembly stress distribution is shown in Fig. 10. The von Mises stresses at which the pins contact area has been predicted and other critical area of stresses also have been reviewed for the better design aspect.

The circumferential or the circumferential stresses which are contributing to the barrel crack according to the design failure mode analysis have been predicted through the FEA, and the maximum stress is induced at the area of spring seating radius area, and the radial displacement of the barrel is predicted, and it is shown in Fig. 11.

From the above analysis, the stresses of the barrel is related with the few parameters among other parameters which was not feasible to take it for the optimization while considering quick design change and ease of manufacturing. Those parameters are barrel spring seating area radius and barrel rim thickness by increasing the outer diameter of the barrel as shown in Fig. 12. Based on the analysis outcome, the optimization parameter function is defined as follows (5). The stress calculation based on the empirical formulae as per the Eq. (2) is the general method which was not predicting the design failure more effectively. Total circumferential stress due to the radius of the spring seating was not able to predict. So, the finite element method was needed to include to consider all the critical geometry of the barrel.

$$\text{One way clutch Barrel Optimisation} = f(r_1, b,) \tag{4}$$

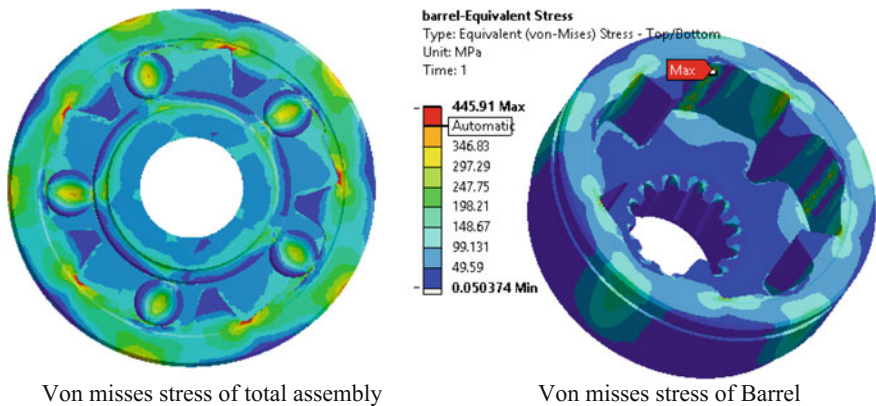


Fig. 10 von Mises stresses of barrel

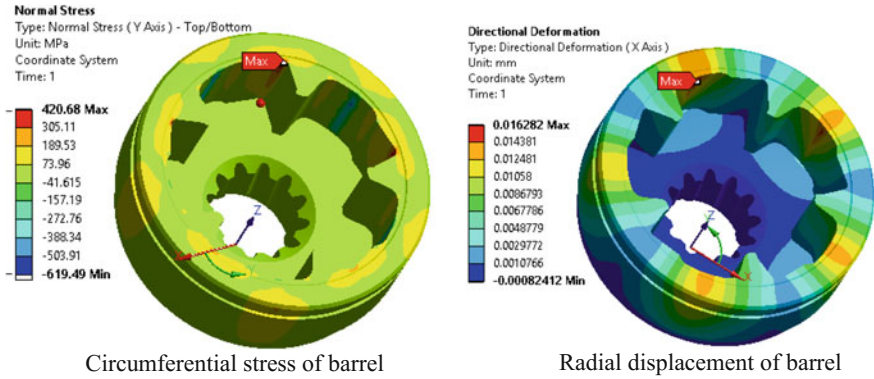


Fig. 11 Circumferential stress and radial displacement

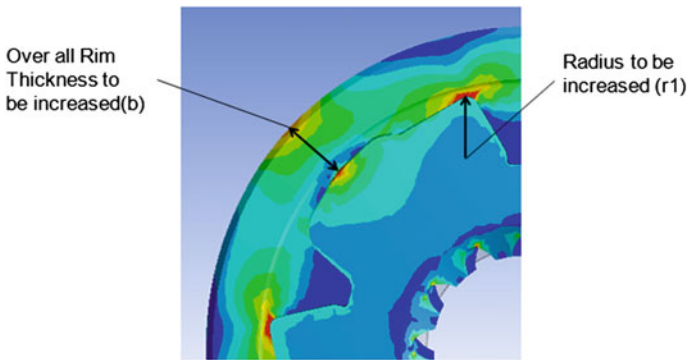


Fig. 12 Stress causing parameters

## 5 Fatigue Calculations

The fatigue calculation and analysis are done with empirical formulae with the superposition of static stress analysis results. The fatigue calculation has separate flow from software inline to stress analysis. The input to fatigue analysis process is having material properties, *S-N* curve, and load cycle.

The observation from the initial design analysis result is that the stress is induced more on the radius (*r1*) and outer radius of the barrel. The circumferential stress is 420.68 MPa which is more contributing to the barrel failure mode is shown in the figure and that has been taken for the fatigue life calculation.

Using the above-calculated circumferential stress from FEA, fatigue life is calculated using the below Gerber theory as the barrel material is hardened and the *S-N* curve [8] used for the calculation is as shown Fig. 13.

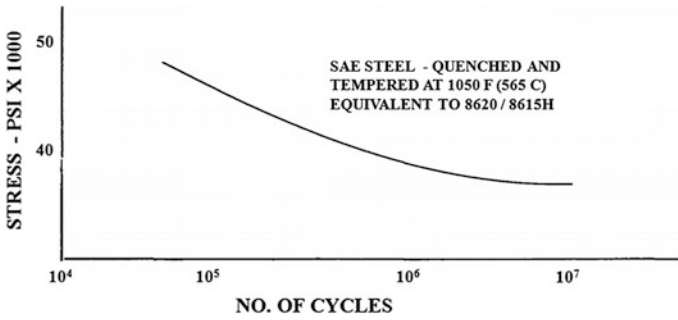


Fig. 13 S-N curve for SAE J404 G8615H steel hardened

The fatigue life calculation is executed with GOODMAN principle as the barrel material is hardened steel [7], and Eq (5),

$$\frac{1}{FOS} = \frac{\sigma_m}{\sigma_u} + \frac{\sigma_a K_f}{\sigma_e K_s K_z} \tag{5}$$

$$K_f = 1 + q(K_t - 1) \tag{6}$$

where

- $\sigma_u$  ultimate stress
- $\sigma_e$  endurance stress limit
- $K_t$  stress concentration factor
- $K_f$  fatigue stress concentration factor
- $K_s$  surface factor
- $K_z$  size factor
- $q$  notch sensitivity factor
- FOS factor of safety

From Eq. (7), endurance stress limit is calculated. The fatigue stress concentration factor [7] and notch sensitivity factor [7] from Fig. 14, surface factor and size factor have been considered as 1.

## 6 Optimization Results

As discussed above, the optimization parameters are set based on the design and manufacturing feasibility constraints, and the parameters are outer diameter of the barrel and barrel spring seating area radius as shown in Table 2. The initial design concept generated with the outer diameter of the barrel is 46.41 mm, and spring seating area radius is 0.8 mm. This design is tested virtually by FEA method and evaluated the stress results in all the view cover critical geometries. Then based on

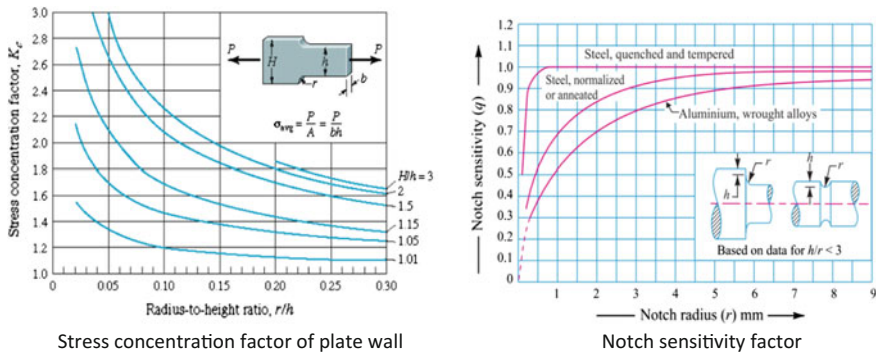


Fig. 14 Stress concentration and notch sensitivity factor chart

Table 2 Optimization parameter

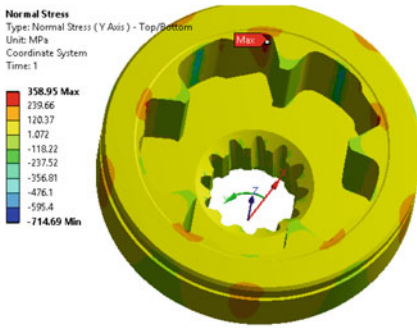
Iteration nos initial design	Outer diameter of barrel (b), mm	Radius (r <sub>1</sub> ), mm
1	46.41	0.8
2	48.41	1.1
3	48.41	1.5
4	49.41	1.1
5	49.41	1.5

the results, the new parameters are set as shown in Table 2 for further iteration or concepts and evaluated using finite element analysis.

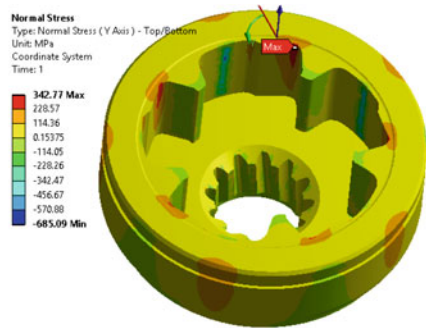
The circumferential stress results of the design iterations are shown in Figs. 15 and 16. The circumferential stress is calculated for the all design iteration using FEA and plotted as shown in Fig. 17 along with the theoretical empirical formulae. The difference we see is because of the radius not being taken into the empirical formulae. This is the reason why the finite element analysis playing the role in validating the complicated design during design cycle.

The initial design stress value was higher, and then the effective optimization procedure was brought to the level of minimum stress which can improve the fatigue life.

As the FEA calculation is reliable and found appropriate method, the circumferential stress calculated from FEA is taken for the fatigue life calculation and plotted using S-N curve in as shown in Fig. 18. The endurance limit for all the design parameters are calculated and used for the fatigue life calculation. The life of the barrel is improved for the operation at which the one-way clutch is assembled into the starter motor. The barrel fatigue cycle is calculated for improved fatigue life. From all the observation of stress analysis and fatigue analysis, the new empirical function is formed to explain the design function for the one-way clutch improved fatigue life.

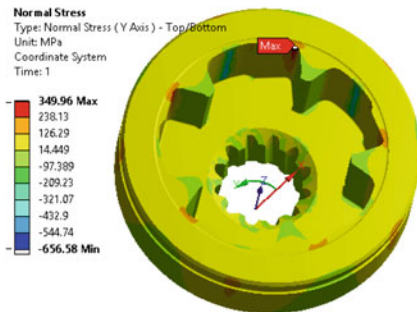


Circumferential stress of barrel Iteration 2

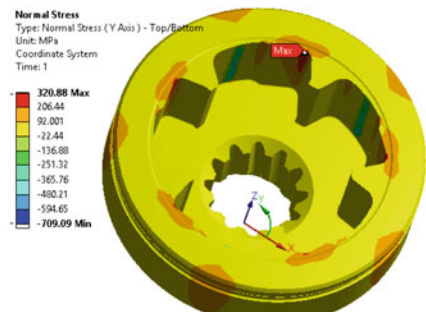


Circumferential stress of barrel Iteration 3

**Fig. 15** Circumferential stress iteration 2&3



Circumferential stress of barrel Iteration 4



Circumferential stress of barrel Iteration 5

**Fig. 16** Circumferential stress iteration 4&5

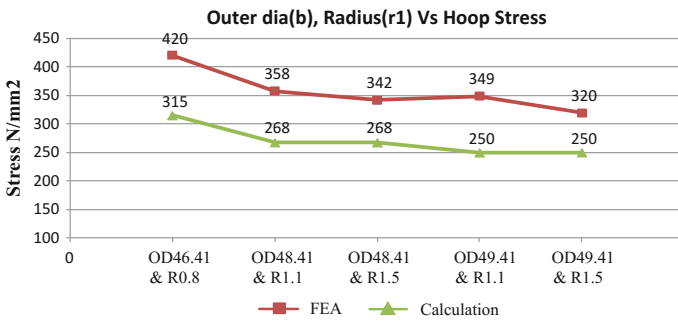


**Fig. 17** FEA optimization

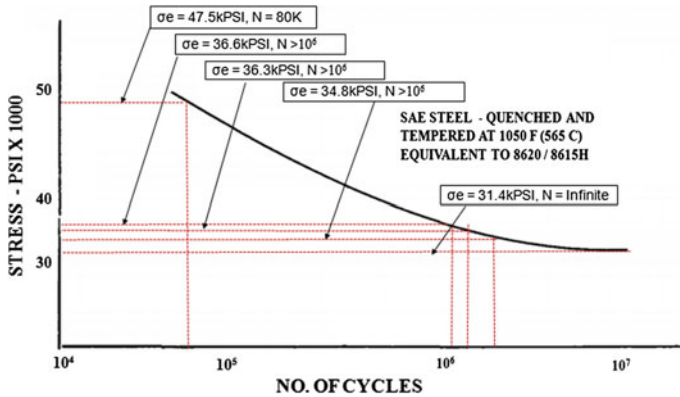


Fig. 18 Fatigue life in S-N curve

$$\text{One way clutch optimisation} = f(S_m, L_o, M_f, F_m, D_v, r, R, a, b, n, \beta, r_1) \quad (7)$$

where

- $S_m$  material strength
- $L_o$  operating loads
- $M_f$  fatigue material data
- $F_f$  fatigue factors
- $D_v$  vehicle duty cycle
- $r_1$  barrel spring seating radius
- $r$  pin radius
- $R$  journal outer radius
- $a$  barrel inner radius
- $b$  barrel outer radius
- $n$  no. of pins
- $\beta$  strut angle
- $T$  pinion torque

## 7 Conclusion

The starter motor one-way clutch fatigue life is improved by redesigning the barrel using FEA and fatigue life calculation approach. The finite element analysis is utilized to understand the stress distribution and importance of all the design geometries for the design requirements which was missing in the empirical calculation method. It is found that one-way clutch optimization is the function of material strength, operating loads, fatigue properties, fatigue factor, and barrel outer diameter, and barrel spring seating radius. The procedure for the starter motor

one-way clutch design analysis and optimization methodology is established and implemented in the design development cycle. The approach explained in this study can be applied to other starter motors' one-way clutch to enhance the overall performance and life improvements at the reduced development cost.

**Acknowledgements** The authors would like to thank M/s. COMSTAR Automotive Technologies Pvt. Ltd. management for giving opportunities to explore and implement a new ideas and methodologies inside the work areas.

## References

1. Aliukov S, Keller A, Alyukov A (2015) On the question of mathematical model of an overrunning clutch. WCE 2015, London, U.K 1–3 July
2. Kumar P, Janaki Manohar N, Fea analysis and optimization of an one way clutch used in automatic transmission based on global parameters. IJRET (eISSN: 2319-1163|pISSN: 2321-7308)
3. Neelakandan V, Jha A, PV SR Hardikar J (2015) Importance of fatigue life in design optimization of off-highway powershift transmission system. JMSSE 3(1):195–201
4. Horng Thin-Lin (2013) The study of contact pressure analyses and prediction of dynamic fatigue life for linear guide ways system. Modern Mech Eng 3:69–76
5. Patadia P, Darji P (2015) A review paper on fatigue life analysis and its improvement of 4-row cylindrical roller bearing used in hot rolling mill. IJEART 3(2)
6. Shelke AA, Galhe DS (2016) Fatigue analysis of bearing. GRD J 1(5)
7. Design data: Data book of engineers by PSG College—Kalaikathir Achchagam—Coimbatore
8. Buyer HE (2010) Atlas of fatigue curves. ASME Int:518
9. Darji PH, Vakharia DP (2011) Fatigue failure analysis of hollow cylindrical roller bearing. Int J Adv Eng Sci 1(2)

# Creep–Fatigue Assessment for Interaction Between IHX Seal Holder and Inner Vessel Stand Pipe in a Pool-Type Fast Reactor as Per RCC-MR

Sanjay Kumar Pandey, S. Jalaldeen, K. Velusamy  
and P. Puthiyavinayagam

**Abstract** Structural analysis of IHX seal holder and inner vessel stand pipe due to interference has been carried out as per RCC-MR code. The phenomenon of progressive deformation/ratcheting, due to combination of primary stress and secondary stress intensity range, has been checked. The damage due to creep–fatigue interaction has been estimation for IV stand pipe, IHX shroud shell and IHX tubes to avoid the failure. The effective primary stress intensities ( $P_1$  and  $P_2$ ) and the plastic plus creep strains are found to be within allowable limits for IV and shroud shell. The detailed 3D analysis of IHX due to 4.5-mm interference between shroud shell and tube of IHX has been carried. The stress in the tube is 320 MPa. The fatigue damage and creep damages are 0.043 and 0.271, respectively.

**Keywords** Fatigue · Creep · Creep–fatigue interaction · Ratcheting  
Progressive deformation

## 1 Introduction

In pool-type sodium-cooled fast reactor (SFR), generally, a mechanical seal is provided in the annular gap between intermediate heat exchanger (IHX) shell and inner vessel (IV) stand pipe to minimize leakage of sodium from hot pool to cold pool. The seal is held by a seal holder, and holder is connected to the IHX shell as shown in Fig. 1. The inside gap (gap between seal holder and stand pipe toward the central axis of main vessel) and outside gap (gap between seal holder and stand pipe away from the central axis of main vessel) change during reactor conditions depending on the temperature of IV, roof slab, etc. The position of IHX and seal holder is designed such that there is no interference between seal holder and stand pipe during full power condition of the reactor. Due to liberal manufacturing tol-

---

S.K. Pandey (✉) · S. Jalaldeen · K. Velusamy · P. Puthiyavinayagam  
Structural Mechanics Section, Reactor Design Group,  
Indira Gandhi Centre for Atomic Research, Kalpakkam 603102, India  
e-mail: pandey@igcar.gov.in

© Springer Nature Singapore Pte Ltd. 2018

S. Seetharamu et al. (eds.), *Proceedings of Fatigue,*

*Durability and Fracture Mechanics*, Lecture Notes

in Mechanical Engineering, [https://doi.org/10.1007/978-981-10-6002-1\\_23](https://doi.org/10.1007/978-981-10-6002-1_23)



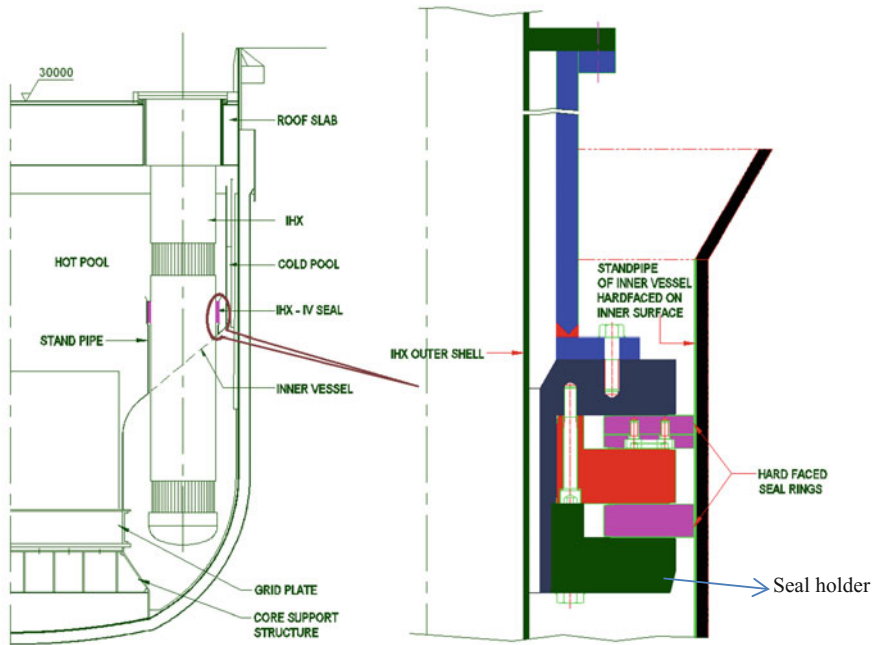


**Fig. 1** Schematic of IHX mechanical seal and its interaction with IV stand pipe

erance, such interference is possible during normal operation and station black-out conditions. Hence, it is required to find out the acceptability of such deviation from creep-fatigue damage consideration of IHX. The scope of the present paper is to evaluate the stresses and deflection due to interference and assess 'structural integrity' as well as risk of 'functional failure' during various reactor conditions. To prevent appearance of progressive deformation/ratcheting at the critical location, detailed thermomechanical analysis is carried out, to verify that the effective primary stress intensity and total inelastic strain (plastic + creep) are within the allowable limits. Creep-fatigue damage evaluation is carried out as per RCC-MRx-2012 to assess the risk of crack initiation.

## 2 Structural Analysis

The focus of the study is interference between IHX seal holder and IV stand pipe. Hence, a finite element model of  $180^\circ$  symmetric sector of IV stand pipe, IV redan shell, IHX seal holder, IHX shroud shell, tube sheets of IHX and equivalent shell for IHX tubes has been generated in the ABAQUS FE software using 20-node quadratic brick, reduced integration elements (C3D20R) as shown in Fig. 2. The tube sheets of IHX are perforated plates. Hence, equivalent solid plate

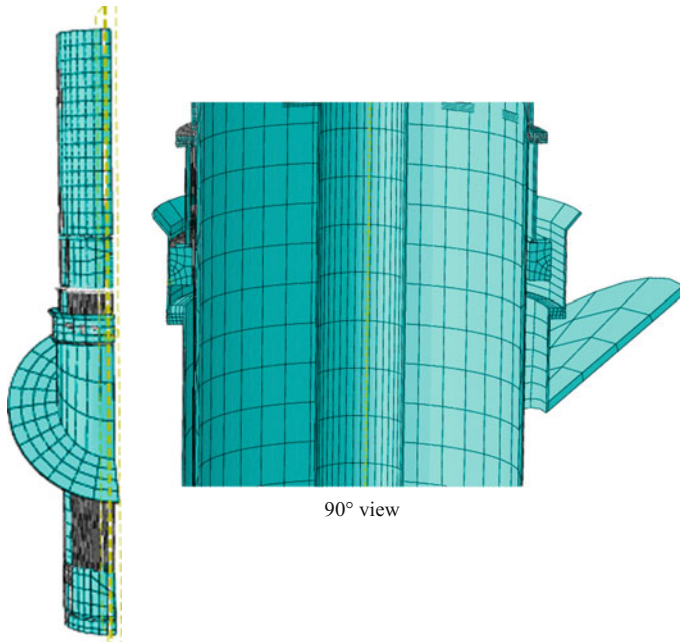


**Fig. 2** Finite element model of 180° sector

concept has been used for the perforated region so that it can be used for conventional structural analysis. The perforated region of plate is idealized as a homogeneous solid plate having the same overall dimensions as perforated region. But, to account for increased flexibility resulting from perforation, modified elastic constant has been used. The tubes of IHX are idealized as shell having equal area moment of inertia for bending. Symmetric boundary condition has been applied for the whole 180° sector. A radial displacement of 9 mm (assumed) has been imposed at the sector model of inner vessel redan, for the results presented in the paper. The thermal stress (self-limiting stress) developed due to 9-mm interference has to be checked for progressive deformation and creep, fatigue damage and creep–fatigue interaction. The stress has been checked with allowable limits, as per RCC-MR. The von Mises stress intensity range and deflection of IHX shell and IV stand pipe have been evaluated for normal operating condition due to radial displacement. The stress contours of IV stand pipe and IHX shroud shell with seal holder are depicted in Figs. 3 and 4, respectively. At the critical locations, the values of membrane plus bending stress intensity range (linearized through the wall thickness),  $\Delta Q$ , and total stress intensity,  $\Delta Q + F$  (peak stress), are presented in Table 1 for the interference.

Since tubes are modeled as equivalent shells, the actual stress in tube cannot be predicted by this model. Hence, a 15° sector of tube with ferrule and antivibration belt has been modeled as depicted in Fig. 5 as shell element to study the effect of interaction on IHX tubes and a radial interaction of 4.5 mm (say). The stress in the tube is found to be 320 MPa. The predicted von Mises stress pattern is depicted in Fig. 6.

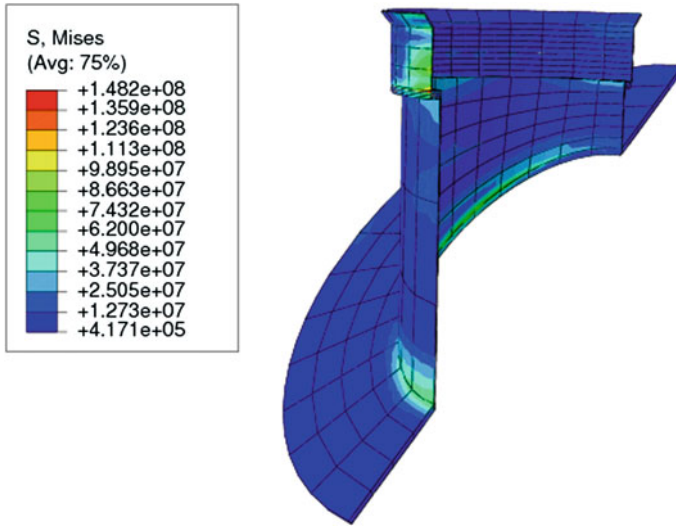


Fig. 3 von Mises stress distribution (Pa) in IV stand pipe

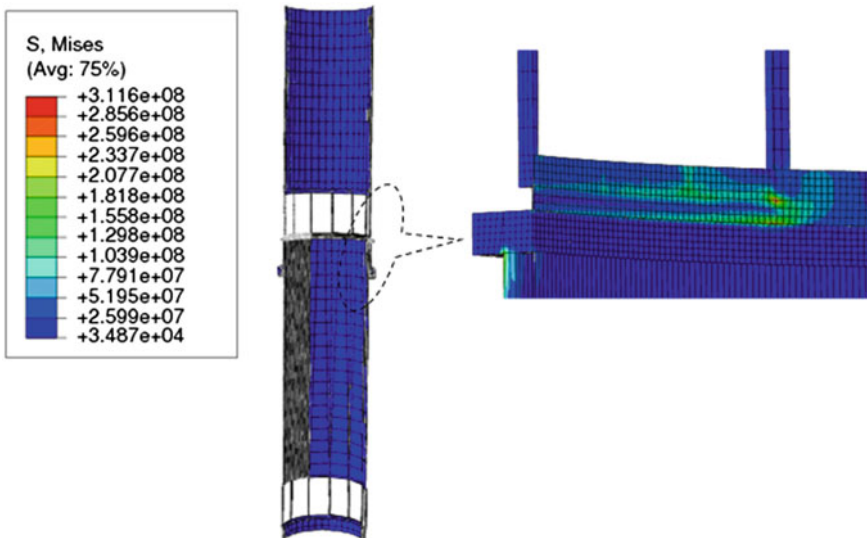


Fig. 4 von Mises stress distribution (Pa) in shroud shell of IHX with seal holder

Table 1 Maximum stress range and total stress intensity

Component	Stress range, $\Delta Q$ (MPa)	Total stress intensity, $\Delta Q + F$ (MPa)
IV stand pipe	106	148
IHX shroud shell	260	312

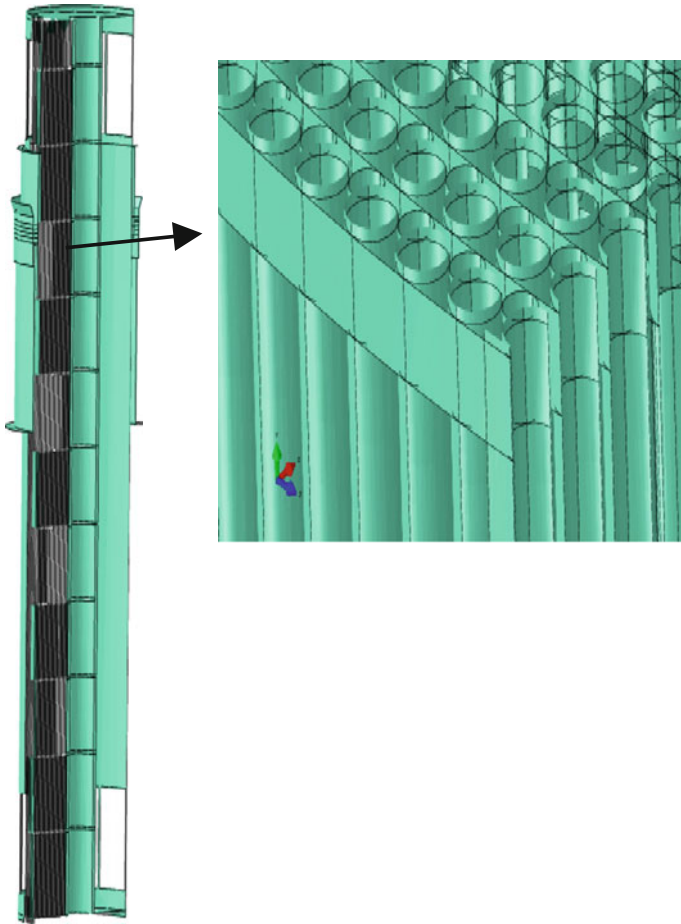


Fig. 5 Finite element model of IHX with stand pipe and seal holder

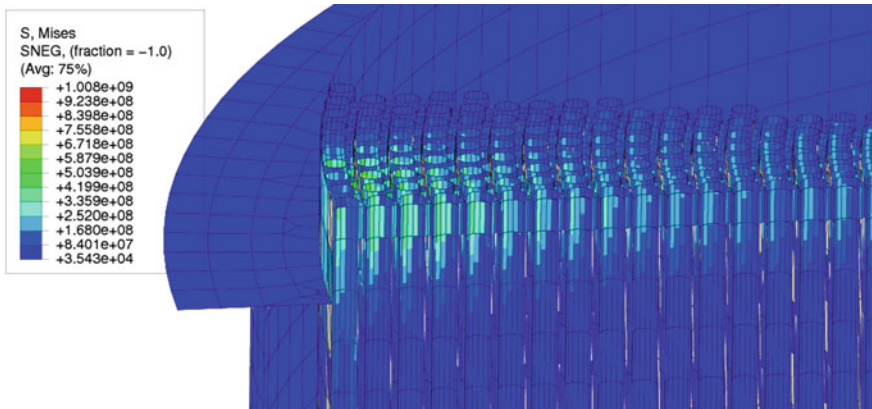


Fig. 6 von Mises stress distribution (Pa) in IHX tubes

### 3 Evaluation of Damage

The damage possibly due to the thermal cyclic stress (secondary stress) and primary stress is (i) progressive deformation (ratcheting) leading to functional failure of component due to large deformation and (ii) creep–fatigue damage leading to failure due to crack/catastrophic rupture without noticeable large deformation.

Design code RCC-MR follows the effective primary stress concept to evaluate the ratcheting, which is derived from maximum primary stress and cyclic secondary stress. The maximum effective primary stress intensity,  $P_1$ , and maximum effective primary stress intensity of the sum of the stresses,  $P_2$ , the plastic strain ( $\varepsilon_p$ ) plus associated creep strain ( $\varepsilon_c$ ) at 1.25 times  $P_1$  and plastic strain plus associated creep strain at 1.25 times  $P_3$  and allowable limits are provided in Table 2 for IV stand pipe and IHX shroud shell.

As per RCC-MR, the fatigue usage fraction and the number of permissible cycles ( $N_p$ ) corresponding to the total strain range ( $\Delta\varepsilon_t$ ) are determined by fatigue design curve at the operating temperature. The fatigue usage fraction,  $V$ , is equal to the ratio of number of actual strain cycles,  $n$ , to the number of permissible cycles. The total strain range, ( $\Delta\varepsilon_t$ ), is the sum of  $\Delta\varepsilon_1$ ,  $\Delta\varepsilon_2$ ,  $\Delta\varepsilon_3$ ,  $\Delta\varepsilon_4$  and  $\Delta\varepsilon_c$ . The strains are calculated as per procedure provided in RCC-MR Appendix A3. The total number of fatigue cycles in the reactor is 861 (total number of shut down).

For the creep rupture usage fraction, the maximum allowable time ( $T_k$ ) corresponding to the highest stress intensity ( $\sigma_k$ ) has been determined by minimum creep rupture curve at maximum temperature of concerned cycle. The creep rupture usage fraction,  $W$ , is calculated as:  $=(t_k/T_k)$  where  $t_k$  is the applicable time (hold time above 450 °C). The total hold time for creep is taken as 262,800 h. The value of  $\sigma_k$  is calculated from,

$$\sigma_k = 0.867 * \sigma_{v.m} + 0.133 * \sigma_r$$

where

$\sigma_{v.m}$  Equivalent stress based on octahedral shear theory (von Mises stress)

$\sigma_r$  Sum of three normal components

The estimated creep ( $W$ ) and fatigue ( $V$ ) damages during the reactor life of 40 y are provided in Table 3; it is seen that the fatigue damage is negligible and the creep damage is  $\sim 0.026$ . The effective creep–fatigue damage has been evaluated as

**Table 2** Effective primary stress intensities and total strain (plastic + creep)

	IV stand pipe	IHX shroud shell	Allowable
$P_1$ (MPa)	23	40	124 (1.3 * $S_m$ )
$P_2$ (MPa)	28	56	187 (1.3 * 1.5 * $S_m$ )
$\varepsilon_p + \varepsilon_c$ (for 1.25 * $P_1$ ) (%)	0.0015	0.0118	1
$\varepsilon_p + \varepsilon_c$ (for 1.25 * $P_3$ ) (%)	0.0028	0.0458	2

**Table 3** Creep–fatigue damage

	IV stand pipe	IHX shroud shell
Total stress intensity range (MPa)	148	312
Fatigue damage, $V$	$\sim 0$	0.043
Creep damage, $W$	0.026	0.027
Effective damage	0.026	0.1

$\sim 0.026$  as per creep–fatigue interaction diagram. Similarly, for IHX shroud shell, it is seen that the fatigue damage and creep damage are 0.043 and 0.027, respectively. The effective creep–fatigue damage has been evaluated as  $\sim 0.1$  as per creep–fatigue interaction diagram. Similarly, the stress found in tube is 320 MPa. The fatigue damage and creep damages as per RCC-MR are 0.043 and 0.271, respectively, and the effective damage is 0.68.

## 4 Conclusion

A systematic approach for structural analysis of IHX seal holder and inner vessel stand pipe due to possible interference between them is proposed. The approach consists of (i) progressive deformation (ratcheting) leading to functional failure of component due to large deformation and (ii) creep–fatigue damage leading to failure due to crack/catastrophic rupture without noticeable large deformation. The approach is adopted to assess the acceptance of 9-mm interference between stand pipe and seal holder. As a part of this procedure, maximum membrane plus bending stress range,  $\Delta Q$ , and total stress range,  $\Delta(Q + F)$ , are determined and IV stand pipe and IHX shroud shell. For a SFR with 40-y design life and 75% load factor, the effective primary stress intensities ( $P_1$  and  $P_2$ ) and the plastic plus creep strains are found to be within limits for IV stand pipe and IHX shell. Hence, the phenomenon of progressive deformation/ratcheting, due to combination of primary stress and secondary stress intensity range, has been ruled out. The creep damage, for IV stand pipe, is found to be 0.026, while the fatigue damage is negligible. Hence, the damage due to creep–fatigue interaction is determined to be 0.026 which is less than the allowable value of 1. Similarly, the creep and fatigue damages, for IHX shell, are found to be 0.027 and  $\sim 0.043$ , respectively. The damage due to creep–fatigue interaction is determined to be 0.1 which is also less than the allowable value of 1.

Similar calculation for tube also indicates that the damage due to creep–fatigue is  $< 1$ .

## References

1. RCC-MRx, Section III, Tome 1, Sub section Z, Technical Appendix A3, 2012
2. RCC-MRx, Section III, Tome 1, Sub section B: Class N1<sub>RX</sub> reactor component and supports, 2012

# Probabilistic Fatigue Life Estimation of Plate with Multiple Stress Concentration Zones

T. Sivaranjani, K. Abhirama and M. Manjuprasad

**Abstract** Fatigue is a complex phenomenon which causes sudden failure of a component subjected to cyclic loading in the elastic region. Fatigue lives of nominally identical specimens subjected to the same nominal cyclic stress display scatter. This phenomenon reflects the stochastic nature of a fatigue damage process. Probabilistic and statistical methods are appropriate for managing the large uncertainties that exist in the fatigue process and provide reliability as a measure of structural performance. In this work, MATLAB was used as a platform to evaluate probabilistic fatigue life of the plate with multiple stress concentration zones using Latin Hypercube sampling. Fatigue reliability was computed by accounting for the scatter present in material properties in terms of random design variables and verified. Among the random design variables, fatigue strength exponent was having higher influence on fatigue life. Fatigue reliability was found to be decreasing with increase in input variation.

**Keywords** Fatigue analysis · Reliability · Latin hypercube sampling · MATLAB

---

T. Sivaranjani (✉) · M. Manjuprasad  
Structural Technologies Division, CSIR-National Aerospace Laboratories,  
Bangalore 560017, India  
e-mail: tsivaranjani@nal.res.in

M. Manjuprasad  
e-mail: manjuprasad@nal.res.in

K. Abhirama  
Department of Mechanical & Manufacturing,  
Manipal Institute of Technology, Manipal 576104, India  
e-mail: abhirambhat144@gmail.com



## 1 Introduction

The history of fatigue failures of machinery, moving vehicles, welded structures, aircraft, etc., has caused catastrophic accidents such as an explosion of a pressure vessel, a collapse of a bridge or complete failure of a large structure. With extensive research and practical experience, much knowledge has been acquired on fatigue of structures and the fatigue mechanism in the material. Fatigue manifests in the form of initiation or nucleation of a crack followed by its growth till the critical crack size under the operating load leads to rupture. The fatigue life is usually split into crack initiation life and crack propagation life. The crack initiation life period has microcrack growth, and those fatigue cracks are very small. In the crack propagation life period, the crack will grow till complete failure [1]. Since the scatter present in the material properties and fatigue data are very high, probability plays a major role in the fatigue life estimation. The probability that an item will perform its intended function under given conditions and defined interval of time is called reliability. By using a probabilistic approach rather than the deterministic approach, all the uncertainties are taken into account so that realistic study on safety of a structure can be performed. This probabilistic technique can show best-to-worst-case scenario [2]. Monte Carlo methods are a broad class of computational algorithms that rely on repeated random sampling to obtain numerical results. Their essential idea is using randomness to solve problems that might be deterministic in principle. They are often used in physical and mathematical problems and are most useful when it is difficult or impossible to use other approaches. Monte Carlo methods are mainly used in three distinct problem classes: optimisation, numerical integration, and generating draws from a probability distribution. But in Monte Carlo, a large number of simulations are required to assess small failure probabilities. Variance reduction techniques (VRTs) improve a “crude” simulation experiment by reducing the variance of the estimators with less computational effort. Latin Hypercube sampling (LHS) is one of the variance reduction techniques, which works by controlling the way that random samples are generated for a probability distribution and it can be applied to multiple variables.

Marian Zaharia [3] carried out fatigue life simulation of mechanical components in order to understand the importance of implementing the Monte Carlo techniques. After comparing the simulation results with experimental results, it was observed that by using the simulation methods, one could obtain good results even in early stage of product design and development. Chen and Yan [4] conducted reliability assessment study of a mechanical spring which was used for various spring deflection applications. Finite element analysis was performed to generate the fatigue stresses and Monte Carlo simulation was realised for  $10^6$  samples. Kala [5] did a study on sensitivity analysis of fatigue behaviour of steel structure under in-plane bending to analyse the influence of some input quantities on the growth analysis of fatigue cracks which occur in steel structures. The Latin Hypercube sampling (LHS) method was used to randomise the input quantities on the fatigue resistance. The initial crack size was modelled by lognormal distribution, and

realizations were performed for 400 runs. It was found that the initial crack size was the important factor influencing the service life. Mrad et al. [6] studied fatigue reliability analysis using Latin Hypercube sampling method on upper arm of a vehicle suspension system. Young's modulus and applied load were randomised using LHS in MATLAB and FORTRAN. From the results, it was observed that the load had a direct and important effect on the fatigue life distribution.

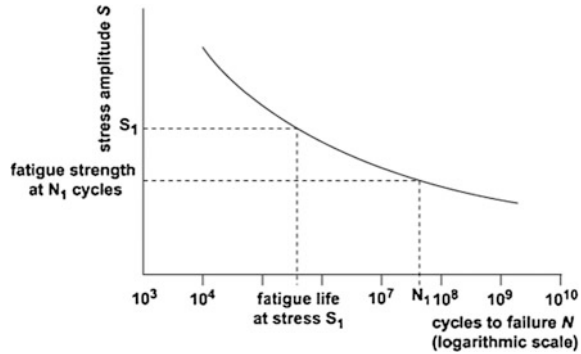
Fatigue is the most common cause for mechanical failures, and stress concentrations will have unique effect on fatigue. Due to irregularity and uncertainty in fatigue parameters, the outcomes of fatigue calculations are also uncertain in nature and prone to errors. Hence, there is a need to establish a tool with which one can effectively study the effect of probabilistic nature of fatigue and can be used in effective design of most critical components of structures. This analysis will help in understanding the impact of each and every fatigue input parameter scatter in designing the life of a component. Hence, in this present work, it is proposed to carry out probabilistic fatigue life prediction of plate with multiple stress concentration zones using Latin Hypercube sampling. The methodology to estimate probabilistic fatigue life prediction of plate with stress concentration zones using MATLAB and FEM was established in this work. First fatigue life of plate with stress concentration zones was estimated using finite element method (FEM) and stress-life approach. Latin Hypercube sampling (LHS) was used to randomize input variables in MATLAB in order to reduce the computation time. Deterministic fatigue life estimation and probabilistic fatigue life estimation was carried out continuously without manual interpretation by integrating MATLAB with Nastran. By using randomised variables, the probabilistic fatigue life of plate with stress concentration zones was estimated. Parametric study of input variables against fatigue life was carried out to establish the sensitivity of the input variable.

## 2 Deterministic Fatigue Life Estimation

### 2.1 Stress-Life Approach

Stress-life approach ( $S-N$  approach) is a standard method of fatigue analysis since mid-1800s. Stress-life approach assumes that all stresses in the component, even local ones, stay below the elastic limit. During fatigue analysis, the test specimen is subjected to alternating loads (constant stress amplitude) until failure. Stress-life fatigue tests are usually carried out on several identically prepared specimens at different fully reversed stress amplitudes.  $S-N$  curves are usually plotted on semi log or log-log coordinates, in which stress amplitude is plotted versus number of cycles to failure (Fig. 1). The number of cycles of stresses or strains that a given specimen sustains before failure is called fatigue life. The portion of the curve with the negative slope is finite life region and the horizontal line is infinite life region. The point of the  $S-N$  curve at which the curve changes from a negative slope to a

**Fig. 1** Typical S-N curve of the specimen



horizontal line is knee of the  $S-N$  curve and represents the fatigue limit or endurance limit. An expression is developed from this log–log plot, and that expression is known as Basquin’s equation. This equation is widely used for fatigue life estimation using  $S-N$  approach.

$$S_{nf} = S_f (N_f)^b \tag{1}$$

where ‘ $S_f$ ’ is the coefficient and represents the value of ‘ $S_u$ ’ or ‘ $S_{nf}$ ’ at one cycle, ‘ $b$ ’ is the slope of straight line, sometimes referred as Basquin’s slope.

$$b = \frac{-(\log S_1 - \log S_2)}{(\log N_2 - \log N_1)} \tag{2}$$

The  $S-N$  curve provides the baseline fatigue data on a given geometry, loading direction and material processing for use in subsequent fatigue analysis. If the loading is other than the fully reversed loading, the mean stress will not be zero. Hence, it is mandatory to use mean stress corrections in order to account the nonzero mean stress. The different mean stress corrections available are Goodman, Gerber and Soderberg mean stress corrections in the stress-life approach. Goodman mean stress criterion equation is given as follows

$$\frac{S_a}{S_{ar}} + \frac{S_m}{S_u} = 1 \tag{3}$$

where  $S_a$  represents stress amplitude and  $S_m$  represents mean stress. In a structure, geometrical notches such as holes cannot be avoided. The notches cause an inhomogeneous stress distribution which is stress concentration at the ‘root of the notch’. The theoretical stress concentration factor  $K_t$  is defined as the ratio of the maximum stress ( $S_{max}$ ) at the root of the notch to the nominal stress ( $S$ ) which would be present if the stress concentration did not occur [7].

$$K_t = \frac{S_{max}}{S} \tag{4}$$

The notch effects are taken into account by using Peterson constant, notch sensitivity factor and notch root radius in the fatigue life estimation. Since the scatter present in the fatigue material properties and fatigue experimental data are enormous, it is necessary to use the probabilistic distributions instead of constant values to accommodate the scatter data present. Probabilistic fatigue life estimation was carried out using the procedures discussed in the next section.

## 2.2 Plate with Single Stress Concentration Zone

### Case A: Plate with a Circular Hole at the Centre

Consider a plate made up of aluminium 2024-T351 material with model dimensions as shown in Fig. 2. The geometric dimensions of the plate with a circular hole at the centre were 5 mm thickness, 150 mm width, 400 mm length and 30 mm hole diameter. The monotonic and cyclic properties of the material are shown in Table 1. The analysis was carried out for constant amplitude loading of magnitude 35 kN with the stress ratios  $R = -1$  (Fully reversed),  $R = 0$  (Pulsating tension) and  $R = 0.1$  (tension–tension).

The plate was modelled in Nastran using CQUAD4 element type. Since the structure was symmetrical with respect to both  $x$  and  $y$  axes, quarter model was considered to perform the analysis. The finite element mesh of a plate with single hole was having element size near the hole as 0.25 mm. Due to symmetry, the constraint conditions of the quarter plate model were ‘UX’ fixed condition on the left end and ‘UY’ fixed condition on the bottom side. The uniform force was applied at every node on the right-end side of the quarter plate model along  $x$  direction. The von Mises stress value at critical location (at the circular hole boundary) was obtained with a magnitude of 150 MPa and its contour plot is shown in Fig. 3.

Fig. 2 Plate with a circular hole at the centre

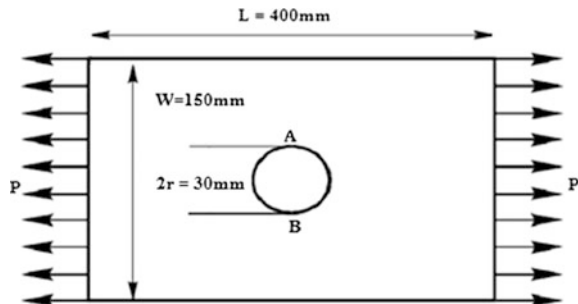


**Table 1** Monotonic and cyclic properties of Al 2024-T351

Monotonic properties		Cyclic properties	
$E$ : Modulus of elasticity	74 GPa	$S'_f$ : Fatigue strength coefficient	1013.53 MPa
$S_{ut}$ : Ultimate tensile strength	477 MPa	$b$ : Fatigue strength exponent	-0.11
$S_y$ : Yield strength	321 MPa		
$\nu$ : Poisson's ratio	0.33		



**Fig. 3** von Mises stress contour of plate with single stress concentration zone

Stress analysis results from Nastran were taken as input for fatigue life calculation using MATLAB. The fatigue material properties considered here were fatigue strength coefficient ( $S'_f$ ) as 1013.53 MPa and fatigue strength exponent ( $b$ ) as  $-0.11$ .  $S-N$  analysis was used to estimate the fatigue life with the proper mean stress corrections. The fatigue analysis was performed for three different stress ratios by considering Goodman mean stress correction wherever required and the results are given in Table 2. The results were compared with literature [8], and it was observed that they were in good agreement.

**Table 2** Fatigue life results for plate with circular hole at the centre

	Literature [8]	Present work using MATLAB
Critical stress	150.97 MPa	149.084 MPa
Stress ratio ( $R$ )	Fatigue life ( $N_f$ ) (cycles)	
$R = -1$	$1.646 \times 10^7$	$1.846 \times 10^7$
$R = 0$	$1.876 \times 10^9$	$2.148 \times 10^9$
$R = 0.1$	$4.116 \times 10^9$	$4.722 \times 10^9$

### 2.3 Plate with Multiple Stress Concentration Zones

#### Case B: Plate with Three Holes Arranged Parallel to Loading Direction

Consider a specimen made up of Al 2024-T351 having three holes arranged parallel to the loading direction as shown in Fig. 4, and the material properties are given in Table 1. The critical stress location after the stress analysis was at the outer holes having a magnitude of 145 MPa. The same procedure as in previous section was carried out here for three different stress ratios, and the obtained fatigue life results are tabulated in Table 3 and compared with the literature [8].

#### Case C: Plate with Three Holes Arranged Perpendicular to Loading Direction with Edge Distance 35 mm

Consider a specimen made up of Al 2024-T351 having three holes arranged perpendicular to the loading direction as shown in Fig. 5 with the edge distance of 35 mm and the material properties are given in Table 1. The stress is critical at the centre hole with the magnitude of 218 MPa. The same procedure as in previous section was carried out here for three different stress ratios and the estimated fatigue life results are tabulated in Table 4 and compared with the literature [8].

#### Case D: Plate with Three Holes Arranged Perpendicular to Loading Direction with Edge Distance 25 mm

Consider a specimen made up of Al 2024-T351 having three holes arranged perpendicular to the loading direction as shown in Fig. 5 with the edge distance of

Fig. 4 Plate with three holes arranged parallel to loading direction

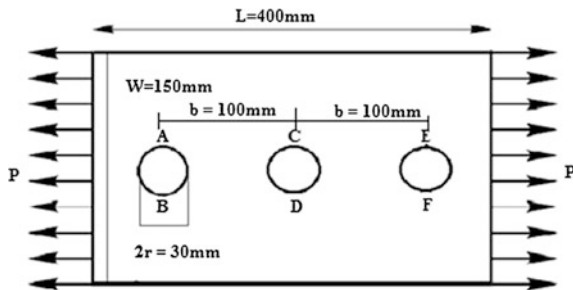
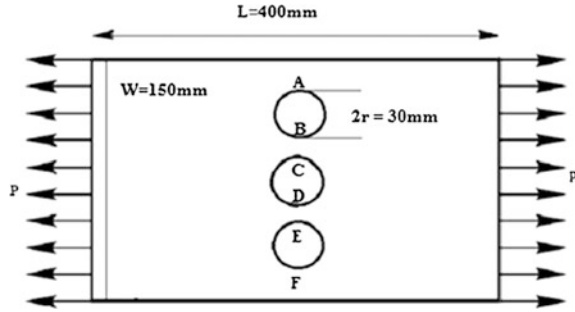


Table 3 Fatigue results for plate with three holes arranged parallel to loading direction (Case B)

	Literature [8]	Present work using MATLAB
Critical stress	146.13 MPa	144.68 MPa
Stress ratio ( $R$ )	Fatigue life ( $N_f$ ) (cycles)	
$R = -1$	$2.214 \times 10^7$	$2.423 \times 10^7$
$R = 0$	$2.664 \times 10^9$	$2.962 \times 10^9$
$R = 0.1$	$5.887 \times 10^9$	$6.552 \times 10^9$

**Fig. 5** Plate with multiple stress concentration zones (Three holes arranged perpendicular to loading direction)



**Table 4** Fatigue results for plate with three holes arranged perpendicular to loading direction (Case C)

	Literature [8]	Present work using MATLAB
Critical stress	218.87 MPa	217.935 MPa
Stress ratio ( $R$ )	Fatigue life ( $N_f$ ) (cycles)	
$R = -1$	$5.627 \times 10^5$	$5.85 \times 10^5$
$R = 0$	$2.872 \times 10^7$	$3.018 \times 10^7$
$R = 0.1$	$5.685 \times 10^7$	$5.985 \times 10^7$

25 mm and the material properties are given in Table 1. The critical stress location was at the outer holes with the magnitude of 226 MPa. The same procedure as in previous section was carried out here for three different stress ratios, and the fatigue life results are tabulated in Table 5 and compared with the literature [8].

It is found that results were in good agreement with the literature [8]. The fatigue life study validated the procedure followed using FEM and MATLAB, and the MATLAB code was also verified. Furthermore, the plate with stress concentration zones perpendicular to loading direction will have less life as compared to the plate with stress concentration zones parallel to loading direction. As the stress concentration zone comes closer to the periphery, it is evident that it will change the critical stress location and hence reduces the fatigue life of the component.

**Table 5** Fatigue results for plate with three holes arranged perpendicular to loading direction (Case D)

	Literature [8]	Present work using MATLAB
Critical stress	225.716 MPa	225.669 MPa
Stress ratio ( $R$ )	Fatigue life ( $N_f$ ) (cycles)	
$R = -1$	$4.254 \times 10^5$	$4.261 \times 10^5$
$R = 0$	$1.994 \times 10^7$	$1.997 \times 10^7$
$R = 0.1$	$3.900 \times 10^7$	$3.910 \times 10^7$

### 3 Probabilistic Fatigue Life Estimation Using Latin Hypercube Sampling

#### 3.1 Probabilistic Approach

Reliability,  $R(t)$ , is a characteristic of an item, expressed by the probability that the item will perform its required function under given conditions for a stated time interval. Probability of failure,  $F(t)$ , of a component or system is defined as the probability that the component or system experiences the first failure or has failed one or more times during the stated time interval [9]. Reliability function gives the probability of an item operating for a certain amount of time without failure.

$$R(t) + F(t) = 1 \quad (5)$$

A probability distribution is a table or an equation that links each outcome of a statistical experiment with its probability of occurrence. Probability density function of a random variable is a function that describes the relative likelihood for the random variable to take on a given value. There are different probability distributions which are used for statistical analysis. Uniform distribution of continuous random variable is one, if all the values belonging to its support have the same probability density. It is also known as rectangular distribution.

The Monte Carlo technique is a numerical method based on a probabilistic interpretation of quantities obtained from algorithmically generated random variables. For reliability purposes, a Monte Carlo simulation can basically be used to estimate a value (e.g. an unknown probability) or simulate (reproduce) the stochastic process describing the behaviour of a complex system [9].

There are various sampling techniques in Monte Carlo simulation which effectively reduces variance and hence computational time. One among the techniques is Latin Hypercube sampling which is used in this study for variance reduction. Latin Hypercube sampling (LHS), a stratified random procedure, provides an efficient way of sampling variables from their distributions. The cumulative distribution for each variable is divided into ' $N$ ' equiprobable intervals. A value is selected randomly from each interval. The ' $N$ ' values obtained for each variable are paired randomly with the other variables. Unlike simple random sampling, this method ensures a full coverage of the range of each variable by maximally stratifying each marginal distribution [10] (Fig. 6).

Using LHS, the fatigue random variables were generated with suitable probability distributions and the probabilistic fatigue life was calculated. The fatigue reliability and fatigue probability of failure were calculated using the generated samples based on the design fatigue life.



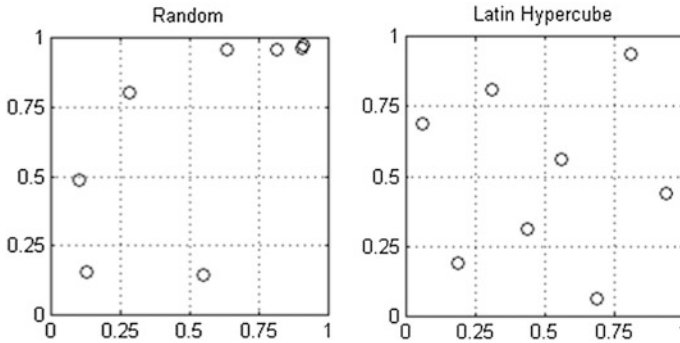


**Fig. 6** Random sampling (Monte Carlo) and Latin Hypercube sampling

### 3.2 Nastran Integration with MATLAB

MSC Nastran was a multidisciplinary structural analysis application used to perform static, dynamic and thermal analysis across the linear and nonlinear domains, all enabled by high-performance computing. Nastran deck provided flexibility in editing parameters when integrated with MATLAB. The specimen was modelled in HyperMesh and FEA was performed using Nastran. The Bulk Data File (.bdf) generated from HyperMesh was solved in the Nastran solver which could be edited for randomising the parameters such as applied load, thickness and Young's Modulus in integration with MATLAB. The fatigue reliability analysis was carried out using the tools MSC Nastran and MATLAB. Random numbers using Monte Carlo or Latin Hypercube sampling were generated in MATLAB, and those random numbers were given as input to the bulk data file of the Nastran, and static stress analysis was carried out. The critical stress value from the output file was taken to the MATLAB file, and the fatigue life was calculated using the MATLAB code. Hence, the 'n' number of fatigue life was generated corresponding to the 'n' number of random input variables. After that based on the design life, the reliability and probability of failure were calculated from the number of samples crossed the design life.

Fatigue reliability analysis was carried out by considering the fatigue material properties, thickness of the plate specimen and the applied load as random input variables which were generated using either Monte Carlo or Latin Hypercube sampling techniques with the help of MATLAB code. The analysis was performed considering one input variable as random at a time, and reliability was calculated. Fatigue strength coefficient ( $S_f$ ), fatigue strength exponent ( $b$ ), applied load and thickness of the plate were treated as random variables. These parameters were varied by 3, 5 and 10% from its deterministic value. These parameters with variations were analysed for constant amplitude loading history with the stress ratios  $R = -1$  (completely reversed),  $R = 0$  (pulsating tension),  $R = 0.1$  (tension-tension). Lognormal distribution was applied for material random variables such as  $S_f$ ,  $b$  and thickness. Normal distribution was used for applied load.

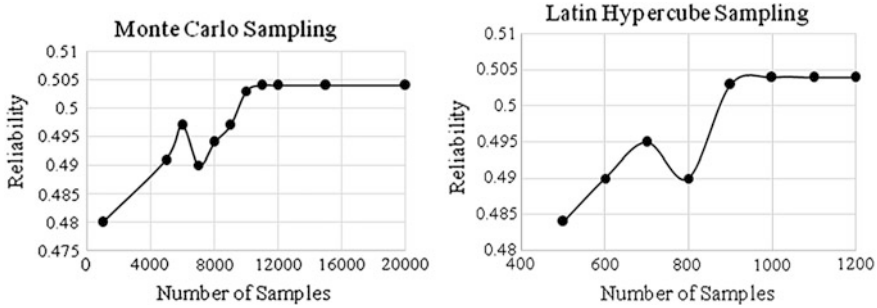


Fig. 7 Convergence study of Monte Carlo sampling method and Latin Hypercube sampling

Sample Convergence Study

Initially, convergence study was carried out by considering a single case (plate with single stress concentration zone for constant amplitude loading history with the stress ratio  $R = 0.1$  (tension–tension) having applied load as a random variable with 5% variation from the mean value) using Monte Carlo and Latin Hypercube sampling techniques. Deterministic fatigue life was taken as the design life for the reliability calculations. The number of samples was increased gradually starting from very less samples, and the results are shown in graph (Fig. 7).

From the graph, it is clear that in the case of Monte Carlo Sampling from 10,000 samples onwards, the reliability result starts to converge, and hence in this study, we used a total of 10,000 samples in the case of Monte Carlo Sampling. But, in the case of Latin Hypercube sampling, even from 1000 samples onwards, the result starts to converge, and because of this, the computation time will be less for LHS method.

Latin Hypercube sampling is a specialised Monte Carlo method with stratified sampling applied to input variables resulting in faster convergence to the mean value with less number of samples as compared to crude Monte Carlo method.

From Fig. 8, it is clear that in the case of LHS even for 10 samples, the deviation from mean value is very less. The similar results are achieved in the Monte Carlo

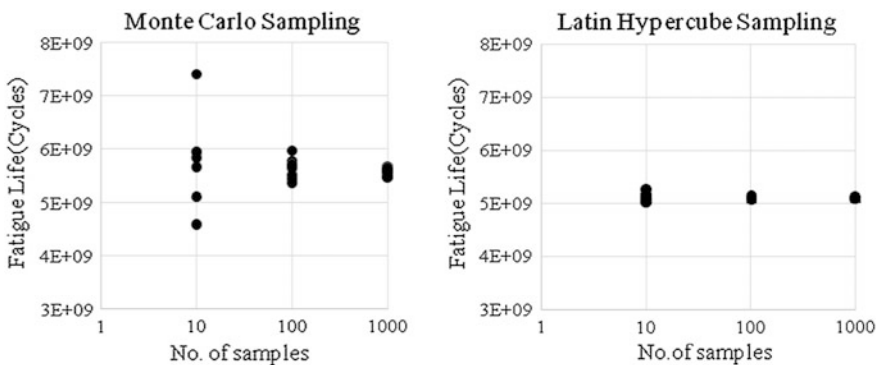


Fig. 8 Convergence towards mean value

**Table 6** Reliability comparison between crude MC method and LHS

Parameter varied	Stress ratio	Std. dev.	Design life	Reliability		
				Crude MC ( $n = 10,000$ samples)		LHS ( $n = 1000$ samples)
				Present work	Literature [11]	
Applied load	$R = 0.1$	5%	$1 \times 10^9$	1.0000	1.0000	1.0000
			$1 \times 10^{10}$	0.5134	0.5130	0.5140
			$1 \times 10^{11}$	0.0000	0.0000	0.0000

Sampling only when 1000 samples are used. Reliability values are tabulated for Latin Hypercube sampling (LHS) method for 1000 samples. Applied load was treated as random variable with 5% variation using normal distribution. Samples were carried out for tension–tension ( $R = 0.1$ ) loading conditions. The reliability values obtained from LHS were compared with that of crude Monte Carlo method (Table 6).

The result shows that LHS method is comparable with the crude MC method with less number of samples. Hence, LHS is used for the further analyses.

### 3.3 Parametric Studies

Reliability values of the plate with single stress concentration zone for a set of design lives were calculated for variation in the input random variables such as  $S_f$ ,  $b$ , force and thickness. The simulations were performed for each individual random variable for 3, 5 and 10% variation from their mean value and also for different stress ratios mentioned earlier. This procedure was followed for other cases B, C and D also. Deterministic fatigue life was considered as the design life value. A sensitivity analysis of all the parameters was performed, and observations were inferred. Table 7 shows the results of the plate with single and multiple stress concentration zones subjected to tension–tension loading. The 1000 random values of all the variables were generated using Latin Hypercube sampling, and the standard deviation of the random variables was 3%.

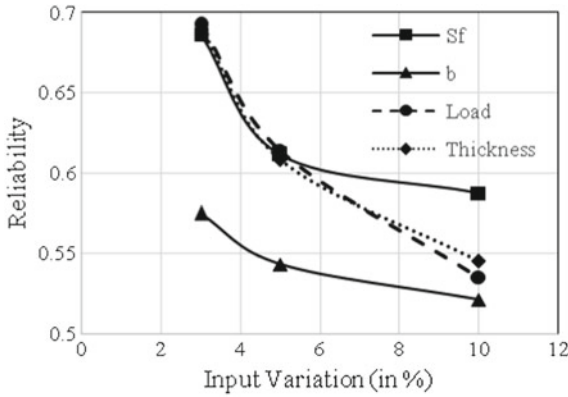
Fatigue life variation was calculated for each and individual random variables, i.e. fatigue strength coefficient ( $s_f$ ), fatigue strength exponent ( $b$ ), applied load ( $p$ ) and thickness of the plate ( $t$ ). Since in Table 7, the design life is not the same, hence, the reliability values could not be compared between the different cases (Case A, B, C and D).

#### Sensitivity analysis

Plate with single stress concentration zone subjected to pulsating loading history ( $R = 0$ ) was considered for the sensitivity analysis. For applied load, normal

**Table 7** Fatigue reliability values for all specimens

Random variables	Reliability n = 1000 samples (3% variation) (Tension-tension loading)			
	Case A (Design life = 5.1E9 cycles)	Case B (Design life = 7.479E9 cycles)	Case C (Design life = 6.554E7 cycles)	Case D (Design life = 4.809E7 cycles)
Fatigue strength coefficient, $S_f$	0.5210	0.5900	0.6290	0.5900
Fatigue strength exponent, $b$	0.5230	0.5410	0.5510	0.5350
Applied load	0.5300	0.5770	0.5900	0.5700
Thickness	0.5310	0.5630	0.5810	0.5710



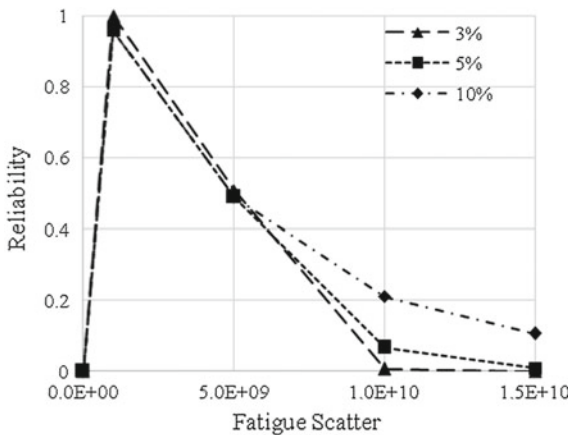
% Variation	$S_f$	$b$	Load	Thickness
3	0.686	0.575	0.692	0.69
5	0.611	0.543	0.614	0.608
7	0.587	0.521	0.535	0.545

Fig. 9 Sensitivity analysis of input random variables

distribution was used, whereas for other parameters, lognormal distribution was used since they should be of positive numbers (Fig. 9).

It was found from the graph that fatigue strength exponent ( $b$ ) had highest influence on fatigue life of the given plate with single stress concentration zones. This is a material property of the given material which is the slope of the  $S-N$  curve. This variable ' $b$ ' forms the exponent part of the Basquin's equation. Hence, minor variation resulted in exponential change in fatigue life of the component.

The effect of scatter and the effect of design life in the fatigue reliability were carried out in this study for the plate with the single stress concentration zone subjected to tension–tension loading having fatigue strength coefficient as the random variable. Fatigue life scatter for the different coefficient of variations were made and plotted as graph against reliability values (Fig. 10).



Design Life	3%	5%	7%
0	0	0	0
1.00E9	0.9997	0.9583	0.9583
5.00E9	0.508	0.4889	0.4889
1.00E10	0.0071	0.0664	0.2107
1.50E10	0	0.009	0.1063

Fig. 10 Fatigue scatter against reliability

As the input random variable scatter increases, the fatigue life scatter also getting increased and was more deviating from the mean value and the reliability value was found to be decreased. As the design life increases, the reliability was drastically decreasing. If the deterministic fatigue life was the design life, 50% reliability can be obtained. Hence, for the particular specimen, the deterministic fatigue life could be the fatigue life with 50% certainty.

## 4 Conclusions

Deterministic fatigue life was estimated for plate with single and multiple stress concentration zone specimens using Nastran and MATLAB, and the results were compared with the literature. Among the various specimens considered, the plate with stress concentration zones perpendicular to loading direction will have less life as compared to the plate with stress concentration zones parallel to loading direction. A probabilistic fatigue life estimation procedure was established using the integration of MSC Nastran and MATLAB. MATLAB was used to generate the random numbers and to calculate the fatigue life and reliability. MSC Nastran was used to find the critical stress location and the magnitude of the specimen. Using Latin Hypercube sampling technique, reduction in computation time was achieved as compared to crude Monte Carlo method in the probabilistic fatigue life estimation. The fatigue strength exponent random variable was affecting the fatigue reliability more when compared to the other three random variables. Coefficient of variation of input variable was directly proportional to the fatigue life scatter and inversely proportional to the reliability.

**Acknowledgements** The authors would like to thank Head, Structural Technologies Division, CSIR-NAL, and the Director, CSIR-NAL, for their support and encouragement to carry out the work reported in this paper. The authors would also like to express their thanks to the people who contributed to this work directly or indirectly.

## References

1. Schijve J (2001) *Fatigue of structures and materials*, 2nd edn. Springer, Berlin. ISBN-13: 978-1-4020-6807-2
2. Dhillon BS (1999) *Design reliability fundamentals and applications*, 1st edn. CRC Press. ISBN 0-8493-1465-8
3. Marian Zaharia S (2015) Fatigue life simulation of the specimens made of mechanical component. In: International conference on scientific paper, AFASES, Brasov, 28–30 May 2015
4. Chen JX, Yan WC (2004) Mechanical spring reliability assessments based on FEA generated fatigue stresses and Monte Carlo simulated stress/strength distributions. In: International conference on compressor engineering, School of Mechanical Engineering Purdue University

5. Kala Z (2006) Sensitivity analysis of fatigue behaviour of steel structure under in-plane bending. *Nonlinear analysis. Modell Control* 11(1):33–45
6. Mrad H, Saudi A, Bouazara M (2011) Fatigue reliability analysis using latin hypercube sampling method. In: *SIMULIA customer conference*. University of Quebec at Chicoutimi, Canada (2011)
7. Lee YL, Pan J, Hathaway R, Barkey M. *Fatigue testing analysis*, 1st edn. Elsevier, Amsterdam. ISBN-0: 7506-7719-8
8. Keerthi HG, Sivaranjani T, Pavan Kumar DVTG, Manjuprasad M, Dinesh SV (2013) Fatigue life prediction of plate with multiple stress concentration zones using FEM. In: *International conference on computer aided engineering* (2013)
9. Biroloni A. *Reliability engineering: theory and practice*, 5th edn. Springer, Berlin. ISBN 978-3-662-05409-3
10. Cochran WG (2007) *Sampling techniques*, 3rd edn. Wiley, New York. ISBN 978-0-471-16240-7
11. Sivaranjani T, Manjuprasad M (2015) *Fatigue reliability analysis of plate with multiple stress concentration zones*. TM-STT/2015/1003, CSIR-NAL Bangalore

# Creep–Fatigue Interaction Study on Gas Turbine Engine Alloy

Neeta Paulose, D. Chandru Fernando, Amborish Banerjee, J.K. Sahu and S.N. Narendra Babu

**Abstract** Alloy IN 718 is used for manufacturing many critical components of gas turbine engine such as compressor blades, discs, and shafts. During engine operation, these components are subjected to cyclic loading along with steady-state operation at high temperatures. These operating conditions induce damage resulting from interaction of creep and fatigue. In order to predict realistically the life of these components, it is necessary to understand creep–fatigue interaction mechanisms and important to carry out test at conditions simulating engine parameters. Therefore, isothermal LCF tests with and without hold time were conducted at a temperature of 600 °C, strain rate of  $10^{-3} \text{ s}^{-1}$  and total strain amplitude varying from 0.4 to 0.6%. Hold time of 1 and 5 min was inserted at maximum strain amplitude to give tensile dwell condition. In gas turbine engine, the presence of centrifugal force of rotating components leads to sustained tensile load in addition to varying loads; therefore, it was decided to have dwell time at peak tensile strains. The investigation revealed that the fatigue life was adversely affected when hold time was introduced at peak strain. The effect on fatigue life with 1- and 5-min hold is discussed. Deformation mechanism of tested samples was also studied using SEM.

---

N. Paulose (✉) · D. Chandru Fernando · S.N. Narendra Babu  
Gas Turbine Research Establishment, DRDO, Bangalore, India  
e-mail: neeta\_paulose@gtre.drdo.in

D. Chandru Fernando  
e-mail: chandruferrando@gtre.drdo.in

S.N. Narendra Babu  
e-mail: narendrababusn@gtre.drdo.in

A. Banerjee · J.K. Sahu  
CSIR-National Metallurgical Laboratory, Jamshedpur, India  
e-mail: amborishbanerjee1205@gmail.com

J.K. Sahu  
e-mail: jksahu@nmlindia.org

A. Banerjee  
University of New South Wales (UNSW), High St., Kensington, NSW 2052, Australia



**Keywords** Iron–nickel-based superalloy • LCF • Creep–fatigue interaction  
Deformation mechanism

## 1 Introduction

IN 718 is an iron–nickel-based precipitation-hardenable wrought superalloy designed to combine excellent strength with good fabrication abilities. The main precipitation strengthening phases are  $\gamma'$  ( $\text{Ni}_3(\text{Al}, \text{Ti})$ -FCC phase),  $\gamma''$  ( $\text{Ni}_3\text{Nb}$ -BCT) and  $\delta$ -phase ( $\text{Ni}_3\text{Nb}$ –orthorhombic).  $\gamma''$  is the primary strengthening phase followed by  $\gamma'$ . Theoretically, volume fraction of  $\gamma'$  and  $\gamma''$  is estimated to be 8 and 13% [1, 2]. The  $\delta$ -phase precipitates initially at grain boundaries, forming a film along the boundary, and some grow into the grains as long but extremely thin plates. As precipitation proceeds,  $\delta$ -phase extends uniformly throughout the microstructure. When present in controlled limit, during hot forging and solution treatment  $\delta$ -phase controls grain growth and grain shape by boundary pinning. In this way, grain morphology is adjusted to enhance low-cycle fatigue resistance [3]. However, higher volume fraction of  $\delta$ -phase reduces indirectly the strength of the fully hardenable alloy by depleting the amount of niobium available for  $\gamma''$  hardening. This is often seen as a precipitate-free zone around the  $\delta$  plates.

$\gamma''$  is metastable phase, which transforms to stable orthorhombic  $\delta$ -phase during long-term exposure at temperature above 650 °C.  $\delta$ -phase is fully incoherent with  $\gamma$  matrix and is less strengthening than  $\gamma''$  phase. The transformation of  $\gamma''$  to  $\delta$ -phase and its relatively rapid coarsening kinetics above 700 °C [4] limit the usage of alloy IN 718 to 650 °C.

IN 718 is widely used for manufacturing compressor aerofoil, disc and shaft of gas turbine engines. These components in gas turbine engines undergo complex loading conditions at high temperature. Therefore, the life-limiting damage mechanisms of these components are low-cycle fatigue (LCF) and creep. In order to actually predict the life of blades and discs, it is important to understand the synergistic effect of creep–fatigue (CF) interaction with environment at high temperature. CF interaction behaviour of material can be studied by conducting experiments on either smooth specimen or notched specimen. Fatigue experiments on smooth specimens provide information on the material behaviour in terms of cyclic hardening/softening, damage accumulation contributed through creep and fatigue in addition to creep–fatigue life [5–9]. On the other hand, notch specimens are employed to study crack growth using fracture mechanics approach [10–12]. In smooth specimen, creep damage can be introduced during isothermal LCF testing either by decreasing the strain rate or by holding the test for some duration at peak strain. The hold time during the course of a strain-controlled LCF test can be introduced at peak strain in either strain-controlled or stress-controlled mode. When the hold time is introduced at peak strain during strain control, the material relaxes, and this is known as a relaxation fatigue (RF) test.

The present study reports the results of RF tests on IN 718 at 600 °C at varying strain amplitudes and hold times. Banerjee et al. [13] have already reported that micro-mechanism of cyclic plastic deformation changes from lower to higher strain amplitude and also during hold-time fatigue exploitation of alloy IN 718. For example, it is observed in [13] that micro-twinning is the predominant mode of plastic deformation at lower strain amplitudes, whereas slip and shearing of precipitates are dominant plastic deformation modes at higher strain amplitude. It is also observed in [13] that the NbC precipitates in IN 718 coarsen during hold-time fatigue tests at 600 °C. However, research reports on fatigue fracture mechanisms during hold-time fatigue tests are scarce. The present paper studies the change in fracture mechanisms when hold time is introduced during fatigue tests of alloy IN 718 at 600 °C.

## 2 Material and Experimental Procedure

IN 718 rods of 15 mm diameter and 500 mm length in fully heat-treated condition (solution-annealed condition (960 °C ± 10 °C-1 h, air cool) and double-aged (720 ± 5 °C-8 h, furnace cooling at 55 °C/h to 620° ± 5 °C, holding at 620 ± 5 °C-8 h, air cool) were used for the present study. The chemical composition of the investigated alloy is given in Table 1.

Microstructure of the material was studied through SEM, and disc-shaped  $\delta$  phases in grain boundary and niobium carbide (NbC) in  $\gamma$  matrix are seen (Fig. 1a). TEM study revealed the presence of primary strengthening phase  $\gamma''$  (needle shape) and secondary strengthening phase  $\gamma'$  (spherical shape).  $\gamma'$  is present as fine-distributed precipitates at the pin of  $\gamma''$  (Fig. 1b).

**Table 1** Chemical composition of IN 718 alloy, wt%

Ni	Cr	Co	Mo	Fe	Si	Mn	Al	Ti	Cu	P	B	Nb + Ta	C
52	19	1	3.05	19	0.35	0.35	0.6	0.9	0.3	0.015	0.006	5.125	0.08

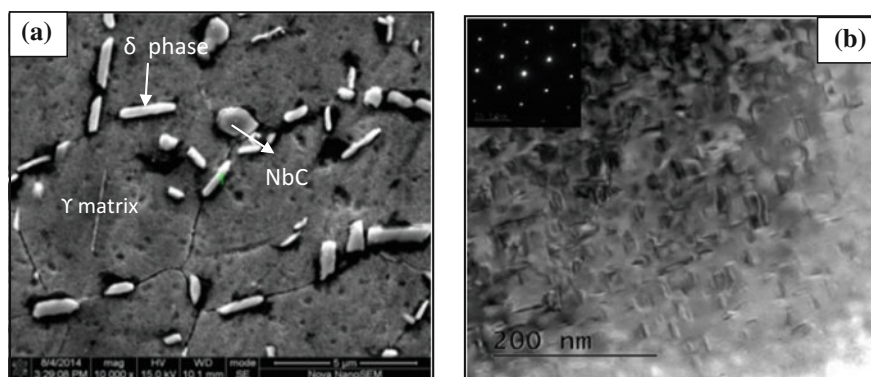


**Fig. 1** a SEM image, b TEM image showing  $\gamma'$  and  $\gamma''$

Test specimens for tensile, LCF and CF tests were fabricated from the fully heat-treated rods. A dimensional drawing of the fatigue test specimen is shown in Fig. 2. Tensile testing was carried out at 600 °C in accordance with ASTM E 21.

Isothermal LCF tests were conducted at 600 °C under fully reversed ( $R = -1$ ) condition at total strain amplitude ( $\Delta\epsilon/2$ ) varying from 0.4 to 0.6% as per ASTM E 606. For CF test, for all strain amplitudes, 5-mins hold time was introduced at maximum tensile strain to replicate engine condition. The waveform used in LCF and CF tests is shown in Fig. 3. To understand the effect of duration of hold time on property degradation, 1-min hold-time test at  $\Delta\epsilon/2$  0.6% was also carried out. Hold-time tests were conducted in accordance with ASTM E 2714. Figure 4 illustrates the corresponding shapes of hysteresis loops of hold and no hold test. The effect of hold time in stress relaxation which leads to creep–fatigue damage is seen (Fig. 4).

Servo-electric Instron 8862 machine of 100 KN capacity was used for the LCF and CF studies. The strain rate was maintained at 0.001/s. The strain amplitudes were selected such that the material undergoes adequate plasticity and represents

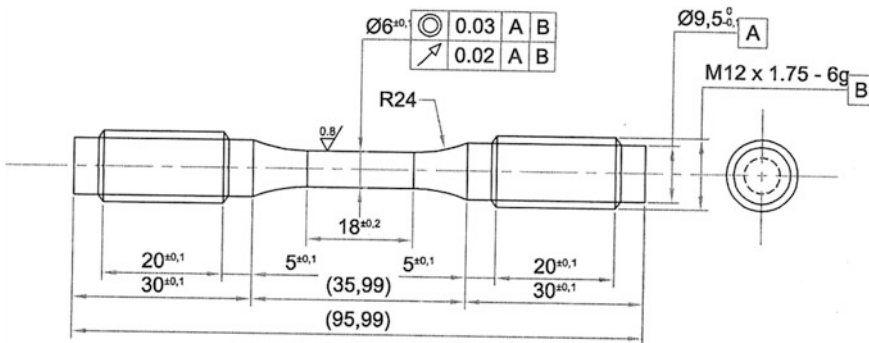
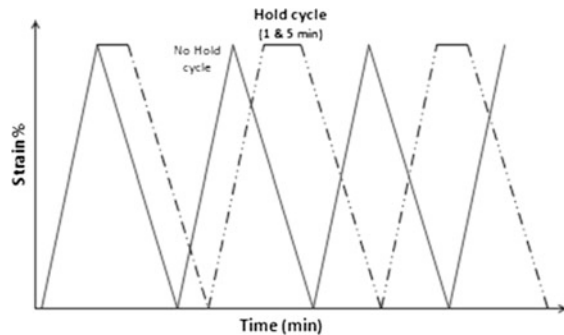
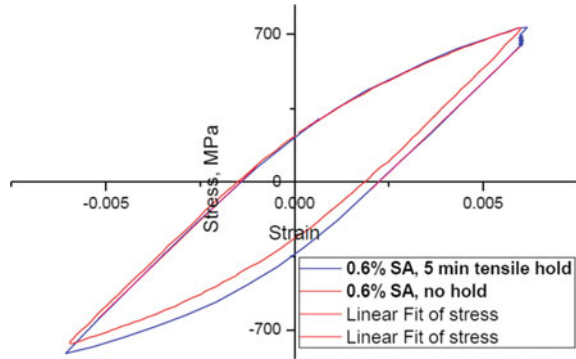


Fig. 2 Dimensional drawing of the specimen

Fig. 3 Waveforms used in the testing



**Fig. 4** Hysteresis loop of test at total strain amplitude 0.6% without hold and with 5-min tensile hold



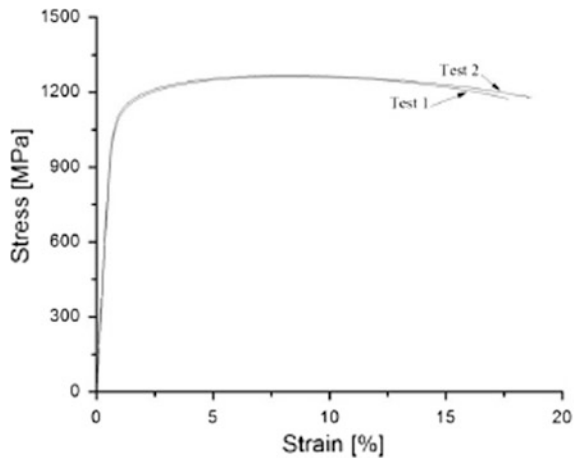
engine conditions. High-temperature extensometers having ceramic rods and a gauge length of 12.5 mm were used for strain measurement. To determine the damage micro-mechanism evolved during LCF and CF interaction tests, fracture surface of the tested samples was studied using SEM.

### 3 Results and Discussion

#### 3.1 Tensile Testing

The stress–strain curve is given in Fig. 5. The average 0.2% offset yield strength, ultimate tensile strength and % elongation of the material at 600 °C are 1152, 1272 MPa and 18%, respectively.

**Fig. 5** Engineering stress–strain curve



### 3.2 LCF and CF Tests

The cyclic hardening/softening curves for all the hold-time tests are plotted as a function of peak tensile/compressive stress amplitude with progress of cyclic life and shown in Fig. 6. It is observed that the tensile/compressive stress relaxes and material exhibits cyclic softening behaviour. Similar cyclic softening behaviour is seen in no-hold fatigue test, which is explained in detail by the authors in Ref. [13].

Total strain amplitude ( $\Delta\epsilon/2$ )-Life ( $N$ ) curve for LCF and CF tests is plotted and given in Fig. 7. As expected, both LCF life and CF life decrease with increase in strain amplitude.

Cyclic life of alloy IN 718 is drastically reduced, when hold time is introduced during fatigue test (Fig. 8). The life reduction factor is listed in Table 2. It is observed that the degradation factor is highly specific to the total strain amplitude.

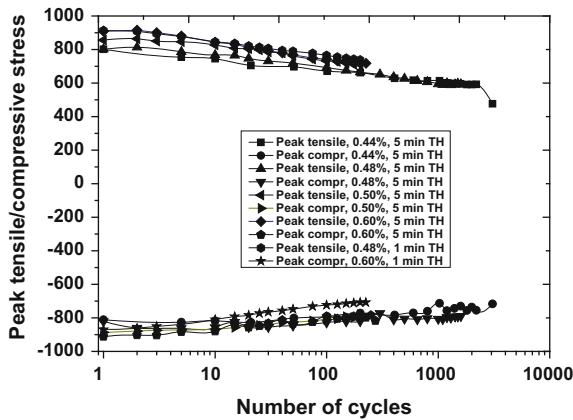


Fig. 6 Cyclic softening and hardening behaviour of CF tests

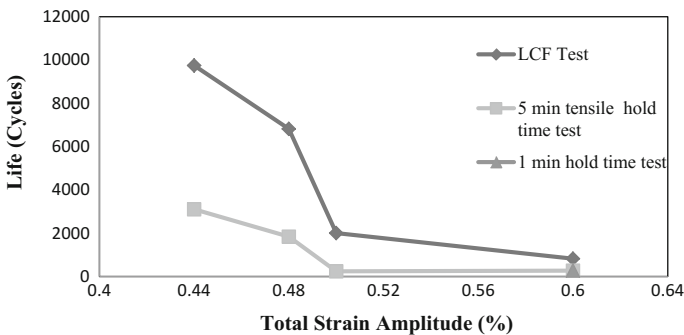
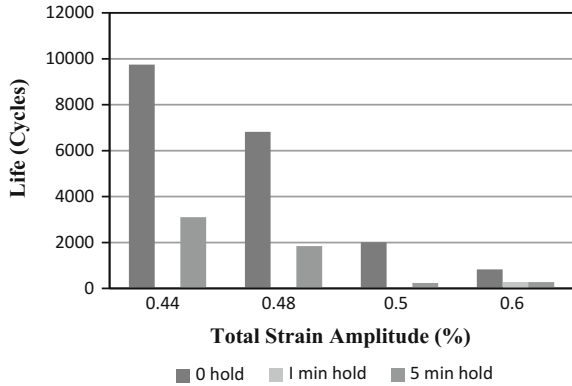


Fig. 7 Strain-life curve at 600 °C

**Fig. 8** Effect of hold time on fatigue life



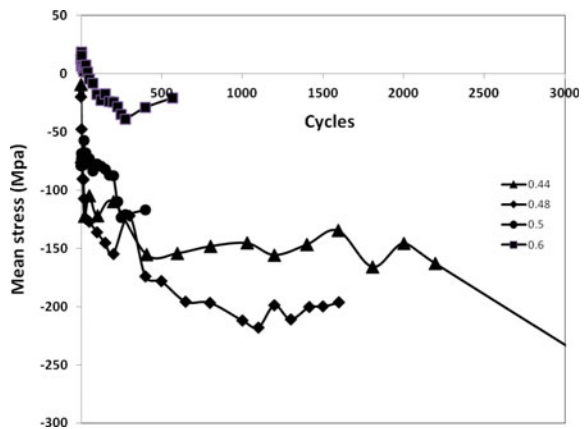
**Table 2** Life reduction factor

Total strain amplitude $\Delta\epsilon/2$	Fatigue life reduction factor (fatigue life-CF life)/fatigue life (without hold)	
	1 min	5 min
0.44	–	0.68
0.48	–	0.54
0.5	–	0.90
0.6	0.53	0.55

Highest degradation is seen at total strain amplitude of 0.5%. More detailed study is required to understand the reason for this phenomenon.

The mean stress developed during hold-time fatigue tests is plotted and shown in Fig. 9. The mean stress is compressive in nature. It has been reported that compressive mean stress is introduced during tensile hold and tensile mean stress during

**Fig. 9** Mean stress in tensile hold-time test



compressive hold. Compressive hold is found to be more damaging than tensile hold [14].

As can be observed from Table 2, duration of hold does not have significant effect on fatigue life. Maximum dwell stress relaxation happens in first few cycles at all strain amplitudes, and this may be the reason for less effect of duration of hold time (Fig. 10).

From the hold-time test, crack initiation time can be predicted. The change in slope of stress ratio/number of cycle indicates crack initiation (Fig. 11).

### 3.3 SEM Analysis

Fracture mechanism of the tested samples was studied using SEM analysis. It is found that the failure is of transgranular nature in pure fatigue test. Striations

**Fig. 10** Dwell stress relaxation at each cycle during fatigue test

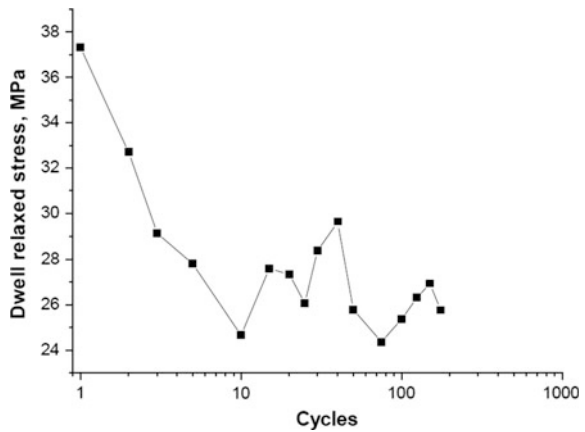
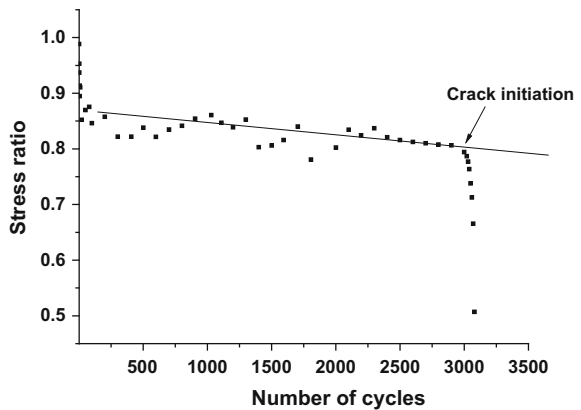


**Fig. 11** Hold-time test at total strain amplitude 0.44% and 5-min tensile hold



indicative of stage II fatigue crack growth and failure are shown in Fig. 12b. In hold-time test, the effect of creep in crack initiation can be seen. Multiple crack origin and intergranular cracks are seen in CF tests (Fig. 13a, b). It is observed that origin of fatigue cracks is of transgranular nature during pure LCF and intergranular nature when hold time is introduced (Figs. 12c and 13c). The intergranularity during hold-time tests might be attributed to cavitations and oxidation of grain boundaries [15].

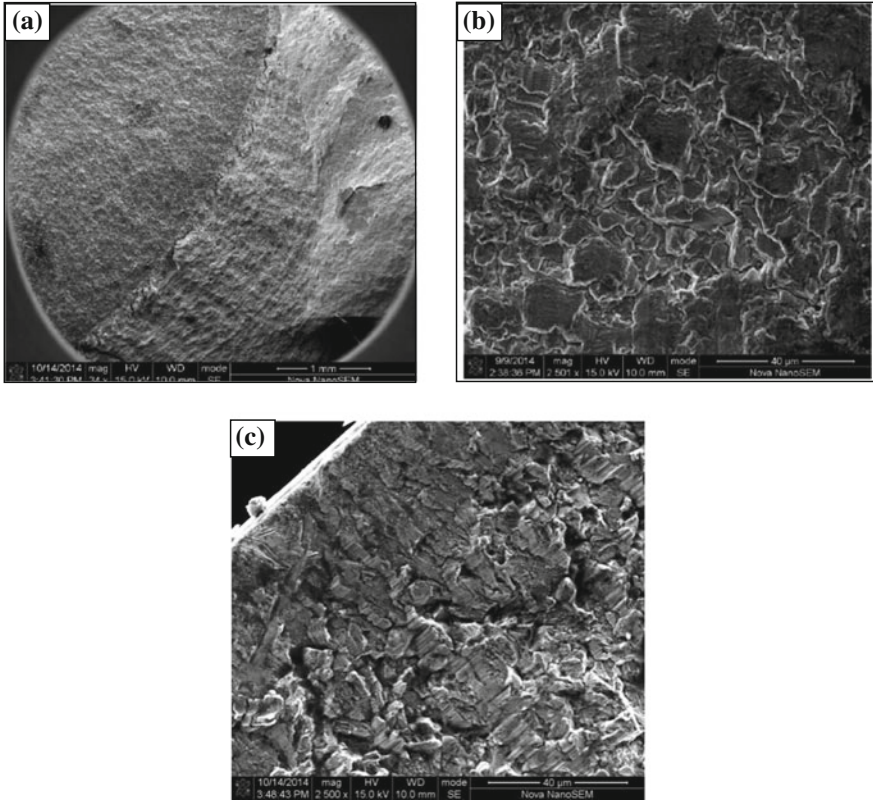
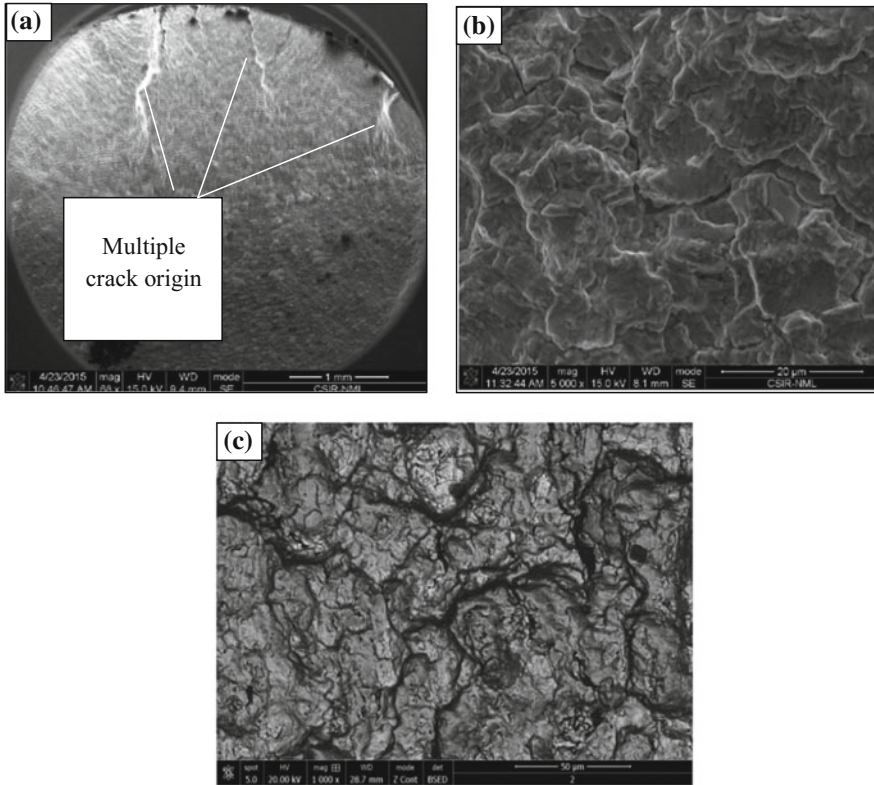


Fig. 12 SEM analysis of LCF tested at 0.4 total strain amplitude at 600 °C





**Fig. 13** SEM analysis CF test (0.6, total strain amplitude, 5-min tensile hold at 600 °C)

## 4 Conclusions

- Cyclic softening is seen during hold-time test.
- Fatigue life significantly dropped when hold time was introduced at tensile peak stress.
- The fatigue life was not affected significantly when hold duration was increased from 1 to 5 min. This may be attributed to max dwell stress relaxation during initial few cycles.
- For the LCF tests the fracture mode is transgranular, and for hold-time test the fracture mode is intergranular.

**Acknowledgements** The authors express their gratitude to DRDO and Director, GTRE for supporting the work and granting permission to publish the data. The support and guidance provided by the Technical and Associate Directors are also gratefully acknowledged. The authors also acknowledge Director, NML for facilitating the mechanical tests at NML.

## References

1. Donachie MJ, Donachie SJ (2002) *Superalloys a technical guide*, 2nd edn. ASM International
2. Wagner HJ, Hall AM (1965) Physical metallurgy of alloy 718. DMIC Report 217
3. Bowers RJ, Lippold JC (1997) The effect of composition and heat treatment cycles on the repair weldability of alloy joining and repair of gas turbine components. ASM International, pp 41–50
4. Richards NL, Benhadad S, Chaturvedi MC (2002) The influence of minor elements on the weldability of an Inconel 718-type superalloy. *Met Trans* 33A:2005–2017
5. Hu D, Wang R (2009) Experimental study on creep-fatigue interaction behaviour of GH4133B superalloy. *Mat Sci Eng A*. 515:183–189
6. Billot T, Villechaise P, Jouiad M, Mendez J (2010) Creep-fatigue interaction behaviour at high temperature of a Udimet 720 nickel-base superalloy. *Int J Fatigue* 32:824–829
7. Tinga T, Brekelmans WAM, Geers MGD (2009) Time-incremental creep-fatigue damage rule for single crystal Ni-base super alloys. *Mater Sci Eng A* 508:200–208
8. Pierce CJ, Palazotto AN, Rosenberger AH (2010) Creep and fatigue interaction in the PWA1484 single crystal nickel-base alloy. *Mater Sci Eng A* 527:7484–7489
9. Totemeier TC, Tian H (2007) Creep-fatigue-environment interactions in Inconel 617. *Mater Sci Eng A* 468:81–87
10. Smith HH, Michel DJ (1986) Effect of environment on fatigue crack propagation behaviour of alloy 718 at elevated temperatures. *Metall Trans A* 17A:370–374
11. Evans WJ, Jones JP, Williams S (2005) The interaction between fatigue, creep and environmental damage in Ti6246 and Udimet 720Li. *Int J Fatigue* 27:1473–1484
12. Yokobori T, Yolobori AT Jr (2001) High temperature creep, fatigue and creep-fatigue interaction in engineering materials. *Int J Pressure Vessels Pip* 78:903–908
13. Banerjee A, Sahu JK, Paulose N, Fernando CD, Ghosh RN (2015) Isothermal low cycle fatigue and creep-fatigue interaction behaviour of nickel based superalloy Inconel 718. *FFEMS* 39(7):877–885
14. Gopinath K, Gupta RK, Sahu JK, Ray PK, Ghosh RN (2015) Designing P92 grade martensitic steel header pipes against creep–fatigue interaction loading condition: damage micromechanisms. *Mat Design* 86:411–420
15. Ostergren WJ (1976) A damage function and associated failure equations for predicting hold time and frequency effects in elevated temperature low cycle fatigue. *J Test Eval* 4(5):327–339

# Evaluation of Implicit Reliability Level Associated with Fatigue Design Criteria of Nuclear Class-1 Piping

J. Mishra and V. Balasubramaniyan

**Abstract** Fatigue design of Class-1 piping of NPP is carried out as per Section-III of American Society of Mechanical Engineers (ASME) Boiler and Pressure Vessel code. The fatigue design criteria of ASME are based on the concept of safety factor, which does not provide means for management of uncertainties for consistently reliable designs. In this regard, a work is taken up to estimate the implicit reliability level associated with fatigue design criteria of Class-1 piping specified by ASME Section III, NB-3650. The methodology employed for reliability evaluation is FORM, HORSIM and MCS, where limit state function is derived using mean fatigue curve developed by Argonne National Laboratory. A number of important aspects related to reliability of various piping product and joints are discussed, and implicit reliability level is evaluated.

**Keywords** ASME · Fatigue · Implicit reliability · FORM · HORSIM · Piping

## Nomenclature

$a$	Constant term of polynomial
$A, B, C$	Constants of Langer equation
$b_{ij}$	Coefficients of univariate basis function
$C_q$	Coefficients of multivariate basis function
$C_1, C_2$	Secondary stress indices for the specific component under investigation
$D$	Expected accumulated damage ratio for the service life
$D_o$	Outside diameter of pipe
$D_f$	Cumulative damage ratio that leads to failure
$f_{X_1, \dots, X_n}(x_1, \dots, x_n)$	Joint probability density function of the random variables $X_i$
$F_{en, nom}$	Nominal environmental fatigue correction factor

---

J. Mishra (✉) · V. Balasubramaniyan  
Safety Research Institute, Atomic Energy Regulatory Board, Kalpakkam 603102, India  
e-mail: jmishra@igcar.gov.in

$F_{en}$	Factor on life due to environmental effects
$F_{se}$	Factor on life due to size effect
$F_{sf}$	Factor on life due to surface finish
$F_{def}$	Factor on life due to conservatism in fatigue definition
$g(X)$	Limit state function
$I$	Moment of inertia
$K_1, K_2$	Peak stress indices
$m, n$	Material parameters
$M_i$	Resultant moment due to a combination of design mechanical loads
$nb$	Number of stress-range levels
$n_{eqv}$	Number of equivalent full temperature load cycles
$N$	Number of cycles
$N_{air,RT}$	Number cycle to failure in the air environment
$N_f$	Fatigue life or total number of cycles to failure
$N_{fi}$	Number of cycles to failure in $i$ th stress-range level
$N_{water}$	Fatigue life in the water at service temperature
$O'$	Transformed DO levels
$P_0$	Range of service pressure
$P_f$	Failure probability
$R_m(x)$	Regular polynomial
$S_a$	Alternating stress intensity
$S_m$	Allowable stress intensity value of the metal
$S_n$	Primary plus secondary stress intensity value
$S_p$	Peak stress intensity value
$T'$	Transformed temperature
$t$	Nominal wall thickness of product
$T_m(x)$	Chebyshev polynomial
$U_i$	Usage factor at the $i$ th stress-range level
$X_i$	Random variables
$Z$	Section modulus
$\varepsilon_a$	Alternating strain amplitude
$\varepsilon'$	Transformed strain rate

## 1 Introduction

The piping design in the American Society of Mechanical Engineers (ASME) Boiler and Pressure Vessel (BPV) code [1] is based on Working Stress Design (WSD) methodology, which relies on the concept of factor of safety in the development of design formulas [2]. This approach began with first ASME code in 1914, which use a single factor to provide adequate protection against particular failure modes. The factor of safety is typically a conservative factor developed to address

various uncertainties in the analytical methods of design, applied loads, strength of material, fabrication, examination, testing and other factors that might affect the performance of the equipment.

Typically, separate factors are used for the various mode of failure such as bursting, plastic deformation, plastic failure, buckling, creep, fatigue or any other mode of failure that is considered significant for the specific problem. This single factor approach of Section-III for each failure modes worked very well for many years, as it indirectly addresses the issue of varying probabilities and consequences of loads on components. Increases in the allowable stresses for occasional loads, such as wind and earthquake loads, in comparison with sustained loads such as pressure and dead weight load reflect the different probability of occurrence. The differentiation of requirements in terms of Class-1, Class-2 and Class-3 components is obviously indirectly related in their importance to the potential consequence or severity of failure.

However, the reliability of a component design by this section varies considerably because the safety factors are based on experience, experimental data and professional expertise, and not through rigorous risk analysis [3]. Recently, a number of ASME code committees have been examining reliability-based requirements with main objective to provide means for the management of uncertainties for consistently reliable and more economical designs, which meets the target level of reliability under various types of loading conditions.

To meet the target reliability and consistency in design it will be a worthwhile exercise to first estimate the implicit reliability level associated with various failure criteria given in the ASME code. The fatigue design criteria of ASME are based on fatigue design curve (FDC) given in Appendix I of Section-III. The FDC curve is derived from the fatigue test data, which has a lot of scatter. Therefore, a work is taken up to estimate the implicit reliability level associated with fatigue failure criteria of ASME code. In this paper a code calibration is performed to estimate the implicit reliability level associated with Class-1 nuclear piping.

## 2 ASME Fatigue Design Criteria

Fatigue is one of the most frequent causes of failure in the pressure vessels and pipelines. The cyclic load in these components mainly occurs because of changes in mechanical and thermal loadings as the system goes from one load set (e.g. pressure, temperature, moment and force loading) to another. During cyclic loading of smooth test specimens, surface cracks of 10  $\mu\text{m}$  or longer develop early in life (i.e. <10% of life) at surface irregularities. These cracks are either already in existence or produced by slip bands, grain boundaries, second-phase particles, etc. The formation of surface cracks and their growth to an engineering size (3-mm deep) are generally considered as the fatigue life of a component [4]. Thus, fatigue life is defined as number of cycles,  $N$  which leads to propagation of cracks from 10 to 3000  $\mu\text{m}$  (3 mm) long, and usually represented by  $\epsilon$ - $N$  curve.

The ASME code was one of the first codes and standards to treat design for fatigue life explicitly and first to include specific code rules to prevent low-cycle fatigue failure. In 1971, Section-III of ASME B&PV included the fatigue based criteria for the evaluation of Class-1, 2 and 3 pipelines of Nuclear Power Plant (NPP). The ASME code, for Class-1 pipelines, used a fatigue evaluation method that is based on fatigue tests of polished bars along with the concept of “stress indices” and with the adjustment for stresses that exceed  $3S_m$  (conceptually, exceed the shakedown limit) [5].

For each class of components, the loads are classified into four different service levels that vary from Level-A through Level-D. Service Level-A corresponds to operating condition, and fatigue failure criteria are mainly concerned with this service level. The Class-1 piping fatigue evaluation method, without significant thermal gradient across wall and devoid of any gross material discontinuities, involves the calculation of the primary plus secondary stress range  $S_n$  by the equation:

$$S_n = C_1 \frac{P_o D_o}{2t} + C_2 \frac{D_o}{2I} M_i \quad (1)$$

and the peak stress range by the equation:

$$S_p = K_1 C_1 \frac{P_o D_o}{2t} + K_2 C_2 \frac{M_i}{Z} \quad (2)$$

If  $S_n > 3S_m$  (conceptually the shakedown limits of  $2S_y$ , but for austenitic steel at high temperature it can become  $2.7S_y$ ),  $S_p$  is divided by 2 to convert from stress range to alternating stress amplitude. If  $S_n > 3S_m$  the strain range corresponding to the elastic-based calculation will not represent the true strain range accumulated in the piping components. In this case, there will be accumulation of plastic strain along with the recoverable elastic strain. Section-III (NB-3228.3) gives a simple way to deal with this condition using a simplified elastic-plastic analysis that involves multiplying  $S_p$  by factor  $K_e$ , where  $K_e$  is given by

$$K_e = 1 + \frac{1-n}{n(m-1)} \left( \frac{S_n}{3S_m} - 1 \right); \quad \text{for } 3S_m \leq S_n \leq 3mS_m \quad (3)$$

$$K_e = \frac{1}{n}; \quad \text{for } S_n \geq 3mS_m \quad (4)$$

where  $m$  and  $n$  are material constant. The values of  $m$  and  $n$  for austenitic steel, which is a commonly used piping material in NPP piping, are 1.7 and 0.3 respectively. From the design fatigue curve (Fig. I-9.2 of ASME Section-III appendix) design cycles  $N$  are estimated using alternating stress amplitude,  $(S_p/2)$ . If the anticipated number of cumulative fatigue cycles in operation is less than  $N$ , then the piping products (e.g. girth butt weld, elbow) are deemed to be acceptable.

If there are more than one stress ranges linear cumulative hypothesis is used for total fatigue damage assessment.

### 3 Fatigue Curve of ASME and ANL

The ASME code fatigue design curves, given in Appendix I of Section-III [5], are based on strain-controlled tests of small polished specimens at room temperature in air. The design curves have been developed from the best-fit curves to the experimental fatigue strain versus life ( $\epsilon_a$  vs.  $N$ ) data, which are expressed in terms of the Langer equation [6] of the form given in (5):

$$\ln(N) = A - B\ln(\epsilon_a - C) \quad (5)$$

where  $\epsilon_a$  is the applied strain amplitude,  $N$  is the fatigue life, and  $A$ ,  $B$  and  $C$  are coefficients of the model. The ASME code mean fatigue curves (till 2004 edition) are from the best-fit curves of the experimental data which for austenitic steel is given as:

$$\ln(N) = 6.954 - 2.0\ln(\epsilon_a - 0.167) \quad (6)$$

This fatigue design curves are obtained from the fatigue best-fit curves by first adjusting for the effects of mean stress using the modified Goodman relationship and subsequently reducing the fatigue life at each point on the adjusted best-fit curve by a factor of 2 on strain (or stress) or 20 on cycles, whichever is more conservative. The factors of 2 and 20 are not safety margins but rather adjustment factors that should be applied to the small-specimen data to obtain reasonable estimates of the lives of actual reactor components. Section III criteria document described that these factors were intended to account for data scatter (including material variability) and differences in surface condition and size between the test specimens and actual components.

Recently, Argonne National Laboratory (ANL) after an extensive study of the fatigue database proposed the fatigue best-fit curves for austenitic stainless steel [7]. The database consists of large pool of 520 tests carried on smooth specimens under fully reversed strain-controlled loading (i.e.  $R = -1$ ). The database can be segregated into Stainless Steel (SS) Type, with 220 nos. of Type 304 SS; 150 nos. of Type 316 SS and 150 nos. of Type 316NG, 304L SS and 316L SS. The data for Type 316 SS are shown in Fig. 1. The proposed fatigue best-fit curves for austenitic steel are

$$\ln(N_f) = 6.891 - 1.920\ln(\epsilon_a - 0.112) \quad (7)$$

The proposed curve is developed by first correcting for mean stress effects, and then reducing the mean stress adjusted curve by a factor of 2 on stress and 12 on

**Fig. 1** Fatigue  $\epsilon-N$  behaviour of 316 austenitic stainless steel in air at various temperatures [7]

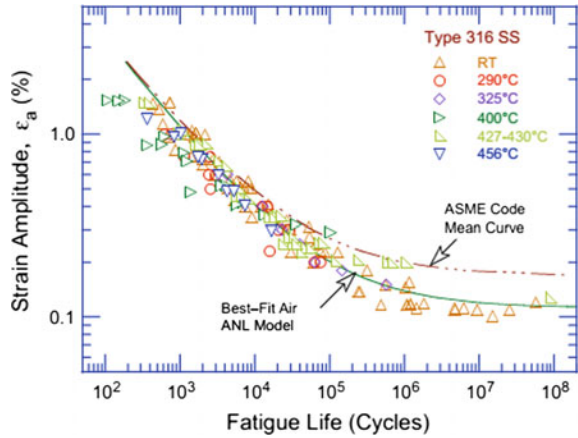
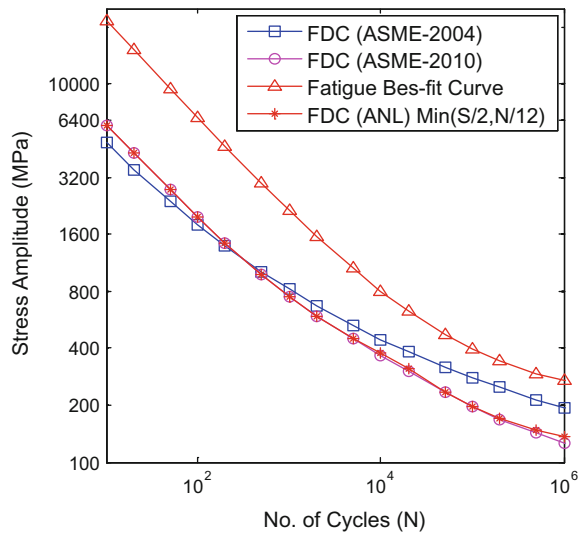


**Fig. 2** Fatigue curves for austenitic stainless steel



cycles, whichever is more conservative. These factors account for the effects of parameters such as mean stress, surface finish, size and geometry, and loading history. A comparison of the ASME (2010) fatigue design curve and ANL fatigue design curve with adjustment factor is given in Fig. 2. Figure 2 shows that the ASME fatigue design curve matches closely with ANL curve. Therefore, for evaluation of implicit reliability associated with fatigue design criteria, limit state formulation is developed based on ANL equation as given in (7).



## 4 Parameters Affecting Fatigue Life of Components

The best-fit fatigue curve given in (7) is derived from the data on material specimens in the controlled environment of laboratory. Even in these controlled environments, there are lot of scatter in the fatigue life represented by number of cycles to failure. However, in the actual operating environment of a component, the fatigue life is affected by many other parameters. These parameters are accounted in the assessment of fatigue life of components by assigning a factor corresponding to each one of them. Considering that effect of these parameters on fatigue life has lot of uncertainties, usually a range of value is assigned to these factors. In this work these parameter are broadly divided into three parts and discussed in following subsections.

### 4.1 Parameters Affecting Fatigue Life in Air Environment

Parameters like surface finish, size and geometry, and loading history are known to reduce the fatigue life of components. These parameters are not explicitly considered in the model given by (7). Table 1 shows the factors on life ( $N$ ) applied to best-fit fatigue curve to account the effects of these parameters. Except the factor for load histories, the factors given in [1, 8, 9] are their mean value, whereas range of factors values is given in [7]. The combined effect of these parameters is given as total adjustment factors in Table 1 and is equal to 20 in [1], 6.0–27.4 in [7], 12.5–31.0 in [8] and 10.0–26.0 in [9].

### 4.2 Parameters Affecting Fatigue Life in Water Environment

The fatigue lives of austenitic stainless steel material further decrease in water environment in comparison to air environments. The key parameters that influence

**Table 1** Factors on the mean fatigue curve to account for effects of various parameters

Parameters	Factors on cycles (or life)			
	ASME Section III [1]	NUREG-CR		
		6909 [7]	6815 [8]	6717 [9]
Material variability and data scatter (min. to mean)	2.0	2.1–2.8	2.0	2.5
Size effect	2.5	1.2–1.4	1.4	1.4
Surface roughness etc.	4.0	2.0–3.5	3.0	2.0–3.0
Loading histories	–	1.2–2.0	1.5–2.5	1.5–2.5
Total adjustment	20	6.0–27.4	12.5–31.0	10.0–26.0

fatigue life in these environments are temperature, dissolved-oxygen (DO) level in water, strain rate and strain (or stress) amplitude. The environmental effects on fatigue life are significant only when these key parameters meet certain threshold values. To quantitatively incorporate these effects, the environmental fatigue correction factor  $F_{en}$  is defined as the ratio of fatigue life in air at room temperature ( $N_{air,RT}$ ) to that in water at the service temperature ( $N_{water}$ ) [4, 7]. For wrought and cast austenitic stainless steel  $F_{en}$  is given as (9).

$$F_{en} = \frac{N_{air,RT}}{N_{water}} \quad (8)$$

$$F_{en} = \exp(0.734 - T' O' \dot{\epsilon}') \quad (9)$$

where  $T'$ ,  $O'$  and  $\dot{\epsilon}'$  are transformed temperature, DO level and strain rate, respectively, defined in [7]. Considering the plant states, the transformed strain rate ( $\dot{\epsilon}'$ ), transformed temperature ( $T'$ ) and transformed DO levels ( $O'$ ) are taken as (-6.91), 0.75 and 0.281, respectively. The nominal environmental fatigue correction factor given by (9) using these values of transformed parameters is 8.93.

### 4.3 Parameters Affecting Fatigue Damage Assessment

Fatigue damage assessment procedure utilises many parameters, which has uncertainties associated with them, leading to the uncertainties in the evaluation of fatigue life of components. In this work, three parameters, namely cumulative fatigue damage ratio, effective full temperature cycles and alternating stress intensity is considered. The mean value of factor associated with these parameters is taken as unity. However, due to uncertainties in their evaluation it plays significant role in the fatigue life estimation.

**Linear Cumulative Damage:** Miner's hypothesis of linear cumulative damage  $D_f$  is a good assumption and used in this work for cumulative damage assessment. However, it is well known from experiment on the un-notched geometries with completely reversed loading condition that loads having the larger stress cycles near the beginning of life tends to accelerate failure leading to  $D_f \leq 1$ . And if the smaller stresses are applied first and progressively higher stresses follow, the cumulative damage ratio for failure  $D_f \geq 1$  [10, 11].

$$D_f = \sum_{i=1}^{nb} U_i \quad (10)$$

where  $U_i$  is the usage factor at the  $i$ th stress-range level, and  $nb$  is the number of stress-range levels in a stress-range histogram. Since the sequence of load cycles

undergone by components is unknown, it adds uncertainties in fatigue damage assessment.

**Effective Full Temperature Cycles:** In practice, component in NPP goes a range of temperature cycles in its useful life. Therefore, it will be useful to convert the range of temperature cycles into an equivalent full temperature cycle, as per procedure similar to given for the ASME Class-2 piping as in (11).

$$D = \sum_{i=1}^{nb} U_i = \sum_{i=1}^{nb} \frac{n_i}{N_{fi}} = \frac{n_{eqv}}{N_f} \tag{11}$$

where  $n_i$  is the expected number of cycles at the  $i$ th stress-range level,  $N_{fi}$  is the number of cycles to failure at the  $i$ th stress-range level,  $n_{eqv}$  is number of equivalent full temperature load cycles, and  $N_f$  is total number of cycles leading to failure.

**Alternating Stress Intensity:** In fatigue damage assessment using ASME criteria, the alternating stress intensity  $S_a$  is obtained as per procedure given in Sect. 2. Various uncertainties creep into the alternating stress intensity evaluation while performing integration of geometric properties, material properties and loads in the discretised domain and subsequent assembling for global response, and enhance the uncertainties in the fatigue life evaluations.

Considering the effect of all above-mentioned parameters and uncertainties associated with them a structural reliability formulation is developed in the following section to evaluate the implicit reliability associated with the fatigue design criteria of Class-1 piping components.

## 5 Formulation for Implicit Reliability Level in Fatigue Design

To evaluate the implicit reliability levels of the code design procedures against a particular failure mode, the first step lies in the definition of a limit state function corresponding to codal provision given for that failure mode. The limit state function can be written as

$$g(X) = g(X_1, X_2, X_3, \dots, X_n) \tag{12}$$

where  $X_i$  represents probabilistically defined variables for the loads and the strength. The function  $g(-)$  is a limit state function that characterises the failure criterion. The probability function is then given by the joint probability distribution of  $X_i$ 's

$$P_f = \int_{g(-) > 0} \int f_{X_1 X_2 \dots X_n}(x_1 x_2 \dots x_n) dx_1 dx_2 \dots dx_n \tag{13}$$

where  $f_{X_1 X_2 \dots X_n}(x_1 x_2 \dots x_n)$  is the joint probability density function (pdf) of the random variables  $X_i$ . The evaluation of failure probability using efficient probabilistic analysis methods like first-order reliability method (FORM) is carried out by locating the most probable point (MPP) with a minimum number of model (function) evaluations, whereas methods like response surface method (RSM) employ the method for better approximation of limit state function. A newly developed method higher-order response surface method (HORSM), which is based on higher-order response surface approximation, approximates the true limit state function using Chebyshev polynomial as basis function  $T_m(x)$  instead of regular polynomial,  $R_m(x)$ . The Chebyshev polynomial and regular polynomial of order  $m$  can be given by  $T_m(x) = \cos(m \cos^{-1}(x))$  and  $R_m(x) = x^m$ , respectively. The approximate limit state of arbitrary order with  $T_x$  as basis function can be given as (12):

$$\widehat{g}(X) = a + \sum_{i=1}^n \sum_{j=1}^{k_i} b_{ij} \cos(j \cos^{-1}(X_i)) + \sum_{q=1}^m c_q \prod_{i=1}^n \cos(p_{iq} \cos^{-1}(X_i)) \quad (14)$$

where the coefficients  $b_{ij}$  correspond to univariate basis function, and the coefficients  $c_q$  correspond to multivariate basis function. The polynomial order  $k_i$ , the total number of mixed terms  $m$  and the order of a random variable in a mixed term  $p_{iq}$  are determined in the various stages of the proposed method. Details of the procedure are given in [12]. The computational procedure for evaluation of implicit reliability levels is given below.

### 5.1 Fatigue Design Limit State Function

The limit state function  $g(X)$  relates the expected accumulated damage ratio for the service life of a pipe  $D$  with the cumulative damage ratio that leads to failure  $D_f$ . When  $g(X) \leq 0$  the component fails, whereas when  $g(X) \geq 0$  a safe design is assured. This can be shown mathematically using (13).

$$g(X) = D_f - D \quad (15)$$

The expected accumulated damage  $D$  at a piping location is computed using the linear damage hypothesis proposed by Palmgren–Miner [10]. Then limit state function using (11) is given by (18).

$$g(X) = D_f - \sum_{i=1}^{nb} U_i = D_f - \frac{n_{eqv}}{N_f} \quad (16)$$

As discussed in Sect. 4,  $N_f$  depends on many variables. Therefore the limit state function using (7) can be written as (17) and (18), which is highly nonlinear function with eight variables.

$$g(X) = D_f - \frac{n_{\text{eqv}}}{N_f} = D_f - \frac{n_{\text{eqv}}}{f(A, S_a, F_{\text{se}}, F_{\text{sf}}, F_{\text{en}}, F_{\text{df}})} \quad (17)$$

$$g(X) = D_f - \frac{n_{\text{eqv}} F_{\text{se}} F_{\text{sf}} F_{\text{en}}}{\exp(A - 1.920 \ln(\frac{100 S_a}{E} - 0.112))} F_{\text{df}} \quad (18)$$

where definition and uncertainties associated with variables  $A, F_{\text{se}}, F_{\text{sf}}, F_{\text{en}}, D_f, S_a, n_{\text{eqv}}$  and  $F_{\text{df}}$  are given in the next section.

## 5.2 Stochastic Characteristics of Variables

The factors associated with each of the variables are treated as the stochastic variables. The stochastic characteristics of each variable are represented with mean value, standard deviation and probability density function. To obtain the stochastic characteristics of the factors related with size and geometry,  $F_{\text{se}}$ , and surface finish,  $F_{\text{sf}}$ , these factors are assumed to follow lognormal distribution with upper and lower limits of these factors representing the 5th and 95th percentile, respectively. In view of insufficient data for density characterisation, assumption of lognormal distribution is reasonably good approximation.

The constant  $A$  of the best-fit fatigue curve (5) has lot of variability due to data scatter and material variability. Hence, constant  $A$  is treated random variables with mean value of 6.891. Also, data analysis of 520 tests by ANL, it is observed that the standard deviation of constant  $A$  is 0.417 [7]. This leads to the coefficient of variation (COV) of  $A$  equal to 0.061.

The factor on fatigue life due to surface finish  $F_{\text{sf}}$  has the range of value 2.0–3.5. This leads to the mean value and standard deviation of  $F_{\text{sf}}$  on life equal 2.68 and 0.46, respectively. Therefore, the COV is equal to 0.17. In the same way, the factor on fatigue life due to size and geometry,  $F_{\text{se}}$ , has the range of value 1.2–1.4. The mean value and standard deviation of this factor on life are equal to 1.29 and 0.061, respectively. From this, the COV for this factor is equal to 0.046. The load histories are taken care in cumulative damage ratio evaluation.

The mean value of the environmental fatigue correction factor,  $F_{\text{en}}$ , is taken as 8.93 as derived in Sect. 4.2. Since, reactor operates at range of temperatures, range of DO levels in coolant as well as at range of strain rate, the  $F_{\text{en}}$  will have large uncertainties in the estimated value. A COV equal to 0.15 is taken for  $F_{\text{en}}$ . The COV of factors for cumulative damage ratio,  $D_f$ , equivalent number of full temperature cycle,  $n_{\text{eqv}}$ , and alternating stress intensity,  $S_a$ , is taken as 0.1. Also, the fatigue failure is considered as over when there is a crack of 3 mm developed the components; however, considerable life will be still there. So, the factor related to

**Table 2** Stochastic variables used for the failure probability estimation

S. No.	Description	Mean	COV	Distribution
1	Constant $A$ from (5)	6.891	0.061	Lognormal
2	Factor on life due to size effect ( $F_{se}$ )	1.30	0.047	Lognormal
3	Factor on life due to surface finish ( $F_{sf}$ )	2.68	0.17	Lognormal
4	Factor on life due to environmental effects ( $F_{en}$ )	8.93	0.15	Lognormal
5	Factor on life due to conservatism in fatigue definition ( $F_{df}$ )	2.0	0.10	Lognormal
6	Uncertainties in the cumulative damage ratio ( $D_f$ )	1.0	0.10	Lognormal
7	Equivalent full temperature cycle ( $n_{eqv}$ )	Based on $S_a$ from (7)	0.1	Lognormal
8	Alternating stress intensity ( $S_a$ )	$(S_p/2)$ —as per (2)	0.10	Lognormal

definition of fatigue failure,  $F_{df}$ , is defined with mean value of 2 and COV of 0.1. Table 2 summarises the stochastic properties of random variables.

### 5.3 Computational Procedure

A computation procedure for evaluation of failure probability of Class-2 nuclear pipeline is given by Avrithi and Ayyub [13]. A similar approach is taken for the computation of implicit reliability level of nuclear Class-1 pipeline using (11). The steps in the evaluation procedure are as follows:

- Evaluate the alternating stress range  $S_a$  corresponding to the cyclic loads.
- Evaluate the equivalent number of maximum temperature cycle  $n_{eqv}$ . In the present case it is taken as number of cycles allowed by ASME fatigue design curve.
- Define limit state function using (18).
- Define the probabilistic characteristic of the variables used for defining the limit state function. These variables are  $A$ ,  $F_{sf}$ ,  $F_{se}$ ,  $F_{df}$ ,  $F_{en}$ ,  $D_f$ ,  $N_{eqv}$  and  $S_a$ .
- Compute the failure probability  $P_f$  and corresponding reliability index  $\beta$  using HORSIM, FORM. The  $\beta$  represents the reliability index associated with code design procedure.

Validate the result with Monte Carlo Simulation (MCS).

## 6 Computation of Implicit Reliability Levels

The reliability, which is complementary of the failure probability, is estimated using the three methods. The first method is FORM, which is very efficient in those cases where analytical expressions of the limit state function are available. Since in the present case the analytical expression is available, FORM is a useful tool for the failure probability estimation.

The second method is HORSM, which presume that limit state function in analytical form is not available. This method is especially suitable for the failure probability estimation of the actual NPP components, where limit state is evaluated using finite element analysis. Since in the present case limit state function is available, failure probability obtained from HORSM and FORM is matching closely. In those cases, where limit is not available in analytical form, HORSM gives better estimate of failure probability. The MCS with  $5 \times 10^7$  iterations is used for the validation of the result obtained from FORM and HORSM method.

### 6.1 Sensitivity Analysis

The sensitivity of limit state function  $g(X)$  with respect to each variable is carried out by varying one variable at a time while keeping all other variables at their mean value. The variables are varied in the range of one standard deviation from mean value, i.e. from  $\mu - \sigma$  to  $\mu + \sigma$  for quantifying the dependence of limit state function on each variable. The sensitivity of variables is compared with the variables in normalised form. It is observed that limit state function is most sensitive to cumulative damage ratio. The constant  $A$  and alternating stress intensity  $S_a$  also have high impact on limit state function. The variables for size effects and equivalent full temperature cycle have lesser effect on the variation of limit state function.

### 6.2 Failure Probability Evaluation

The failure probability of piping products and joints is estimated using FORM, HORSM and MCS. Two parametric studies are carried out to assess the variation of the failure probability with primary plus secondary stress range. For a typical case, a pipeline made up of austenitic steel SS304L and operating at 300 °C, which is typically the operating temperature of the NPP reactors, is taken for failure probability evaluation.

**Failure Probability of Butt-Welding Elbow:** The failure probabilities for butt-welding elbow are evaluated for different value of primary plus secondary stress range  $S_n$ . The  $S_n$  is gradually varied from shakedown limit to twice of this limit, i.e.  $3.0S_m$  to  $6.0S_m$ . Here,  $S_m$  is the maximum allowable stress intensity given

in the ASME Section-II. The  $S_m$  value for the austenitic steel SS304L at 300 °C is 98 MPa. When  $S_n$  is varied in this range of 3.0  $S_m$  to 6.0  $S_m$ , the number of allowable fatigue life from ASME Section-III is in the range of 500 cycles to  $4 \times 10^5$  cycles. The failure probabilities for elbow are given in Table 3 and Fig. 3. The values obtained from all three methods, namely MCS, FORM and HORSM are nearly same. The maximum value of the failure probability of  $\sim 4.0 \times 10^{-3}$  is observed when allowable number of cycles is in the range of 5000–10000. The corresponding  $S_n$  is nearly 1.25–1.35 times of shakedown limit. It is also observed that when allowable number of cycles is 1000, which is generally the design criteria on number of cycles for pipelines, the failure probability is nearly  $\sim 1.0 \times 10^{-3}$ .

**Failure Probability of Piping Products and Joints:** A parametric study is also carried out to compare the failure probabilities of the various pipe products and joints with respect to  $S_n$ . Five piping products like butt-welding elbow, girth butt weld in the flush and as-welded condition, longitudinal butt weld in the as-welded condition and branch connection are taken for the comparison. The  $S_n$  is gradually varied from half of the shakedown limit to twice of this limit, i.e. 1.5  $S_m$  to 6.0  $S_m$ . The results are plotted in Fig. 4, with X-axis representing the stress range  $S_n$  in the normalised form.

It is observed from this figure that for the piping product with higher value of peak stress indices  $K_2$  the curve shifts towards left inferring that failure will occur at the lower value of  $S_n$ . At the shakedown limit the failure probability evaluated for butt-welding elbow, girth butt weld (flushed), longitudinal butt weld (as-welded), girth butt weld (as-welded) and branch connection are  $1.0 \times 10^{-6}$ ,  $2.5 \times 10^{-6}$ ,  $4.7 \times 10^{-5}$ ,  $1.4 \times 10^{-3}$ ,  $2.2 \times 10^{-3}$ , respectively. This shows that failure probability of branch connection is three orders higher than butt-welding elbow. However, for piping products and joints with same value of peak stress indices,  $K_2$  like straight pipe, butt-welding elbows, butt-welding tees, the failure probabilities at the shakedown limits will be same.

**Table 3** Failure probability of the Class-I butt-welded elbow, designed as per the ASME Section III

S. No.	Primary plus secondary stress	No. of cycles from FDC of ASME	Failure probability		
			HORSM	FORM	MCS
1	294.0	414060	1.00E-07	1.00E-07	6.01E-07
2	323.4	69486	7.05E-04	5.86E-04	4.95E-04
4	352.8	21575	5.14E-03	5.04E-03	4.58E-03
6	411.6	4014	8.85E-03	7.67E-03	7.22E-03
8	470.4	1175	4.10E-03	3.62E-03	3.43E-03
10	543.9	602	2.98E-03	2.82E-03	2.66E-03
11	588.0	493	2.84E-03	2.60E-03	2.46E-03



**Fig. 3** Failure probability of Class-1 butt-welding elbows designed as per ASME Section III with respect to allowable number of cycles

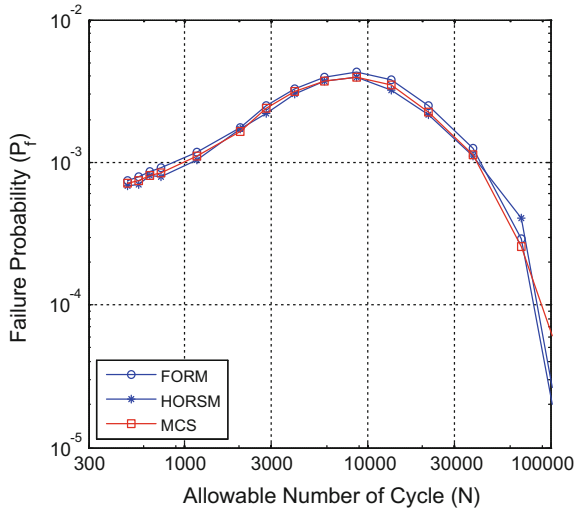
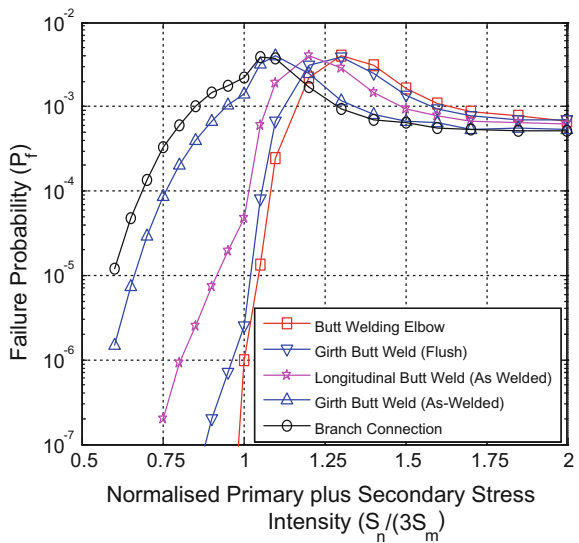


**Fig. 4** Failure probability of Class-1 piping components designed as per Class-III with respect to primary plus secondary stress intensity ( $S_n$ )



## 7 Conclusion

The paper describes a procedure to estimate the implicit reliability level associated with the fatigue design criteria of Class-1 piping specified by ASME BPV Code, Section III, NB-3650. The reliability evaluation is carried out using mean fatigue curve given by ANL because it matches closely with ASME fatigue design curve when a factor of 2 on stress and 12 on life is applied on them. Limit state function

for reliability evaluation, which is based on linear damage hypothesis proposed by Palmgren–Miner, is developed using eight parameters affecting the fatigue life. The sensitivity analysis of the limit state function suggests that it is strongly sensitive to cumulative damage ratio, constant  $A$  of fatigue mean curve and alternating stress intensity, whereas geometry (i.e. size) and equivalent temperature cycle have less predominant effect.

It is observed that the maximum value of the failure probability of butt-welding elbow is  $\sim 4.0 \times 10^{-2}$ , which is observed when allowable number of cycles is in the range of 5000–10000. The corresponding  $S_n$  is nearly 1.25–1.35 times of shakedown limit. Also, the failure probability is lower for those pipe products and joints which have higher value of peak stress indices. Due to this reason failure probability of branch connection is three orders higher than those of butt-welding elbow. Therefore, it is concluded that the failure probabilities of piping products and joints of pipeline, which is designed as per ASME Section-III fatigue design criteria, will have large variations.

## References

1. American Society of Mechanical Engineers (ASME), Rules for construction of nuclear facility components, ASME Boiler & Pressure Vessel Code (2010)
2. Gupta A, Choi B (2003) Reliability-based load and resistance factor design for piping: an exploratory case study. *Nucl Eng Des* 224:161–178
3. Hill III RS (2004) Probabilistic & system—based methods for design—development of reliability-based load and resistance factor design methods for piping. ASME Nuclear Codes and Standards Workshop, New Orleans, LA
4. Chopra OK (2002) Mechanism and estimation of fatigue crack initiation in austenitic stainless steels in LWR environments, NUREG/CR-6787
5. American Society of Mechanical Engineers, Rules for construction of nuclear facility components. ASME Boiler and Pressure Vessel Code, Section-III, Appendix-I (2010)
6. Langer BF (1962) Design of pressure vessels for low-cycle fatigue. *ASME J Basic Eng* 84:389–402
7. Chopra OK, Shack WJ (2007) Effect of LWR coolant environments on the fatigue life of reactor materials—final report, NUREG/CR-6909 and ANL-06/08
8. Chopra OK, Shack WJ (2003) Review of the margins for ASME code design curves—effects of surface roughness and material variability, NUREG/CR-6815, ANL-02/39
9. Chopra OK, Shack WJ (2001) Environmental effects on fatigue crack initiation in piping and pressure vessel steels, NUREG/CR-6717, ANL-00/27
10. Miner MA (1945) Cumulative damage in fatigue. *J Appl Mech* 12:A159–A164
11. Fatemi A, Yang L (1998) Cumulative fatigue damage and life prediction theories: a survey of the state of the art for homogeneous materials. *Int J Fatigue* 20(1):9–34
12. Mishra J, Chellapandi P, MeherPrasad A, Narayanan S (2014) Evaluation of failure probability of expansion bellow at RCB containment penetration of PFBR using higher order response surface method. *SRESA Int J Life Cycle Reliab Safety Eng* 3(2):15–24
13. Avrithi K, Ayyub BM (2010) A reliability-based approach for low-cycle fatigue design of class 2 and 3 nuclear piping. *J Press Vessel Technol* 132

# The Tensile Fatigue Behaviour of Aligned MWNT/Epoxy Nanocomposites

Sasidhar Jangam, A. Hema Devi, S. Raja, K. Hemachandra Reddy and G. Vijay Kumar

**Abstract** The emergence of carbon nanotubes (CNTs) has created new opportunities for the fabrication of polymer composites that possess strong potential for a wide spectrum of applications. The one-dimensional structure of carbon nanotubes has a very high anisotropic nature and unusual mechanical properties, which made them as promising nanofiller for the composite structures. But the particle-level exceptional properties are not completely utilised when they are used as reinforcement in composites due to inadequate and immature processing techniques. In the present work, we have made an attempt to utilise the strong anisotropic nature of multi-walled carbon nanotubes (MWNTs) for improving the fatigue life of nanocomposites, especially for very low weight percentages. The MWNTs anisotropy was imparted to the nanocomposites by aligning them in the epoxy matrix with DC electric field during curing. Nanocomposites were made for 0.1 wt% MWNT loading. Totally, three categories of nanocomposites were prepared: nanocomposites with aligned CNT (with electric field), nanocomposites without CNT alignment (without electric field), and neat epoxy for the comparison purpose. The tensile fatigue behaviour was investigated under stress control mode by applying cyclic sinusoidal load with the frequency range of 1–3 Hz and stress ratio of  $R = 0.1$ . The specimens were tested for the fatigue load until the failure or  $1E+05$  cycles. The fractured surfaces were examined through scanning electron microscope to analyse the fatigue fracture behaviour.

---

S. Jangam (✉) · A. Hema Devi · S. Raja  
Structural Technologies Division, CSIR National Aerospace Laboratories,  
Bangalore 560017, India  
e-mail: sasidhar.jangam@gmail.com

S. Jangam · K. Hemachandra Reddy  
Department of Mechanical Engineering, Jawaharlal Nehru Technological University,  
Anantapur 515002, India

A. Hema Devi · G. Vijay Kumar  
Department of Mechanical Engineering, P.V.P. Siddhartha Institute of Technology,  
Vijayawada 520007, India

**Keywords** Multi-walled carbon nanotubes (MWNTs) · Nanocomposites  
Fatigue · Nanotube alignment · Digital image correlation (DIC)  
Toughening mechanisms

## 1 Introduction

With the discovery of carbon nanotubes (CNTs) by Iijima [1] in 1991, a new era in science and technology called nanotechnology has emerged and boomed up with in no time because of its potential applications. The CNTs can be envisioned as coaxially arranged concentric graphene layers around central hollow core. In general, CNTs can be classified based on the number of concentric cylindrical shells, as single-walled carbon nanotubes (SWNTs), double-walled carbon nanotubes (DWNTs), and multi-walled carbon nanotubes (MWNTs).

As the CNTs exhibit excellent mechanical, electrical, and thermal properties, they became promising nanofillers [2] for automotive, electronics, aerospace, and biomedical sectors. In addition to these exceptional properties, CNTs offer very strong interfacial bonding with the matrix [3], which made CNTs most compatible with many matrices, especially with polymers to deliver astonishing results. All these extraordinary properties to the CNTs are mainly due to its one-dimensional structure and the high aspect ratios (>1000) [4].

The CNTs have shown Young's modulus of 1–1.5 TPa and tensile strength of 50–200 GPa in particle level [5], but when these CNTs are incorporated into the matrix the difference in mechanical properties compared to the particle level is very huge. This may be due to the agglomeration, poor dispersion, and random orientation. Many research works have been conducted in the last two decades to retain and transfer the particle-level unusual and exceptional properties of CNTs to the composites when they incorporated into the matrix. Researchers have come up with different sonication techniques (probe sonication, bath sonication) [6] and functionalisation (defect, covalent, non-covalent functionalisation) of CNTs [7] in order to attain a good quality of dispersion. At the same time, many attempts were made to improve the anisotropic nature of the nanocomposites by aligning the CNTs in the matrix [8]. Among many techniques, electric field alignment (AC, DC, and both) [9–11], magnetic field alignment [12], shear flow [13], acoustic wave [14], and dip coating [15] were popular. Again the properties of the nanocomposites depend on several parameters like type of CNTs used, wt% of CNT used, type of dispersion, time of dispersion, alignment technique, etc.

Contemporarily many research works have been conducted to improve the fatigue life of composites by incorporating rubber nanoparticles [16], nanosilica [17], nanotitanium, nanoalumina, CNT [18] as reinforcement. Out of all reinforcements, CNTs became very popular to improve both static and fatigue properties due to its high anisotropy, compatibility, and good interfacial strength. However, the full utilisation of CNTs unique properties has not been successful till date, due to difficulty in imparting the anisotropy of CNTs to the composites by

aligning them in the matrix. Much research has been conducted in improving the tensile, compressive, flexural and electrical properties by aligning the CNTs, but the fatigue studies have been neglected.

In the present work, we have studied the effect of CNT alignment on the fatigue life of the nanocomposites compared to the randomly oriented nanocomposites. We adopted DC electric field alignment technique to align the MWNTs in the matrix. We prepared majorly the two categories of specimen random nanocomposites and aligned nanocomposites with specific MWNT loading (0.1 wt%). Neat epoxy specimens were also prepared for the comparison purpose.

## 2 Experimental

### 2.1 Materials

The nanocomposites were prepared by using diglycidyl ether bisphenol A (DGEBA) as resin and triethylenetetramine (TETA) as hardener. The resin-to-hardener mix ratio was 100:12. Both resin and hardener were procured from Sigma-Aldrich chemicals, USA. Polyvinyl acrylate was used as releasing agent for easy removal of the specimen. The MWNTs (supplied by Nanoshell, USA) used in this study were produced through catalytic chemical vapour deposition (>99% C) method and functionalised with COOH group. As per the supplier's specification, the average diameter and length of MWNTs were ranged between 10–20 nm and 10–15  $\mu\text{m}$ , respectively.

### 2.2 Specimen Preparation

The as-received MWNTs were added to the epoxy for a given wt% loading (0.1%), and the mixture of both MWNT and epoxy was sonicated for one hour for better dispersion. The temperature of the mixture during sonication was maintained constant in order to avoid overheating problem. The MWNT/epoxy mixture was then degassed for 15 min in a vacuum oven to remove entrapped air, otherwise blow holes may form in the composites. Now the hardener was added to the perfectly sonicated and degassed MWNT/epoxy mixture at the 100:12 resin to hardener ratio and then gently stirred manually for 15 min to get homogeneous solution. Then, the solution was poured into two similar moulds to prepare randomly oriented and aligned nanocomposite laminates. DC electric field of 200 V/cm was applied for one hour to prepare aligned nanocomposites [19], whereas no electric field was applied for randomly oriented nanocomposites. Figure 1 shows the schematic of nanocomposite fabrication. Both randomly and

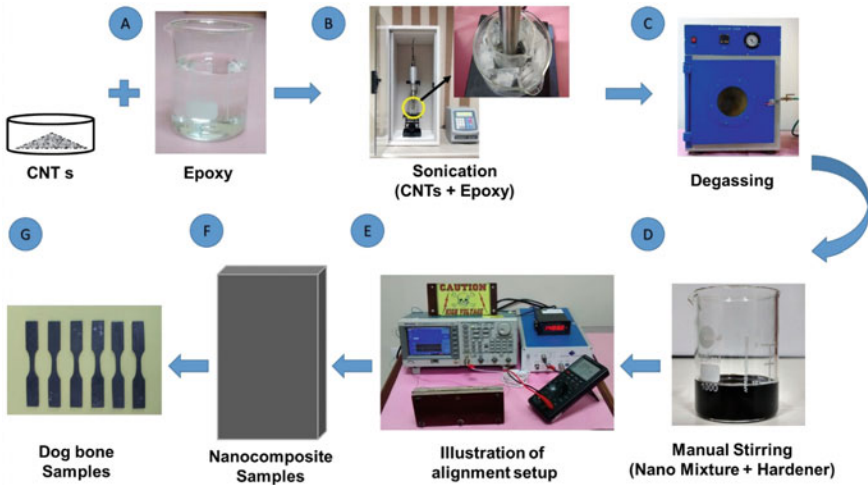


**Fig. 1** Schematic of nanocomposite fabrication

aligned nanocomposite laminates were cured at room temperature for 24 h and post-cured at 50 °C for 30 min, 70 °C for 60 min, and 85 °C for 2 h in the oven [20]. Then, the nanocomposite laminates were cut into dog-bone specimens as per the ASTM D638, type-v [21], for both tensile tests and fatigue tests. Figure 2 shows different nanocomposite specimens prepared for the tests.

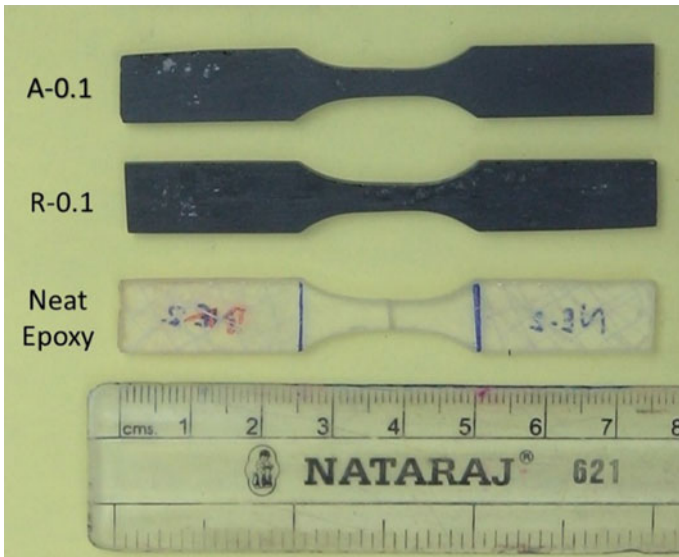


**Fig. 2** Nanocomposite specimen (dog-bone-shaped)

### 2.3 Testing Procedure

The tensile tests were carried out on Instron E3000 machine, under position control with the constant crosshead movement of 0.5 mm/min. The tensile properties, including tensile modulus ( $E$ ) and ultimate tensile strength of all specimens, were determined according to the ASTM D638. For each material, five specimens were tested and the average was considered to reduce the experimental error. The tensile cyclic fatigue tests were conducted on Instron E3000 machine, under the stress control mode with the following fatigue test parameters: stress ratio  $R = 0.1$  ( $R = \frac{\sigma_{min}}{\sigma_{max}}$ ), sinusoidal cyclic frequency  $f = 3$  Hz. Totally, six specimens were tested for each category. For all the specimens, the cyclic load was applied up to the failure or  $1.5E+05$  cycles. Figure 3 shows the test set-up of tensile and fatigue tests.

Microscopic analysis was performed to check the quality of dispersion and the alignment of MWNT in the matrix. Along with this analysis, the fatigue fracture behaviour was also studied by examining the fractured surfaces. ZEISS supra 40VP field emission scanning electron microscope was used for microscopic analysis.

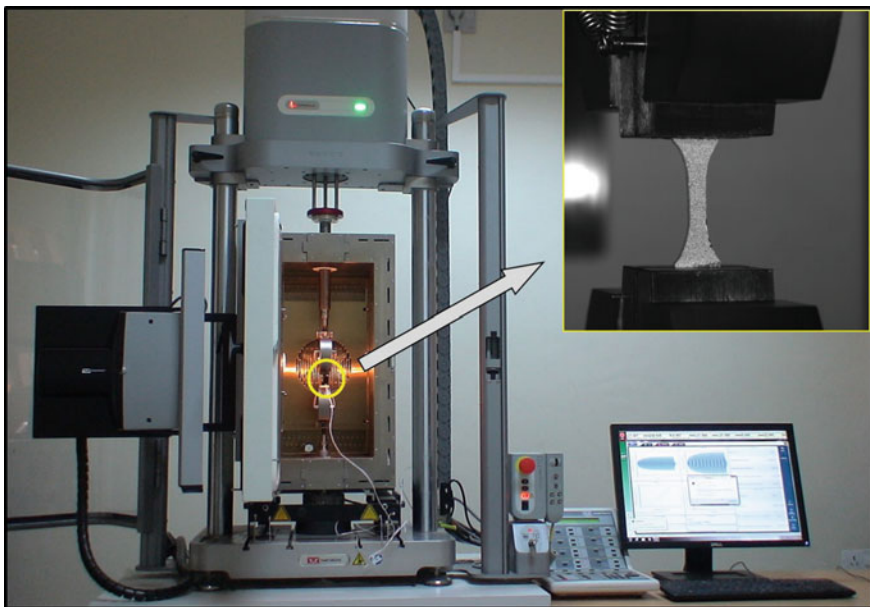


Fig. 3 Test set-up of tensile and fatigue tests

### 3 Results and Discussion

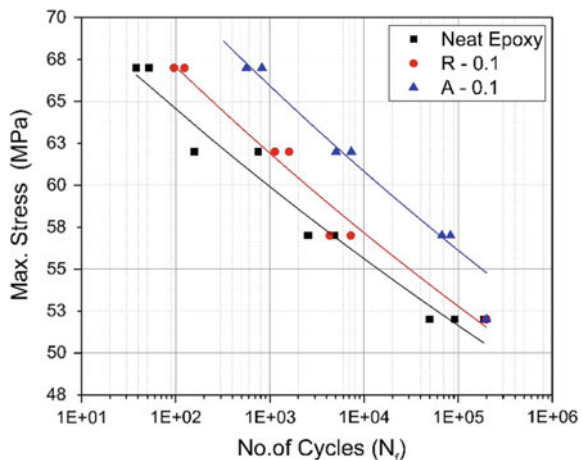
The tensile properties of all materials determined as per the ASTM D638 [21] are listed in Table 1. It is very clear that the dispersion of MWNT (randomly oriented nanocomposites) has increased the modulus by 7% than neat epoxy. Furthermore, for the same wt% of MWNT the modulus has increased 9%, which is just because of aligned MWNT networks in the matrix. It is noteworthy that the nanoparticle alignment process has improved the modulus by twofold than the conventional dispersion alone, for the same nanoparticle loading. Similar kind of trend can be seen for the ultimate tensile strength.

Figure 4 shows the tensile fatigue test results obtained for nanocomposites for the stress ratio,  $R = 0.1$ . It can be clearly seen that the addition of MWNT to the epoxy matrix has improved the fatigue lives of both randomly oriented and the aligned nanocomposites than the neat epoxy over the entire range of stress levels investigated. It is very interesting to notice that the addition of MWNT in small quantity (0.1 wt%, randomly oriented) has enhanced the fatigue life about 2–3 times when compared to the neat epoxy, whereas for the same amount of MWNT addition but with the aligning process it has improved the fatigue life about 6–8 times than neat epoxy and 3–5 times than randomly oriented nanocomposites. It is very clear that the orientation of nanoparticles has significant influence over anisotropic properties of nanocomposites, which again may cause the enhancement of the

**Table 1** Tensile properties of the samples

Specimen	Tensile modulus— $E$ (GPa)	Ultimate tensile strength— $\sigma_U$ (MPa)
NE	2.75	81.25
R-0.1	2.93	83.63
A-0.1	3.21	85.28

**Fig. 4** Stress versus fatigue life (S–N) curves of nanocomposites





fatigue life. It is noteworthy that the results obtained are in agreement with the similar research works where the fatigue lives have been improved by modifying the epoxy matrices with the nanoparticles (carbon nanotubes, carbon nanofibres, nanosilicate) [17, 22–24].

The dispersion, as well as the orientation of MWNTs in the cured nanocomposites with the electric field and without an electric field, was examined using the micrographs, obtained from the fractured surfaces. Figure 5a, b shows the fractured surfaces of nanocomposites in the longitudinal and lateral directions, respectively. MWNTs were seen like tiny lengthy objects and small dots when the longitudinal and lateral fractured surface was examined, respectively, which confirms the orientation/alignment of MWNTs in the applied electric field direction. Figure 5c, d shows the fatigue failure pattern.

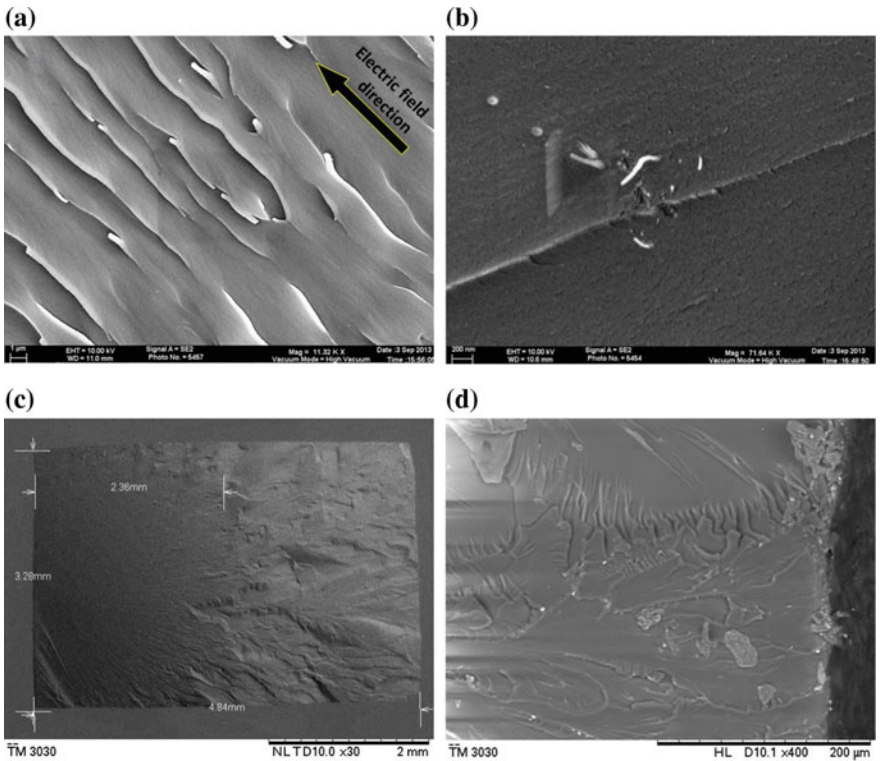


**Fig. 5** a Fractured surface-longitudinal direction, b fractured surface-lateral direction, c failure pattern of fatigue fracture, d failure pattern of fatigue fracture

## 4 Conclusions

In summary, the work has addressed how the MWNT alignment has improved the fatigue performance of nanocomposites for low MWNT wt%. The 0.1wt% MWNT dispersion alone has improved the fatigue life by a factor of about 2–3 times than neat epoxy, whereas for the MWNT loading the dispersion along with the alignment has improved the fatigue life further more by 3–5 times, and overall improvement about 6–8 times than net epoxy. With the above experimental results, it is clear that the electrical alignment process significantly improves the fatigue life of nanocomposites, and it can be used as the promising technique for fatigue life enhancement.

**Acknowledgements** The authors would like to acknowledge the financial support received from the 12th Five Year Plan of Council of Scientific and Industrial Research (CSIR), India (Project No. ESC-02-12-02).

## References

1. Iijima S (1991) Helical microtubules of graphitic carbon. *Nature* 354:56–58
2. Goh PS, Ismail AF, Ng BC (2014) Directional alignment of carbon nanotubes in polymer matrices: contemporary approaches and future advances. *Compos Part A* 56:103–126
3. Rahmat M, Hubert P (2011) Carbon nanotube—polymer interactions in nanocomposites: a review. *Compos Sci Technol* 72(1):72–84
4. Coleman JN, Khan U, Blau WJ, Gun'ko YK (2006) Small but strong: a review of the mechanical properties of carbon nanotube-polymer composites. *Carbon N Y* 44(9):1624–1652
5. Wernik JM, Meguid SA (2010) Recent developments in multifunctional nanocomposites using carbon nanotubes. *Appl Mech Rev* 63(5):050801
6. Ma P, Siddiqui NA, Marom G, Kim J (2010) Dispersion and functionalization of carbon nanotubes for polymer-based nanocomposites: a review. *Compos Part A* 41(10):1345–1367
7. Gopal N, Rana S, Whan J, Li L, Hwa S (2010) Progress in polymer science polymer nanocomposites based on functionalized carbon nanotubes. *Prog Polym Sci* 35(7):837–867
8. Ma Y, Wang B, Wu Y, Huang Y, Chen Y (2011) The production of horizontally aligned single-walled carbon nanotubes. *Carbon N Y* 49(13):4098–4110
9. Sengezer EC, Seidel GD, Bodnar RJ (2015) Phenomenological characterization of fabrication of aligned pristine-SWNT and COOH-SWNT nanocomposites via dielectrophoresis under AC electric field. *Polym Compos* 1266–1279
10. Khan SU, Pothnis JR, Kim J-K (2013) Effects of carbon nanotube alignment on electrical and mechanical properties of epoxy nanocomposites. *Compos Part A Appl Sci Manuf* 49:26–34
11. Kumar S, Sharma A, Tripathi B, Srivastava S, Agrawal S, Singh M (2010) Enhancement of hydrogen gas permeability in electrically aligned MWCNT-PMMA composite membranes. *Micron* 41(7):909–914
12. Aldajah S, Haik Y (2012) Transverse strength enhancement of carbon fiber reinforced polymer composites by means of magnetically aligned carbon nanotubes. *J Mater* 34:379–383
13. Qiu L, Wang X, Su G, Tang D, Zhe X, Zhu J (2016) Remarkably enhanced thermal transport based on a flexible horizontally-aligned carbon nanotube array film. *Nature Scientific Reports*
14. Lim WP, Yao K, Chen Y (2007) Alignment of carbon nanotubes by acoustic manipulation in a fluidic medium. *J Phys Chem C* 100:16802–16807

15. Spotnitz ME, Stone HA (2004) Dip coating for the alignment of carbon nanotubes on curved surfaces. *J Mater Chem* 14:1299–1302
16. Pearson RA (1996) Fatigue of rubber-modified epoxies: effect of particle size and volume fraction. *J Mater Sci* 31:3777–3789
17. Manjunatha CM, Taylor AC, Kinloch AJ, Sprenger S (2009) The cyclic-fatigue behaviour of an epoxy polymer modified with micron-rubber and nano-silica particles. *J Mater Sci* 44 (16):4487–4490
18. Parvaneh V, Shariati M (2015) Experimental analysis of the low cycle fatigue of a spray-coated layered multi-walled carbon nanotubes/polyvinyl chloride nanocomposite. *J Compos Mater* 0(0):1–8
19. Jangam S, Raja S, Maheswar Gowd BU (2016) Influence of multiwall carbon nanotube alignment on vibration damping of nanocomposites. *J Reinf Plast Compos* 35(8):617–627
20. Rao S (2008) An emerging, energy-efficient cure process for rapid composite manufacture. In: International conference on aerospace science and technology, Bangalore, India
21. American Society for Testing and Materials (2014) Standard test method for tensile properties of plastics, ASTM D638-14, Annual book of ASTM Standards, vol 8.01. American Society for Testing and Materials, PA, USA
22. Böger L, Sumfleth J, Hedemann H, Schulte K (2010) Composites: part A improvement of fatigue life by incorporation of nanoparticles in glass fibre reinforced epoxy. *Compos Part A* 41:1419–1424
23. Borrego LP, Costa JDM, Ferreira JAM, Silva H (2014) Composites: part B fatigue behaviour of glass fibre reinforced epoxy composites enhanced with nanoparticles. *Compos Part B* 62:65–72
24. Bortz DR, Merino C, Martin-gullon I (2011) Carbon nanofibers enhance the fracture toughness and fatigue performance of a structural epoxy system. *Compos Sci Technol* 71 (1):31–38

# Thermo-Mechanical Creep and Recovery of CTBN–Epoxy Shape Memory Polymers Under Saline Environment

A. Revathi, M. Sendil Murugan and Sandhya Rao

**Abstract** In the present study, the creep and recovery experiments of unmodified epoxy SMP and 5% carboxyl-terminated butadiene acrylonitrile (CTBN) modified epoxy SMPs were carried out after being exposed to saline environment (5% NaCl, 35 °C/98% RH). The creep results of the SMP specimens before and after exposure to saline environment, obtained through short-term tensile creep test at different temperatures (i.e., 25, 80, 103 and 120 °C) and loading conditions, were compared. Prior to exposure to saline environment, the creep strain was found to increase with increasing temperature and reached a maximum around the glass transition temperature (i.e., 103 °C). A higher creep recovery ratio was noticed in the CTBN-modified epoxy SMP particularly at high-temperature conditions. The creep strain was higher in saline environment at 25, 80 and 103 °C; however, at 120 °C both the SMPs could not withstand the applied load. The creep recovery ratio was unaffected by the saline environment in both the SMPs.

**Keywords** Themo-mechanical · Creep · Recovery · CTBN · SMP · Saline

## 1 Introduction

Shape memory polymers (SMPs) are the emerging smart materials for different applications, especially in biomedical, aerospace, and construction engineering fields. SMPs are those materials that have the ability to “memorize” a permanent shape and can be “fixed” to a temporary shape under specific conditions of temperature and stress [1–4]. The polymeric materials, when placed in service, are exposed to a variety of environmental conditions such as high temperature, relative humidity (RH), ultraviolet and solar radiation, chemicals, saline water, dust, hydraulic fuels and also different types of mechanical loading. Therefore, SMPs

---

A. Revathi (✉) · M. Sendil Murugan · S. Rao  
Centre for Societal Missions and Special Technologies (CSMST),  
CSIR-National Aerospace Laboratories (NAL), Bangalore, India  
e-mail: revs@nal.res.in

must perform under environmental conditions combined with mechanical stresses. The present study is a baseline assessment of the durability of epoxy-based shape memory polymers when exposed to saline environment. Creep behavior is characteristic of the viscoelastic behavior of SMPs and depends heavily on the material temperature. Also this is the most important parameter in characterizing the shape memory effect of SMPs. Moisture absorption in polymers may increase toughness and decrease strength and stiffness, thereby leading to increased creep strains. Creep response of viscoelastic polymers is strongly related to the moisture content and the overall diffusion process [5]. Many researchers have pointed out that the change in temperature and the moisture absorption [6, 7] lead to a decrease in the tensile, compressive, fatigue, and creep properties in carbon fiber/epoxy composites. Characterization of viscoelastic behavior of epoxy SMP systems was investigated by Song et al. [8]. He studied the stress–strain hysteresis, stress relaxation, and creep behavior at different temperatures. Yousef et al. [9] studied the effect of different environmental conditions (tap water and sea water) on the creep behavior of concrete beams reinforced with glass fiber-reinforced polymer (GFRP) bars under sustained loads. The results show that the creep effect due to sustained loads was significant for all environments and the highest effect was observed under sea-water immersion conditions. Influence of water absorption (distilled water for 24 h at 90 °C and frozen for 24 h at –16 °C in refrigerator) on creep behavior of carbon fiber/epoxy laminates was studied by Kim and Kenichi [7]. The results show that the steady-state creep of the moisture absorbed and frozen specimens rapidly increased at 100 °C. Maksimov et al. [10] investigated the creep profiles of PN-3 polyester resin at various temperatures and moisture contents. The results showed that time–temperature–moisture superposition can apply in creep under various temperatures and moisture conditions. Kawai and Mauko [11] examined the high-temperature creep behavior of UD T800H/3631 carbon/epoxy composites at relatively high stress levels and simulated using the classical laminated plate theory. Excellent agreement between the predicted and observed results was demonstrated on taking into account the fiber rotation induced by deformation.

In this background, it is important to understand the effect of saline environment on creep behavior of CTBN–epoxy SMPs and to assess the effects on shape memory performance. Therefore, in the present study, the creep deformation and recovery of epoxy shape memory polymers with 5 wt% CTBN are investigated at different temperatures and stress levels after conditioning in saline environment.

## 2 Experimental

### 2.1 Material and Specimen Preparation

A thermosetting epoxy-based SMP was obtained by co-reacting L552 epoxy resin (epoxy equivalent weight (EEW) of 156 g/eq) with K552, a cycloaliphatic amine

hardener, supplied by M/s. Atul India (P) Ltd. (Mumbai, India). This SMP was modified with 40 wt% CTBN-epoxy adduct (Albipox 1000, EEW=330 g/eq), procured from Nanoresins (Geesthacht, Germany) so as to yield 5 % CTBN (by weight)-modified epoxy SMP matrices.

The unmodified and CTBN modified SMPs were prepared as per the procedure mentioned elsewhere [13]. Before subjecting to tests, the specimens were thermally cycled between 25°C and 100°C so as to remove the thermal strains accumulated during fabrication.

## 2.2 Creep Tests

The creep and recovery tests were performed using a custom-built thermo-mechanical creep facility fitted with a microprocessor-based temperature controller to control the temperature (M/s Spranktronics Pvt Ltd, Bengaluru). Test specimens with dimensions of 90 mm × 10 mm × 3 mm were used for the creep tests. The specimens were mounted carefully in a fixture and aligned to avoid any twisting or buckling of the specimens. The distance between the tension grips was maintained at 40 mm, and this was considered as the gauge length. The preselected constant stress was applied on to the specimen for 3600 s, then load was removed immediately, and recovery was continued for a period of 3600 s [13]. Creep tests were performed at different stress levels and temperatures (25, 80, 103, and 120 °C) after exposure to saline environment.

## 2.3 Salt Spray Test

SMPs were exposed to saline media (i.e., 5% NaCl solution) in salt spray chamber (M/s Weiss tecknic, USA) maintained at 35 °C/98% RH according to ASTM D-117. The test profile was configured in the microprocessor-based controller by using the SIMPAC software in segment wise. Saline water flow quantity limiter position was set for 750 cm<sup>3</sup>/h. Laboratory Reagent (LR) grade 5% NaCl was mixed with demineralised water in the mixing ratio of 100:5. The compressed air pre-pressure was maintained at 1.1 bar so that the salt solution could be sprayed through nozzle.

The initial weights of specimens were recorded before the exposure. Precautions were taken to remove the water from specimen surfaces, by carefully wiping them before testing. Specimens were conditioned up to 1000 h.

### 3 Results and Discussions

#### 3.1 Influence of Temperatures and Loads

The creep and recovery profiles as a function of time for unmodified epoxy SMP and 5% CTBN–epoxy SMP after exposure to saline environment are presented in Figs. 1a–d and 2a–d, respectively. The creep strain increases with increasing temperature and shows maximum around the  $T_g$  in both the SMPs. It can also be seen from Figs. 1 and 2 that the creep strain increased with the increasing load at 25 and 103 °C; however, at 80 °C the creep strain decreased slightly with increasing load in both the SMPs. This may be due to the accumulation of unrecovered strain from the first load. The same trend was noticed for unexposed specimens which is shown in Tables 1 and 2 [13].

#### 3.2 Influence of CTBN and Saline Environment

Tables 1, 2, 3 and 4 show the creep strain and recovery ratio of the SMPs before and after exposure to saline environment. From the tables, it can be seen that the creep strain of 5% CTBN–epoxy SMP is lower than that of the epoxy SMP under all the temperatures and loads considered. This implies that the creep behavior is improved due to the presence of CTBN phase [14] in the epoxy SMP. Compared to

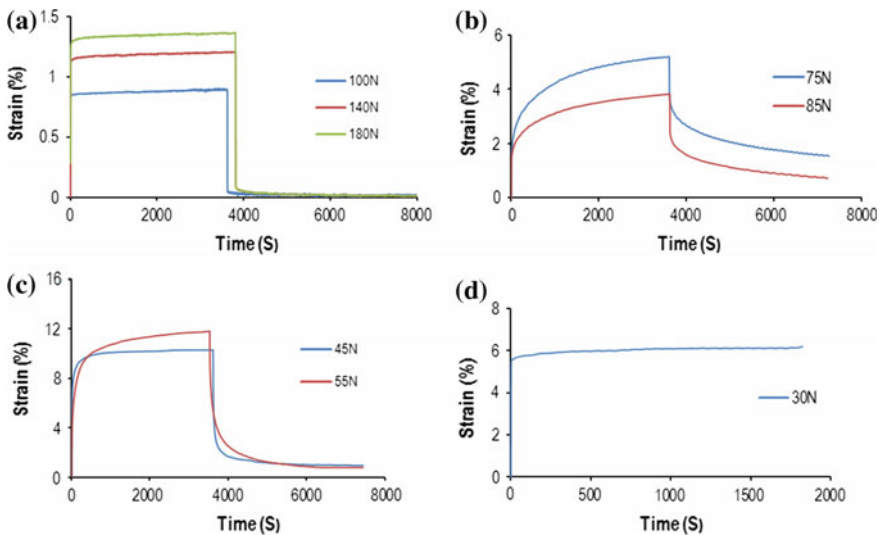


**Fig. 1** Creep and recovery of epoxy SMP after exposure to saline environment, **a** 25 °C **b** 80 °C **c** 103 °C and **d** 120 °C

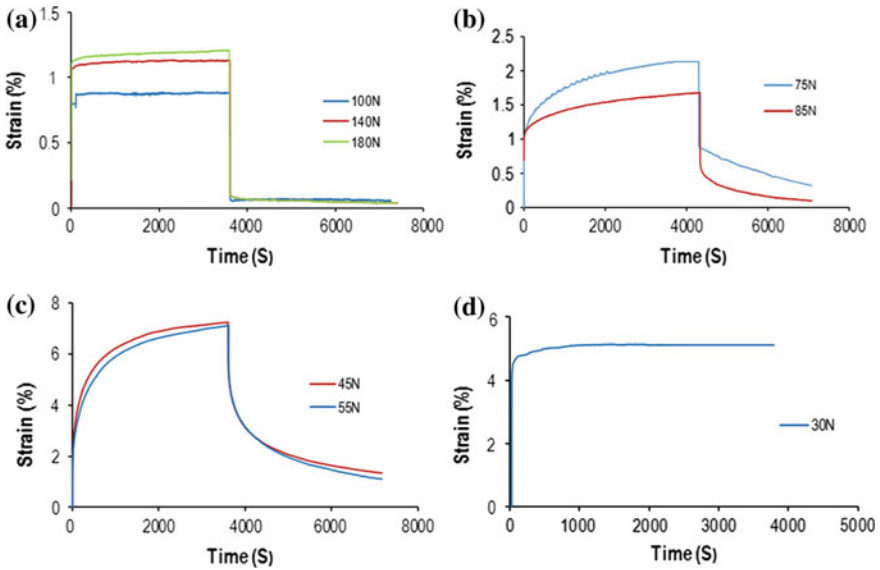


**Fig. 2** Creep and recovery of 5% CTBN–epoxy SMP after exposure to saline environment, **a** 25 °C **b** 80 °C **c** 103 °C and **d** 120 °C

**Table 1** Creep strain, residual strain, and recovery ratio for epoxy SMP before exposure

Temperature (°C)	Loads (N)	Creep strain (%)	Residual strain (%)	Recovery ratio (%)
25	100	0.71	0.02	97.18
	140	0.89	0.01	98.87
	180	1.19	0.02	98.31
80	75	2.33	0.62	73.51
	85	1.84	0.29	83.85
103	45	9.98	0.92	90.78
	55	10.75	0.86	92.00
120	30	7.83 (specimen broken)		

unmodified epoxy SMP, 5% CTBN–epoxy SMP shows lower residual strains, indicating that incorporation of CTBN decreases the permanent deformation remarkably and as a result, the recovery ratio also increased particularly in high-temperature regimes. At 120 °C, the 5% CTBN–epoxy SMP could withstand all the three loads (Table 2) due to the flexibility and toughening effect of the rubber particles dispersed in the epoxy SMP. It can be observed from the Tables 3 and 4 that the creep strain was higher at all the temperatures except 120 °C after exposure to saline environment. The creep strain increased significantly at 80 and 103 °C; however at 120 °C, both the SMPs could not withstand the load. It can be explained that absorbed moisture would have led to plasticization of the matrix (the mobility



**Table 2** Creep strain, residual strain and recovery ratio for 5% CTBN–epoxy SMP before exposure

Temperature (°C)	Loads (N)	Creep strain (%)	Residual strain (%)	Recovery ratio (%)
25	100	0.84	0.01	98.22
	140	0.93	0.01	98.92
	180	1.06	0.02	98.11
80	75	1.25	0.09	92.40
	85	1.19	0.07	94.53
103	45	5.54	0.45	91.87
	55	5.72	0.53	90.73
120	30	5.20	0.13	97.50
	40	6.44	0.02	99.68
	50	8.16	0.08	99.01

**Table 3** Creep strain, residual strain and recovery ratio for epoxy SMP after exposure

Temperature (°C)	Loads (N)	Creep strain (%)	Residual strain (%)	Recovery ratio (%)
25	100	0.89	0.02	97.75
	140	1.20	0.01	99.16
	180	1.36	0.03	97.79
80	75	5.20	1.40	73.07
	85	3.82	0.72	81.15
103	45	10.29	0.96	90.67
	55	11.80	0.80	93.22
120	30	6.28 (specimen broken)		

**Table 4** Creep strain, residual strain and recovery ratio for 5% CTBN–epoxy SMP after exposure

Temperature (°C)	Loads (N)	Creep strain (%)	Residual strain (%)	Recovery ratio (%)
25	100	0.88	0.02	97.72
	140	1.13	0.01	99.11
	180	1.20	0.02	98.33
80	75	2.13	0.22	89.67
	85	1.68	0.15	91.07
103	45	7.11	0.45	93.67
	55	7.24	0.49	93.23
120	30	5.11 (specimen broken)		

of polymer chains increases) causing increase in toughness and decrease strength and stiffness, thereby leading to increased creep strains [7, 15]. However, the creep recovery ratio was unaffected by the saline environment in both the SMPs.

## 4 Conclusions

The creep behavior of 5% CTBN-epoxy SMP at different temperatures and loads has been compared with that of the corresponding unmodified epoxy SMP before and after exposure to saline environment. The following conclusions were drawn:

The creep strain increases with increasing temperature and shows maximum around the  $T_g$  in both the SMPs. Also the creep strain increased with the increasing load at 25 and 103 °C; however, at 80 °C the creep strain decreased with increasing load. Compared to unexposed specimen, the creep strain is more in saline environment especially at higher temperatures (i.e., at 80 and 103 °C). This may be due to the plasticizing effect of moisture in the saline environment. However, at 120 °C both the SMPs could not withstand the load. Incorporation of CTBN into epoxy SMP produced a significant decrease in the residual strain; therefore, a higher percentage creep recovery behavior was noticed particularly in high-temperature regimes as compared to the unmodified epoxy SMP. The creep recovery ratio was unaffected by the saline environment in both the SMPs.

## References

1. Otsuka K, Wayman CM (1998) Shape memory materials. Cambridge University Press, New York
2. Lendlein AS, Kelch S (2002) Shape-memory polymers. *Angew Chem* 41:2034–2057
3. Lendlein AS, Kelch S, Kratz K, Schulte J (2005) Shape-memory polymers. In: *Encyclopedia of Materials*, Elsevier, Amsterdam, pp 1–9
4. Nakayama K (1991) Properties and application of shape-memory polymers. *Int J Polym Sci Technol* 18:T43–T48
5. Venkata SC, Derrick R (2010) Dean, Gregg, M. Janowski.: Effect of environmental weathering on flexural creep behavior of long fiber-reinforced thermoplastic composites. *Polym Degrad Stab* 95:2628–2640
6. Arao Y, Koyanagi J, Utsunomiya S, Takeda S, Kawada H (2009) Analysis of time-dependent deformation of a CFRP mirror under hot and humid conditions. *Mech Time-Depend Mater* 13:183–197
7. Kim H, Takemura K (2011) Influence of water absorption on creep behaviour of carbon fiber/epoxy laminates. *Procedia Eng* 10:2731–2736
8. Song WB, Wang ZD (2013) Characterization of viscoelastic behavior of shape memory epoxy systems. *J Appl Polym Sci* 128:199–205
9. Al-Salloum YA, Almusallam TH (2007) Creep effect on the behavior of concrete beams reinforced with GFRP bars subjected to different environments. *Constr Build Mater* 21:1510–1519
10. Maksimov RD, Sokolov EA, Mochalov VP (1975) Effect of temperature and moisture on the creep of polymeric materials. One-dimensional extension under stationary Temperature–moisture conditions. *Inst Polym Mech* 3:393–399
11. Kawai M, Mauko Y (2004) Creep behavior of unidirectional and angle-ply T800/3631 laminates at high temperature and simulations using a phenomenological viscoplasticity model. *Compos Sci Technol* 64:2373–2384
12. Kavitha, Revathi A, Rao S, Srihari S, Dayananda GN (2012) Characterization of shape memory behaviour of CTBN-epoxy resin system. *J Polym Res* 19:1–7

13. Revathi A, Murugan MS, Rao S, Rao KV (2016) Estimation of creep and recovery of carboxyl-terminated butadiene acrylonitrile-epoxy shape memory polymers under tensile loading. *Ind J Adv Chem Sci* S1:39–44
14. Brahmananda P, Raju Mantena P (2011) Viscoelastic response of graphite platelet and CTBN reinforced vinyl ester nanocomposites. *Mater Sci Appl* 2:1667–1674
15. Vlasveld DPN, Bersee HEN, Picken SJ (2005) Creep and physical ageing of PA6. *Polymer* 46:12539–12545

# Fatigue Life Estimation of Components Mounted on PCB Due to Vibration

Debadatta Mishra, Manish Trikha, D. Kamesh, K. Venkatesh and M. Ravindra

**Abstract** A spacecraft consists of a number of electronic packages to meet the functional requirements. An electronic package is generally an assembly of printed circuit boards placed in a mechanical housing. A number of electronic components are mounted on the printed circuit board (PCB). A spacecraft experiences various types of loads during its launch such as vibration, acoustic and shock loads. Prediction of response for printed circuit boards due to vibration loads is important for mechanical design and reliability of electronic packages. Dynamic analysis of printed circuit boards is carried out using finite element method. The components mounted on PCB experience stresses due to curvature of the board and inertia loads. The response of the component depends on its natural frequency as well as PCB dynamic characteristics. The objective of this paper is to predict the fatigue life of components mounted on printed circuit boards due to vibration. A case study of a typical component mounted on PCB is taken up and dynamic analysis is carried out for base excitation. Modal analysis and frequency response analysis are carried out using FEM. The component lead stresses due to vibration are determined. The fatigue life is estimated for sine and random vibration environment.

**Keywords** Printed circuit board (PCB) · Spacecraft · Vibration analysis  
Component stress · Fatigue life

---

D. Mishra  
Liquid Propulsion Systems Center, HAL 2nd Stage HPO,  
Bangalore 560008, Karnataka, India

M. Trikha (✉) · D. Kamesh · K. Venkatesh · M. Ravindra  
ISRO Satellite Centre, Vimanapura Post, Bangalore 560017, Karnataka, India  
e-mail: mtrikha1@yahoo.com

## 1 Introduction

A spacecraft experiences various types of loads during its launch such as vibration, acoustic and shock loads. The electronic packages are designed to withstand the launch vibration environment. Electronics packages are subjected to vibration testing to establish adequate margins. Package component failures due to vibration loads have been observed in the past. The four basic failure modes of components mounted on PCB due to vibration environment are the results of the following conditions: high acceleration levels, high stress levels, large displacement amplitudes and electrical signals out of tolerance [1].

It is possible to predict the probability of mechanical failure by a two-stage Physics of Failure (POF) approach. The first stage of this approach is defined as the response prediction stage. In this stage, vibration response of the board is calculated through a finite element (FE) model of the PCB component system. The second stage relates this calculated response to some pre-determined component failure criteria, to show whether the attached components can withstand this curvature or acceleration.

Sophisticated electronic systems are often simulated using simple masses, springs and dampers to estimate the dynamic characteristics of the system. Simple one and two degree of freedom systems are used to approximate the electronic systems. More complicated finite element models of electronic systems are created to study the dynamic characteristics of the system and to estimate the fatigue life of critical components mounted on the PCB. Finite element models can be either simplified or detailed. Detailed finite element models are built by modeling the PCB and the components. The simple geometry of the board is modeled and meshed using 2-D finite elements (i.e., by using flat shell elements).

In this paper, modeling and simulation of a typical component mounted on a PCB used for space applications is carried out. First, vibration analysis of a PCB with components is carried out using FEM to determine the natural frequencies. The PCB is modeled using 2D shell elements. The FEM model is validated by conducting vibration tests on the PCB and comparing the simulation and test results. The transistor component is modeled as a 1-D cantilever beam with end mass. The stress analysis of PCB with components is carried out for out of plane sine vibration input and fatigue life of the component pin is calculated. Modal analysis of the transistor component fixed at the base is carried out. Frequency response analysis and stress analysis of component are done for in-plane sine vibration input. Subsequently, the fatigue life of the component pin is calculated for in-plane sine and random vibration input.

## 2 Literature Review

Suhir [2] showed the simplest way to predict the fundamental (lowest) natural frequency of “free” vibrations of a heavy electronic component mounted on a printed circuit board by assuming certain boundary conditions. He also derived a

formula to find out the prediction of the fundamental lowest natural frequency. He explains that Idealization of an actual structure as a cantilever beam with a lumped mass at the end a formula for this case can be found in the majority of textbooks which can lead to a significant overestimation of the fundamental frequency, i.e., result in a nonconservative and even misleading information. Schaller [3] has carried out the finite element analysis of printed circuit board by commercial FEM software, and he expressed that FEM analysis for electronic components was safer and reliable when the PCB is more complex mounted with of several components of different material which properties starts from metals such as copper to non-metals like ceramic. He proved the effectiveness of FEM by a case study and explained its advantage in the present electronic industry scenario where the component rerouting on the PCB and design changes is frequent and unavoidable. Silva et al. [4] devised a simplified FEM model of a component to compare the vibration analytical solution especially stress induced at the component pins with the FEM simulation result. He verified his study with an example and stated that his methodology can be applied to any complicated PCB model with component with suitable assumptions. Jung et al. [5] made the FEM analysis of PCB with components and found out the natural frequencies with the corresponding mode shapes for fatigue life prediction. Then they did the vibration test to validate the natural frequencies derived for the FEM analysis. They concluded that along with FEM analysis if the test can be carried out on PCB, then the fatigue life prediction will be more accurate than only theoretical study. The method explained in their work can be used in space program as well as equally applicable for electronic home appliances. Pitarresi [6] carried out a comparison study between computational and experimental study to find out the natural frequencies and mode shapes for printed circuit board subject to vibration for the first few modes. He explored some simplification in the FEM modeling to avoid the modeling complication. Finally, he proofed his methodology with a valid example. Liguore et al. [7] describes a test program in this paper which was performed to obtain structural fatigue data for SMT solder joints exposed to a random vibration environment. He used a number of PCB cards with surface mounted components to predict the physics of “why and how” SMT solder joints fail under vibration loads. In his work, he recorded the vibration time to failure data for individual solder joints of the SMT components for understanding under vibration loading fatigue life of the solder joints. Dehbi et al. [8] used the Steinberg vibration model to predict the fatigue life cycle of electronic sensors mounted on automobile platforms. He calculated the fatigue life of the tantalum capacitors populated boards using FEM analysis and validated his analysis with sine vibration test as input to the PCB. Chen et al. [9] carried out the FEA of the component mounted on printed wiring board (PWB) and did the vibration test by giving the sine vibration load as input the PWB to estimate the fatigue life of the component. He applied the Miner’s rule in calculating the fatigue damage index for those test components when failed.

### 3 Vibration Analysis of a PCB Mounted with Transistors

In this study, a six-layer PCB used for space applications is considered. The PCB is modeled as isotropic plate with equivalent material properties such as Young's modulus, Poisson's ratio and mass density. Details of the PCB and components are summarized in Tables 1, 2 and 3. The PCB and the four transistors mounted on the PCB as shown in Fig. 1 are modeled using HYPERMESH as pre-processor, and MSC.NASTRAN is used as solver. The PCB is meshed with 6567 quadrilateral 2-D shell elements (2.5 mm element size) with appropriate thickness. Fixed boundary conditions are applied at nine locations (PCB mounting locations) by arresting six degrees of freedom for the nodes on the boundary of holes in PCB as shown in Fig. 1. The transistor component is shown in Fig. 2. The leads of the transistor are modeled as single 1-D beams with end mass. The mass of the transistor is equally distributed as end mass to the three leads (1-D beams). The end mass is lumped at an offset from the free end of the beam at the C.G. of the transistor body.

#### 3.1 Modal Analysis of PCB with Four Transistors

Normal mode analysis was conducted using FEM to extract natural frequencies for PCB mounted with transistors. The first two natural frequencies are 341 and 373 Hz for PCB FEM model. The FEM results are compared with the natural frequencies obtained from vibration tests, and the results are shown in Table 4. The results are matching well.

#### 3.2 Stress Analysis of PCB with Four Transistors

##### Out of Plane Vibration (Sine Vibration)

The frequency response analysis is carried out for out of plane sine vibration input of 10 g from 5 to 2000 Hz. Damping ratio of 2% is assumed for the analysis. The component pin/lead stresses are determined. Maximum stress of 10.05 MPa is obtained for one of the transistor pins at 373 Hz (Mode-2 frequency). The lead stress versus input frequency plot for the transistor pin is shown in Fig. 3.

**Table 1** Details of PCB

Parameter	Value
PCB size	0.19 * 0.216 * 0.0017 m
Mass of bare PCB	138 g
Young's modulus of bare PCB	20 GPa
Poisson's ratio	0.12
Boundary condition	Fixed @9 locations

**Table 2** Details of component

(Dia * H) of Component	7.75 * 6.10 mm
Length of lead/pin	1.5 mm
Diameter of lead/pin	0.46 mm
CG of the transistor body from the lead end	0.7 mm

**Table 3** Mechanical Properties of component leads

Component lead/pin properties	
Young's modulus	160 GPa
Poisson's ratio	0.33
Density	8359 kg/m <sup>3</sup>
Yield strength	276 MPa
Ultimate tensile strength	518 MPa

**Geometry With Boundary Condition For PCB with Transistor**

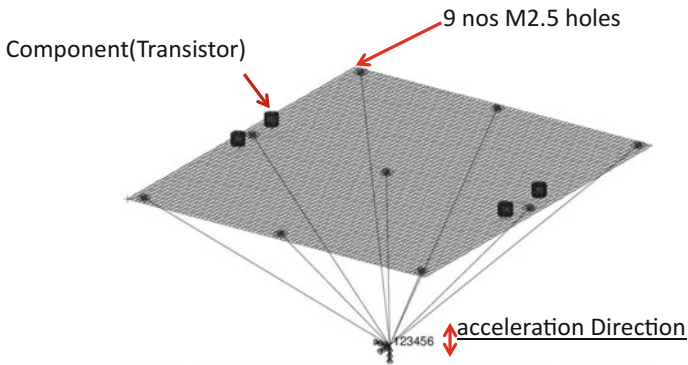


**Fig. 1** FE model of PCB with components

**Fig. 2** Transistor component

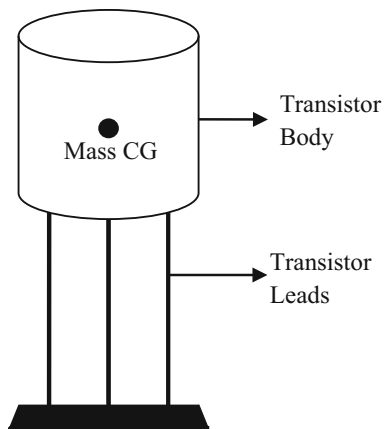




**Table 4** Comparison of natural frequencies obtained from FEM and vibration tests

Mode#	Natural frequency from FEM simulation (Hz)	Natural frequency from test (Hz)	% Difference
MODE-1	341	318	-7.2
MODE-2	373	363	-2.7

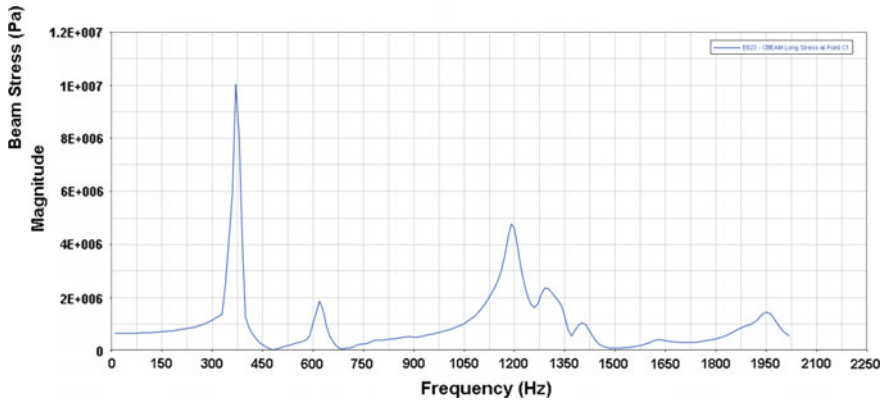


**Fig. 3** Component lead stress versus input frequency plot for transistor pin

We consider this maximum stress induced at the pin/lead and compare with the *S-N* curve of the component lead material to calculate the fatigue life of the pin.

### 3.3 Fatigue Life Calculation for the Component Pin

#### Out of Plane Vibration Condition

The maximum stress induced at the component pin from the FEM results is 10.05 MPa at 373 Hz. The ultimate tensile strength for the pin material is 518 MPa.

The equation for calculating the fatigue life of a component lead/pin is given by [1]:

$$N_1 S_1^b = N_2 S_2^b$$

where

$N_2$  1000 cycles to fail at 518 MPa

$S_2$  518 MPa (Ultimate Tensile strength of pin material)

$b$  6.4 (for stress concentration factor of 2, from the *S-N* curve)

For  $N_1 = 10^8$  cycles,  $S_1 = 96$  MPa (Endurance Limit of the pin material)

From FEM analysis results, maximum stress induced at the pin = 10.05 MPa at 373 Hz. Since, the maximum stress is less than the endurance limit; hence the component will not fail due to fatigue for the out of plane vibration input.

## 4 Vibration Analysis of Transistor Alone

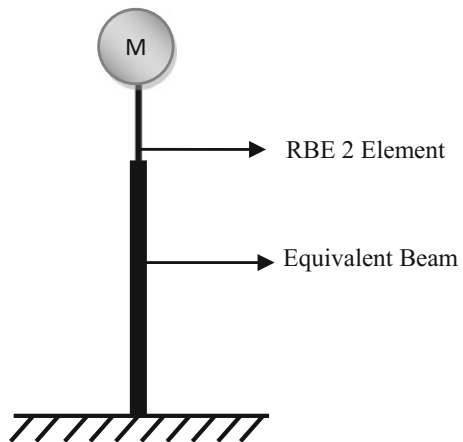
The FEM model of the transistor is developed using commercial FEM package HYPERMESH as pre-processor. The analysis is done using MSC. NASTRAN as solver. The three leads of the transistor are modeled as equivalent 1-D beam with equivalent cross-sectional area and moment of inertia. The body of the transistor component is modeled as concentrated mass element (CMASS2) with mass lumped at the C.G. of the body. One end of the equivalent beam is fixed, and the free end is connected to the mass element through rigid body element (RBE2) as shown in Fig. 4. The modal analysis is carried out, and the first natural frequency is 1520 Hz. This is the beam cantilever mode.

### 4.1 Frequency Response Analysis of Transistor

#### In-Plane Sine Vibration

The frequency response analysis is carried out for in-plane sine vibration input of 10 g from 5 to 2000 Hz. The frequency response function (FRF) for the mass is shown in Fig. 5, and an amplification of 16.7 is obtained at the first mode. Damping ratio of 3% is assumed for the analysis. The bending moment at the fixed end of the beam is plotted in Fig. 6 and the maximum bending moment ( $M$ ) is 0.012 Nm.

**Fig. 4** Equivalent beam model for the transistor component



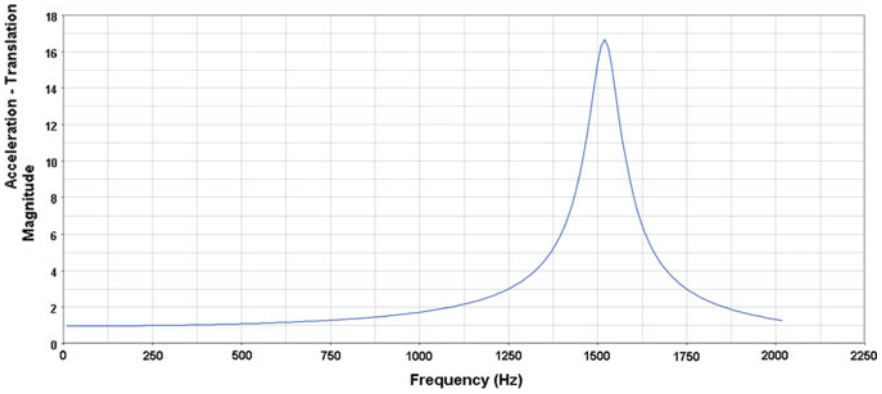


Fig. 5 FRF for in-plane sine vibration input

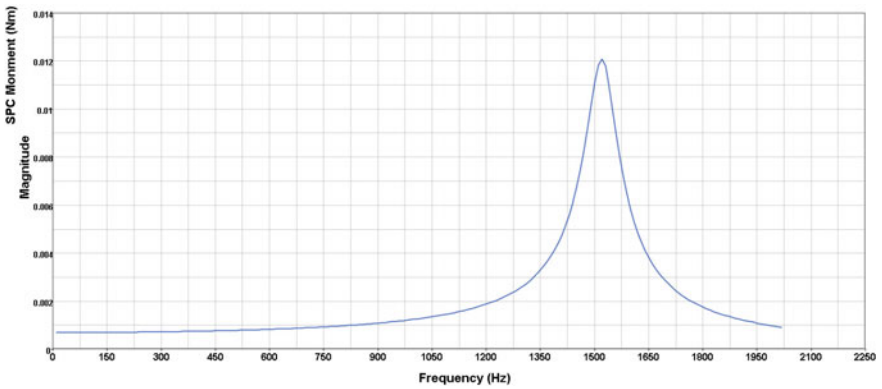


Fig. 6 Bending moment at the fixed end of the beam

### 4.2 *Fatigue Life Calculation for the Component Pin Due to Sine Vibration*

The fatigue life for the component pin is calculated for in-plane sine vibration input of 10 g from 5 to 2000 Hz. From the maximum bending moment ( $M$ ) at the fixed end of the beam (for first mode frequency), the bending moment at the fixed end of the pin/lead is obtained as  $1/3 * M$ . The bending stress ( $\sigma$ ) at the fixed end of the pin/lead is obtained as,

$$\sigma = (M/I) * (d/2)$$

where  $I$  is the area moment of inertia and  $d$  is diameter of the pin.

$\sigma$  418.75 MPa

The equation for calculating the fatigue life of a component lead/pin is given by:

$$N_1 S_1^b = N_2 S_2^b$$

where

$N_2$  1000 cycles to fail at 518 MPa

$S_2$  518 MPa (Ultimate Tensile strength of pin material)

$b$  6.4 (for stress concentration factor of 2, from the  $S-N$  curve)

For,  $S_1 = 418.75$  MPa,  $N_1 = 3901$  cycles to fail.

Time taken to failure at the natural frequency (1520 Hz) of the transistor =  $3901/1520 = 2.57$  s.

### 4.3 Fatigue Life Calculation for the Component Pin Due to Random Vibration

The fatigue life for the component pin is calculated for in-plane random vibration input of  $0.1 \text{ g}^2/\text{Hz}$  from 5 to 2000 Hz. The root mean square (rms) response of the mass ( $G_{\text{out}}$ ) to the broadband random vibration input is given by [1]:

$$G_{\text{out}} = \sqrt{\frac{\pi P f_n Q}{2}}$$

where

$P$   $0.1 \text{ g}^2/\text{Hz}$  is the input PSD,

$f_n$  1520 Hz is the natural frequency,

$Q$  16.7 is the amplification at the natural frequency,

Hence,  $G_{\text{out}} = 63.12 \text{ g (rms)}$

The bending moment at the fixed end of each pin/lead = 1.498 N mm (rms).

Bending stress ( $\sigma$ ) = 156.87 MPa (rms)

Assuming, Gaussian distribution for the random vibration and using three-band method [1],

The instantaneous accelerations,  $1\sigma$  values occur 68.3% of the time,

$2\sigma$  values occur 27.1% of the time and

$3\sigma$  values occur 4.33% of the time.

The approximate number of stress cycles  $N_1$  required to produce a fatigue failure in the component lead/pin for the  $1\sigma$ ,  $2\sigma$  and  $3\sigma$  stresses can be obtained from the following equation [1]:

$$N_1 S_1^b = N_2 S_2^b$$

where

$N_2$  1000 cycles to fail at 518 MPa

$S_2$  518 MPa (Ultimate Tensile strength of pin material)

$b$  6.4 (for stress concentration factor of 2, from the  $S-N$  curve)

### For $1\sigma$ (rms) stress

$S_1 = 156.87$  MPa,  $N_1 = 2.09 * 10^6$  cycles to fail

Time taken to failure =  $2.09 * 10^6 / 1520 = 22.9$  min

### For $2\sigma$ stress

$S_1 = (2 * 156.87) = 313.74$  MPa,  $N_1 = 2.47 * 10^4$  cycles to fail

Time taken to failure =  $2.47 * 10^4 / 1520 = 16.3$  s

### For $3\sigma$ stress

$S_1 = (3 * 156.87) = 470.61$  MPa,  $N_1 = 1.84 * 10^3$  cycles to fail

Time taken to failure =  $1.84 * 10^3 / 1520 = 1.2$  s

For in-plane random vibration test of 1 min duration for the given input, the component lead/pin will experience  $3\sigma$  stresses for 4.33% of the time, i.e., 2.6 s. Comparing this, with the time taken to failure for  $3\sigma$  stresses, the component is likely to fail for the given random vibration input.

## 5 Conclusions

The fatigue life estimation of components mounted on PCB due to vibration is carried out. Modal analysis of a PCB mounted with transistors is carried out, and the results are compared with the vibration tests on PCB. The results are matching well. Frequency response analysis of a PCB mounted with transistors is carried out for out of plane sine vibration input, and the component lead stresses are determined. The fatigue life for the component lead/pin is calculated, and it is observed that component does not fail for the given vibration input. Next, modal analysis and frequency response analysis of transistor alone are done for in-plane vibration input. The fatigue life for the component lead/pin is estimated for sine and random in-plane vibration input. The time taken for fatigue failure is calculated, and the results show that the component is likely to fail for the given in-plane vibration input.

**Acknowledgements** The authors would like to thank Mr. Anand, M. Tech Project student at ISAC for his help in FEM simulations.

## References

1. Steinberg DS (2000) *Vibration analysis for electronic equipment*, 3rd edn. Wiley, New York
2. Suhir E (2000) Predicted fundamental vibration frequency of a heavy electronic component mounted on a printed circuit board. *J Electron Packag* 122(1):3–5
3. Schaller A (1988) Finite element analysis of microelectronic component-state of the art. In: CH2629-4/88/0000-0057 @1988 IEEE conference
4. Silva GHC, Gonçalves PJP (2013) A model for computing vibration induced stresses of electronic components in a general flexible mounting. *J Sound Vib* 332:5192–5206
5. Jung IH, Park TW, Han SW, Seo JH, Kim SH (2004) Structural vibration analysis of electronic equipment for satellite under launch environment. *J Korean Soc Precis Eng* 21(8):1440–1445
6. Pitarresi JM (1990) Modeling of printed circuit cards subject to vibration. Department of Mechanical and Industrial Engineering, State University of New York at Binghamton, Binghamton, New York 13901, pp 2104–2107
7. Liguore S, Followell D (1995) Vibration fatigue of surface mount technology (SMT) solder joints. In: *Proceedings annual reliability and maintainability symposium*, pp 18–26
8. Dehbi A, Ousten Y, Danto Y, Wondrak W (2005) Vibration lifetime modelling of PCB assemblies using steinberg model. *Microelectron Reliab* 45:1658–1661
9. Chen YS, Wang CS, Yang YJ (2008) Combining vibration test with finite element analysis for the fatigue life estimation of PBGA components. *Microelectron Reliab* 48:638–644

# Modified Rainflow Counting Algorithm for Fatigue Life Calculation

Vaibhav Shinde, Jyoti Jha, Asim Tewari and Sushil Miashra

**Abstract** Fatigue life calculation of a varying load spectrum is a complex task. There are various approaches suggested to simplify the load spectrum into simple major and minor cycle. One such approach is rainflow counting methodology. In this paper, a new Microsoft Excel-based algorithm for the modified graphical rainflow counting method is presented. Validity and accuracy of algorithm have been demonstrated by various simple as well as complex examples. This method allows the application of Miner's rule in order to assess the fatigue life of a structure subject to complex loading.

**Keywords** Cycle counting · Rainflow counting algorithm · Fatigue analysis Hysteresis loop

## 1 Introduction

It has been estimated that 90% of the structure failure is due to the fatigue. Fatigue failure occurs due to the varying load with respect to time. The fatigue life of the component which is subjected to constant varying load can easily be calculated using  $S-N$  curve; however, when the varying load is random it is difficult to estimate the fatigue life. Several methodologies have been suggested to convert the random load spectrum to simpler cycles, and one such approach is cycle counting. In the cycles counting methodology, same cycles grouped together and Miner's rule used to calculate the damage and fatigue life. There are number of methods for the cycle counting, i.e., (1) level crossing cycle counting, (2) peak counting method, (3) simple-range counting method, (4) rainflow counting method, (5) Range-pair counting method, (6) two-parametric fatigue characteristics [1–4].

---

V. Shinde · J. Jha (✉) · A. Tewari · S. Miashra  
National Centre for Aerospace Innovation and Research, Indian Institute of Technology  
Bombay, Powai, Mumbai 400076, India  
e-mail: jyoti.jha@iitb.ac.in

© Springer Nature Singapore Pte Ltd. 2018  
S. Seetharamu et al. (eds.), *Proceedings of Fatigue, Durability and Fracture Mechanics*, Lecture Notes  
in Mechanical Engineering, [https://doi.org/10.1007/978-981-10-6002-1\\_30](https://doi.org/10.1007/978-981-10-6002-1_30)

Rainflow counting method is widely practiced across the industry to convert the fatigue load spectrum to simpler cycle. This method is the most accurate and also it gives the average value [5].

## 2 Concept of Rainflow Counting Method

It has been estimated that 90% of the structure failure is due to the fatigue. Fatigue failure occurs due to the varying load with respect to time. The fatigue life of the component which is subjected to constant varying load can easily be calculated using  $S-N$  curve; however, when the varying load is random it is difficult to estimate the fatigue life. There are several methodology has been suggested to convert the random load spectrum to simpler cycles and one such approach is cycle counting. In the cycles counting methodology, same cycles grouped together and Miner's rule used to calculate the damage and fatigue life. There are number of methods for the cycle counting, i.e., (1) level crossing cycle counting, (2) peak counting method, (3) simple-range counting method, (4) rainflow counting method, (5) range-pair counting method, (6) two-parametric fatigue characteristics [1–4].

Rainflow counting method is widely practiced across the industry to convert the fatigue load spectrum to simpler cycle. This method is the most accurate and also it gives the average value [5] (Fig. 1).

To get a cycle count from the variable amplitude loading, we have to find out the sequences of the peak and valleys. To get a peak and valleys, turn the sheet clockwise  $90^\circ$  as shown in figure. Drops of water released from each maximum and minimum value of the loading. The drop will stop when the peak (or valley) value is greater than or equal (or smaller than or equal) to the value of the peak (or valley) from where the water drop starts. The water drop also stops when it merges with the path of the previous drops path (point 2' as shown in Fig. 2).

**Fig. 1** Variable amplitude loading

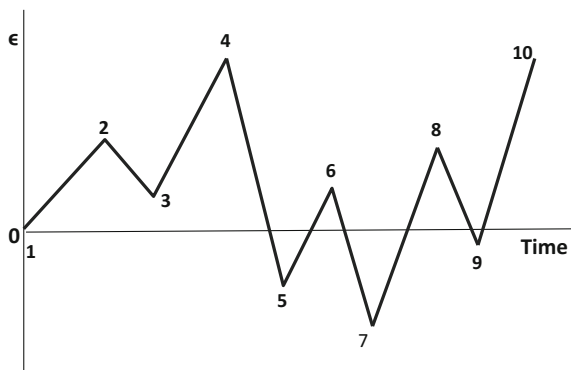
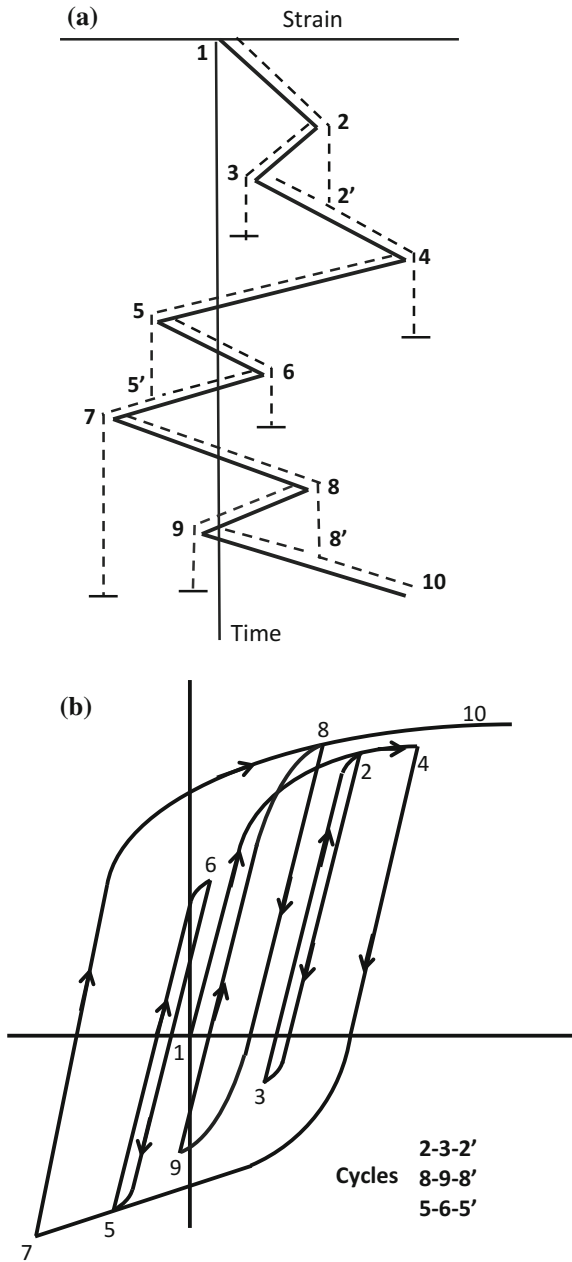




**Fig. 2** Rainflow counting method. **a** Load sequence and, **b** its stress-strain history



The whole concept of the MGRM has been clearly illustrated in figure. In this figure, one can see the cycles count for the closed hysteresis loop. Whole cycles and half-cycles are shown in Fig. 2b.

### 3 Computer Programming of MGRM

Before giving data to program, it is necessary to filter it or one can say to arrange the data in such a way that there should be a successive extreme value. This can be done by adjusting equal value points with the only one point of the corresponding value and polygonal line processing [6]. By using these techniques, we can obtain a data in such way that each point in the data is either local maximum or minimum. We can also use a filter to eliminate the cycles which are less than the threshold value (8, page No. 10).

The algorithm developed for the modified rainflow counting has been explained in the following flowchart. Load the data and the time sequence in the form of array  $S[i]$  and  $T[i]$ , respectively. At the starting of the data, if  $S[1] > S[2]$ , then  $S[1]$  will be the peak or else it would be the valley. For the other peaks and valleys, go to step 1.

- (1) If  $S[i] < S[i + 1]$ , then go to the valley or else go to the peak (i.e., step 2)
- (2) If  $S[i] = \text{peak}$  (i.e., values of the peaks stores for the particular  $i$  in the step 5), then  $i + 1$  and go back for the next loop, or else go to the step 3.
- (3) Let  $j = i + 1$ , and check for the condition  $S[j] \leq S[i - 1]$  with the  $j += 2$ , if condition satisfied at the  $j = b$ , then go to step 4 or else go to step 6.
- (4) Peak = maximum value of the range ( $S[i]$ – $S[b]$ ) and store this peak for the particular corresponding  $i$  value. In this, if  $(b - i) = 1$ , then  $S[i]$  itself a peak value, store this value and go to step 1 or else go to step 5.
- (5) In this step, effect of the step 4 will be implemented on the peaks which are present between the  $S[i]$  and  $S[b]$ . Thus one can get the peaks for the values between  $S[i]$  and  $S[b]$  (which used to check in step 2). For this let  $x = b$  with the  $x - = 2$ , then search for the value  $S[x] = \text{peak}$  and when this condition satisfies then peak at  $i = b$  is equal to the maximum value of range  $(x - 2-i)$ . That has to be stored so that when in step 2,  $i$  comes equal to  $b$  it goes to next loop. Thus loop of  $x$  is repeated as shown in flowchart. After reaching  $x$  at  $i + 2$ , go to the step 1.
- (6) This is same as step 5 but instead of going up to  $b$  we have to go up to the last of the data, i.e.,  $S[n]$ . All other procedures and conditions are same as step 5.

Flowchart of the valley is also same like peak, but the conditions are the reverse of the peak. After getting peaks and valleys, the data have been processed and arranged in a Microsoft Excel Macro to get the closed cycles.

### 4 Illustrative Example

Whole algorithm can be explained well with the following simple example (based on Fig. 1).

Loads sequence: 0, 10, 5, 15, -4, 3, -9, 6, -1, 20. Peaks and valleys for the given load sequence can be obtained with the help of computer program (Fig. 3) as shown in Table 1.

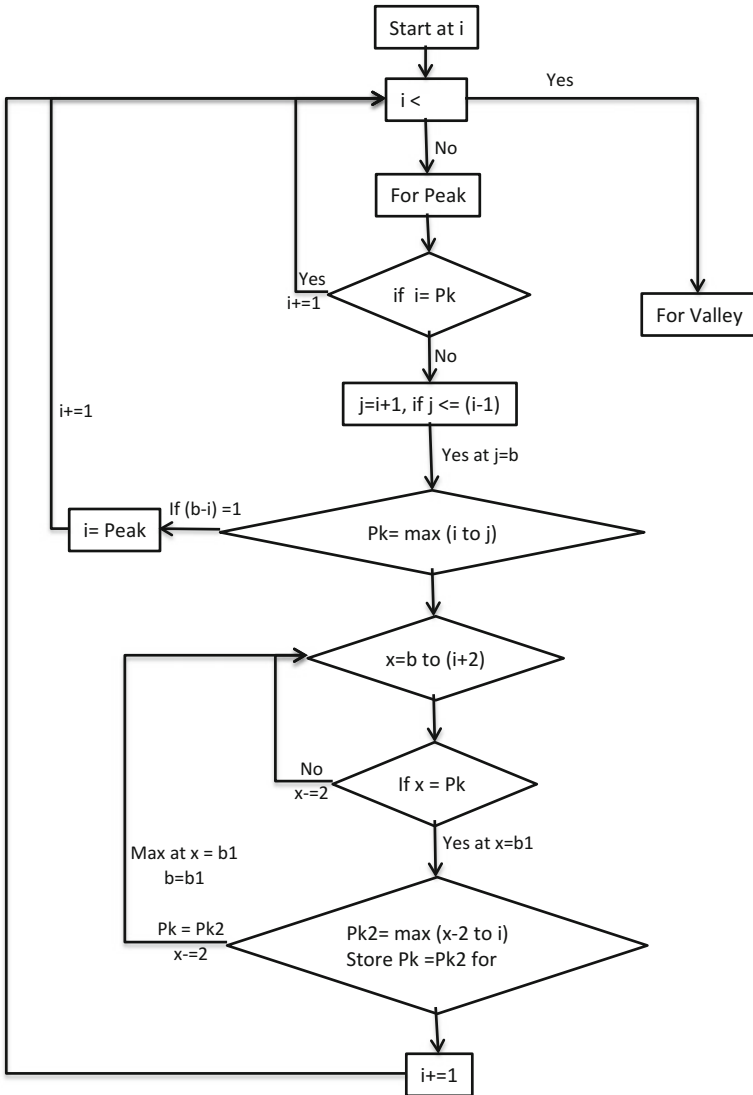


Fig. 3 Flowchart for obtaining peak and valley

**Table 1** Peaks and valleys

Valley	Peaks
0	15
5	10
-9	3
-4	20
-1	6

**Table 2** Half-reversals

Stress from sequence (X), MPa	Peak/valley (Y), MPa	No. of cycles
0	15	0.5
10	5	0.5
5	10	0.5
15	-9	0.5
-4	3	0.5
3	-4	0.5
-9	20	0.5
6	-1	0.5
-1	6	0.5
20	-	-

**Table 3** Number of complete cycles

From (MPa)	To (MPa)	Sigma max	Sigma min	Range	Sigma Alt	Sigma mean	No. of cycles
10	5	10	5	5	2.5	7.5	1
-4	3	3	-4	7	3.5	-0.5	1
6	-1	6	-1	7	3.5	2.5	1

After getting peaks and valleys, we have to arrange the data as shown in Table 2. Thus half-reversal obtained as shown in Table 2.

In Table 2, we have to write the peaks and valleys alternatively in the column Y and stress sequence in the column X with help of simple computer code. When first value (starting value, i.e., 0 in our example) in stress sequence is valley, then in the Y column, we have to start with the peak and vice versa. When  $X_i = Y_k$  and at the corresponding  $X_k = Y_i$ , then closed cycle will form. After getting full cycles, cycles the same Maximum and minimum values of closed cycles bunched together. Output from above table by using simple code will be shown in Table 3.

## 5 Conclusion

Modified graphical method using Microsoft Excel Macro has been explained in this paper. Since the entire data can be processed in the excel sheet, it can easily used for fatigue life calculation.

## References

1. Ligaj B (2011) An analysis of the influence of cycle counting methods on fatigue life calculations of steel. *Sci Prob Mach Oper Maintenance* 4(168):25–43
2. Hong N (1991) A modified rainflow counting method. *Int J Fatigue* 13:465–469
3. Schluter LL, Sutherland HJ (1991) User's guide for LIFE2's rainflow counting algorithm. Sandia National Laboratories, New Mexico and Livermore, California
4. American Society for Testing and Materials (ASTM) (2005) Standard Practices for Cycle Counting in Fatigue Analysis, ASTM E1049-85((Reapproved 2005). ASTM International, West Conshohocken, Pennsylvania
5. Mainka K, Thoben M, Schilling O (2011) Counting methods for lifetime calculation of power modules. Infineon Technologies AG, Warstein, Germany
6. Deng Q, Yuan H (2011) The algorithm for graphic method of rain-flow counting in programming. In: School of reliability and System Engineering. Beihang University, Beijing, China
7. Massarelli PJ, Baber TT (2001) Fatigue reliability of steel highway bridge details. Virginia transportation research council. Charlottesville, Virginia
8. GopiReddy L, Tolbert LM, Ozpineci B (2012) Lifetime Prediction of IGBT in a STATCOM using modified-graphical rainflow counting algorithm. The University of Tennessee, Oak Ridge National Laboratory, USA
9. McInnes CH, Meehan PA (2008) Equivalence of four-point and three-point rainflow cycle counting algorithms. *Int J Fatigue* 30:547–559 CRC Mining, School of Engineering
10. Singh KL, Ranganath VR (2007) Cycle counting using rainflow algorithm for fatigue analysis, NAL. Bangalore, India
11. Yin F, Cerkovnik M (2014) Assessment of Fatigue Damage from Variable Amplitude Loads in Risers. University of Windsor, Windsor, ON, Canada
12. Amzallag C, Gery JP, Robert JL, Bahaud J (1993) Standardization of the Rainflow counting method for fatigue analysis. France

# Damage Prognosis of Plain Concrete Under Low-Cycle Fatigue Using Piezo-Based Concrete Vibration Sensors

Anjaneya Dixit, Abhinav Bindal and Suresh Bhalla

**Abstract** The recent advent of smart materials in structural health monitoring (SHM) has paved the path for research as well as varied applications of piezo-sensors in the field of engineering. As a smart material, lead–zirconate–titanate (PZT) has proven to be an indispensable tool for SHM due to its easy availability in varying sizes and shapes, cost-effectiveness, high damage sensitivity and ease of installation. Existing research shows that PZT sensors, coupled with the electromechanical impedance (EMI) technique, can identify as well as quantify the damages induced in concrete and metals with appreciable accuracy. The study presented here employs the admittance signatures from the PZT sensors to monitor the accumulating damage in plain concrete specimens under low-cycle fatigue loading. PZT patches in the form of embeddable concrete vibration sensors (CVSs) are used for sensing purposes. Three cube specimens of size 150 mm were prepared: two cubes with single embedded CVS (acting in self-sensing mode) and one with a pair of CVS. The specimens were subjected to loading and unloading cycles until failure using a 3000 kN compressive testing machine. Admittance signatures were recorded from the CVS using a LCR meter at various damage stages. These signatures were then analyzed, and the root-mean-square deviation (RMSD) plots were generated to get a full damage profile of the specimens. The results reflect the effectiveness of the PZT sensors to identify the fatigue-induced damages in the concrete using PZT sensors.

**Keywords** Structural health monitoring (SHM) · Electromechanical impedance (EMI) · Fatigue · Concrete vibration sensors · Lead–zirconate–titanate (PZT)

---

A. Dixit (✉) · A. Bindal · S. Bhalla  
Department of Civil Engineering, Indian Institute of Technology Delhi,  
New Delhi, India  
e-mail: anjaneya.dixit@gmail.com

A. Bindal  
e-mail: bindal.abhinav@gmail.com

S. Bhalla  
e-mail: sbhalla@civil.iitd.ac.in

# 1 Introduction

With the advancement in material science, high-quality and economic smart materials have found multifarious usage in different fields of engineering. Smart materials are new-generation materials capable of adapting to the changes in their environment, vis-à-vis stresses or strains, with intrinsic intelligence. They tend to change their physical properties specifically to respond to corresponding stimulus which may be induced thermally, electrically and/or magnetically, chemically, hydrostatically, by pressure or nuclear radiation. Piezo-sensors are active smart materials capable of modifying their geometrical and material properties under external load (mechanical or electrical) and find wide ranging applications for structural health monitoring (SHM). Piezoelectric effect is observed in anisotropic crystals in which electric dipoles are generated under mechanical loads which culminate as electrical charge. These charges are superficial and generated in response to the applied mechanical stress (direct effect). Conversely, these materials experience deformations when subjected to an electric field (converse effect). The constitutive equation to represent this phenomenon is given by [1]:

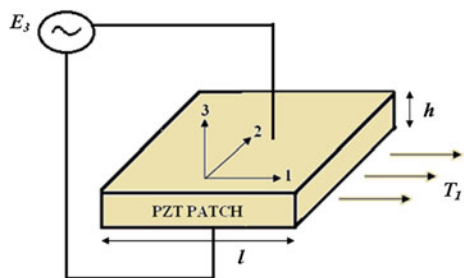
$$D_3 = \overline{\epsilon_{33}^T} E_3 + d_{31} T_1 \tag{1}$$

$$S_1 = \frac{T_1}{\overline{Y^E}} + d_{31} E_3 \tag{2}$$

where, referring to Fig. 1,  $S_1$  is the strain in direction ‘1,’  $D_3$  the electric displacement over the PZT patch,  $d_{31}$  the piezoelectric strain coefficient, and  $T_1$  the axial stress in direction ‘1.’  $\overline{Y^E} = Y^E(1 + \eta j)$  is the complex Young’s modulus of elasticity of the PZT patch at constant electric field, and  $\overline{\epsilon_{33}^T} = \epsilon_{33}^T(1 - \delta j)$  the complex electric permittivity (in direction ‘3’) at constant stress. Here,  $\eta$  and  $\delta$  are the mechanical loss factor and the dielectric loss factor, respectively, of the PZT material. Equation (1) finds usage in sensing applications, while Eq. (2) in actuation applications of the piezoelectric materials.

Lead–zirconate–titanate (PZT) is a widely used smart material owing to its lightweight, low-cost, small size, high sensitivity and good dynamic response,

**Fig. 1** PZT patch under stress and electric field (1D interaction)



which has been the focus of this present study. The EMI technique employs the direct and converse piezoelectric effects simultaneously. The collocated electromechanical admittance, which forms the health signature of the structure, can be mathematically expressed as [2].

$$\bar{Y} = G + Bj = 4\omega j \frac{l^2}{h} \left[ \frac{\epsilon_{33}^T}{(1-\nu)} - \frac{2d_{31}^2 \bar{Y}^E}{(1-\nu)} + \frac{2d_{31}^2 \bar{Y}^E}{(1-\nu)} \left( \frac{Z_{a,eff}}{Z_{s,eff} + Z_{a,eff}} \right) \bar{T} \right] \quad (3)$$

Here,  $Z_{a,eff}$  is defined as the effective mechanical impedance of the PZT patch. The mechanical impedance of the host structure is represented by  $Z_{s,eff}$ . The complex tangent ratio,  $\bar{T}$ , is given by

$$\bar{T} = \frac{\tan(\kappa l)}{\kappa l}; \quad \kappa = \omega \sqrt{\frac{\rho(1-\nu^2)}{\bar{Y}^E}} \quad (4)$$

Any damage (incipient or otherwise) induced to the host structure will change the mechanical impedance and, hence, the admittance signature. SHM is performed using the EMI technique by analyzing these changes in the admittance signature and associating with the corresponding damage. The real part of the signature, conductance, is used for damage analysis.

For the present study, the commercially available PZT (10 mm × 10 mm 0.2 mm), as shown in Fig. 2a, has been used. This PZT patch has been used in embedded form as concrete vibration sensor (CVS). The CVS (Fig. 2b) is a proprietary product of the Smart Structures and Dynamics and Laboratory (SSDL), IIT Delhi [3], developed specifically for SHM of reinforced concrete structures. The concrete matrix of the sensor houses the fragile PZT patch, protecting it from the severe conditions during casting, and provides high compatibility with surrounding concrete post installation.

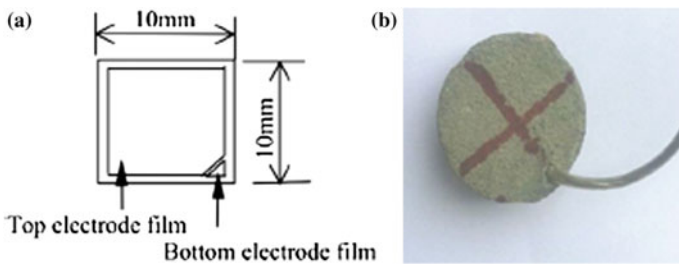


Fig. 2 a Commercially available PZT sensor, b concrete vibration sensor



## 2 High-Stress Low-Cycle Compressive Fatigue

This section describes the experimental procedure for performing the compressive fatigue analysis and the study of the compressive fatigue behavior using admittance signatures. Concrete specimens were subjected to high-stress compressive fatigue using automatic compressive testing machine (CTM). Admittance signatures of the local sensor were acquired at various damage states over high-frequency range using LCR meter. These signatures were analyzed, and the damages induced in the specimens were monitored with the change in the admittance signatures.

### 2.1 Experimental Program

Tests were conducted on three  $150 \times 150 \text{ mm}^3$ . CVS was embedded at the center of the cubes as shown in Fig. 3. The samples were subjected to compressive fatigue load using the CTM at 90% of their maximum load carrying capacity (560 kN) (Fig. 4). The LCR meter readings were acquired whenever observable damage was visible on the specimen surface. The admittance signatures (conductance,  $G$ , and susceptance,  $B$ ) of the PZT sensor in pristine state and after each state of damage till failure were measured. These admittance signatures were then analyzed to study the damage induced.

### 2.2 Data Analysis and Results

Repetitive compressive loads at high-stress ranges were applied on the three cubes with embedded CVS. The samples failed at 40 cycles, 33 cycles and 36 cycles, respectively. The fatigue load applied was within load range of 0–90% of the 28-day compressive strength.

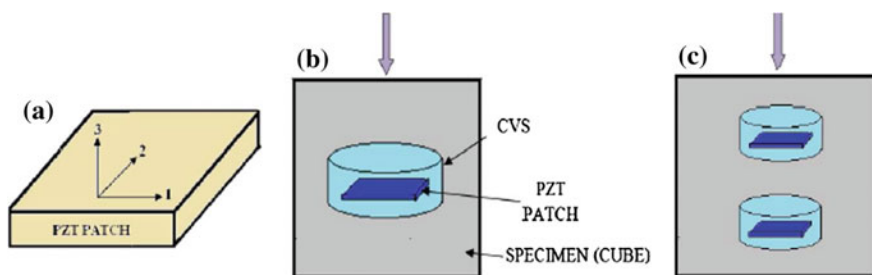


**Fig. 3** a Axes orientation for PZT patch, b PZT patch/CVS orientation during fatigue tests, c specimen with dual sensors

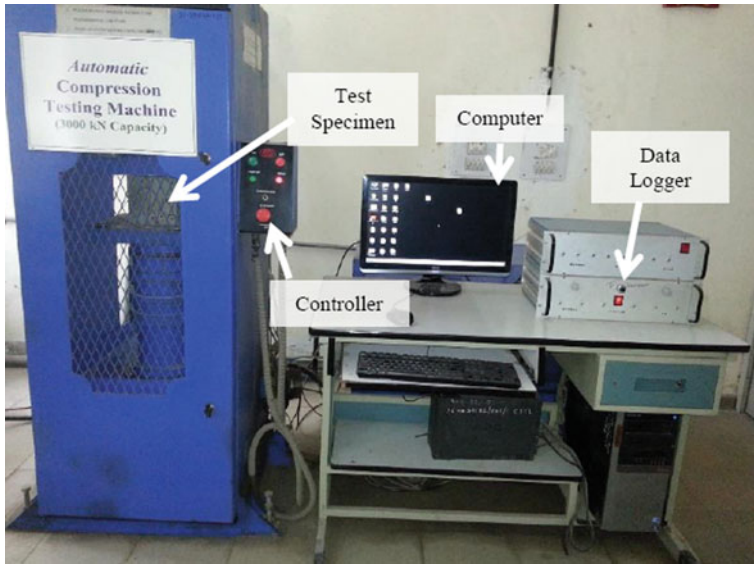
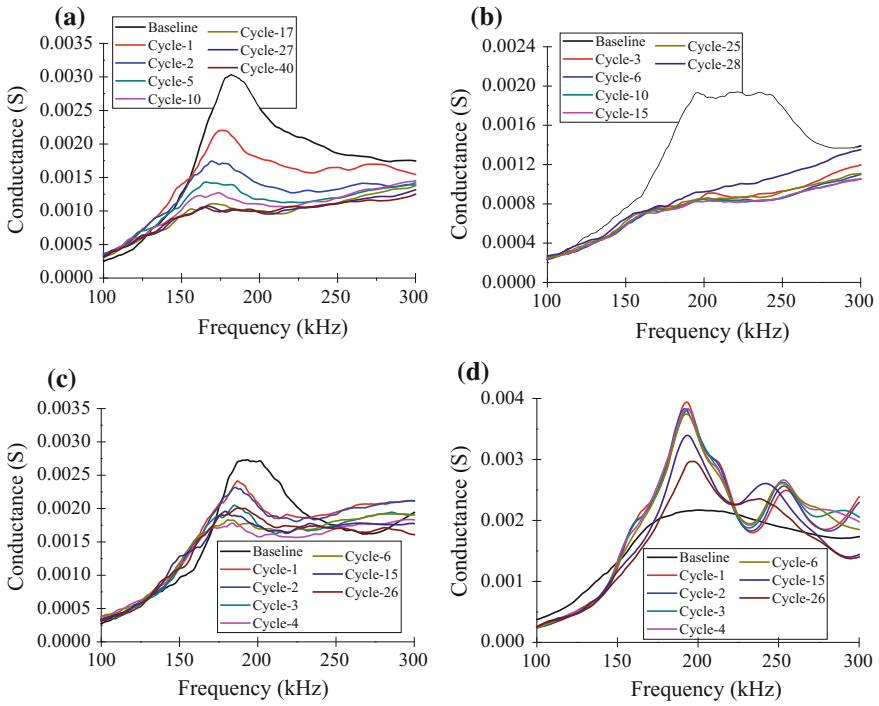


Fig. 4 Experimental setup for low-cycle fatigue tests

Figure 5a–d shows the variation in the conductance signature with increasing damage. From the figures, it is observed that with the onset of damage to the cubes, there is a noticeable change in the conductance signature, vis-à-vis the shifting of the positions of the peaks as well as the change in their magnitudes. Additionally, new peaks might be observed as well. These changes provide clear indications of damage to the host structure. Previous researchers conducting EMI studies have utilized various statistical methods such as the root-mean-square deviation or RMSD [4], the difference of transfer function between damaged and pristine states and the mean absolute percent deviation or MAPD. In this study, RMSD index has been used, which is defined as

$$RMSD(\%) = \sqrt{\frac{\sum_{i=1}^N (G_i^1 - G_i^0)^2}{\sum_{i=1}^N (G_i^0)^2}} \times 100 \tag{5}$$

Here,  $G_i^1$  represents the conductance of the patch at a given damage state,  $G_i^0$  represents the conductance in pristine state, and  $i$  is the frequency index. Using the RMSD data of all the sensor at different stages, a damage assessment index profile is developed to monitor the increment in damage. The RMSD plots developed for varying states of damages are shown in Figs. 6, 7, and 8. From these figures, the consistent rise of the index with increasing number of cycles can be clearly noted, except for cube 3 (Fig. 8).



**Fig. 5** Conductance versus frequency with varying damage for cubes **a** 1, **b** 2, **c** 3 (sensor 1), **d** 3 (sensor 2)

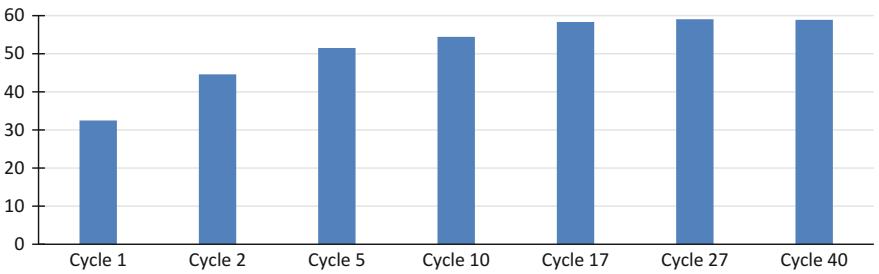


**Fig. 6** RMSD plot for cube 1

Gradual drop in conductance signature was observed with increasing cycles of compressive fatigue. Sharp drop in conductance signature was observed initially, after which the overall nature of the conductance signatures remained similar till failure. In the RMSD values, a general trend of increasing RMSD with increasing number of cycles is observed. The RMSD for cube 3, sensor 2, however, deviates from the pattern.

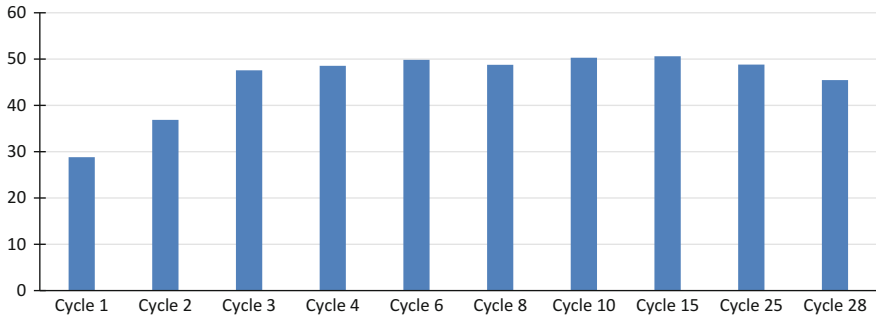


Fig. 7 RMSD plot for cube 2

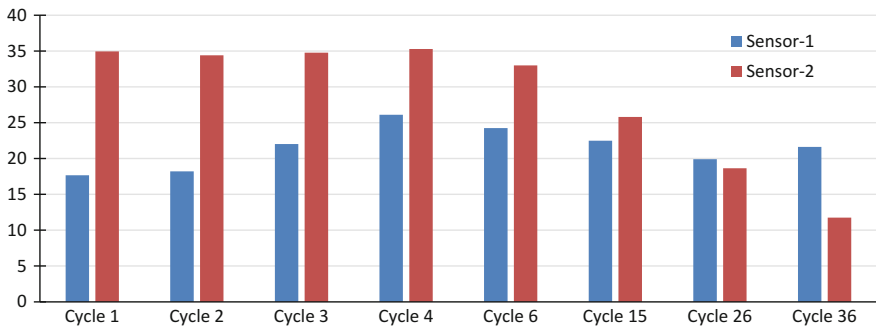


Fig. 8 RMSD plot for cube 3

### 3 Conclusions

The PZT-based concrete vibration sensor has detected the fatigue-induced damages in concrete with appreciable sensitivity. In general, the change in conductance signatures was sharper initially as compared to advanced stages of fatigue loading. This is also reflected in the RMSD values of the specimens, which show a noticeable change between the initial cycles, followed by minor variations thereafter. With the exception of cube 3 (sensor 2), the repetitive trend of increasing RMSD with number of cycles suggests that RMSD plots can be employed to monitoring accumulating damages such as fatigue, which have the potential to evade visual inspections. The CVS was found to operate well even when the specimens were approaching failure, indicating that they are robust and can outperform the host structure (cube).

## References

1. Shankar R, Bhalla S, Gupta A, Kumar MP (2011) Dual use of PZT patches as sensors in global dynamic and local electromechanical impedance techniques for structural health monitoring. *J Intell Mater Syst Struct* 22(16):1841–1856
2. Bhalla S, Soh CK (2004) Structural health monitoring by piezo-impedance transducers. I: modeling. *J Aerosp Eng* 17(4):154–165, 166. [http://doi.org/10.1061/\(ASCE\)0893-1321](http://doi.org/10.1061/(ASCE)0893-1321)
3. Bhalla S, Gupta A (2007) A novel vibration sensor for concrete structures. Patent application no. 1011/DEL/2011
4. Giurgiutiu V, Reynolds A, Rogers CA (1999) Experimental investigation of E/M impedance health monitoring for spot-welded structural joints. *J Intell Mater Syst Struct* 10(10):802–812. <http://doi.org/10.1106/N0J5-6UJ2-WIGV-Q8MC>
5. Bhalla S, Vittal PA, Veljkovic M (2012) Piezo-impedance transducers for residual fatigue life assessment of bolted steel joints. *Struct Health Monit* 11(6):733–750. <http://doi.org/10.1177/1475921712458708>
6. Giurgiutiu V, Rogers CA (1998) Recent advancements in the electro-mechanical (E/M) impedance method for structural health monitoring and NDE. In: SPIEs 5th annual international symposium on smart structures and materials, 1–5 Mar 1998
7. Rogers CA (1988) Workshop summary. In: Proceedings U.S. army research office workshop on smart materials, structures and mathematical issues. Technomic Publishing Co., pp 1–12
8. Rogers CA, Barker DK, Jaeger CA (1988) Introduction to smart materials and structures. In: Proceedings of U.S. army research office workshop on smart materials, structures and mathematical issues. Virginia Polytechnic Institute and State University, Technomic Publishing Co., pp 17–28

# Asymmetric Cyclic Behaviour of Fine- and Coarse-Grained Commercially Pure Copper and Aluminium

Jayanta Kumar Mahato, Partha Sarathi De, Amrita Kundu  
and Pravash Chandra Chakraborti

**Abstract** In the present study, uniaxial ratcheting behaviour of annealed copper and aluminium with two different grain sizes has been investigated. Engineering stress-control tests have been performed at various combinations of stress amplitudes and mean stresses. To account for grain size variation, stress amplitudes were selected keeping the constant ratio of equivalent stress amplitude and tensile strength. It is found that ratcheting life of fine- and coarse-grained copper and aluminium is inversely related to both stress amplitude and mean stress. However, the effect of stress amplitude on ratcheting life is more as compared to mean stress for both the FCC metals. It is also found out that the ratcheting life of fine-grained FCC metals is more compared to coarse-grained FCC metals. The ratcheting strain rate follows three stages irrespective of stress combination and grain size of both FCC metals. It is observed that for both the FCC metals, the average steady state ratcheting strain rate follows perfect power relationship with cycles to failure.

**Keywords** Grain size · Ratcheting phenomena · Ratcheting lives  
Ratcheting strain rate · Stress parameter

## 1 Introduction

There are many reasons for failure of engineering components during service. Among these fatigue, failure is one of the major concerns in case of cyclically loaded components. The fatigue behaviour of materials is commonly studied under completely reversed cyclic stressing or straining. Because of such symmetric cyclic

---

J.K. Mahato (✉) · P.S. De · A. Kundu · P.C. Chakraborti  
Metallurgical and Material Engineering Department, Jadavpur University,  
Kolkata 700032, India  
e-mail: jayanta.mahato@gmail.com

J.K. Mahato · A. Kundu · P.C. Chakraborti  
Centre of Excellence in Phase Transformation and Product Characterisation,  
Jadavpur University, Kolkata 700032, India

loading failure occurs without any gross plastic deformation and the fatigue life depends upon the imposed stress or strain amplitudes. But, during asymmetric cyclic stress, i.e., cyclic loading with non-zero mean stress, along with fatigue damage cycle-by-cycle inelastic strain, is accumulated in the specimen and final failure occurs on accumulation of certain amount of inelastic deformation. Such accumulation of inelastic strain during asymmetric cyclic stressing is known as “ratcheting deformation.” The damage occurring due to ratcheting deformation deteriorates the cyclic life of specimens and components as compared to what happens in case of symmetric cyclic stressing. It is, therefore, essential to understand the ratcheting behaviour of different materials for safety and structural integrity purpose of cyclically loaded components. In last two decades, many researchers were studied both uniaxial and multi axial ratcheting behaviours of different materials [1–16].

The effect of stress parameters on ratcheting life or ratcheting strain rate evolution can be investigated in two different ways: (i) using different combinations of mean stress and stress amplitude and (ii) using different stress ratios for constant maximum or minimum stress level. It is well reported in literature that ratcheting strain evolution increases with increase in mean stress for a variety of materials having different hardening/softening characteristics [17–19]. The mean stress and stress amplitude-dependent asymmetric cyclic plastic behaviour, mainly ratcheting life, ratcheting strain and ratcheting strain rate have been studied by researchers over a variety of materials like: IF steel [20], SA 333 Gr. C-Mn Steel [21], SA 333 Steel [22], SS 304 Stainless Steel [23], Inconel 718 [19] and Cu [24]. The three stage ratcheting rate evolution has been studied by some of the above researchers, and the variation has been looked into with respect to the mean stress and stress amplitude. But the effect of mean stress and stress amplitude on average steady state ratcheting strain rate has not been clearly reported by these researchers. As ratcheting life and ratcheting strain evolution during stress-control cyclic loading is dependent on the ratcheting strain rate, it is expected that there should be a relation between average steady state ratcheting strain rate and ratcheting life irrespective of stress combinations. Such type of relationship has not been reported as yet.

In general, it is known that slip homogenization in fine-grained materials improves fatigue performance. Lukas et al. [25] have first shown that cyclic saturation stress depends on the grain size of the polycrystalline materials. They also pointed out that strain localization in persistent slip band (PSB) is greater in case of fine-grained material. Such plastic strain localization in PSB causes significant changes in the shape of the hysteresis loop. In case of fine-grained polycrystalline material, cyclic saturation stress is higher than that of coarse-grained materials. It is worth mentioning here that while there is some information available regarding the grain size effect on symmetric cyclic loading behaviour, the grain size effect on ratcheting behaviour is very scanty in open literature domain. In our previous work [26], it was observed that in case of engineering stress-control ratcheting tests, the number of cycles required for accumulation of constant amount of ratcheting strain depends upon grain size of the specimens. More number of cycles is required for fine-grained specimens as compared to the coarse-grained specimens. Therefore, it

can be said that number of cycles to failure or total ratcheting strain accumulation during ratcheting deformation will depend on the grain size. But the comparison study of grain size effect on ratcheting behaviour is not straightforward because of the difficulties in the selection of stress parameters for different grain sizes. This happens because of the grain size-dependent strength variation. To avoid this difficulty, the present investigation has been carried out by keeping constant ratio between equivalent stress amplitude ( $\sigma_a^{eq}$ ) estimated from the modified Goodman equation [24] to ultimate tensile strength (UTS) of the material with different grain sizes.

## 2 Experimental Procedure

Experiments were performed on commercially available high purity (99.97%) polycrystalline copper and Aluminium (98.48%). Cylindrical specimen blanks of copper were annealed at 520 and 770 °C for one hour and then quenched to generate different grain sizes. In case of Al, cylindrical specimen blanks were heated at 325 and 500 °C for two hours and finally slowly cooled in the furnace.

Small metallographic specimens were extracted from these heat-treated specimen blanks and polished following usual metallographic procedure. After polishing, etching of copper specimens was done with  $FeCl_3$  solution. Kellers reagent was used for etching of aluminium specimens. The polished and etched specimens were observed in an inverted optical microscope, Leica DMILM. Microstructures were grabbed by using a digital camera, Leica DC 300 coupled with a personal computer. The average grain size was measured by using linear intercept method following ASTM standard E112 method.

Cylindrical tensile specimens of 30 mm gauge length and 6.25 mm gauge diameter were fabricated out of heat-treated specimen blanks. The tensile tests were performed at room temperature under strain control mode at strain rate of  $10^{-3} s^{-1}$  in a computer controlled servohydraulic universal testing machine, Instron 8501 of  $\pm 100$  kN load capacity using Bluehill 2, tensile testing software.

Before stress-control ratcheting tests, all the specimens having 28 mm gauge length and 7 mm gauge diameter were manually polished with very fine polishing paper so to obtain very good surface finish of the test specimens. A set of stress-control asymmetric cyclic loading was performed at different combinations of mean stress and stress amplitude until complete failure of the specimens. The stress amplitude and mean stress was selected in such a way so to keep the ratio of equivalent stress amplitude ( $\sigma_a^{eq}$ ) and tensile strength ( $\sigma_{UTS}$ ) constant. This was done in order to take account of the grain size effect on the variation of yield and tensile strength of the materials. The equivalent stress amplitude ( $\sigma_a^{eq}$ ) has been estimated using the modified Goodman equation. The test matrix used for asymmetric cyclic loading has been shown in Tables 1 and 2. Tests were done using a triangular waveform at a stress rate of  $200 MPa s^{-1}$ . All the tests were done at room



**Table 1** Ratcheting test matrix at different combination of stress parameters for annealed copper

Fine grain				Coarse grain					
Mean stress	Stress amp	$\sigma_a/\sigma_{UTS}$	Ratcheting strain (%)	Ratcheting life	Mean stress	Stress amp	$\sigma_a/\sigma_{UTS}$	Ratcheting strain (%)	Ratcheting life
$\sigma_m$ (MPa)	$\sigma_a$ (MPa)			$N_f$	$\sigma_m$ (MPa)	$\sigma_a$ (MPa)			$N_f$
20	180	0.82	69	200	19	170	0.82	66	114
20	160	0.72	89	954	19	154	0.72	80	336
20	140	0.63	95	6,972	19	135	0.62	90	1,663
40	180	0.9	73	110	38	170	0.9	52	39
40	160	0.8	80	414	38	154	0.8	61	209
40	140	0.7	84	3,163	38	135	0.7	70	934
40	120	0.6	65	40,930	38	115	0.6	76	8,957
60	160	0.88	67	154	56	154	0.88	52	61
60	140	0.77	76	1,177	56	135	0.77	67	401
60	120	0.66	73	17,353	56	115	0.66	78	4,345
80	140	0.87	74	350	77	135	0.87	54	91
80	120	0.75	64	4,065	77	115	0.75	59	791



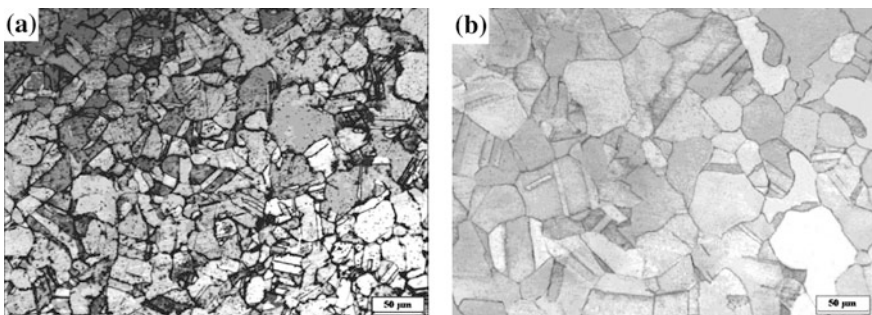
temperature in a computer controlled servoelectric universal testing machine, Instron 8862, of  $\pm 100$  kN load capacity. Tests were controlled, and data acquisition was accomplished using a general purpose fatigue testing software, Instron, WaveMatrix 1.5. An extensometer 25 mm gauge length and  $-10$  to  $100\%$  full range capacity was used to record cycle-by-cycle ratcheting strain accumulation. In most cases, tests were continued until complete failure of the specimens.

### 3 Results and Discussion

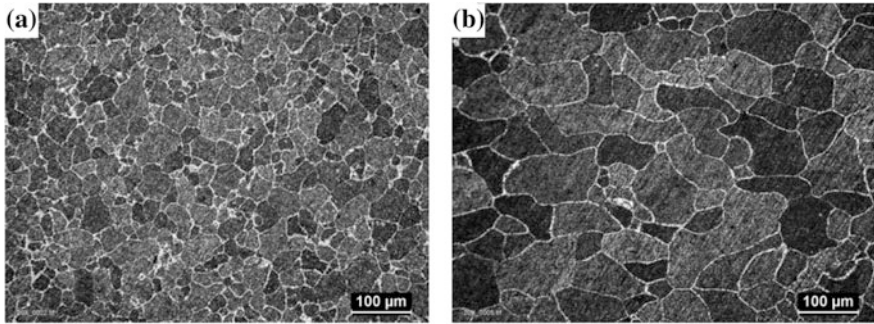
#### 3.1 Microstructure and Tensile Properties

Figure 1a, b shows the optical micrographs of the annealed copper. It is found that the microstructure consists of polyhedral grains with annealing twins interspersed in some grains. Depending upon the annealing conditions the two-dimensional average grain size of annealed copper was obtained as 36 and 51  $\mu\text{m}$  respectively. The specimens with fine- and coarse-grained copper have been identified as FG-Cu and CG-Cu. In case of aluminium, it is found that microstructure only consists of polyhedral grains, Fig. 2a, b, the two-dimensional average grain size being 37 and 82  $\mu\text{m}$ , respectively. The striking difference between the microstructure of copper and aluminium specimen is that in contrast to copper the microstructure of aluminium specimens does not contain any annealing twin because of its higher stacking fault energy.

Tensile properties of annealed copper and aluminium have been tabulated in Tables 3 and 4, respectively. It is found that in both FCC metals yield strength and ultimate tensile strength is more in case of fine-grained specimens due to grain size strengthening effect. It is also observed that strength, ductility and work hardening exponent is much higher in case of annealed copper due to its low value of stacking fault energy (SFE) as compared to annealed Al.



**Fig. 1** Optical micrographs of OFHC copper, solution annealed at **a** 520 and **b** 770  $^{\circ}\text{C}$



**Fig. 2** Optical micrographs of pure aluminium, annealed at **a** 325 and **b** 500 °C

### 3.2 Ratcheting Deformation Behaviour

The ratcheting curves of fine- and coarse-grained copper deformed under engineering stress-control mode of experiments at different stress combinations are shown in Figs. 3a–c and 4a–c. It is observed that during asymmetric cyclic loading, either at constant mean stress or at constant stress amplitude, elongation of the specimen occurs without any plastic shakedown effect due to accumulation of inelastic strain in the direction of mean stress. It is very clear from Figs. 3a–c and 4a–c that accumulation of ratcheting strain occurs in three different stages. In the first stage, ratcheting strain evolution increases rapidly irrespective of stress combinations. This is followed by a steady state; finally ratcheting strain accumulation occurs very rapidly due to increase in true stress caused by large decrease of specimen cross-sectional area. From Figs. 3a–c and 4a–c, it is observed that the steady state region is lower in case of CG-Cu as compared to FG-Cu specimens for any mean stress and stress amplitude combination. It is found that in case of FG-Cu

**Table 3** Tensile properties of annealed OFHC copper

Specimen ID	Grain size (µm)	YS (MPa)	UTS (MPa)	Uniform strain (%)	Total strain (%)	$n$	$K$ (MPa)	Reduction in area (%)
FG-Cu	36	72.0	239.0	39.0	57.0	0.39	504	73.20
CG-Cu	51	63.0	231.0	39.0	56.0	0.40	502	76.50

**Table 4** Tensile properties of annealed aluminium

Specimen ID	Grain size (µm)	YS (MPa)	UTS (MPa)	Uniform strain (%)	Total strain (%)	$n$	$K$ (MPa)	Reduction in area (%)
FG-Al	37	82.0	133.0	7.0	27.0	0.21	258	83.88
CG-Al	82	48.0	103.0	16.0	31.0	0.24	196	92.91

specimens the ratcheting strain to failure is more as compared to CG-Cu specimens. This means that fine-grained materials can sustain large amount of deformation before complete failure. The mean stress and stress amplitude effect on ratcheting life ( $N_f$ ) for both fine- and coarse-grained copper and aluminium is shown in Fig. 5a, b. It is observed that ratcheting life follows a power law relationship with stress amplitude. But similar relationship is not observed between  $N_f$  and mean stress. It is also found that the effect of stress amplitude on decreasing the ratcheting life is more as compared to the effect of mean stress for both fine- and coarse-grained copper and aluminium. Such behaviour is almost universal in all types of materials. It is also clear from Figs. 3a–c and 4a–c that ratcheting lives are more in case of fine-grained copper (FG-Cu) as compared to coarse-grained copper (CG-Cu) irrespective of stress combinations. This is attributed to homogenization of cyclic slip homogenization in case fine-grained materials and the consequent higher fatigue resistance.

Similar to annealed copper, the ratcheting curves of fine- and coarse-grained aluminium shown in Fig. 6a–c also reveal different stages of deformation. But the significant difference is that more ratcheting strain occurs in case of CG-Al

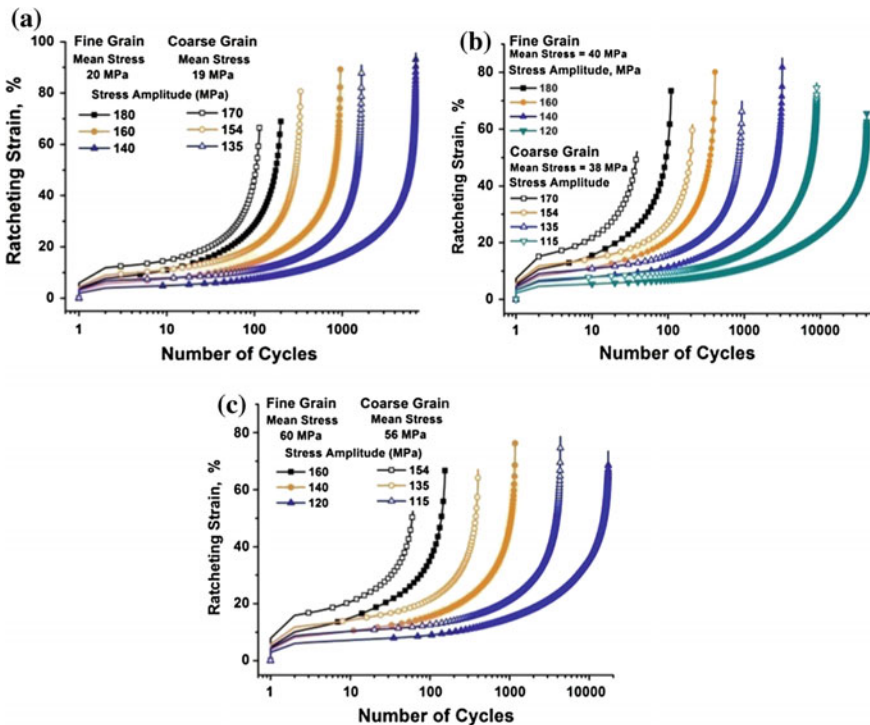


**Fig. 3** Ratcheting curve at different stress amplitude and constant mean stress levels; for fine-grained copper constant mean stresses: **a** 20, **b** 40 and **c** 60 MPa and for coarse-grained copper constant mean stresses: **a** 19, **b** 38 and **c** 56 MPa

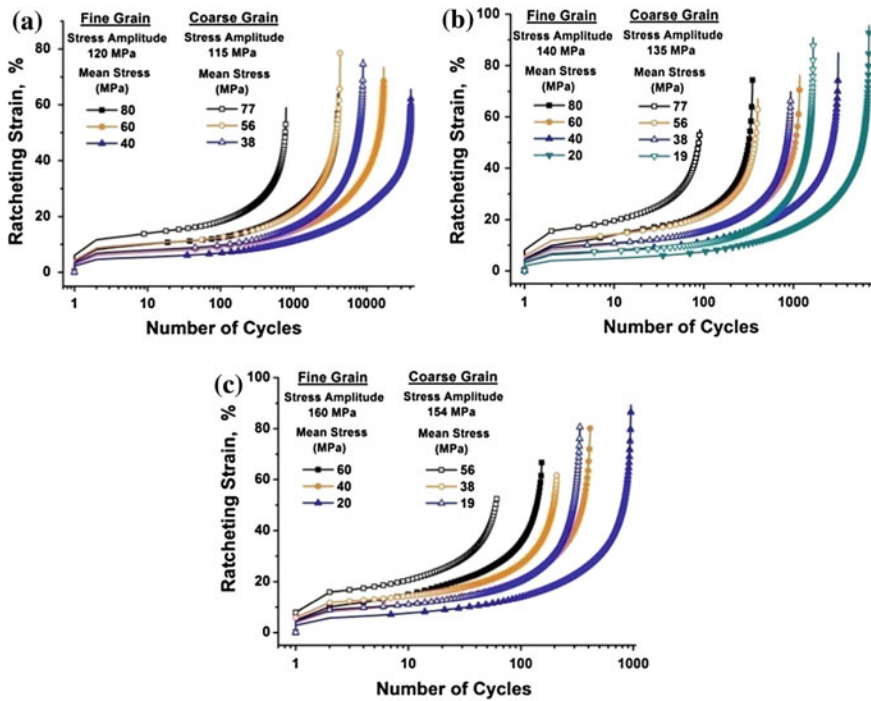


**Fig. 4** Ratcheting curve at different mean stress and constant stress amplitude levels; for fine-grained copper constant stress amplitudes: **a** 120, **b** 140 and **c** 160 MPa and for coarse-grained copper constant stress amplitudes: **a** 115, **b** 135 and **c** 154 MPa

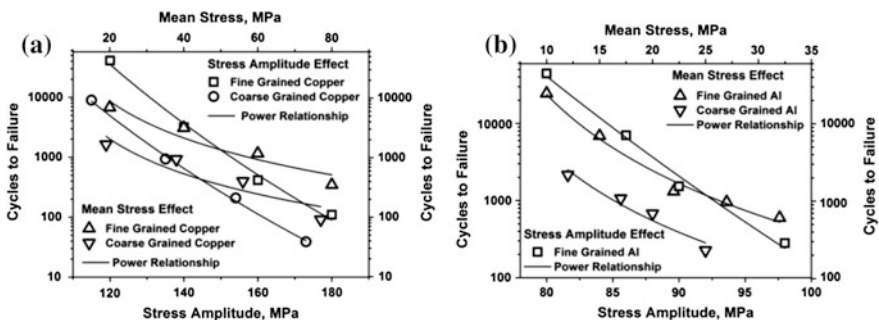


**Fig. 5** Stress amplitude and mean stress effect on ratcheting lives of both fine- and coarse-grained **a** copper and **b** aluminium

compared to FG-Al specimens. It is also interestingly observed that plastic shakedown occurs in CG-Al specimens at certain stress combinations for which the maximum stress is below 80 MPa. In these cases after accumulation of about 17–20% strain, no strain is accumulated with progression of cyclic loading and the tests

were discontinued. During the cyclic deformation at the earliest stage of ratcheting deformation, the loosely tangled dislocation structure developed due to less interaction of dislocations in case of CG-Al specimens [27]. On further cycling, the loosely tangled structure transformed into a stable dislocation structure. This hinders further ratcheting deformation in CG-Al specimens at lowest maximum stress (below 80 MPa). It is also clear from Fig. 6a–c that similar to annealed copper, the ratcheting lives are more in case of fine-grained aluminium as compared to coarse-grained aluminium irrespective of stress combinations.

### 3.3 Ratcheting Strain Rate Evolution

It is clear from Figs. 7a, b and 8a, b that ratcheting strain rate ( $\dot{\epsilon}_r$ ) evolution with number of cycles follows three distinct stages irrespective of stress combination and grain size of both the FCC metals. In the first stage  $\dot{\epsilon}_r$  rapidly decreases within first few cycles. This is followed by steady state ratcheting rate. Finally,  $\dot{\epsilon}_r$  again

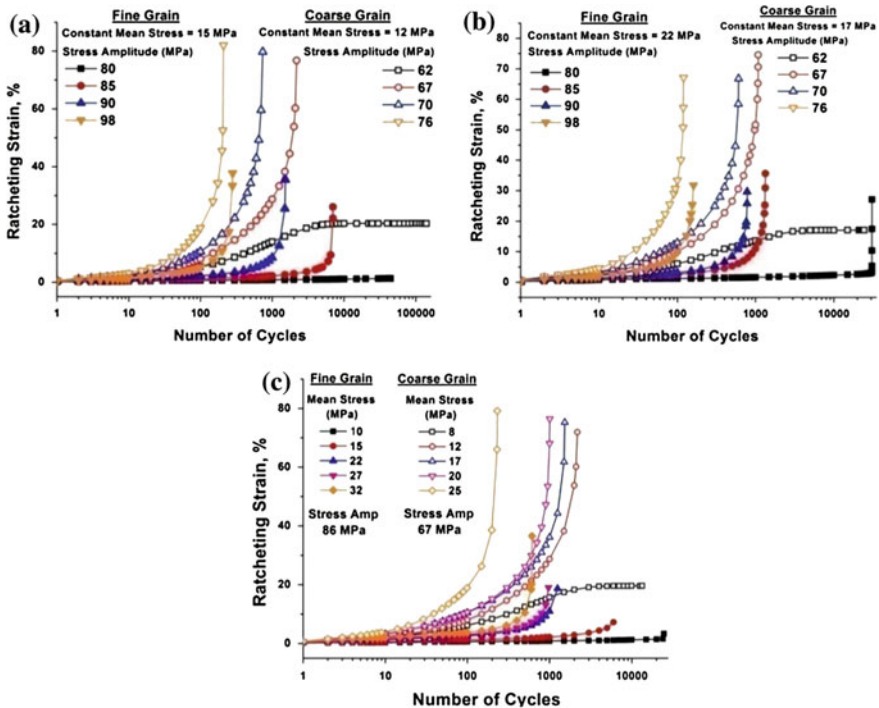


**Fig. 6** Ratcheting curve of fine- and coarse-grained aluminium: **a** different stress amplitude and constant mean stress of 15 MPa (for FG-Al) and 12 MPa (for CG-Al), **b** different stress amplitude and constant mean stress of 22 MPa (for FG-Al) and 17 MPa (for CG-Al) and **c** different mean stress and constant stress amplitude of 86 MPa (for FG-Al) and 67 MPa (for CG-Al)

increases until complete failure of the specimens due to increase in true stress for substantial reduction in specimen cross-sectional area. The initial as well as throughout the cyclic deformation,  $\dot{\epsilon}_r$  is more for higher  $\sigma_a$  or higher  $\sigma_m$  value and decreases with decrease in  $\sigma_a$  or  $\sigma_m$  value at constant  $\sigma_m$  and  $\sigma_a$  respectively. As  $\dot{\epsilon}_r$  increases with increase in either  $\sigma_a$  or  $\sigma_m$  value, the ratcheting life decreases with increase in either  $\sigma_a$  or  $\sigma_m$  value as discussed earlier. Similar types of ratcheting strain rate variation have been observed for both fine- and coarse-grained copper, but the only difference is in the magnitude of  $\dot{\epsilon}_r$  CG-Cu specimens produce more  $\dot{\epsilon}_r$  throughout the cyclic deformation for any combination of  $\sigma_a$  and  $\sigma_m$ . Hence, the ratcheting life is less in case of CG-Cu specimens compared to FG-Cu specimens.

Similar to annealed copper, three distinct stages of ratcheting strain rate behaviour have been found irrespective of stress combination in case of annealed aluminium, Fig. 8a, b. But the initial as well as in the steady state region  $\dot{\epsilon}_r$  is more in case of annealed copper as compared to annealed aluminium. It is also observed that increase in either  $\sigma_a$  or  $\sigma_m$  value at constant  $\sigma_m$  or  $\sigma_a$ , respectively, the ratcheting strain rate increases for annealed aluminium irrespective of grain size. But CG-Al specimens produce more  $\dot{\epsilon}_r$  throughout the cyclic deformation for any combination of  $\sigma_a$  and  $\sigma_m$  leading to early failure of the specimens. The ratcheting strain rate falls down at steady state region and tends to be zero in case of  $\sigma_m = 12$  MPa,  $\sigma_a = 62$  MPa and  $\sigma_m = 8$  MPa,  $\sigma_a = 67$  MPa stress combination for CG-Al specimen due to the plastic shakedown.

The average steady state ratcheting rate ( $\dot{\epsilon}_r^{sat}$ ) has been calculated from the ratcheting strain rate curves of fine- and coarse-grained copper and aluminium. It has found that increase in either  $\sigma_a$  or  $\sigma_m$  value at constant  $\sigma_m$  or  $\sigma_a$ , respectively, the average ratcheting strain rate ( $\dot{\epsilon}_r^{sat}$ ) increases for both annealed copper and aluminium irrespective of grain size. The interesting observation is that the average ratcheting strain rate follows a power relationship with the cycles to failure irrespective of stress combination and grain size for both the FCC metals, Fig. 9a, b. From this relationship, the ratcheting lives can be fairly estimated as the steady state constitutes the major fraction of the cyclic life. Such type of observation has not yet

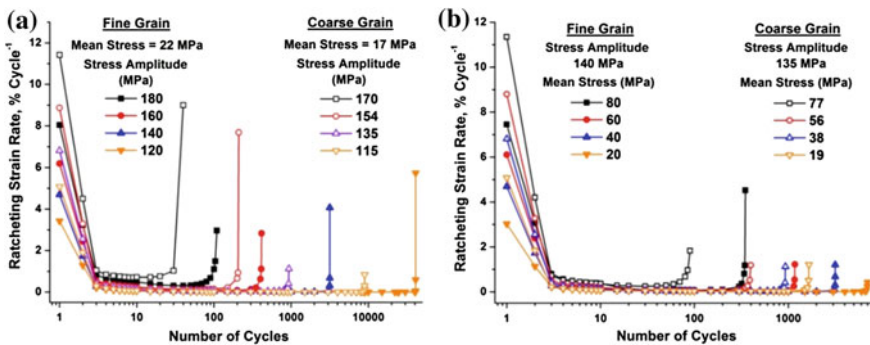
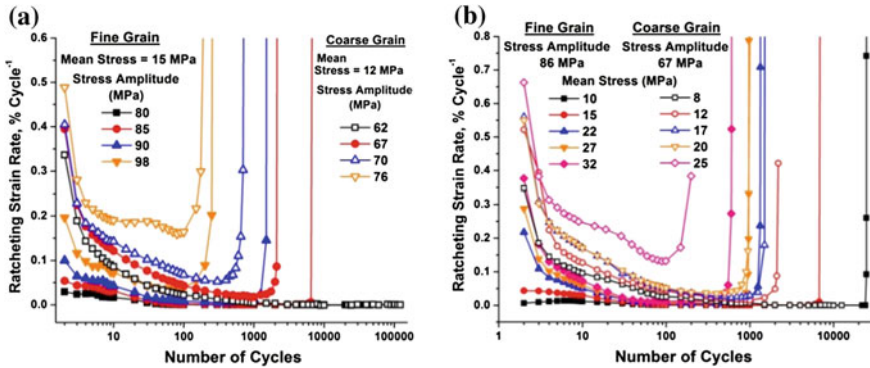


Fig. 7 Ratcheting strain rate variation for annealed copper at a constant mean stress and b constant stress amplitude level





**Fig. 8** Ratcheting strain rate variation for annealed aluminium at **a** constant mean stress and **b** constant stress amplitude level

been reported by any researcher. From the power law relationship, it is clear that the absolute value of exponent is more in case of coarse-grained material as compared to fine-grained ones and this difference is more in case of annealed aluminium.

### 3.4 Fractography

Fractographs of annealed copper and aluminium specimens failed due to asymmetric cyclic loading under different stress combination are shown in Figs. 10a–c, 11a–c and 12a–c, respectively. It is clear that both irrespective of grain size and stress combinations the annealed copper specimens material failed in a ductile manner following void nucleation and growth mechanisms. Substantially, no difference in void morphology is observed in fine or coarse-grained specimens.

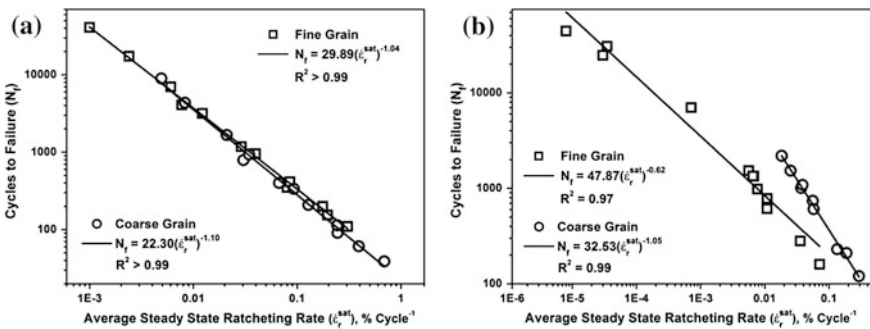


**Fig. 9** Co-relationship between average steady state ratcheting rate with ratcheting lives irrespective of stress combination for both grain size of **a** annealed copper and **b** annealed aluminium

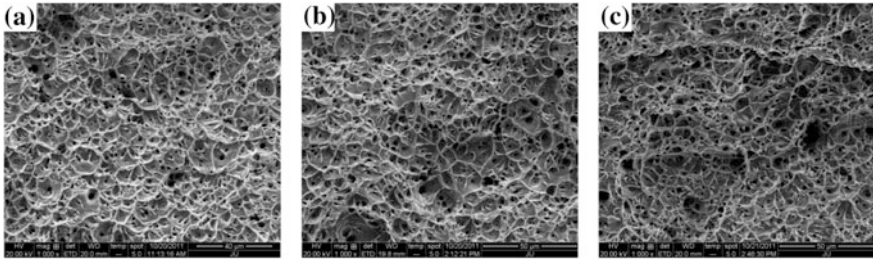


**Fig. 10** Fractographs of ratcheting failure FG-Cu specimens under stress combination of **a**  $\sigma_m = 60$  MPa,  $\sigma_a = 120$  MPa, **b**  $\sigma_m = 60$  MPa,  $\sigma_a = 140$  MPa and **c**  $\sigma_m = 60$  MPa,  $\sigma_a = 160$  MPa

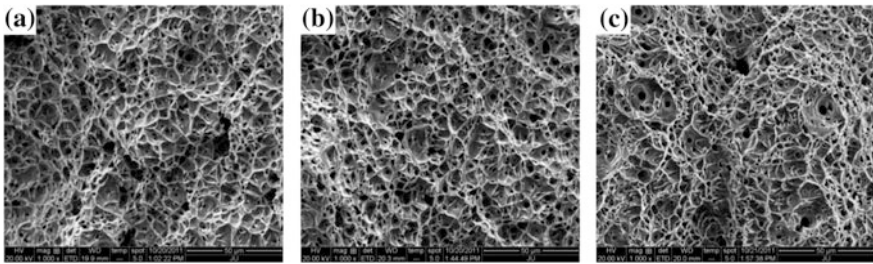


**Fig. 11** Fractographs of ratcheting failure FG-Cu specimens under stress combination of **a**  $\sigma_m = 80$  MPa,  $\sigma_a = 120$  MPa, **b**  $\sigma_m = 40$  MPa,  $\sigma_a = 160$  MPa and **c**  $\sigma_m = 20$  MPa,  $\sigma_a = 180$  MPa

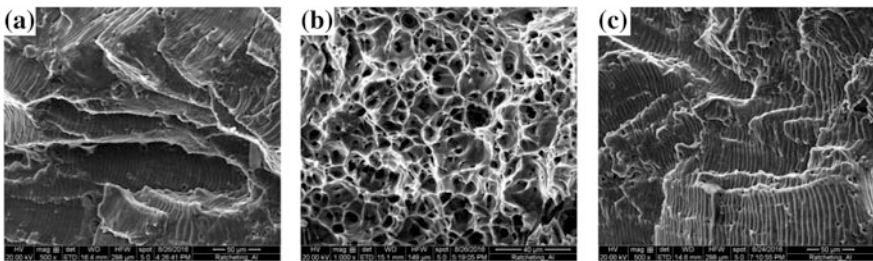


**Fig. 12** Fractographs of ratcheting failure FG-Al specimens under stress combination of **a**  $\sigma_m = 10$  MPa,  $\sigma_a = 86$  MPa, **b**  $\sigma_m = 22$  MPa,  $\sigma_a = 80$  MPa and **c**  $\sigma_m = 15$  MPa,  $\sigma_a = 80$  MPa

Similar failure mechanisms are also observed in case of annealed aluminium specimens except for the stress combinations of  $\sigma_m = 10$  MPa,  $\sigma_a = 86$  MPa and  $\sigma_m = 15$  MPa,  $\sigma_a = 80$  MPa in case of FG-Al specimens. Fatigue striations observed in Fig. 12a, c suggest that fatigue damage is the chief failure mechanism for these stress combinations. It is observed from Fig. 6a, c that for these two

specific stress combinations ratcheting deformation is extremely less. Hence, it is inferred that during asymmetric cyclic loading if the ratcheting deformation becomes very less, failure would occur primarily due to accumulation of fatigue damage and ratcheting life would also be higher.

## 4 Conclusions

From the present investigation, the following conclusions have been drawn

1. During engineering stress-control asymmetric cyclic loading, accumulation of ratcheting strain occurs in three distinct stages irrespective of stress combinations and grain size in both FCC metals. While in case of aluminium ratcheting strain accumulation is more in case of coarse grain structure, ratcheting strain accumulation is more in fine-grained copper. This opposite phenomenon is attributed to the difference in stacking fault energy between two FCC metals.
2. Ratcheting life decrease with increase in stress amplitude and mean stress for both fine- and coarse-grained copper and aluminium. However, the effect of stress amplitude on decreasing ratcheting fatigue life is more as compared to mean stress. The ratcheting life is more in case of fine-grained specimens as compared to coarse-grained specimen for both FCC metals.
3. Ratcheting strain rate follows three different paths with number of cycles. It decreases rapidly within first few cycles and then a steady state is reached. Finally, the ratcheting strain rate increases up to the complete failure of the specimens. A power law relationship can be drawn between average steady state ratcheting strain rate and ratcheting lives irrespective of stress combination and grain size of both FCC metals. The ratcheting strain rate all through the cyclic life is more in case of coarse-grained specimens irrespective of stress combination except when plastic shake down occurs.

**Acknowledgements** The authors would like to thank CoE, TEQIP Phase-II and Jadavpur University for providing funding and facilities, respectively, for carrying out the research work.

## References

1. Ohno N (1997) Recent progress in constitutive modeling for ratcheting. *Mater Sci Res Int* 3 (1):1–10
2. Bari S, Hassan T (2002) An advancement in cyclic plasticity modeling for multiaxial ratcheting simulation. *Int J Plast* 18:873–894
3. Abdel Karim M (2005) Shakedown of complex structures according to various hardening rules. *Int J Press Vessels Pip* 82:427–458
4. Chen X, Jiao R, Kim KS (2005) On the Ohno-Wang kinematic hardening rules for multiaxial ratcheting modeling of medium carbon steel. *Int J Plast* 21:161–184

5. Chen X, Jiao R (2004) Modified kinematic hardening rule for multiaxial ratcheting prediction. *Int J Plast* 20:871–898
6. Kang GZ, Li YG, Zhang J, Sun YF, Gao Q (2005) Uniaxial ratcheting and failure behaviours of two steels. *J Theor Appl Fract Mech* 43:199–209
7. Kang GZ, Kan QH, Zhang J, Sun YF (2006) Time-dependent ratcheting experiments of SS304 stainless steel. *Int J Plast* 22:858–894
8. Kang GZ, Li YG, Gao Q, Kan QH, Zhan J (2006) Uniaxial ratcheting in steels with different cyclic softening/hardening behaviours. *Fatigue Fract Eng Mater Struct* 29:93–103
9. Feaugas X, Gaudin C (2004) Ratcheting process in the stainless steel AISI316L at 300K: an experimental investigation. *Int J Plast* 20:643–662
10. Mayama T, Sasaki K, Ishikawa H (2004) Biaxial ratcheting deformation of type 304 stainless steel: effect of memorization of back stress. *J Mech Eng Sci* 218:901–908
11. Abdel-Karim M (2005) Numerical integration method for kinematic hardening rules with partial activation of dynamic recovery term. *Int J Plast* 21:1303–1321
12. Gupta C, Chakraborti JK, Reddy GR, Benerjee S (2005) Uniaxial cyclic deformation behaviour of SA 333 Gr 6 piping steel at room temperature. *Int J Press Vessels Pip* 82:459–469
13. Johansson G, Ekh M, Runesson K (2005) Computational modeling of inelastic large ratcheting strains. *Int J Plast* 21:955–980
14. Khoei AR, Jamali N (2005) On the implementation of a multi-surface kinematic hardening plasticity and its applications. *Int J Plast* 21:1741–1770
15. Yaguchi M, Takahashi Y (2005) Ratcheting of viscoplastic material with cyclic softening, part I: experiments on modified 9Cr-Mo steel. *Int J Plast* 21:43–65
16. Yaguchi M, Takahashi Y (2005) Ratcheting of viscoplastic material with cyclic softening part II: application of constitutive model. *Int J Plast* 21:835–860
17. Yang X (2005) Low cycle fatigue and cyclic stress ratcheting failure behavior of carbon steel 45 under uniaxial cyclic loading. *Int J Fatigue* 27:1124–1132
18. Chen G, Chen X, Niu C (2006) Uniaxial ratcheting behavior of 63Sn37Pb solder with loading histories and stress rates. *Mater Sci Eng A* 341:238–244
19. Park SJ, Kim KS, Kim HS (2007) Ratcheting behaviour and mean stress considerations in uniaxial low-cycle fatigue of Inconel 718 at 649 °C. *Fatigue Fract Eng Mater Struct* 30:1076–1108
20. Dutta K, Ray KK (2013) Ratcheting strain in interstitial free steel. *Mater Sci Eng A* 575:127–135
21. Paul SK, Sivaprasad S, Dhar S, Tarafder S (2010) True stress control asymmetric cyclic plastic behavior in SA 333 C-Mn steel. *Int J Press Vessels Pip* 87:440–446
22. Paul SK, Sivaprasad S, Dhar S, Tarafder S (2010) Ratcheting and low cycle fatigue behavior of SA333 steel and their life prediction. *J Nucl Mater* 401:17–24
23. Kang G, Liu Y, Li Z (2006) Experimental study on ratcheting-fatigue interaction of SS304 stainless steel in uniaxial cyclic stressing. *Mater Sci Eng A* 435–436:396–404
24. Lim CB, Kim KS, Seong JB (2009) Ratcheting and fatigue behavior of a copper alloy under uniaxial cyclic loading with mean stress. *Int J Fatigue* 31:501–507
25. Lukas P, Kunz L (1987) Effect of grain size on the high cycle behaviour of polycrystalline copper. *Mater Sci Eng* 85:5–75
26. Mahato JK, De PS, Sarkar A, Kundu A, Chakraborti PC (2016) Effect of deformation mode and grain size on Bauschinger behavior of annealed copper. *Int J Fatigue* 83:42–52
27. Oh YJ, Hwang TB, Shin BM (2005) A comparison of low-cycle fatigue properties in stainless steel types 347 N and 316 N. *Mater Trans* 46:317–322

# High-Temperature Fatigue Crack Growth Behaviour of SS 316LN

M. Nani Babu, G. Sasikala and Shaju K. Albert

**Abstract** FCG behaviour of SS 316LN steel is evaluated in the temperature range 300–823 K. While there is a general increase in FCG rate with temperature and load ratio, specifically at low applied stress intensity factor ranges, for intermediate temperatures (623–723 K) and applied stress intensity factors (15–25 MPa m<sup>1/2</sup>), a cross over in the crack growth rate is observed. The Paris exponents for different temperatures varied between 2.4 and 3.7. The variations in the crack growth rates are examined by considering the crack closure and dynamic strain ageing (DSA) effects. Attempts have been made to rationalize these variations with the temperature dependence of Young's modulus and yield strength. The stress intensity factor range normalized with yield strength gives a better correlation with FCG rates at different temperatures. The unified data for all the temperatures was fitted to a Paris-type correlation, viz.,  $\frac{da}{dN} = C \cdot \left(\frac{\Delta K}{\sigma_{ys}}\right)^m$  with  $C = 4.5$  nm/cycle and  $m = 2.73$ .

**Keywords** High-temperature fatigue crack growth · Load ratio  
Dynamic strain ageing

## 1 Introduction

SS 316L(N) is used worldwide as a high-temperature structural material for nuclear industry owing to the combination of good high-temperature mechanical properties, compatibility with coolant liquid sodium, good weldability, and superior resistance to intergranular stress corrosion cracking (IGSCC) by reducing the carbon content and adding nitrogen. Based on the international and in-house research experience, SS 316L(N) has been chosen for high-temperature structural components of the

---

M. Nani Babu (✉) · G. Sasikala · S.K. Albert  
Materials Technology Division, Metallurgy and Materials Group, Indira Gandhi Centre  
for Atomic Research, Kalpakkam 603102, India  
e-mail: nanibm@igcar.gov.in

500 MWe prototype fast breeder reactor (PFBR) which is in an advanced stage of construction at Kalpakkam. PFBR operating temperature range is 623–823 K. Many of these components are subjected to static, cyclic thermo-mechanical and flow-induced vibrational loads, which induce different types of damage like creep, fatigue, creep–fatigue interaction and high cycle fatigue etc. Several research reports are available on the evaluation of tensile, creep and fatigue properties of this material [1–5]. For the structural integrity assessment procedure of these high-temperature components, the fatigue crack growth and fracture properties are required. In previous studies, the fatigue crack growth and fracture properties were examined at ambient test condition for SS 316LN base material with different nitrogen contents [6, 7] and the weld metal of 0.08 wt% nitrogen variant, SS 316 (N) [8, 9]. However, the base line FCG data for SS 316L(N) steel at different temperatures were not established. Therefore, a campaign was initiated to study the effect of temperature on fatigue crack growth behaviour of SS 316L(N).

It is well established that the stage II fatigue crack growth behaviour of any material can explained by the well-known Paris equation [10],

$$da/dN = C(\Delta K)^m \quad (1)$$

where the  $da/dN$  is the fatigue crack growth rate,  $\Delta K$  is the stress intensity factor range ( $\Delta K = K_{\max} - K_{\min}$ ),  $K_{\max}$  and  $K_{\min}$  are maximum and minimum stress intensity factors respectively, coefficient,  $C$ , and the exponent,  $m$ , are constants which depend on the material and test condition.

FCG is influenced by several factors such as microstructure, environment, temperature,  $R$ -ratio, crack closure, overloads, cold work, cyclic loading frequency etc. The effect of crack closure on the crack growth behaviour near threshold is predominant than in the Paris regime. There are several publications, reports and books are available in literature ever since the closure phenomenon was discovered [11–14]. Crack closure provides a mechanism whereby the effective crack growth driving force (cyclic stress intensity factor range) near crack tip ( $\Delta K_{\text{eff}} = K_{\max} - K_{\text{cl}}$  where  $K_{\text{cl}}$  is closure stress intensity factor) differs from the nominally applied value ( $\Delta K$ ). For better prediction of the crack growth behaviour of material, the extent of the crack closure contribution is essential. The evaluation of predominant crack closure mechanisms will also help to understand and interpret the crack growth results. Several crack closure mechanisms have been discussed in the literature depending on the material and test conditions. The crack closure mechanism can be broadly classified as: plasticity induced, roughness induced, oxide induced and transformation induced [12]. Plasticity-induced closure is dominant in ductile materials, while oxide-induced crack closure is a high-temperature mechanism. Roughness-induced crack closure is important when the mating surfaces are rough due to the crack path deviations during crack growth, for example, when the crack follows interfaces like phase/grain boundaries [15]. Transformation-induced crack closure can be important when there is a phase transformation at the crack tip, e.g. strain-induced martensite formation as in the case of metastable austenitic stainless steels such as SS 304.

In this paper, the influence of temperature on FCG behaviour of SS 316L(N) in the Paris regimes is presented. The results are examined incorporating crack closure effects at different temperatures. Attempts have been made to establish an empirical model for crack growth by taking the temperature-dependent mechanical properties into account.

## 2 Experimental

The chemical composition of SS 316L(N) used in this study is presented in Table 1. Specimen blanks of approximately  $(70 \times 65 \times 30 \text{ mm}^3)$  dimensions were prepared from the SS 316L(N) plates of 30 mm thick with 0.08 wt% nitrogen. Compact tension (CT) specimens of 20 mm thickness were fabricated from the blanks as shown in Fig. 1. The CT specimens were pre-cracked as per the standard before the actual test. The FCG tests were conducted in laboratory air at different temperatures in the range 300–823 K, according to ASTM E647 [16] for a constant  $R$  value 0.1 and cyclic frequency 15 Hz in a fully automated servo hydraulic machine. Crack length measurements were carried out using a suitably calibrated direct current potential drop (DCPD) system. The extent of crack closure was estimated using compliance offset method (ASTM E647).

## 3 Results and Discussion

### 3.1 FCG Results

FCG results without and with crack closure correction obtained in the temperature range 300–823 K are presented in Fig. 2a, b. Paris parameters determined from FCG plots are presented in Table 2. It is observed that crack growth rate increases with temperature at a given  $\Delta K$ . The difference in the crack growth rate is high at low  $\Delta K$  ( $<25 \text{ MPa m}^{1/2}$ ) levels when compared to high  $\Delta K$ . However, the crack growth rates at 673 and 723 K are of the same order in  $\Delta K$  range 10–30  $\text{MPa m}^{1/2}$ .

From Table 2, it can be seen that  $\log C$  increases, while change in  $m$  remains constant up to 723 K when crack closure is not accounted for, i.e. when applied  $\Delta K$  is used for correlation. Even after closure correction, the trends in  $\log C$  and  $m$  with temperature are retained up to 673 K. Beyond this,  $\log C$  and  $m$  show non-monotonic behaviour.

**Table 1** Chemical composition of SS316LN

Element	C	N	Mn	Cr	Mo	Ni	Si	S	P	Fe
wt%	0.027	0.08	1.7	17.53	2.49	12.2	0.22	0.0055	0.013	Bal.

**Fig. 1** CT sample dimensions all are in mm

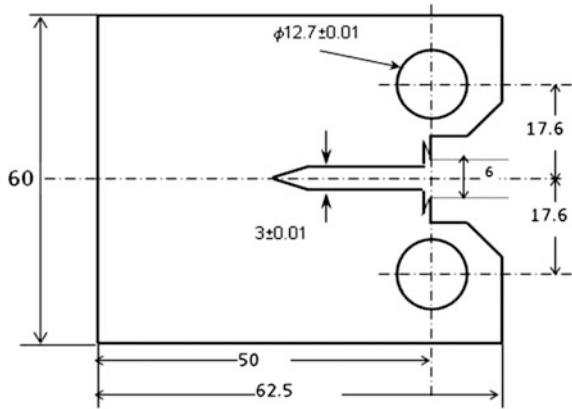


**Fig. 2** Fatigue crack growth results **a** without and **b** with crack closure correction

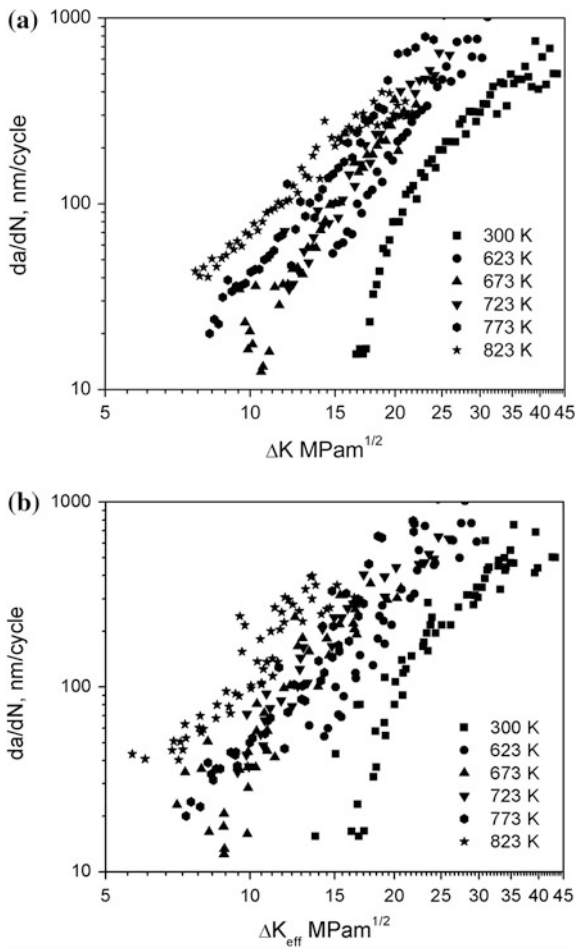




**Table 2** Paris parameters

Temperature (K)	Paris constants			
	$\Delta K$		$\Delta K_{eff}$	
	$m$	$\log C, \text{ nm/cycle}$	$m$	$\log C, \text{ nm/cycle}$
300	3.4721	-2.7053	3.3079	-2.3919
623	3.9264	-2.8442	3.7494	-2.4943
673	3.8369	-2.5510	3.3450	-1.7057
723	3.8311	-2.5160	2.8471	-1.0956
773	3.4288	-1.8217	3.2886	-1.5712
823	2.3766	-0.5106	2.5518	-0.4478

The general increase in  $\log C$  (Table 2) is a consequence of the temperature-dependent decrease in the strength of the material, while the decrease in  $m$  at high temperature, i.e. lower sensitivity of the crack growth rate to  $\Delta K$ , indicates the increased significance of thermally activated mechanisms in damage accumulation. However, at intermediate temperatures, the phenomenon of dynamic strain ageing (DSA) plays a major role in deciding the mechanical behaviour of the material, which is manifested as (i) increase in strength (ii) decrease in ductility (iii) increase in work hardening rate and (iv) negative strain rate sensitivity of flow stress. The consequent changes in tensile properties of material at different temperatures can lead to the observed non-monotonic variations in  $\log C$  and  $m$ . Therefore, FCG results have been further examined by considering the temperature-dependent variations in elastic modulus (since  $\Delta K$  is a linear elastic fracture mechanics parameter) and the yield strength.

### 3.2 Effect of Crack Closure and Dynamic Strain Ageing (DSA) on FCG

Results of the estimation of crack closure are presented in Fig. 3 in the form of  $K_{cl}/K_{max}$  as a function of  $\Delta K$ . It is clear that the extent of crack closure is different at different temperatures. Also, the extent of crack closure is low for the test temperatures viz, 300, 623 and 773 K, while it is high at 673, 723 and 823 K in the  $\Delta K$  range 10–25 MPa m<sup>1/2</sup>. This observation indicates the possibility of contributions from more than one phenomenon to crack closure in this temperature range. After incorporating the crack closure correction, the crack growth rates for 673, 723 and 773 K fall in the same scatter band. The same crack growth rate is attributed to the dynamic strain ageing effects operating in this material in this temperature range, which is corroborated with tensile properties. Tensile properties of SS 316LN at different temperatures are presented in Table 3. The yield strength rapidly decreases from room temperature to 623 K. However, the rate of decrease in the yield strength at 673 K is low, and a small peak in YS is observed at 723 K. In

**Fig. 3** Crack closure results at different temperature

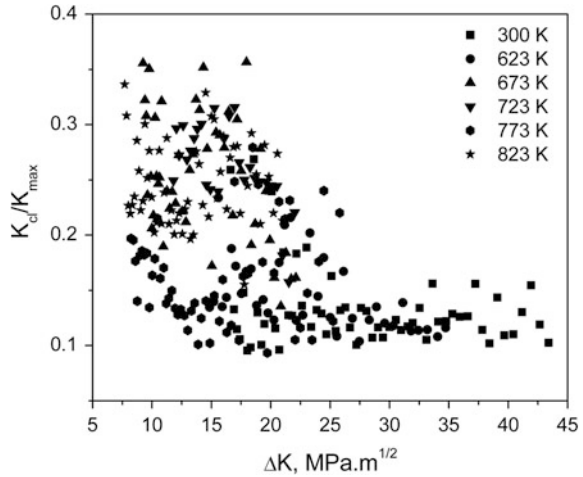


**Table 3** Tensile properties of SS 316L(N) steel at different temperatures (strain rate:  $3 \times 10^{-4} \text{ s}^{-1}$ )

Temperature (K)	300	623	673	723	773	823
Yield strength (MPa)	290	160	155	163	147	146

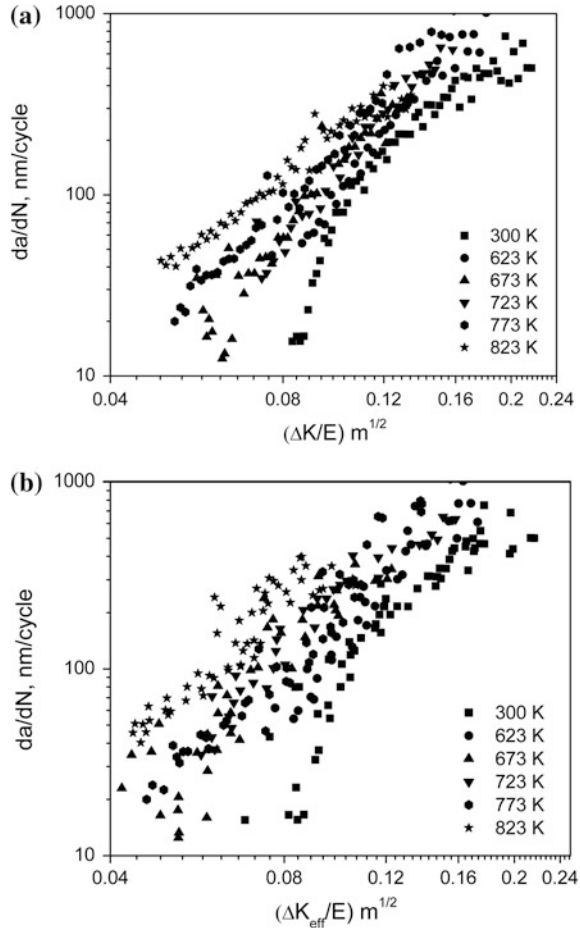
addition, yield strength is more or less same at 773 and 823 K can be seen in Table 3.

This kind of yield strength variation with temperature is attributed to DSA [17]. DSA is a characteristic phenomenon of the dynamic interaction between the moving dislocations and the diffusing solute elements, and its extent is a function of strain rate and temperature. The effects of DSA on different mechanical properties have been discussed in literature [18]. The effect of test control mode on the manifestation of DSA has been further discussed in an earlier study [19]. In FCG tests which are generally conducted in the load control mode, DSA causes crack tip strengthening, thereby leading to a decrease in the crack growth rate.

### 3.3 Effect of Modulus (E) and Yield Strength ( $\sigma_y$ ) on FCG

The temperature dependence of crack growth behaviour may be linked to those of the basic mechanical properties, viz., elastic modulus, yield strength, and ultimate tensile stress. The concept of using normalized stress intensity factors for correlating FCG data was initially introduced by Pearson [20] and applied to various materials at ambient test condition [21]. Hence, the effect of temperature dependency of Young’s modulus (E) on the FCG properties has been examined by normalizing  $\Delta K$  and  $\Delta K_{eff}$  with E (Fig. 4a, b). From Fig. 4a, it is obvious that the

**Fig. 4** FCG data by normalising **a**  $\Delta K$  and **b**  $\Delta K_{eff}$  with modulus ( $E$ )



FCG curves for all temperatures lie in a relatively closer scatter band than in Fig. 2a; however, the temperature dependence still remains largely. It indicates that the role of  $E$  on the crack growth behaviour is not significant. These observations are in agreement with previous reports [20, 21] that the variations in elastic modulus cannot account for the differences in FCG rates for different materials.

It is known that the crack tip plastic zone size is a function of applied  $\Delta K$  and yield strength  $r_p = \frac{1}{2\pi} \left( \frac{\Delta K}{\sigma_y} \right)^2$ , where  $r_p$  is plastic zone size. Therefore, we examine the possibility of accounting for the temperature induced variations in FCG data by normalizing  $\Delta K$  and  $\Delta K_{eff}$  with the yield strength; the results are presented in

**Fig. 5** FCG data by normalising **a**  $\Delta K$  and **b**  $\Delta K_{\text{eff}}$ , with yield strength ( $\sigma_{ys}$ )

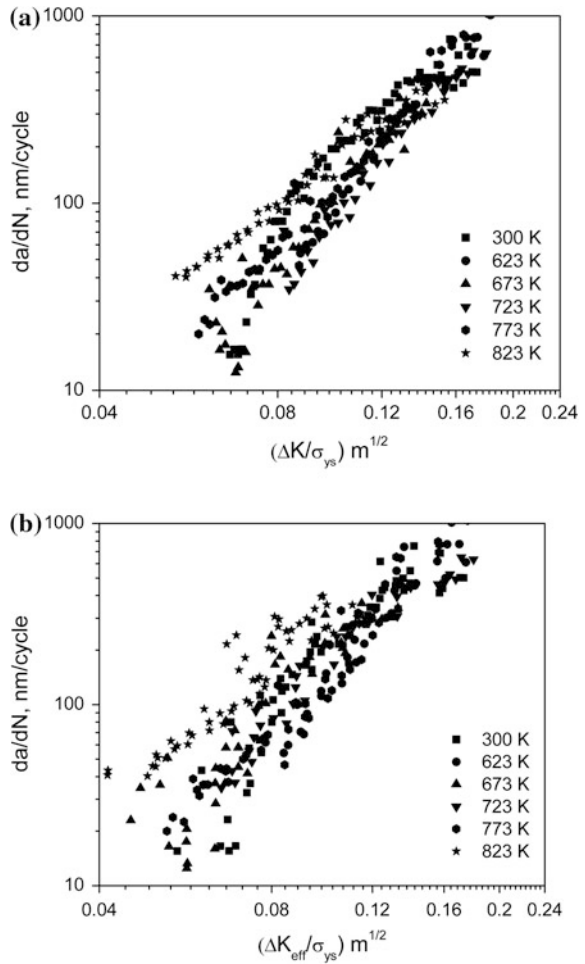


Fig. 5a, b. As seen from Fig. 5a, the crack growth rate for all the test temperatures lie in a single scatter band. The unified data for all the temperatures were fitted to a Paris-type correlation as given below.

$$\frac{da}{dN} = C \cdot \left( \frac{\Delta K}{\sigma_{ys}} \right)^m$$

with  $C = 4.5$  nm/cycle and  $m = 2.73$ .

It is interesting to note that the Paris exponent  $m$  in the normalized correlation is close to 3, that is expected for this class of steels.

## 4 Conclusions

Fatigue crack growth behaviour of SS 316LN steel in the temperature range 300–823 K has been evaluated. The effect of temperature and crack closure on the FCG has been examined. It was observed that the crack closure effects are significant at low  $\Delta K$  levels. Also the intrinsic crack growth rate at the intermediate temperature range 673–773 K is in the same order, and it is attributed to dynamic strain ageing. The effect of modulus and yield strength on FCG properties have been evaluated by normalizing  $\Delta K$  and  $\Delta K_{\text{eff}}$  with modulus and yield strength in the test temperature range. The effect of modulus on FCG behaviour is insignificant. However, the FCG rates gives a better correlation with the stress intensity factor range normalized with yield strength in this temperature range. The unified data for all the temperatures were fitted to a Paris-type correlation.

**Acknowledgements** The authors would like to acknowledge Mr. Syed Kaleem and Ms. Shanthi for experimental support. Also authors wish to acknowledge Dr. A.K. Bhaduri, Director, IGCAR, for continuous support and encouragement.

## References

1. Ganesan V, Mathew MD, Bhanu K, Rao S (2009) Influence of nitrogen on tensile properties of 316 LN SS. *Mater Sci Technol* 25:614–618
2. Reddy GVP, Sandhya R, Rao KBS, Sankaran S (2010) Influence of nitrogen alloying on dynamic strain ageing regimes in low cycle fatigue of AISI 316LN stainless steel. *Procedia Eng* 2:2181–2188
3. Mathew MD, Kim DW, Ryu WS (2008) A neural network model to predict low cycle fatigue life of nitrogen-alloyed 316L stainless steel. *Mater Sci Eng A* 474:247–253
4. Sasikala G, Mathew MD, Rao KBS, Mannan SL (2004) Creep deformation and fracture behaviour of type 316 and 316LN stainless steels and their welds. *Metall Mater Trans A* 31A:1175–1185
5. Ganesan V, Mathew MD, Parameswaran P, Rao KBS (2010) Creep strengthening of low carbon grade type 316 LN stainless steel by nitrogen. *Trans Indian Inst Met* 63:417–421
6. Dutt BS, Shanthi G, Sasikala G, Babu MN, Venugopal S, Albert SK, Bhaduri AK, Jayakumar T (2014) Effect of Nitrogen addition and test temperatures on elastic-plastic fracture toughness of SS 316LN. *Procedia Eng* 86:302–307
7. Babu MN, Dutt BS, Venugopal S, Sasikala G, Albert SK, Bhaduri AK, Jayakumar T (2013) Fatigue crack growth behavior of 316LN stainless steel with different nitrogen contents. *Procedia Eng* 55:716–721
8. Samuel KG, Sasikala G, Ray SK (2011) On  $R$  ratio dependence of threshold stress intensity factor range for fatigue crack growth in type 316(N) stainless steel weld. *Mat Sci Tech* 27:371–377
9. Babu MN, Dutt SB, Venugopal S, Sasikala G, Bhaduri AK, Jayakumar T, Raj B (2010) On the anomalous temperature dependency of fatigue crack growth of SS 316(N) weld. *Mat Sci Eng* 527:5122–5129
10. Paris PC, Gomez M, Anderson W (1961) The rational analytical theory of fatigue. *Tren Eng* 13:9–14
11. Elber W (1970) Fatigue crack closure under cyclic tension. *Eng Fract Mech* 2:37–45

12. Suresh S (1991) *Fatigue of materials*. Cambridge University Press
13. Ritchie RO (1988) Mechanisms of fatigue crack propagation in metals, ceramics and composites: role of crack-tip shielding. *Mater Sci Eng A* 103:15–28
14. Ritchie RO, Gilbert CJ, McNaney JM (2000) Mechanics and mechanism of fatigue damage and crack growth in advanced materials. *Intl J Solids Struct* 37:311–329
15. Calonne V, Gourgues AF, Pineau A (2004) Fatigue crack propagation in cast duplex stainless steels: thermal ageing and microstructural effects. *Fatigue Fract Eng Mat Struct* 27:31–43
16. E647-08e1 (2010) *Annual book of ASTM Standards*. ASTM, USA
17. Rodriguez P (1984) Serrated plastic flow. *Bull Mater Sci* 6:653–663
18. Rodriguez P (2000) Dynamic strain ageing: is it really a damage mechanism? In: Raj B, Rao KBS, Jayakumar T, Dayal RK (eds) *Proceeding international symposium on materials ageing and life management*. Allied Publishers Limited, Chennai, pp K1–14
19. Babu MN, Sasikala G, Dutt SB, Venugopal S, Albert SK, Bhaduri AK, Jayakumar T (2012) Investigation on influence of dynamic strain ageing on fatigue crack growth behaviour of modified 9Cr–1Mo steel. *Int J Fat* 43:242–245
20. Pearson S (1966) Fatigue crack propagation in metals. *Nature* 211(3):1077
21. Lal DN (1996) On the combined influences of young's modulus and stress ratio on the LEFM fatigue crack growth process: a new mechanistic approach. *Eng Fract Mech* 54(6):761–790

# Numerical Simulation of Fracture in Coatings Subjected to Sudden Temperature Change Using Element-Free Galerkin Method

Sahil Garg and Mohit Pant

**Abstract** The article presented broadens the dexterity of element-free Galerkin method (EFGM) for analysis of thermal fracture in case of materials with coatings under plane stress conditions. A conjugated modeling approach developed and employed in this work by amalgamation of jump function approach and enrichment criterion. This approach allows the successful modeling of multiple weak and strong discontinuities in one domain. To distinguish the interface of two materials, jump function methodology is used, while for capturing the stress field oscillations around the crack tip an intrinsic enrichment criterion is put to use. The interaction integral scheme for thermal fracture has been modified to compensate thermal strains for generating mode-I stress intensity factors (SIFs). The effect of mechanical properties on crack under sudden temperature change is compared using three cases in which Zinc and Steel substrates are used (Steel/Zinc/Steel configuration and Zinc/Steel/Zinc configuration) and compared with results of mono-material configuration.

**Keywords** EFGM · SIF · Thermal fracture · Coatings

## 1 Introduction

The evolution of technology and the need of swift computational tools require advance techniques such as EFGM [1, 2] which can ameliorate the primitive mesh-based methods such as finite element method (FEM). The EFGM shape functions are derived using the moving least squares [3] interpolants, which require only nodal data without the need of making elements and defining elemental connectivity. The advantages of this method are that continuous differentiable

---

S. Garg (✉) · M. Pant  
National Institute of Technology, Hamirpur, HP, India  
e-mail: sahil.garg1017@gmail.com

M. Pant  
e-mail: mohitpant.iitr@gmail.com

approximations can be obtained so that the partial derivatives of approximations such as strains in elastic problems are smooth, and also the need of requirement of post-processing is eliminated and mainly applied in moving boundary problems such as crack propagation [4, 5], where nodes were constantly shifted or added to track the crack tip. Initially, domain partitioning [6] and Lagrange multiplier [7] approaches were quite popular but, in dealing with discontinuities, the continuity of meshless approximations causes some trouble in cases where the exact solution possesses discontinuities [7] in the derivatives. The most common examples of such cases involve treatment of material interfaces [8] such as bi-materials or inclusions. In this regard, jump function approaches [9] provided discontinuities in the derivatives of primary variable across a material interface using a special shape function.

Coatings have been used widely for thermal barrier applications [10] in aerospace industries and also in automotive industries [11] for protection of major components. The work presents the judicious use of jump function scheme in analyzing the cracks in coatings.

This article aims at analysis of thermal fracture and effects of material properties in coatings using meshless methods. Motivated by the wide application of coated materials, this work extends the applicability of EFGM for simulating layered materials under thermal loads.

## 2 Derivation of EFGM Shape Functions

To find the interpolation function,  $u$  is the MLS approximation, and  $u^h(x)$  can be given as:

$$u^h(\mathbf{x}) = \sum_{j=1}^m p_j(\mathbf{x}) a_j(\mathbf{x}) \equiv \mathbf{p}^T(\mathbf{x}) \mathbf{a}(\mathbf{x}) \quad (1)$$

where  $p(x)$  stands for basis function.

To determine the shape function, first the value of  $a(x)$  has to be acquired at any random point  $x$ . This can be achieved by minimization of weighted least squares sum of the difference between local approximation,  $u^h(x)$ , and field function nodal parameters,  $u_I$ .

Lets represent the weighted least squares sum expressed by  $\mathcal{L}(x)$ ; therefore,

$$L(\mathbf{x}) = \sum_{I=1}^n w(\mathbf{x} - \mathbf{x}_I) [\mathbf{p}^T(\mathbf{x}) \mathbf{a}(\mathbf{x}) - u_I]^2 \quad (2)$$

$w(\mathbf{x} - \mathbf{x}_I)$  here represents the weight function.



By completing the minimization process using  $\partial L/\partial \mathbf{a} = 0$ , the following set of linear equation is obtained:

$$A(x)a(x) = B(x)u \tag{3}$$

By replacement of Eq. (3) in (1), the approximation function is obtained as:

$$u^h(\mathbf{x}) = \sum_{I=1}^n \Phi_I(\mathbf{x})u_I \tag{4}$$

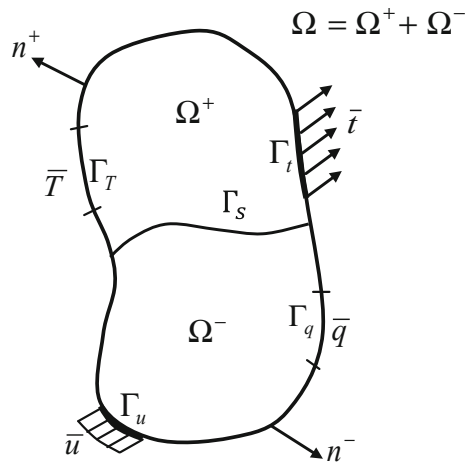
### 3 Jump Function Approach for Interface Modeling

One of the best approaches in EFGM to handle the weak discontinuity problems is the use of jump functions for their ability to hold compact support which results in banded matrix equations. Consider two distinguishable materials separated by a single interface,  $\Gamma_s$  as shown in Fig. 1. A perfect interface is assumed; thereby, the traction, displacement, temperature and heat flux are assumed to be continuous across the interface  $\Gamma_s$ . An approximation of displacement with jump function becomes

$$u^h(\mathbf{x}) = u^{EFGM}(\mathbf{x}) + q^J(s)\Psi_J(r) \tag{5}$$

where  $u^{EFGM}$  is the standard EFGM approximation,  $q^J$  are amplitude parameters of the jump shape function, and  $\Psi_J(r)$  are the jump shape functions.  $s$  provides parameterization of the line of discontinuity, and  $q^J$  is discretized as follows

**Fig. 1** Two-dimensional inhomogeneous body



$$q^J(s) = \sum_I N_I(s) q_I^J \tag{6}$$

where  $N_I(s)$  are one-dimensional shape functions.

The jump function used in the present work is given by

$$\Psi_J(\bar{r}_J) = \begin{cases} \frac{-1}{6} \bar{r}_J^3 + \frac{1}{2} \bar{r}_J^2 - \frac{1}{2} \bar{r}_J + \frac{1}{6} & \bar{r}_J \leq 1 \\ 0 & \bar{r}_J \geq 1 \end{cases} \tag{7}$$

$\psi_J$  is the jump function and  $r_J$  stands for the distance to  $J$ th point of discontinuity.

### 4 Computation of SIFs by Employing Interaction Integral Scheme

The generalized mathematical equation of  $J$  integral for an isotropic cracked body is given as [12]

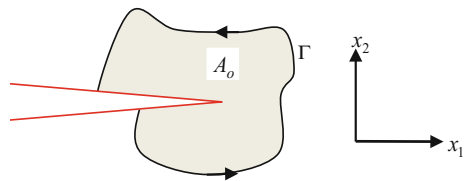
$$J = \int_{\Gamma} \left( W \delta_{ij} - \sigma_{ij} \frac{\partial u_i}{\partial x_1} \right) n_j d\Gamma \tag{8}$$

where  $W = \int_0^{\epsilon} \sigma d\epsilon$  represents the strain energy density,  $\sigma$  stands for stress, and  $n$  is the outward unit normal vector to an discretional curve surrounding the crack tip (Fig. 2). In problems concerning linear elastic material models, it is known that  $W = \sigma_{ij} \epsilon_{ij} / 2$ . The line integral in Eq. (8) is transformed into an area integral by means of Green’s theorem.

$$J = \int_A \left( \sigma_{ij} \frac{\partial u_i}{\partial x_1} - W \delta_{ij} \right) \frac{\partial q}{\partial x_j} dA \tag{9}$$

where  $A$  is the area of the arbitrary curve surrounding the and  $q$  is a plateau function picked in such a way that it holds a value of unity at the crack tip, zero along the boundary of the domain and random at other places.

**Fig. 2** Crack surrounded by an arbitrary path  $\Gamma$  of area  $A_o$



For a closed path  $\Gamma$  as shown in Fig. 2, the final form of thermal interaction integral [12] can be given by:

$$\int_{\Gamma} \left[ \left( W - \frac{\beta}{2} T \varepsilon_{kk} \right) \delta_{ij} - \sigma_{ij} \frac{\partial u_i}{\partial x_1} \right] n_j d\Gamma + \beta \int_{A_o} \frac{\partial T}{\partial x_1} \varepsilon_{kk} dA \tag{10}$$

where  $\beta$  is coefficient of thermal expansion,  $T$  is applied temperature, and  $\varepsilon_{kk}$  is thermal strain.

### 5 Numerical Execution

MATLAB is used to generate the EFGM code for simulation and modeling of the problem. Since the mutual interaction of weak and strong discontinuities is modeled, the crack has been represented using intrinsic enrichment while the interface is characterized using the jump function criterion. The problem domain is bifurcated using 25 regularly dispersed nodes along the length, i.e.,  $x$ -axis, and 37 nodes along  $y$ -axis making a total of 925 ( $25 \times 37$ ) nodes and 864 ( $24 \times 36$ ) background cells. The rectangular plate subjected to tensile load preferred as a model for this study has dimensions height ( $B$ ) = 3 units and width ( $W$ ) = 2 units, and the sudden temperature change of 100 °C is applied under plane stress conditions. The thickness of each layer is kept to be 0.5 units. The position of primary crack is fixed in all the simulations at coordinates  $x = 0$  and  $y = B/2$ , i.e., 1.5 units from the base with an orientation  $\alpha = 0^\circ$  ( $\alpha = 0^\circ$  here means that the crack is parallel to the horizontal axis). The effect of variation of substrate rigidity and variation of material properties on outer layer with crack is discussed. Three cases are discussed in this work: First, the SIFs are calculated for mono-material (Zinc and Steel), in second case calculations for SIFs are made with Zinc as middle material while Steel on both sides (Steel/Zinc/Steel configuration), and finally, Steel is taken in middle while Zinc is placed on each of the sides (Zinc/Steel/Zinc configuration). The maximum variation between FEM and EFGM results in case of all simulations was around 3–5%. The mechanical characteristics of the materials essential for the calculations are given in Table 1. The proposed model works well using EFGM as the relative error compared to FEM results is low. Table 2 depicts results calculated using EFGM.

**Table 1** Materials and their mechanical properties

S. No.	Material	Young’s modulus (GPa)	Poisson’s ratio	Coefficient of thermal expansion (m/(m K))
1	Steel	210	0.3	$12 \times 10^{-6}$
2	Zinc	100	0.3	$29 \times 10^{-6}$

**Table 2** Values of mixed mode SIFs for all the configurations<sup>a</sup>

Single edge crack (crack length $a = 0.2$ )	SIFs for Steel/Zinc/Steel configuration		SIFs for Zinc configuration		SIFs for Zinc/Steel/Zinc configuration		SIFs for steel configuration	
	$K_I$ (KN m <sup>1/2</sup> )	$K_{II}$ (KN m <sup>1/2</sup> )	$K_I$ (KN m <sup>1/2</sup> )	$K_{II}$ (KN m <sup>1/2</sup> )	$K_I$ (KN m <sup>1/2</sup> )	$K_{II}$ (KN m <sup>1/2</sup> )	$K_I$ (KN m <sup>1/2</sup> )	$K_{II}$ (KN m <sup>1/2</sup> )
Crack inclination angle (°)								
0	2.0049	0.0185	2.2140	0.0179	2.1402	0.0154	1.9238	0.0156
10	1.7234	0.1863	1.9134	0.2884	1.8574	0.2032	1.6627	0.1811
20	1.9699	0.4385	2.1814	0.4888	2.1147	0.4759	1.8956	0.4247
30	1.7632	0.5120	1.9564	0.5707	1.9007	0.5562	1.7001	0.4959
40	1.4324	0.6113	1.6019	0.6850	1.5657	0.6705	1.3920	0.5952
50	1.1147	0.7747	1.2510	0.8873	1.2270	0.8660	1.0871	0.7624
60	0.9010	0.7718	1.1195	0.8167	1.0063	0.8083	0.8859	0.7097

<sup>a</sup>All values of SIFs are to be multiplied by 10<sup>5</sup>

### 5.1 Edge Crack Under Thermal Load

The plate with above-mentioned dimensions is taken for this analysis. An edge crack with crack length equal to 0.2 units is taken at 1.5 units above the base edge as shown in Fig. 3. The crack inclination angle is varied from 0° to 60°, and results are plotted in Fig. 4. The mode-1 SIF ( $K_I$ ) keeps on decreasing with increase in inclination angle, and mode-2 SIF ( $K_{II}$ ) keeps on rising as crack enters mixed mode conditions. The result worth mentioning here is that the SIFs of mono-material configuration vary primarily due to the variation of coefficient of thermal expansion of Zinc or Steel (which would otherwise be same in case of mechanical loading) as shown in Table 2.

The values in Table 2 show that a homogeneous plate of Steel has lowest value of mode-I SIF due to low thermal expansion coefficient, thereby causing less expansion as compared to other configurations. The stress distribution plots of stress in “y” direction for all the configurations are shown in Fig. 5a–c.

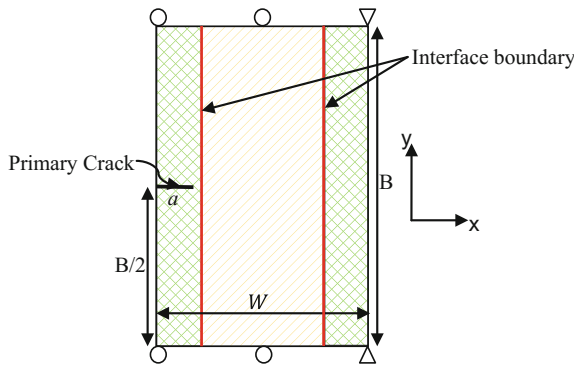


Fig. 3 Problem geometry along with boundary conditions

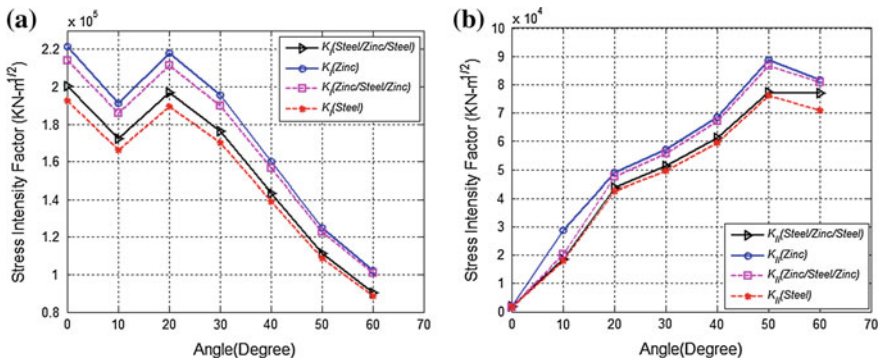
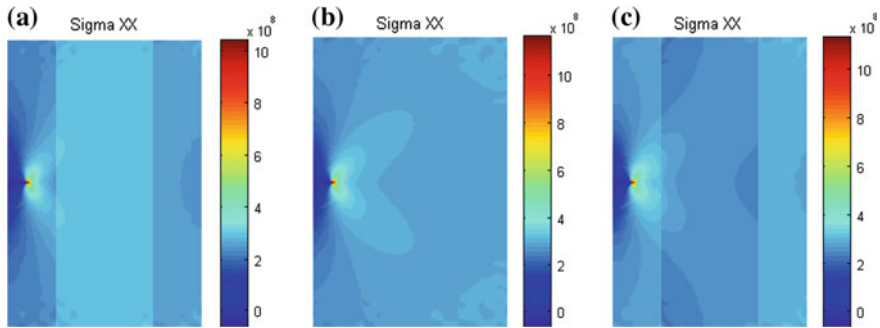


Fig. 4 Plots of SIFs a mode-I and b mode-II



**Fig. 5** Contour plot of  $\sigma_{yy}$  **a** Steel/Zinc/Steel configuration, **b** Mono-material configuration, **c** Zinc/Steel/Zinc configuration

## 6 Conclusion

The work presents a judicial extension of EFGM and jump function approach in analyzing thermal fracture in coatings. The results by EFGM are validated by comparing them with FEM results and are well in agreement. The following conclusions can be drawn from the simulated results:

1. The substrate rigidity immensely effects the SIFs of crack, harder the substrate less is the SIF for the primary crack and vice versa; hence, it can be concluded that a softer layer of material will protect the hard material compared to mono-material configuration due to lower SIF.
2. The effect of coefficient of thermal expansion greatly influences the SIFs of the crack. In order to protect a material from damage, the coating material should be selected such that it has lower rigidity compared to substrate and lower value of coefficient of thermal expansion.

The future scope of work can be extended to analysis of crack interaction effects and to simulate the effect of various discontinuities on fatigue crack growth in coatings.

## References

1. Belytschko T, Lu YY, Gu L (1994) Element-free Galerkin methods. *Int J Numer Meth Eng* 37:229–256
2. Lu YY, Belytschko T, Gu L (1994) A new implementation of the element element-free Galerkin method. *Comput Methods Appl Mech Eng* 113:397–414
3. Lancaster P, Salkauskas K (1981) Surfaces generated by moving least squares methods. *Math Comput* 37:141–158
4. Belytschko T, Lu YY, Gu L (1995) Crack propagation by element-free Galerkin methods. *Eng Fract Mech.* 51:295–315

5. Belytschko T, Krongauz Y, Fleming M, Organ D (1996) Smoothing and accelerated computations in element-free Galerkin method. *J Comput Appl Math* 74:111–126
6. Liu GR (2003) Mesh free methods—moving beyond the finite element method. CRC Press, USA
7. Cordes LW, Moran B (1996) Treatment of material discontinuity in the element free Galerkin method. *Comput Methods Appl Mech Eng* 139:75–89
8. Belytschko T, Gracie R (2007) On XFEM applications to dislocations and interfaces. *Int J Plast* 23:1721–1738
9. Krongauz Y, Belytschko T (1998) EFG approximation with discontinuous derivatives. *Int J Numer Meth Eng* 41:1215–1233
10. Arai M, Okajima Y, Kishimoto K (2007) Mixed-mode interfacial fracture toughness for thermal barrier coating. *Eng Fract Mech* 74:2055–2069
11. Nasri K, Abbadi M, Zenasni M, Ghammouri M, Azari Z (2014) Double crack growth analysis in the presence of a bi-material interface using XFEM and FEM modelling. *Eng Fract Mech* 132:189–199
12. Pant M, Singh IV, Mishra BK (2010) Numerical simulation of thermo-elastic fracture problems using element free Galerkin method. *Int J Mech Sci* 52:1745–1755

# Measurement of Residual Stress Distribution and Fatigue Life Assessment of Similar and Dissimilar Butt-Welded Joint

Varun Ravichandran, E.R. Revanth, D. Varun Kumar, M. Sandeep  
and A. Harish

**Abstract** The residual stresses developed during welding are deleterious to fatigue life. Tensile stresses tend to pull apart the surface of the material. Cracks are developed when subjected to high tensile stress. By altering the residual stress level, fatigue life can be improved significantly. The intent of this work is to measure the residual stress distribution and fatigue life assessment of butt-welded joint with similar (M.S IS 2062) and dissimilar (SS304L & M.S IS 2062) materials. The residual stress level in these joints is evaluated accurately by X-ray diffraction, before and after the surface modification. Shot peening is the surface modification method employed to enhance fatigue life of the joint. Based on the experimental results, it is observed that fatigue life of the welded joint has been improved.

**Keywords** Residual stress · Shot peening · Fatigue life · Butt welding

## 1 Introduction

Fatigue is a phenomenon exhibited by materials under repeated cycles of stress and strain which causes localized structural damage and results in progressive fracture. Fatigue occurs at stresses well within the tensile strength of the material. When the

---

V. Ravichandran (✉) · E.R. Revanth · D. Varun Kumar · M. Sandeep · A. Harish  
Mechanical Engineering Department, BNM Institute of Technology, Bangalore, India  
e-mail: ferrari.var@gmail.com

E.R. Revanth  
e-mail: revabob@gmail.com

D. Varun Kumar  
e-mail: varunkumarvaru.6@gmail.com

M. Sandeep  
e-mail: sandmech619@gmail.com

A. Harish  
e-mail: harishbba@gmail.com



component is subjected to torsion or bending load, tensile stresses pull apart the material which initiates crack propagation. The number of cycles of fluctuating stresses and strains that a material will sustain before failure occurs is known as fatigue life. One of the main factors affecting fatigue life is surface residual stress.

Residual stresses are locked-up stresses in engineering components which are developed mainly due to non-uniform volumetric change in metallic component. Residual stresses in welds develop due to differential weld thermal cycle in the heat-affected region. The type and magnitude of the residual stresses vary continuously during different stages of welding, i.e., heating and cooling. During cooling as the metal starts to shrink, tensile residual stresses develop and their magnitude keeps on increasing until the room temperature is attained. Residual stresses are generally desirable when they are applied opposite to the stress due to load. Introducing compressive residual stresses within the outer layer of the work piece can nullify or reduce the effect of external tensile stresses.

Shot peening is a cold working process which is extensively employed to reduce premature fatigue failure and increase fatigue life of the machine components. In shot peening, small metallic pellets traveling at a high velocity hit the material surface inducing compressive stresses.

Hardness is the resistance of a material to indentation or penetration by means of drilling, scratching or wear and is measured by hardness tests such as Brinell, Rockwell or Vickers. Normally the hardness of a body is determined by creating a small indentation on the surface of the body, and the characteristics of this indentation can be studied to determine the hardness of the body.

Scanning electron microscope (SEM) is a microscope that provides a highly magnified image of the surface under observation by building an image from the electrons reflected from each point. Due to the high resolution and three-dimensional images, SEM is critical in fields that require characterization of solid materials. Scanning electron microscope can easily detect and analyze surface fractures and provide precise information on microstructures.

The objective of this study is to estimate residual stresses induced by welding and to modify the residual stress with the use of shot peening method. Two different materials, mild steel and stainless steel 304L are used which are joined by butt welding. The two specimens are prepared by welding of similar and dissimilar material. Similar metal weld joints are used in many areas for economic purposes and at the places where temperatures are same throughout. Similar metals weld the joint of mild steel in low-temperature application. It cannot be used in high-temperature application because of its corrosion issues. For high-temperature application, SS304L is used along with mild steel. The part of plant where temperature is high SS304L is used and for the part where temperature is low mild steel is used. By using these two materials along with each other, the cost will reduce. For that reason, dissimilar weld joint is extensively used in many power plants, pressure vessels, etc., for economic and efficient operation. Similar weld joint is made between mild steel and mild steel, and dissimilar weld joint is made between mild steel and stainless steel. Mild steel and stainless steel are used in many areas such as to construct bridges and building, mechanical equipment, machines,

pressure vessels, nozzles, oil refinery plants, etc. In the above-mentioned area, these materials undergo various temperature condition, pressure condition and loading condition. These materials can fail during the periodic operation. So, it is important to understand the characteristic behavior of these materials under various conditions.

## 2 Experimental Details

In this study, mild steel and stainless steel plates of 4 mm thickness are used and dumbbell specimens are prepared in accordance with ASTM E647 specifications. Plates of  $110 \times 20$  mm size are used for welding and a single V-joint with bevel angle of  $35^\circ$  and root face 3 mm is prepared. Figure 1 shows the dumbbell specimen used in this study. The plates are butt welded using shielded metal arc welding with E-6013 electrode. We weld two types of materials, mild steel (MS) and stainless steel (SS 304L) to obtain similar (MS to MS) and dissimilar (MS to SS) welded joints. To weld MS to MS, mild steel wire is used as filler material and to weld MS to SS, SS 304L wire is used as filler material. Test specimens are joined under the following welding conditions: welding current 180 A, arc voltage 21 V, welding speed 1100 mm/min and weld width 3–4 mm. The plate for 30 min after welding (Fig. 2, Tables 1 and 2).

The specimen on which shot peening is to be performed is placed on the machine fixture and S330 type shot ball of diameter ranging from 0.7 to 1.20 mm is made to strike on the specimen at an angle of  $45^\circ$  with a velocity of  $47 \text{ ms}^{-1}$  for 25 s at an intensity of 0.53 mm.

To determine the residual stresses induced on the specimen due to shot peening, X-ray diffraction is used. This non-destructive testing method is preferred because the low scattering angles obtained from this setup is well suited for plate geometry of the specimen. The specimen is first placed on the plate of the machine, and the X-ray beam is incident on the surface of specimen at an angle. The angle used for

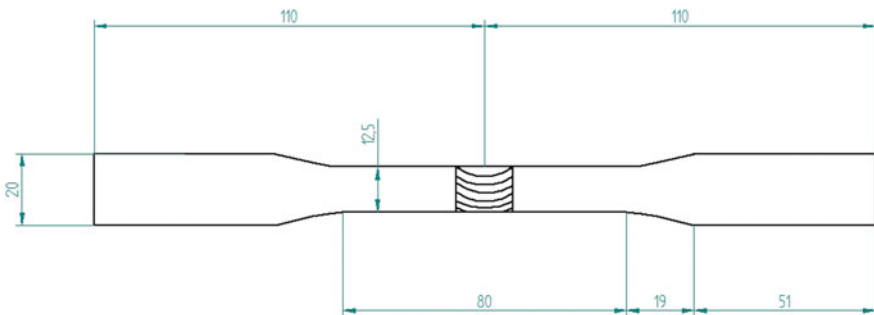


**Fig. 1** Dumbbell specimen prepared for experimental testing (all dimensions in mm)

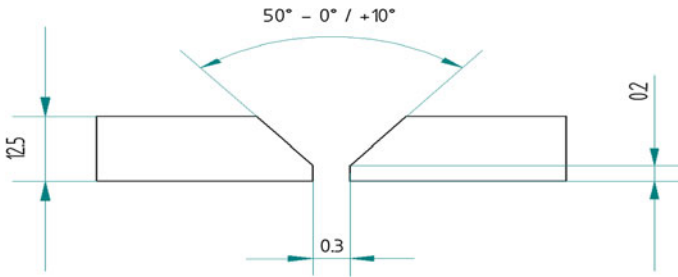


**Fig. 2** Joint design

**Table 1** Composition ranges of MS IS 2062

Element	C	Mn	Si	P	S
Content	0.05–0.18%	0.7–0.9%	0.40% max	0.040% max	0.040% max

**Table 2** Composition ranges of SS304L

Element	C	Mn	Si	P	S	Cr	Mo	Ni	N	Fe
Content	<0.03%	<2.0%	<0.75%	0.045%	<0.03%	18–20%	2–3%	8–12%	<0.1%	Balance

steel specimen is 155°–157°. Each time when the X-ray travels from one end to other end of specimen, it gives a pick point. This is seen on the computer screen using the software Lapos. The beam is made to travel on the specimen surface for a certain period of time, and each time it gives a pick point. The distance between these pick points is known as the  $d$ -spacing. With the use of this  $d$ -spacing which is a distance between two adjacent crystallographic planes, the strain in the specimen can be calculated and so stress in the component measured by using Hook's law.

The fatigue specimen is gripped at two ends: One end has a motor to rotate the specimen, while the other end is subjected to load. The specimen is subjected to tensile and compressive stresses in the lower and upper parts when rotated about its longitudinal axis. The test is performed till the specimen fails. The number of cycle for which the specimen withstands without any failure is noted down. To obtain the number of cycles to failure, a revolution counter is used. The number of cycles to failure reduces with increase in cyclic stress. Likewise, the number of cycles to failure increases with reduction in cyclic stress. At the fatigue endurance limit, specimen failure will not occur for a certain value of the cyclic stress.

Hardness of a specimen is an important factor which indicates its strength. Hardness of a specimen is determined by making small indentations on its surface and is represented as HRC. Common indenters used are made of hardened steel or diamond. Here we make use of Rockwell hardness testing equipment to find

**Fig. 3** Microstructure of MS to MS welded specimen before shot peening

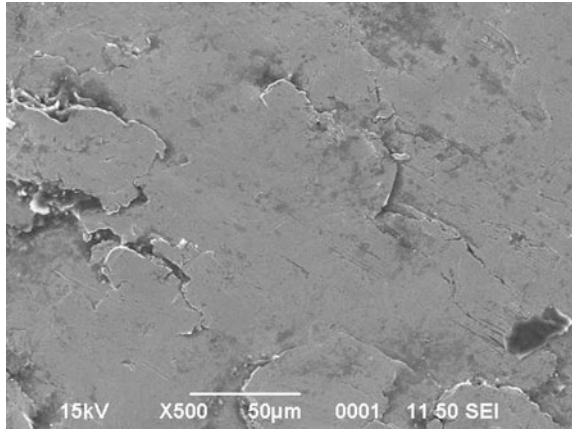
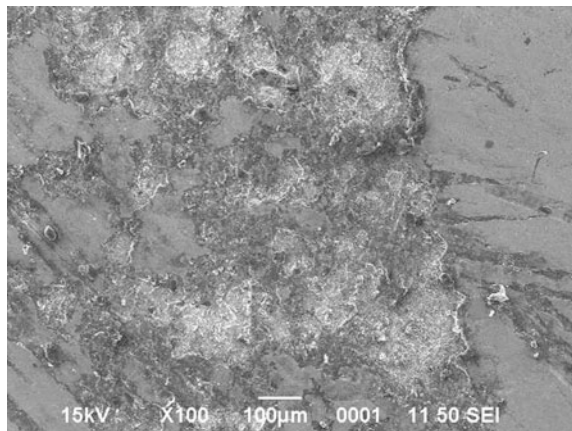


**Fig. 4** Microstructure of MS to MS welded specimen after shot peening



hardness of material. In this project work, we are measuring the hardness on steel surface. So, scale used in this case is 'A', indenter used is diamond and dial used is black. During the experiment, first the specimen is placed on the anvil surface. Then the indenter ball is brought in contact with the specimen surface, and a load of 60 kgf is applied by means of load lever. The readings are noted down, and the experiment is repeated at different points on the specimen surface. The value of hardness is average of these obtained values.

The material analysis is done using SEM. The purpose of this is to observe the changes in surface topography due to shot peening. Microstructure of the specimens is shown in Figs. 3, 4, 5 and 6.

**Fig. 5** Microstructure of MS to SS welded specimen before shot peening

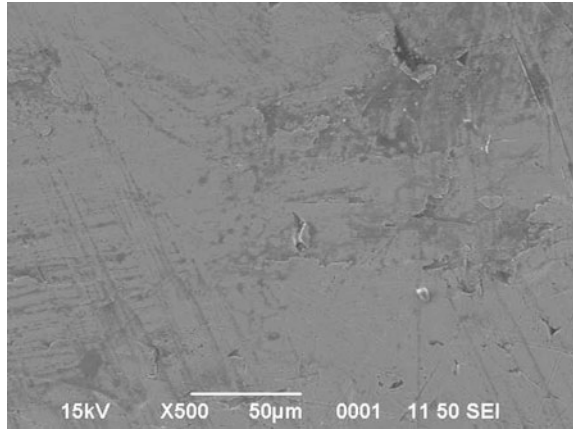
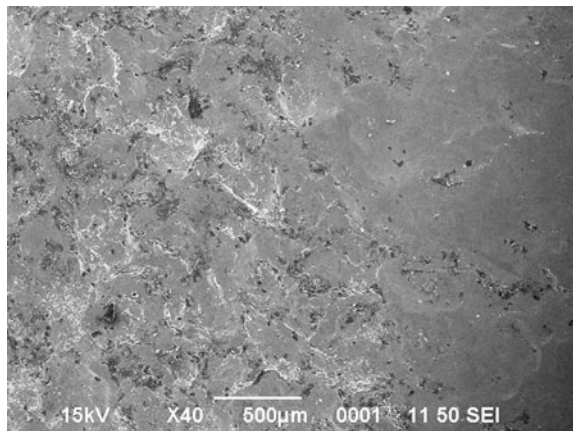


**Fig. 6** Microstructure of MS to SS welded specimen after shot peening



### 3 Results and Discussions

#### 3.1 *Effect of Shot Peening on Residual Stress*

The residual stress induced before and after shot peening of MS to MS and MS to SS specimens is shown in Tables 3 and 4 (Figs. 7 and 8).

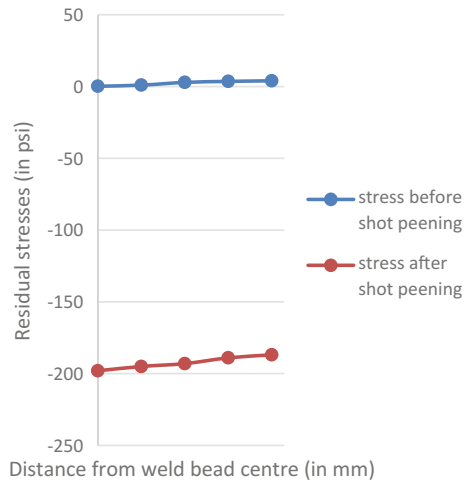
**Table 3** Experimental result of residual stress in MS to MS specimen before and after shot peening

S. No.	Distance from weld bead center (mm)	Stress before shot peening (Psi)	Stress after shot peening (Psi)
1	0	0.2	-198.0
2	1.16	1.0	-195.0
3	2.33	2.9	-193.0
4	3.49	3.6	-189.0
5	4.66	4.0	-186.9

**Table 4** Experimental result of residual stress in MS to SS specimen before and after shot peening

S. No.	Distance from weld bead center (mm)	Stress before shot peening (Psi)	Stress after shot peening (Psi)
1	0	0.15	-1000.0
2	1.16	1.1	-960.35
3	2.33	2.4	-930.5
4	3.49	3.1	-920.12
5	4.66	3.75	-910.8

**Fig. 7** Effect of shot peening on residual stress distribution for MS to MS



### 3.2 Effect of Shot Peening on Fatigue Life

The fatigue life of the specimens for load of 25 N and 2500 rpm, before and after shot peening of MS to MS and MS to SS specimens, is shown in Tables 5 and 6 (Figs. 9 and 10).

**Fig. 8** Effect of shot peening on residual stress distribution for MS to SS

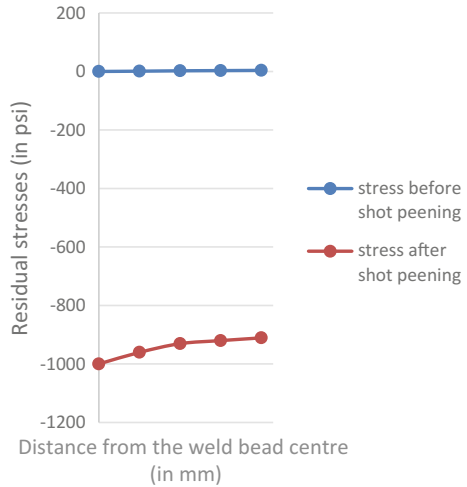


**Table 5** Experimental result of fatigue life of MS to MS specimen before and after shot peening

S. No.	Stress (MPa)	Number of cycles to failure before shot peening	Number of cycles to failure after shot peening
1	60	120,000	205,000
2	80	80,000	150,000
3	100	70,000	140,000
4	200	60,000	111,000

**Table 6** Experimental result of fatigue life of MS to SS specimen before and after shot peening

S. No.	Stress (MPa)	Number of cycles to failure before shot peening	Number of cycles to failure after shot peening
1	60	200,000	310,000
2	80	130,000	250,000
3	100	90,000	185,000
4	200	70,000	100,000

### 3.3 Effect of Shot Peening on Hardness

The shot peening is carried out for the specimen MS to MS and MS to SS. The hardness of the material before and after shot peening is shown in Tables 7 and 8.

It is seen that the material hardness increases by means of shot peening operation. Thus when a welded component undergoes shot peening operation, the residual tensile stress in the specimen reduces and compressive stress induced. The residual tensile stress reduces the hardness of material and material with high compressive stress has high hardness (Fig. 11).

**Fig. 9** Effect of shot peening on fatigue strength of welded joint for MS to MS

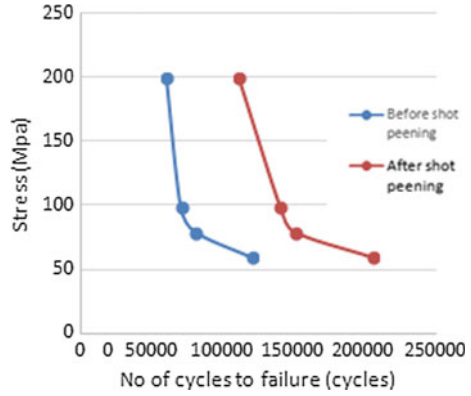


**Fig. 10** Effect of shot peening on fatigue strength of welded joint for MS to SS

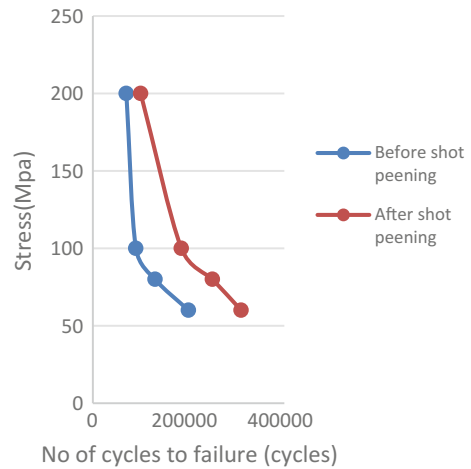


**Table 7** Experimental result of hardness on the heat-affected zone in the MS to MS specimen before and after shot peening

S. No.	Distance from weld bead center (mm)	Load (kgf)	Hardness before shot peening (HRC)	Hardness after shot peening (HRC)
1	0		42	53
2	1.16		44	56
3	2.33	60	48	60
4	3.49		51	61
5	4.66		52	63

It is evident from the table that the residual stress in the specimens before shot peening is positive, i.e., tensile stress but it becomes negative, i.e., compressive stress after shot peening. From Tables 3 and 4, it is evident that shot peening



**Table 8** Experimental result of hardness on the heat-affected zone in the MS to SS specimen before and after shot peening

S. No.	Distance from weld bead center (mm)	Load (kgf)	Hardness before shot peening (HRC)	Hardness after shot peening (HRC)
1	0		47	55
2	1.16		51	57
3	2.33	60	53	59
4	3.49		54	63
5	4.66		57	65

**Fig. 11** Effect of shot peening on hardness distribution for MS to MS

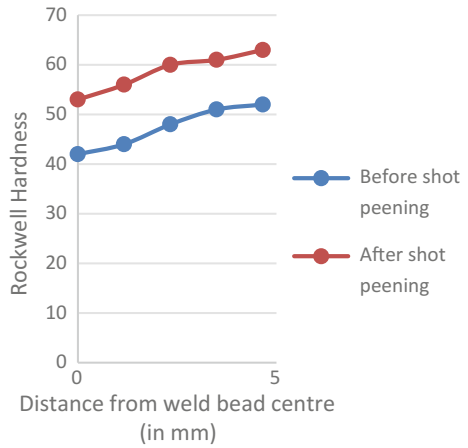
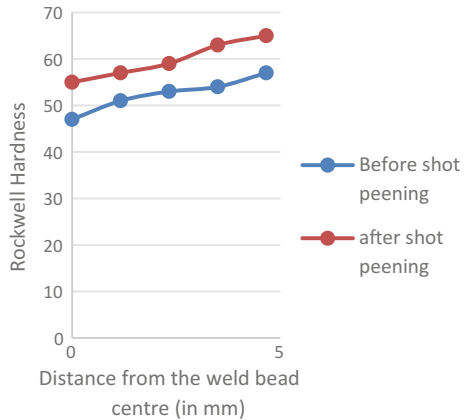


**Fig. 12** Effect of shot peening on hardness distribution for MS to SS



reduces the residual tensile stress and induces residual compressive stresses in the weld specimens.

Tables 5 and 6 show that the fatigue life of component increases after the shot peening process. Also, the fatigue life of MS to SS specimen is greater than that of MS to MS specimen before and after shot peening process. The fatigue life of the welded specimen has increased by 28.97% in the case of MS to MS welded joint and by 12.31% in the case of MS to SS welded joint.

It can be inferred from these results that the fatigue life of the specimen is greatly improved due to residual stresses induced by shot peening process, and thus components subjected to compressive residual stresses will exhibit increased fatigue life (Fig. 12).

## 4 Conclusions

Conclusions drawn based on the results obtained from experimental and numerical methods are summarized as follows:

1. The residual tensile stresses which are detrimental to fatigue life can be reduced by shot peening process.
2. The fatigue life of welded joint is improved significantly by subjecting it to shot peening process.
3. The durability of the welded joint increases when it is subjected to shot peening process.

## References

1. Molzen MS, Hornbach D Evaluation of welding residual stress levels through shot peening and heat treating
2. Chataigner S, Dieng L, Guit K, Grasset M (2013) Improving welded joint fatigue life using shot peening or grinding, France, Jan 2013
3. Hasegawa M, Suzuki H (2010) Improvement of the fatigue strength of aluminium alloy welded joints by high hardness and large specific gravity shot peening. *Weld Int* 19
4. Saini M, Arora N, Pandey C, Mehdi H (2014) Mechanical properties of bimetallic weld joint between sa 516 grade 65 carbon steel and SS 304 l for steam generator application
5. Cheng X, Prask HJ, Gnaeupel Herold T, Luzin V, Fisher JW Neutron diffraction measurements for residual stresses in AL-6XN stainless steel welded beams
6. (Johnny) Johnson MH Fatigue life improvement techniques for welds, Process Barron Alabama
7. Baptista R, Infante V, Branco CM Experimental and numerical analysis of fatigue life improvement techniques in welded joints of stainless steels, Lisbon, Portugal

# Fatigue Life Prediction of Spot Welded Joints: A Review

Vipin Wagare

**Abstract** Resistance spot welding (RSW) is a major sheet metal joining process. It is widely used in many industries, such as the automotive, aircraft and spacecraft industries. Resistance spot welding (RSW) is dominant joining method which is very complicated process including close interaction of electrical, thermal, mechanical, and metallurgical phenomena. In the present automobile sector, vehicle contains about 4000–5000 spot welded joints, which has been subjected to continuous variable type loading condition. The life and structural integrity of this spot welded joints depends on many parameters. This is a review work that looks into the fatigue behavior of spot welded tensile lap shear specimen under cyclic loading condition. The main objective is to study the effects of different processes, designs, material parameters on the fatigue behavior of spot welded joints. The design parameters of spot welded lap specimens like distance between spot, number of spots as well as process parameters like nugget diameter weld time, electric current, etc., are varied and the effects on the structural integrity and fatigue behavior of spot weld joints have been observed.

**Keywords** Fatigue life · Fatigue damage · Strain life criterion  
Cycles to crack initiation

## 1 Introduction

Spot welding is one among the oldest welding processes. It is a kind of resistance welding that could be a methodology of welding two or a lot of metal sheets along while not victimizing any filler material by applying pressure and heat to the world to be welded. Resistance spot welding could be a widely used connection method for fabricating sheet assemblies like vehicles, truck cabins, rail vehicles and residential applications as a result of its blessings in welding efficiency and quality for

---

V. Wagare (✉)

Department of Mechanical, AISSMS College of Engineering, Pune 411001, India  
e-mail: wagarevipin@gmail.com

© Springer Nature Singapore Pte Ltd. 2018

S. Seetharamu et al. (eds.), *Proceedings of Fatigue, Durability and Fracture Mechanics*, Lecture Notes

in Mechanical Engineering, [https://doi.org/10.1007/978-981-10-6002-1\\_36](https://doi.org/10.1007/978-981-10-6002-1_36)

automation. As an example, a contemporary automotive body assembly wants 8000–10,000 spots of welding.

So it is required to look at the weight reduction of car and improve the fuel economy as well as to reduce exhaust emission gases by the use of lightweight materials like aluminum alloys. Aluminum alloys have applications in designed vehicles, trunks and doors.

The objective of this study is to review the knowledge about the influencing design, process and fatigue parameters on the fatigue life of spot welded specimen, and numerical techniques for fatigue life calculation and to discuss the future trends in spot welding to improve its joint strength and life.

Sohn [1] proposed the best method to determine fatigue design criteria for spot welded joint specimen of specific geometry details and materials. The method has been verified by the theory of Weibull probability distribution since fatigue strength of the spot weld affects structural rigidity and durability of the spot welded structures; safety and structural integrity of the structure are determined by fatigue strength of spot welded joint.

Therefore, correct stress analysis and systematical fatigue strength analysis of spot welded joint area unit important to work out its long fatigue design criterion. However, it is terribly troublesome to workout the fatigue design criterion with the particular structure directly. Thus, when estimating fatigue strength with simulated specimen satisfying the structural characteristic of the particular structures, the fatigue design criterion is mostly determined and applied to fatigue design of the spot welded structures.

Rahman [2] conducted the parametric studies of design parameter of spot weld on fatigue life of joint. It has been predicted as position of the weakest weld nugget during variable amplitude loading condition.

Ahmet [3] has investigated the fatigue lives of spot welded lap shear specimen which is made of low carbon steel under variable amplitude load condition. Experimental fatigue testing has been carried out for two types of resistance welding, i.e., manual type and automated type. The virtual testing simulation work has been carried out using commercial CAE tool and parametric study performed on fatigue lives of spot weld joint using coffin monsoon, morrows means stress models.

Gean [4] has conducted static and fatigue experimental testing of 1.2-mm aluminum alloy. Extensive work has been done, and investigated nuggets porosity, surface indentation, nugget size have no major effect on fatigue life of spot weld joint.

Spot welding is widely used sheet metal joining method in automobile sector because of its speed of welding, spot precision, efficiency and cost reductions. The spot welding process is used to join sheet materials using copper electrode and apply pressure with electrical current through the worksheet. In these steps during the current flow, the parts locally get heated and the material volume in-between the electrodes is yielded and squeezed and then it melts, destroying the interface between the worksheets. When the electric current supply has been switched off, the “nugget” of molten materials is formed. The material is with having high electrical

resistivity and low thermal conductivity than the electrode used is suitable to choose such as steel because it making welding relatively easy. For another material such as aluminum, its electrical resistance and thermal conduction is nearer to that of copper; however, the melting point for this material is less than copper, so creating a weld is feasible (Kalpakjian et al.). In the spot welding, some of its parameters need to be thought about. These parameters can have an effect on the standard of the spot welds and its strength. The right combination of the spot welding parameter can manufacture a robust connection kind of joint. Spot welding parameters include:

- (1) Electrode force
- (2) Diameter of the electrode contact surface
- (3) Squeeze time
- (4) Weld time
- (5) Hold time
- (6) Weld current

The fatigue strength of the joint during this method depends on the quantity and size of spot welded structure of the welds. The diameters for spot weld vary from 3 to 12.5 mm (Milleer 2004). To analyze the strength of spot welds in terms of the specimen pure mathematics, attachment parameter, attachment schedule, base metal strength, checking speed and testing configuration, the tensile test methodology can also be used to analyze the strength of the spot weld.

## 2 Models for Fatigue Life Assessment

Different fatigue life prediction techniques have been suggested in the literature. They are classified on the basis of strain- and stress-based approaches in general.

- *Stress-Based Approaches*

These are the earliest, but the most widely used approaches. They are based on the assumption that the range of values for stress controls the fatigue behavior of a component. They involve empirical relations between uniaxial fully reversed stress and fatigue life ( $S-N$  curves), which are obtained through the standard rotating bending testing. However, mechanical components are usually subject to stresses oscillating about an average stress level. For these cases, a number of models were proposed [5–9, 20–25]:

$$\frac{S_a}{S_f} + \frac{S_m}{S_{ut}} = 1 \text{ (Modified Goodman, England-1899)}$$

$$\frac{S_a}{S_f} + \frac{S_m}{\sigma_f} = 1 \text{ (Morrow, USA-1960s)}$$

where  $S_a$  is the alternating stress,  $S_m$  is the mean stress,  $S_f$  is the fully reversed fatigue strength of the specimen,  $S_{ut}$  is the ultimate tensile strength. There is a controversy on how the equivalent stress should be calculated. Use of the maximum principal stress

$$S_{ea} = \sigma_{a1}$$

maximum shear stress

$$S_{ea} = \sigma_{a1} - \sigma_{a3}$$

or von Mises stress

$$S_{ea} = \frac{1}{\sqrt{2}} \sqrt{(\sigma_{a1} - \sigma_{a2})^2 + (\sigma_{a1} - \sigma_{a3})^2 + (\sigma_{a2} - \sigma_{a3})^2}$$

was suggested as representative of equivalent alternating stress,  $S_{ea}$ . Here,  $\sigma_{a1}$ ,  $\sigma_{a2}$  and  $\sigma_{a3}$  are principal alternating nominal stresses with  $\sigma_{a1} > \sigma_{a2} > \sigma_{a3}$ . For equivalent mean stress,  $\sigma_{em}$ , similar suggestions were made [26]. For example, use of von Mises stress

$$S_{em} = \frac{1}{\sqrt{2}} \sqrt{(\sigma_{m1} - \sigma_{m2})^2 + (\sigma_{m1} - \sigma_{m3})^2 + (\sigma_{m2} - \sigma_{m3})^2}$$

or sum of the normal mean stresses

$$S_{em} = \sigma_{m1} + \sigma_{m2} + \sigma_{m3} = \sigma_{mx} + \sigma_{my} + \sigma_{mz}$$

was suggested as representative of equivalent mean stress,  $S_{em}$  [26]. Equivalent stress approaches are extensions of the yield criteria to fatigue.

- *Strain-Based Approaches*

According to these models, the range of values for strain controls fatigue life. They also take into account the effect of plastic strain. They are therefore especially suitable for cases where plastic effects dominate fatigue behavior. Although most engineering structures are designed such that the nominal stresses stay elastic, stress concentrations typically cause plastic strains to develop within the locality of notches, e.g., spot welds in our case. Fatigue cracks usually nucleate due to plastic straining at the notches. The total strain amplitude is resolved into elastic and plastic strain elements, all of that was shown to be correlative with fatigue life in an exceedingly linear fashion victimization log-log scale for many metals [7].

One method, referred to as ‘‘Morrow’s mean stress method,’’ can be written as [10, 24, 26],

$$\frac{\Delta \epsilon}{2} = \epsilon_a = \frac{\Delta \epsilon_e}{2} + \frac{\Delta \epsilon_p}{2} = \frac{\sigma'_f - \sigma_m}{E} (2N_f)^b + \epsilon' (2N_f)^c$$

where  $\sigma'_f$  is the fatigue strength coefficient,  $\epsilon'_f$  is the fatigue ductility coefficient,  $b$  and  $c$  are exponents determined by experiments, and  $\sigma_m$  is the mean stress.

In the case of multiaxial stress and strain state, equivalent alternating strain is calculated [7, 9, 21] using either maximum principal strain

$$\epsilon_{qa} = \epsilon_{a1}$$

or maximum shear strain

$$\epsilon_{qa} = \frac{\epsilon_{a1} - \epsilon_{a3}}{1 + \nu}$$

or octahedral shear strain

$$\epsilon_{qa} = \frac{\sqrt{(\epsilon_{a1} - \epsilon_{a2})^2 + (\epsilon_{a2} - \epsilon_{a3})^2 + (\epsilon_{a3} - \epsilon_{a1})^2}}{\sqrt{2}(1 + \nu)}$$

where  $\epsilon_{a1}$ ,  $\epsilon_{a2}$  and  $\epsilon_{a3}$  are principal alternating strains with  $\epsilon_{a1} > \epsilon_{a2} > \epsilon_{a3}$ .

One more equation derived by Smith, Watson, and Topper (often called “SWT parameter”) is given by [6, 20, 21],

$$\sigma_{\max} \epsilon_a E = (\sigma'_f)^2 (2N_f)^{2b} + \sigma'_f \epsilon'_f E (2N_f)^{b+c}$$

In addition to these equations, there are two more universal relations which are used in fatigue life calculations proposed in the literature based on the experimental data. These relations are “Muralidharan and Manson” and “Brinell hardness” equations written as the following.

$$\frac{\Delta \epsilon}{2} = \epsilon_a = 0.623 \left( \frac{S_{ut}}{E} \right)^{0.832} (2N_f)^{-0.09} + 0.0196 (\epsilon_f)^{0.155} \left( \frac{S_{ut}}{E} \right)^{-0.53} (2N_f)^{-0.56}.$$

### 3 Design and Process Parameters

#### 3.1 Specimen Thickness and Nugget Diameter

Figure 1 shows the result of the sheet thickness and spot diameter on the fatigue lifetime of the spot weld structure. Spot weld diameter of 2.5–8.5 mm and sheet thickness for one and a couple of zero. From 2 to 1.2 mm are thought of during this study, the spot weld diameter and therefore the thickness of the sheet metals

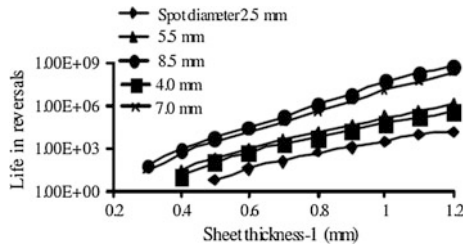


Fig. 1 Effect of the sheet thickness

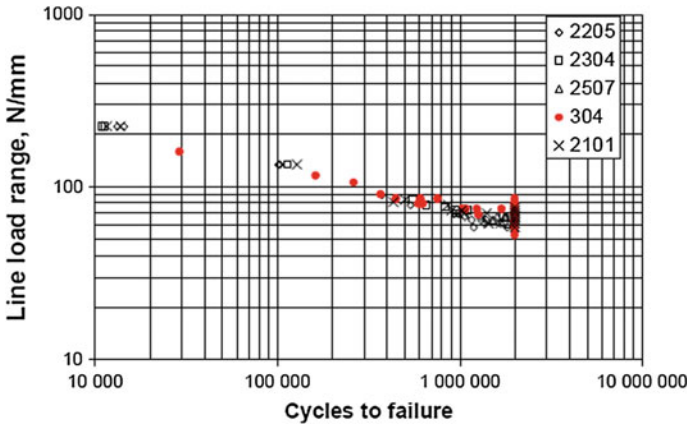


Fig. 2 Effect of the sheet thickness

influences the fatigue lifetime of the structure. It is discovered that the fatigue lifetime of the structure will increase with the increase in the spot weld diameter and thickness of the sheet. Increase in shear strength may be stopped with the increase in sheet thickness. Less thickness sheet probably failed in pull-out-type failure mode during testing. It is observed that there is gradual increase in strength after the thickness of sheet is increased. Because of more thickness, more surface contact area is formed in-between the weld and specimen. The strength of spot weld joint increases as the diameter of nugget significantly increase in strength of spot weld joint. It occurs because more nugget diameter contains more volume of metal which is nothing but more surfaces in joint so more shear strength obtained. In graph smooth linear curve has been obtained from experiment. So, we can say that by the increase in nugget diameter we can also increase the shear strength of spot weld joint (Fig. 2).



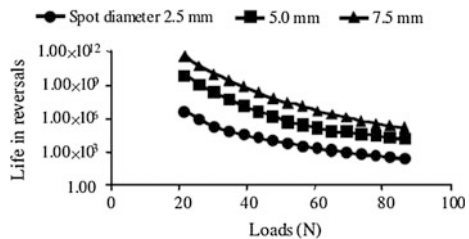
### 3.2 Effect of Material Strength

Linder and his colleagues [11–13] have studied the spot welded joint with explicit relevancy fatigue characteristic. A separate study by Marples [10] is additionally according during this section. Three completely different joint configurations (test specimen types) are studied as shown in Fig. 3. Nord [4] has tested spot and projection welded 1.5-mm temper-rolled AISI 301 employing a forty six-millimeter-wide sort 3 specimen. Yield and tensile strengths were 1072 and 1391 MPa severally. The amount of specimens tested for every series of spot welded joints was depleted for a calculation of confidence limits and however brought along as in Fig. 8; the fatigue strength at  $2 \times 10^6$  cycles will be calculable to be 1.68 kN or 70 N/mm, forward a 24-mm pitch. The uncertainty is calculable as  $\pm 10$  N/mm. Lump size was 6.4 mm. For a smaller lump size, 5.3 mm, the fatigue strength is reduced; however, looking at series it was too tiny to make sure a big distinction. These results are almost like those of the medium-strength AISI 304 on top of the Ueda and Kawataka [12]-tested single row, multiple spot joints of 1.5-mm-thick AISI 301. The fatigue testing was done on a 120-mm-wide specimen with 35-mm overlap and 192-mm grip distance. Over the breadth, a pair of, 3, 4, 6 and 12 nuggets with 7 mm diameter were welded. This resulted in pitch distances of 60, 40, 30, 20 and 10 mm. The results are shown in Fig. 12. It has been shown many times that fatigue properties for joints in steel sheets with completely different parent material strengths are similar. This is often illustrated in Fig. 16 to be the case even for untainted steels. In this figure, the fatigue results for various untainted steels with yield strengths within 290 and 725 MPa are compared. For spherical clenched joints, there are indications that accumulated strength results in accumulated fatigue strength; however, at intervals a restricted vary since use of the clinching method set limitations on the clinch ability of thicker material.

### 3.3 Effects of the Loads

Figure 3 shows the consequences of the masses and confidence of survival on the fatigue life on the spot weld structure. From the obtained results, it is often seen from Fig. 11 that the fatigue life decreases linearly with the increase in hundreds;

**Fig. 3** Effect of the sheet thickness



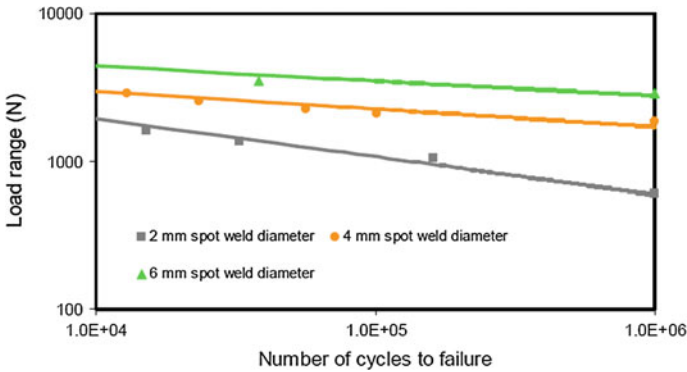


Fig. 4 Fatigue lives predicted using “Coffin and Manson’s approach” for TS specimen [3]

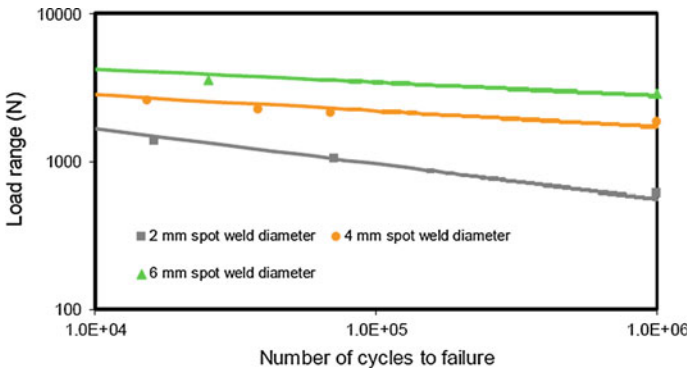


Fig. 5 Fatigue lives predicted using “Morrow’s mean stress approach” for TS specimen [3]

however, the fatigue life increases with the increase in spot weld diameter. The obtained results from Fig. 12 clearly show that the fatigue life influences the arrangement of survival parameter that is predicated on the quality error of the  $S-N$  curves.

### 3.4 Distance Between Two Spot

It is observed that as the distance between two spots is increased the curve linearly increases and shear strength of weld is increased. In our experiment, distance between two spots varies from 9 to 13 mm. As the distance between spot weld joints increases, there is after certain limit a decrease in strength because bending action takes place and failure occurs. Above given distances are least it means if less distance then there will be overlapping of the nugget diameter which affect

strength of weld and if more than upper then decrease In lap shear strength of spot weld joints.

### ***3.5 Effect of Corrosive Field***

The result of a corrosive (3% NaCl aqueous) setting on the fatigue properties of spot welded AISI 304 and duplex SAF 2304 chrome steel is reportable by Linder and Melander [14]. The study was created on four metric linear unit sheet material victimization specimens sort one at close temperature and 50 cps. In the fatigue testing, the run-out was set at 107 cycles, and therefore, the testing time was up to 60 h. Result of testing setting. Testing in aggressive third common salt setting reduces the fatigue strength of spot welded AISI 304 chrome steel joints at long lives by up to four-hundredth. Exposure of up to 2000 h before testing failed to have more effect on the fatigue strength. Though not tested a similar response is anticipated for tight joints and optical maser welded joints. Unblemished to galvanized steel joints have not been tested in aggressive environments; however, area unit is expected to be terribly sensitive owing to galvanic corrosion. Connection ways. Spot welded and projection welded joints show similar fatigue strengths. Within the thickness from 0.8 to 1.5 metric linear unit spot attachment, optical maser attachment and adhesive bonding have similar fatigues strength, 70 N/mm. Dry setting adhesive bonding and combination of spot attachment and adhesives have potential to present very high fatigue strengths compared with spot attachment. The result of adhesives is larger for thicker materials. At around one metric linear unit, thickness spot attachment and rectangular clinches offer similar fatigue strengths, generally 1.2 kN per lump or clinch. Spherical clinches offer some double this fatigue strength.

### ***3.6 Numerical Modeling***

In the FE model, a 3D 10-node tetrahedral solid part, SOLID92, was used for the bottom metal [3]. This part has physical property, stress stiffening, massive deflection and huge strain capabilities. On the other hand, the nugget was sculptured employing a two-node beam part, BEAM188. Contact and target parts, Targe170 and Conta175, were created on the inner surfaces of the plates round the spots. The beam part, BEAM188, is predicated on Timoshenko beam theory. Shear deformation effects are thus enclosed that are particularly vital for brief beams. This part has six degrees of freedom at every node. As a result of the nugget experiencing low stresses, its material model was chosen as linearly elastic. In welding method, heat treatment does not have an effect on the mechanical properties of the fabric. Therefore, it is necessary to use identical material properties for the hunk and base metal. Hence during this study, base metal and spot weld hunk square measure

modeled victimization identical material properties that young's modulus and poisson's quantitative relation as  $2.07E5$  Mpa and 0.25, respectively [3]. First, the strain and strain values of the essential nodes of spot welded MTS and TS for various spot weld diameters were calculated employing a nonlinear finite component analysis (FEM). Once these calculations were done, it was clear that a stress concentration or singularity exists at the interception of the hunk boundary with the interface of joined sheets as a result of all von Misses stresses, tensile stresses, bending stresses, etc., having their most magnitudes close to the hunk boundary (that is the inner surfaces of flanged or center items of TS specimens on the peripheries of the spots). These stress distributions make a case for with success the development that why the fractures square measure usually initial created round the nugget for the spot welded joints. Peak tensile stress values on  $x$ ,  $y$  and  $z$  directions were found at the inner edges of the spot welds, whereas peak compression stress values were found at the external edges of the spot welds. Thence, it may be aforesaid that the high tensile stresses along with the high tearing stresses square measured all settled at the perimeters of the spot welds within the spot welded joints and can cause bending of the lap zones of the specimens though this bending values in tensile shear specimens (TS) do not seem to be therefore essential. Using differing kinds of fatigue life prediction techniques, typical spot weld fatigue results for various pure mathematics and spot weld diameters are given through Figs. 4 and 5[3].

## 4 Conclusion

The fatigue life of the spot welded specimens depended most importantly on the kind of specimen, applied load amplitudes and off beam the spot weld diameter. The behavior of diameter of spot weld and sheet thicknesses are important parameters in stress distribution close to spot welds. The uninheritable results show that the spot diameter and thickness of the sheets greatly influence the fatigue lifetime of the spot welded structures. The results of the loading and geometric configuration on the fatigue lifetime of spot welded joints may be directly incorporated within the structural stress methodology. Equivalent stress approaches have been commonly used because of their simplicity, but their success in correlating multiracial fatigue data has been limited to a few materials and loading conditions. In addition, they should be used only for proportional loading conditions, in which the principal axes directions remain fixed during the loading cycle. It is familiar that the failure modes for tensile and changed tensile loading cases depended totally on the magnitude of the applied mean load and therefore the nugget diameter. It absolutely was determined that the amplitude of the applied load seems less of an impact on the ultimate failure mode, though this had a major result on the specimen fatigue life.

## References

1. Sohn I, Bae D (2000) A study on the fatigue life prediction method of the spot-welded lap joint. Seoul 2000 FISITA World Automotive Congress
2. Rahman MM, Rosli AB, Noor MM, Sani MSM, Julie JM (2009) Effects of spot diameter and sheets thickness on fatigue life of spot welded structure based on FEA approach. *Am J Appl Sci* 6(1):137–142
3. Ertas AH, Sonmez FO (2007) A parametric study on fatigue life behavior of spot welded joints. In: Proceedings of 8th international fracture conference. Istanbul, Turkey, 7–9 Nov 2007
4. Gean A, Westgate SA, Kucza JC, Ehrstrom JC Static and fatigue behavior of spot-welded -0 aluminum alloy sheet
5. Davidson JA (1982) A review of the fatigue properties of spot-welded sheet steels. SAE International Congress and Exposition, Detroit, MI
6. Dannbauer H, Gaier C, Hofwimmer K (2005) Fatigue analysis of welding seams and spot joints in automotive structures. SAE International Congress and Exposition, Detroit, MI
7. Adib H, Gilbert J, Pluvinage G (2004) Fatigue life duration prediction for welded spots by volumetric method. *Int J Fatigue* 26:81–94
8. Hou Z, Wang Y, Li C, Chen C (2006) An analysis of resistance spot welding. *Weld J (Miami, FL, U.S.)* 85(3):36–40
9. Socie DF (1977) Fatigue-life prediction using local stress-strain concepts. *Exp Mech* 17:50–56
10. Kan YR (1976) Fatigue resistance of spotwelds—an analytical study. *Met Eng Q* 16(4):26–36
11. Linder J, Thuvander A, Melander A, Gustavsson A, Bergengren Y (1997) A finite element study of spot welded stainless sheet steels. Swedish Institute for Metals Research, Report IM-3475
12. Linder J, Melander A, Larsson M, Bergengren Y (1998) Fatigue data and design methods for spot welded austenitic and duplex stainless sheet steels. In: *Stainless steels in transport industry*. Espoo, Finland
13. Linder J, Melander A, Larsson M, Bergengren Y Fatigue design of spot welded austenitic and duplex stainless steels. *Fatigue Fract Eng*
14. Pan N (2000) Fatigue life study of spot welds, Ph.D. thesis. Stanford University, Stanford, CA
15. Nordberg H (2005) Fatigue properties of stainless steel lap joints. 2005 SAE International
16. Gero BM (1997) Acousto-ultrasonic evaluation of cyclic fatigue of spot welded structures, MS thesis. Virginia Polytechnic Institute and State University, Blacksburg, VA
17. Ertas AH (2004) Fatigue behavior of spot welds, MS thesis. Bogazici University, Istanbul, Turkey
18. El-Sayed MEM, Stawiarski T, Fruntiger R (1996) Fatigue analysis of spot-welded joints under variable amplitude load history. *Eng Fract Mech* 55(3):363–369

# Crystal Orientation Effect on SIF in Single Crystals: A Study Based on Coupled Framework of XFEM and Crystal Plasticity Model

Rajwinder Singh and Dhiraj K. Mahajan

**Abstract** A coupled framework of extended finite element method (XFEM) and crystal plasticity (CP) is proposed for investigating the effect of crystal orientation on Mode I stress intensity factor (SIF) in pre-cracked single crystals. While XFEM is used to evaluate the local displacement fields in front of the crack tip, CP provides anisotropic material response in front of the crack tip. Three different orientations of single crystal nickel with and without crack having Euler angles  $(0^\circ, 0^\circ, 0^\circ)$ ,  $(30^\circ, 0^\circ, 0^\circ)$  and  $(45^\circ, 0^\circ, 0^\circ)$  are investigated using the proposed framework. The lattice orientation highly influences the activation of slip system, which consequently results in the change in cumulative plastic slip. Under the action of similar applied displacement loading, higher stresses are observed in  $(45^\circ, 0^\circ, 0^\circ)$  oriented cracked and uncracked single nickel crystal followed by  $(30^\circ, 0^\circ, 0^\circ)$  and  $(0^\circ, 0^\circ, 0^\circ)$  lattice orientations. The proposed framework can be extended to study the short fatigue crack propagation in polycrystalline metals which is highly influenced by local microstructural features such as grain orientation, grain boundaries, phase difference and inclusions.

**Keywords** XFEM · Crystal plasticity · Crystal orientation · Crack Stress intensity factor

## 1 Introduction

About 75% of the component's fatigue life is spent in stage 1 of fatigue crack propagation which is associated with crack initiation and propagation phase of microstructurally short cracks. These microstructurally short cracks are of the order of grain size of the material [1]. Under the action of cycling loading, these short cracks propagate along high shear planes at higher rate compared to long cracks as

---

R. Singh · D.K. Mahajan (✉)

Department of Mechanical Engineering, Indian Institute of Technology Ropar,  
Rupnagar 140001, Punjab, India  
e-mail: dhiraj.mahajan@iitrpr.ac.in

© Springer Nature Singapore Pte Ltd. 2018

S. Seetharamu et al. (eds.), *Proceedings of Fatigue, Durability and Fracture Mechanics*, Lecture Notes

in Mechanical Engineering, [https://doi.org/10.1007/978-981-10-6002-1\\_37](https://doi.org/10.1007/978-981-10-6002-1_37)

they are less prone to crack closure effect [2]. In addition, these short cracks start propagating at much lower value of stress intensity factor range ( $\Delta K$ ) compared to threshold value ( $\Delta K_{th}$ ) defined for long cracks [3]. It is therefore important to study short crack growth behavior as crack growth laws defined for long cracks are not valid in short crack regime [4]. In short crack regime, the crack growth is highly influenced by the microstructural features of the material such as grain orientations, grain boundaries, phase difference and inclusions [3, 5, 6]. The growth rate of short cracks drops when they reach near the grain or phase boundaries [7]. The change in slip plane from one grain to another due to the difference in grains orientations results in zigzag pattern of short crack growth path [8, 9]. Experimental investigations have shown strong influence of crystal orientation on the stress intensity factor range [10]. The variation in grains orientations along the short crack growth direction may lead to acceleration or deceleration of growth rate. These microstructural features may also lead to the short crack arrest [11, 12]. The coupling of XFEM with CP will provide a promising modeling framework to study such short fatigue crack growth.

In this paper, a coupled framework of extended finite element method (XFEM) and crystal plasticity (CP) is introduced that can be used to study the effect of microstructure on short fatigue crack growth. While XFEM is used to evaluate the local displacement fields in front of the crack tip, CP provides anisotropic material response in front of the crack tip. The coupling of XFEM with CP will provide a promising modeling framework. The proposed framework is used for investigating the effect of crystal orientation on Mode I stress intensity factor (SIF) in a pre-cracked single crystal. For the sake of simplicity, the material being used for investigation is single crystal nickel bearing an FCC structure.

The paper is divided into six sections. Material modeling based on crystal plasticity formulation is discussed in Sect. 2. A brief introduction to XFEM formulation used for modeling discontinuities like sharp crack is given in Sect. 3. Simulation details such as model geometry, meshing and boundary conditions used in modeling single crystal nickel are explained in Sect. 4. The results, discussion and conclusion are included in Sects. 5 and 6 respectively. The tensors, vectors and scalars constituting the equations in this paper are represented by standard indicial notations. The quantities with four and two indexes in the subscript represent fourth- and second-order tensors, respectively. The quantities with single index in the subscript represent vectors and the quantities with no index represent scalars. Also, the quantities written in capital bold letters represent tensors, in small bold letters represent vectors and in unbold letters represent scalars.

## 2 Crystal Plasticity Based Material Modeling

The basis of kinematics of crystals is laid by Taylor, Hill, Rice and Asaro [13–18]. The theory of kinematics of crystal is discussed in Sect. 2.1. In single crystal, only crystallographic dislocations are assumed to cause the plastic deformation. Here,

resolved shear stress also called as Schmid stress is assumed to be responsible for slip movement.

### 2.1 Kinematics

Under the action of applied load, the crystal lattice undergoes elastic deformation, rigid body rotation and plastic deformation. The deformation gradient  $F_{ij}$  then can be decomposed into elastic component  $F_{ik}^e$  and plastic component  $F_{kj}^p$  as

$$F_{ij} = F_{ik}^e F_{kj}^p \tag{1}$$

where the lattice stretching as well as lattice rotation are given by the elastic component and plastic deformation caused by crystalline slip is given by the plastic component. The elastic-plastic deformation of crystal is illustrated in Fig. 1.

The deformation and rotation of crystal lead to the stretching and rotation of lattice vectors. The orientation of unit vector of the slip direction  $\mathbf{s}^{(\alpha)}$  and unit vector of the normal to the slip plane  $\mathbf{m}^{(\alpha)}$  of the  $\alpha$ th slip system in deformed configuration can be written as

$$s_i^{*(\alpha)} = F_{ij}^e s_j^{(\alpha)} \tag{2}$$

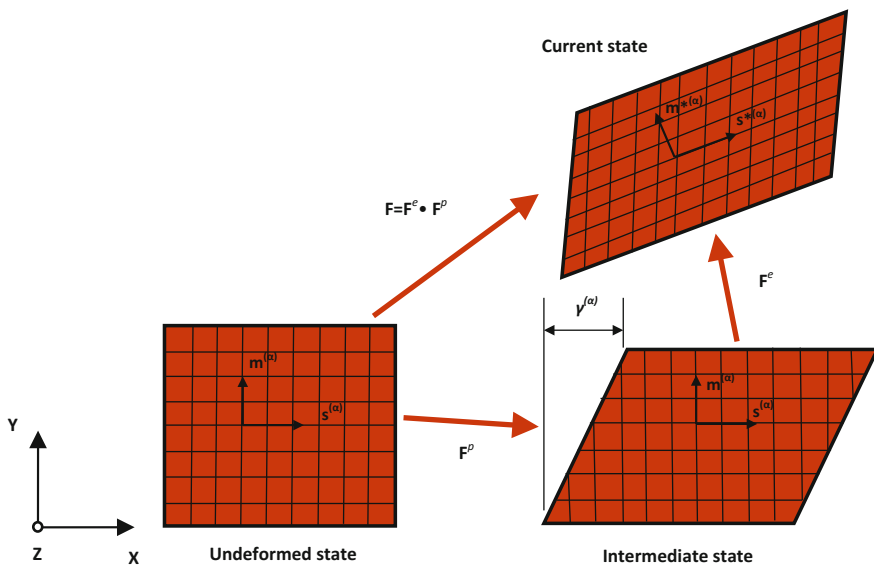


**Fig. 1** Schematic representation of elastic-plastic deformation in single crystal caused by crystalline slip



$$m_j^{*(\alpha)} = m_j^{(\alpha)} F_{ij}^{e-1} \quad (3)$$

In the current state, the standard formula for velocity gradient  $\mathbf{L}$  can be written as

$$L_{ij} = \dot{F}_{ik} F_{kj}^{-1} = F_{ik}^e F_{kj}^{e-1} + F_{ik}^e \dot{F}_{km}^p F_{ml}^{p-1} F_{lj}^{e-1} \quad (4)$$

The velocity gradient  $\mathbf{L}$  can be split into symmetric and antisymmetric components. The symmetric part represents rate of deformation  $\mathbf{D}$ , while the antisymmetric part represents the continuum spin  $\mathbf{W}$ . The velocity gradient  $\mathbf{L}$  then can be decomposed as

$$L_{ij} = D_{ij} + W_{ij} = \left( D_{ij}^e + D_{ij}^p \right) + \left( W_{ij}^e + W_{ij}^p \right) \quad (5)$$

Since it is assumed that only crystalline slip is responsible for plastic deformation, therefore in current state the plastic part of velocity gradient  $\mathbf{L}^p$  can be defined as

$$L_{ij}^p = D_{ij}^p + W_{ij}^p = \sum_{\alpha} \dot{\gamma}^{(\alpha)} s_i^{*(\alpha)} m_j^{*(\alpha)} \quad (6)$$

where  $\dot{\gamma}^{(\alpha)}$  is the slipping rate on all the slip systems. For every slip system, we can define the Schmid tensor  $\mu_{ij}^{(\alpha)}$  and tensor  $\omega_{ij}^{(\alpha)}$  as

$$\mu_{ij}^{(\alpha)} = \frac{1}{2} \left( s_i^{*(\alpha)} m_j^{*(\alpha)} + s_j^{*(\alpha)} m_i^{*(\alpha)} \right) \quad (7)$$

$$\omega_{ij}^{(\alpha)} = \frac{1}{2} \left( s_i^{*(\alpha)} m_j^{*(\alpha)} - s_j^{*(\alpha)} m_i^{*(\alpha)} \right) \quad (8)$$

The plastic part of deformation rate and continuum spin can be defined as

$$D_{ij}^p = \sum_{\alpha} \dot{\gamma}^{(\alpha)} \mu_{ij}^{(\alpha)} \quad (9)$$

$$W_{ij}^p = \sum_{\alpha} \dot{\gamma}^{(\alpha)} \omega_{ij}^{(\alpha)} \quad (10)$$

## 2.2 Constitutive Laws

Hill and Rice [16] established the crystal elastic law for large deformation as

$$\overset{\nabla}{\boldsymbol{\sigma}} + \boldsymbol{\sigma} \text{tr}(\mathbf{D}^e) = \mathbf{L} : \mathbf{D}^e \quad (11)$$

where  $\mathbf{L}$  is the elastic moduli fourth-order tensor and  $\overset{\nabla}{\boldsymbol{\sigma}}$  is the material Jaumann rate of stress which is the corotational stress rate formed on axes that rotate with the crystal lattice. The Jaumann rate  $\overset{\nabla}{\boldsymbol{\sigma}}$  is related to the Cauchy stress rate  $\dot{\boldsymbol{\sigma}}$  as

$$\overset{\nabla}{\sigma}_{ij} = \dot{\sigma}_{ij} - W_{ik}^e \sigma_{kj} + \sigma_{ik} W_{kj}^e \quad (13)$$

The resolved shear stress or Schmid stress  $\tau^{(\alpha)}$  can be defined for slip system  $\alpha$  as

$$\tau^{(\alpha)} = \mu_{ij}^{(\alpha)} \sigma_{ij} \quad (14)$$

Asaro [18] derived the relation between rate of change of Schmid stress  $\Delta\tau^{(\alpha)}$  and strain increment  $\Delta\varepsilon_{ij}$  as

$$\Delta\tau^{(\alpha)} = \left[ L_{ijkl} \Delta\varepsilon_{kl} + \omega_{ik}^{(\alpha)} \sigma_{jk} + \omega_{jk}^{(\alpha)} \sigma_{ik} \right] \left[ \Delta\varepsilon_{ij} - \sum_{\beta} \mu_{ij}^{(\beta)} \Delta\gamma^{(\beta)} \right] \quad (15)$$

The increment of corotational stress  $\Delta\sigma_{ij}$  is given by

$$\Delta\sigma_{ij} = L_{ijkl} \Delta\varepsilon_{kl} - \sigma_{ij} \Delta\varepsilon_{kk} - \sum_{\alpha} \left[ L_{ijkl} \mu_{kl}^{(\alpha)} + \omega_{ik}^{(\alpha)} \sigma_{jk} + \omega_{jk}^{(\alpha)} \sigma_{ik} \right] \Delta\gamma^{(\alpha)} \quad (16)$$

The Jacobian matrix,  $J_{ijkl} = \partial\Delta\sigma_{ij} / \partial\Delta\varepsilon_{kl}$  can be evaluated from Eq. (16) as

$$J_{ijkl} = L_{ijmn} \delta_{mk} \delta_{nl} - \sigma_{ij} \delta_{mk} \delta_{ml} - \sum_{\alpha} \left[ L_{ijmn} \mu_{mn}^{(\alpha)} + \omega_{im}^{(\alpha)} \sigma_{jm} + \omega_{jm}^{(\alpha)} \sigma_{im} \right] \frac{\partial\Delta\gamma^{(\alpha)}}{\partial\Delta\varepsilon_{kl}} \quad (17)$$

where  $\delta$  is the Kronecker delta.

### 2.3 Hardening Law

Based on Hutchinson simple power law for polycrystalline creep [19], the slipping rate of the  $\alpha$ th slip system in a rate-dependent crystalline solid is determined by the corresponding Schmid stress or resolved shear stress  $\tau^{(\alpha)}$  as given by Eq. (18). It is assumed that the yielding will occur when the Schmid stress becomes greater than the current critical shear stress  $g^{(\alpha)}$ .

$$\dot{\gamma}^{(\alpha)} = \dot{a}^{(\alpha)} \left( \frac{\tau^{(\alpha)}}{g^{(\alpha)}} \right) \left( \left| \frac{\tau^{(\alpha)}}{g^{(\alpha)}} \right| \right)^{n-1} \quad (18)$$

where  $\dot{a}^{(\alpha)}$  is reference strain rate,  $n$  is the strain rate sensitivity parameter and  $g^{(\alpha)}$  is the current strain hardening state of the crystal.

$$\dot{g}^{(\alpha)} = \sum_{\beta} h_{\alpha\beta} \dot{\gamma}^{(\beta)} \quad (19)$$

where  $h_{\alpha\beta}$  are the slip hardening moduli.

The hardening law proposed by Pierce et al. [20] and Asaro [18] is implemented in the current formulation. They defined the self hardening and latent hardening moduli as

$$h_{\alpha\alpha} = h(\gamma) = h_o \sec h^2 \left| \frac{h_o \gamma}{\tau_s - \tau_o} \right| \quad (20)$$

$$h_{\alpha\beta} = qh(\gamma), (\alpha \neq \beta) \quad (21)$$

where  $h_o$  is initial hardening modulus,  $\tau_s$  is saturation stress,  $\tau_o$  is initial critical resolved shear stress,  $q$  is the hardening factor, and  $\gamma$  is the cumulative slip which is defined as

$$\gamma = \sum_{\alpha} \int_0^t |\dot{\gamma}^{(\alpha)}| dt. \quad (22)$$

### 3 Extended Finite Element Method (XFEM)

By using XFEM, the discontinuities like sharp cracks in a body can be modeled efficiently. In XFEM, the nodes of the elements that contain the crack are enriched by providing additional degree of freedom in order to model the crack discontinuity. Figure 2 shows the meshing of the cracked portion of the body using XFEM [21].

The circled nodes are enriched with additional two degree of freedom, which lead to total of four degree of freedom to the circled nodes. The squared nodes are enriched with additional eight degree of freedom, which lead to total of ten degree of freedom to the squared nodes. In the domain of discontinuities, the displacement field at a particular node with nodal coordinates  $X_i$  can be approximated as

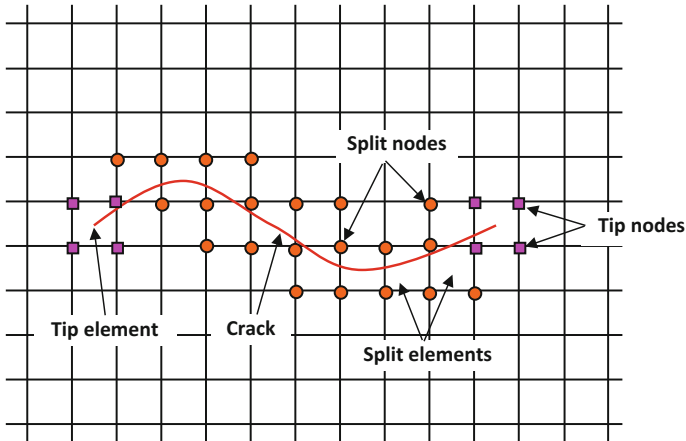


**Fig. 2** Schematic of node enrichment in 2-D XFEM framework

$$\begin{aligned}
 \mathbf{u}_{\text{XFEM}}(X) = & \sum_{i \in I} N_i(X) u_i + \sum_{i \in J} N_i(X) [H(X) - H(X_i)] a_i \\
 & + \sum_{i \in K} \left[ N_i(X) \sum_{\alpha=1}^4 [F_\alpha(X) - F_\alpha(X_i)] b_{i\alpha} \right]
 \end{aligned}
 \tag{23}$$

where  $I$  = set of all nodes in the mesh,  $N_i(X)$  = Lagrange basis shape function,  $u_i$  = standard displacement field variables of node  $i$ ,  $J$  = set of nodes belonging to split elements,  $H(X)$  = Heaviside function for split elements,  $a_i$  = additional degree of freedom associated with  $H(X)$ ,  $K$  = set of nodes belonging to crack tip element,  $F_\alpha(X)$  = crack tip enrichment function and  $b_{i\alpha}$  = degree of freedom associated with  $F_\alpha(X)$ . The material model based on crystal plasticity has been implemented as FORTRAN code which is coupled with XFEM module in ABAQUS software through UMAT subroutine. For constitutive modeling of material’s mechanical behavior, the material Jacobian matrix,  $\partial \Delta \sigma_{ij} / \partial \Delta \varepsilon_{kl}$ , must be provided in UMAT subroutine and the stresses must be updated at the end of every increment. In crystal plasticity model, the calculations of material Jacobian matrix and stress increment,  $\Delta \sigma_{ij}$ , are discussed in Sect. 2.2. The coupled framework of XFEM and CP is used for all simulations presented in next sections.

## 4 Numerical Modeling

A 2D model of single crystal nickel with dimensions  $4 \text{ mm} \times 4 \text{ mm}$  with an initial edge crack of length  $a = 1 \text{ mm}$  as shown in Fig. 3 is used to carry out the simulations. The meshing and boundary conditions applied on the model are shown in

**Fig. 3** Meshing and boundary conditions applied on the 2D model of an edge cracked single crystal nickel

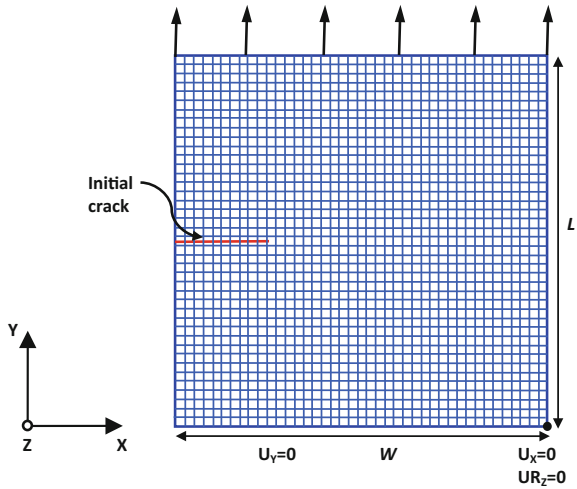


**Table 1** Constants used in present study to model material behavior of single crystal nickel

C11 (GPa)	C12 (GPa)	C44 (GPa)	$\dot{\alpha}$ (per sec)	$n$	$h_o$ (MPa)	$h_{\alpha\alpha}$	$h_{\alpha\beta}$	$\tau_s$ (MPa)	$\tau_o$ (MPa)
250.8	150	123.5	0.001	10	541.5	1	1	109.5	60.8

Fig. 3 as well. The meshing is done using 4-noded bilinear CPE4 plane strain elements. The total numbers of elements used to mesh the model are 1764. The boundary conditions applied on the bottom edge and bottom right corner of the 2D model are ( $U_y = 0$ ) and ( $U_x = 0, U_z = 0$ ), respectively. The ramped displacement of  $U_y = 3.3 \mu\text{m}$  has been applied on the upper edge. This displacement is sufficient to activate several slip systems in all the three orientations to be analyzed.

The material parameters used to model the single crystal nickel behavior are listed in Table 1 [22]. Three independent elastic constants are required to model FCC single crystal.

In this work, only crystalline slip is assumed to be responsible for causing plastic deformation. The FCC structured crystals have twelve active slip systems, which are composed of four slip planes and three slip directions. The active slip systems used in this modeling are listed in Table 2 [23].

Depending upon the stress  $\sigma$  being produced far away from the crack under the action of the displacement  $U_y = 3.3 \mu\text{m}$ , the stress intensity factor  $K_I$  in front of the crack can be computed theoretically [9] as

$$K_I = C\sigma\sqrt{\pi a}, C = \left[ 1.12 - 0.23\left(\frac{a}{W}\right) + 10.6\left(\frac{a}{W}\right)^2 - 21.7\left(\frac{a}{W}\right)^3 + 30.4\left(\frac{a}{W}\right)^4 \right] \tag{21}$$

**Table 2** Active slip systems in FCC metals

Slip system	Slip plane	Slip direction
S1; $\alpha = 1$	(111)	$[0\bar{1}1]$
S2; $\alpha = 2$	(111)	$[10\bar{1}]$
S3; $\alpha = 3$	(111)	$[\bar{1}10]$
S4; $\alpha = 4$	$(\bar{1}11)$	$[101]$
S5; $\alpha = 5$	$(\bar{1}11)$	$[110]$
S6; $\alpha = 6$	$(\bar{1}11)$	$[0\bar{1}1]$
S7; $\alpha = 7$	$(1\bar{1}1)$	$[011]$
S8; $\alpha = 8$	$(1\bar{1}1)$	$[110]$
S9; $\alpha = 9$	$(1\bar{1}1)$	$[10\bar{1}]$
S10; $\alpha = 10$	$(11\bar{1})$	$[011]$
S11; $\alpha = 11$	$(11\bar{1})$	$[101]$
S12; $\alpha = 12$	$(11\bar{1})$	$[\bar{1}10]$

where  $C$  is a constant, which depends upon the geometry of the model and the applied loading.

## 5 Results and Discussion

### 5.1 Effect of Lattice Orientation on Deformation Behavior of Single Crystal

The single nickel crystal with and without crack has been simulated for three different orientations with Euler angles  $(0^\circ, 0^\circ, 0^\circ)$ ,  $(30^\circ, 0^\circ, 0^\circ)$  and  $(45^\circ, 0^\circ, 0^\circ)$ . As shown in Fig. 4, the change in lattice orientation with respect to the applied strain significantly influenced the  $\sigma - \varepsilon$  response of the monocrystal nickel. The stiffness of monocrystal nickel has increased as the lattice orientation about  $Z$ -axis is changed from  $0^\circ$  to  $45^\circ$ .

The normal stress distribution in  $Y$  direction  $\sigma_{YY}$  over the monocrystal nickel for three different orientations under the action of same displacement loading is shown as contour plots in Fig. 5. The contour plots show that the  $\sigma_{YY}$  stress distribution is homogeneous for all the three orientations, but the magnitude of stresses is different. This change in stress-strain response is due to difference in activation of slip systems caused by initial lattice rotation.

As shown in Fig. 6 the total of four slip systems, i.e., S4, S5, S9 and S12 are active in  $(0^\circ, 0^\circ, 0^\circ)$  oriented monocrystal nickel without crack. Only two slip systems, i.e., S6 and S7 are active in nickel crystal oriented with Euler angles

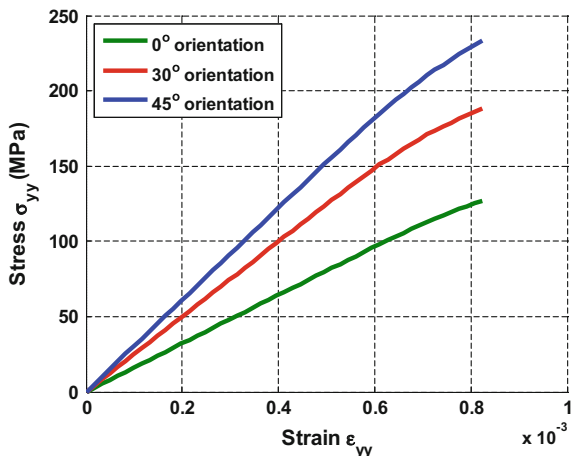


Fig. 4 Effect of grain orientation on stress–strain response of single Ni crystal

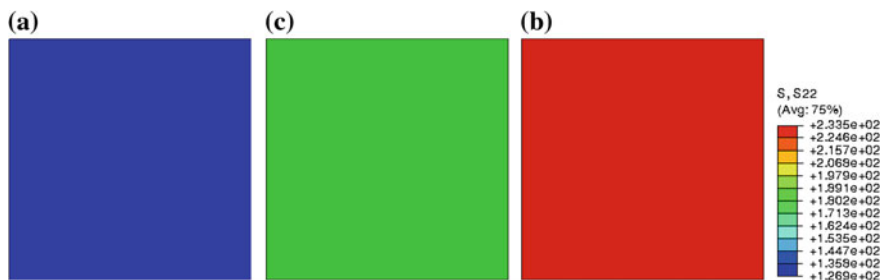
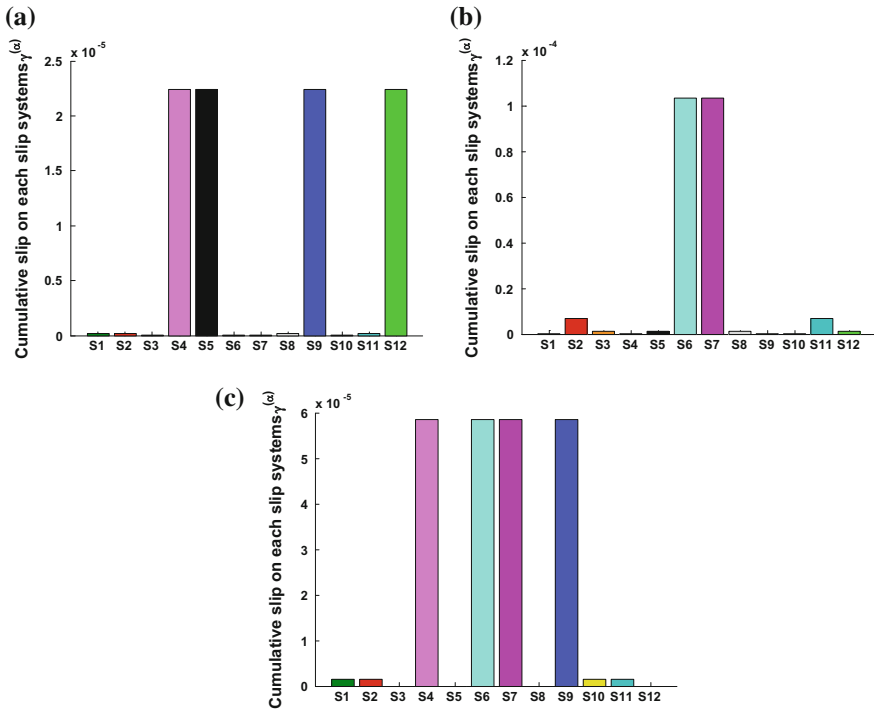


Fig. 5 Contour plots of  $\sigma_{yy}$  stress in a 0° b 30° and c 45° oriented single Ni crystal

(30°, 0°, 0°). In case of nickel crystal with initial lattice rotation (45°, 0°, 0°), four slip systems, i.e., S4, S6, S7 and S9 are active. The cumulative slip ( $\gamma$ ) on all the slip systems in (0°, 0°, 0°), (30°, 0°, 0°) and (45°, 0°, 0°) oriented nickel crystals is  $9.05044 \times 10^{-5}$ ,  $2.25441 \times 10^{-4}$  and  $2.39403 \times 10^{-4}$ , respectively. The cumulative slip on all the slip systems has increased with the increase in orientation angle from 0° to 45° about Z-axis. Under the action of the similar applied strain, the lattice orientation with greater cumulative slip on all the slip systems will have higher inbuilt stresses.



**Fig. 6** Comparison of cumulative slip on each slip system in the absence of crack for **a**  $0^\circ$ , **b**  $30^\circ$  and **c**  $45^\circ$  oriented single Ni crystals

### 5.2 Effect of Crystal Orientation on Mode I Stress Intensity Factor ( $K_I$ )

The contour plots of normal stress distribution in Y direction  $\sigma_{YY}$  over the single edge cracked monocrystal nickel for three different orientations, under the action of same displacement loading is shown in Fig. 7. The magnitude of stresses in the vicinity of the crack tip is changing with the change in the lattice orientation. The stresses are high in the vicinity of the crack tip as compared to away from the crack tip. In the vicinity of the crack tip, the complex scenario of slip system activation for three orientations is shown as inset for Fig. 7a, b, c.

In the presence of crack in monocrystal nickel, all twelve slip systems are active in the vicinity of the crack tip for all three orientations as shown in Fig. 8. This shows that the pre-existing crack serves as a stress raiser that results in localization of shear stresses on slip system which otherwise would have been inactive. For all the three orientations, the values of  $\sigma_{YY}$  stress far away from the crack in the edge cracked single nickel crystals as shown in Fig. 7 matches with the values of  $\sigma_{YY}$



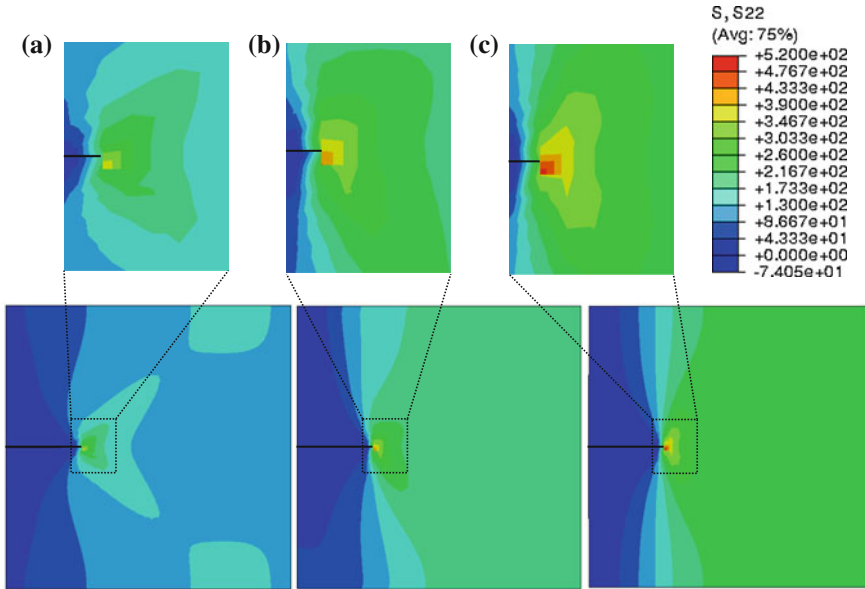


Fig. 7 Contour plots of  $\sigma_{yy}$  stress in a  $0^\circ$ , b  $30^\circ$  and c  $45^\circ$  oriented edge cracked single Ni crystal

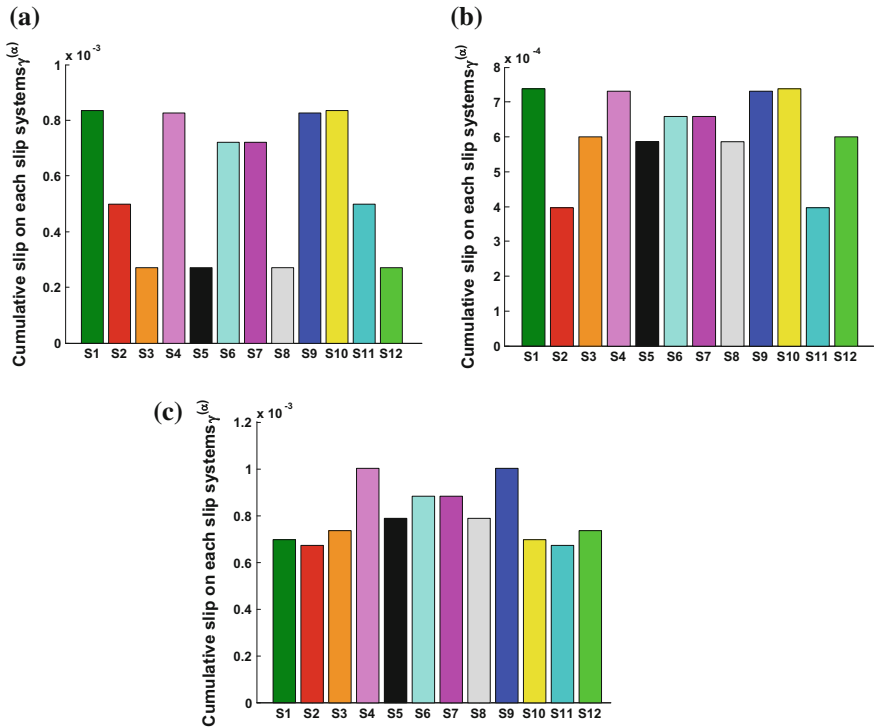
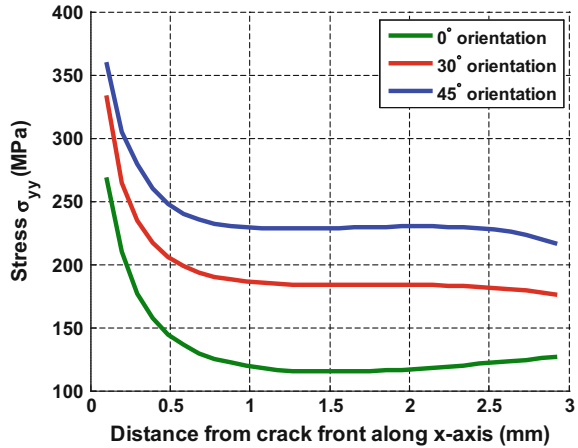


Fig. 8 Comparison of cumulative slip on each slip system in front of the crack tip for a  $0^\circ$ , b  $30^\circ$  and c  $45^\circ$  oriented single Ni crystals

**Fig. 9** Comparison of stresses along the crack front for three different orientations of single Ni crystal

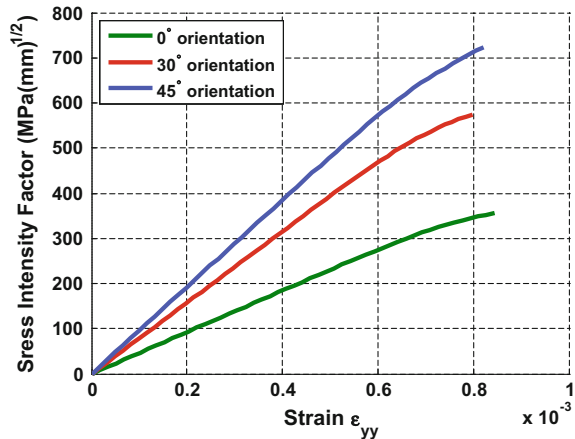


stress in uncracked single nickel crystal as shown in Fig. 5 under the action of the same displacement loading of 3.3  $\mu\text{m}$ .

The cumulative slip ( $\gamma$ ) on all the slip systems in the vicinity of the crack tip for  $(0^\circ, 0^\circ, 0^\circ)$ ,  $(30^\circ, 0^\circ, 0^\circ)$  and  $(45^\circ, 0^\circ, 0^\circ)$  oriented single edge cracked nickel crystals is  $6.8471 \times 10^{-3}$ ,  $7.41478 \times 10^{-3}$  and  $9.547495 \times 10^{-3}$ , respectively. The variation of stresses along the crack front for three orientations of monocrystal nickel is shown in Fig. 9. Under the action of the similar applied strain, the orientation with greater cumulative slip on all the slip systems in the vicinity of the crack tip is having high stresses in front of the crack tip.

The variation of stress intensity factor  $K_I$  with applied strain  $\epsilon_{yy}$  in differently oriented monocrystal nickel is shown in Fig. 10. The orientation with high inbuilt stresses is having high value of stress intensity factor near the crack tip.

**Fig. 10** Comparison of stress intensity factor in front of crack tip for three different orientations of single Ni crystal



## 6 Conclusions

The effect of crystalline orientations on activation of slip system in the absence and presence of crack in single Nickel crystal has been studied numerically. The following conclusions are drawn:

- The crystalline orientation effects the activation of slip system and extent of slipping.
- The stress–strain response of crystalline material is highly affected by the number of active slip systems.
- Near the vicinity of the crack tip all slip systems get activated whereby only two to four slip systems are active in the absence of crack.
- The stresses near the vicinity of the crack tip depend upon the degree of slipping near the crack tip.
- This model can be extended further to simulate fatigue crack growth in polycrystalline metals.

## References

1. Miller KJ (1982) The short crack problem. *Fract Eng Mater Struct* 5(3):223–232
2. McEvily AJ, Eiffler D, Macherauch E (1991) An analysis of the growth of short fatigue cracks. *Eng Fract Mech* 40(3):571–584
3. Hussain K (1997) Short fatigue crack behaviour and analytical models: a review. *Eng Fract Mech* 58(4):327–354
4. Leis BN, Hopper AT, Ahmad J, Broek D, Kanninen MF (1986) Critical review of the fatigue growth of short cracks. *Eng Fract Mech* 23(5):883–898
5. Miller KJ (1987) The behaviour of short fatigue cracks and their initiation Part II-A general summary. *Fatigue Fract Eng Mater Struct* 10(2):93–113
6. Hussain K, De Los Rios ER, Navarro A (1993) A two-stage micromechanics model for short fatigue cracks. *Eng Fract Mech* 44(3):425–436
7. Kumar A, Singh SB, Ray KK (2008) Short fatigue crack growth behaviour in ferrite-bainitic dual-phase steels. *ISIJ Int* 48(9):1285–1292
8. Krupp U, Düber O, Christ H-J, Künkler B, Köster P, Fritzen C-P (2007) Propagation mechanisms of microstructurally short cracks—factors governing the transition from short- to long-crack behavior. *Mater Sci Eng, A* 462(1–2):174–177. doi:10.1016/j.msea.2006.03.159
9. Suresh S (1998) *Fatigue of materials*, second addition. Cambridge University Press, Cambridge
10. Aswath PB (1994) Effect of orientation on crystallographic cracking in notched nickel-base superalloy single crystal subjected to far-field cyclic compression. *Metall Mater Trans A* 25A (February):287–297
11. Tvergaard V, Wei Y, Hutchinson JW (2001) Edge cracks in plastically deforming surface grains. *Eur J Mech A/Solids* 20:731–738
12. Zhai T, Wilkinson AJ, Martin JW (2000) A crystallographic mechanism for fatigue crack propagation through grain boundaries. *Acta Mater* 48(20):4917–4927
13. Taylor GI (1938) Plastic strain in metals. *J Inst Metals* 62:307–324
14. Hill R (1966) Generalized constitutive relations for incremental deformation of metal crystals by multislip. *J Mech Phys Solids* 14:95–102

15. Rice JR (1971) Inelastic constitutive relations for solids: an internal-variable theory and its applications to metal plasticity. *J Mech Phys Solids* 19:433–455
16. Hill R, Rice JR (1972) Constitutive analysis of elastic-plastic crystals at arbitrary strain. *J Mech Phys Solids* 20:401–413
17. Asaro RJ, Rice JR (1977) Strain localization in ductile single crystals. *J Mech Phys Solids* 25:309–338
18. Asaro RJ (1983) Crystal plasticity. *J Appl Mech* 50(December):921–934
19. Hutchinson JW (1977) Creep and plasticity of hexagonal polycrystals as related to single crystal slip. *Metall Trans A* 8A(September):1465–1469
20. Peirce D, Asaro RJ, Needleman A (1982) An analysis of nonuniform and localized deformation in ductile single crystals. *Acta Metall* 30:1087–1119
21. Giner E, Sukumar N, Tarancón JE, Fuenmayor FJ (2009) An Abaqus implementation of the extended finite element method. *Eng Fract Mech* 76(3):347–368
22. Cagin T (1999) Thermal and mechanical properties of some fcc transition metals. *Phys Rev B* 59(5):3468–3473
23. Groves GW, Kelly A (1963) Independent slip systems in crystals. *Phil Mag* 8(89):877–887